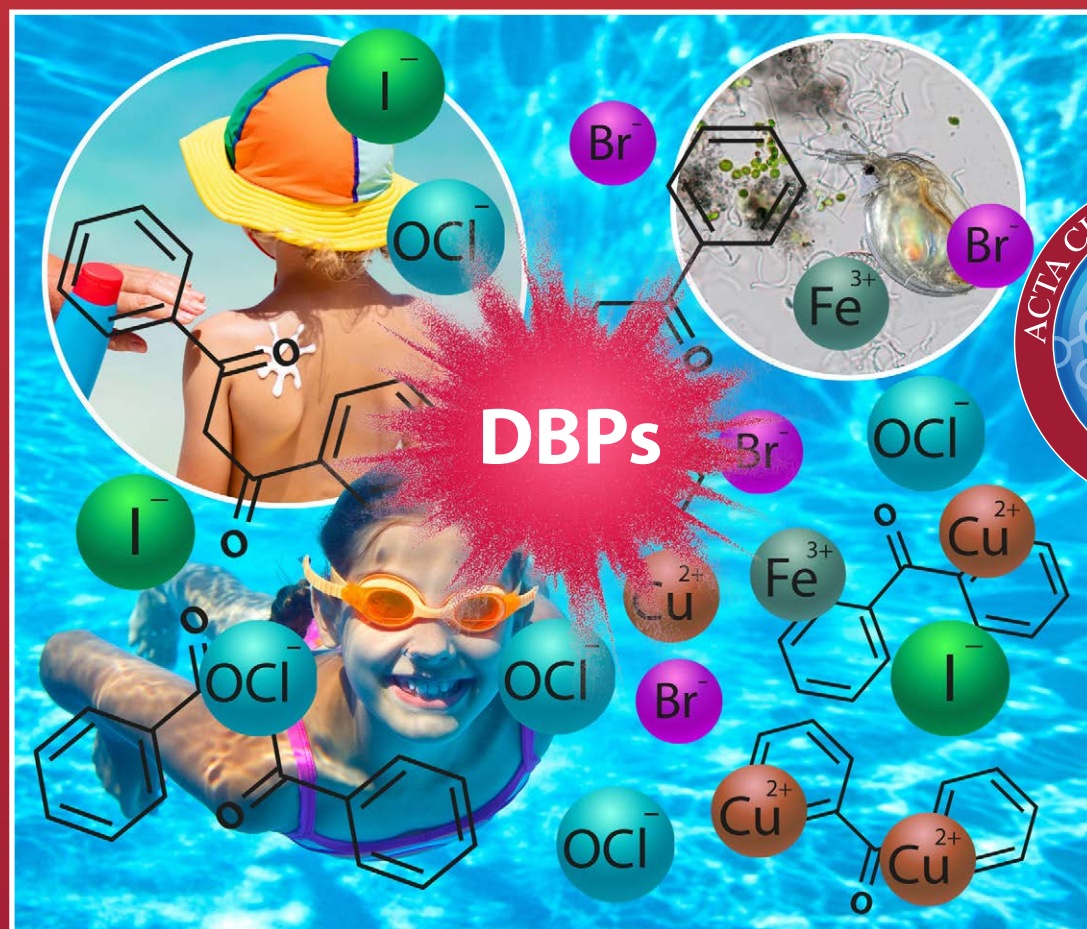




# Acta Chimica Slo Acta Chimica Slo Slovenica Acta C

4



70/2023



---

## EDITOR-IN-CHIEF

FRANC PERDIH

University of Ljubljana, Faculty of Chemistry and Chemical Technology, Večna pot 113, SI-1000 Ljubljana, Slovenija  
E-mail: ACSi@fkk.uni-lj.si, Telephone: (+386)-1-479-8514

## ASSOCIATE EDITORS

**Alen Albreht**, National Institute of Chemistry, Slovenia  
**Aleš Berlec**, Jožef Stefan Institute, Slovenia  
**Janez Cerkovnik**, University of Ljubljana, Slovenia  
**Mirela Dragomir**, Jožef Stefan Institute, Slovenia  
**Krištof Kranjc**, University of Ljubljana, Slovenia  
**Matjaž Kristl**, University of Maribor, Slovenia  
**Maja Leitgeb**, University of Maribor, Slovenia

**Helena Prosen**, University of Ljubljana, Slovenia  
**Jernej Stare**, National Institute of Chemistry, Slovenia  
**Irena Vovk**, National Institute of Chemistry, Slovenia

## ADMINISTRATIVE ASSISTANT

**Eva Mihalinec**, Slovenian Chemical society, Slovenia

---

## EDITORIAL BOARD

**Wolfgang Buchberger**, Johannes Kepler University, Austria  
**Alojz Demšar**, University of Ljubljana, Slovenia  
**Stanislav Gobec**, University of Ljubljana, Slovenia  
**Marko Goličnik**, University of Ljubljana, Slovenia  
**Günter Grampp**, Graz University of Technology, Austria  
**Wojciech Grochala**, University of Warsaw, Poland  
**Danijel Kikelj**, University of Ljubljana  
**Janez Košmrlj**, University of Ljubljana, Slovenia  
**Mahesh K. Lakshman**, The City College and  
The City University of New York, USA  
**Blaž Likozar**, National Institute of Chemistry, Slovenia

**Janez Mavri**, National Institute of Chemistry, Slovenia  
**Jiří Pinkas**, Masaryk University Brno, Czech Republic  
**Friedrich Sreenc**, University of Minnesota, USA  
**Walter Steiner**, Graz University of Technology, Austria  
**Jurij Svete**, University of Ljubljana, Slovenia  
**David Šarlah**, University of Illinois at Urbana-Champaign, USA;  
Università degli Studi di Pavia, Italy  
**Ivan Švancara**, University of Pardubice, Czech Republic  
**Gašper Tavčar**, Jožef Stefan Institute, Slovenia  
**Ennio Zangrando**, University of Trieste, Italy  
**Polona Žnidaršič Plazl**, University of Ljubljana, Slovenia

---

## ADVISORY EDITORIAL BOARD

**Chairman**  
Branko Stanovnik, Slovenia

### Members

Udo A. Th. Brinkman, The Netherlands  
Attilio Cesaro, Italy  
Vida Hudnik, Slovenia  
Venčeslav Kaučič, Slovenia

Željko Knez, Slovenia  
Radovan Komel, Slovenia  
Stane Pejovnik, Slovenia  
Anton Perdih, Slovenia  
Slavko Pečar, Slovenia  
Andrej Petrič, Slovenia  
Boris Pihlar, Slovenia  
Milan Randić, Des Moines, USA

Jože Škerjanc, Slovenia  
Đurđa Vasić-Rački, Croatia  
Marjan Veber, Slovenia  
Gorazd Vesnaver, Slovenia  
Jure Zupan, Slovenia  
Boris Žemva, Slovenia  
Majda Žigon, Slovenia

---

*Acta Chimica Slovenica* is indexed in: *Academic Search Complete*, *Central & Eastern European Academic Source*, *Chemical Abstracts Plus*, *Chemical Engineering Collection (India)*, *Chemistry Citation Index Expanded*, *Current Contents (Physical, Chemical and Earth Sciences)*, *Digitalna knjižnica Slovenije (dLib.si)*, *DOAJ*, *ISI Alerting Services*, *PubMed*, *Science Citation Index Expanded*, *SciFinder (CAS)*, *Scopus*, *Web of Science and Portico*. Impact factor for 2021 is IF = 1.524.



Articles in this journal are published under the  
Creative Commons Attribution 4.0 International License

### Izdaja – Published by:

**SLOVENSKO KEMIJSKO DRUŠTVO – SLOVENIAN CHEMICAL SOCIETY**  
Naslov redakcije in uprave – Address of the Editorial Board and Administration  
Hajdrihova 19, SI-1000 Ljubljana, Slovenija  
Tel.: (+386)-1-476-0252; Fax: (+386)-1-476-0300; E-mail: chem.soc@ki.si

### Izdajanje sofinancirajo – Financially supported by:

National Institute of Chemistry, Ljubljana, Slovenia  
Jožef Stefan Institute, Ljubljana, Slovenia  
Faculty of Chemistry and Chemical Technology, University of Ljubljana, Slovenia  
Faculty of Chemistry and Chemical Engineering, University of Maribor, Slovenia  
University of Nova Gorica, Slovenia

Slovensko kemijsko društvo  
Slovenian Chemical Society

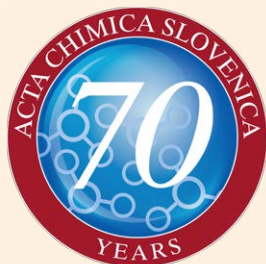


*Acta Chimica Slovenica* izhaja štirikrat letno v elektronski obliki na spletni strani <http://acta.chem-soc.si>. V primeru posvečenih številk izhaja revija tudi v tiskani obliki v omejenem številu izvodov.

*Acta Chimica Slovenica* appears quarterly in electronic form on the web site <http://acta.chem-soc.si>. In case of dedicated issues, a limited number of printed copies are issued as well.

Transakcijski račun: 02053-0013322846 Bank Account No.: SI56020530013322846-Nova Ljubljanska banka d. d., Trg republike 2, SI-1520 Ljubljana, Slovenia, SWIFT Code: LJBA SI 2X

Oblikovanje ovitka – Design cover: KULT, oblikovalski studio, Simon KAJTNA, s. p. Grafična priprava za tisk: OSITO, Laura Jankovič, s.p.



## 70<sup>th</sup> anniversary of *Acta Chimica Slovenica*

Dear readers of *Acta Chimica Slovenica*,

In this year *Acta Chimica Slovenica*, the journal published by Slovenian Chemical Society, is celebrating 70<sup>th</sup> anniversary. Already in 1951 *Kemijski zbornik* was published as a kind of its predecessor and already then, its editors expressed the wish to launch a scientific journal. However, the first volume appeared only in 1954 as *Vestnik Slovenskega kemijskega društva* (*Bulletin of the Slovenian Chemical Society*). Several renowned Slovenian scientists have served as editors and the journal was developing international recognition. Several milestones have to be mentioned that had crucial influence on the development of *Acta Chimica Slovenica*. In 1978 (vol. 25) a new editorial board with Drago Kolar as the editor, Marko Razinger as the technical editor and Branko Stanovnik as the chairman of the editorial board started to publish *Vestnik Slovenskega kemijskega društva* on a regular basis as four issues per year. They also started to



publish review articles and plenary lectures delivered at symposia and congresses organized by the Slovenian Chemical Society as well as special issues dedicated to prominent chemists. In 1993 (vol. 40) the name of the journal was changed to *Acta Chimica Slovenica*. In 1998 two major steps were achieved by the editor Andrej Petrič - alongside with the printed version of articles also electronic version was published and *Acta Chimica Slovenica* started to be indexed in Web of Science. Two years later, in 2000, *Acta Chimica Slovenica* obtained its first impact factor. The journal further developed under the editors Janez Košmrlj, Aleksander Pavko and Ksenija Kogej. Under their leadership modern information technologies have been fully employed enabling the transition from the printed to the electronic articles, greatly facilitating the accessibility of the journal, thus increasing the international reach of the journal and, of course, significantly increasing the impact of scientific papers published in *Acta Chimica Slovenica* on the development of chemistry, chemical engineering, biochemistry, chemical education and other related disciplines. The broad international coverage of the journal due to the free access of the online articles and due to the indexing in various scientific databases such as Web of Science, PubMed, CrossRef, Chemical Abstract Plus, Scopus, SciFinder (CAS), Portico and others, as well as due to introduction of DOI numbers, have enabled *Acta Chimica Slovenica* to establish a strong presence in the international scientific community. The quality of the journal's publications is also demonstrated by the fact that the most cited articles published in the time span 1998–2023 have more than 200 citations. Many years of dedicated work of the editors and editorial boards, the strong support provided by the Slovenian Chemical Society and the support of Slovenian universities, faculties and institutes have enabled 70 years of development and progress in the field of publishing the Slovenian scientific journal *Acta Chimica Slovenica*. This has given the journal an excellent platform for further activities. It was a great privilege for me to serve *Acta Chimica Slovenica* for many years as co-editor in the field of Inorganic Chemistry and to become Editor-in-Chief in January 2023 at the beginning of the 70<sup>th</sup> anniversary of our journal.

The contribution of *Acta Chimica Slovenica* and Slovenian Chemical Society as its publisher to the scientific community can be assessed by data accessible in Web of Science. These data are available since the year 1998 when *Acta Chimica Slovenica* started to be indexed in Web of Science. We can see interesting transition and development of the journal. In the period 1998–2001, *Acta Chimica Slovenica* published between 40 and 50 articles per year (WoS statistics include scientific and professional articles), however, by 2002 the number of articles per year had almost doubled (Figure 1). The number of articles published additionally increased in 2007, when 132 articles were published, about three times as many as in 1998. The number of articles published annually since 2007 has fluctuated around 120, with the highest number of articles published in 2008 (146 articles) and the lowest number in the last year, when 94 articles were published. The number of citations has also increased markedly since 1998, confirming the international relevance and importance of the scientific results published in the journal (Figure 1).

International involvement can also be monitored by the proportion of publications by foreign authors. In the period 1998–2022, the journal published papers having authors from 89 countries. Slovenian authors contributed

the majority of the articles to *Acta Chimica Slovenica* during this period (35.3%), followed by the authors from Iran (11.2%), China (6.8%), India (6.7%), Turkey (6.4%) and Croatia (4.1%) (Figure 2). Between 2% and 4% per country were contributed by the authors from Egypt, Romania, Serbia, the Czech Republic, the USA and Germany. Between 1 and 2% per country were contributed by the researchers from Poland, Bulgaria, France, Pakistan, Ukraine, Italy, Slovakia, Hungary and Austria. Less than 1% per country came from the 68 countries, representing a total of 17.3%.

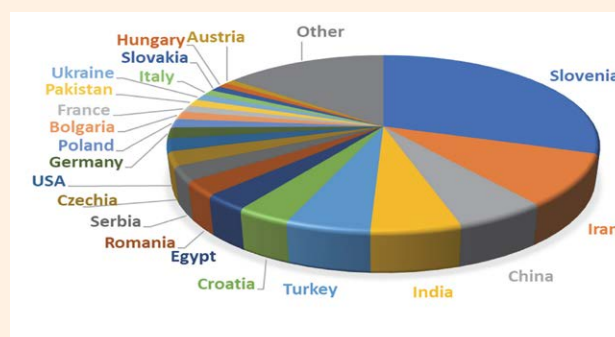


Figure 2: Publication shares by country.

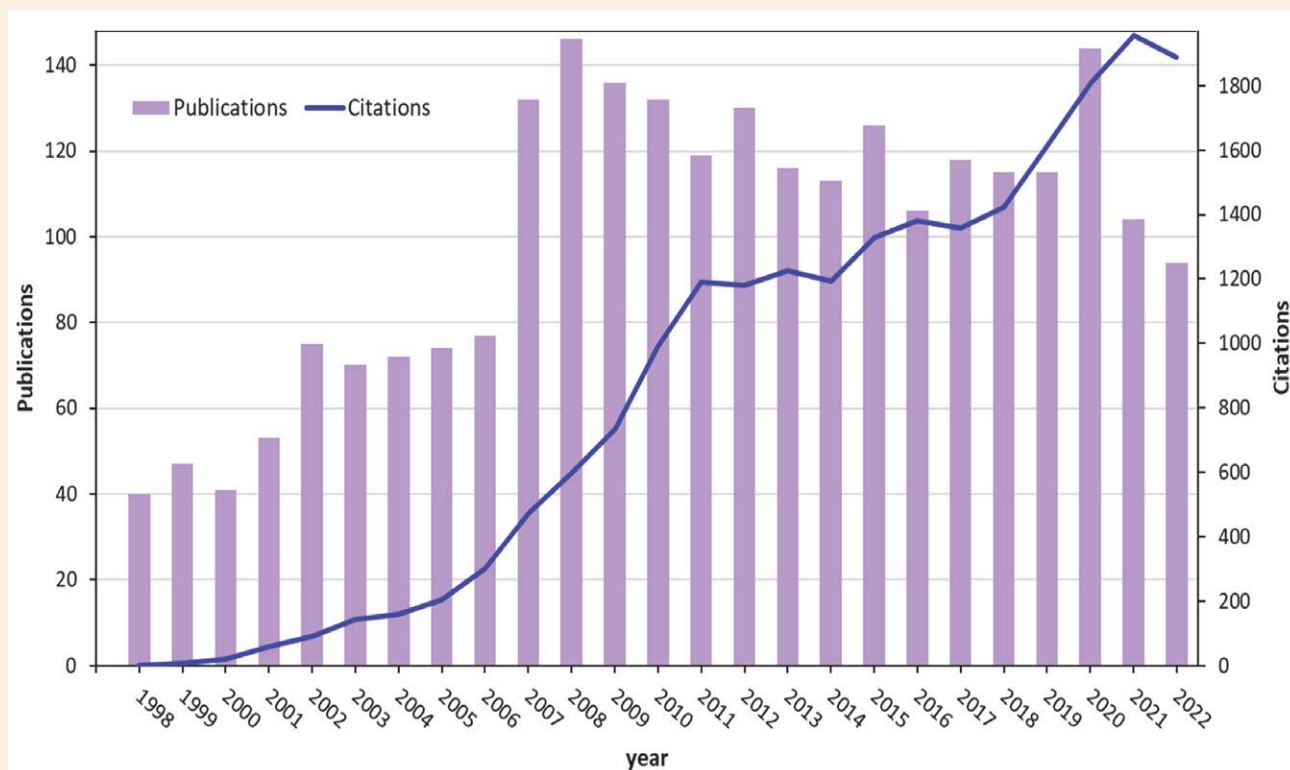


Figure 1: Number of publications in *Acta Chimica Slovenica* and number of all citations per year.

A breakdown by the continent shows that during the period 1998–2022, contributions from Europe dominated (69.3%), followed by those from Asia (37.6%), Africa (5.9%), the Americas (4.8%), and Australia and Oceania (0.7%) (Figure 3).

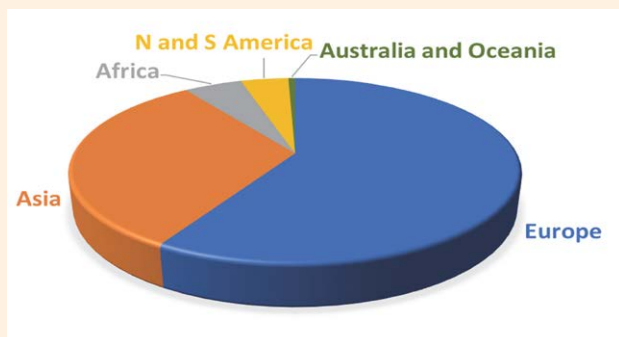


Figure 3: Publication shares by continent.

The free online access of articles and indexing of the journal content in the most important scientific databases are the cornerstones of international accessibility, making the content available to all researchers worldwide thus creating opportunities for the visibility of the research published. *Acta Chimica Slovenica* fulfils all these conditions and thus enables authors to disseminate their results efficiently. We can clearly see that articles published in *Acta Chimica Slovenica* can achieve international visibility and recognition in the scientific community as demonstrated by many highly cited articles in our journal. Below follow short presentations of the articles published in the time period 1998–2022 that received more than 100 citations.

The two most cited articles in *Acta Chimica Slovenica* in the time period 1998–2022 have both 232 citations (data access December 5<sup>th</sup> 2023). Article entitled *Characterization of phenol-formaldehyde prepolymer resins by in line FT-IR spectroscopy* published in 2005 by Slovenian authors I. Poljanšek and M. Krajnc reports on different resol phenol-formaldehyde prepolymer resins synthesized with different formaldehyde/phenol ratios. The phenolic resin composition depends on monomer ratio, catalyst, reaction conditions, and residual free monomers. Temperature and pH conditions under which reactions of phenols with formaldehyde are carried out have a profound effect on the characteristics of the resulting products. Three reaction sequences must be considered: formaldehyde addition to phenol, chain growth or prepolymer formation and finally the cross linking or curing reaction. Two prepolymer types are obtained depending on pH, novolacs in an acidic pH region whereas resols

by alkaline reaction. Resol resins are synthesized with a molar excess of formaldehyde ( $1 < F/P < 3$ ). These are mono- or polynuclear hydroxymethylphenols which are stable at room temperatures, but are transformed into three dimensional, cross linked, insoluble and infusible polymers by the application of heat. An ATR-FTIR spectrometry technique (ReactIR 4000) with light conduit and diamond-composite sensor was used to perform in-line monitoring of phenol-formaldehyde prepolymer synthesis. This technique was found to be ideal for determining residual free phenol and formaldehyde, individual phenol and formaldehyde conversions and prepolymer composition changes as a function of time when the condensation reaction was carried out. The kinetics data obtained through the ReactIR 4000 in-line reaction analysis system agreed well with those determined by the traditional titration method. ReactIR technology replaces time consuming and inaccurate off-line methodology (*Acta Chim. Slov.* **2005**, 52, 283–244).

Another contribution with the same number of citations entitled *Biodegradation of malachite green by Kocuria rosea MTCC 1532* published in 2006 by Indian authors G. Parshetti, S. Kalme, G. Saratale and S. Govindwar reports on completely decolorized malachite green under static anoxic condition within 5 h by bacteria *Kocuria rosea* MTCC 1532; however decolorization was not observed at shaking condition. *K. rosea* have also shown decolorization of azo, triphenylmethane and industrial dyes (cotton blue, methyl orange, reactive blue 25, direct blue-6, reactive yellow 81, and red HE4B). Semi-synthetic media containing molasses, urea and sucrose have shown 100, 91, 81% decolorization respectively. Induction in the activities of malachite green reductase and DCIP reductase was observed during MG decolorization suggesting their involvement in the decolorization process. UV-Visible absorption spectrum, HPLC and FTIR analysis showed degradation of MG. Toxicity study revealed the degradation of MG into non-toxic products by *K. rosea* (*Acta Chim. Slov.* **2006**, 53, 492–498).

The third most cited contribution with 152 citations entitled *Equilibrium sorption study of Al<sup>3+</sup>, Co<sup>2+</sup> and Ag<sup>+</sup> in aqueous solutions by fluted pumpkin (Telfairia occidentalis HOOK f) waste biomass* was published in 2005 by Nigerian authors M. Horsfall Jnr and A. I. Spiff. Authors combined an ensemble of equilibrium sorption techniques to study the influence of ionic radius on the sorption characteristics of Al<sup>3+</sup>, Co<sup>2+</sup> in Ag<sup>+</sup> by fluted pumpkin waste biomass. The experimental results were analyzed in terms of five two-parameter adsorption isotherm equations-the Langmuir, Freundlich, Temkin, Dubinin-Radushkevich and Flory-Huggins isotherms. According to the evaluation us-

ing Langmuir equation, the monolayer sorption capacity obtained was 16.98 mg/g, 10.34 mg/g and 8.03 mg/g for  $\text{Al}^{3+}$ ,  $\text{Co}^{2+}$  in  $\text{Ag}^+$  respectively. The data further showed that, the Freundlich and Langmuir isotherms described the data appropriate than Temkin, Dubinin-Radushkevich and Flory-Huggins isotherms. The result showed that fluted pumpkin waste could be used for the removal of  $\text{Al}^{3+}$ ,  $\text{Co}^{2+}$  in  $\text{Ag}^+$  from wastewater and ionic radius influences the rate of metal ion migration to the biomass surface and the adsorption intensity of the metal (*Acta Chim. Slov.* **2005**, 52, 174–181).

The fourth contribution with 139 citations entitled *Kinetics and mechanism of reactive red 141 degradation by a bacterial isolate Rhizobium radiobacter MTCC 8161* was published in 2008 by Indian authors A. Telke, D. Kalyani, J. Jadhav and S. Govindwar. Authors isolated a bacterium *Rhizobium radiobacter* MTCC 8161 from effluent treatment plant of textile and dyeing industry of Ichalkaranji, India. The bacterial isolate *Rhizobium radiobacter* MTCC 8161 was capable of decolorizing various azo, triphenylmethane (TPM), disperse and reactive textile dyes with decolorizing efficiency varying from 80–95%. This strain decolorized (90%) a deep red sulfonated diazo dye Reactive Red 141 (50 mg/L) with 0.807 mg of dye reduced/g of dry cells/h of specific decolorization rate in static anoxic condition at optimum pH 7.0 and temperature 30 °C with 83.33% reduction in COD. The degradation efficiency of this strain using urea and yeast extract showed fast decolorization among different carbon, nitrogen source. The induction of various oxidative and reductive enzymes indicates involvement of these enzymes in color removal. Phytotoxicity studies revealed less toxic nature of decolorized products (1000 mg/L) as compared to original dye. FTIR spectroscopy and GC-MS analysis indicated naphthalene diazonium, *p*-dinitrobenzene and 2-nitroso naphthol as the final products of Reactive Red 141 (*Acta Chim. Slov.* **2008**, 55, 320–329).

A contribution with 132 citations entitled *Evaluation of the hydration of Portland cement containing various carbonates by means of thermal analysis* was published in 2006 by Slovenian authors R. Gabrovšek, T. Vuk and V. Kaučič. Authors report on hydration of portland cement containing a fixed amount of mineral admixtures (calcium carbonate or dolomite or magnesite) at 60 °C for 7- and 28 days. Phase compositions were evaluated by thermogravimetric analysis and by powder X-ray diffraction. Measurements of surface area indicated the development of the hydrated microstructure. Detailed analysis of DTG decomposition profiles of portlandite and carbonate enabled the evaluation of certain admixture-related parameters concerning portlandite formation and also indicated the

behavior of specific carbonates during the hydration process (*Acta Chim. Slov.* **2006**, 53, 159–165).

A contribution with also 132 citations entitled *A comparative study of several transition metals in Fenton-like reaction systems at circum-neutral pH* was published in 2003 by Slovenian authors M. Strlič, J. Kolar, V.-S. Šelih, D. Kočar and B. Pihlar. Authors used *N,N'*-(5-nitro-1,3-phenylene)bisglutaramide hydroxylation assay for spectrophotometric determination of the rate of oxidising species generation in Fenton-like systems to obtain comparative data for Cd(II), Co(II), Cr(III), Cu(II), Fe(III), Mn(II), Ni(II), and Zn(II). The pH range of interest was 5.5–9.5 and was controlled by addition of an appropriate phosphate buffer. The temperature of the reaction mixture was controlled in the range 25–80 °C. The rates of production of oxidising species at pH 7 decrease in the following order: Cu(II) > Cr(III) > Co(II) > Fe(III) > Mn(II) > Ni(II), while Cd(II) and Zn(II) did not exhibit any catalytic activity and Ni(II) only led to a significant production of oxidising species at pH > 7.5. In mixtures of Cu(II) and Fe(III) the rate of oxidising species production may be considered as the sum of contributions of individual metals. This was not the case of a mixture containing additional small amounts of Zn(II), Co(II) and Mn(II). The later two had strong pro-oxidative effects, the addition of Zn(II) had an anti-oxidative effect. Apparent activation energies for oxidising species generation are in the range 75–110 kJ mol<sup>-1</sup>, and decrease in the following order: Cu(II) > Ni(II) > Mn(II) > Fe(III) > Co(II) (*Acta Chim. Slov.* **2003**, 50, 619–632).

A contribution with 120 citations entitled *Application of polyaniline and its composites for adsorption/recovery of chromium(VI) from aqueous solutions* was published in 2006 by an Iranian author R. Ansari. The paper deals with adsorption of Cr(VI) from aqueous solutions using sawdust coated by polyaniline (SD/PAN) and polyaniline composites with nylon 66 and polyurethane. Nylon and polyurethane are available common polymers that can be easily dissolved in the solvents of PAN (formic acid and NMP). So, the PAN composites with these polymers can be readily prepared via solvent cast method. Polyaniline (PAN) was synthesized chemically and coated on the surface of sawdust (SD) from formic acid via cast method. It was found that polyaniline in the acid doped form (e.g. HCl), can be used for Cr(VI) ion removal in acidic aqueous solutions (pH ≤ 2). Adsorption occurs only under acidic conditions and it decreases with increasing the pH of solution significantly. The proposed mechanism for adsorption of Cr(VI) with our currently developed adsorbent seems to be mostly occurring via an anion exchange process. Adsorption of Cr(VI) from water using SD/PAN

column is both a simple and efficient method compared to the other adsorbents reported by previous investigators (*Acta Chim. Slov.* **2006**, *53*, 88–94).

A contribution with 119 citations entitled *Sol-gel prepared NiO thin films for electrochromic applications* was published in 2006 by Slovenian authors R. Cerc Korošec and P. Bukovec. The paper summarizes on the topic of changes in optical properties of electrochromic material in the visible part of the spectrum under a certain applied potential. The change is reversible and the material returns to its original state under the opposite electric field. Recently, electrochromism has been applied in electrochromic devices, where in a battery-like assembly the throughput of solar light is controlled by the voltage and is usually termed a smart window. In the first part of this article a brief theoretical introduction to electrochromism and the functioning of smart windows is given. Since in the last decade nickel oxide has been extensively studied as an ion-storage material in electrochromic devices, some properties of nickel oxide are explained in the following part. The electrochromic response (reversibility during potential switching and the degree of coloration) of a nickel oxide thin film, used in an electrochromic device, strongly depends on the degree of heat treatment. Thermal analysis of thin films can give valuable information about a suitable temperature and the duration of heat-treatment when thin films are prepared by chemical methods of deposition. Since thermal analysis of thin films deposited on a substrate is not a common analytical technique, basic strategies are also summarized in the article. After this theoretical introduction, the application of TG analysis to optimisation of the electrochromic response of sol-gel prepared Ni oxide thin films is presented. The electrochromic properties of thin films, thermally treated to different degrees, were tested using spectroelectrochemical methods. Additional techniques (IR, TEM, AFM and EXAFS) were indispensable in following structural and morphological changes during the heat treatment (*Acta Chim. Slov.* **2006**, *53*, 136–147).

A contribution with 105 citations entitled *Characterization of Cobalt Oxide Nanoparticles Prepared by the Thermal Decomposition of  $[\text{Co}(\text{NH}_3)_5(\text{H}_2\text{O})](\text{NO}_3)_3$  Complex and Study of Their Photocatalytic Activity* was published in 2016 by Iranian authors S. Farhadi, M. Javanmard and G. Nadri. The authors report on thermal decomposition of the  $[\text{Co}(\text{NH}_3)_5(\text{H}_2\text{O})](\text{NO}_3)_3$  precursor complex under solid state conditions. Thermal analysis (TG/DTA) showed that the complex was easily decomposed into the  $\text{Co}_3\text{O}_4$  nanoparticles at low temperature (175 °C) without using any expensive and toxic solvent or a complicated equipment. The obtained product was identified by X-ray diffraction

(XRD), Fourier transform infrared spectroscopy (FT-IR), Raman spectroscopy, scanning electron microscopy (SEM), transmission electron microscopy (TEM) and energy-dispersive X-ray spectroscopy (EDX). Optical and magnetic properties of the products were studied by UV-visible spectroscopy and a vibrating sample magnetometer (VSM), respectively. FT-IR, XRD and EDX analyses confirmed the formation of highly pure spinel-type  $\text{Co}_3\text{O}_4$  phase with cubic structure. SEM and TEM images showed that the  $\text{Co}_3\text{O}_4$  nanoparticles have a sphere-like morphology with an average size of 17.5 nm. The optical absorption spectrum of the  $\text{Co}_3\text{O}_4$  nanoparticles showed two band gaps of 2.20 and 3.45 eV, which in turn confirmed the semiconducting properties. The magnetic measurement showed a weak ferromagnetic order at room temperature. Photocatalytic degradation of methylene blue (MB) demonstrated that the as-prepared  $\text{Co}_3\text{O}_4$  nanoparticles have good photocatalytic activity under visible-light irradiation (*Acta Chim. Slov.* **2016**, *63*, 335–343).

A contribution with 102 citations entitled *Removal of methylene blue from aqueous solutions by wheat bran* was published in 2007 by Algerian authors O. Hamdaoui and M. Chiha. In this work, a fundamental investigation on the removal of methylene blue from aqueous solutions by wheat bran is conducted in batch conditions. Removal kinetic data are determined, and the effects of different experimental parameters, such as wheat bran mass, initial concentration of methylene blue, agitation speed, solution pH, particle size, temperature, and ionic strength on the kinetics of methylene blue removal are investigated. The cationic dye recovery increases with an increase of sorbent mass, solution pH, and temperature. Methylene blue removal decreases with an increase of initial concentration, particle size, and ionic strength. The agitation speed showed a limited influence on the removal kinetics. Modeling of kinetic results shows that sorption process is best described by the pseudo-second order model, with determination coefficients higher than 0.996 under all experimental conditions. The applicability of both internal and external diffusion models shows that liquid-film and particle diffusion are effective sorption mechanisms. The activation energy of sorption calculated using the pseudo-second order rate constants is found to be 13.41 kJ mol<sup>-1</sup> from an Arrhenius plot. The low value of the activation energy indicates that sorption is an activated and physical process. Thus, wheat bran, a low cost and easily available biomaterial, can be efficiently used as an excellent sorbent for the removal of dyes from wastewater. It can be safely concluded that wheat bran is much economical, effectual, viable, and can be an alternative to more costly adsorbents (*Acta Chim. Slov.* **2007**, *54*, 407–418).

However, the number of citations gives only a partial insight into the impact of an article, as older articles may have an advantage over more recent articles due to the longer period of time they can be cited. Another possible insight into scientific importance is provided by the average number of citations per year. Here, we can highlight two contributions with very high average number of citations per year that were not presented above. Contribution with 89 total citations and an average number of citations per year 14.8 entitled *Synthesis and Characterization of Zinc Oxide Nanoparticles with Small Particle Size Distribution* was published in 2018 by Malaysian authors N. M. Shamhari, B. S. Wee, S. F. Chin, K. Y. Kok. The authors report on a solvothermal synthesis having a great potential to synthesize zinc oxide nanoparticles (ZnO NPs) with less than 10 nm size. In this study, a rapid synthesis of ZnO NPs was presented in which ZnO NPs with more uniform shape and highly dispersed were synthesized using zinc acetate dihydrate ( $\text{Zn}(\text{CH}_3\text{COO})_2 \cdot 2\text{H}_2\text{O}$ ) and potassium hydroxide (KOH) as a precursor and absolute ethanol as solvent via solvothermal method. Few techniques were exploited to characterize synthesized ZnO NPs including X-ray diffraction (XRD), transmission electron microscope (TEM), Brunauer-Emmett-Teller (BET), energy-dispersive X-ray spectroscopy (EDX), fourier transform infrared (FT-IR) spectroscopy, and ultraviolet visible (UV-Vis) spectroscopy. Synthesized ZnO NPs that were prepared via solvothermal synthesis method at 60 °C for 3 hours exhibited a wurtzite structure with a crystalline size of 10.08 nm and particle size of  $7.4 \pm 1.2$  nm. The UV-vis absorption spectrum has shown peak at 357 nm indicate the presence of ZnO NPs. Hence, better quality with uniform size ZnO NPs can be easily synthesized with reduced amount of time via solvothermal synthesis method rather than using other complicated and lengthy synthesis methods (*Acta Chim. Slov.* **2018**, 65, 578–585).

A contribution with 88 total citations and average number of citations per year 8.8 entitled *An Overview of the Optical and Electrochemical Methods for Detection of DNA – Drug Interactions* was published in 2014 by Serbian authors M. M. Aleksić, V. Kapetanović. This review paper gives an overview on a large number of inorganic and or-

ganic compounds that are able to bind to DNA and form complexes. Among them, drugs are very important, especially chemotherapeutics. This paper presents the overview of DNA structural characteristics and types of interactions (covalent and non-covalent) between DNA molecule and drugs. Covalent binding of the drug is irreversible and leads to complete inhibition of DNA function, what conclusively, causes the cell death. On the other hand, non-covalent binding is reversible and based on the principle of molecular recognition. Special attention is given to elucidation of the specific sites in DNA molecule for drug binding. According to their structural characteristics, drugs that react non-covalently with DNA are mainly intercalators, but also minor and major groove binders. When the complex between drug and DNA is formed, both the drug molecule, as well as DNA, experienced some modifications. This paper presents the overview of the methods used for the study of the interactions between DNA and drugs with the aim of detection and explanation of the resulting changes. For this purpose many spectroscopic methods like UV/VIS, fluorescence, infrared and NMR, polarized light spectroscopies like circular and linear dichroism, and fluorescence anisotropy or resonance is used. The development of the electrochemical DNA biosensors has opened a wide perspective using particularly sensitive and selective electrochemical methods for the detection of specific DNA interactions. The presented results summarize literature data obtained by the mentioned methods. The results are used to confirm the DNA damage, to determine drug binding sites and sequence preference, as well as conformational changes due to drug–DNA interaction (*Acta Chim. Slov.* **2014**, 61, 555–573).

The 70<sup>th</sup> anniversary of *Acta Chimica Slovenica* is thus an excellent opportunity to highlight the achievements and enthusiasm of all editorial team members that served in the past seventy years and those that still serve in this capacity. The anniversary gives also a new impetus for further development, growth and improvement in order to serve the scientific community even better and to address all the challenges we are facing and will be facing in the contemporary fast-changing world of science, research and dissemination of the results.

**Franc Perdih**  
*Editor-in-Chief*



# Graphical Contents



Acta Chimica Slo  
Acta Chimica Slo  
Slovenica Acta C

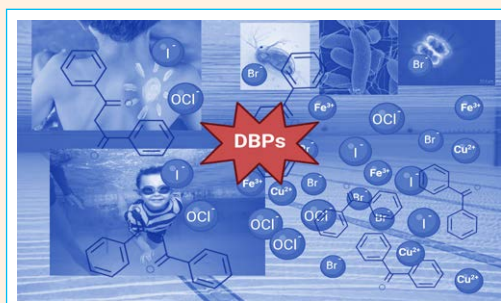
Year 2023, Vol. 70, No. 4

## FEATURE ARTICLE

601–610 Feature Article

### Chlorination of UV Filters with Antioxidant Shield in Swimming Pool Waters – Products Identification and Toxicity Assessment

Mojca Bavcon Kralj, Albert T. Lebedev and Polonca Trebše



## REVIEW ARTICLE

467–478 Review articles

### Rise of Gold Nanoparticles as Carriers of Therapeutic Agents

Chandrashekar Thalluri, Kalpana Swain and Satyanarayan Pattnaik

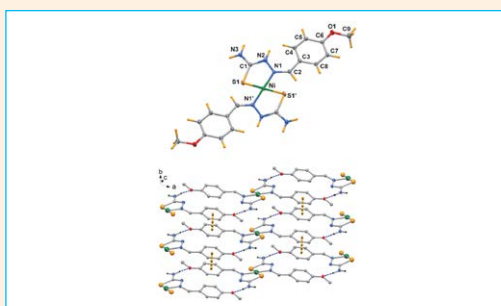


## SCIENTIFIC PAPER

479–488 Organic chemistry

### A novel nickel(II) Complex with N,S-donor Schiff Base: Structural Characterisation, DFT, TD-DFT Study and Catalytic Investigation

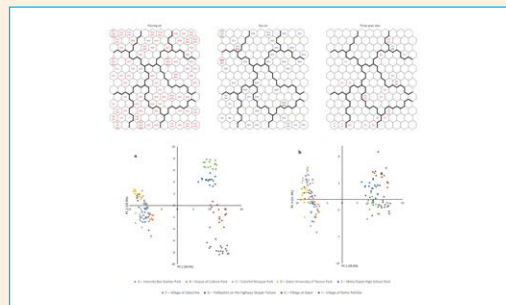
Manas Chowdhury, Niladri Biswas, Sandepta Saha, Ennio Zangrando, Nayim Sepay and Chirantan Roy Choudhury



489–499 Analytical chemistry

## X-ray Powder Diffraction and Supervised Self-Organizing Maps as Tools for Forensic Classification of Soils

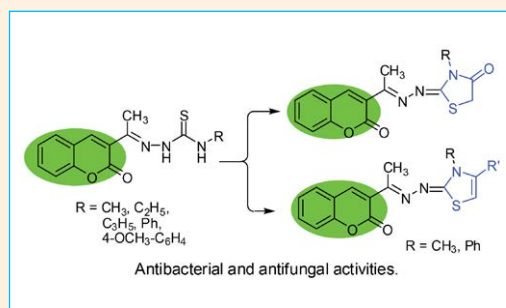
Hirijete Idrizi, Mile Markoski, Metodija Najdoski and Igor Kuzmanovski



500–508 Organic chemistry

## Synthesis of New of 4-Thiazolidinone and Thiazole Derivatives Containing Coumarin Moiety with Antimicrobial Activity

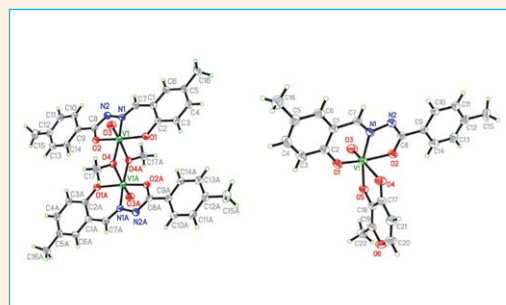
Reem A. K. Al-Harbi, Marwa A. M. Sh. El-Sharief and Samir Y. Abbas



509–515 Inorganic chemistry

## Synthesis, Characterization and X-Ray Crystal Structures of Oxidovanadium(V) Complexes Derived from *N*'-(2-Hydroxy-5-methylbenzylidene)-4-methylbenzohydrazide with Antibacterial Activity

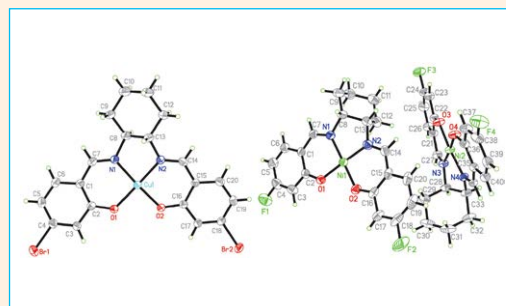
Xue-Rong Tan, Wei Li, Meng-Meng Duan and Zhonglu You



516–523 Inorganic chemistry

## Copper(II) and Nickel(II) Complexes Derived from Isostructural Bromo- and Fluoro-Containing Bis-Schiff Bases: Syntheses, Crystal Structures and Antimicrobial Activity

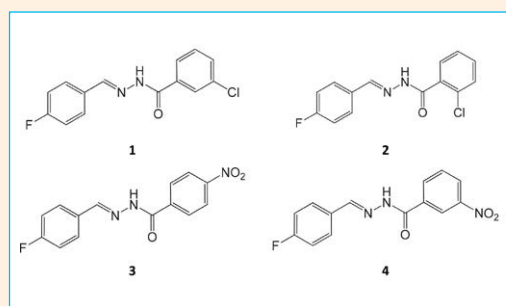
Ke-Sheng Cao, Ling-Wei Xue and Qiao-Ru Liu



524–532 Organic chemistry

## Syntheses, Characterization, Crystal Structures and Xanthine Oxidase Inhibitory Activity of Hydrazones

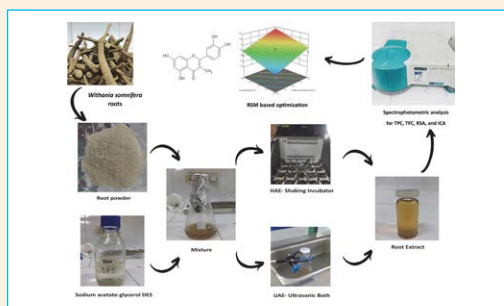
Xiao-Jun Zhao, Ling-Wei Xue and Qiao-Ru Liu



533–544 Organic chemistry

## Comparison of Deep Eutectic Solvent-based Ultrasound and Heat-assisted Extraction of Bioactive Compounds from *Withania somnifera* and Process Optimization Using Response Surface Methodology

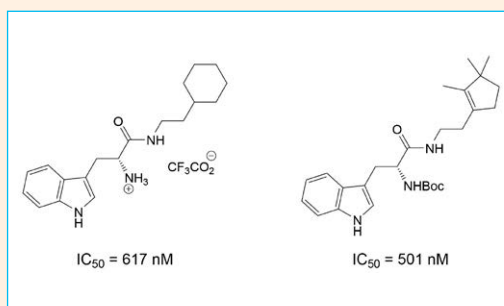
Faizan Sohail and Dildar Ahmed



545–559 Organic chemistry

## Synthesis and Cholinesterase Inhibitory Activity of Selected Indole-Based Compounds

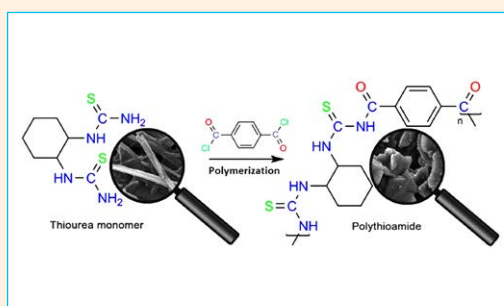
Marija Gršič, Anže Meden, Damijan Knez, Marko Jukič, Jurij Svete, Stanislav Gobec and Uroš Grošelj



560–573 Materials science

## Synthesis and Characterization of Multicolor Luminescent and Thermally Stable Thioureas and Polythioamides

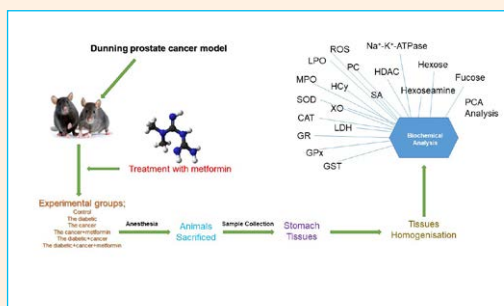
Farah Qureshi, Muhammad Yar Khuhawar, Taj Muhammad Jahangir and Abdul Hamid Channar



574–587 Biochemistry and molecular biology

## Glycoprotein Levels and Oxidative Stomach Damage in Diabetes and Prostate Cancer Model: Protective Effect of Metformin

Onur Ertik, Pınar Koroglu Aydin, Omur Karabulut Bulan and Refiye Yanardag



588–600 General chemistry

## Synergistic, Additive and Antagonistic Interactions of Some Phenolic Compounds and Organic Acids Found in Grapes

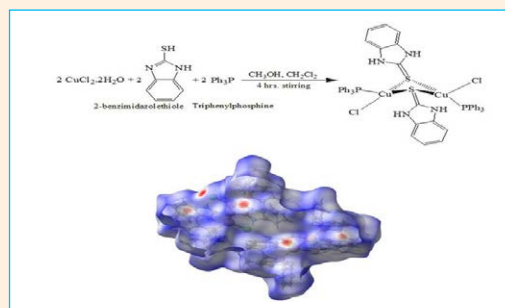
Crina Vicol and Gheorghe Duca



611–619 Inorganic chemistry

## Synthesis, Crystal Structure, Hirshfeld Surface Analysis, and DFT Calculations of the New Binuclear Copper(I) Complex Containing 2-Benzimidazolethiole and Triphenylphosphine Ligands

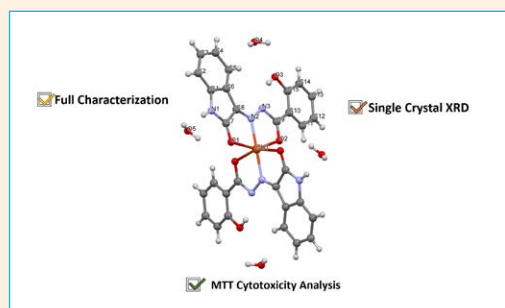
Karwan Omer Ali



620–627 Inorganic chemistry

## Synthesis, Crystal Structure and In Vitro Cytotoxicity of Novel Cu(II) Complexes Derived from Isatin Hydrazide-Hydrazone Ligands

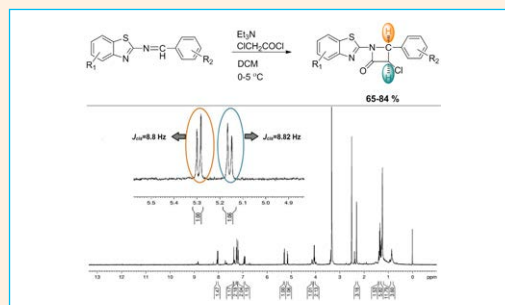
Cansu Topkaya



628–633 Organic chemistry

## Synthesis of Novel *cis*-2-Azetidinones from Imines and Chloroacetyl Chloride Using Triethylamine

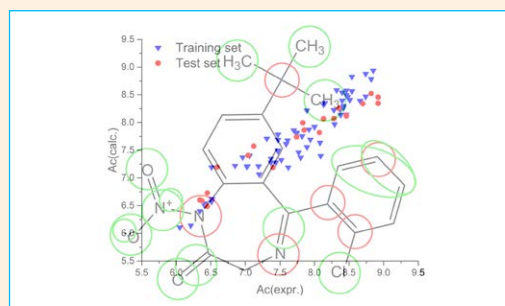
Handan Can Sakarya and Aslı Ketrez



634–641 Physical chemistry

## Development of QSAR Model Based on Monte Carlo Optimization for Predicting GABA<sub>A</sub> Receptor Binding of Newly Emerging Benzodiazepines

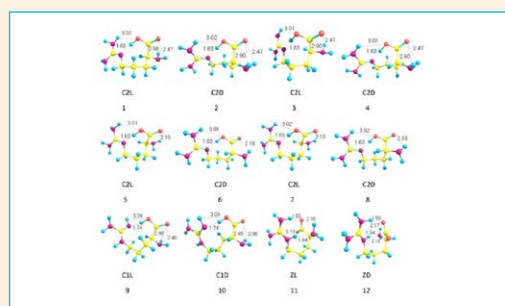
Aleksandra Antović, Radovan Karadžić, Jelena V. Živković and Aleksandar M. Veselinović



642–650 Physical chemistry

## The Role of Nitrogen-Rich Moieties in the Selection of Arginine's Tautomeric Form at Different Temperatures

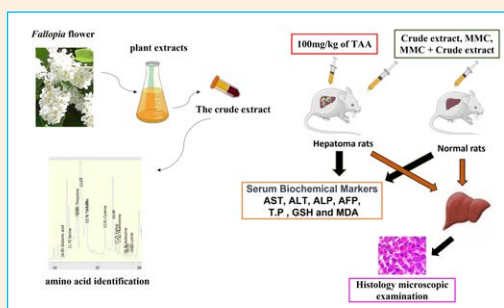
Aned de Leon, José Luis Cabellos, César Castillo-Quevedo, Martha Fabiola Martín-del-Campo-Solis and Gerardo Martínez-Guajardo4



651–660 Biochemistry and molecular biology

## The Role of *Fallopia baldschuanica* Plant Extract in the Regression of Induced Hepatocellular Carcinoma in Rats

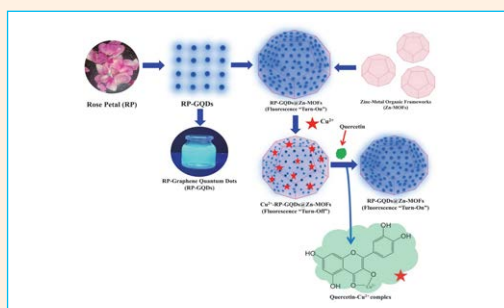
Luma Abd Almunim Baker, Shaymaa Zuhir Jalal Aldin and Hamza N Hameed



661–673 Analytical chemistry

## Zinc Metal-Organic Frameworks- Graphene Quantum Dots Nanocomposite Mediated Highly Sensitive and Selective Fluorescence “On-Off-On” Probe for Sensing of Quercetin

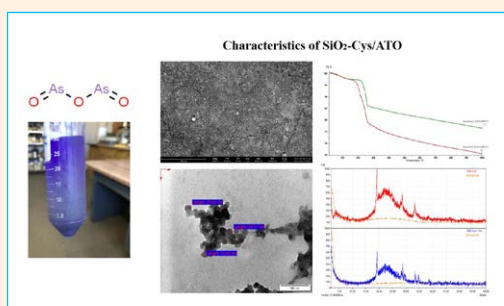
Sopan N. Nangare<sup>1</sup>, Premnath M. Sangare, Ashwini G. Patil and Pravin O. Patil



674–689 Inorganic chemistry

## Synthesis and Characterization of a Nanosilica-Cysteine Composite for Arsenic(III) Ion Removal

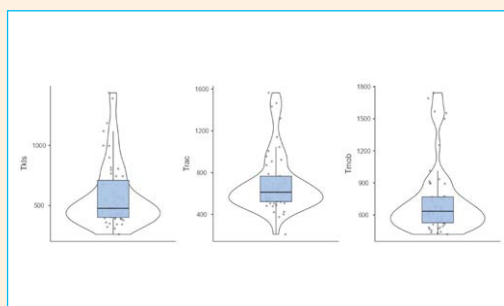
Omar Alnasra and Fawwaz Khalili



690–698 Chemical education

## The Comparison of the Speed of Solving Chemistry Calculation Tasks in the Traditional Way and with the use of ICT

Brina Dojer<sup>1</sup>, Matjaž Kristl and Andrej Šorgo



699–701

## AUTHOR INDEX



Review article

# Rise of Gold Nanoparticles as Carriers of Therapeutic Agents

Chandrashekar Thalluri,<sup>1</sup> Kalpana Swain<sup>2</sup> and Satyanarayan Pattnaik<sup>2,\*</sup><sup>1</sup> Faculty of Pharmaceutical Science, Assam Down Town University, Panikhaiti, Guwahati, Assam 781026, India<sup>2</sup> Division of Advanced Drug Delivery, Talla Padmavathi College of Pharmacy, Warangal, India.

\* Corresponding author: E-mail: drsatyapharma@gmail.com

Tel: +91-7386752616

Received: 04-25-2023

## Abstract

Nanoparticles are typically nanoscopic materials with at least one of the dimensions below 100 nm having diverse applications in many industries. The latest developments in nanotechnology provide a wide range of methods for studying and monitoring various medical and biological processes at the nanoscale. Nanoparticles can help diagnose and treat diseases, such as cancer, by carrying drugs directly to cancer cells. They can also be used to detect disease biomarkers in the body, helping to provide early diagnosis. It is plausible that nanoparticles could be used in theranostic applications and targeted drug delivery. This could significantly improve patient outcomes and reduce the amount of time, effort, and money needed to diagnose and treat diseases. It could also reduce the side effects of treatments, providing more precise and effective treatments. Nanoparticles for biomedical applications include polymeric and metal nanoparticles; liposomes and micelles; dendrimers and quantum dots; etc. Among the nanoparticles, gold nanoparticles (GNPs) have emerged as a promising platform for drug delivery applications. GNPs are highly advantageous for drug delivery applications due to their excellent biocompatibility, stability, and tunable physical and chemical properties. The present review provides an in-depth discussion of the various approaches to GNPs synthesis and drug delivery applications.

**Keywords:** Bio-degradable; gold nanoparticles; drug delivery; drug targeting; cancer therapy; gene delivery; protein delivery; Vaccine delivery; siRNA delivery.

## 1. Introduction

Researchers across the world have offered viable solutions for the optimal delivery of challenging therapeutic agents so as to achieve the best clinical outcomes in diverse disease conditions. In this scenario, nanotechnology-driven technology platforms stood very effective for drug delivery and other biomedical applications.<sup>1–8</sup> One of the first metals discovered, gold, has had a long and illustrious study and implementation chronology. Arab, Chinese, and even Indian researchers attempted to create colloidal gold as early as the fifth and fourth century BC, according to early treatises on the subject. European alchemist laboratories investigated and used colloidal gold during the Middle Ages for the treatment of various ailments including syphilis, leprosy, plague, epilepsy, diarrhea, and mental disorders. In the last few years, nanoparticles based on gold chemistry have drawn considerable research and practical attention. They are versatile biological agents that can be used in a variety of applications, including very sen-

sitive analytical assessments, the creation of ablation heat and radiation, and the transfer of drugs and genes.<sup>9–11</sup> In order to interact with cells or biomolecules in biomedical applications, gold nanoparticles (GNPs) must be externally functionalized. A high surface area to volume ratio, the ability to be modified with ligands containing functional groups such as thiols, phosphines, and amines, and the ability to bind to gold surfaces are some of the unique properties of the GNP that have been developed.<sup>12–14</sup> Additional moieties, including proteins, oligonucleotides, and antibodies, can be attached to the ligands using these functional groups. Compared to GNPs, silver nanoparticles can be more reactive and prone to oxidation, potentially limiting their stability and performance over time.<sup>15</sup>

While silver nanoparticles have antimicrobial properties, excessive release of silver ions from the nanoparticles can raise toxicity concerns, particularly in biological and environmental contexts. GNPs are favored for their biocompatibility, stability, and functionalization capabil-

ities, making them suitable for biomedical and targeted delivery applications. These nanoparticles can be easily functionalized with biomolecules, such as antibodies and peptides, for targeted drug delivery and molecular interactions. The stability of GNPs ensures that these functionalized coatings remain intact, allowing for precise and controlled interactions with biological systems. GNPs exhibit unique catalytic properties, particularly in selective oxidation reactions. While silver nanoparticles also possess catalytic activity, the selectivity and efficiency of GNPs make them preferable for certain catalytic applications. These unique physical and chemical properties of GNPs allow for various applications. Recent research suggests that GNPs can be used as efficient medication carriers since they can enter organelles in addition to infiltrating blood vessels to reach the tumor's site.<sup>14,16</sup> GNPs can also release their payload at the target spot in response to an internal or external stimulus. Our review makes an effort to present a thorough overview of the most promising uses of GNPs in contemporary scientific studies, while also taking into account the amount of data produced and the rate at which it is updated.

## 2. Synthesis of GNPs

Synthesis of GNPs follows the same "Top-Down" and "Bottom-Up" methodologies as other inorganic and metal nanoparticle synthesis. Synthesizing GNPs from bulk material and breaking them down into nanoparticles in a variety of ways is the top-down approach. On the other hand, nanoparticles are synthesized using the bottom-up method, which begins at the atomic level. Laser ablation, ion sputtering, ultraviolet, and infrared irradiation, and aerosol technology are all examples of top-down approaches to synthesis, while the reduction of gold III ions ( $\text{Au}^{3+}$ ) is an example of a bottom-up strategy.<sup>17</sup> The synthesis strategies are discussed in the following section. (Figure 1).



Figure 1: Strategies for synthesis of gold nanoparticles.

### 2. 1. Citrate Reduction (Turkevich Method)

Most methods of synthesizing GNPs require reducing an aqueous gold solution to gold nanoparticles (in

fact, elemental gold) using specific reducing chemicals, followed by stabilizing the newly created nanoparticles. In the second stage of stabilization, sulfonated and non-sulfonated sulphur compounds, polymers, and surfactants are all utilized to prevent GNPs from aggregating.<sup>18,19</sup>

Recently few green approaches have also been introduced for the fabrication process. Green chemistry refers to chemical synthesis techniques that are safe for the environment and do not harm live organisms.<sup>18</sup> There is evidence that the biomaterial Egg shell membrane (ESM) can be used to effectively produce GNPs via green biosynthesis.<sup>19</sup>

The most popular technique for generating GNPs is the Turkevich reductive approach.<sup>20</sup> In this process, sodium citrate ( $\text{Na}_3\text{C}_6\text{H}_5\text{O}_7$ ) and chloroauric acid ( $\text{HAuCl}_4$ ) react to produce colloidal gold.<sup>21</sup> The reduction of citrate was modified by the group of scientists led by Frens to get GNPs with sizes ranging from 2 to 330 nanometers.<sup>22,23</sup> The particle size of the GNPs fabricated via the Turkevich method is grossly affected by various parameters like the molar ratio of the reactants, production batch size, reaction temperature, pH, and the order of addition of reactants.<sup>20</sup>

### 2. 2. Brust-Schiffirin Strategy

GNPs with lower dispersion values may be produced via Brust Schiffirin reaction.<sup>21</sup> The procedure involves producing GNPs from chloroauric acid ( $\text{HAuCl}_4$ ) in a non-aqueous solution by reducing Au(III) with sodium borohydride and tetraoctyl ammonium bromide.<sup>22</sup> The addition of the reducing agent causes the organic phase to change color from orange to dark brown. This demonstrates the existence of GNPs.

The Brust-Schiffirin strategy has been widely applied in the preparation of GNPs, and it has played a significant role in the advancement of nanotechnology.<sup>22</sup> GNPs have unique properties due to their small size and high surface area-to-volume ratio, making them attractive for various applications in catalysis, electronics, medicine, and more. Let's explore how the Brust-Schiffirin strategy is helpful in the preparation of gold nanoparticles:

**Core Formation:** The first step in the Brust-Schiffirin method involves functional group transformations.<sup>24</sup> In the context of GNPs synthesis, this step focuses on creating a gold core with the desired size. Usually, a gold precursor, such as gold chloride ( $\text{AuCl}_3$ ), is reduced using a suitable reducing agent. For example, sodium borohydride ( $\text{NaBH}_4$ ) is a common reducing agent in this context. The reduction reaction leads to the formation of tiny gold clusters or nuclei.<sup>24</sup>

**Surfactant-Mediated Growth:** The Brust-Schiffirin strategy relies on surfactants, which are molecules that can stabilize and control the growth of nanoparticles. In the case of GNPs, ligands like alkanethiols or alkylamines are commonly used as surfactants.<sup>24</sup> These surfactants bind to



the GNPs' surfaces, preventing them from agglomerating and stabilizing their size and shape.

**Convergent Assembly:** After obtaining the gold nuclei, the next step is the convergent assembly, where the small gold clusters are brought together to grow into larger nanoparticles.<sup>24</sup> In this process, the surfactants play a crucial role. They act as linkers, guiding the gold clusters toward each other, resulting in the formation of larger nanoparticles.

**Protecting Group Strategy:** In the context of GNPs synthesis, the protecting group strategy is not directly involved, as it is typically applied in multi-step organic synthesis.<sup>22</sup> However, the surfactants mentioned earlier can be considered akin to protecting groups, as they prevent the gold clusters from coalescing and facilitate controlled growth.

The Brust-Schiffrin strategy in GNPs synthesis has many advantages. The modular nature of the strategy allows for the synthesis of GNPs with different sizes and surface functionalities. By controlling the starting materials, surfactants, and reaction conditions, researchers can fine-tune the properties of the nanoparticles for specific applications. The strategy enables precise control over the size of the resulting nanoparticles. The initial size of the gold nuclei can be adjusted by varying the amount of reducing agent and reaction time. The surfactants further regulate the growth of the nanoparticles, ensuring a uniform and controlled size distribution. Furthermore, the use of surfactants in the Brust-Schiffrin method promotes the formation of monodisperse nanoparticles, meaning that the particles have a narrow size distribution. This is crucial for many applications where consistent particle size is desirable. The Brust-Schiffrin strategy often yields a high percentage of monodisperse nanoparticles, contributing to its efficiency and cost-effectiveness. Hence, the Brust-Schiffrin strategy has proven to be a valuable approach for the preparation of GNPs. It offers control over the size, shape, and surface properties of the nanoparticles, making them suitable for various applications in nanotechnology and beyond. The ability to synthesize GNPs with precise characteristics has opened up new possibilities in fields such as catalysis, sensing, imaging, and targeted drug delivery.<sup>22</sup>

### 2. 3. Electrochemical Strategy

GNPs can be created electrochemically in a two-electrode cell with the cathode reduced and the anode oxidized. Reetz and Helbig (1994) introduced the concept of creating nanoparticles via electrochemical techniques.<sup>23</sup> This method has been considered preferable to other ways of nanoparticle synthesis because of its low processing temperature, low cost, high quality, simple equipment, and ease of process management.<sup>25</sup> The electrochemical synthesis method was used to create GNPs on the surface of multi-walled carbon nanotubes with glassy carbon electrodes.<sup>26</sup> Tetra dodecyl ammonium bromide as a sur-

factant stabilizer has been used to stabilize the size-controlled GNPs fabricated via electrochemical synthesis.<sup>27</sup>

In an electrochemical cell, the cathode is immersed in an electrolyte solution containing gold ions, such as HAuCl<sub>4</sub>. An external power source, such as a battery or a potentiostat, is connected to the cathode and anode, creating an electric potential between the two electrodes. At the cathode, gold ions (Au<sup>3+</sup>) from the electrolyte solution gain electrons and undergo reduction, resulting in the formation of elemental gold (Au<sup>0</sup>) nanoparticles on or near the cathode surface.<sup>28</sup> This reduction process is the key step in the electrochemical synthesis of GNPs. Simultaneously, at the anode, a counterreaction occurs to balance the reduction process at the cathode. In the case of an aqueous electrolyte, water molecules may be oxidized to produce oxygen gas and protons (H<sup>+</sup>). The size and shape of the synthesized GNPs can be controlled by adjusting the experimental parameters, such as the applied potential, the concentration of gold ions in the electrolyte, and the reaction time.

Electrochemical methods offer several advantages for GNPs synthesis, including precise control over the size and shape of the nanoparticles and the ability to perform the synthesis in a more environmentally friendly manner. Additionally, this approach can be easily scaled up for large-scale production of GNPs.

**Role of Electrodes:** The cathode is the electrode where reduction reactions occur. In the case of GNPs synthesis, the cathode serves as the site for the reduction of gold ions (Au<sup>3+</sup>) to elemental gold (Au<sup>0</sup>) that forms the nanoparticles.<sup>28</sup> Electrons from an external power source are supplied to the cathode, promoting the reduction reaction. Typically, the cathode is made of a conductive material, such as a metal or a conductive glass substrate. On the other hand, the anode is the electrode where oxidation reactions occur. During the electrochemical synthesis of GNPs, the anode is typically made of an inert material that does not participate in chemical reactions. Its primary function is to provide a site for the oxidation of a counter-reaction that balances the reduction occurring at the cathode. For example, in an aqueous solution, water molecules can be oxidized to produce oxygen gas and protons (H<sup>+</sup>), thus balancing the reduction of gold ions at the cathode.<sup>28,29</sup>

### 2. 4. Seeding Growth Strategy

Since several years ago, attention has been focused on the large-scale synthesis of GNPs in order to meet the huge demand for these materials. Using Oleyl amine as a reducing and stabilizing agent, GNPs with an average diameter of 9 nm were created in toluene.<sup>30</sup> These GNPs operate as seeds for subsequent growth reactions in which the identical precursors are progressively added to the reaction vessel (Figure 2). Tan et al (2015) synthesized stable GNPs (size ranging 7–30 nm) using a seeding growth

technique.<sup>31</sup> The dispersion is highly disseminated and consistent with the particle size, as seen by the Transmission electron microscopy (TEM) images and optical absorption spectra of the GNPs.

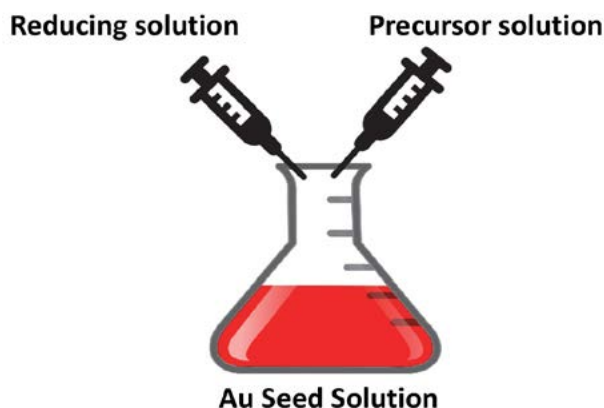


Figure 2. Synthesis of gold nanoparticle via seeding growth strategy.

In this approach, the synthesis is initiated using pre-formed seed nanoparticles with specific crystal facets. The seed nanoparticles act as nuclei for further crystal growth, guiding the formation of anisotropic shapes like gold nanorods, nanostars, nanocubes, and nanoplates.<sup>32</sup>

Compared to other synthesis methods, the seeding growth strategy offers several advantages. One notable advantage is the ability to precisely control the size and shape of the nanoparticles by adjusting the seed size and growth conditions. This level of control is particularly important in nanotechnology and nanoscience applications where specific shapes are required to tailor the nanoparticles' properties for different uses.

Once the seed nanoparticles are synthesized, they can be used as templates for the large-scale production of anisotropic GNPs.<sup>32</sup> The ability to synthesize a large number of nanoparticles with consistent shapes and sizes is advantageous for industrial applications, where reproducibility and scalability are critical factors.

Furthermore, the seeding growth method enables the synthesis of complex nanoparticle shapes that might be challenging to achieve using other techniques. For example, gold nanostars, with their unique sharp protrusions, have specific plasmonic properties that make them attractive for biomedical imaging and therapeutic applications.

In research and industrial settings, large-scale synthesis of GNPs with controlled shapes is essential for various applications. For instance, in the field of catalysis, well-defined nanoparticle shapes can enhance catalytic activity and selectivity. In biomedicine, the size and shape of GNPs play a crucial role in their interactions with biological systems, influencing their behavior as drug carriers, imaging agents, or therapeutics.

To demonstrate the significance of the seeding

growth strategy, researchers often specify the number of nanoparticles synthesized. The ability to produce grams or even kilograms of anisotropic GNPs with reproducible shapes and properties showcases the suitability of this method for practical applications.<sup>33</sup>

Overall, the seeding growth strategy for GNPs synthesis is a versatile and efficient method for large-scale production of nanoparticles with tunable shapes. Its potential for creating well-defined anisotropic shapes makes it an attractive choice for various technological and biomedical applications. Researchers continue to refine and optimize this method to meet the increasing demand for tailored nanoparticles with precise properties and functionalities.

## 2. 5. Photochemical Strategy

Due to the improved spatial and temporal control that these technologies provide, photochemical approaches have attracted a lot of attention in the production of metallic NPs.<sup>34</sup> A typical experiment involves irradiation of visible or ultraviolet (UV) light on solutions containing the metal precursors. Photochemical routes in nanotechnology are preferable to other approaches, such as chemical approaches, because they avoid the use of toxic or harmful compounds, do not require expensive equipment or highly skilled personnel, and, most importantly, can be completed at ambient conditions, such as room temperature and atmospheric pressure.<sup>34–36</sup>

The photochemical method for GNPs synthesis is a versatile and widely used approach that involves the use of light energy to drive the reduction of gold ions and the subsequent formation of GNPs.<sup>37</sup> This method typically employs a photosensitive compound, known as a photosensitizer or a stabilizer, which absorbs light and transfers the energy to the gold ions, initiating the reduction process (Figure 3).

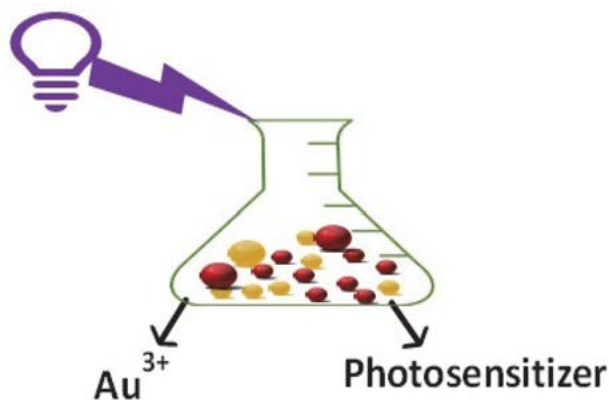


Figure 3. Photochemical synthesis of gold nanoparticles.

The key steps involved in the photochemical synthesis of GNPs are as follows:

**Photosensitizer Selection:** The choice of a suitable photosensitizer is crucial in this method. Photosensitizers are molecules that have the ability to absorb light energy and undergo a photochemical reaction. These molecules should be compatible with the gold precursor solution and facilitate the reduction of gold ions when excited by light.

**Light Irradiation:** The photosensitizer-bound gold precursor solution is exposed to light of a specific wavelength that matches the absorption spectrum of the photosensitizer.<sup>37</sup> This light irradiation leads to the activation of the photosensitizer, resulting in the generation of reactive species or electrons with high reducing potential.

**Gold Ion Reduction:** The activated photosensitizer transfers the energy to the gold ions present in the solution. The excited gold ions then undergo reduction to form GNPs. The reaction typically involves the transfer of electrons from the excited state of the photosensitizer to the gold ions, leading to the conversion of Au<sup>3+</sup> (gold ions) to Au<sup>0</sup> (elemental gold).

**Nanoparticle Stabilization:** As the reduction process proceeds, the formed GNPs are often stabilized and capped by the surrounding stabilizing agents or the photosensitizer itself. These stabilizing agents prevent the nanoparticles from aggregating and aid in controlling the size and shape of the nanoparticles.

The photochemical method offers several advantages for GNPs synthesis. One of the significant advantages is the ease of control over the size and shape of the nanoparticles. By adjusting the light intensity, duration of light exposure, and concentration of the photosensitizer, researchers can tune the synthesis conditions to obtain GNPs with specific properties tailored for different applications.<sup>37</sup>

Moreover, the photochemical method is relatively fast, allowing for rapid nanoparticle synthesis. It also offers the potential for spatial control over nanoparticle formation, enabling localized synthesis in specific regions using patterned light sources or photomasks.

Researchers have explored various photosensitizers for GNPs synthesis, including organic dyes, metal complexes, and semiconductor nanomaterials like quantum dots.<sup>38</sup> Each type of photosensitizer has its specific advantages and can lead to different nanoparticle properties.

The photochemical method has found applications in diverse fields, including nanomedicine, catalysis, and sensing. The ability to use light as a trigger for nanoparticle synthesis offers unique opportunities for on-demand and controlled nanoparticle production, making it a promising technique for future advancements in nanotechnology and nanoscience.

It is worth noting that while the photochemical method is powerful, the choice of the photosensitizer, light source, and reaction conditions should be carefully optimized to achieve desired nanoparticle properties and prevent unwanted side reactions.<sup>39</sup> Therefore, researchers continue to explore and develop this method, advancing the synthesis of GNPs for a wide range of applications.

## 2. 6. Ultrasound-aided Synthesis of GNP

Sonochemistry, a rapidly growing area of chemistry that is focused on the ultrasonic (US) effect and acoustic cavitation, has grown significantly during the past several decades. In a liquid media, US-induced pressure variations cause bubbles to develop, expand, and implosively collapse. There is a significant buildup of energy inside the bubble as a result of the bubble collapsing. The tiny bubbles may potentially deagglomerate nanoparticles, break larger particles into smaller ones, or collapse at the surface of a solid substrate and activate it. Researchers across the world tried this technology for the fabrication of GNPs.<sup>40–44</sup> GNPs synthesized with ultrasound have been shown to have a smaller particle size (13.65 nm vs 16.80 nm), and greater yield than their non-ultrasound counterparts.<sup>44</sup> In another effort, Chen et al (2011) reported a single-step fabrication of spherical and plate-shaped GNPs using the ultrasonication method.<sup>43</sup>

### Significance of the Cavitation Process

In the ultrasound-aided synthesis of GNPs, the phenomenon of cavitation plays a crucial role in enhancing the nanoparticle formation process. Cavitation is a physical process that occurs when ultrasound waves pass through a liquid medium, leading to the formation, growth, and implosion of microscopic bubbles.

During the ultrasound-assisted synthesis of GNPs, the gold precursor solution is exposed to ultrasonic waves.<sup>45,46</sup> These waves create alternating high-pressure and low-pressure regions in the liquid medium. When the pressure in the low-pressure regions drops below the vapor pressure of the liquid, small gas bubbles are formed. These bubbles continue to grow during the low-pressure phase of the ultrasound wave.

As the ultrasound wave progresses to its high-pressure phase, the surrounding pressure rapidly increases. The rapid change in pressure causes the bubbles to violently collapse or implode. This implosion generates intense localized energy, resulting in high temperatures and pressures in the vicinity of the collapsing bubbles. These extreme conditions trigger the reduction of gold ions present in the solution, leading to the formation of GNPs.<sup>45</sup>

The cavitation process during ultrasound-aided GNP synthesis enhances the kinetics of the reduction reaction and promotes the formation of smaller and more uniform nanoparticles. The violent collapse of bubbles generates hotspots with high energy, which facilitate the reduction of gold ions to elemental gold more efficiently. Additionally, the turbulence created by cavitation helps in mixing and homogenizing the reaction mixture, leading to better control over nanoparticle size and shape.

Furthermore, the cavitation phenomenon can aid in the reduction of polydispersity, resulting in a narrower size distribution of the synthesized GNPs.<sup>47</sup> The rapid and localized nature of the cavitation process also enables the

synthesis of GNPs with shorter reaction times compared to conventional methods.

The ultrasound-aided synthesis of GNPs through cavitation has found applications in various fields, including catalysis, biomedical imaging, and drug delivery. The ability to control nanoparticle size and morphology with enhanced efficiency makes this approach valuable for tailoring GNPs for specific applications.

However, it is important to carefully optimize the ultrasound parameters, such as frequency, power, and exposure time, to avoid undesired effects like overheating or the formation of non-uniform nanoparticles.<sup>45,47,48</sup> Researchers continue to explore and refine ultrasound-aided synthesis methods to harness the benefits of cavitation for precise and controlled nanoparticle synthesis.

## 2. 7. Laser Ablation Synthesis of GNPs

Pulsed lasers are utilized nowadays to treat materials and advance numerous chemical reactions. When a target submerged in a liquid is exposed to pulsed laser energy, the target and solution form a dispersion after cavitation bubbles, shock waves, and secondary photons are produced.

By using laser ablation, precise and repeatable results have been achieved in terms of both form and size. Sahebi et al (2019) reported the fabrication of colloidal GNPs using pulsed laser ablation reduction of aqueous gold precursor.<sup>49</sup> By applying the laser ablation approach with a low-power neodymium yttrium aluminum garnet (Nd:YAG) laser at the fundamental wavelength, high-purity GNPs have been effectively produced by Khumaeni et al.<sup>50</sup> In order to create GNPs, an experimental pulse laser beam was focused onto a high-purity gold sheet, which was then placed into deionized water. GNPs were produced in tetrahydrofuran utilizing the pulsed laser ablation approach in another investigation.<sup>51</sup> The average size of produced GNPs was reduced from 11 nm to 6 nm after 30 minutes of ablation. According to the report, these observations were triggered by the quick laser pulse's forced convection flow and shock waves, which fragmented the ablated GNPs even more into tiny sizes.

In recent times, pulsed lasers have been used to treat materials and enhance various chemical reactions. When a target is immersed in a liquid and exposed to pulsed laser energy, the target, and solution form a dispersion due to the formation of cavitation bubbles, shock waves, and secondary photons.<sup>52</sup>

In summary, the use of pulsed lasers in the preparation of GNPs has shown promising results, with researchers achieving high purity and controlled sizes by utilizing the laser ablation approach. The technique offers a reliable and efficient way to synthesize GNPs with potential applications in various fields, including catalysis, biomedicine, and nanotechnology.

## 2. 8. Biological Method

The biosynthesis of nanoparticles is a straightforward, one-step, green process. The dissolved metal ions are converted into nanometals by biochemical reactions in biological agents. For the production of metal nanoparticles, many biological agents are used, such as plant tissues, fungi, bacteria, etc.<sup>53</sup> To begin the synthesis of GNPs, the biological extract (such as bacterial, fungal, or plant material) is added to the gold (III) chloride (HAuCl<sub>4</sub>) solution and thoroughly mixed. Gold III (Au<sup>3+</sup>) is reduced to gold with a neutral charge (Au<sup>0</sup>) in the first stage of biosynthesis, and then GNPs are formed as a result of agglomeration of atoms and stabilization in the second step.<sup>53</sup> It's interesting to note that a wide range of bio-compounds, including enzymes, phenols, sugars, and others, can take part in both the stabilization and capping of nanoparticles as well as the reduction of gold.<sup>54</sup>

Eco-friendly extracellular production of metallic GNPs was carried out using leaf extracts from two plants, *Magnolia kobus* and *Diopyros kaki*.<sup>55</sup> By employing plant leaf extracts as reducing agents to process an aqueous chloroauric acid (HAuCl<sub>4</sub>) solution, stable GNPs were created. Scanning electron microscopy SEM and Transmission electron microscopy (TEM) pictures revealed that smaller spherical forms were produced at higher temperatures and leaf broth concentrations, while a mixture of plate (triangles, pentagons, and hexagons) and spherical structures (size, 5–300 nm) were generated at lower temperatures and leaf broth concentrations.<sup>55</sup> In another study, Brazilian Red Propolis extract was used for the biosynthesis of GNPs.<sup>56</sup> The outcomes revealed a potential low-cost green technique to create GNPs with considerable biological characteristics by using Brazilian red propolis. GNPs with spherical shape and an average size of 15 nm were synthesized at 20–50 °C using different volumes of the using *Platycodon grandiflorum* plant leaf extracts.<sup>57</sup> The diverse phenolic compounds present in the natural extracts has the potential to reduce Au (III).<sup>56,57</sup> Brazilian Red Propolis is a unique type of propolis found in Brazil, specifically in the state of Alagoas, and is known for its distinct red color and potent biological properties.<sup>56,57</sup> Propolis is a resinous substance that bees collect from various plants and trees, which they then modify by mixing it with their enzymes and beeswax. The resulting propolis is used by bees to seal and protect their hives from external threats, such as bacteria, fungi, and other pathogens.

## 3. Morphology of GNPs

GNPs can be synthesized using various methods, each yielding nanoparticles with different shapes and morphologies. The Brust-Schiffrin method typically results in the formation of spherical GNPs. In this method, gold ions are reduced by sodium borohydride in the presence of a capping agent like alkylthiols, which controls the nanopar-

ticle size and stabilizes the particles in a spherical shape.<sup>22,58</sup> Similarly, the Turkevich method predominantly produces spherical GNPs with sizes ranging from 10 to 100 nanometers.<sup>20,59</sup> In this approach, gold ions are reduced with citrate ions, leading to the formation of well-defined spherical nanoparticles.

Anisotropic GNPs with diverse shapes can be synthesized through the seed-mediated growth method. Depending on the reaction conditions, growth time, and surfactant types, this method can yield gold nanorods, nanostars, nanocubes, and nanospheres. Seed-mediated growth relies on controlling the crystal growth direction and adding seeds with specific crystal facets to induce anisotropic growth and shape control. Electrochemical synthesis of GNPs can also produce various shapes depending on the applied potential and reaction conditions.<sup>27,28</sup> This method can yield gold nanospheres, nanorods, nanowires, and nanoplates. By controlling the potential and electrolytes, researchers can tailor the shape and size of the nanoparticles to suit specific applications.

Template-assisted synthesis involves using templates such as porous materials or dendrimers to guide the formation of unique GNPs shapes. Depending on the structure and dimensions of the templates, this method can produce gold nanotubes, nanocages, or nanowells. Microwave-assisted synthesis is a rapid and controlled method that can produce various shapes of GNPs, including nanospheres, nanorods, and nanoplates. The use of microwave irradiation allows for fast and efficient heating, leading to controlled nanoparticle growth.<sup>60</sup>

To accurately determine the shape of synthesized GNPs, researchers often use advanced characterization techniques such as transmission electron microscopy (TEM), scanning electron microscopy (SEM), atomic force microscopy (AFM), or X-ray diffraction (XRD).<sup>2</sup> These techniques allow researchers to visualize and con-

firm the morphology and size of the nanoparticles, ensuring the desired properties for specific applications. The ability to control the shape of GNPs is crucial as it impacts their physical, chemical, and optical properties, making them suitable for a wide range of applications in catalysis, biomedical imaging, drug delivery, and sensing.

## 4. Delivery of Therapeutic Agents Using GNPs

Recent years have seen a significant increase in interest in drug delivery techniques for the best and safest delivery of therapeutic agents.<sup>6–71</sup> Nanotechnology-based platforms are among the cutting-edge methods for delivering pharmacologically active compounds that are the subject of extensive research.<sup>5,6,63,64</sup> Diverse categories of nanocarriers have been exploited by researchers to deliver challenging therapeutic molecules. Metal nanoparticles are also in the race and GNPs found many applications in drug delivery apart from other biomedical applications. The following section discusses the recent drug delivery applications of GNPs. However, delivery strategies of protein conjugates and antibodies for the treatment of cancers are not included in this review. A very brief overview of the drug delivery aspects of GNPs is presented in Table 1.

### 4.1. Small Molecule Drugs Delivery

GNPs have become increasingly popular for delivering small-molecule drugs during the last few decades. These nanosized carriers provide a suitable method of delivering small compounds as well as biomacromolecules to cells/tissues due to their distinct size-dependent physicochemical properties, flexibility, sub-cellular size, and bio-compatibility.

**Table 1.** Overview of gold nanoparticles in drug delivery applications.

Therapeutic agent delivered	Objective of delivery	Level of proof	References
5-fluorouracil, and doxorubicin	Targeted delivery	Glioblastoma cell model	[64]
Doxorubicin, and aptamer	Targeted delivery	A549 and 4T1 cells	[65]
Doxorubicin	Extended delivery	MDA-MB-468, $\beta$ TC-3, and HFb cell lines	[66]
Withaferin A	Targeted delivery	Murine melanoma cells, Chinese hamster ovary, and mouse embryonic fibroblast cells	[67]
Betulinic Acid	Targeted delivery	Human Caco-2, HeLa and MCF-7 cancer cell lines	[68]
Doxorubicin	pH dependent targeted delivery	Human breast, cervical, and hepatocellular carcinoma cell lines	[69]
Linalool	Targeted delivery	breast cancer cell line	[70]
Doxorubicin	Targeted delivery	HeLa cells	[71]
EGFR siRNA	Lung cancer treatment	BEAS-2B, and A549 cells	[72]
Bcl-2 siRNA and doxorubicin	Breast cancer treatment	Triple-negative breast cancer, and MCF7 cell line	[73]
siRNA	Targeted controlled release	Immunodeficient mice bearing A549 tumor xenograft	[74]
siRNA	Laser transfection	Canine pleomorphic adenoma ZMTH3 cells	[75]
siRNA	Topical delivery	Normal human keratinocytes, spontaneously immortalized cells, and HeLa cells	[79]

A pH-responsive drug delivery system composed of GNPs and chitosan with aptamer was reported to deliver anticancer agents (5-fluorouracil and doxorubicin).<sup>65</sup> The drug-loaded GNPs were found monodispersed with a mean size of  $196.2 \pm 2.89$  nm. Cellular internalization of the nanoparticles was also confirmed by transmission electron microscopic investigations.<sup>65</sup> In another intriguing research, GNPs-chitosan conjugates with aptamers were deployed successfully for the targeted delivery of doxorubicin.<sup>66</sup> The tumor specificity of the nano drug delivery system was confirmed in the *in vivo* studies.<sup>66</sup> Surface functionalization of GNPs with chondroitin sulfate and chitosan was successful for extended delivery of doxorubicin.<sup>67</sup> Glucocorticoid receptor-dependent cancer cell-selective cytotoxicity was demonstrated by GNPs conjugated with thiol-modified dexamethasone and with-aferin.<sup>68</sup> These compounds also inhibited the growth of an aggressive mouse melanoma tumor, decreased mouse mortality, and prevented tumor cell metastasis. A successful mitochondrial targeting of betulinic acid was reported deploying functionalized GNPs.<sup>69</sup> The effectiveness of mitochondrial targeting was shown by these conjugated GNPs, which significantly inhibited the development of cancer cells. *In vitro*, the targeted nano complexes recorded  $IC_{50}$  values in the range of 3.12–13.2 micromolar ( $\mu M$ ) compared to that of the free betulinic acid (BA) (9.74–36.31  $\mu M$ ). High amplitude mitochondrial depolarization, caspase 3/7 activation, and an associated arrest at the G0/G1 phase of the cell cycle were implicated in their modes of action.<sup>69</sup> Spherical-shaped GNPs fabricated with sodium tripolyphosphate as a linking agent and functionalized with chitosan and folate-linked chitosan exhibited a pH-dependent doxorubicin release.<sup>70</sup> The nanoconjugates were found superior to free doxorubicin in terms of chemotherapeutic activities against cancer cell lines. Linalool-loaded GNPs conjugated with a penta peptide Cys-Ala-Leu-Asn-Asn (CALNN) peptide exhibited promising anticancer activities against breast cancer Michigan Cancer Foundation (MCF-7) cell line.<sup>71</sup> Doxorubicin was delivered using GNPs made from *Azadirachta indica* leaf extract.<sup>72</sup> The GNPs were found to be stable due to the biological capping agents. The resulting complex was found less hazardous to normal cells Madin-Darby canine kidney (MDCK cells) and highly toxic to malignant cells (HeLa cells).<sup>72</sup>

## 4. 2. Nucleic acids / Small Interfering RNAs Delivery

Small interfering RNAs (siRNAs), among other nucleic acids, are commonly delivered using nanosized carriers in therapeutic settings. Cell membrane interaction is essential for controlling absorption in different delivery modalities. Different portals that enter mammalian cells have different types, sizes, destinations, and cargo fates. A nucleic acid's ability to be released at its site of action

and function depends on the mechanism of cellular entry. For delivering siRNA-loaded nanoparticles to specific intracellular locations for a distinct biological impact, small, monodisperse nanoparticles with a defined potential and surface chemistry work best. siRNA therapies have made great progress, but optimal delivery remains a problem before they can be used clinically.

However, siRNAs are large, negatively charged molecules, which makes it difficult for them to passively diffuse through the cell membrane. They require assistance to enter the target cells. Techniques that focus on changing the size and surface characteristics of nanoparticles make excellent models for understanding drug targeting and cellular absorption. siRNA and oligonucleotides have been delivered into cells using GNPs.

GNPs were fabricated with biocompatible collagen to improve siRNA loading capacity carrying epidermal growth factor receptor siRNA to treat lung cancer.<sup>73</sup> The conjugated GNPs were biocompatible to normal airway is a well-established and widely used human bronchial epithelial cell line epithelial cells (BEAS-2B) than to cancer cells (A549). The nanocomplexes were comparable or even more efficient, compared with lipofetamine, in carrying siRNA to knock down Epidermal Growth Factor Receptor (EGFR of A549) cells.<sup>73</sup> Tunc et al. (2022) made an intriguing effort by implementing an approach that combined the use of gene therapy and chemotherapy.<sup>74</sup>

For the regulated delivery of siRNAs to the target cells, a nanoconjugate of GNP and oligonucleotides was created.<sup>75</sup> In comparison to the commercial transfection reagent lipofectamine 3000, the core 3D shell nanoconstruct with the outer coating made up of aptamer-incorporated Y-shaped backbone-rigidified triangular DNA bricks was more effective at inducing tumor cell apoptosis. It also effectively reduced the expression of PLK1 mRNA, refers to the messenger RNA (mRNA) molecule that encodes for the PLK1 gene (PLK1 mRNA) and PLK1 protein.<sup>75</sup> In order to successfully bind siRNA at the right weight ratio by electrostatic force and produce well-dispersed nanoparticles, polyethyleneimine-capped GNPs were created.<sup>76</sup> Although confocal laser scanning microscopy observation and fluorescence-activated cell sorting analyses have shown more internalized polyethyleneimine (PEI) and small interfering RNA (siRNA) (PEI/siRNA) complexes in cells, polyethyleneimine-capped GNPs induced more significant and enhanced reduction in targeted green fluorescent protein expression in metastatic ductal adenocarcinoma (MDA-MB-435s) cells with siRNA binding.<sup>76</sup> Topical routes of drug delivery have been greatly exploited for the clinical management of diseases which largely manifest on the skin. However, macromolecules or proteins cannot penetrate through the epidermal barrier when delivered via the transdermal route due to their large size.<sup>77–79</sup> Spherical nucleic acid nanoparticle conjugates were created for simultaneous transfection and gene regulation in another intriguing study.<sup>80</sup> These nanoparticle conjugates didn't

need to be altered or transfected with cationic components to stimulate cellular entrance. Nearly all of the cells in the more than 50 cell lines, primary cells, cultured tissues, and whole organs that these nanostructures entered.<sup>80</sup>

## 5. Cellular Uptake Mechanism of GNPs

Cellular entry mechanisms, especially related to GNPs, involve various processes by which these nanoparticles are taken up by mammalian cells. GNPs have gained considerable attention in biomedical research due to their unique physicochemical properties and potential applications in drug delivery, imaging, and therapeutics. Understanding the mechanisms of cellular entry is crucial for optimizing GNP-based applications and ensuring their safe and effective use. Endocytosis is a fundamental cellular process through which cells internalize extracellular materials, including nanoparticles, into intracellular vesicles. Several types of endocytosis exist, and the most relevant to GNPs are clathrin-mediated endocytosis, caveolae-mediated endocytosis, and macropinocytosis.<sup>81–83</sup> Clathrin-mediated endocytosis involves the formation of clathrin-coated pits on the cell membrane, which then invaginate and pinch off to form clathrin-coated vesicles containing the GNPs. Caveolae are small invaginations of the cell membrane that play a role in the uptake of certain nanoparticles, including GNPs. In micropinocytosis, the cell engulfs extracellular fluid along with the GNPs into large endocytic vesicles called macropinosomes. For small-sized GNPs (less than 5–6 nm), passive diffusion across the cell membrane can occur. However, this mechanism is not as prevalent for larger-sized GNPs, as their entry is hindered by the cell's lipid bilayer.<sup>84</sup>

Some GNPs can exploit specific cell surface receptors by attaching ligands (e.g., peptides, antibodies) to their surface. This ligand-receptor interaction facilitates receptor-mediated endocytosis, leading to the internalization of the GNP-receptor complex into the cell.<sup>85</sup> Certain types of GNPs, particularly those functionalized with fusogenic peptides or lipids, can undergo direct membrane fusion with the cell membrane. This process allows the GNPs to enter the cell cytoplasm without the need for endocytosis.<sup>86</sup>

It's important to note that the cellular entry mechanisms of GNPs can be influenced by various factors, including their size, shape, surface charge, surface functionalization, and the type of mammalian cell involved.<sup>82,84,85,87</sup> Additionally, the cellular entry pathways may vary depending on the specific GNP formulation and the cellular context.

Researchers continue to investigate these mechanisms to optimize GNP-based applications and improve their targeting, delivery, and safety profiles. Understanding the cellular entry of GNPs is a critical step in harnessing their potential for various biomedical applications.

## 6. Conclusion

The biocompatibility, variable size, and easy functionalization make GNPs appealing delivery vehicles for nucleic acids. GNP-based covalent and non-covalent nucleic acid carriers alter cellular uptake, endosomal escape, and nucleic acid release. To present, the promise of these systems has primarily been shown in vitro; nonetheless, there remain difficulties to overcome before GNP-nucleic acid conjugates may be used in clinical settings. First, short- and long-term GNP cytotoxicity must be reduced. Numerous studies have shown the biocompatibility of therapeutic NPs using basic cytotoxicity trials.<sup>88–93</sup> However, a full toxicological assessment (cell membrane damage, oxidative stress, genotoxicity, etc.) must be addressed. To reduce negative effects, these vehicles must be targeted to particular organs and tissues. This targeting can be achieved by decorating delivery vehicles with specific antibodies targeting disease cells and (ii) grafting non-interacting functional groups (e.g., polyethylene glycol and zwitter ionic entities) on the surface to avoid plasma protein adsorption, improving pharmacokinetics and evading immune surveillance. Immunological concerns must be investigated before the clinical usage of any novel substance. AuNPs offer a platform with all the features needed to tackle these problems and should continue to provide essential in vitro tools and therapeutically relevant delivery vehicles.

## Conflict of Interest

The authors declare no conflict of interest. The authors alone are responsible for the content and writing of the article.

## 7. References

1. S. Pattnaik, K. Swain, In: Inamuddin, A. M. Asiri, A. Mohamad (Ed.): Applications of Nanocomposite Materials in Drug Delivery, Woodhead Publishing, **2018**, pp. 589–604. DOI:10.1016/B978-0-12-813741-3.00025-X
2. K. Pathak, S. Pattnaik, In: S. Bajaj, S. Singh (Ed.): Methods for Stability Testing of Pharmaceuticals. Methods in Pharmacology and Toxicology. Humana Press, New York, **2018**, pp. 293–305. DOI:10.1007/978-1-4939-7686-7\_13
3. S. Pattnaik, K. Swain, J. V. Rao, T. Varun, K. B. Prusty, S. K. Subudhi, *RSC Adv.* **2015**, 5, 91960–91965. DOI:10.1039/C5RA20411A
4. S. Pattnaik, K. Pathak, *Curr. Pharm. Des.* **2017**, 23, 467–480. DOI:10.2174/1381612822666161026162005
5. S. Pattnaik, K. Swain, P. Manaswini, E. Divyavani, J. V. Rao, V. Talla, S. K. Subudhi, *J. Drug Deliv Sci Technol.* **2015**, 29, 199–209. DOI:10.1016/j.jddst.2015.07.021
6. S. Pattnaik, K. Swain, Z. Lin, *J. Mater. Chem. B.* **2016**, 4, 7813–7831. DOI:10.1039/C6TB02086K

7. Y. C. Yadav, S. Pattnaik, *Drug Dev. Ind. Pharm.* **2023**, *49*, 240–247. DOI:10.1080/03639045.2023.2201625
8. S. Chakraborty, M. Dhivar, A. Das, K. Swain, S. Pattnaik, *Recent Adv. Drug Deliv. Formul.* **2023**. DOI:10.2174/2667387817666230726140745
9. J. Soutschek, A. Akinc, B. Bramlage, K. Charisse, R. Constien, M. Donoghue, S. Elbashir, A. Gelck, P. Hadwiger, J. Harborth, M. John, V. Kesavan, G. Lavine, R. K. Pandey, T. Racie, K. S. Rajeev, I. Röhl, I. Toudjarska, G. Wang, S. Wuschko, D. Bumcrot, V. Kotellansky, S. Limmer, M. Manoharan, H. P. Vornlocher, *Nature* **2004**, *432*, 173–178. DOI:10.1038/nature03121
10. J. C. G. Jeaynes, C. Jeaynes, M. J. Merchant, K. J. Kirkby, *Analyst* **2013**, *138*, 7070–7074. DOI:10.1039/c3an01406a
11. M. Horisberger, J. Rosset, H. Bauer, *Experientia* **1975**, *31*, 1147–1149. DOI:10.1007/BF02326761
12. X. Qian, X. H. Peng, D. O. Ansari, Q. Yin-Goen, G. Z. Chen, D. M. Shin, L. Yang, A. N. Young, M. D. Wang, S. Nie, *Nat. Biotechnol.* **2008**, *26*, 83–90. DOI:10.1038/nbt1377
13. C. M. Niemeyer, *Nucleic Acids Res.* **2003**, *31*, 1–7. DOI:10.1093/nar/gng090
14. D. J. Javier, N. Nitin, M. Levy, A. Ellington, R. Richards-Kortum, *Bioconjug. Chem.* **2008**, *19*, 1309–1312. DOI:10.1021/bc8001248
15. S. B. Yaqoob, R. Adnan, R. M. Rameez Khan, M. Rashid, *Front. Chem.* **2020**, *8*, 1–15. DOI:10.3389/fchem.2020.00376
16. H. Yang, Z. Chen, L. Zhang, W. Y. Yung, K. C. F. Leung, H. Y. E. Chan, C. H. J. Choi, *Small* **2016**, *12*, 5178–5189. DOI:10.1002/smll.201601483
17. S. Ramanathan, S. C. B. Gopinath, M. K. M. Arshad, P. Pooalan, V. Perumal, In: S. C. B. Gopinath, F. Gang (Ed.): *Nanoparticles in Analytical and Medical Devices*, Elsevier, **2021**, pp. 31–43. DOI:10.1016/B978-0-12-821163-2.00002-9
18. S. Pattnaik, G. Arun, K. Swain, In: Inamuddin, A. Asiri, (Ed.): *Advanced Nanotechnology and Application of Supercritical Fluids. Nanotechnology in the Life Sciences*, Springer, **2020**, pp. 1–14. DOI: org/10.1007/978-3-030-44984-1\_1
19. B. Zheng, L. Qian, H. Yuan, D. Xiao, X. Yang, M. C. Paau, M. M. F. Choi, *Talanta* **2010**, *82*, 177–183. DOI:10.1016/j.talanta.2010.04.014
20. J. Dong, P. L. Carpinone, G. Pyrgiotakis, P. Demokritou, B. M. Moudgil, *Kona* **2020**, *37*, 224–232. DOI:10.14356/kona.2020011
21. R. Herizchi, E. Abbasi, M. Milani, A. Akbarzadeh, *Artif. Cells Nanomed. Biotechnol.* **2016**, *44*, 596–602. DOI:10.3109/21691401.2014.971807
22. P. J. G. Goulet, R. B. Lennox, *J. Am. Chem. Soc.* **2010**, *132*, 9582–9584. DOI:10.1021/ja104011b
23. M. T. Reetz, W. Helbig, *J. Am. Chem. Soc.* **1994**, *116*, 7401–7402. DOI:10.1021/ja00095a051
24. P. Zhao, N. Li, D. Astruc, *Coord. Chem. Rev.* **2013**, *257*, 638–665. DOI:10.1016/j.ccr.2012.09.002
25. M. T. Reetz, W. Helbig, S. A. Quaiser, U. Stimming, N. Breuer, R. Vogel, *Science* **1995**, *267*, 367–369. DOI:10.1126/science.267.5196.367
26. Y. Z. Song, X. Li, Y. Song, Z. P. Cheng, H. Zhong, J. M. Xu, J. S. Lu, C. G. Wei, A. F. Zhu, F. Y. Wu, J. Xu, *Russ. J. Phys. Chem. A* **2013**, *87*, 74–79. DOI:10.1134/S0036024413010275
27. C. J. Huang, P. H. Chiu, Y. H. Wang, K. L. Chen, J. J. Linn, C. F. Yang, *J. Electrochem. Soc.* **2006**, *153*, D193. DOI:10.1149/1.2358103
28. I. Saldan, O. Dobrovetska, L. Sus, O. Makota, O. Pereviznyk, O. Kuntiyi, O. Reshetnyak, *J. Solid State Electrochem.* **2018**, *22*, 637–656. DOI:10.1007/s10008-017-3835-5
29. H. Ma, B. Yin, S. Wang, Y. Jiao, W. Pan, S. Huang, S. Chen, F. Meng, *Chem. Phys. Chem.* **2004**, *5*, 68–75. DOI:10.1002/cphc.200300900
30. C. Stanglmair, S. P. Scheeler, C. Pacholski, *Eur. J. Inorg. Chem.* **2014**, 3633–3637. DOI:10.1002/ejic.201402467
31. K. H. Tan, H. A. Tajuddin, M. R. Johan, *J. Nanomater.* **2015**, 537125, 1–8. DOI:10.1155/2015/537125
32. C. Ziegler, A. Eychmüller, *J. Phys. Chem. C* **2011**, *115*, 4502–4506. DOI:10.1021/jp1106982
33. Q. Yao, X. Yuan, V. Fung, Y. Yu, D. T. Leong, D. E. Jiang, J. Xie, *Nat. Commun.* **2017**, *8*, 927. DOI:10.1038/s41467-017-00970-1
34. N. Jara, N. S. Milán, A. Rahman, L. Mouheeb, D. C. Boffito, C. Jeffryes, S. A. Dahoumane, *Molecules* **2021**, *26*, 4585. DOI:10.3390/molecules26154585
35. J. Castillo, L. Bertel, E. Páez-Mozo, F. Martínez, *Nanomater. Nanotechnol.* **2013**, *3*, 1–6. DOI:10.5772/57144
36. G. N. Abdelrasoul, R. Cingolani, A. Diaspro, A. Athanassiou, F. Pignatelli, *J. Photochem. Photobiol. A* **2014**, *275*, 7–11. DOI:10.1016/j.jphotochem.2013.10.008
37. K. L. McGilvray, C. Fasciani, C. J. Bueno-Alejo, R. Schwartz-Narbonne, J. C. Scaiano, *Langmuir* **2012**, *28*, 16148–16155. DOI:10.1021/la302814v
38. V. Mallikarjun, M. Balaji, T. Chandrashekar, A. Shanmugarithnam, G. Bhaskar, H. Roy, *BioNanoSci.* **2023**, *13*, 576–587. DOI:10.1007/s12668-023-01102-4
39. M. L. Marin, K. L. McGilvray, J. C. Scaiano, *J. Am. Chem. Soc.* **2008**, *130*, 16572–16584. DOI:10.1021/ja803490n
40. P. Kesharwani, R. Ma, L. Sang, M. Fatima, A. Sheikh, M. A. S. Abourehab, N. Gupta, Z.S. Chen, Y. Zhou, *Mol. Cancer* **2023**, *22*, 98. DOI:10.1186/s12943-023-01798-8
41. P. T. Huynh, G. D. Nguyen, K. Thi Le Tran, T. Minh Ho, V. Q. Lam, T. V. K. Ngo, *Processes* **2021**, *9*, 1–16. DOI:10.3390/pr9010112
42. M. A. Bhosale, D. R. Chenna, B. M. Bhanage, *Chemistry Select.* **2017**, *2*, 1225. DOI:10.1002/slct.201601851
43. H. J. Chen, D. Wen, *Nanoscale Res. Lett.* **2011**, *6*, 198. DOI: org/10.1186/1556-276X-6-198
44. L. Gao, S. Mei, H. Ma, X. Chen, *Ultrason. Sonochem.* **2022**, *83*, 105940. DOI:10.1016/j.ultsonch.2022.105940
45. J. A. Fuentes-García, J. Santoyo-Salzar, E. Rangel-Cortes, G. F. Goya, V. Cardozo-Mata, J. A. Pescador-Rojas, *Ultrason. Sonochem.* **2021**, *70*, 105274. DOI:10.1016/j.ultsonch.2020.105274
46. A. Shanei, H. Akbari-Zadeh, N. Attaran, M. R. Salamat, M. Baradaran-Ghahfarokhi, *Ultrasonics* **2020**, *102*, 106061. DOI:10.1016/j.ultras.2019.106061



47. A. Shanei, M. M. Shanei, *Ultrason. Sonochem.* **2017**, *34*, 45–50. DOI:10.1016/j.ultsonch.2016.05.010
48. A. Veeren, M. O. Ogunyankin, J. E. Shin, J. A. Zasadzinski, *Pharmaceutics* **2022**, *14*, 701. DOI:10.3390/pharmaceutics14040701
49. F. Sahebi, M. Ranjbar, M. T. Goodarzi, *Appl. Phys. A* **2019**, *125*, 1–8. DOI:10.1007/s00339-019-3138-z
50. C. Shalichah, A. Khumaeni, S. Abdulateef, A. Omar, M. Mat Jafri, A. Khumaeni, W. Setia Budi, H. Sutanto, J. Soedhartha, *J. Phys. Conf. Ser.* **2017**, *909*, 1–4. DOI:10.1088/1742-6596/909/1/012037
51. N. Z. A. Naharuddin, N. Z. A. Naharuddin, A. R. Sadrolhosseini, M. H. A. Bakar, N. Tamchek, M. A. Mahdi, *Opt. Mater. Express* **2020**, *10*, 323–331. DOI:10.1364/OME.381427
52. L. Gentile, H. Mateos, A. Mallardi, M. Dell'Aglio, A. De Giacomo, N. Cioffi, G. Palazzo, *J. Nanopart. Res.* **2020**, *23*, 1–12. DOI:10.1007/s11051-021-05140-5
53. K. X. Lee, K. Shameli, Y. P. Yew, S. Y. Teow, H. Jahangirian, R. Rafiee-Moghaddam, T. J. Webster, *Int. J. Nanomedicine.* **2020**, *15*, 275–300. DOI:10.2147/IJN.S233789
54. E. O. Mikhailova, *J. Funct. Biomater.* **2021**, *12*, 70. DOI:10.3390/jfb12040070
55. J. Y. Song, H. K. Jang, B. S. Kim, *Process Biochem.* **2009**, *44*, 1133–1138. DOI:10.1016/j.procbio.2009.06.005
56. C. E. A. Botteon, L. B. Silva, G. V. Ccana-Ccapatinta, T. S. Silva, S. R. Ambrosio, R. C. S. Veneziani, J. K. Bastos, P. D. Marcato, *Sci. Rep.* **2021**, *11*, 1–16. DOI:10.1038/s41598-021-81281-w
57. P. Anbu, S. C. B. Gopinath, S. Jayanthi, *Nanomater. Nanotechnol.* **2020**, *10*, 1–9. DOI:10.1177/1847980420961697
58. R. Lévy, N. T. K. Thanh, R. Christopher Doty, I. Hussain, R. J. Nichols, D. J. Schiffrin, M. Brust, D. G. Fernig, *J. Am. Chem. Soc.* **2004**, *126*, 10076–10084. DOI:10.1021/ja0487269
59. J. Kimling, M. Maier, B. Okenve, V. Kotaidis, H. Ballot, A. Plech, *J. Phys. Chem. B* **2006**, *110*, 15700–15707. DOI:10.1021/jp061667w
60. S. K. Seol, D. Kim, S. Jung, Y. Hwu, *Mater. Chem. Phys.* **2011**, *131*, 331–335. DOI:10.1016/j.matchemphys.2011.09.050
61. S. Pattnaik, K. Swain, J. V. Rao, T. Varun, K. B. Prusty, S. K. Subudhi, *RSC Adv.* **2015**, *5*, 91960–91965. DOI:10.1039/C5RA20411A
62. S. Pattnaik, K. Pathak, *Curr. Pharm. Des.* **2016**, *23*, 467–480. DOI:10.2174/1381612822666161026162005
63. D. S. Panda, N. K. Alruwaili, S. Pattnaik, K. Swain, *Acta Chim. Slov.* **2022**, *69*, 483–488. DOI:10.17344/acs.2022.7370
64. S. Pattnaik, K. Swain, S. Ramakrishna, *Wiley Interdiscip. Rev. Nanomed. Nanobiotechnol.* **2023**, *15*, e1859. DOI:10.1002/wnan.1859
65. A. Sathiyaseelan, K. Saravanakumar, A. V. A. Mariadoss, M. H. Wang, *Carbohydr Polym.* **2021**, *262*, 1–14. DOI:10.1016/j.carbpol.2021.117907
66. Z. Khademi, P. Lavaee, M. Ramezani, M. Alibolandi, K. Abnous, S. M. Taghdisi, *Carbohydr. Polym.* **2020**, *248*, 1–40. DOI:10.1016/j.carbpol.2020.116735
67. T. Chandrashekar, A. Ruhul, M. Jithendar Reddy, G. Amel, E. Talha Bin, B. K. Dey, A. Roy, M. S. Alqahtani, M. S. Refat, S. Z. Safi, A. M. Alsuhaibani, M. Asariha, S. H. Kiaie, S. Izadi, F. H. Pirhayati, M. Fouladi, M. Gholamhosseinpour, *BioMed Res. Inter.* **2022**, *2467574*, 1–13. DOI:10.1155/2022/2467574
68. P. Agarwalla, S. Mukherjee, B. Sreedhar, R. Banerjee, *Nanomed.* **2016**, *11*, 2529–2546. DOI:10.2217/nnm-2016-0224
69. O. Oladimeji, J. Akinyelu, A. Daniels, M. Singh, *Int. J. Mol. Sci.* **2021**, *22*, 1–24. DOI:10.3390/ijms22105072
70. J. Akinyelu, O. Oladimeji, A. Daniels, M. Singh, *J. Drug. Deliv. Sci. Technol.* **2022**, *67*, 102978. DOI:10.1016/j.jddst.2021.102978
71. A. S. S. Majid S. Jabir, Ali A. Taha, Usama I. Sahib, Zainab J. Taqi, Ahmed M. Al-Shammari, *Mater. Sci. Eng. C.* **2019**, *94*, 949–964. DOI:10.1016/j.msec.2018.10.014
72. R. Dharmatti, C. Phadke, A. Mewada, M. Thakur, S. Pandey, M. Sharon, *Mater. Sci. Eng. C* **2014**, *44*, 92–98. DOI:10.1016/j.msec.2014.08.006
73. A. Y. H. Yu, R. H. Fu, S. hui Hsu, C. F. Chiu, W. H. Fang, C. A. Yeh, C. M. Tang, H. H. Hsieh, H. S. Hung, *Mater. Today Adv.* **2021**, *12*, 100191. DOI:10.1016/j.mtdadv.2021.100191
74. C. Ü. Tunç, O. Aydin, *J. Drug. Deliv. Sci. Technol.* **2022**, *74*, 103603. DOI:10.1016/j.jddst.2022.103603
75. C. Xue, S. Hu, Z. H. Gao, L. Wang, M. X. Luo, X. Yu, B. F. Li, Z. Shen, Z. S. Wu, *Nat. Com.* **2021**, *12*, 1–12. DOI:10.1038/s41467-021-23250-5
76. D. Heinemann, M. Schomaker, S. Kalies, M. Schieck, R. Carlson, H. M. Escobar, T. Ripken, H. Meyer, A. Heisterkamp, *PLoS One.* **2013**, *8*, e58604. DOI:10.1371/journal.pone.0058604
77. K. Swain, S. Pattnaik, N. Yeasmin, S. Mallick, *Eur. J. Drug Metab. Pharmacokinet.* **2011**, *36*, 237–241. DOI:10.1007/s13318-011-0053-x
78. S. Pattnaik, K. Swain, J. V. Rao, T. Varun, S. Mallick, *Medicina* **2015**, *51*, 253–261. DOI:10.1016/j.medic.2015.07.002
79. S. Pattnaik, K. Swain, P. Choudhury, P. K. Acharya, S. Mallick, *Int. Braz. J. Urol.* **2009**, *35*, 716–729. DOI:10.1590/S1677-55382009000600010
80. D. Zheng, D. A. Giljohann, D. L. Chen, M. D. Massich, X. Q. Wang, H. Iordanov, C. A. Mirkin, A. S. Paller, *Proc. Natl. Acad. Sci. U S A.* **2012**, *109*, 11975–11980. DOI:10.1073/pnas.1118425109
81. S. H. Wang, C. W. Lee, A. Chiou, P. K. Wei, *J Nanobiotechnol.* **2010**, *8*, 1–33. DOI:10.1186/1477-3155-8-33
82. D. Yilmaz, M. Culha, *Talanta* **2021**, *225*, 122071. DOI:10.1016/j.talanta.2020.122071
83. A. M. Alkilany, C. J. Murphy, *J. Nanopart. Res.* **2010**, *12*, 2313–2333. DOI:10.1007/s11051-010-9911-8
84. Y. J. Lee, E. Y. Ahn, Y. Park, *Nanoscale Res. Lett.* **2019**, *14*, 2–14. DOI:10.1186/s11671-019-2967-1
85. A. Kapara, V. Brunton, D. Graham, K. Faulds, *Chem. Sci.* **2020**, *11*, 5819–5829. DOI:10.1039/D0SC01255F
86. M. A. Tahir, Z. P. Guven, L. R. Arriaga, B. Tinao, Y. S. S. Yang, A. Bekdemir, J. T. Martin, A. N. Bhanji, D. Irvine, F. Stellacci, A. Alexander-Katz, *Proc. Natl. Acad. Sci. USA.* **2020**, *117*, 18470–18476. DOI:10.1073/pnas.1902597117
87. X. Xie, J. Liao, X. Shao, Q. Li, Y. Lin, *Sci. Rep.* **2017**, *7*, 1–9. DOI:10.1038/s41598-017-04229-z

88. R. Shukla, V. Bansal, M. Chaudhary, A. Basu, R. R. Bhonde, M. Sastry, *Langmuir* **2005**, *21*, 10644–10654. DOI:10.1021/la0513712
89. H. R. Ali, M. R. K. Ali, Y. Wu, S. A. Selim, H. F. M. Abdelaal, E. A. Nasr, M. A. El-Sayed, *Bioconjug. Chem.* **2016**, *27*, 2486–2492. DOI:10.1021/acs.bioconjchem.6b00430
90. Y. Pan, S. Neuss, A. Leifert, M. Fischler, F. Wen, U. Simon, G. Schmid, W. Brandau, W. Jahnen-Dechent, *Small* **2007**, *3*, 1941–1949. DOI:10.1002/smll.200700378
91. A. Chompoosor, K. Saha, P. S. Ghosh, D. J. MacArthy, O. R. Miranda, Z. J. Zhu, K. F. Arcaro, V. M. Rotello, *Small* **2010**, *6*, 2246–2249. DOI:10.1002/smll.201000463
92. E. E. Connor, J. Mwamuka, A. Gole, C. J. Murphy, M. D. Wyatt, *Small* **2005**, *1*, 325–327. DOI:10.1002/smll.200400093
93. R. Amin, C. Thalluri, A.O. Docea, J. Sharifi-Rad, D. Calina, *eFood* **2022**, *3*, 1–14. DOI:10.1002/efd2.33

## Povzetek

Nanodelci so običajno nanoskopski materiali z vsaj eno od dimenzij pod 100 nm, ki se uporabljajo v številnih panogah. Najnovejši razvoj na področju nanotehnologije omogoča široko paleto metod za proučevanje in spremljanje različnih medicinskih in bioloških procesov na nanometrski ravni. Nanodelci lahko pomagajo pri diagnosticiranju in zdravljenju bolezni, kot je rak, saj dostavljajo zdravila neposredno do rakavih celic. Uporabljajo se lahko tudi za odkrivanje bioloških označevalcev bolezni v telesu, kar pomaga pri zgodnjem diagnosticiranju. Verjetno je, da bi se nanodelci lahko uporabljali v teranostičnih aplikacijah in pri ciljni dostavi učinkovin. To bi lahko bistveno izboljšalo izide zdravljenja bolnikov ter zmanjšalo količino časa, truda in denarja, potrebnega za diagnosticiranje in zdravljenje bolezni. Prav tako bi lahko zmanjšalo stranske učinke zdravljenja ter zagotovilo natančnejše in učinkovitejše zdravljenje. Nanodelci za uporabo v biomedicini vključujejo polimerne in kovinske nanodelce, liposome in micelle, dendrimere, kvantne pike itd. Med nanodelci so se zlati nanodelci (GNP) izkazali kot obetavna platforma za uporabo pri dostavi zdravil. GNP so zaradi svoje odlične biokompatibilnosti, stabilnosti ter nastavljivih fizikalnih in kemijskih lastnosti zelo primerni za dostavo zdravil. Pregledni članek vsebuje poglobljeno razpravo o različnih pristopih k sintezi GNP in aplikacijah za dostavo učinkovin.



Except when otherwise noted, articles in this journal are published under the terms and conditions of the Creative Commons Attribution 4.0 International License

Scientific paper

# A novel nickel(II) Complex with N,S-donor Schiff Base: Structural Characterisation, DFT, TD-DFT Study and Catalytic Investigation

Manas Chowdhury,<sup>1</sup> Niladri Biswas,<sup>1,2</sup> Sandeeptha Saha,<sup>1,3</sup> Ennio Zangrando,<sup>4</sup>  
Nayim Sepay<sup>5</sup> and Chirantan Roy Choudhury<sup>\*,1</sup>

<sup>1</sup> Department of Chemistry, West Bengal State University, Barasat, Kolkata-700126, India

<sup>2</sup> Department of Biotechnology, Institute of Genetic Engineering, No. 30, Thakurhat Road, Badu, Madhyamgram, Kolkata, West Bengal 700128, India

<sup>3</sup> Sripur High School, Madhyamgram Bazar, Kolkata-700130, India

<sup>4</sup> Department of Chemical and Pharmaceutical Sciences, University of Trieste, 34127 Trieste, Italy

<sup>5</sup> Department of Chemistry, Lady Brabourne College, Kolkata-700017, India.

\* Corresponding author: E-mail: crchoudhury2000@yahoo.com;  
Tel: + 91-9836306502; Fax: +91-33-2524-1577

Received: 03-012-2023

## Abstract

One new mononuclear nickel(II) thiosemicarbazone complex (**1**), has been synthesised from the Schiff base ligand derived from *p*-anisaldehyde and thiosemicarbazide. Complex **1** was characterized by using different spectroscopic techniques and single crystal X-ray structural analysis. The time dependent density functional theory (TD-DFT) was applied to simulate the electronic spectra of the complex **1** with the help of Polarizable Continuum Model (PCM). Complex **1** acts as functional model towards catecholase activity and the catalytic property has been evaluated from Lineweaver-Burk plot using the Michaelis-Menten approach of enzyme catalysis with a  $k_{\text{cat}}$  value of the order of  $708 \text{ h}^{-1}$ .

**Keywords** Catecholase-like activity, crystal structure, DFT study, Ni(II) complex, Schiff base

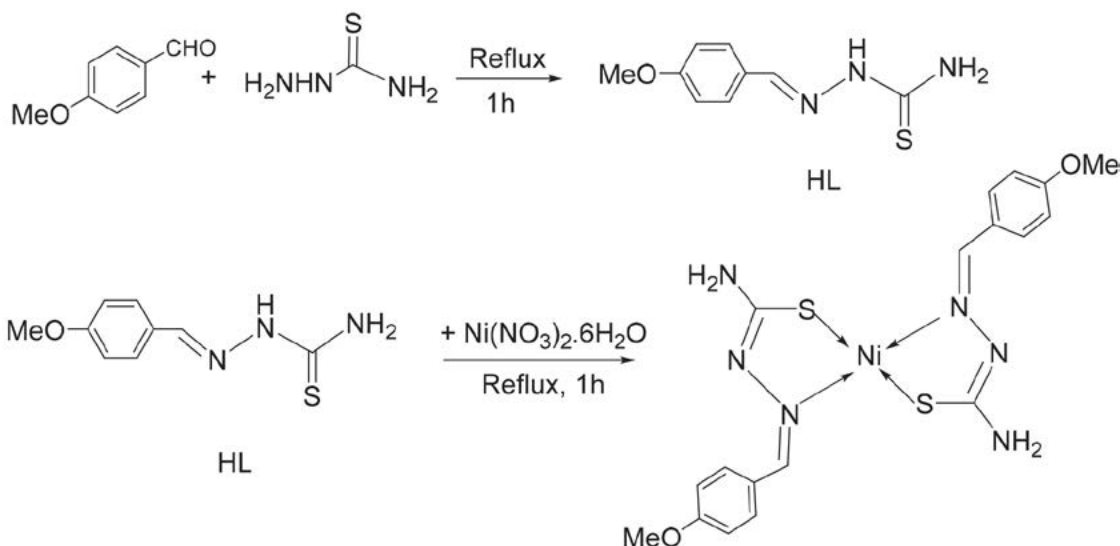
## 1. Introduction

Biomimetic models of metalloenzymes have emerged as an important class of compounds for their application to catalytic organic conversions which are otherwise difficult to achieve.<sup>1–4</sup> In catecholase metalloenzyme one hydroxide ion forms a bridge between the dinuclear copper(II) active site.<sup>5–6</sup> Among different Schiff bases, thiosemicarbazones are considered as extremely suitable ligands for their different coordination behaviour, as it can bind in both anionic as well as neutral form.<sup>7–10</sup> Various copper(II) complexes showing catecholase activity have been reported<sup>11–13</sup> along with complexes of other transition metals such as manganese(II),<sup>14</sup> nickel(II),<sup>15</sup> iron(III),<sup>16</sup> cobalt(II/III),<sup>5,17</sup> and zinc(II).<sup>18</sup> In particular it was observed that catecholase-like activity was

exhibited by metal complexes comprising of ligands with *N,N*-, *N,O*- or *N,S*-donor set.<sup>19–25</sup>

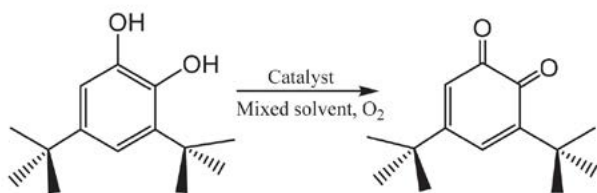
Till date dinuclear nickel(II) metal complexes have been frequently studied for their catecholase activity,<sup>26–29</sup> but systematic reports of mononuclear nickel(II) complexes which can be used as catecholase mimicking systems are less reported.<sup>30,31</sup> These facts prompted us to synthesise a nickel(II) complex with the Schiff base ligand 2-(4-methoxybenzylidene)hydrazine-1-carbothioamide(HL) bearing both hard and soft *N,S*-donor site (Scheme 1). The present Ni(II) complex has been reported earlier together with Cu and Pd derivative containing the same ligand, but not supported by X-ray single crystal analysis.<sup>32</sup>

The catalytic efficiency of the complex **1** towards catecholase-like activity was studied in detail and it was revealed that it is an efficient species for the oxidation of



Scheme 1. Synthesis of ligand HL and complex 1.

3,5-di-*tert*-butylcatechol (3,5-DTBC) to 3,5-di-*tert*-butylbenzoquinone (3,5-DTBQ) (Scheme 2).



Scheme 2. Catecholase-like activity exhibited by the complex 1.

## 2. Experimental Section

### 2.1. Materials

All materials were of reagent grade and were used without further purification. Nickel(II) nitrate hexahydrate  $[\text{Ni}(\text{NO}_3)_2 \cdot 6\text{H}_2\text{O}]$ , thiosemicarbazide (Sigma Aldrich), and *p*-anisaldehyde (Sigma-Aldrich) were used as received.

### 2.2. Physical Techniques

Fourier Transform Infrared spectrum (4000–400  $\text{cm}^{-1}$ ) of the complex 1 was recorded on a Perkin-Elmer SPECTRUM-2 FT-IR spectrophotometer in solid KBr matrices. Electronic spectrum was recorded at 300 K on a Perkin-Elmer Lambda-35 UV-Vis spectrophotometer in DMSO. C, H, N microanalyses were carried out with a Perkin-Elmer 2400 II elemental analyzer. Electrochemical studies were performed in DMSO with a CH 660E cyclic voltammeter at a scan rate of 50  $\text{mV sec}^{-1}$  by using saturated calomel electrode (SCE) as a reference in a three-electrode system and tetrabutylammonium perchlorate as supporting electrolyte. Nitrogen gas was bubbled through the sample solution at a constant rate for 1 minute.

### 2.3. Synthesis

#### 2.3.1. Synthesis of Schiff Base (HL)

A methanolic solution of *p*-anisaldehyde (608.35  $\mu\text{L}$ , 5 mmol) was added to a methanolic solution of thiosemicarbazide (0.4557 g, 5 mmol) in same ratio and the reaction mixture was refluxed for two hours. Then the reaction mixture was cooled at room temperature and used without further purification.

#### 2.3.2. Synthesis of Nickel(II) Complex (1)

$\text{Ni}(\text{NO}_3)_2 \cdot 6\text{H}_2\text{O}$  (0.183 g, 1 mmol) in methanol medium was added into the solution of the Schiff base in 1:1 millimolar ratio and the reaction mixture was refluxed for two hours. Then the solution was filtered and left for slow evaporation. After a few days, brown coloured single crystals were obtained and separated out. Yield: 68%. Anal. Calc. for  $[\text{C}_{18}\text{H}_{20}\text{N}_6\text{NiO}_2\text{S}_2]$ : C, 45.45; H, 4.21; N, 17.68% Found: C, 45.41; H, 4.18; N, 17.66%. IR bands: ( $\nu$ ,  $\text{cm}^{-1}$ ) 1609  $\nu(\text{C}=\text{N})$ ; 560  $\nu(\text{Ni}-\text{N})$ ; 493  $\nu(\text{Ni}-\text{S})$ , 671  $\nu(\text{C}-\text{S})$ , 3466  $\nu(\text{O}-\text{H})$ . UV-Vis:  $\lambda_{\text{max}}$  (nm) (DMSO): 283, 401, 565.

#### 2.3.4. Crystallographic Data Collection and Refinement

Diffraction data collection of the complex 1 was performed at the X-ray diffraction beam line (XRD1) of the Elettra Synchrotron of Trieste (Italy), with a Pilatus2M image plate detector. Complete dataset was collected at 100(2) K with a monochromatic wavelength of 0.7000 Å. The diffraction data were indexed, integrated, and scaled using XDS.<sup>33</sup> The structure was solved by direct methods using SIR2014.<sup>34</sup> Fourier analysis and refinement were performed by the full-matrix least-squares methods based on  $F^2$  implemented in SHELXL-2019/2.<sup>35</sup> All non-hydrogen

atoms were refined anisotropically. The molecular graphics and crystallographic illustrations complex were prepared using DIAMOND 4<sup>36</sup> program. All the relevant crystallographic data and details of structure refinement are summarized in Table 1.

**Table 1.** Crystal data and details of structure refinement of complex 1.

empirical formula	C <sub>18</sub> H <sub>20</sub> N <sub>6</sub> NiO <sub>2</sub> S <sub>2</sub>
formula weight (g mol <sup>-1</sup> )	475.23
Crystal system	Monoclinic
Space group	P2 <sub>1</sub> /c
<i>a</i> (Å)	12.473(3)
<i>b</i> (Å)	5.5140(11)
<i>c</i> (Å)	14.195(3)
$\beta$ (deg)	101.88(3)
<i>V</i> (Å <sup>3</sup> )	955.4(3)
<i>Z</i>	2
<i>d</i> <sub>calc</sub> (g cm <sup>-3</sup> )	1.652
<i>M</i> (mm <sup>-1</sup> )	1.203
<i>F</i> (000)	492
crystal size (mm <sup>3</sup> )	0.11 × 0.30 × 0.32
Collected reflections	29501
Independent reflections	2907
<i>R</i> <sub>int</sub>	0.0264
Goodness-of-fit on <i>F</i> <sup>2</sup>	1.099
Final <i>R</i> <sub>1</sub> , <i>wR</i> <sub>2</sub> indices [ <i>I</i> > 2 $\sigma$ ( <i>I</i> )]	0.0272, 0.0684
<i>R</i> <sub>1</sub> , <i>wR</i> <sub>2</sub> indices (all data)	0.0279, 0.0689
Residuals (eÅ <sup>-3</sup> )	0.505, -0.597

### 2. 3. 5. DFT Studies

The energy minimized structure of the complex **1** (in the isolated form) was obtained using density functional theory (DFT) calculation. For this study, B3LYP dispersion corrected hybrid functional along with mixed basis sets LANL2DZ for Ni(II) ion and 6-311G(d,p) for other atoms were used with spin-unrestricted scheme. The initial coordinates for structure optimization were taken from the X-ray crystallographic structure. The Gaussian 09 software with D1 revision and Gauss View<sup>537,38</sup> were used for DFT calculations and molecular visualization software, respectively. Using the optimized structure, the electronic absorption spectrum, at the same level of theory, was calculated in DMSO solvent using the Polarizable Continuum Model (PCM). Frontier molecular orbitals (FMOs) like HOMO and LUMO were drawn by Gauss View6. Gauss Sum was utilized to get the contribution of orbitals and outcome obtained in TD-DFT.

## 3. Result and Discussion

### 3. 1. Infrared Spectra Study

The FT-IR-spectrum of complex **1**, shown in Fig. S1, exhibited a distinctive band at 1609 cm<sup>-1</sup>, which can be as-

signed to the C=N<sup>39</sup> stretching frequency of azomethine group. The bands at 560 and 493 cm<sup>-1</sup> are due to the formation of Ni-N and Ni-S bonds<sup>39,40</sup> and the band detected in the region of 671 cm<sup>-1</sup> can be attributed to the C-S stretching frequency.<sup>41</sup> In addition, the complex showed a prominent IR band at 3466 cm<sup>-1</sup> due O-H stretching frequency.

### 3. 2. Electronic Spectral Study

The electronic spectrum of complex **1** in DMSO solution at a concentration of 10<sup>-3</sup> M is shown in Fig. S2. The complex exhibited three characteristics peaks in the region 283–565 nm. The sharp high intensity band observed at 283 nm can be attributed to  $\pi \rightarrow \pi^*$  transition<sup>42</sup> of coordinated imine of the ligand. A moderate intense peak observed at 401 nm was assigned to  $n \rightarrow \pi^*$  transition<sup>43</sup> and a very low intensity band, detected at 565 nm correspondent to  $d \rightarrow d$  transition. The electronic spectrum of **1** was carried out for three successive days maintaining same concentration and same solvent, but no significant change was detected.

### 3. 3. Cyclic Voltammetric Study

The cyclic voltammogram of complex **1** (displayed in Fig. S3) shows one irreversible oxidative peak at +1.30 V (versus SCE) in the anodic region that can be attributed to the oxidation of Ni(II) to Ni(III). The irreversible reductive peak at -0.65 V (versus SCE) in the cathodic region is due to the reduction of Ni(II) to Ni(I).

### 3. 4. Structural Description

Brown single crystals of complex **1** were obtained by slow evaporation of a saturated methanolic solution. The X-ray structural analysis shows that the geometry of complex **1** is square planar.

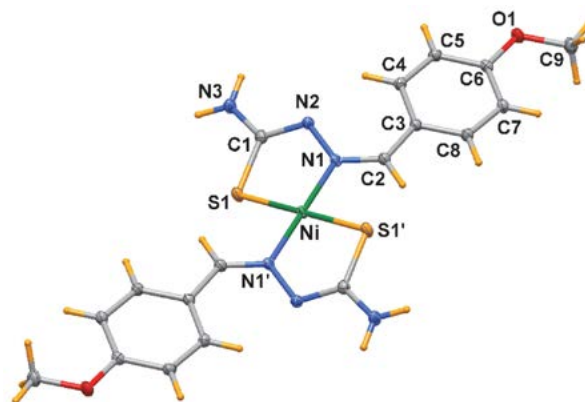


**Fig. 1.** ORTEP diagram (ellipsoid probability at 50%) of the centrosymmetric complex **1** (primed atoms at  $-x, -y + 1, -z + 1$ ).

The molecular structure consists of a centrosymmetric neutral complex species [Ni(L)<sub>2</sub>], with the nickel atom located at an inversion center, so that the asymmetric unit

comprises only half complex. An ORTEP view of the complex along with the atom numbering scheme is depicted in Fig. 1 and a selection of bond lengths and angles is given in Table 2 and 3, respectively, along with calculated values obtained from the DFT approach. The thiosemicarbazone ligands chelate the Ni(II) center via *N,S*-donor atoms in trans configuration resulting in two five membered rings. The Ni–N1 and Ni–S1 bond distances are of 1.9210(12) and 2.1820(5) Å with a chelating angle of 84.83(4)°. The ligand atoms are not coplanar and the phenyl ring forms a dihedral angle of 23.22(6)° with the coordination plane NiN<sub>2</sub>S<sub>2</sub>. These bonding parameters are in good agreement with the coordinating pattern of similar square planar Ni complexes with thiosemicarbazone ligands,<sup>44</sup> where Ni–N and Ni–S bond distances were found in to fall in the range 1.906(2)–1.9310(19) and 2.1735(7)–2.1796(6) Å, respectively.

**Table 2.** Experimental and DFT calculated bond distances (Å) for complex **1**.

Complex <b>1</b>		
Bond distances	X-ray	DFT
Ni–N1	1.9210(12)	1.9522
Ni–S1	2.1820(5)	2.1142

**Table 3.** Experimental and DFT calculated bond angles (°) for complex **1**.

Complex <b>1</b>		
Bond angles	X-ray	DFT
S1–Ni–N1	84.83(4)	84.42
S1–Ni–S1 <sup>i</sup>	180.00	180.00
S1–Ni–N1 <sup>i</sup>	95.17(4)	95.64
N1–Ni–N1 <sup>i</sup>	180.00	180.00

Symmetry code for primed atoms:  $-x, -y + 1, -z + 1$

Upon coordination the bond lengths in thiosemicarbazone ligand undergo some changes compared to the values measured in the free ligand.<sup>44</sup> In particular, the C1–S1 bond length of 1.670(2) Å elongates to 1.7387(14) Å, while the C1–N2 bond distance from 1.350(2) Å shortens to 1.3000(17) Å in the complex. These features are consistent with the acquisition of a partial single bond character in the former, and a partial double bond in the latter.

In addition, the square-planar coordination geometry with the N<sub>2</sub>S<sub>2</sub> donor atoms involves the thiolato sulphur and the nitrogen N1 atoms in *Z* configuration (Fig. 1) indicating that the complexation occurs after a 180° rotation around the C1–N2 bond.<sup>44</sup>

The crystal packing evidences phenyl rings  $\pi$ -stacking with distance between centroids of 3.6343(11) Å, in addition to weak H bonds involving the amino group NH<sub>2</sub>

with O1 leading to a 2D supramolecular network (N3...O1 = 3.0962(18) Å) as shown in Fig 2. Finally, the amino group NH<sub>2</sub> interact also with S1 (N3...S1 = 3.5493(18) Å) giving rise a 3D architecture.

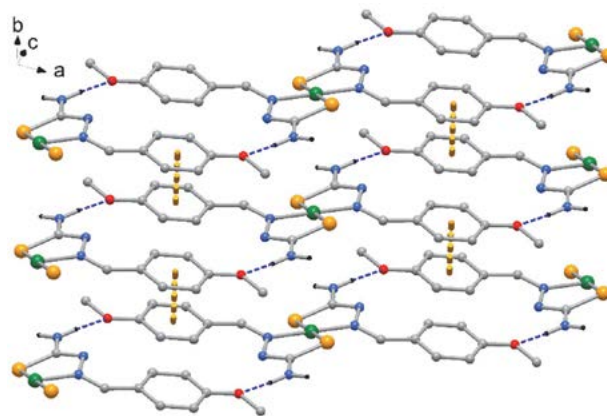


**Fig. 2.** Detail of crystal packing of complex **1** with indication of  $\pi$ -stacking between phenyl ring and N-H...O hydrogen bonds (only H atoms at N3 are shown for clarity).

### 3. 5. DFT Studies

Density functional theory approach can be used to evaluate the experimental properties of the complex.<sup>45</sup> The structure of the complex **1** obtained from X-ray crystallography was optimized with the help of DFT method leading to a self-consistent field total energy and dipole moment of  $-3588436.369697$  kJ/mol and 0.005993 Debye, respectively. The structure of the complex **1** obtained after energy minimization is reported in Fig. 3a. Atom-by-atom overlay of asymmetric unit of X-ray crystal structure (orange) with energy minimized structure (violet) of the complex is displayed in Fig 3b. The difference of root mean square deviation of these structures was found to be 0.3623 Å, and most of the bond lengths and angles of the optimised structures corroborates with those of the corresponding X-ray structure. Few changes were observed for the atoms in the coordination sphere of the Ni center. The bond distances Ni–S, C–S, C=N, N–N, and N–Ni in the crystal structure are 2.18, 1.74, 1.31, 1.39, and 1.92 Å, respectively, whereas they are 2.11, 1.54, 1.42, 1.44, and 1.95, respectively, in the case of optimised structure. Such structural differences can be attributed to the fact the experimental structure is obtained in the solid state and theoretical structure obtained in vacuum.

The electronic spectrum of the complex **1** was simulated in the DMSO medium by using the time dependent density functional theory (TD-DFT) and compared with the experimental one. The simulated spectrum shows a strong absorption band at  $\lambda_{\max} = 410$  nm (oscillator strength 0.87), while the complex shows an absorption band at  $\lambda_{\max} = 401$  nm (Fig. 3c). The TD-DFT calculation shows that HOMO to LUMO (99%) and HOMO-1 to LU-

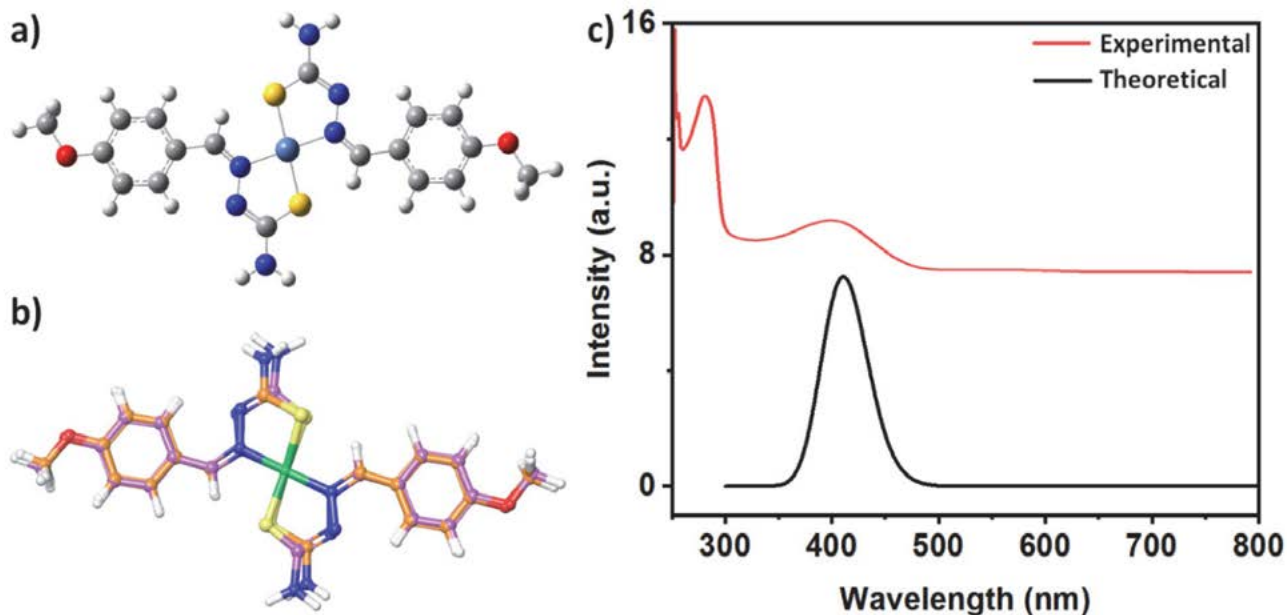


Fig. 3. (a) DFT energy minimized structure of the complex 1, (b) overlay of energy minimized (violet) and X-ray crystal structure (orange) of the complex 1, and (c) experimental and theoretical absorption spectra of the complex 1.

MO transition are responsible for the above mentioned absorption band.

In the formation of metal complexes, energy and electron density in the complexes show drastic changes from those of the ligand. The chemical reactivity of a molecule depends upon the difference in energy between the highest occupied molecular orbital (HOMO) and lowest unoccupied molecular orbital (LUMO).<sup>46</sup> In fact, high energy of HOMO facilitates the interaction of the molecule with other molecules through electron donation whereas, molecule with low energy LUMO can accept electron easily from other molecules.<sup>46,47</sup> It is interesting to note that

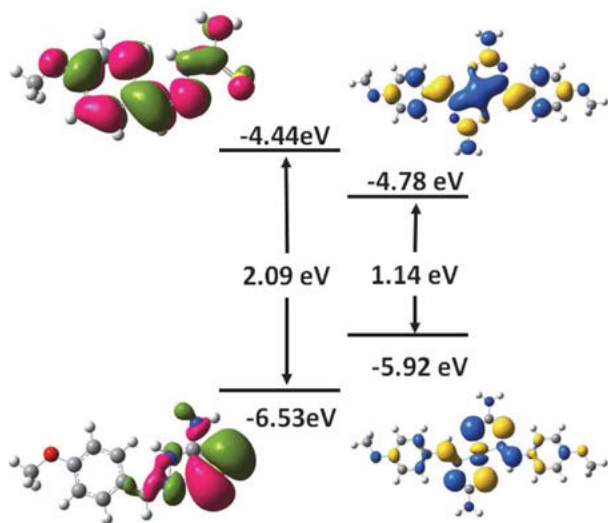


Fig. 4. HOMO and LUMO molecular orbitals and their energy of ligand and in complex 1.

assembly of the Ni(II) ion with (*Z*)-2-(4-methoxybenzylidene)hydrazine-1-carbothioamide ligands induces lowering of the LUMO and enhancement of the HOMO energy with respect to the HL in the complex (Fig. 4). As a result, the energy gap between HOMO and LUMO of HL (2.09 eV) is much higher than that of the complex (1.14 eV). Therefore, the complex 1 is more soft in nature and capable of interaction with other molecules through both electron donation and electron acceptance. In addition, the electron density of HOMO is concentrated over the large planar aromatic moiety, while in the case of LUMO, it is spread also over Ni atom ( $d_{xy}$ ). As a result, the complex 1 can accept electron very easily at the metal centre in LUMO. All the aforesaid electronic and energy features make the complex a good catalyst.

### 3. 6. Catecholase Activity

In order to assess the strength of the complex 1 to mimic the catecholase activity, the substrate 3,5-di-*tert*-butylcatechol (3,5-DTBC)<sup>29</sup> appears to be the most efficient substrate.<sup>48</sup> This molecule has allow redox potential that facilitates oxidation process and bears bulky *tert*-butyl substituents hindering any further over oxidation reaction and ring opening. The stability of the oxidised product 3,5-di-*tert*-butylbenzoquinone (3,5-DTBQ) is very high and the maximum absorption is shown at 400 nm in pure DMSO.<sup>49</sup>

#### 3. 6. 1. Reaction with 3,5-DTBC as Substrate

A solution of  $1 \times 10^{-4}$  M of complex 1 in DMSO was mixed with a DMSO solution of 3,5-DTBC ( $1 \times 10^{-2}$  M) at

room temperature. The UV-Vis spectra of the mixture were recorded at regular intervals of 5 mins.<sup>48</sup> After addition of the complex **1** to the solution of 3,5-DTBC, a steady rise in absorbance was observed with the appearance of a new band at 402 nm, correspond to the formation of 3,5-di-*tert*-butylbenzoquinone (3,5-DTBQ) (Fig. 5).<sup>50</sup>

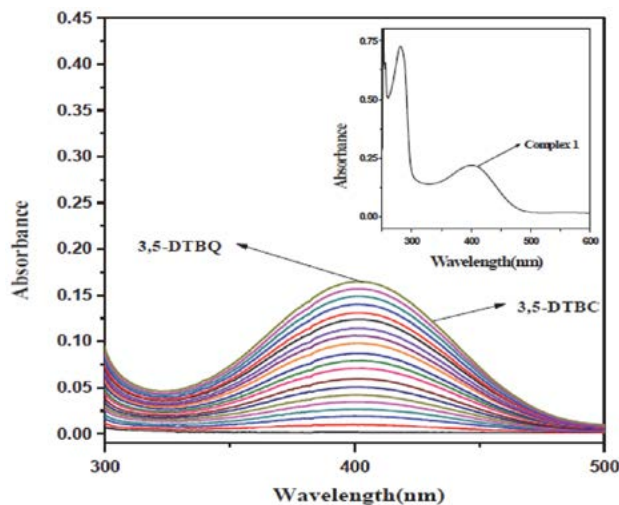


Fig. 5. Increase of the absorbance after the addition of 100 equivalents of 3,5-DTBC to a  $10^{-4}$  M solution of complex **1**. The spectra were recorded at intervals of 5 min.

The  $\log[A_{\alpha}/(A_{\alpha} - A_t)]$  versus time plot was utilised to determine the rate constant for a specific complex substrate mixture (Fig. 6).<sup>48,49</sup>

Since saturation kinetics is followed by initial rate methods at higher substrate concentration, the Michaelis-Menten model was used for the study of enzyme kinetics and the Lineweaver-Burk plot was employed to compute the various kinetics parameters for the complex **1**. The Michaelis binding constant ( $K_m$ ), maximum velocity ( $V_{max}$ ) values and the rate constant for the dissociation of the substrate (i.e. turnover frequency,  $K_{cat}$ ) were all calculated from the Lineweaver-Burk graph  $1/V$  vs.  $1/[S]$  (Fig. 7) by utilizing the equation  $1/V = \{K_m/V_{max}\}\{1/[S]\} + 1/V_{max}$ .

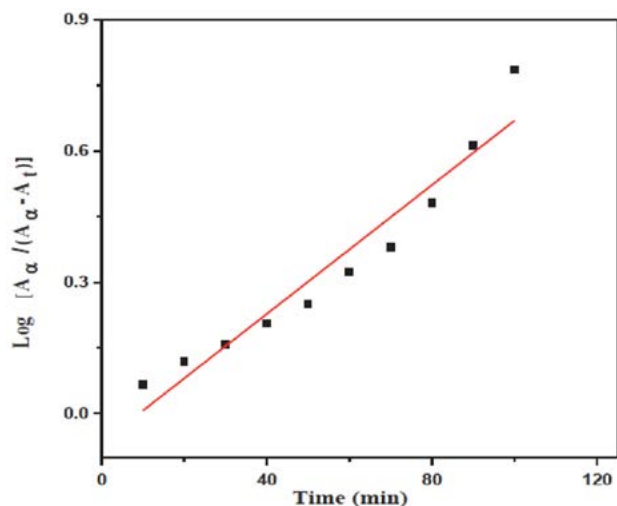


Fig. 6. Change in absorption maxima at 402 nm with time for complex **1**.

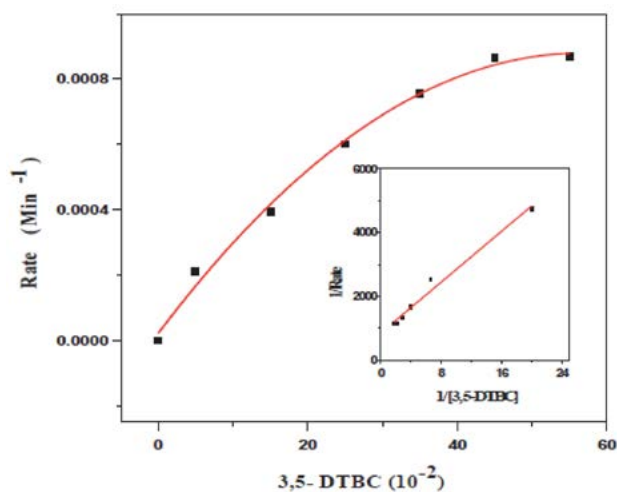


Fig. 7. Plot of rate vs substrate concentration for complex **1**. Inset shows the Lineweaver-Burk plot.

The  $V_{max}$ ,  $K_m$ , and  $K_{cat}$  kinetic parameters for the complex **1** were found to be  $1.18 \times 10^{-3}$  M  $\text{min}^{-1}$ , 0.235 M and  $708 \text{ h}^{-1}$  respectively.<sup>40,44,48,49,51</sup>

Table 4.  $K_{cat}$  values for the oxidation of 3,5-DTBQ catalyzed by reported mononuclear Ni(II) complex along with other metal complexes.

Complex	Solvent	$K_{cat}$	References
[Ni(L) <sub>2</sub> ] Complex <b>1</b>	DMSO	708	This work
[Ru(PPh <sub>3</sub> )Cl <sub>2</sub> (L) <sub>2</sub> ]	DMSO	$2.346 \times 10^3$	23
[Ni(L <sub>3</sub> )ClO <sub>4</sub> ]	CH <sub>3</sub> OH	$8 \times 10^3$	40
[Ni(L <sub>4</sub> )ClO <sub>4</sub> ]	CH <sub>3</sub> OH	$2.7 \times 10^3$	40
[Ni(L <sub>5</sub> ) <sub>2</sub> ]	DMSO	116	44
[Cu(L <sub>6</sub> )(CCl <sub>3</sub> COO)(H <sub>2</sub> O)].H <sub>2</sub> O	DMSO	1452.00	48
[Cu(L <sub>7</sub> )(H <sub>2</sub> O)Cl] <sub>2</sub>	DMSO	1458.00	48
{[Cu(HL <sub>8</sub> )(H <sub>2</sub> O)](NO <sub>3</sub> ) <sub>n</sub> }	DMSO	$5.19 \times 10^3$	49
[Cu <sub>2</sub> (L <sub>8</sub> ) <sub>2</sub> (H <sub>2</sub> O) <sub>3</sub> ] <sub>n</sub>	DMSO	$5.56 \times 10^3$	49
[Ni(L <sub>9</sub> ) <sub>2</sub> ]	CH <sub>3</sub> OH	140.72	50



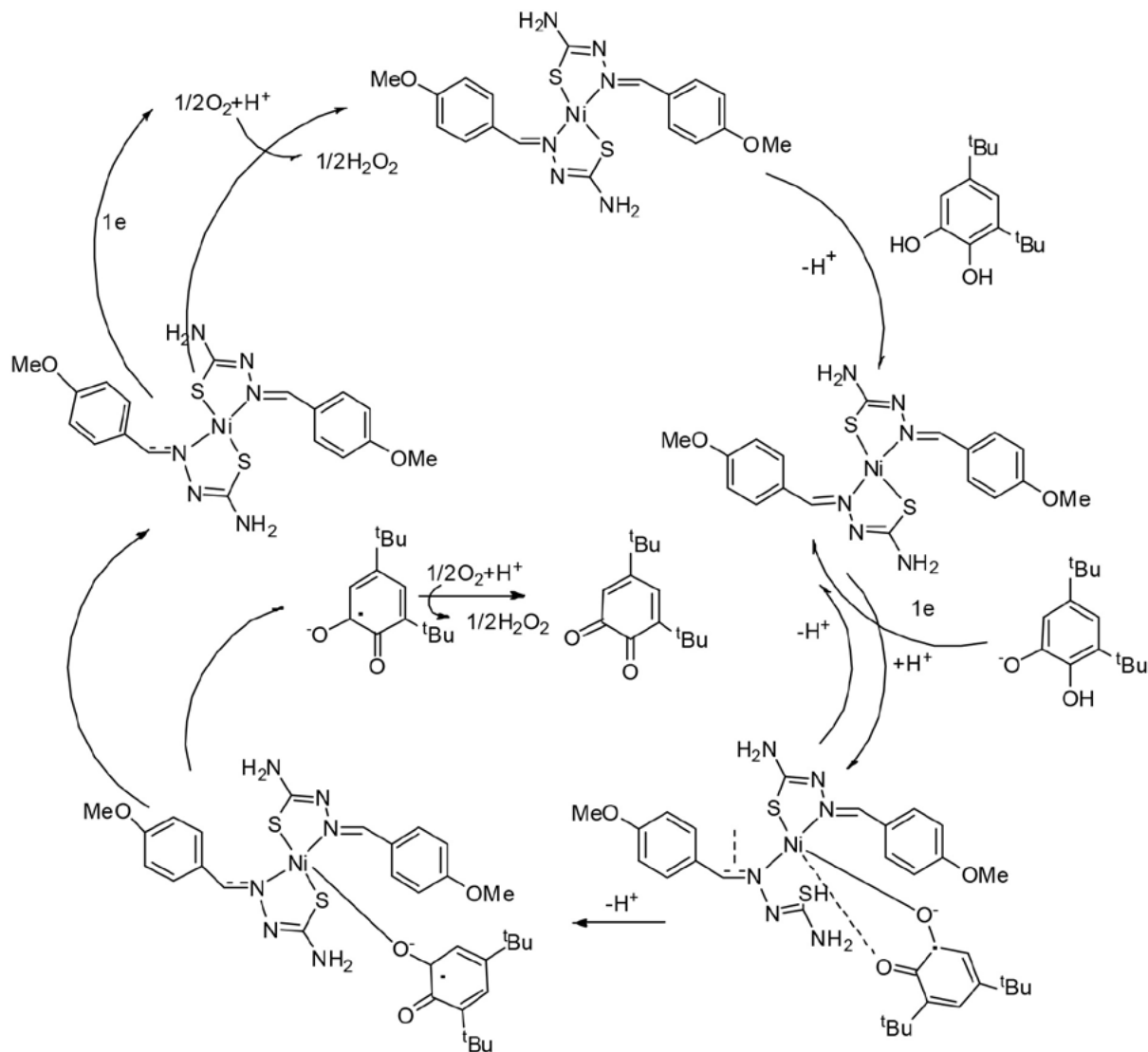
Key: HL<sub>2</sub> = (*E*)-4-chloro-2-(((2-(dimethylamino)ethyl)imino)methyl)phenol. HL<sub>3</sub> = 1-Phenyl-3-(2-piperazin-1-yl-ethylimino)-but-1-en-1-ol. HL<sub>4</sub> = 4-((2-(piperazin-1-yl)ethyl)imino)pent-2-en-2-ol. HL<sub>5</sub> = [N-(diethylaminothiocarbonyl)-benzimidoylchloride-2-aminoacetophenone-*N*-methylthiosemicarbazone]. HL<sub>6</sub> = Hpymab = (*E*)-2-((pyridine-2-yl)methyleneamino) benzoic acid. HL<sub>7</sub> = HPmyaib = (HPmyaib = 4-iodo-2-((*E*)-(pyridin-2-yl)methyleneamino)benzoic acid). [H<sub>2</sub>L<sub>8</sub> = H<sub>2</sub>Pymat = (*E*)-2-(1-(pyridin-2-yl)-methyleneamino) terephthalic acid]. HL<sub>9</sub> = 1,1'-(1*E*,1*E*)-(propane-1,3-diylbis(azan-1-yl-1-ylidene)bis(methan-1-yl-1-ylidene)dinaphthalene-2-ol.

### 3. 6. 2. Reaction Mechanism

The probable mechanism of 3,5-DTBC oxidation by complex **1** is shown in Scheme 3. When a mixture of starch

and potassium iodide was added to a solution of the complex **1** and 3,5-DTBC, the formation of a blue colour indicate that H<sub>2</sub>O<sub>2</sub> was produced during the progress of the reaction. Meanwhile it is noteworthy that no colouration was observed in presence of only 3,5-DTBC. The mechanism of formation of H<sub>2</sub>O<sub>2</sub>, obtained as a byproduct during the oxidation of 3,5-DTBC to 3,5-DTBCQ catalysed by the complex **1** followed similar mechanism found in the literature.<sup>52</sup>

Following the generalized mechanism of catecholase reaction induced by the complex **1** (Scheme 3), it can be stated that the Ni(II) metal centre is the main facilitator for the transfer of electrons that delocalise more easily through the C=N bond of the Schiff base to the neighbouring conjugate system. In other words, the chelation of Schiff bases to the metal expands the aromatic system consisted of delocalized  $\pi$ -electrons with an achievable thione-thiol tautomerism (Scheme 3).<sup>10</sup>



Scheme 3. Plausible mechanism for the oxidation of 3,5-DTBC by complex **1**.

### 3. 6. 3. Comparison with Previous Related Studies: Significant Aspects

Single crystal X-ray structure characterizations is of paramount importance to ascertain structure-property relationships.<sup>19</sup> In recent times, researchers have been describing many transition metal(II) systems to mimic Catecholase activity. Some of the metal complexes are mononuclear, while a large number of metal complexes are dinuclear in nature, and it was found that some model catalysts demonstrate high turnover number ( $K_{cat}$ ), whereas opposite results were also presented.<sup>20</sup> Therefore, we can make a conclusive remark, as per the available data of the Table 4, that a simple relationship between the nuclearity of the system and the observed  $K_{cat}$  value is not possible due to numerous variables involved, such as metal-metal distance, flexibility and electronic/steric properties of the ligand, exogenous bridging ligand, and coordination geometry around the metal centre.<sup>48,49</sup>

## 4. Conclusion

- (i) The present work focuses the synthesis and characterization of one nickel (II) thiosemicarbazone complex (**1**) of the Schiff base ligand (*Z*)-2-(4-methoxybenzylidene)hydrazine-1-carbothioamide (**L**) derived from *p*-anisaldehyde and thiosemicarbazide.
- (ii) Complex **1** was well characterized by elemental analysis, cyclic voltammetry and spectroscopic measurements like FT-IR, UV-Vis spectroscopy, cyclic voltammetry along with single crystal X-ray analysis.
- (iii) Time dependent density functional theory (TD-DFT) was performed to simulate the electronic spectra of the complex **1** with the help of Polarizable Continuum Model (PCM) which was further supported by Frontier molecular orbitals (FMOs).
- (iv) Complex **1** exhibits significant catecholase activity towards the aerial oxidation of 3,5-di-*tert*-butyl catechol to the corresponding quinone in DMSO.

## 5. Acknowledgements

N. Biswas acknowledges CSIR, New Delhi, Govt. of India, for awarding junior research fellowship (Project No: 01/2537/11- EMR - II). M. Chowdhury acknowledges UGC, New Delhi, Govt. of India, for awarding Senior research fellowship (Sr. No. 2121410140, Ref. No. 21/12/2014 (II) EU-V). C. Roy Choudhury acknowledges DST- FIST (Project No. SR/FST/CSI-246/2012) New Delhi, Govt. of India for instrumental support under capital heads.

## Appendix A. Supplementary data

CCDC 2239973 contains the supplementary crystallographic data for complex **1**. These data can be obtained free of charge via <http://www.ccdc.cam.ac.uk/conts-re->

[trieving.html](http://www.ccdc.cam.ac.uk/conts-retrieving.html), or from the Cambridge Crystallographic Data Centre, 12 Union Road, Cambridge CB2 1EZ, UK; fax: (+44) 1223-336-033; or e-mail: [deposit@ccdc.cam.ac.uk](mailto:deposit@ccdc.cam.ac.uk). Supplementary data associated with this article can be found, in the online version, at <http://>

## Disclosure statement

No potential conflict of interest was reported by the authors.

## 6. References

1. A. K. Maji, A. Chatterjee, S. Khan, B. K. Ghosh, *J. Mol. Struct.* **2017**, *1146*, 821–827. DOI:10.1016/j.molstruc.2017.06.077
2. S. K. Dey, A. Mukherjee, *Coord. Chem. Rev.* **2016**, *310*, 80–115. DOI:10.1016/j.ccr.2015.11.002
3. R. Rahaman, B. Chakraborty, T. K. Paine, *Angew. Chem. Int. Ed.* **2016**, *55*, 13838–13842. DOI:10.1002/ange.201607044
4. (a) S. K. Chatterjee, R. C. Maji, S. K. Barman, M. M. Olmstead, A. K. Patra, *Angew. Chem. Int. Ed.* **2014**, *53*, 10184–10189. DOI:10.1002/ange.201404133  
(b) S. Dasgupta, I. Majumder, P. Chakraborty, E. Zangrando, A. Bauzá, A. Frontera, D. Das, *Eur. J. Inorg. Chem.* **2017**, 133–145. DOI:10.1002/ejic.201600985
5. C. Eicken, B. Krebs, J. C. Sacchettini, *Curr. Opin. Struct. Biol.* **1999**, *9*, 677–683. DOI:10.1016/S0959-440X(99)00029-9
6. T. Klabunde, C. Eicken, J. C. Sacchettini, B. Krebs, *Nat. Struct. Biol.* **1998**, *5*, 1084–1090. DOI:10.1038/4193
7. B. Shaabani, A. A. Khandar, F. Mahmoudi, S. S. Balula, L. Cunha-Silva, *J. Mol. Struct.* **2013**, *1045*, 55–61. DOI:10.1016/j.molstruc.2013.03.049
8. N. Biswas, S. Khanra, A. Sarkar, S. Bhattacharjee, D. P. Mandal, A. Chaudhuri, S. Chakraborty, C. R. Choudhury, *New J. Chem.* **2017**, *41*, 12996–13011. DOI:10.1039/C7NJ01998J
9. J. Haribabu, K. Jeyalakshmi, Y. Arun, N. S. P. Bhuvanesh, P. T. Perumal, R. Karvembu. *RSC Adv.* **2015**, *5*, 46031–46049. DOI:10.1039/C5RA04498G
10. N. Biswas, S. Saha, S. Khanra, A. Sarkar, D. P. Mandal, S. Bhattacharjee, A. Chaudhuri, S. Chakraborty, C. R. Choudhury, *J. Biomol. Struct. Dyn.* **2018**, *37*, 2801–2822. DOI:10.1080/07391102.2018.1503564
11. (a) M. Merkel, N. Moller, M. Piacenza, S. Grimme, A. Rompel, B. Krebs, *Chem. Eur. J.* **2005**, *11*, 1201–1209. DOI:10.1002/chem.200400768  
(b) B. Sreenivasulu, F. Zhao, S. Gao, J. J. Vittal, *Eur. J. Inorg. Chem.* **2006**, 2656–2670. DOI:10.1002/ejic.200600022
12. (a) S. Majumder, S. Sarkar, S. Sasmal, E. Carolina Sãnudo, S. S. Mohanta, *Inorg. Chem.* **2011**, *50*, 7540–7554. DOI:10.1021/ic200409d  
(b) A. Biswas, L. K. Das, M. G. B. Drew, C. Diaz, A. Ghosh, *Inorg. Chem.* **2012**, *51*, 10111–10121. DOI:10.1021/ic300319s  
(c) S. Mandal, J. Mukherjee, F. Lloret, R. Mukherjee, *Inorg. Chem.* **2012**, *51*, 13148–13161. DOI:10.1021/ic3013848
13. M. Mitra, A. K. Maji, B. K. Ghosh, G. Kaur, A. R. Choudhury,

- C.-H. Lin, J. Ribas, R. Ghosh, *Polyhedron* **2013**, *61*, 15–19.  
DOI:10.1016/j.poly.2013.05.017
14. (a) M. Maiti, D. Sadhukhan, S. Thakurta, E. Zangrando, G. Pilet, A. Bauzá, A. Frontera, B. Dede, S. Mitra, *Polyhedron* **2014**, *75*, 40–49. DOI:10.1016/j.poly.2014.03.005  
(b) A. Guha, K. S. Banu, A. Banerjee, T. Ghosh, S. Bhattacharya, E. Zangrando, D. Das, *J. Mol. Catal. A: Chem.* **2011**, *338*, 51–57. DOI:10.1016/j.molcata.2011.01.025  
(c) P. Kar, Y. Ida, T. Kanetomo, M. G. B. Drew, T. Ishida, A. Ghosh, *Dalton Trans.* **2015**, *44*, 9795–9804.  
DOI:10.1039/C5DT00709G  
(d) P. Chakraborty, I. Majumder, K. S. Banu, B. Ghosh, H. Kara, E. Zangrando, D. Das, *Dalton Trans.* **2016**, *45*, 742–752.  
DOI:10.1039/C5DT03659C  
(e) S. Mukherjee, T. Weyhermüller, E. Bothe, K. Wieghardt, P. Chaudhuri, *Dalton Trans.* **2004**, *22*, 3842–3853.  
DOI:10.1039/B410842F  
(f) P. Chakraborty, S. Majumder, A. Jana, S. Mohanta, *Inorg. Chim. Acta* **2014**, *410*, 65–75. DOI:10.1016/j.ica.2013.10.013
15. P. K. Basu, M. Mitra, A. Ghosh, L. Thander, C.-H. Lin, R. Ghosh, *J. Chem. Sci.* **2014**, *126*, 1635–1640.  
DOI:10.1007/s12039-014-0742-5
16. (a) R. Singh, A. Banerjee, K. K. Rajak, *Inorg. Chim. Acta.* **2010**, *363*, 3131–3138. DOI:10.1016/j.ica.2010.05.027  
(b) M. Mitra, A. K. Maji, B. K. Ghosh, P. Raghavaiah, J. Ribas, R. Ghosh, *Polyhedron* **2014**, *67*, 19–26.  
DOI:10.1016/j.poly.2013.08.064
17. (a) S. Majumder, S. Mondal, P. Lemonie, S. Mohanta, *Dalton Trans.* **2013**, *42*, 4561–4569. DOI:10.1039/c2dt32629a  
(b) L. Mandal, S. Sasmal, H. A. Sparkes, J. A. K. Howard, S. Mohanta, *Inorg. Chim. Acta.* **2014**, *412*, 38–45.  
DOI:10.1016/j.ica.2013.12.004  
(c) X. Jing, C. He, Y. Yang, C. Duan, *J. Am. Chem. Soc.* **2015**, *137*, 3967–3974. DOI:10.1021/jacs.5b00832
18. (a) A. Guha, T. Chattopadhyay, N. D. Paul, M. Mukherjee, S. Goswami, T. K. Mondal, E. Zangrando, D. Das, *Inorg. Chem.* **2012**, *51*, 8750–8759. DOI:10.1021/ic300400v  
(b) S. K. Mal, M. Mitra, C. S. Purohit, R. Ghosh, *Polyhedron.* **2015**, *101*, 191–195. DOI:10.1016/j.poly.2015.08.039
19. A. Chatterjee, H. R. Yadav, A. R. Choudhury, A. Ali, Y. Singh, R. Ghosh, *Polyhedron* **2018**, *141*, 140–146.  
DOI:10.1016/j.poly.2017.11.040
20. (a) Y. Matoba, T. Kumagai, A. Yamamoto, H. Yoshitsu, M. Sugiyama, *J. Biol. Chem.* **2006**, *281*, 8981–8990.  
DOI:10.1074/jbc.M509785200  
(b) H. Decker, T. Schweikardt, F. Tuzcek, *Angew. Chem. Int. Ed.* **2006**, *45*, 4546–4550. DOI:10.1002/anie.200601255
21. C. Citek, C. T. Lyons, E. C. Wasinger, T. D. P. Stack, *Nat. Chem.* **2012**, *4*, 317–322. DOI:10.1038/nchem.1284
22. Y. Thio, X. Yang, J. J. Vittal, *Dalton Trans.* **2014**, *43*, 3545–3556. DOI:10.1039/c3dt52829d
23. N. Biswas, S. Saha, E. Zangrando, A. Frontera, C. R. Choudhury, *Acta Chim. Slov.* **2021**, *68*, 212–221.  
DOI:10.17344/acsi.2020.6379
24. A. Bhattacharjee, S. Halder, K. Ghosh, C. Rizzoli, P. Roy, *New J. Chem.* **2017**, *41*, 5696–5706. DOI:10.1039/C7NJ00846E
25. S. K. Mal, M. Mitra, H. R. Yadav, C. S. Purohit, A. R. Choudhury, R. Ghosh, *Polyhedron* **2016**, *111*, 118–122.  
DOI:10.1016/j.poly.2016.03.033
26. A. Biswas, L. K. Das, M. G. B. Drew, G. Aromí, P. Gamez, A. Ghosh, *Inorg. Chem.* **2012**, *51*, 7993–8001.  
DOI:10.1021/ic202748m
27. T. Chattopadhyay, M. Mukherjee, A. Mondal, P. Maiti, A. Banerjee, K. S. Banu, S. Bhattacharya, B. Roy, D. J. Chattopadhyay, T. K. Mondal, M. Nethaji, E. Zangrando, D. Das, *Inorg. Chem.* **2010**, *49*, 3121–3129.  
DOI:10.1021/ic901546t
28. L. K. Das, A. Biswas, J. S. Kinyon, N. S. Dalal, H. Zhou, A. Ghosh, *Inorg. Chem.* **2013**, *52*, 11744–11757.  
DOI:10.1021/ic401020m
29. T. Ghosh, J. Adhikary, P. Chakraborty, P. K. Sukul, M. S. Jana, T. K. Mondal, E. Zangrando, D. Das, *Dalton Trans.* **2014**, *43*, 841–852. DOI:10.1039/C3DT51419F
30. J. Adhikary, P. Chakraborty, S. Das, T. Chattopadhyay, A. Bauzá, S. K. Chattopadhyay, B. Ghosh, F. A. Mautner, A. Frontera, D. Das, *Inorg. Chem.* **2013**, *52*, 13442–13452.  
DOI:10.1021/ic401819t
31. A. Guha, K. S. Banu, S. Das, T. Chattopadhyay, R. Sanyal, E. Zangrando, D. Das, *Polyhedron.* **2013**, *52*, 669–678.  
DOI:10.1016/j.poly.2012.07.088
32. G. Borah, J. Baruah, D. Kardong, *Ind. J. Chem.* **2014**, *53A*, 1520–1525
33. W. Kabsch, *Acta Cryst. D* **2010**, *66*, 125–132.  
DOI:10.1107/S0907444909047337
34. M. C. Burla, R. Caliandro, B. Carrozzini, G. L. Casciarano, C. Cuocci, C. Giacovazzo, M. Mallamo, A. Mazzone, G. Polidori, *J. Appl. Cryst.* **2015**, *48*, 306–309.  
DOI:10.1107/S1600576715001132
35. G. M. Sheldrick, *Acta Cryst.* **2008**, *64*, 112–122.  
DOI:10.1107/S0108767307043930
36. K. Brandenburg, DIAMOND, Crystal Impact GbR, Bonn, Germany, **1999**.
37. Gaussian 09, Revision D.01; Gaussian, Inc.: Wallingford, CT, 2009. Gaussian 09, Revision D.01; Gaussian, Inc.: Wallingford, CT, **2009**.
38. GaussView, Version 5; Gaussian, Inc.: Wallingford, CT, 2009. GaussView, Version 5; Gaussian, Inc.: Wallingford, CT, **2009**
39. K. Nakamoto, *Infrared and Raman Spectra of Inorganic and Coordination Compounds*, Wiley, New York, 1997, vol. 23.
40. N. Beyazit, B. Catikkas, S. Bayraktar, C. Demetgül, *J. Mol. Struct.* **2016**, *1119*, 124–132.  
DOI:10.1016/j.molstruc.2016.04.047
41. R. M. El-Shazly, G. A. A. Al-Hazmi, S. E. Ghazy, M. S. El-Shahawi, A. A. El Asmy, *Spectrochim. Acta Part A* **2005**, *61*, 243–252. DOI:10.1016/j.saa.2004.02.035
42. A. Hazari, L. K. Das, R. M. Kadam, A. Bauzá, A. Frontera, A. Ghosh, *Dalton Trans.* **2015**, *44*, 3862–3876.  
DOI:10.1039/C4DT03446E
43. S. Mondal, B. Pakhira, A. J. Blake, M. G. B. Drew, S. K. Chattopadhyay, *Polyhedron* **2016**, *117*, 327–337.  
DOI:10.1016/j.poly.2016.05.052
44. (a) M. Hakimi, R. Takjoo, V. Erfaniyan, E. Schuh, F. Mohr,

- Trans. Met. Chem.* **2010**, *35*, 959–965.  
DOI:10.1007/s11243-010-9417-3
- (b) K. Begum, E. Zangrando, M. S. Begum, C. Sheikh, R. Miyatake, *IUCrData*, **2018**, *3*, x181684.  
DOI:10.1107/S241431461801684X
- (c) S. S. Khan, M. B. H. Howlader, M. C. Sheikh, R. Miyatake, E. Zangrando, *Acta Cryst.*, **2023**, *E79*, 714–717.  
DOI:10.1107/S2056989023005935
45. M. Ghosh, N. Sepay, C. Rizzoli, C. K. Ghosh, A. Banerjee, S. Saha, *New J. Chem.* **2021**, *45*, 2995–3006.  
DOI:10.1039/D0NJ04610H
46. N. Sepay, R. Mondal, M. K. Al-Muhanna, D. Saha, *New J. Chem.* **2022**, *46*, 9735–9744. DOI:10.1039/D2NJ00389A
47. N. Sepay, P. C. Saha, Z. Shahzadi, A. Chakraborty, U. C. Halder, *Phys. Chem. Chem. Phys.* **2021**, *23*, 7261–7270.  
DOI:10.1039/D0CP05714B
48. B. K. Biswas, S. Saha, N. Biswas, M. Chowdhury, A. Frontera, C. Rizzoli, R. R. Choudhury, C. R. Choudhury, *J. Mol. Struct.*, **2020**, *1217*, 128398. DOI:10.1016/j.molstruc.2020.128398
49. S. Saha, N. Biswas, A. Sasmal, C. J. Gómez-García, E. Garribba, A. Bauzá, A. Frontera, G. Pilet, G. M. Rosair, S. Mitra, C. R. Choudhury, *Dalton Trans.* **2018**, *47*, 16102–16118.  
DOI:10.1039/C8DT02417K
50. S. Mistri, H. Puschmann, S. C. Manna, *Polyhedron*. **2016**, *115*, 155–163. DOI:10.1016/j.poly.2016.05.003
51. P. Adak, B. Ghosh, A. Bauzá, A. Frontera, A. J. Blake, M. Corbella, C. D. Mukhopadhyay, S. K. Chattopadhyay, *RSC Adv.* **2016**, *6*, 86851–86861. DOI:10.1039/C6RA14059A
52. (a) P. Vijayan, P. Viswanathamurthi, K. Velmurugan, R. Nandhakumar, M. D. Balakumaran, P. T. Kalaiichelvan, J. G. Malecki, *RSC Adv.* **2015**, *5*, 103321–103342.  
DOI:10.1039/C5RA18568H
- (b) J. P. Chyn, F. L. Urbach, *Inorg. Chim. Acta* **1991**, *189*, 157–163. DOI:10.1016/S0020-1693(00)80184-X

## Povzetek

Sintetizirali smo nov enojedrni nikljev(II) kompleks s tiosemikarbazonom (**1**), pri čemer smo kot ligand uporabili Schiffovo bazo pripravljeno iz *p*-anisaldehida in tiosemikarbazida. Spojino **1** smo karakterizirali z uporabo različnih spektroskopskih tehnik in z monokristalno rentgensko strukturno analizo. Za simulacijo elektronskih spektrov spojine **1** smo uporabili časovno odvisno teorijo gostotnih funkcionalov (TD-DFT) z uporabo modela PCM. Kompleks **1** deluje kot funkcionalni model za oksidacijo katehola, pri čemer smo katalitske lastnosti določali iz Lineweaver-Burkovega diagrama z uporabo Michaelis-Mentenovega pristopa prista katalize z vrednostjo  $k_{\text{cat}} = 708 \text{ h}^{-1}$ .



Except when otherwise noted, articles in this journal are published under the terms and conditions of the Creative Commons Attribution 4.0 International License

Scientific paper

# X-ray Powder Diffraction and Supervised Self-Organizing Maps as Tools for Forensic Classification of Soils

Hirijete Idrizi,<sup>1,2</sup> Mile Markoski,<sup>3</sup> Metodija Najdoski<sup>1</sup> and Igor Kuzmanovski<sup>1,\*</sup>

<sup>1</sup> Ss Cyril and Methodius University, Institute of Chemistry, Faculty of Natural Sciences and Mathematics, Str. Arhimedova 5, Skopje 1000, Republic of North Macedonia

<sup>2</sup> State University of Tetovo, Faculty of Natural Sciences and Mathematics, Bul. Ilinden bb, Tetovo 1200, Republic of North Macedonia

<sup>3</sup> Ss Cyril and Methodius University, Faculty of Agricultural Sciences and Food, Str. 16-ta Makedonska Brigada 3, 1000 Skopje, Republic of North Macedonia

\* Corresponding author: E-mail: shigor@pmf.ukim.mk

Received: 05-01-2023

## Abstract

Due to its transferability, the soil has been commonly used as evidence in criminal investigations. In this work, 172 soil samples were taken from five urban parks from the town of Tetovo (North Macedonia) and from additional four rural locations in its vicinity. The soil samples were examined using X-ray powder diffraction. The collected diffractograms were used for development of classification models based on supervised self-organizing maps for determination of their origin. The examination of generalization performances of the developed models showed that they were able to correctly classify between 95.6 and 97.8% of the samples from the independent test set. The influence of the weather and the seasonal changes on the composition of the soil was also examined. For this purpose, three years after the initial soil samples were collected, additional 28 samples were analyzed from different locations. The best models presented in this work were able to successfully classify 27 of these additional samples.

**Keywords:** Chemometrics, soil analysis, forensic analysis, X-ray powder diffraction

## 1. Introduction

An aerial view, on the agricultural land, in the right season, could reveal plots of land with variety of colors. It is amazing how relatively close these plots of land could be but their color can still differ. For a chemist, the difference in the soil color or nuance of the soil color is the first clue that could lead to a conclusion about possible difference in its chemical composition. The soil color is influenced by the minerals, the water and the organic matter present in it. For example, the soils with high concentration of calcium tend to be white, those with high concentration of iron are reddish, and those high in humus are dark brown to black.<sup>1</sup> The soil color is significant indicator of the chemical composition and a Munsell color chart could be enough for classification of soils for agricultural purposes. However, this approach is not enough for forensic investigations. Due to its high mineral content X-ray powder diffraction analysis of the soils can provide additional and sufficient data

which could be used as forensic evidence. The idea behind the soil as a forensic evidence comes from its divisibility and transferability.<sup>2</sup> Namely, the soil taken from a perpetrator's shoes, car tires or tools, can be linked to a crime scene.<sup>3</sup>

The soil samples have specific chemical and physical composition that has been analyzed with a variety of analytical methods. Scanning electron microscopy has been applied to identify unusual particles. This technique has also been coupled with EDS.<sup>4–6</sup> The potential use of the soil as forensic evidence has been studied with atomic absorption spectrometry,<sup>7,8</sup> inductively coupled plasma, with mass spectrometry,<sup>9,10</sup> gas chromatography coupled with mass spectrometry,<sup>11,12</sup> Raman spectroscopy,<sup>13–15</sup> infrared absorption spectroscopy and infrared reflectance spectroscopy.<sup>16–23</sup> The IR spectroscopy has been used for determination of both (1) organic and (2) mineral components of the soil.<sup>18,24,25</sup>

X-ray powder diffraction (XRD) is a nondestructive technique that can provide a rapid and accurate miner-

logical analysis of multicomponent mixtures without a need for extensive sample preparation.<sup>26</sup> In addition to this, we have to state here that, for forensic purposes, X-ray powder diffraction has been previously used.<sup>19,20,27,28</sup>

In this work, we present our efforts for the development of chemometric method based on supervised self-organizing maps (SOM) used for classification of soil samples for determination of their origin for forensic purposes.<sup>29</sup> Chemometrics by itself has already found its application in forensic science.<sup>30–39</sup> In our previous work, we successfully developed models for classification of urban soils for forensic analysis from five locations using infrared spectroscopy as an experimental technique.<sup>40</sup> However, the signals (the bands) in infrared spectra are highly overlapped most of the time. That was the reason why, in order to obtain successful classification of the samples, we used one-against-the-rest approach. The performances of the one-against-the-rest approach were considerably better compared to a single model approach used for classification of all five types of urban soil samples.<sup>40</sup>

Compared to the signals in the infrared spectra, the signals obtained by X-ray powder diffraction are less overlapped. Having this information in mind, in this work we decided to use X-ray powder diffraction as an experimental technique for classification of samples from nine locations. Five urban location from the town of Tetovo, and four rural locations.

## 2. Experimental

For this purpose, the soil samples were collected from (1) five different parks from the town of Tetovo (North Macedonia) and from (2) four additional rural locations in its vicinity. These locations are presented on Table 1 and in Figure 1.

**Table 1.** Locations from which the soil samples were collected, the description of the locations and their labels.

Label	Location
A	Intercity Bus Station Park
B	House of Culture Park
C	Colorful Mosque Park
D	State University of Tetovo Park
E	Moša Pijade High School Park
F	Village of Džepčište (north exit of the town)
G	Near the tollbooths on the highway Skopje–Tetovo (east exit)
H	Near the village of Gajre (west exit of the town)
I	Near the village of Dolno Palčište (south exit of the town)

Three of the five parks (locations: A, B and C) are located at approximate distances between 1 and 1.5 km. The distance between these three parks from the remaining two (locations: D and E) is about 2.5 km. It is also important

to note that the distance between the remaining two parks (D – State University of Tetovo Park and E – Moša Pijade High School Park) is about 250–300 m. These two parks were selected in this way in order to examine whether the smaller distance will have influence on the performances of the classification models due to the possible similarities of the composition of the soils. The distances between center of the town and the remaining four rural locations (F, G, H and I) are between 4.5 and 5 km.

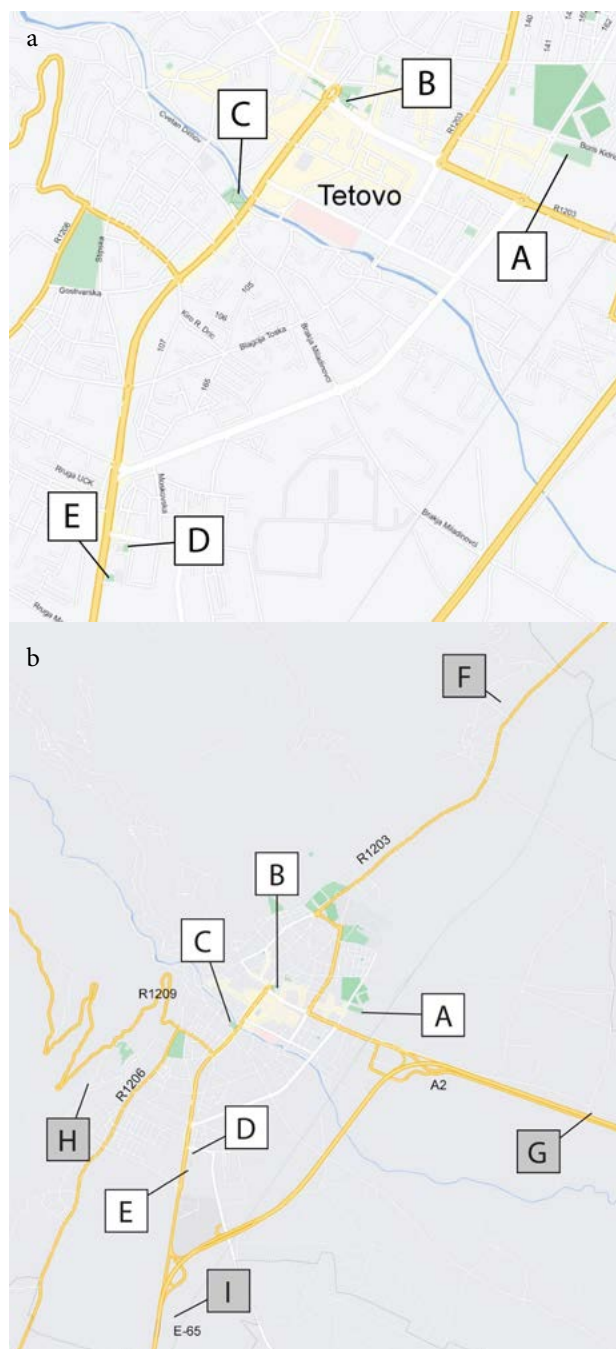


**Figure 1.** The nine locations (a) inside and (b) around town of Tetovo. Locations A, B, C, D and E represent the five parks located in the town, while locations F, G, H and I represent locations from which rural samples were collected.

Total number of 144 soil samples were collected from all nine locations. Sixteen samples were collected from each location. Each of the sixteen samples was taken from the predetermined square grid with area of about 9 m<sup>2</sup> (Figure 2). The distance between the sampling positions on the grid was about 1 m. The samples were collected from top soil layer (10 cm).

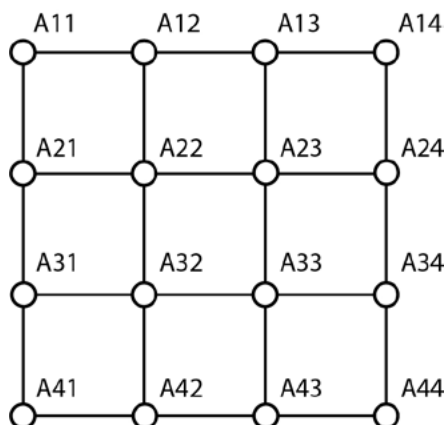


**Figure 2.** The grid used for soil sampling. The indices which are used on this grid are also used for labeling the different samples taken from the same location.

In order to properly analyze the results, it was important to label the collected samples in a systematic manner. For this purpose, each of the samples were labeled as shown in Figure 2. On this figure each of the nodes, which correspond to different samples taken on location A, were labeled as: A11, A12, A13, A14; A21, A22 ... A44.

Three years later (in the autumn of 2019), additional 28 new soil samples were collected from seven of the nine locations. The selected locations were B, D, E (from three parks in Tetovo) as well as all four rural locations (F, G, H and I). This was performed in order (1) to validate our models with new data, but also (2) to examine the influence of the seasonal changes and the weather on the composition of the soil in these parks.

In addition to this, we did not get any information from the local Police Department that these locations were scene of the crime in order to validate our models with their data.

Also, it has to be stated that at this point of our experimental work (in the autumn of 2019), we did not take new samples from the locations A and C because, during these three years, larger horticultural interventions were performed in these two parks by the Municipality of Tetovo.

The samples of the soil were dried at ambient conditions for few days. They were sieved with 20 mesh Tyler sieve. The material that passed the sieve was collected and marked. Collected samples were dried at temperature of 110 °C. The dried samples were kept in desiccator. In ad-

dition to this, before the diffractograms were recorded the samples were powdered in a mortar with a pestle.

The X-ray diffractograms of all samples were recorded using the Rigaku Ultima IV powder X-ray diffractometer in the Bragg-Brentano geometry with CuK<sub>α</sub> radiation ( $\lambda = 1.54178 \text{ \AA}$ ) at room temperature. The sample holder was a 2 mm thick glass plate with dimensions 60 mm × 35 mm and 20 mm × 20 mm depression for the sample. The depression in the holder was filled with sample and was flattened. The mass of the analyzed samples was approximately 200 mg.

Diffraction patterns were measured in the  $2\theta$  range from 5° to 60° with a step size of 0.02° and scanning speed of 20° per minute. The accelerating voltage and the electric current were set to 40 kV and 40 mA, respectively. The divergence slit parameter (DivSlit) was 2/3 degrees, the height limiting slit parameter (DivH.L.Slit) was 10 mm and the anti-scatter slit parameter (SctSlit) was 8.0 mm.

## 2. 1. Data Pre-processing and Algorithms Used

In order to properly prepare the data for optimization of the SOMs, it was necessary to pre-process the obtained diffractograms. The experimentally collected diffractograms of the soil samples were stored in a single data matrix. The data matrix was composed of 172 diffractograms (rows) and 2749 intensities at different  $2\theta$  values (columns).

In this study, the first step in the pre-processing (see Figure 3) was the baseline correction of the diffractograms. After that, baseline corrected diffractograms were normalized to unit area under the curve. Further, in order to make the (1) optimization faster, (2) to reduce the noise in the diffractograms as well as (3) to reduce the number of data points because most of the intensities on different  $2\theta$  values are correlated, data reduction was performed by averaging each consecutive non-overlapping interval composed of 11 intensities using the following formula:

$$d'_{im} = \frac{\sum_{j=i-(m-1)11+1}^{i+11} d_j}{11} \quad (1)$$

$d_{ij}$  in the equation (1) represents the data point from pre-processed matrix consisting of diffractograms,  $i$  – is the sample number,  $j$  – represent the intensity values at different  $2\theta$  values, whereas  $d'_{im}$  is data point from  $i$ -th sample and  $m$ -th column in the reduced data matrix. Using this approach, the number of intensities were reduced from 2749 down to 259 (Figure 3). The diffractograms obtained using this data pre-processing procedure were stored in single data matrix ( $D$ ).

The previously obtained data matrix ( $D$ ) was further reduced using principal component analysis (PCA). In order to perform PCA the variables (the columns in  $D$ ) were auto-scaled. Using PCA we were able to extract the largest fraction of the information stored in  $D$  into small number of principal components. Finally, the obtained princi-

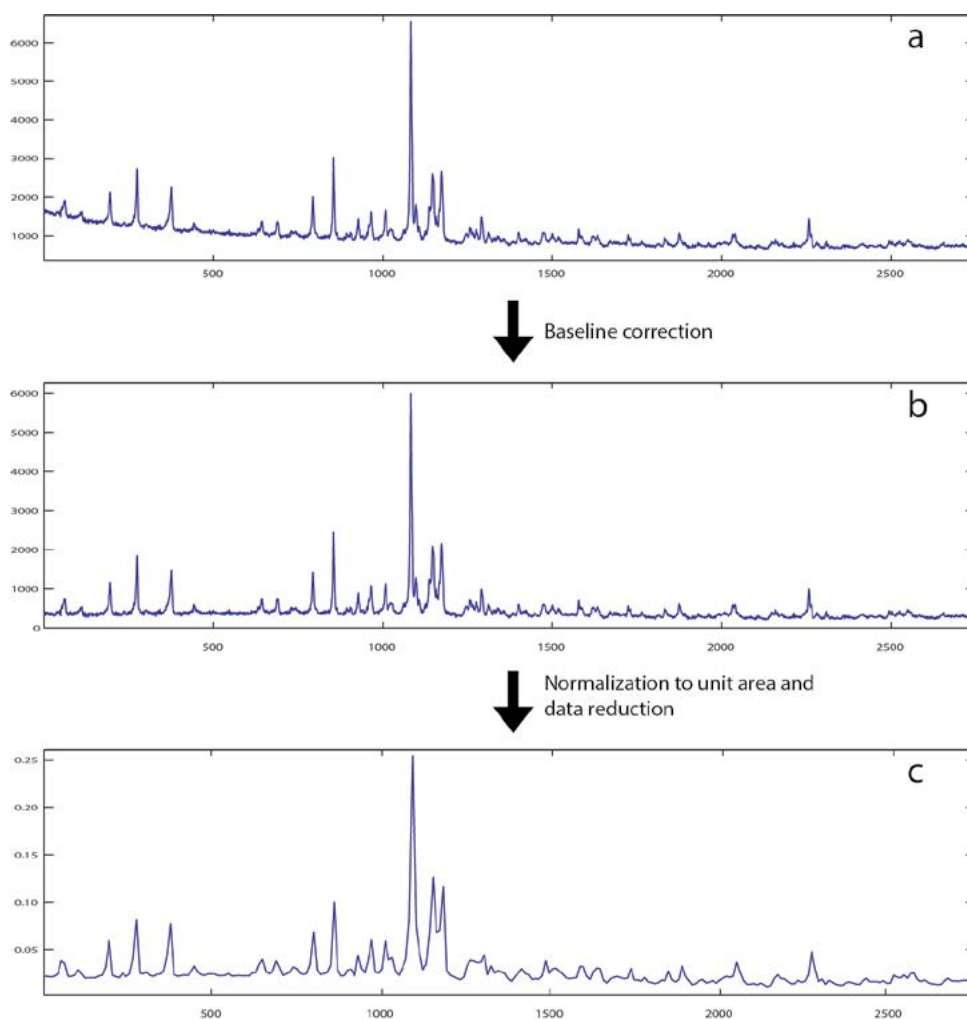


**Figure 3.** Illustration of the main steps of the preprocessing of the experimentally obtained diffractograms. a – original diffractogram; b – baseline corrected diffractogram; c – normalized diffractogram to unit area under the curve with data points reduced down to 259 using equation (1).

pal components were used for training of the supervised self-organizing maps.

## 2. 2. Supervised Self-organizing Maps

According to its inventor, Teuvo Kohonen, self-organizing maps (alternative names: Kohonen maps or Kohonen neural networks) were originally developed as algorithm for unsupervised learning.<sup>29,41</sup> In chemistry and related sciences, most often the unsupervised version of this algorithm is used.<sup>42,43</sup> Today, the unsupervised variant of the algorithm is simply called *self-organizing maps* or *Kohonen neural networks*. While the supervised version of the algorithm, which is not used as frequently as the previously mentioned version, is called *supervised self-organizing maps*. The supervised version of SOM is used in cases when there is not a clear separation among different types of samples.<sup>29</sup> In order to adapt the SOM algorithm for classification purposes (see Figure 4), it is necessary to augment each training vector ( $\mathbf{d}_s$ ) with unit vector ( $\mathbf{d}_u$ ) assigned into one of the nine classes of samples in our case

(Figure 4a). This augmentation of the training set vectors (samples) with  $\mathbf{d}_u$  helps in better separation of the different types of samples during the training.

During the prediction phase the weight levels which correspond to the unit vectors ( $\mathbf{w}_u$ ) are removed (Figure 4b). In other words, for each sample in the training set  $\mathbf{d}_s$  the corresponding  $\mathbf{d}_u$  must be used during training. While during the prediction phase, for the unknown samples –  $\mathbf{x}$  only,  $\mathbf{x}_s$  part is compared with the corresponding part of the weight vectors ( $\mathbf{w}_u$ ) of the trained supervised SOM.

Supervised self-organizing maps were implemented in Matlab<sup>44</sup> programming language using SOM Toolbox developed by J. Vesanto<sup>45–47</sup> on a Windows computer.

## 2. 3. Genetic Algorithms

In this work, the optimization of the supervised SOM models was performed in automated manner using genetic algorithms. Genetic algorithms have been used successfully for solving different problems in the field of chemistry and related sciences since the beginning of the last decade of



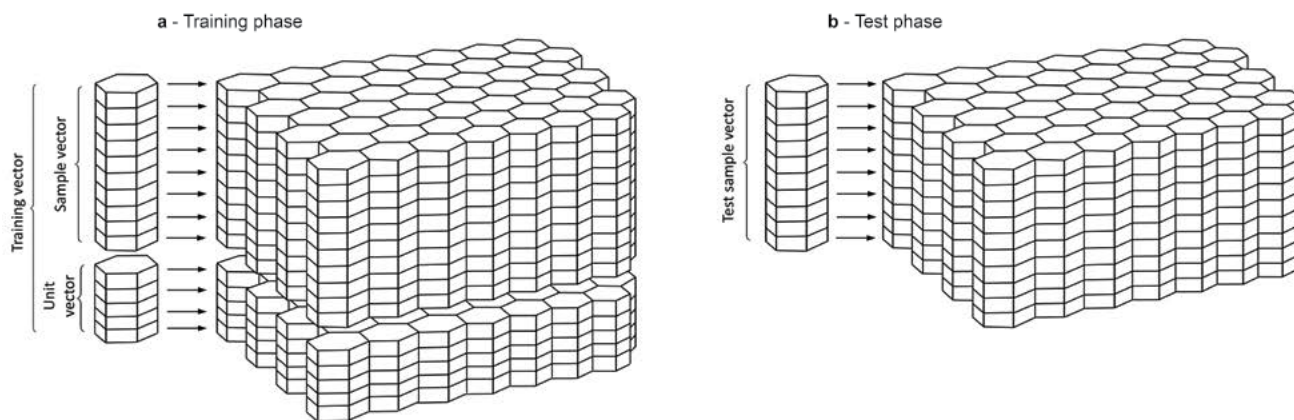


**Figure 4.** Illustration of the structure of the supervised self-organizing maps during the phases of (a) training and (b) prediction. As shown on this figure in the training phase the vector which represents samples is augmented with different unit vector for five different classes of samples. While using the supervised SOM for prediction purposes, the weight levels that correspond to unit vectors are removed.

the 20<sup>th</sup> century.<sup>48–51</sup> The theory of genetic algorithms has been described several times in the chemometric literature during the same decade.<sup>52–54</sup> We have to mention here that, most often, in chemometrics GAs have been used for selection of variables.<sup>52–54</sup> In our work, we use GAs not only as a variable selection tool but also in order to find optimal parameters of the developed models.<sup>40,55,56</sup>

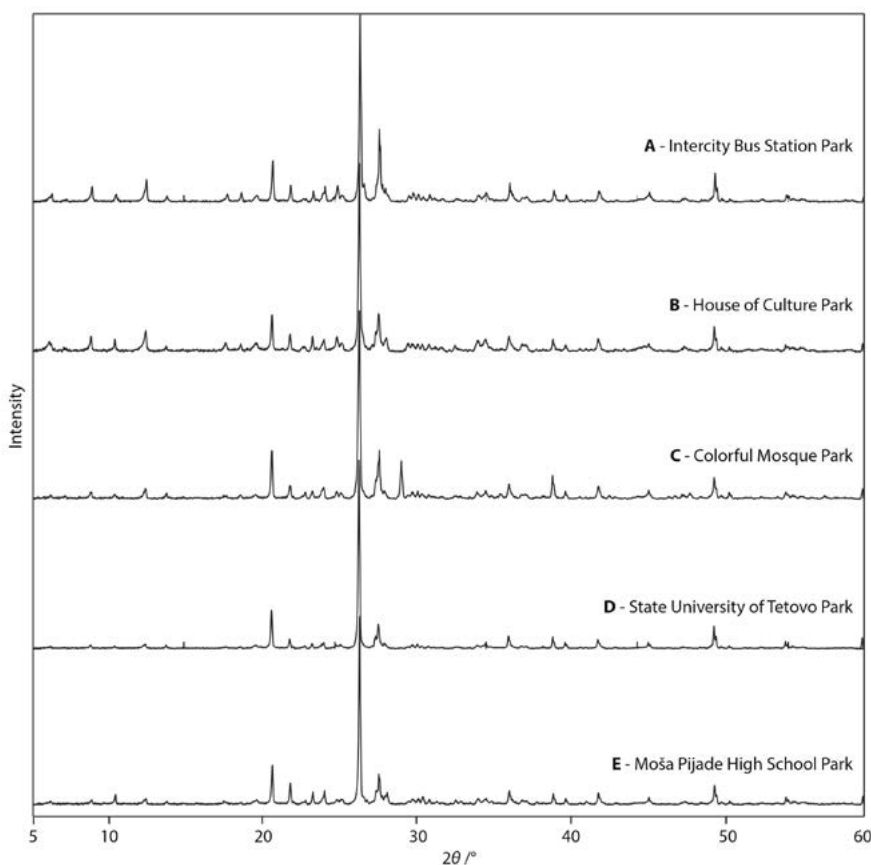
Genetic algorithms were also implemented in Matlab programming language. For this purpose, Genetic Al-

used.<sup>57</sup>

### 3. Results and Discussion

#### 3.1. Main Mineralogical Components

It is important to state that diffractograms from different locations are similar (see Figure 5 for the urban samples and Figure 6 for the rural samples). For more de-



gorithm Toolbox developed at University of Sheffield was

tailed comparison all diffractograms are available in the

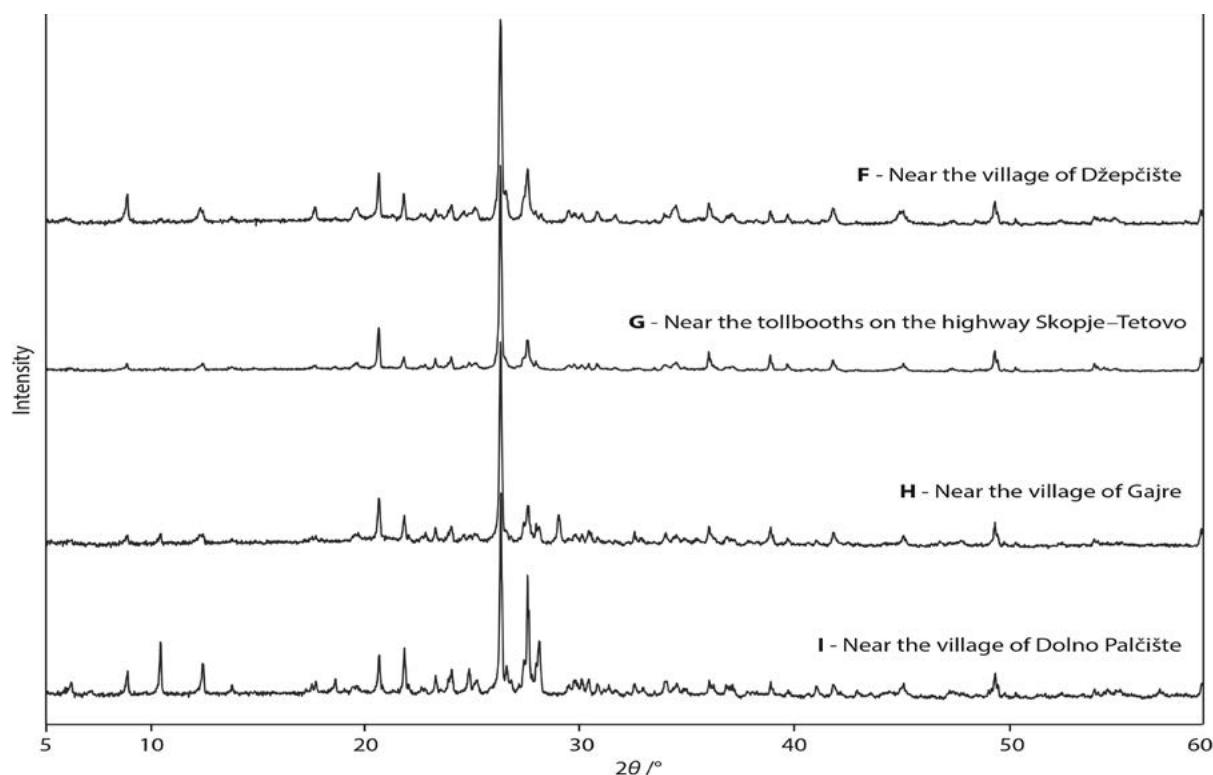


**Figure 6.** X-ray powder diffractograms for the selected samples from four rural locations. (The files with all samples from these five locations are given as Supplementary Material.)

Supplementary Material together with some additional figures. One can notice that the main differences in the diffractograms are in the relative intensities of the major components of the soil samples.

Main mineralogical components of the analyzed soil samples were found by comparing the obtained diffractograms with the diffractograms stored in COD<sup>58–64</sup> and PDF-2 databases<sup>65</sup> using Match! software.<sup>66</sup> The results show that the main component in the samples is SiO<sub>2</sub> (silicon dioxide) in a form of quartz. Three additional minerals with lower mass fractions were also detected as possible constituents of the samples. It is interesting to state that they all have an empirical formula MAlSi<sub>3</sub>O<sub>8</sub>, where M represents potassium or sodium. When M represents sodium, the mineral is known as albite. In the case when M is potassium, the mineral is orthoclase (which can make solid solutions with albite). The third mineral present in our samples is, probably, the high-temperature polymorph of albite known as sanidine.

It is important to state here that there are diffraction peaks in the recorded diffractograms which do not correspond to the previously mentioned minerals. These signals probably belong to the additional mineral components. However, due to the fact that their mass fraction and consequently the intensities of their signals are weak we were not able to identify them using previously described approach. Also, earlier we pointed out that the diffractograms from all locations are similar (Figure 5 and Figure

6). Most of the differences among the diffractograms are in the regions with diffraction peaks that have smaller intensities. This is one of the reasons why genetic algorithm was used for variable selection. In cases like this, optimization using GA performs selection of the intensities at  $2\theta$  values which can help in finding better classification models and, at the same time, it eliminates the intensities at  $2\theta$  values which are similar for all samples.

### 3. 2. Principal Component Analysis

The principal component analysis (PCA) which was performed on the auto-scaled data matrix showed us that about 92% of the variance in the pre-processed diffractograms was captured by first 16 principal components (PCs). As previously stated, these PCs were used for development of the SOM models which will be able to classify the samples according to their geographic origin. However, before the development of the models started, we used PCA as an auxiliary tool in order to evaluate whether the samples from different location were at least partially separated. This is important since the main goal of this work is determination of the origin of the soil samples. The first two principal components (labeled as: PC1 and PC2) are presented on Figure 7a. The first (PC1) and third (PC3) principal components are presented on Figure 5b. A careful examination of these two figures (Figure 7a and b) shows that all samples taken from the rural locations (F, G,

H and I) are grouped in the first and fourth quadrant. Having in mind that these two figures are projections of the three-dimensional space defined by PC1, PC2 and PC3, it is easy to see that the samples from these four locations form well separated clusters. The reason for this might be the fact that most of the rural locations from which the samples were collected are at distances larger than 4 km. Only the distance between locations H and I is smaller than 4 km.

In the second and third quadrant, the remaining samples from the urban location are grouped. Here it could be seen that there is a partial overlap among the samples from all urban locations. Also, most of the samples from location C are well separated from the remaining samples (see Figure 7b). Likewise, the reason for larger overlap between these clusters might be the fact that these locations are closer one to another. As previously stated, the distanc-

tions composed of 100 binary chromosomes. The initial values of genes in the chromosomes were randomly generated. Different parts of these chromosomes were responsible for decoding different parameters for the supervised SOMs. In this case 259 genes were used for variable selection. After the variable selection was performed, PCA was applied on the selected intensities. The number of PCs used during the optimization varied between 1 and 16. For this purpose, four additional genes were allocated in the chromosomes. Eight more genes were allocated for decoding the width and length of the supervised SOM. These two parameters were changed in the interval between 7 and 22. Four more genes were dedicated for selection of the number of epochs in the rough training phase, which is performed in larger neighborhood and larger learning rate. The number of epochs here was changed in the interval between 10 and 25. Finally, for the number of epochs in

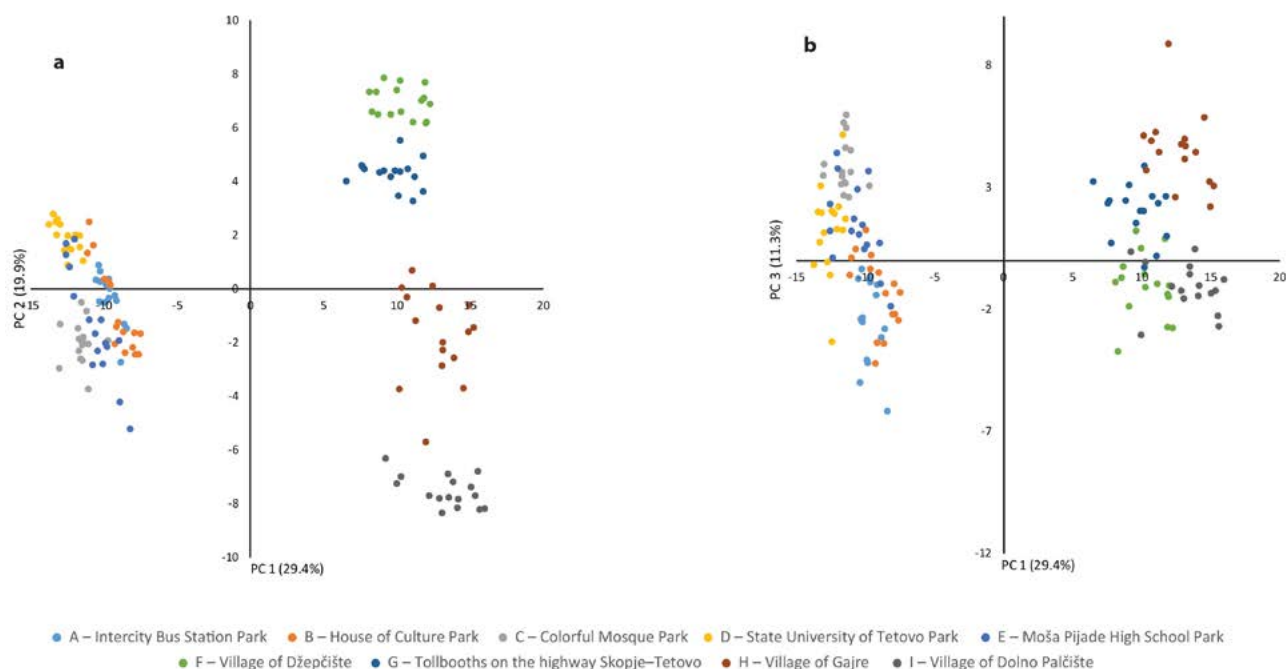


**Figure 7.** The soil samples presented in the space defined by first (PC1) and second (PC2) as well as the first (PC1) and third (PC3) principal component obtained from autoscaled matrix.

es between the parks (1) next to the Intercity Bus Station (labeled as A), (2) House of Culture Park (labeled as B) and (3) Colorful Mosque Park (labels: C) vary between 1 and 1.5 km. While the distance between the park labeled as D (State University of Tetovo Park) and park labeled as E (Moša Pijade High School Park) is only about 300 m.

### 3. 3. Optimization of the SOM Models Using Genetic Algorithms

As earlier stated, the optimization of the models based on supervised self-organizing maps was performed using GAs. For optimization purposes, we used popula-

the fine-tuning phase, additional seven genes were selected. The use of seven binary genes could produce the maximal number of epochs 127 and the minimal number of epoch zero. In order to avoid the zero which appears here, but also to be sure that number of epochs in the fine-tuning phase is larger than that obtained in the rough training phase, the number of epochs obtained by these genes was increased by the number of epochs obtained for the rough training phase.

Before the optimization with GA started, we had to properly separate the data set into training and test data sets in order to obtain good generalization performances. The training data set was used for the optimization of

**Table 2.** Six selected models with best performances (misclassified samples). The size of the network, the training parameters, the number of principal components used for training of supervised SOMs, as well as the labels of the misclassified samples are also presented.

Model	Size of the SOM		Training epochs		No of principal components	Misclassified samples				Labels for the misclassified samples					
	Width	Length	Rough	Fine		Training	Cross validation	Test	Real	Test set			Real samples		
										A42	D41	E11	E3	E4	H4
1	14	11	16	228	8	0	0	2	1		E	C	D		
2	15	9	17	131	9	0	1	2	1		E	C			G
3	17	9	13	260	6	0	1	2	2	B	E		D	A	
4	8	20	16	101	7	0	3	2	1		E	C			G
5	12	13	15	91	6	0	1	1	2	B				B	G
6	21	8	17	163	7	0	1	1	1			C	D		

the models. During the optimization, the generalization performances of the models were controlled by cross-validation. After the optimization was finished, additional validation of the models was performed using the test set composed of samples which were not used during the training of the models. The original data set (*D*) was divided into training and test set using Kennard-Stone algorithm separately for each location.<sup>67</sup> Using this algorithm, five of the sixteen diffractograms from each location were selected to be part of the test set. The remaining eleven samples were stored into the training data set. As a result, our training set was composed of 99 diffractograms and the test set was composed of the remaining 45 diffractograms.

The entire search for optimal classification model performed by GA was repeated several times. Using this approach, we were able to obtain more than 100 models with good generalization performances. Some of the best models are presented on Table 2. The criteria for selection of these models for presentation were: (1) The size of the SOMs should be different; (2) If the only difference between the models were in number of the training epochs, then the one with smaller number of epochs was selected; (3) Finally, the most important criteria was the performances on the independent test set.

The examination of the results obtained for the test set (presented in Table 2) shows that three soil samples are most often misclassified. Two of these samples (labeled as D41 and E11) are from the locations that are at a distance of about 300 m. These two locations are: D – State University of Tetovo Park and E – Moša Pijade High School Park. As an illustration, the trained supervised SOM, which corresponds to model 1 in Table 2, is presented on Figure 6. Percentage of incorrectly classified samples from the test set which was used for examination of the generalization performances of the trained SOM vary between 2.2% for the model number 6 up to 4.4% for all other models presented in Table 2.

In our previous work, when we developed different models for classification of the urban soils based on infrared spectroscopy, the samples from these two parks were most often misclassified, probably due to smaller difference in the composition of the soils on these two lo-

cations.<sup>40</sup> In this case, the sample D41 is misclassified as a sample from Moša Pijade High School Park (label: E). However, the second of these samples (label: E11) is classified together with the samples taken from the park which is in the neighborhood of the Colorful Mosque (labels: C).

The third misclassified sample was taken from Intercity Bus Station Park (labels: A). This sample was classified together with the samples from House of Culture Park (labels: B) by two of the presented models.

Compared to the results which we obtained using infrared spectra of the urban soils, where only one sample was misclassified, we have to state that, in that case, due to higher overlap between signals in the infrared spectra there we were not able to develop good classification models which will be able to classify all five urban soils samples.<sup>40</sup> In that case, as stated earlier, we were forced to use *one-against-the-rest* approach and, consequently, we developed five separate models in order to obtain good classification models for all five locations.

Due to exposure to (1) seasonal changes, (2) biological processes and (3) the changing weather conditions, the composition of the soil is slowly changing. Sometimes, during the forensic investigations, by order of court or in the cases where the crime has been detected few years after it has been committed, in order to perform reliable detection of the origin of the soils, it is important to know how these variations in composition of the soils could influence the results. In order to examine the influence of the previously mentioned factors on the performances of the models developed here, three years after the initial samples were collected four more samples were collected from seven of nine original locations used in this study. The seven selected locations are labeled: B, D, E, F, G, H and I (see Table 1 for more details). Total number of newly collected samples was 28. These samples were treated in a same way as the initial 144 samples from all nine locations (see Experimental part).

As shown in Figure 8 which represents model 1 (presented in Table 2), only one sample from location E (with label E3) is misclassified as a sample from the nearby park (State University of Tetovo Park).

For the remaining models, the misclassified samples are also presented in Table 2. Here one can see that only

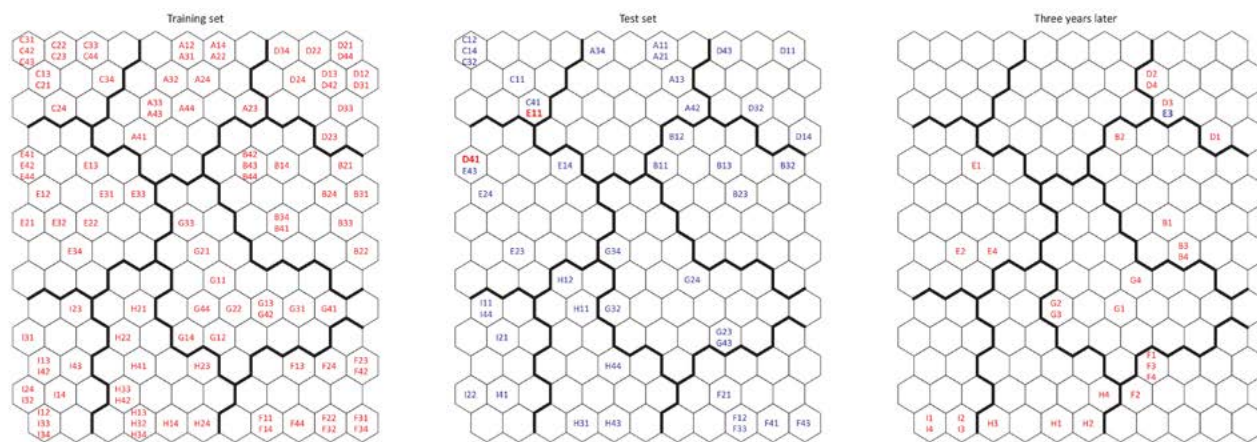


**Figure 8.** Supervised self-organizing map which corresponds to model 1 in Table 2 labelled with (a) samples from the training set, (b) samples from the test set and (c) with samples collected three years later in order to examine the influence of the weather and the seasonal changes on the composition of the soil on different locations. The misclassified samples are labelled with bold characters in different color than the remaining labels.

three of these samples are misclassified by more than one model. One of these samples (E3) was already discussed. The remaining two samples are labeled as E4 and H4. Two of the samples are from Moša Pijade High School Park (E3 and E4). Here the sample labeled as E4 is mapped once in the part of the supervised SOM that serves for recognition of the samples from location A and the second time it is misclassified together with the samples from location B.

## 4. Conclusion

In this study 144 samples from five urban and four rural locations were analyzed using supervised self-organizing maps. As a tool for automated search for the best models, genetic algorithms were used. Performances of the models during the optimization were controlled using cross-validation. Further, the generalization performances were examined using the test set which was not used during the training. The best models obtained and presented in this study were able to correctly classify between 95.6 and 97.8% of the test samples.

Having in mind that in our previous work, where the classification was performed using infrared spectra of the analyzed samples, due to the highly overlapping signals we had to develop five different models for successful classification of the samples from five urban locations. In this study, probably because the signals from the minor components of the analyzed soils in the X-ray diffractograms were well separated and, with the help from GA, we were able to select intensities which could help in better discrimination of the soil sample we were able to successfully classify most of the samples from all nine locations with a single model.

The performances of the models obtained here are comparable to those obtained in our previous work.<sup>40</sup> However, there in order to perform successful classification of the samples from the five locations there we had

to develop separate models for each location. While here, using X-ray diffractograms of the samples, with only one model, we were able to correctly classify between 95.6 and 97.8% of the samples.

As previously stated in this study, it is also important to check the robustness of the model on the changes of the composition of the samples due to the changes of the environment. For this purpose, additional 28 samples were collected from seven locations (B, D, E, F, G, H and I). The best models presented here are capable of correctly classifying 27 of 28 samples collected three years after the initial soil samples were analyzed.

## 5. References

1. P. R. Owens, E. M. Rutledge, *Morphology*, chapter in *Encyclopedia of soils in the environment*, D. Hillel (Ed.), Elsevier, Amsterdam, **2005**.
2. K. Inmana, N. Rudin, *Forensic Sci. Int.* **2002**, *126*, 11–16. DOI:10.1016/s0379-0738(02)00031-2.
3. D. Werner, C. Burnier, Y. Yu, A. R. Marolf, Y. Wang, G. Massonnet, *Sci. Justice* **2019**, *59*, 643–653. DOI:10.1016/j.scijus.2019.07.004
4. K. Pye, D. Croft, *Forensic Sci. Int.* **2007**, *165*, 52–63. DOI:10.1016/j.forsciint.2006.03.001.
5. B. G. Rawlins, S. J. Kemp, E. H. Hodgkinson, J. B. Riding, C. H. Vane, C. Poulton, K. Freeborough, *J. Forensic Sci.* **2006**, *51*, 832–845. <http://doi.10.1111/j.1556-4029.2006.00152.x>
6. S. Cengiza, A. C. Karaca, I. Çakır, H. B. Üner, A. Sevindik, *Forensic Sci. Int.* **2004**, *141*, 33–37. DOI:10.1016/j.forsciint.2003.12.006.
7. P. A. Bull, A. Parker, R. M. Morgan, *Forensic Sci. Int.* **2006**, *162*, 6–12. DOI:10.1016/j.forsciint.2006.06.075.
8. R. M. Morgan, P. A. Bull, *Environ. Forensics* **2006**, *7*, 325–334. DOI:10.1080/15275920600996248.
9. L. Arroyo, T. Trejos, T. Hosick, S. Machermer, J. R. Almirall, P.

- R. Gardinali, *Environ. Forensics* **2010**, *11*, 315–327. DOI:10.1080/15275922.2010.494949.
10. L. Reidy, K. Bu, Murrell, G. James, V. Cizdziel, *Forensic Sci. Int.* **2013**, *233*, 37–44. DOI:10.1016/j.forsciint.2013.08.019.
11. J. M. L. Mazzetto, V. F. Melo, E. J. Bonfleura, P. Vidal-Torradob, J. Dieckowa, *Sci. Justice* **2019**, *59*, 635–642. DOI:10.1016/j.scijus.2019.07.003.
12. P. M. Medeiros, B. R. T. Simoneit, *J. Sep. Sci.* **2007**, *30*, 1516–1536. DOI:10.1002/jssc.200600399.
13. S. C. Jantzi, J. R. Almirall, *Anal. Bioanal. Chem.* **2011**, *400*, 3341–3351. DOI:10.1007/s00216-011-4869-7
14. B. W. Kamrath, A. Koutrakos, J. Castillo, C. Langley, D. H. Jones, *Forensic Sci. Int.* **2018**, *285*, e25–e33. DOI:10.1016/j.forsciint.2017.12.034
15. K. Ritz, L. Dawson, D. Miller (Eds.), *Criminal and Environmental Soil Forensics*. Soil Forensics International, Edinburgh Conference Centre, Springer, **2008**.
16. X. Xu, C. Du, F. Ma, Y. Shen, J. Zhou, *Forensic Sci. Int.* **2020**, *310*, 110222. DOI:10.1016/j.forsciint.2020.110222
17. R. J. Cox, H. L. Peterson, J. Young, C. Cusik, E. O. Espinoza, *Forensic Sci. Int.* **2000**, *108*, 107–116. DOI:10.1016/S0379-0738(99)00203-0
18. B. A. Weinger, J. A. Reffner, P. R. De Forest, *J. Forensic Sci.* **2009**, *54*, 851–856. DOI:10.1111/j.1556-4029.2009.01064.x
19. L. A. Dawson, S. Hillier, *Surf. Interface Anal.* **2010**, *42*, 363–377. DOI:10.1002/sia.3315
20. M. D. Suarez, R. J. Southard, S. J. Parikh, *J. Forensic Sci.* **2015**, *60*, 894–905. DOI:10.1111/1556-4029.12762.
21. J. M. Soriano-Disla, L. J. Janik, R. A. V. Rossel, L. M. Macdonald, M. J. McLaughlin, *Appl. Spectrosc. Rev.* **2014**, *49*, 139–186. DOI:10.1080/05704928.2013.811081
22. V. Sharma, J. Yadav, R. Kumar, D. Tesarova, A. Ekielski, P. K. Mishrad, *Vib. Spectrosc.* **2020**, *110*, 103097. DOI:10.1016/j.vibspec.2020.103097.
23. V. Sharma, S. Bhardwaj, R. Kumar, *Vib. Spectrosc.* **2019**, *101*, 81–91. DOI:10.1016/j.vibspec.2019.02.006.
24. R. R. E. Artz, S. J. Chapman, A. H. J. Robertson, J. M. Potts, F. Laggoun-Défarge, S. Gogo, L. Comont, J. R. Disnar, A. J. Francez, *Soil Biol. Biochem.* **2008**, *40*, 515–527. DOI:10.1016/j.soilbio.2007.09.019.
25. Š. Matějková, T. Šimon, *Plant Soil Environ.* **2012**, *58*, 192–195. DOI:10.17221/317/2011-PSE
26. S. Bashir, J. Liu, *Advanced nanomaterials and their applications in renewable energy*, Elsevier, Amsterdam, **2015**.
27. L. V. Prandel, V. F. Melo, A. M. Brinatti, S. C. Saab, F. A. S. Salvador, *J. Forensic Sci.* **2018**, *63*, 251–257. DOI:10.1111/1556-4029.13476.
28. A. Ruffella, P. Wiltshire, *Forensic Sci. Int.* **2004**, *145*, 13–23. DOI:10.1016/j.forsciint.2004.03.017.
29. T. Kohonen, *Self-Organizing Maps*, 3rd Edition, Springer, Berlin, **2001**.
30. R. Chauhan, R. Kumar, V. Sharma, *Microchem. J.* **2018**, *139*, 74–84. DOI:10.1016/j.microc.2018.02.020
31. V. Sharma, R. Kumar, *TrAC – Trends Anal. Chem.* **2018**, *107*, 181–195. DOI:10.1016/j.trac.2018.08.006
32. R. Kumar, V. Sharma, *TrAC – Trends Anal. Chem.* **2018**, *105*, 191–201. DOI:10.1016/j.trac.2018.05.010
33. M. Baron, J. G. Rodriguez, R. Croxton, R. Gonzalez, R. Jimenez, *J. Appl. Spectrosc.* **2011**, *65*, 1151–1161. DOI:10.1366/10-06197
34. R. Chauhan, R. Kumar, P. K. Diwan, V. Sharma, *Forensic Chem.* **2020**, 100191. DOI:10.1016/j.forc.2019.100191
35. M. E. Sigman, M. R. Williams, *WIREs Forensic. Sci.* **2020**, *2*, e1368. DOI:10.1002/wfs2.1368
36. C. S. Leea, T. M. Sung, H. S. Kim, C. H. Jeon, *J. Anal. Appl. Pyrol.* **2012**, *96*, 33–42. DOI:10.1016/j.jaap.2012.02.017
37. M. I. Kaniu, K. H. Angeyo, *Geoderma* **2015**, *241–242*, 32–40. DOI:10.1016/j.geoderma.2014.10.014.
38. N. C. Thanasoulas, E. T. Piliouris, M. S. E. Kotti, N. P. Evmiridis, *Forensic Sci. Int.* **2002**, *130*, 73–82. DOI:10.1016/s0379-0738(02)00369-9.
39. M. Baron, J. Gonzalez-Rodriguez, R. Croxton, R. Gonzalez, R. Jimenez-Perez, *Appl. Spectrosc.* **2011**, *65*, 1151–1161. DOI:10.1366/10-06197.
40. H. Idrizi, M. Najdoski, I. Kuzmanovski, *J. Chemom.* **2021**, *35*, e3328. DOI:10.1002/cem.3328
41. T. Kohonen, *Computer*, **1988**, *21*, 11–22.
42. J. Zupan, M. Novic, I. Ruisánchez, *Chemometr. Intell. Lab. Syst.* **1997**, *38*, 1–23. DOI:10.1016/S0169-7439(97)00030-0
43. J. Zupan, J. Gasteiger, *Neural Networks in Chemistry and Drug Design*. WCH: Weinheim, **1999**.
44. MATLAB 7.12 (R2011a), 1984–2011, MathWorks.
45. J. Vesanto, J. Himberg, E. Alhoniemi, J. Parhankangas, *SOM Toolbox for Matlab 5*, Technical Report A57, Helsinki University of Technology, **2000**.
46. <http://www.cis.hut.fi/projects/somtoolbox/> (assessed: July 15, 2023).
47. J. Vesanto, *Intell. Data Anal.* **1999**, *6*, 111–126.
48. C. B. Lucasius, S. Werten, A. Vanaert, G. Kateman, M. J. J. Blommers, *Lect. Notes Comput. Sci.* **1991**, *496*, 90–97.
49. D. Jouan-Rimbaud, D. L. Massart, R. Leardi, O. E. de Noord, *Anal. Chem.* **1995**, *67*, 4295–4301. DOI:10.1021/ac00119a015
50. C. B. Lucasius, G. Kateman, *TrAC – Trends Anal. Chem.* **1991**, *10*, 254–261.
51. M. Bos, H. T. Weber, *Anal. Chim. Acta* **1991**, *247*, 97–105. DOI:10.1002/bip.360320107
52. R. Leardi, A. Lupiañez Gonzales, *Chemometr. Intell. Lab. Syst.* **1998**, *41*, 195–207.
53. H. Handels, T. Roß, J. Kreuzsch, H. H. Wolff, S. J. Pöppel, *Artif. Intell. Med.* **1999**, *16*, 283–297.
54. S. S. So, M. Karplus, *J. Med. Chem.* **1996**, *39*, 5246–5256.
55. I. Kuzmanovski, M. Trpkovska, B. Šoptrajanov, *J. Mol. Struct.* **2005**, *744–747*, 833–838.
56. N. Stojić, S. Erić, I. Kuzmanovski, *J. Mol. Graph. Model.* **2010**, *29*, 450–460.
57. A. Chipperfield, P. Fleming, H. Pohlheim, C. Fonseca, *Genetic algorithm toolbox user's guide*, University of Sheffield, Sheffield, **1994**.
58. A. Merkys, A. Vaitkus, A. Grybauskas, A. Konovalovas, M. Quirós, S. Gražulis, *J. Cheminformatics* **2023**, *15*(25). DOI:10.1186/s13321-023-00692-1

59. A. Vaitkus, A. Merkys, S. Gražulis, *J. Appl. Crystallogr.* **2021**, 54(2), 661–672. DOI:10.1107/S1600576720016532
60. M. Quirós, S. Gražulis, S. Girdzijauskaitė, A. Merkys, A. Vaitkus, *J. Cheminformatics* **2018**, 10(23). DOI:10.1186/s13321-018-0279-6
61. A. Merkys, A. Vaitkus, J. Butkus, M. Okulič-Kazarinas, V. Kairys, S. Gražulis, *J. Appl. Crystallogr.* **2016**, 49. DOI:10.1107/S1600576715022396
62. S. Gražulis, A. Merkys, A. Vaitkus, M. Okulič-Kazarinas, *J. Appl. Crystallogr.* **2015**, 48, 85–91. DOI:10.1107/S1600576714025904
63. S. Gražulis, A. Daškevič, A. Merkys, D. Chateigner, L. Lutterotti, M. Quirós, N. R. Serebryanaya, P. Moeck, R. T. Downs, A. LeBail, *Nucleic Acids Res.* **2012**, 40, D420–D427. DOI:10.1093/nar/gkr900
64. S. Gražulis, D. Chateigner, R. T. Downs, A. T. Yokochi, M. Quiros, L. Lutterotti, E. Manakova, J. Butkus, P. Moeck, A. Le Bail, *J. Appl. Crystallogr.* **2009**, 42, 726–729. DOI:10.1107/S0021889809016690
65. ICDD, PDF-2 2011 (Database), S. Kalakkodu (Ed.), Newtown Square: Int. Centre Diffraction Data, **2011**.
66. Match! - Phase Analysis using Powder Diffraction, Version 3.x, Crystal Impact - Dr. H. Putz & Dr. K. Brandenburg GbR, Kreuzherrenstr. 102, 53227 Bonn, Germany, <https://www.crystalimpact.de/match>.
67. R. W. Kennard, L. A. Stone, *Dent Tech.* **1969**, 11, 137–148.

## Povzetek

Zaradi svoje prenosljivosti se tla pogosto uporabljajo kot dokazni material v kriminalnih preiskavah. V tej raziskavi smo odvzeli 172 vzorcev tal iz petih urbanih parkov v mestu Tetovo (Severna Makedonija) in iz dodatnih štirih podeželskih lokacij v njegovi bližini. Vzorce tal smo preiskali z uporabo X-žarkovne praškovne difrakcije. Zbrane difraktogramne smo uporabili za razvoj klasifikacijskih modelov za določitev njihovega izvora, ki temeljijo na nadzorovanih samoorganiziranih mapah. Preiskava generalizacijske sposobnosti razvitih modelov je pokazala, da so bili zmožni pravilno klasificirati med 95,6 in 97,8 % vzorcev iz neodvisnega testnega niza. Preučili smo tudi vpliv vremenskih in obdobjnih sprememb na sestavo tal. Za ta namen smo tri leta po začetnem zbiranju vzorcev tal analizirali dodatnih 28 vzorcev iz različnih lokacij. Najboljši modeli, predstavljeni v tej raziskavi, so bili zmožni uspešno klasificirati 27 od teh dodatnih vzorcev.



Except when otherwise noted, articles in this journal are published under the terms and conditions of the Creative Commons Attribution 4.0 International License

Scientific paper

# Synthesis of New of 4-Thiazolidinone and Thiazole Derivatives Containing Coumarin Moiety with Antimicrobial Activity

Reem A. K. Al-Harbi,<sup>1</sup> Marwa A. M. Sh. El-Sharief<sup>2</sup> and Samir Y. Abbas<sup>3,\*</sup><sup>1</sup> Chemistry Department, Faculty of Science, Taibah University, Almadinah Almunawwarah, Saudi Arabia.<sup>2</sup> Applied Organic Chemistry Department, National Research Centre, Cairo, Egypt.<sup>3</sup> Organometallic and Organometalloid Chemistry Department, National Research Centre, Cairo, Egypt.

\* Corresponding author: E-mail: samiryoussef98@yahoo.com; sy.abbas@nrc.sci.eg

Received: 06-19-2023

## Abstract

Synthesizing hybrid molecules is one of the best manners to achieve novel promising agents. Consequently, series of new thiazoles having coumarin nucleus were synthesized from 3-acetylcoumarin thiosemicarbazones. Cyclization of thiosemicarbazone derivatives with ethyl 2-chloroacetate, 1-chloropropan-2-one and 2-bromo-1-phenylethanone afforded the corresponding 4-thiazolidinones, 4-methylthiazoles and 4-phenylthiazoles, respectively. The expected antimicrobial properties for the synthesized thiosemicarbazone and thiazole derivatives were investigated. The thiosemicarbazones and thiazolidin-4-ones showed moderate activities against Gram-positive and Gram-negative bacteria.

**Keywords:** Thiazoles; Coumarin; Benzopyrone; Chromenes; Thiosemicarbazones; Antibacterial and antifungal activities.

## 1. Introduction

Most of microbial infections are the reason of serious diseases. The microbial resistance against the well known antimicrobial drugs is the most common antimicrobial medication problem. The infections with resistant organisms cannot be treated by using common antibiotic drugs. One of the strategies that was exercised to overcome this problem is design of novel pharmacophores. So, recently the main tasks of medicinal chemists are creation of novel antimicrobial drugs against novel molecular targets. To get powerful synergistic effect, researches were directed to combine different pharmacophores in one structure.<sup>1–4</sup>

Coumarin is family of benzopyrones and it is frequently found in nature. Coumarin is considered to be one of significant members of the family of benzopyrone scaffolds. So, the design and synthesis of coumarins are an attractive developing topic for medicinal chemists. Due to the versatility of the coumarin moiety, it is an amazing material suitable for many applications. Coumarins have been reported as anticoagulant, antioxidant, antimicrobial, anticancer, anti-diabetic, analgesic, antineurodegenerative, and anti-inflammatory agents.<sup>5–11</sup> Coumarin and its deriv-

atives are used in several anticoagulants, including warfarin, acenocoumarin, phenprocoumon, choleraicin A, hymecromone (umbelliferone) and the antibiotic novobiocin.<sup>12</sup> On the other hand, coumarins have a wide range of applications such as perfumes, cosmetics, industrial additives and aroma enhancers in tobaccos and certain alcoholic drinks.<sup>13–15</sup> Coumarin-based ion receptors, fluorescent probes, and biological stains are a quickly growing area and have extensive applications to monitor timely enzyme activity, complex biological events, as well as accurate pharmacological and pharmacokinetic properties in living cells.<sup>16</sup>

Thiazole is a privileged scaffold in medicinal chemistry; so, it has displayed crucial role in the medicinal chemistry research. Thiazole ring appears in many structures of natural compounds and some of the synthesized biologically active agents.<sup>1,17–20</sup> Thiazole nucleus constitutes an interesting class of bioactive molecules where it exhibits broad spectra of biological activities such as anti-HIV,<sup>21</sup> antimicrobial,<sup>1</sup> anticancer,<sup>22</sup> hypnotic,<sup>23</sup> anticonvulsant,<sup>17</sup> analgesic,<sup>24</sup> and anti-inflammatory<sup>24</sup> activities. Moreover, some of the derivatives of thiazole have been reported as potent antimicrobial drugs. Some examples of drugs con-



taining thiazole scaffold that are approved for medical uses are penicillin and its analogous (Figure 1) that were the first successful antibiotic drugs.

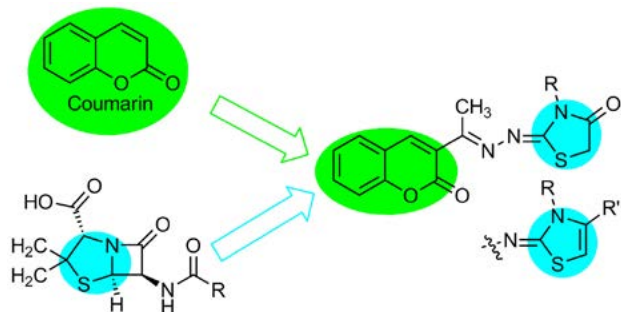


**Figure 1.** Design of new hybrids of coumarin and thiazole moieties as antimicrobial agents

Penicillins play critical roles in the therapy of the bacterial diseases.<sup>25</sup> Some examples of thiazole-based drugs are ravuconazole (antifungal agent), ritonavir (anti-HIV), tiazofurin (antineoplastic agent), dasatinib (antineoplastic agent), nitazoxanide (antiparasitic agent), thiamethoxam (insecticide), fentiazac (anti-inflammatory agent), fanetizole (anti-inflammatory agent), meloxicam (anti-inflammatory agent) and nizatidine (antiulcer agent).<sup>26</sup>

The design of our structures was depended on the validation of coumarins and some of their analogues as drugs. Many studies reported the potency of many thiazole containing compounds. In this direction, previously, we synthesized quinoline derivatives having a thiazole moiety. The thiazole derivative had a potent antimicrobial activity toward eight of the tested strains including Gram-positive and Gram-negative bacteria and fungi.<sup>1</sup>

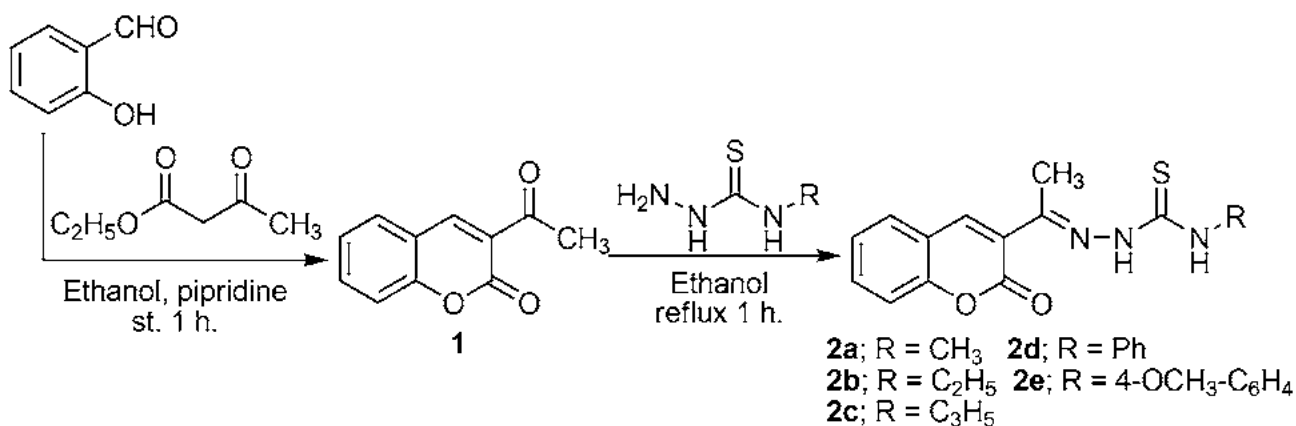
Moreover, heterocyclic compounds have been reported as a significant class of organic molecules where they are the main scaffolds for the variety of bioactive compounds.<sup>27,28</sup> So, depending on our experience in the synthesis of the thiazole derivatives,<sup>29</sup> we aim to synthesize series of coumarins bearing thiazole nucleus. Thus, the de-

rivatives of thiosemicarbazone will be subjected to ring closure by ethyl chloroacetate, chloroacetone and phenacyl bromide in the hope of obtaining potent antimicrobial thiazole derivatives.

## 2. Results and Discussion

Coumarins are usually synthesized from salicylaldehyde derivatives *via* tandem condensation Knoevenagel reaction with ester derivatives containing active methylene group in the presence of basic medium to give intermediates that are subjected to intramolecular cyclization.<sup>8</sup> Thus, 3-acetylcoumarin (**1**) was prepared in good yield by using a reported procedure with some modification<sup>14</sup> by treating salicylaldehyde with ethyl acetoacetate in ethanol containing piperidine as the catalyst. The 3-acetylcoumarin thiosemicarbazones **2a–e** were prepared as illustrated in Scheme 1.

Thiosemicarbazones of 3-acetylcoumarin were prepared through the condensation reactions between 3-acetylcoumarin (**1**) and some selected thiosemicarbazides in ethanol containing catalytic amount of acetic acid under reflux. IR spectrum of thiosemicarbazone **2a**, as an example of the formed thiosemicarbazones **2a–e**, displayed bands at: 3326, 3365, 3312  $\text{cm}^{-1}$  for NH groups, and a band at 1708  $\text{cm}^{-1}$  for the carbonyl group. Its <sup>1</sup>H NMR spectrum displayed two diagnostic aliphatic signals for two methyl groups at  $\delta$  2.26 ( $\text{CH}_3\text{-C=N}$ ) and 3.03 ppm ( $\text{NHCH}_3$ ). Beside the characteristic signal at  $\delta$  8.36 for proton at C-4 of chromene, the other protons of chromene ring appeared as two doublet signals ( $\text{C}_8\text{-H}$  at 7.43 and  $\text{C}_5\text{-H}$  at 7.79 ppm) and two triplet signals ( $\text{C}_6\text{-H}$  at 7.40 and  $\text{C}_7\text{-H}$  at 7.65 ppm). Two signals for NH groups at  $\delta$  8.50 ( $\text{NHCH}_3$ ) and 10.44 ppm ( $\text{N-NH-CS}$ ) were displayed. <sup>13</sup>C NMR spectrum of compound **2a** showed two diagnostic signals in the aliphatic region at  $\delta$  16.34 and 31.41 ppm for two methyl groups. The signals resonating in the deshielded region at 153.68, 159.74 and 179.10 ppm were assigned to the carbons of  $\text{C=N}$ ,  $\text{C=O}$  and  $\text{C=S}$ , respectively.

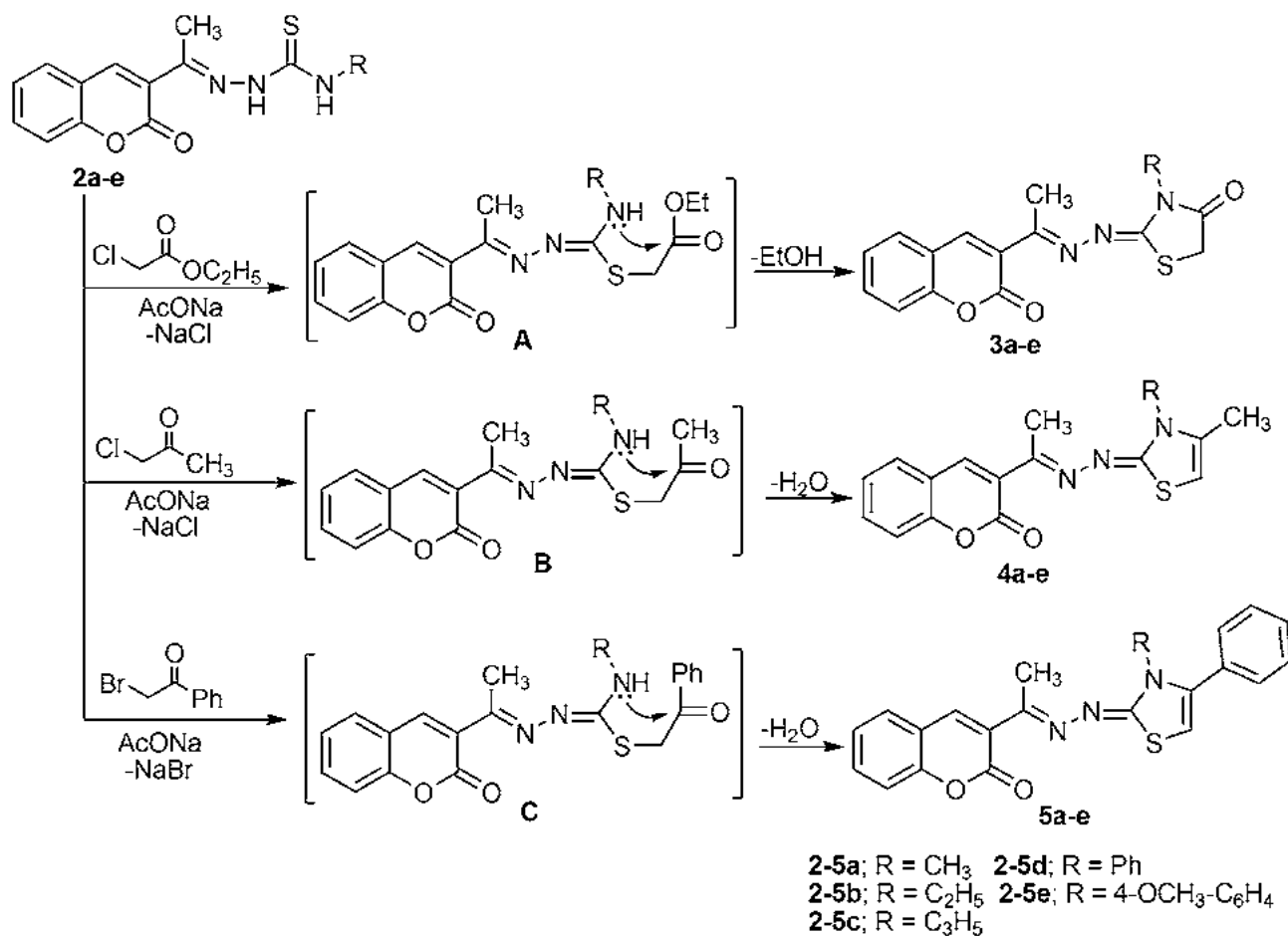


**Scheme 1.** Synthesis of the 3-acetylcoumarin thiosemicarbazones **2a–e**

Thiosemicarbazone derivatives **2a–e** were subjected to cyclize with three various halo compounds. The thiosemicarbazones **2a–e** reacted with ethyl chloroacetate in tetrahydrofuran under reflux condition resulted in the formation of the 4-thiazolidone derivatives **3a–e** in high yields as shown in Scheme 2. The formation of 4-thiazolidones **3a–e** initially takes place *via* *S*-alkylation of the thiosemicarbazones to obtain the intermediate **A**, then intramolecular cyclization occurred through the elimination of ethanol. In IR spectrum of 4-thiazolidone **3a**, a diagnostic band at  $1712\text{ cm}^{-1}$  for carbonyl group was observed. Its  $^1\text{H}$  NMR spectrum revealed three characteristic aliphatic signals for two methyl groups and  $\text{CH}_2$ -thiazole at  $\delta$  2.37, 3.21 and 3.96 ppm, respectively. The chromene protons were assigned at 7.40 (triplet,  $\text{C}_6\text{-H}$ ), 7.46 (doublet,  $\text{C}_8\text{-H}$ ), 7.68 (triplet,  $\text{C}_7\text{-H}$ ), 7.88 (doublet,  $\text{C}_5\text{-H}$ ), and 8.21 ppm (singlet,  $\text{C}_4\text{-H}$ ). Under the same reaction conditions, cyclocondensation of thiosemicarbazone derivatives **2a–e** with 1-chloropropan-2-one furnished the corresponding 4-methylthiazole derivatives **4a–e**. The formation of 4-methylthiazoles **4a–e** was carried out through *S*-alkylation of thiosemicarbazones to obtain intermediate **B**, then intramolecular cyclization occurred through the elimina-

tion of a molecule of water. IR spectrum of **4a** exhibited a diagnostic band at  $1716\text{ cm}^{-1}$  for carbonyl group. Its  $^1\text{H}$  NMR spectrum exhibited two diagnostic aliphatic singlet signals for methyl protons at  $\delta$  2.17 ( $\text{CH}_3$ -thiazole) and 2.32 ppm (s, 3H,  $\text{CH}_3\text{-C=N}$ ). The characteristic H-5 proton of thiazole was found at  $\delta$  6.09 ppm. The diagnostic  $\text{C}_4\text{-H}$  of chromene appeared at  $\delta$  8.11 ppm.

Moreover, similarly to the above mentioned condition, ring closing of thiosemicarbazones **2a–e** by 2-bromo-1-phenylethanone (phenacyl bromide) furnished the corresponding 4-phenylthiazole derivatives **5a–e**. Also, the formation of 4-phenylthiazoles **5a–e** was carried out through *S*-alkylation of thiosemicarbazones to obtain intermediate **C**, then intramolecular cyclization occurred through the elimination of a molecule of water. IR spectrum of **5a** exhibited diagnostic absorption band for carbonyl group at  $1710\text{ cm}^{-1}$ .  $^1\text{H}$  NMR spectrum of **5a** displayed two diagnostic signals for two methyl group at  $\delta$  2.35 ( $\text{CH}_3\text{-C=N}$ ), 3.36 ppm ( $\text{NCH}_3$ ). The proton of  $\text{CH}$ -thiazole was displayed at  $\delta$  6.448 ppm. The protons of chromene ring were displayed at 7.38 ( $\text{C}_6\text{-H}$ ), 7.44 ( $\text{C}_8\text{-H}$ ), 7.63 ( $\text{C}_7\text{-H}$ ), 7.86 ( $\text{C}_5\text{-H}$ ), 8.15 ppm ( $\text{C}_4\text{-H}$ ), while the protons of phenyl ring were displayed at 7.53 ppm. Its  $^{13}\text{C}$



**Scheme 2.** Syntheses of 4-thiazolidinone derivatives **3a–e**, 4-methyl-2,3-dihydrothiazole derivatives **4a–e** and 4-phenyl-2,3-dihydrothiazole derivatives **5a–e**.

NMR spectrum exhibited four diagnostic signals at  $\delta$  16.96 and 33.98 ppm for two methyl carbons. Three signals were observed in the deshielded region at 153.63, 159.91 and 170.44 ppm for carbons of  $2 \times \text{C}=\text{N}$  and  $\text{C}=\text{O}$ .

## 2. 1. Antibacterial and Antifungal Activities

For all new synthesized thiosemicarbazones **2a–e**, 4-thiazolidinones **3a–e**, 4-methylthiazoles **4a–e** and 4-phenylthiazoles **5a–e** were evaluated their antibacterial and antifungal properties. For the screening of antibacterial activity, diffusion agar technique<sup>1</sup> was applied at 5 mg/mL concentration (50  $\mu\text{L}$  was tested), well diameter 6.0 mm. The obtained inhibition zone diameters are given in Table 1. The following three microbial categories were estimated. Category 1: Gram-positive bacteria: *Staphylococcus aureus* (ATCC25923) and *Bacillus subtilis* (RCMB015 NR-RL B-543). Category 2: Gram-negative bacteria: *Escherichia coli* (ATCC25922) and *Proteus vulgaris* (RCMB004 ATCC13315). Category 3: Fungi: *Aspergillus fumigatus* (RCMB002008) and *Candida albicans* (RCMB005003 ATCC10231).

Few compounds showed good effects towards some bacteria. All of the compounds gave no effects towards fungi. Definite interpretation will be clarified. The 3-acetyl coumarin thiosemicarbazone derivatives **2a–e** carried various substituents at terminal nitrogen atom. The prosperity of each substituent was estimated. Changing the substituent on nitrogen atom from methyl to ethyl to allyl to phenyl to 4-methoxyphenyl (**2a** / **2b** / **2c** / **2d** / **2e**) was

used to estimate the variation between them. It was noted that there is a moderate variation in antimicrobial property between the thiosemicarbazone derivatives; this suggested that the main antimicrobial activity may be due to the presence of the coumarin and thiosemicarbazone scaffolds. All thiosemicarbazones **2a–e** showed moderate activity toward Gram-positive bacteria. Almost all of the thiosemicarbazones **2a–e** displayed moderate activity toward Gram-negative bacteria. Ring closure of thiosemicarbazones **2a–e** with ethyl chloroacetate to give the 4-thiazolidinones **3a–e** does not improve the antimicrobial activity. The thiazolidin-4-ones **3a–e** gave nearly the same effects as thiosemicarbazone derivatives **2a–e** toward the tested organisms. Ring closure of the thiosemicarbazone derivatives **2a–e** with chloroacetone to give the 4-methylthiazoles **4a–e** decreased the antimicrobial activity. The 4-methylthiazoles **4a–e** gave lesser effects than their thiosemicarbazone derivatives **2a–e** against the tested organisms. Ring closure of the thiosemicarbazones **2a–e** with phenacyl bromide to give the 4-phenylthiazoles **5a–e** gave bad effects where the 4-phenylthiazoles **5a–e** gave no effects towards all the tested organisms.

## 3. Conclusion

To investigate new antimicrobial drugs, five 3-acetyl coumarin thiosemicarbazones **2a–e**, five 4-thiazolidinones **3a–e**, five 4-methylthiazoles **4a–e** and five 4-phenylthiazoles **5a–e** were efficiently synthesized. The antibacterial

Table 1. The mean inhibition zones measured for the pathogenic microorganisms (in mm)

Compd. No	Gram-positive bacteria		Gram-negative bacteria		Fungi	
	<i>S. aureus</i>	<i>B. subtilis</i>	<i>E. coli</i>	<i>P. vulgaris</i>	<i>A. fumigatus</i>	<i>C. albicans</i>
2a	11	22	NA	12	NA	NA
2b	13	20	NA	13	NA	NA
2c	15	21	13	15	NA	NA
2d	13	15	11	14	NA	NA
2e	14	17	12	13	NA	NA
3a	10	9	11	10	NA	NA
3b	11	12	13	12	NA	NA
3c	13	13	10	13	NA	NA
3d	14	18	11	15	NA	NA
3e	15	17	9	12	NA	NA
4a	10	NA	NA	NA	NA	NA
4b	9	10	NA	NA	NA	NA
4c	11	15	NA	12	NA	NA
4d	10	17	NA	13	NA	NA
4e	12	NA	11	NA	NA	NA
5a	NA	NA	10	NA	NA	NA
5b	NA	NA	NA	NA	NA	NA
5c	NA	NA	NA	NA	NA	NA
5d	NA	NA	NA	NA	NA	NA
5e	NA	NA	NA	NA	NA	NA
Gentamycin	24	26	30	25	—	—
Ketoconazole	—	—	—	—	17	20

and antifungal properties were investigated. Few thiosemicarbazone and thiazole derivatives gave good activity against some microorganisms. The thiosemicarbazones **2a–e** and thiazolidin-4-ones **3a–e** showed moderate effect toward Gram-negative and Gram-positive bacteria. The 4-phenylthiazoles **5a–e** gave no effects towards all the tested organisms. None of the derivatives gave any effect toward fungi.

### 3. 1. Experimental Section

NMR spectra were recorded on Bruker spectrometer ( $^1\text{H}$  NMR at 400 MHz and  $^{13}\text{C}$  NMR at 101 MHz) in deuterated dimethylsulfoxide ( $\text{DMSO}-d_6$ ) with chemical shift in  $\delta$  from internal standard TMS. Elemental analyses were determined on EuroVector apparatus C, H, N analyzer EA3000 Series.

### 3. 2. Preparation of 3-Acetyl-2H-chromen-2-one (1)

To a solution of salicylaldehyde (10 mmol, 1.22 g) in ethanol (20 mL), ethyl acetoacetate (12 mmol, 1.56 g) was added while stirring. After that, piperidine (catalytic amount) was added. The stirring was continued for 1 h at room temperature. The obtained solid product was formed. The pure precipitate was collected by filtration and washed with cold methanol. The obtained 3-acetyl-coumarin (**1**) was used for further reactions without purification.

### 3. 3. Synthesis of 3-Acetylcoumarin Thiosemicarbazone Derivatives 2a–e

A mixture of 3-acetylcoumarin **1** (0.01 mol, 1.88 g) and the selected thiosemicarbazide derivatives (0.01 mol) (namely: *N*-methylthiosemicarbazide (1.05 g), *N*-ethylthiosemicarbazide (1.19 g), *N*-allylthiosemicarbazide (1.31 g), *N*-phenylthiosemicarbazide (1.67 g), or *N*-(4-methoxyphenyl)-thiosemicarbazide (1.97 g) was heated in a mixture of ethanol (60 mL) and acetic acid (3 mL) for 1 h under reflux. The resultant precipitated products were collected by filtration and recrystallized from dioxane.

**N-Methyl-2-(1-(2-oxo-2H-chromen-3-yl)ethylidene)hydrazinecarbothioamide (2a).** Yield 2.2 g (80%); m.p. 197–198 °C (m.p. lit. 192–194 °C<sup>30</sup>). IR:  $\nu$  3365, 3312 ( $2\times\text{NH}$ ), 3033 (CH-Ar), 2934, 2989 (CH-aliph.), 1708 (C=O), 1605  $\text{cm}^{-1}$  (C=N);  $^1\text{H}$  NMR:  $\delta$  2.26 (s, 3H,  $\text{CH}_3\text{-C=N}$ ), 3.03 (d, 3H,  $J = 4.6$  Hz,  $\text{NHCH}_3$ ), 7.40 (t, 1H,  $J = 7.5$  Hz,  $\text{C}_6\text{-H}$  of chromene), 7.43 (d, 1H,  $J = 8.2$ ,  $\text{C}_8\text{-H}$  of chromene), 7.65 (t, 1H,  $J = 7.8$  Hz,  $\text{C}_7\text{-H}$  of chromene), 7.79 (dd, 1H,  $J = 7.7$ , 1.3 Hz,  $\text{C}_5\text{-H}$  of chromene), 8.36 (s, 1H,  $\text{C}_4\text{-H}$  of chromene), 8.50 (d, 1H,  $J = 4.4$  Hz,  $\text{NHCH}_3$ ), 10.44 (s, 1H, N-NH-CS);  $^{13}\text{C}$  NMR:  $\delta$  16.34 ( $\text{CH}_3$ ), 31.41 ( $\text{CH}_3$ ), 116.52 (C), 119.20 (C), 125.24 (C), 126.30 (CH),

129.54 (CH), 132.87 (CH), 142.30 (CH), 146.11 (CH), 153.68 (C=N), 159.74 (C=O), 179.10 (C=S); MS:  $m/z$  (%) 275 ( $\text{M}^+$ ; 39.8). Anal. Calcd for  $\text{C}_{13}\text{H}_{13}\text{N}_3\text{O}_2\text{S}$  (275.33): C, 56.71; H, 4.76; N, 15.26. Found: C, 56.66; H, 4.74; N, 15.30.

**N-Ethyl-2-(1-(2-oxo-2H-chromen-3-yl)ethylidene)hydrazinecarbothioamide (2b).** Yield 2.457 g (85%); m.p. 206–208 °C (m.p. lit. 170–172 °C<sup>30</sup>; 293–295 °C<sup>31</sup>). IR:  $\nu$  3350, 3157 ( $2\times\text{NH}$ ), 2971, 2885 (CH-aliph.), 1722 (C=O), 1607  $\text{cm}^{-1}$  (C=N);  $^1\text{H}$  NMR:  $\delta$  1.15 (t, 3H,  $J = 7.1$  Hz,  $\text{CH}_2\text{CH}_3$ ), 2.26 (s, 3H,  $\text{CH}_3\text{-C=N}$ ), 3.61 (q, 2H,  $J = 7.0$  Hz,  $\text{CH}_2\text{CH}_3$ ), 7.30–7.51 (m, 2H,  $\text{C}_6\text{-H}$ ,  $\text{C}_8\text{-H}$  of chromene), 7.64 (t, 1H,  $J = 7.8$  Hz,  $\text{C}_7\text{-H}$  of chromene), 7.79 (dd, 1H,  $J = 7.7$ , 1.4 Hz,  $\text{C}_5\text{-H}$  of chromene), 8.34 (s, 1H,  $\text{C}_4\text{-H}$  of chromene), 8.51 (t, 1H,  $J = 5.8$  Hz,  $\text{NHCH}_2$ ), 10.37 (s, 1H, N-NH-CS);  $^{13}\text{C}$  NMR:  $\delta$  13.96, 16.34, 31.41, 116.36, 119.20, 125.24, 126.28, 129.59, 132.87, 142.30, 146.11, 153.69, 159.74, 179.10; MS:  $m/z$  (%) 289 ( $\text{M}^+$ ; 71.4). Anal. Calcd for  $\text{C}_{14}\text{H}_{15}\text{N}_3\text{O}_2\text{S}$  (289.35): C, 58.11; H, 5.23; N, 14.52. Found: C, 58.07; H, 5.21; N, 14.47.

**N-Allyl-2-(1-(2-oxo-2H-chromen-3-yl)ethylidene)hydrazinecarbothioamide (2c).** Yield 2.559 g (85%); m.p. 138–139 °C. IR:  $\nu$  3366, 3209 (NH), 2989 (CH-aliph.), 1716, 1697, 1645 (C=O), 1619, 1606  $\text{cm}^{-1}$  (C=N);  $^1\text{H}$  NMR:  $\delta$  2.28 (s, 3H,  $\text{CH}_3\text{-C=N}$ ), 4.24 (t, 2H,  $J = 5.6$  Hz,  $\text{NHCH}_2$ ), 5.04–5.24 (m, 2H,  $\text{CH}_2\text{-olefinic}$ ), 5.87–5.89 (m, 1H,  $\text{CH-olefinic}$ ), 7.25–7.48 (m, 2H,  $\text{C}_6\text{-H}$ ,  $\text{C}_8\text{-H}$  of chromene), 7.65 (t, 1H,  $J = 7.8$  Hz,  $\text{C}_7\text{-H}$  of chromene), 7.80 (d, 1H,  $J = 7.7$  Hz,  $\text{C}_5\text{-H}$  of chromene), 8.36 (s, 1H,  $\text{C}_4\text{-H}$  of chromene), 8.63 (t, 1H,  $J = 5.7$  Hz,  $\text{NHCH}_2$ ), 10.51 (s, 1H, N-NH-CS);  $^{13}\text{C}$  NMR:  $\delta$  16.50 ( $\text{CH}_3$ ), 46.35 ( $\text{CH}_2$ ), 116.19 ( $=\text{CH}_2$ ), 116.43 (C), 119.26 (C), 125.21 (C), 126.42 (CH), 129.56 (CH), 132.85 (CH), 135.17 (CH), 142.2 (CH), 146.40 (CH), 153.77 (C=N), 159.51 (C=O), 178.85 (C=S); MS:  $m/z$  (%) 301 ( $\text{M}^+$ ; 46.5). Anal. Calcd for  $\text{C}_{15}\text{H}_{15}\text{N}_3\text{O}_2\text{S}$  (301.36): C, 59.78; H, 5.02; N, 13.94. Found: C, 59.81; H, 5.03; N, 13.89.

**2-(1-(2-Oxo-2H-chromen-3-yl)ethylidene)-N-phenylhydrazinecarbothioamide (2d).** Yield 3.033 g (90%); m.p. 192–193 °C (m.p. lit. 183–185 °C<sup>31</sup>). IR:  $\nu$  3219, 3178 (NH), 3113, 3048 (CH-Ar), 2887, 2292 (CH-aliph.), 1707 (C=O), 1604, 1593  $\text{cm}^{-1}$  (C=N);  $^1\text{H}$  NMR:  $\delta$  2.35 (s, 3H,  $\text{CH}_3\text{-C=N}$ ), 7.19 (t, 1H,  $J = 7.5$  Hz, Ar-H), 7.33–7.62 (m, 6H, Ar-H), 7.66 (d, 1H,  $\text{C}_7\text{-H}$  of chromene), 7.80 (d, 1H,  $\text{C}_5\text{-H}$  of chromene), 8.50 (s, 1H,  $\text{C}_4\text{-H}$  of chromene), 10.16 (s, 1H, NPh), 10.85 (s, 1H, N-NH-CS); MS:  $m/z$  (%) 337 ( $\text{M}^+$ ; 51.4). Anal. Calcd for  $\text{C}_{18}\text{H}_{15}\text{N}_3\text{O}_2\text{S}$  (337.40): C, 64.08; H, 4.48; N, 12.45. Found: C, 64.08; H, 4.48; N, 12.45.

**N-(4-Methoxyphenyl)-2-(1-(2-oxo-2H-chromen-3-yl)ethylidene)hydrazinecarbothioamide (2e).** Yield 3.303 g (90%); m.p. 183–185 °C (m.p. lit. 285–287 °C<sup>31</sup>). IR:  $\nu$  3327, 3282 (NH), 3066 (CH-Ar), 2954, 2847

(CH-aliph.), 1721  $\text{cm}^{-1}$  (C=O);  $^1\text{H}$  NMR:  $\delta$  2.34 (s, 3H,  $\text{CH}_3\text{-C=N}$ ), 3.76 (s, 3H,  $\text{OCH}_3$ ), 6.92 (d, 2H,  $J = 7.8$  Hz, Ar-H), 7.21–7.50 (m, 4H, Ar-H), 7.65 (t, 1H,  $J = 7.8$  Hz,  $\text{C}_7\text{-H}$  of chromene), 7.78 (d, 1H,  $J = 6.7$  Hz,  $\text{C}_5\text{-H}$  of chromene), 8.50 (s, 1H,  $\text{C}_4\text{-H}$  of chromene), 10.02 (s, 1H, NH-Ar-H), 10.75 (s, 1H, N-NH-CS); MS:  $m/z$  (%) 367 ( $\text{M}^+$ ; 55.8). Anal. Calcd for  $\text{C}_{19}\text{H}_{17}\text{N}_3\text{O}_3\text{S}$  (367.42): C, 62.11; H, 4.66; N, 11.44. Found: C, 62.07; H, 4.64; N, 11.38.

### 3. 4. Synthesis of 4-Thiazolidinone Derivatives 3a–e

To the mixture of 3-acetylcoumarin thiosemicarbazone derivatives **2a–e** (3 mmol) and ethyl chloroacetate (0.61 g; 5 mmol) in 50 mL THF, freshly prepared fused sodium acetate (0.492 g; 6 mmol) was added. The reaction mixture was heated for 4 h under reflux condition and left to cool. The obtained solid products were filtrated and recrystallized from THF.

**3-Methyl-2-((1-(2-oxo-2H-chromen-3-yl)ethylidene)hydrazono)thiazolidin-4-one (3a).** Yield 0.756 g (80%); m.p. 285–287 °C (m.p. lit. 280–282 °C<sup>30</sup>). IR:  $\nu$  1712  $\text{cm}^{-1}$  (C=O);  $^1\text{H}$  NMR:  $\delta$  2.37 (s, 3H,  $\text{CH}_3\text{-C=N}$ ), 3.21 (s, 3H,  $\text{NCH}_3$ ), 3.96 (s, 2H,  $\text{CH}_2\text{-thiazole}$ ), 7.40 (t, 1H,  $J = 7.4$  Hz,  $\text{C}_6\text{-H}$  of chromene), 7.46 (d, 1H,  $J = 8.3$  Hz,  $\text{C}_8\text{-H}$  of chromene), 7.68 (t, 1H,  $J = 7.1$  Hz,  $\text{C}_7\text{-H}$  of chromene), 7.88 (d, 1H,  $J = 7.7$  Hz,  $\text{C}_5\text{-H}$  of chromene), 8.21 (s, 1H,  $\text{C}_4\text{-H}$  of chromene);  $^{13}\text{C}$  NMR:  $\delta$  17.34, 27.65, 32.37, 116.52, 119.25, 125.23, 126.86, 129.82, 133.13, 142.23, 154.13, 159.45, 161.13, 164.11, 172.45; MS:  $m/z$  (%) 315 ( $\text{M}^+$ ; 72.3). Anal. Calcd for  $\text{C}_{15}\text{H}_{13}\text{N}_3\text{O}_3\text{S}$  (315.35): C, 57.13; H, 4.16; N, 13.33. Found: C, 57.08; H, 4.14; N, 13.26.

**3-Ethyl-2-((1-(2-oxo-2H-chromen-3-yl)ethylidene)hydrazono)thiazolidin-4-one (3b).** Yield 0.839 g (85%); m.p. 220–222 °C (m.p. lit. 213–215 °C<sup>30</sup>). IR:  $\nu$  2983, 2951 (CH-aliph.), 1714 (C=O), 1618, 1595  $\text{cm}^{-1}$  (C=N);  $^1\text{H}$  NMR:  $\delta$  1.22 (t, 3H,  $J = 7.0$  Hz,  $\text{CH}_2\text{CH}_3$ ), 2.36 (s, 3H,  $\text{CH}_3\text{-C=N}$ ), 3.79 (q, 2H,  $J = 7.0$  Hz,  $\text{CH}_2\text{CH}_3$ ), 3.97 (s, 2H,  $\text{CH}_2\text{-thiazole}$ ), 7.30–7.53 (m, 2H,  $\text{C}_6\text{-H}$ ,  $\text{C}_8\text{-H}$  of chromene), 7.67 (t, 1H,  $J = 7.8$  Hz,  $\text{C}_7\text{-H}$  of chromene), 7.87 (d, 1H,  $J = 7.7$  Hz,  $\text{C}_5\text{-H}$  of chromene), 8.22 (s, 1H,  $\text{C}_4\text{-H}$  of chromene);  $^{13}\text{C}$  NMR:  $\delta$  12.65 ( $\text{CH}_3$ ), 17.34 ( $\text{CH}_3$ ), 32.66 ( $\text{CH}_2$ ), 38.37 ( $\text{CH}_2$ ), 116.50 (C), 119.15 (C), 125.26 (C), 126.86 (CH), 129.81 (CH), 133.13 (CH), 142.18 (CH), 154.00 (CH), 159.44 (C=N), 161.13 (C=N), 163.99 (C=O), 172.40 (C=O); MS:  $m/z$  (%) 329 ( $\text{M}^+$ ; 38.9). Anal. Calcd for  $\text{C}_{16}\text{H}_{15}\text{N}_3\text{O}_3\text{S}$  (329.37): C, 58.34; H, 4.59; N, 12.76. Found: C, 58.29; H, 4.60; N, 12.81.

**3-Allyl-2-((1-(2-oxo-2H-chromen-3-yl)ethylidene)hydrazono)thiazolidin-4-one (3c).** Yield 0.767 g (75%); m.p. 215–217 °C. IR:  $\nu$  1710  $\text{cm}^{-1}$  (C=O);  $^1\text{H}$  NMR:  $\delta$  2.31 (s, 3H,  $\text{CH}_3\text{-C=N}$ ), 4.57 (m, 2H,  $\text{NCH}_2$ ), 5.17–5.19 (m, 2H,  $\text{CH}_2\text{-olefinic}$ ), 5.88–6.05 (m, 1H,  $\text{CH-olefinic}$ ),

3.96 (s, 2H,  $\text{CH}_2\text{-thiazole}$ ), 7.30–7.50 (m, 2H,  $\text{C}_6\text{-H}$ ,  $\text{C}_8\text{-H}$  of chromene), 7.66 (t, 1H,  $J = 7.8$  Hz,  $\text{C}_7\text{-H}$  of chromene), 7.88 (d, 1H,  $J = 7.7$  Hz,  $\text{C}_5\text{-H}$  of chromene), 8.22 (s, 1H,  $\text{C}_4\text{-H}$  of chromene); MS:  $m/z$  (%) 341 ( $\text{M}^+$ ; 46.5). Anal. Calcd for  $\text{C}_{17}\text{H}_{15}\text{N}_3\text{O}_3\text{S}$  (341.38): C, 59.81; H, 4.43; N, 12.31. Found: C, 59.78; H, 4.41; N, 12.26.

**2-((1-(2-Oxo-2H-chromen-3-yl)ethylidene)hydrazono)-3-phenylthiazolidin-4-one (3d).** Yield 0.905 g (80%); m.p. 175–177 °C. IR:  $\nu$  2927 (CH-aliph.), 1711 (C=O), 1589  $\text{cm}^{-1}$  (C=N);  $^1\text{H}$  NMR:  $\delta$  2.13 (s, 3H,  $\text{CH}_3\text{-C=N}$ ), 4.07 (s, 2H,  $\text{CH}_2\text{-thiazole}$ ), 7.36–7.50 (m, 7H, Ar-H,  $\text{C}_6\text{-H}$  of chromene and  $\text{C}_8\text{-H}$  of chromene), 7.67 (t, 1H,  $J = 7.8$  Hz,  $\text{C}_7\text{-H}$  of chromene), 7.87 (d, 1H,  $J = 7.8$  Hz,  $\text{C}_5\text{-H}$  of chromene), 8.20 (s, 1H,  $\text{C}_4\text{-H}$  of chromene); MS:  $m/z$  (%) 377 ( $\text{M}^+$ ; 41.6). Anal. Calcd for  $\text{C}_{20}\text{H}_{15}\text{N}_3\text{O}_3\text{S}$  (377.42): C, 63.65; H, 4.01; N, 11.13. Found: C, 63.58; H, 3.99; N, 11.20.

**3-(4-Methoxyphenyl)-2-((1-(2-oxo-2H-chromen-3-yl)ethylidene)hydrazono)thiazolidin-4-one (3e).** Yield 1.038 g (85%); m.p. 254–256 °C. IR:  $\nu$  2998 (CH-aliph.), 1726  $\text{cm}^{-1}$  (C=O);  $^1\text{H}$  NMR:  $\delta$  2.12 (s, 3H,  $\text{CH}_3\text{-C=N}$ ), 3.82 (s, 3H,  $\text{OCH}_3$ ), 4.08 (s, 2H,  $\text{CH}_2\text{-thiazole}$ ), 7.07 (d,  $J = 8.9$  Hz, 2H, Ar-H, AB), 7.33 (d, 2H,  $J = 8.9$  Hz, Ar-H, AB), 7.40–7.44 (m, 2H,  $\text{C}_6\text{-H}$ ,  $\text{C}_8\text{-H}$  of chromene), 7.67 (t, 1H,  $J = 7.8$  Hz,  $\text{C}_7\text{-H}$  of chromene), 7.87 (d, 1H,  $J = 7.8$  Hz,  $\text{C}_5\text{-H}$  of chromene), 8.20 (s, 1H,  $\text{C}_4\text{-H}$  of chromene); MS:  $m/z$  (%) 407 ( $\text{M}^+$ ; 54.0). Anal. Calcd for  $\text{C}_{21}\text{H}_{17}\text{N}_3\text{O}_4\text{S}$  (407.44): C, 61.90; H, 4.21; N, 10.31. Found: C, 61.94; H, 4.19; N, 10.26.

### 3. 5. Synthesis of 4-Methyl-2,3-dihydrothiazole Derivatives 4a–e

To the mixture of 3-acetylcoumarin thiosemicarbazone derivatives **2a–e** (3 mmol) and chloroacetone (0.46 g; 5 mmol) in 50 mL THF, fused sodium acetate (0.492 g; 6 mmol) was added. The reaction mixture was heated for 6 h under reflux condition then the solution was concentrated and left to cool. The obtained products were filtrated and recrystallized from ethanol.

**3-(1-((3,4-Dimethylthiazol-2(3H)-ylidene)hydrazono)ethyl)-2H-chromen-2-one (4a).** Yield 0.563 g (60%); m.p. 156–157 °C (m.p. lit. 210–212 °C<sup>30</sup>). IR:  $\nu$  1716 (C=O), 1603  $\text{cm}^{-1}$  (C=N);  $^1\text{H}$  NMR:  $\delta$  2.16 (s, 3H,  $\text{CH}_3$ ), 2.32 (s, 3H,  $\text{CH}_3$ ), 2.40 (s, 3H,  $\text{CH}_3$ ), 6.09 (s, 1H, thiazole-H), 7.23–7.53 (m, 2H,  $\text{C}_6\text{-H}$ ,  $\text{C}_8\text{-H}$  of chromene), 7.62 (t, 1H,  $J = 7.2$  Hz,  $\text{C}_7\text{-H}$  of chromene), 7.83 (d, 1H,  $J = 7.0$  Hz,  $\text{C}_5\text{-H}$  of chromene), 8.11 (s, 1H,  $\text{C}_4\text{-H}$  of chromene);  $^{13}\text{C}$  NMR:  $\delta$  14.96, 16.14, 33.93, 100.57, 116.33, 119.39, 125.21, 127.50, 130.83, 132.51, 140.63, 141.05, 153.29, 153.64, 159.91, 170.44; MS:  $m/z$  (%) 313 ( $\text{M}^+$ ; 42.4). Anal. Calcd for  $\text{C}_{16}\text{H}_{15}\text{N}_3\text{O}_2\text{S}$  (313.37): C, 61.32; H, 4.82; N, 13.41. Found: C, 61.28; H, 4.80; N, 13.36.

**3-(1-((3-Ethyl-4-methylthiazol-2(3H)-ylidene)hydrazono)ethyl)-2H-chromen-2-one (4b).** Yield 0.638 g (65%); m.p. 133–135 °C (m.p. lit. 232–234 °C<sup>30</sup>). IR:  $\nu$  3276 (CH-Ar), 2974 (CH-aliph.), 1726 (C=O), 1605 cm<sup>-1</sup> (C=N); <sup>1</sup>H NMR:  $\delta$  1.26 (t, 3H,  $J = 6.9$  Hz, CH<sub>2</sub>CH<sub>3</sub>), 2.18 (s, 3H, CH<sub>3</sub>-thiazole), 2.31 (s, 3H, CH<sub>3</sub>-C=N), 3.84 (q, 2H,  $J = 7.0$  Hz, CH<sub>2</sub>CH<sub>3</sub>), 6.05 (s, 1H, thiazole-H), 7.21–7.51 (m, 2H, C<sub>6</sub>-H, C<sub>8</sub>-H of chromene), 7.61 (t, 1H,  $J = 7.2$  Hz, C<sub>7</sub>-H of chromene), 7.82 (d, 1H,  $J = 7.0$  Hz, C<sub>5</sub>-H of chromene), 8.12 (s, 1H, C<sub>4</sub>-H of chromene); <sup>13</sup>C NMR:  $\delta$  12.33, 14.96, 16.21, 38.78, 99.39, 116.36, 119.69, 125.20, 127.56, 129.41, 130.83, 132.56, 140.62, 141.40, 153.62, 160.99, 170.29; MS:  $m/z$  (%) 327 (M<sup>+</sup>; 63.2). Anal. Calcd for C<sub>17</sub>H<sub>17</sub>N<sub>3</sub>O<sub>2</sub>S (327.40): C, 62.36; H, 5.23; N, 12.83. Found: C, 62.42; H, 5.21; N, 12.79.

**3-(1-((3-Allyl-4-methylthiazol-2(3H)-ylidene)hydrazono)ethyl)-2H-chromen-2-one (4c).** Yield 0.661 g (65%); m.p. 115–117 °C. IR:  $\nu$  1726 cm<sup>-1</sup> (C=O); <sup>1</sup>H NMR:  $\delta$  2.14 (s, 3H, CH<sub>3</sub>-thiazole), 2.29 (s, 3H, CH<sub>3</sub>-C=N), 4.55 (m, 2H, NCH<sub>2</sub>), 5.17–5.19 (m, 2H, CH<sub>2</sub>-olefinic), 5.88–6.05 (m, 1H, CH-olefinic), 6.59 (s, 1H, thiazole-H), 7.37–7.43 (m, 2H, C<sub>6</sub>-H, C<sub>8</sub>-H of chromene), 7.62 (t, 1H,  $J = 7.2$  Hz, C<sub>7</sub>-H of chromene), 7.83 (d, 1H,  $J = 7.8$  Hz, C<sub>5</sub>-H of chromene), 8.13 (s, 1H, C<sub>4</sub>-H of chromene); <sup>13</sup>C NMR:  $\delta$  13.51, 16.96, 34.98, 100.55, 116.33, 119.39, 125.21, 129.06, 129.31, 129.41, 129.67, 132.51, 140.63, 141.05, 153.29, 153.64, 159.91, 170.44; MS:  $m/z$  (%) 339 (M<sup>+</sup>; 46.5). Anal. Calcd for C<sub>18</sub>H<sub>17</sub>N<sub>3</sub>O<sub>2</sub>S (339.41): C, 63.70; H, 5.05; N, 12.38. Found: C, 63.66; H, 5.03; N, 12.42.

**3-(1-((4-Methyl-3-phenylthiazol-2(3H)-ylidene)hydrazono)ethyl)-2H-chromen-2-one (4d).** Yield 0.788 g (70%); m.p. 198–200 °C. IR:  $\nu$  3106, 3069 (CH-Ar), 2918 (CH-aliph.), 1709 (C=O), 1600 cm<sup>-1</sup> (C=N); <sup>1</sup>H NMR:  $\delta$  1.87 (s, 3H, CH<sub>3</sub>-thiazole), 2.05 (s, 3H, CH<sub>3</sub>-C=N), 6.25 (s, 1H, thiazole-H), 7.36–7.50 (m, 5H, Ar-H), 7.54–7.58 (m, 2H, C<sub>6</sub>-H, C<sub>8</sub>-H of chromene), 7.62 (t, 1H, C<sub>7</sub>-H of chromene), 7.84 (d, 1H,  $J = 7.7$  Hz, C<sub>5</sub>-H of chromene), 8.12 (s, 1H, C<sub>4</sub>-H of chromene); <sup>13</sup>C NMR:  $\delta$  14.46, 16.96, 100.57, 116.33, 119.39, 125.21, 128.13, 129.06 (2C), 129.31 (2C), 129.41, 129.67, 130.43, 132.51, 140.63, 141.05, 153.29, 153.64, 157.44, 170.44; MS:  $m/z$  (%) 375 (M<sup>+</sup>; 45.7). Anal. Calcd for C<sub>21</sub>H<sub>17</sub>N<sub>3</sub>O<sub>2</sub>S (375.44): C, 67.18; H, 4.56; N, 11.19. Found: C, 67.11; H, 4.55; N, 11.24.

**3-(1-((3-(4-Methoxyphenyl)-4-methylthiazol-2(3H)-ylidene)hydrazono)ethyl)-2H-chromen-2-one (4e).** Yield 0.911 g (75%); m.p. 218–219 °C. IR:  $\nu$  2922 (CH-aliph.), 1728 cm<sup>-1</sup> (C=O); <sup>1</sup>H NMR:  $\delta$  1.87 (s, 3H, CH<sub>3</sub>-thiazole), 2.07 (s, 3H, CH<sub>3</sub>-C=N), 3.83 (s, 3H, OCH<sub>3</sub>), 6.22 (s, 1H, thiazole-H), 7.07 (d, 2H,  $J = 8.7$  Hz, Ar-H, AB), 7.34 (d, 2H,  $J = 8.6$  Hz, Ar-H, AB), 7.37–7.42 (m, 2H, C<sub>6</sub>-H, C<sub>8</sub>-H of chromene), 7.62 (t, 1H, C<sub>7</sub>-H of chromene), 7.82 (d, 1H,  $J = 7.7$  Hz, C<sub>5</sub>-H of chromene), 8.11 (s, 1H, C<sub>4</sub>-H of chromene); MS:  $m/z$  (%) 405 (M<sup>+</sup>; 36.5). Anal.

Calcd for C<sub>22</sub>H<sub>19</sub>N<sub>3</sub>O<sub>3</sub>S (405.47): C, 65.17; H, 4.72; N, 10.36. Found: C, 65.24; H, 4.73; N, 10.26.

### 3. 6. Synthesis of 4-Phenylthiazole Derivatives 5a–e

To the mixture of 3-acetylcoumarin thiosemicarbazone derivatives **2a–e** (3 mmol) and phenacyl bromide (0.995 g; 5 mmol) in 50 mL THF, fused sodium acetate (0.492 g; 6 mmol) was added. The reaction mixture was heated for 5 h under reflux condition and left to cool. The obtained solid products were filtrated and recrystallized from dioxane.

**3-(1-((3-Methyl-4-phenylthiazol-2(3H)-ylidene)hydrazono)ethyl)-2H-chromen-2-one (5a).** Yield 0.9 g (80%); m.p. 165–167 °C (m.p. lit. 161–163 °C<sup>30</sup>). IR:  $\nu$  3086 (CH-Ar), 2946, 2906 (CH-aliph.), 1710 cm<sup>-1</sup> (C=O); <sup>1</sup>H NMR:  $\delta$  2.35 (s, 3H, CH<sub>3</sub>-C=N), 3.36 (s, 3H, NCH<sub>3</sub>), 6.44 (s, 1H, thiazole-H), 7.38 (t, 1H,  $J = 7.5$  Hz, C<sub>6</sub>-H of chromene), 7.44 (d, 1H,  $J = 8.3$  Hz, C<sub>8</sub>-H of chromene), 7.53 (m, 5H, Ph-H), 7.63 (t, 1H,  $J = 7.8$  Hz, C<sub>7</sub>-H of chromene), 7.86 (d, 1H,  $J = 7.7$  Hz, C<sub>5</sub>-H of chromene), 8.15 (s, 1H, C<sub>4</sub>-H of chromene); <sup>13</sup>C NMR:  $\delta$  16.96 (CH<sub>3</sub>), 33.98 (CH<sub>3</sub>), 100.56 (C), 116.33 (C), 119.39 (C), 125.20 (C), 127.49 (C), 129.06 (2CH), 129.31 (2CH), 129.42 (CH), 129.67 (CH), 130.82 (CH), 132.51 (CH), 140.63 (CH), 141.05 (CH), 153.28 (CH), 153.63 (C=N), 159.91 (C=N), 170.44 (C=O); MS:  $m/z$  (%) 375 (M<sup>+</sup>; 38.3). Anal. Calcd for C<sub>21</sub>H<sub>17</sub>N<sub>3</sub>O<sub>2</sub>S (375.44): C, 67.18; H, 4.56; N, 11.19. Found: C, 67.23; H, 4.55; N, 11.23.

**3-(1-((3-Ethyl-4-phenylthiazol-2(3H)-ylidene)hydrazono)ethyl)-2H-chromen-2-one (5b).** Yield 0.875 g (75%); m.p. 176–178 °C (m.p. lit. 158–160 °C<sup>30</sup>). IR:  $\nu$  3099, 3055 (CH-Ar), 2971, 2936 (CH-aliph.), 1717 (C=O), 1690 cm<sup>-1</sup> (C=N); <sup>1</sup>H NMR:  $\delta$  1.16 (t, 3H,  $J = 7.0$  Hz, CH<sub>2</sub>CH<sub>3</sub>), 2.35 (s, 3H, CH<sub>3</sub>-C=N), 3.84 (q, 2H,  $J = 7.0$  Hz, CH<sub>2</sub>CH<sub>3</sub>), 6.39 (s, 1H, thiazole-H), 7.38 (t, 1H,  $J = 7.5$  Hz, C<sub>6</sub>-H of chromene), 7.44 (d, 1H,  $J = 8.3$  Hz, C<sub>8</sub>-H of chromene), 7.48–7.53 (m, 5H, Ph-H), 7.66 (t, 1H,  $J = 7.8$  Hz, C<sub>7</sub>-H of chromene), 7.85 (dd, 1H,  $J = 7.7, 1.2$  Hz, C<sub>5</sub>-H of chromene), 8.16 (s, 1H, Ar-H at C<sub>4</sub>-H of chromene); MS:  $m/z$  (%) 389 (M<sup>+</sup>; 58.1). Anal. Calcd for C<sub>22</sub>H<sub>19</sub>N<sub>3</sub>O<sub>2</sub>S (389.47): C, 67.84; H, 4.92; N, 10.79. Found: C, 67.81; H, 4.94; N, 10.83.

**3-(1-((3-Allyl-4-phenylthiazol-2(3H)-ylidene)hydrazono)ethyl)-2H-chromen-2-one (5c).** Yield 0.962 g (80%); m.p. 168–170 °C. IR:  $\nu$  1718 cm<sup>-1</sup> (C=O); <sup>1</sup>H NMR:  $\delta$  2.31 (s, 3H, CH<sub>3</sub>-C=N), 4.45 (d, 2H,  $J = 4.7$  Hz, NCH<sub>2</sub>), 4.94 (dd, 1H,  $J = 17.3, 1.4$  Hz, CH-olefinic), 5.14 (dd, 1H,  $J = 10.5, 1.3$  Hz, CH-olefinic), 5.80–5.89 (m, 1H, CH-olefinic), 6.44 (s, 1H, thiazole-H), 7.40 (t, 1H,  $J = 7.6$  Hz, C<sub>6</sub>-H of chromene), 7.45 (d, 1H,  $J = 8.4$  Hz, C<sub>8</sub>-H of chromene), 7.48–7.53 (m, 5H, Ph-H), 7.64 (t, 1H,  $J = 7.8$  Hz, C<sub>7</sub>-H of

chromene), 7.86 (dd, 1H,  $J = 7.7, 1.2$  Hz, C<sub>5</sub>-H of chromene), 8.17 (s, 1H, Ar-H at C<sub>4</sub>-H of chromene); MS:  $m/z$  (%) 401 (M<sup>+</sup>; 46.5). Anal. Calcd for C<sub>23</sub>H<sub>19</sub>N<sub>3</sub>O<sub>2</sub>S (401.48): C, 68.81; H, 4.77; N, 10.47. Found: C, 68.78; H, 4.75; N, 10.44.

**3-(1-((3,4-Diphenylthiazol-2(3H)-ylidene)hydrazono)ethyl)-2H-chromen-2-one (5d)**. Yield 1.049 g (80%); m.p. 210–212 °C. IR:  $\nu$  1732 (C=O), 1600, 1589 cm<sup>-1</sup> (C=N); <sup>1</sup>H NMR:  $\delta$  2.14 (s, 3H, CH<sub>3</sub>-C=N), 6.67 (s, 1H, thiazole-H), 7.18 (m, 2H, Ar-H), 7.21–7.28 (m, 3H, Ar-H), 7.29 (m, 3H, Ar-H), 7.38 (m, 3H, Ar-H), 7.43 (d, 1H,  $J = 8.3$  Hz, C<sub>8</sub>-H of chromene), 7.66 (t, 1H,  $J = 7.8$  Hz, C<sub>7</sub>-H of chromene), 7.85 (d, 1H,  $J = 7.7$  Hz, C<sub>5</sub>-H of chromene), 8.15 (s, 1H, C<sub>4</sub>-H of chromene); MS:  $m/z$  (%) 437 (M<sup>+</sup>; 53.3). Anal. Calcd for C<sub>26</sub>H<sub>19</sub>N<sub>3</sub>O<sub>2</sub>S (437.51): C, 71.38; H, 4.38; N, 9.60. Found: C, 71.42; H, 4.36; N, 9.57.

**3-(1-((3-(4-Methoxyphenyl)-4-phenylthiazol-2(3H)-ylidene)hydrazono)ethyl)-2H-chromen-2-one (5e)**. Yield 1.191 g (85%); m.p. 291–293 °C. IR:  $\nu$  3114, 3068, 3009 (CH-Ar), 2942, 2841 (CH-aliph.), 1726 (C=O), 1603 cm<sup>-1</sup> (C=N); <sup>1</sup>H NMR:  $\delta$  2.13 (s, 3H, CH<sub>3</sub>-C=N), 3.85 (s, 3H, OCH<sub>3</sub>), 6.65 (s, 1H, thiazole-H), 7.15–7.40 (m, 10H, Ar-H), 7.44 (d, 1H,  $J = 8.3$  Hz, C<sub>8</sub>-H of chromene), 7.67 (t, 1H,  $J = 7.8$  Hz, C<sub>7</sub>-H of chromene), 7.84 (d, 1H,  $J = 7.7$  Hz, C<sub>5</sub>-H of chromene), 8.16 (s, 1H, C<sub>4</sub>-H of chromene); MS:  $m/z$  (%) 467 (M<sup>+</sup>; 63.0). Anal. Calcd for C<sub>27</sub>H<sub>21</sub>N<sub>3</sub>O<sub>3</sub>S (467.54): C, 69.36; H, 4.53; N, 8.99. Found: C, 69.28; H, 4.51; N, 9.03.

## 4. References

- S. I. Eissa, A. M. Farrag, S. Y. Abbas, M. F. El Shehry, A. Ragab, E. A. Fayed, Y. A. Ammar, *Bioorg. Chem.* **2021**, *110*, 104803. DOI:10.1016/j.bioorg.2021.104803
- S. Y. Abbas, M. A. M. Sh. El-Sharief, R. A. K. Al-Harbi, E. W. El-Gammal, A. M. Sh. El-Sharief, *Med. Chem.* **2021**, *17*, 638–645. DOI:10.2174/1573406416666191227112648
- M. F. El Shehry, M. M. Ghorab, S. Y. Abbas, E. A. Fayed, S. A. Shedid, Y. A. Ammar, *Eur. J. Med. Chem.* **2018**, *143*, 1463–1473. DOI:10.1016/j.ejmech.2017.10.046
- M. F. El Shehry, S. Y. Abbas, A. M. Farrag, S. I. Eissa, S. A. Fouad, Y. A. Ammar, *Med. Chem. Res.* **2018**, *27*, 2287–2296. DOI:10.1007/s00044-018-2235-4
- M. A. Salem, S. Y. Abbas, M. H. Helal, A. Y. Alzahrani, *Polycycl. Aromat. Compd.* **2023**, *43*, 1081–1091. DOI:10.1080/10406638.2021.2024583
- M. A. Salem, S. Y. Abbas, M. H. Helal, A. Y. Alzahrani, *J. Heterocycl. Chem.* **2021**, *58*, 2117–2123. DOI:10.1002/jhet.4335
- S. A. Fouad, S. A. Hessein, S. Y. Abbas, A. M. Farrag, Y. A. Ammar, *Croat. Chem. Acta* **2018**, *91*, 99–107.
- M. A. Salem, M. H. Helal, M. A. Gouda, Y. A. Ammar, M. S. A. El-Gaby, S. Y. Abbas, *Synth. Commun.* **2018**, *48*, 1534–1550. DOI:10.1080/00397911.2018.1455873
- S. A. Hessein, M. A. M. El-Sharief, S. Y. Abbas, H. K. Thabet, Y. A. Ammar, *Croat. Chem. Acta* **2016**, *89*, 91–100. DOI:10.5562/cca2811
- L. Fernández-Peña, M. J. Matos, E. López, *Mar. Drugs* **2023**, *21*, 37. DOI:10.3390/md21010037
- F. Annunziata, C. Pinna, S. Dallavalle, L. Tamborini, A. Pinto, *Int. J. Mol. Sci.* **2020**, *21*, 4618. DOI:10.3390/ijms21134618
- T. I. Verhoef, W. K. Redekop, A. K. Daly, R. M. F. van Schie, A. de Boer, A.-H. M.-v. der Zee, *Br. J. Clin. Pharmacol.* **2014**, *77*, 626–641. DOI:10.1111/bcp.12220
- X. Wang, Z. Guo, S. Zhu, Y. Liu, P. Shi, H. Tian, W.-H. Zhu, *J. Mater. Chem. B* **2016**, *4*, 4683–4689. DOI:10.1039/C6TB01096B
- I. Yahaya, N. Seferoğlu, Z. Seferoğlu, *Tetrahedron* **2019**, *75*, 2143–2154. DOI:10.1016/j.tet.2019.02.034
- S. Chen, M. Zhang, C. Zhu, H. Lu, M. Zhao, X. Tian, Q. Zhang, S. C. De Souza, F. Rong, H. Zhou, J. Wu, Y. Tian, *Dyes Pigm.* **2018**, *148*, 429–436. DOI:10.1016/j.dyepig.2017.09.047
- A. Carneiro M. J. Matos, E. Uriarte, L. Santana, *Molecules* **2021**, *26*, 501. DOI:10.3390/molecules26020501
- A. A. Farag, S. N. Abd-Alrahman, G. F. Ahmed, R. M. Ammar, Y. A. Ammar, S. Y. Abbas, *Arch. Pharm. Life Sci.* **2012**, *345*(9), 703–712. DOI:10.1002/ardp.201200014
- M. A. Salem, S. Y. Abbas, M. A. M. Sh. El-Sharief, M. H. Helal, M. A. Gouda, M. A. Assiri, T. E. Ali, *Acta Chim. Slov.* **2021**, *68*, 990–996. DOI:10.17344/acsi.2021.6980
- S. Y. Abbas, M. M. Abd El-Aziz, S. M. Awad, M. S. Mohamed, *Synth. Commun.* **2023**, *53*, 68–75. DOI:10.1080/00397911.2022.2150086
- A. E. M. Abdallah, R. M. Mohareb, M. H. E. Helal, G. J. Mofeed, *Acta Chim. Slov.* **2021**, *68*, 604–616. DOI:10.17344/acsi.2020.6446
- C. Deng, H. Yan, J. Wang, B.-s. Liu, K. Liu, Y.-m. Shi, *Arabian J. Chem.* **2022**, *15*, 104242. DOI:10.1016/j.arabj.2022.104242
- C. Sharma, K. K. Bansal, A. Sharma, D. Sharma, A. Deep, *Eur. J. Med. Chem.* **2020**, *188*, 112016. DOI:10.1016/j.ejmech.2019.112016
- Z.-X. Niu, Y.-T. Wang, S.-N. Zhang, Y. Li, X.-B. Chen, S.-Q. Wang, H.-M. Liu, *Eur. J. Med. Chem.* **2023**, *250*, 115172. DOI:10.1016/j.ejmech.2023.115172
- C. B. Reodl, D. Vogt, S. B. M. Kretschmer, K. Ihlefeld, S. Barzen, A. Brüggerhoff, J. Achenbach, E. Proschak, D. Steinhilber, H. Stark, B. Hofmann, *Eur. J. Med. Chem.* **2014**, *84*, 302–311. DOI:10.1016/j.ejmech.2014.07.025
- E. Lane Miller, *J. Midwifery Womens Health* **2002**, *47*, 426–434. DOI:10.1016/S1526-9523(02)00330-6
- A. Ayati, S. Emami, A. Asadipour, A. Shafiee, A. Foroumadi, *Eur. J. Med. Chem.* **2015**, *97*, 699–718. DOI:10.1016/j.ejmech.2015.04.015
- R. M. Mohareb, Y. R. Milad, A. A. Masoud, *Acta Chim. Slov.* **2021**, *68*, 72–87. DOI:10.17344/acsi.2020.6182
- N. Y. M. Abdo, R. M. Mohareb, *Acta Chim. Slov.* **2022**, *69*, 700–713. DOI:10.17344/acsi.2021.6886
- K. A. M. El-Bayouki, W. M. Basyouni, E. A. Mostafa, S. Y. Abbas, *Synth. React. Inorg. Met.-Org.* **2014**, *44*, 537–540. DOI:10.1080/15533174.2013.763274

- 30 D. H. Dawood, R. Z. Batran, T. A. Farghaly, M. A. Khedr, M. M. Abdulla, *Arch. Pharm. Chem. Life Sci.* **2015**, *348*, 875–888. DOI:10.1002/ardp.201500274
- 31 R. H. Vekariya, K. D. Patel, D. P. Rajani, S. D. Rajani, H. D. Patel, *J. Assoc. Arab Univ. Basic Appl. Sci.* **2017**, *23*, 10–19. DOI:10.1016/j.jaubas.2016.04.002

## Povzetek

Priprava hibridnih molekul je eden izmed najboljših načinov izdelave novih biološko aktivnih spojin. Skladno s tem načelom smo iz tiosemikarbazonov 3-acetilkumarina pripravili serijo novih tiazolov, ki vsebujejo kumarinski fragment. S ciklizacijo tiosemikarbazonskih derivatov z etil 2-kloroacetatom, 1-kloropropan-2-onom in 2-bromo-1-feniletanonom smo pripravili ustrezne 4-tiazolidinone, 4-metiltiazole in 4-feniltiazole. Za vse pripravljene tiosemikarbazone in tiazole smo raziskali antimikrobne lastnosti. Tiosemikarbazoni in tiazolidin-4-oni so izkazali zmerne aktivnosti proti Gram-pozitivnim in Gram-negativnim bakterijam.



Except when otherwise noted, articles in this journal are published under the terms and conditions of the Creative Commons Attribution 4.0 International License



Scientific paper

# Synthesis, Characterization and X-Ray Crystal Structures of Oxidovanadium(V) Complexes Derived from *N*'-(2-Hydroxy-5-methylbenzylidene)-4-methylbenzohydrazide with Antibacterial Activity

Xue-Rong Tan,<sup>1</sup> Wei Li,<sup>1,\*</sup> Meng-Meng Duan<sup>2</sup> and Zhonglu You<sup>2</sup>

<sup>1</sup> Department of Radiology, The Second Hospital of Dalian Medical University, Dalian 116023, P.R. China

<sup>2</sup> Department of Chemistry and Chemical Engineering, Liaoning Normal University, Dalian 116029, P. R. China

\* Corresponding author: E-mail: liwei\_dlm@126.com

Received: 07-29-2023

## Abstract

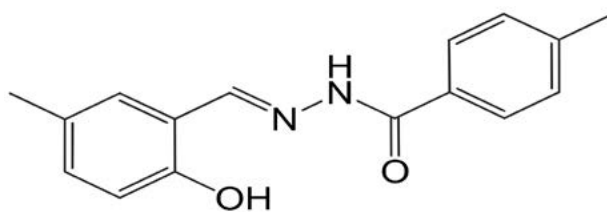
A dinuclear oxidovanadium(V) complex [V<sub>2</sub>O<sub>2</sub>L<sub>2</sub>(OMe)<sub>2</sub>] (1) was synthesized from *N*'-(2-hydroxy-5-methylbenzylidene)-4-methylbenzohydrazide (H<sub>2</sub>L) and VO(acac)<sub>2</sub> in MeOH. Reaction of complex 1 with 3-hydroxy-2-methyl-4-pyrone (HL') afforded a mononuclear oxidovanadium(V) complex [VOLL'] (2). The hydrazone and both complexes were characterized by IR, UV and <sup>1</sup>H NMR spectroscopy, as well as X-ray single crystal determination. X-ray powder diffraction of the complexes was performed. The V atoms in the two complexes are in octahedral coordination. The molecules of complex 2 are linked through non-classical hydrogen bonds of type C–H...O to form one-dimensional chains running along the *a* axis. The biological assay indicates that the complexes have good antimicrobial activities on the bacteria strains *P. aeruginosa*, *S. aureus*, *B. subtilis* and *E. coli*.

**Keywords:** Hydrazone; Oxidovanadium complex; X-Ray crystal structure; Antibacterial activity.

## 1. Introduction

Vanadium compounds have received considerable attention for their various biological properties like normalizing the blood glucose levels and modeling haloperoxidases.<sup>1</sup> Hydrazones are a special kind of Schiff bases, which possess the characteristic functional group CH=N–NH–C(O). The compounds are well known for their facile synthesis and excellent coordinate capability to a number of metal ions. Hydrazones and metal complexes have been widely studied on their broadly biological applications.<sup>2</sup> Recently, we have reported the structures and biological activities of some vanadium complexes.<sup>3</sup> The solvents such as MeOH and EtOH usually coordinate to the V atoms through neutral or deprotonated form as terminal ligands.<sup>4</sup> Interestingly, they can act as bridging ligands to form dinuclear complexes.<sup>5</sup> When administered with bidentate ligands, it can obtain vanadium complexes with mixed ligands.<sup>6</sup> Maltol is used as food additive, flavor and fragrance. Maltol complexes of vanadium can regulate alkaline phosphatase activity and osteoblast-like cell

growth.<sup>7</sup> In this paper, a new dinuclear oxidovanadium(V) complex [V<sub>2</sub>O<sub>2</sub>L<sub>2</sub>(OMe)<sub>2</sub>] (1) and a new mononuclear oxidovanadium(V) complex [VOLL'] (2), where H<sub>2</sub>L is *N*'-(2-hydroxy-5-methylbenzylidene)-4-methylbenzohydrazide (Scheme 1), and HL' is maltol, are presented.



Scheme 1. H<sub>2</sub>L

## 2. Experimental

### 2.1. Materials and Measurements

5-Methylsalicylaldehyde, 4-methylbenzohydrazide and maltol were purchased from Sigma-Aldrich

and used as received. Solvents and other reagents were commercial obtained. Elemental analyses for C, H and N were performed with a Perkin-Elmer elemental analyzer. IR spectra were recorded on a Nicolet AVATAR 360 spectrometer as KBr pellets.  $^1\text{H}$  NMR spectrum was carried out on a Bruker 500 MHz instrument. Powder X-ray diffraction was performed with a Bruker D8 Advance X-ray diffractometer using Cu K $\alpha$  radiation ( $\lambda = 1.548 \text{ \AA}$ ) generated at 40 kV and 40 mA. The powder XRD spectra were recorded in a  $2\theta$  range of  $2\text{--}50^\circ$  using a 1D Lynxeye detector under ambient conditions. X-ray single crystal structures for the complexes were collected at 298(2) K using a Bruker D8 VENTURE PHOTON diffractometer with MoK $\alpha$  radiation ( $\lambda = 0.71073 \text{ \AA}$ ).

## 2. 2. Synthesis of $\text{H}_2\text{L}$

5-Methylsalicylaldehyde (1.0 mmol, 0.14 g) and 4-methylbenzohydrazide (1.0 mmol, 0.15 g) were respectively dissolved in 20 mL MeOH and mixed together. The mixture was reflux for 20 min give a colorless solution. The solvent was removed by distillation to obtain white solid, which was re-crystallized from MeOH to give colorless crystalline product. Yield: 0.24 g (89%). Analysis: Found: C 71.45%, H 6.12%, N 10.53%. Calculated for  $\text{C}_{16}\text{H}_{16}\text{N}_2\text{O}_2$ : C 71.62%, H 6.01%, N 10.44%. IR data (KBr,  $\text{cm}^{-1}$ ):  $\nu$  3439 (m, OH), 3293 and 3205 (w, NH), 1648 (s, C=O), 1617 (s, C=N). UV-Vis in MeOH ( $\lambda$ , nm ( $\epsilon$ ,  $\text{L mol}^{-1} \text{ cm}^{-1}$ )): 240 (23,750), 290 (32,022), 300 (31,120), 333 (17,020), 396 (4,250).  $^1\text{H}$  NMR ( $d_6$ -DMSO, ppm)  $\delta$  12.04 (s, 1H, OH), 11.09 (s, 1H, NH), 8.61 (s, 1H, CH=N), 7.88 (d, 2H, ArH), 7.36 (d, 3H, ArH), 7.14 (d, 1H, ArH), 6.86 (d, 1H, ArH), 2.41 (s, 3H,  $\text{CH}_3$ ), 2.27 (s, 3H,  $\text{CH}_3$ ).

## 2. 3. Synthesis of $[\text{V}_2\text{O}_2\text{L}_2(\text{OMe})_2]$ (1)

$[\text{VO}(\text{acac})_2]$  (0.10 mmol, 26 mg) and  $\text{H}_2\text{L}$  (0.10 mmol, 27 mg) were respectively dissolved in MeOH (20 mL) and mixed together. The mixture was stirred at room temperature for 30 min to give a deep brown solution. The mixture was filtered and with the filtration allowed to slow evaporate for a week. Brown block like single crystals were formed. The crystals were isolated by filtration. Yield: 19 mg (53%). Analysis: Found: C 55.87%, H 4.78%, N 7.58. Calculated for  $\text{C}_{34}\text{H}_{34}\text{N}_4\text{O}_8\text{V}_2$ : C 56.05%, H 4.70%, N 7.69%. IR data (KBr,  $\text{cm}^{-1}$ ):  $\nu$  1610 (s, C=N), 961 (V=O). UV-Vis in MeOH ( $\lambda$ , nm ( $\epsilon$ ,  $\text{L mol}^{-1} \text{ cm}^{-1}$ )): 227 (21,320), 268 (23,215), 325 (15,630), 406 (4,655). Molar conductivity in MeOH at concentration of  $10^{-4} \text{ mol L}^{-1}$ :  $26 \Omega^{-1} \text{ cm}^2 \text{ mol}^{-1}$ .

## 2. 4. Synthesis of $[\text{VOLL}']$ (2)

Maltol (0.20 mmol, 26 mg) was dissolved in MeOH (15 mL) and added dropwise to a 10 mL methanolic solu-

tion of complex **1** (0.10 mmol, 73 mg). The mixture was stirred at room temperature for 30 min to give a deep brown solution. The mixture was filtered and with the filtration allowed to slow evaporate for a week. Brown block like single crystals were formed. The crystals were isolated by filtration. Yield: 43 mg (47%). Analysis: Found: C 57.78%, H 4.10%, N 6.19. Calculated for  $\text{C}_{22}\text{H}_{19}\text{N}_2\text{O}_6\text{V}$ : C 57.65%, H 4.18%, N 6.11%. IR data (KBr,  $\text{cm}^{-1}$ ):  $\nu$  1608 (s, C=N), 970 (V=O). UV-Vis in MeOH ( $\lambda$ , nm ( $\epsilon$ ,  $\text{L mol}^{-1} \text{ cm}^{-1}$ )): 221 (22,175), 273 (28,190), 327 (14,370), 410 (3,575). Molar conductivity in MeOH at concentration of  $10^{-4} \text{ mol L}^{-1}$ :  $35 \Omega^{-1} \text{ cm}^2 \text{ mol}^{-1}$ .

## 2. 5. X-ray Crystallography

The collected data by the diffractometer were reduced with SAINT.<sup>8</sup> Multi-scan absorption corrections were applied with SADABS.<sup>9</sup> Structures of both complexes were solved by direct method and refined by full-matrix least-squares method against  $F^2$  with SHELXL-TL.<sup>10</sup> The non-hydrogen atoms were refined anisotropically, while the hydrogen atoms were placed in idealized positions and constrained to ride on their parent atoms. The crystallographic data are listed in Table 1. Coordinate bond lengths and bond angles are summarized in Table 2.

**Table 1.** Crystallographic data and refinement parameters for the complexes

	<b>1</b>	<b>2</b>
Chemical formula	$\text{C}_{34}\text{H}_{34}\text{N}_4\text{O}_8\text{V}_2$	$\text{C}_{22}\text{H}_{19}\text{N}_2\text{O}_6\text{V}$
$M_r$	728.53	458.33
Crystal color, habit	Brown, block	Brown, block
Crystal system	Monoclinic	Monoclinic
Space group	$P2_1/n$	$P2_1/c$
Unit cell parameters		
$a$ ( $\text{\AA}$ )	8.7163(12)	14.319(2)
$b$ ( $\text{\AA}$ )	20.5798(16)	10.295(2)
$c$ ( $\text{\AA}$ )	9.5130(12)	14.335(2)
$\beta$ ( $^\circ$ )	105.194(2)	114.437(2)
$V$ ( $\text{\AA}^3$ )	1646.8(3)	1923.9(5)
$Z$	2	4
$D_{\text{calc}}$ ( $\text{g cm}^{-3}$ )	1.469	1.582
$T$ (K)	298(2)	298(2)
$\mu$ ( $\text{mm}^{-1}$ )	0.626	0.561
$F(000)$	752	944
Number of unique data	3049	3228
Number of observed data	1597	1395
$[I > 2\sigma(I)]$		
Number of parameters	220	283
Number of restraints	0	0
$R_1, wR_2 [I > 2\sigma(I)]$	0.0537, 0.0982	0.0762, 0.1867
$R_1, wR_2$ (all data)	0.1294, 0.1226	0.1491, 0.2323
Goodness of fit on $F^2$	0.977	0.909

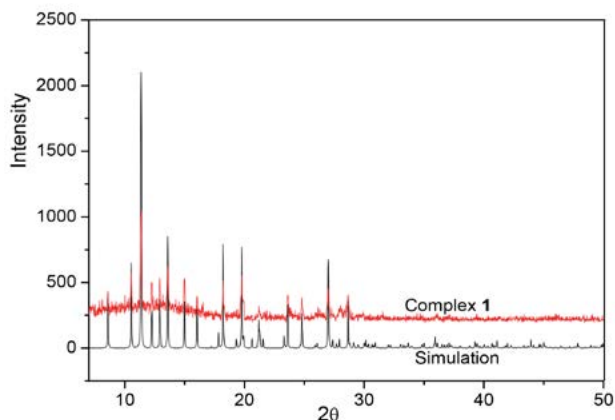
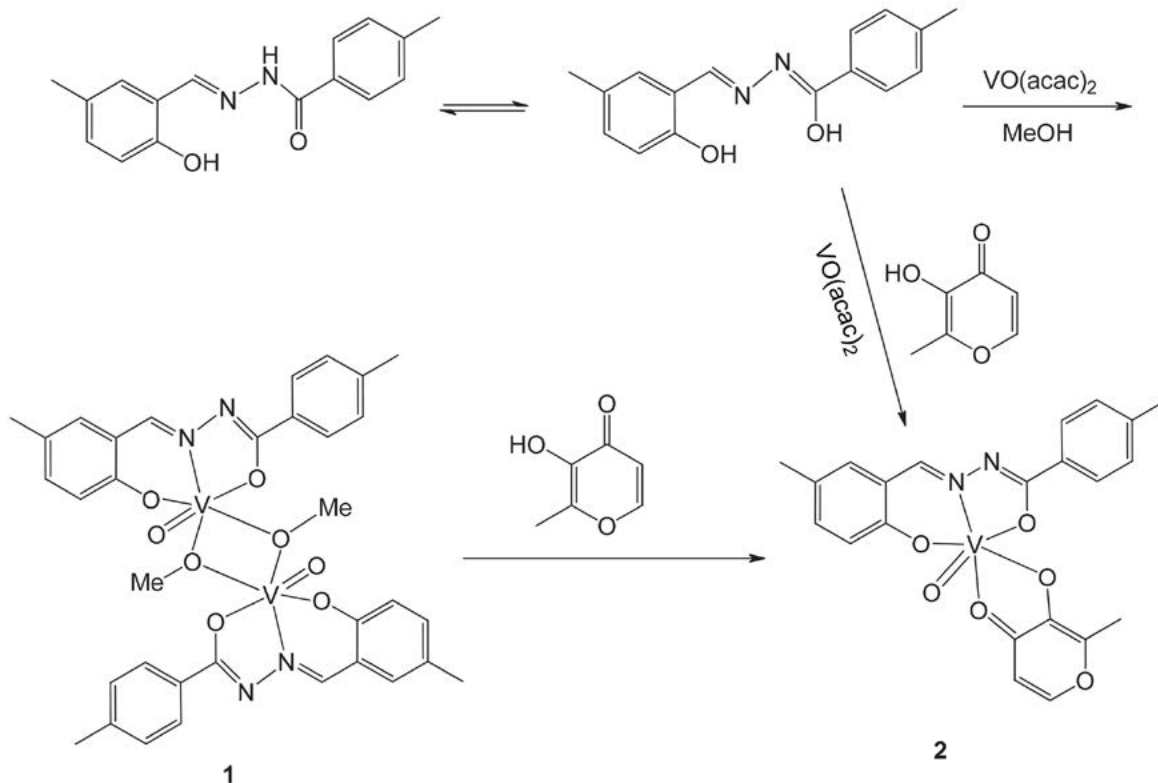
**Table 2.** Selected bond distances (Å) and angles (°) for the complexes

<b>1</b>			
V1–O1	1.823(3)	V1–O2	1.933(3)
V1–O3	1.581(3)	V1–O4	1.827(3)
V1–N1	2.093(3)	V1–O4A	2.373(3)
O3–V1–O1	101.18(14)	O3–V1–O4	102.17(13)
O1–V1–O4	106.12(12)	O3–V1–O2	99.38(13)
O1–V1–O2	151.25(12)	O4–V1–O2	88.81(11)
O3–V1–N1	96.84(14)	O1–V1–N1	83.55(13)
O4–V1–N1	156.35(13)	O2–V1–N1	74.21(12)
O3–V1–O4A	176.23(12)	O1–V1–O4A	81.37(11)
O4–V1–O4A	74.36(11)	O2–V1–O4A	79.23(10)
N1–V1–O4A	86.18(11)		
<b>2</b>			
V1–O1	1.865(4)	V1–O2	1.800(4)
V1–O3	1.531(4)	V1–O4	2.207(4)
V1–O5	1.831(4)	V1–N2	2.068(5)
O3–V1–O1	96.7(2)	O3–V1–O5	99.8(2)
O1–V1–O5	95.6(2)	O3–V1–O2	100.8(2)
O1–V1–O2	154.0(2)	O5–V1–O2	100.0(2)
O3–V1–N2	99.4(2)	O1–V1–N2	75.4(2)
O5–V1–N2	159.6(2)	O2–V1–N2	83.0(2)
O3–V1–O4	175.9(2)	O1–V1–O4	81.0(2)
O5–V1–O4	77.1(2)	O2–V1–O4	82.5(2)
N2–V1–O4	83.4(2)		

Symmetry operation for A: 1 - x, 1 - y, 1 - z.

### 3. Results and Discussion

Complex **1** was synthesized by reaction  $[\text{VO}(\text{acac})_2]$  with  $\text{H}_2\text{L}$  in MeOH (Scheme 2). Reaction of complex **1** with maltol afforded complex **2** (Scheme 2). Complex **2** can also be directly synthesized by reaction  $[\text{VO}(\text{acac})_2]$ ,  $\text{H}_2\text{L}$  and maltol in MeOH. The  $\text{V}^{\text{IV}}$  in  $[\text{VO}(\text{acac})_2]$  was oxidized to  $\text{V}^{\text{V}}$  by oxygen in air during the reaction and crystallization. Molar conductivities of the complexes at the concentration of  $10^{-4}$  mol  $\text{L}^{-1}$  are 26–35  $\Omega^{-1} \text{cm}^2 \text{mol}^{-1}$ , prove them as non-electrolytes.<sup>11</sup> The experimental and simulated powder XRD patterns of the complexes are shown in Figures 1 and 2, which confirm the purity of the bulk materials.

**Figure 1.** Experimental and simulated powder XRD patterns of complex **1**.**Scheme 2.** The synthetic procedure for the two complexes

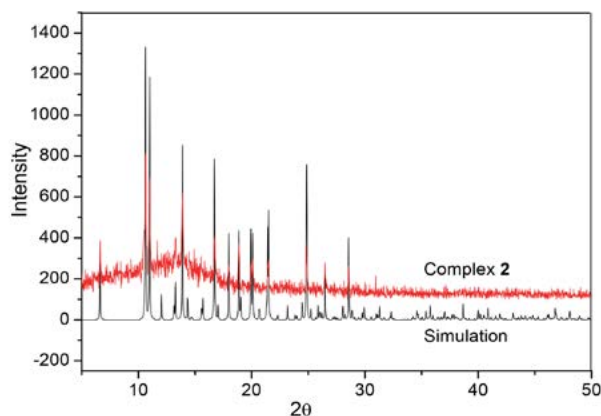


Figure 2. Experimental and simulated powder XRD patterns of complex 2.

### 3. 1. Crystal Structure Description of $[V_2O_2L_2(OMe)_2]$ (1)

Molecular structure of complex 1 is presented in Figure 3. The molecule possesses crystallographic inversion center symmetry. The two V atoms with a distance of 3.363(2) Å are bridged by two methanolate ligands. The V atoms in the complex are in octahedral coordination, which are coordinated by the three donor atoms (N1, O1, O2) of the dianionic hydrazone ligand, two oxygens (O4 and O4A) from two methanolate ligands, and one oxo oxygen (O3). The methanolate O4 atom is coordinated *trans* to the oxo oxygen, which gives a long distance than V1–O4. This is not unusual for the *trans* effect of oxo group.<sup>3–5</sup> The V1–O3 bond length of 1.581(3) Å is within normal values for reported oxidovanadium(V) complexes.<sup>4</sup> The V–O and V–N bond lengths are comparable to the dinuclear vanadium complexes bridged by methanolate or ethanolate ligand.<sup>5</sup> The angular distortion about V coordinate bonds in the octahedral geometry is due to the strain of

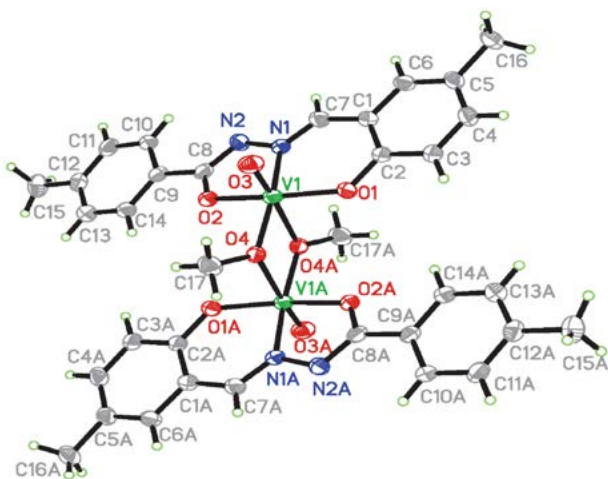


Figure 3. ORTEP plot of molecular structure of complex 1. Displacement ellipsoids of non-hydrogen atoms are drawn at the 30% probability level.

the four- and five-membered chelate rings V1–O4–V1A–O4A and V1–N1–N2–C8–O2 taken by the hydrazone ligand, with angles of 74.36(11)° and 74.21(12)°, respectively. The bond angles in the octahedral coordination are 74.36(11)–106.12(12)° for the perpendicular and 151.25(12)–176.23(12)° for the diagonal angles, also show distortion about the octahedral geometry. The V atom displaced out of the plane defined by O1, N1, O2 and O4 toward the oxo group by 0.336(2) Å. The benzene rings C1–C6 and C9–C14 form a dihedral angle of 5.9(3)°.

### 3. 2. Crystal Structure Description of $[VOLL']$ (2)

Molecular structure of complex 2 is presented in Figure 4. The V atom in the complex is in octahedral coordination, which are coordinated by the three donor atoms (N1, O1, O2) of the dianionic hydrazone ligand, two donor atoms (O4 and O5) of the maltolate ligand, and one oxo oxygen (O3). The carbonyl O4 atom is coordinated *trans* to the oxo oxygen, which gives a long distance than V1–O5. This is not unusual for the *trans* effect of oxo group.<sup>3–5</sup> The V1–O3 bond length of 1.531(4) Å is comparable to that of complex 1, and within normal values for reported oxidovanadium(V) complexes.<sup>5</sup> The angular distortion about V coordinate bonds in the octahedral geometry is due to the strain of the five-membered chelate rings V1–O4–C17–C18–O5 and V1–N2–N1–C8–O2 taken by the hydrazone and maltolate ligands, with angles of 77.1(2)° and 75.4(2)°, respectively. The bond angles in the octahedral coordination are 75.4(2)–100.8(2)° for the perpendicular and 154.0(2)–175.9(2)° for the diagonal angles, also show distortion about the octahedral geometry. The V atom displaced out of the plane defined by O1, N1, O2 and O5 toward the oxo group by 0.303(2) Å. The benzene rings C1–C6 and C9–C14 form a dihedral angle of 3.2(3)°.

In the crystal structure of the complex, the vanadium complexes are linked through intermolecular C–H...O hydrogen bonds (Table 3), to form one dimensional chains running along the *a* axis (Figure 5).

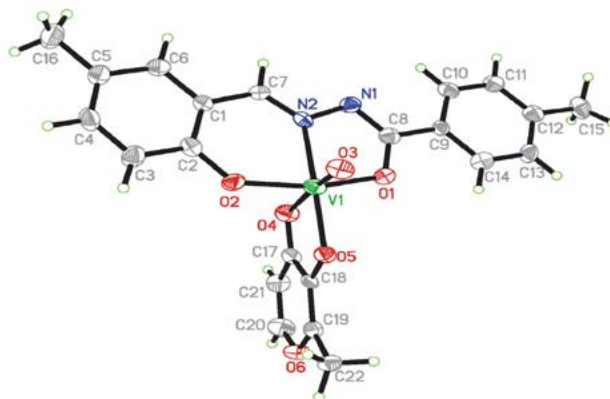
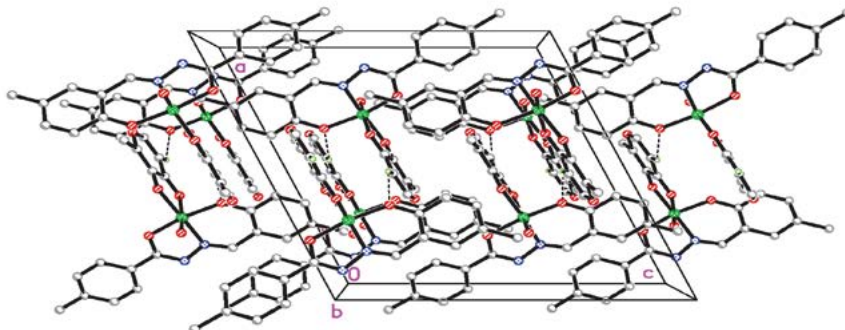


Figure 4. ORTEP plot of molecular structure of complex 2. Displacement ellipsoids of non-hydrogen atoms are drawn at the 30% probability level.

**Table 3.** Hydrogen bond distances (Å) and bond angle (°) for complex **2**

D–H...A	$d(D-H)$ , Å	$d(H...A)$ , Å	$d(D...A)$ , Å	Angle (D–H...A), °
C21–H21...O1 <sup>i</sup>	0.93	2.56	3.243	131

Symmetry code: i)  $1 - x, \frac{1}{2} + y, \frac{1}{2} - z$ .**Figure 5.** Molecular packing diagram of complex **2**, viewed along the  $b$  axis. Hydrogen atoms not related to hydrogen bonding are omitted. Hydrogen bonds are shown as dashed lines.

### 3. 3. Infrared and UV-Vis Spectra

The spectrum of  $H_2L$  showed vibrations which can be attributed to C=O, C=N, C–OH, and NH at 1648, 1617, 1154, 3290 and 3205  $cm^{-1}$ , respectively.<sup>12</sup> The bands at 961  $cm^{-1}$  for **1** and 961  $cm^{-1}$  for **2** are assigned to the characteristic vibration of V=O bond.<sup>13</sup> In the spectra of the complexes, the  $\nu_{C=O}$  and  $\nu_{NH}$  are absent, but new C–O stretches appeared at 1283  $cm^{-1}$  (**1**) and 1257  $cm^{-1}$  (**2**). This indicates the presence of *keto*-imine tautomerization of the hydrazone ligand after complexation.<sup>12</sup> The  $\nu_{C=N}$  observed at 1617  $cm^{-1}$  in the spectrum of  $H_2L$  shifted to 1608–1610  $cm^{-1}$  for the complexes upon coordination to V ions.<sup>14</sup>

In the UV-Vis spectra of  $H_2L$  and the complexes, the absorptions in the ranges 220–240 and 300–333 nm can be assigned as  $\pi \rightarrow \pi^*$  and  $n \rightarrow \pi^*$  transitions, respectively. The absorptions at 268 nm for **1** and 273 nm for **2** are due to LMCT of V=O, which is observed at 274 nm for  $[VO(acac)_2]$ .<sup>15</sup>

### 3. 4. Antibacterial Activity

The hydrazone  $H_2L$  and the complexes were assayed for antibacterial activity against *P. aeruginosa*, *S. aureus*, *B. subtilis* and *E. coli* at 50  $\mu g mL^{-1}$  using ethanol as solvent and control, and using tetracyclin as the standard drug. The minimum inhibitory concentrations (MICs) were determined by broth micro-dilution method.<sup>16</sup> The MIC values are listed in Table 4. The antibacterial activity was evaluated by measuring the zone of inhibition in mm. Ethanol has no antibacterial activity on the bacteria at the concentration studied. The results indicate that  $H_2L$  and the oxido vanadium complexes have weak to strong activities against the microorganisms. The two complexes showed stronger activities than  $H_2L$ . The least MIC value of 8  $\mu g$

$mL^{-1}$  was observed for the dinuclear complex **1** against *E. coli*. Complex **2** has good activities against *S. aureus* and *E. coli*, with the MIC values of 11 and 10  $\mu g mL^{-1}$ , respectively. The present two complexes have better activity on *B. subtilis* and *E. coli*, while similar activity on *S. aureus* when compared to the vanadium(V) complexes with fluoro- and chloro-substituted benzohydrazone ligands.<sup>12</sup>

**Table 4.** Minimum inhibitory concentrations (MICs,  $\mu g mL^{-1}$ ) of the compounds

Compound	<i>P. aeruginosa</i>	<i>S. aureus</i>	<i>B. subtilis</i>	<i>E. coli</i>
$H_2L$	> 50	45	39	27
<b>1</b>	> 50	13	17	8
<b>2</b>	> 50	11	14	10

## 4. Supplementary Material

CCDC–2285223 (1) and 2285222 (2) contain the supplementary crystallographic data for this paper. These data can be obtained free of charge at <http://www.ccdc.cam.ac.uk/const/retrieving.html> or from the Cambridge Crystallographic Data Centre (CCDC), 12 Union Road, Cambridge CB2 1EZ, UK; fax: +44(0)1223-336033 or e-mail: deposit@ccdc.cam.ac.uk.

## 5. References

- (a) A. Shaik, V. Kondaparthi, R. Aveli, D. Das Manwal, *J. Mol. Struct.* **2022**, *1261*, 132825; DOI:10.1016/j.molstruc.2022.132825

- (b) M. J. Pereira, E. Carvalho, J. W. Eriksson, D. C. Crans, M. Aureliano, *J. Inorg. Biochem.* **2009**, *103*, 1687–1692; DOI:10.1016/j.jinorgbio.2009.09.015
- (c) Z. L. Chen, *Coord. Chem. Rev.* **2022**, *457*, 214404; DOI:10.1016/j.ccr.2021.214404
- (d) O. Yalcin, J. E. M. Erwin, D. Gerceker, I. Onal, I. E. Wachs, *ACS Catal.* **2020**, *10*, 1566–1574; DOI:10.1021/acscatal.9b02450
- (e) C. C. McLauchlan, H. A. Murakami, C. A. Wallace, D. C. Crans, *J. Inorg. Biochem.* **2018**, *186*, 267–279. DOI:10.1016/j.jinorgbio.2018.06.011
2. (a) A. J. Ressler, M. Frate, A. Hontoria, A. Ream, E. Timms, H. F. Li, L. D. Stettler, A. Bollinger, J. E. Poor, M. A. Parra, H. Ma, N. P. Seeram, S. M. Meschwitz, G. E. Henry, *Bioorg. Med. Chem.* **2023**, *90*, 117369; DOI:10.1016/j.bmc.2023.117369
- (b) I. Khan, W. Rehman, F. Rahim, R. Hussain, S. Khan, L. Rasheed, M. M. Alanazi, A. S. Alanazi, M. H. Abdellattif, *ACS Omega* **2023**, *8*, 22508–22522; DOI:10.1021/acsomega.3c00702
- (c) Y. U. Cebeci, O. O. Batur, H. Boulebd, *J. Mol. Struct.* **2023**, *1289*, 135791; DOI:10.1016/j.molstruc.2023.135791
- (d) H. Kekecmammed, M. Tapera, E. Aydogdu, E. Saripinar, E. A. Karatas, E. M. Uc, M. Akyuz, B. Tuzun, I. Gulcin, R. E. Bora, I. O. Ilhan, *Chem. Biodivers.* **2023**, *20*, DOI: 10.1002/cbdv.202200886; DOI:10.1002/cbdv.202200886
- (e) O. M. I. Adly, M. Shebl, E. M. Abdelrhman, B. A. El-She-tary, *Appl. Organomet. Chem.* **2023**, *37*, DOI:10.1002/aoc.7036
- (f) K. Akdag, F. Tok, S. Karakus, O. Erdogan, O. Cevik, B. Kocyigit-Kaymakcioglu, *Acta Chim. Slov.* **2022**, *69*, 863–875; DOI:10.17344/acsi.2022.7614
- (g) G. X. He, L. W. Xue, *Acta Chim. Slov.* **2021**, *68*, 567–574; DOI:10.17344/acsi.2020.6333
- (h) Z.-Q. Sun, S.-F. Yu, X.-L. Xu, X.-Y. Qiu, S.-J. Liu, *Acta Chim. Slov.* **2020**, *67*, 1281–1289. DOI:10.17344/acsi.2020.6236
3. (a) L.-X. Li, Y. Sun, Q. Xie, Y.-B. Sun, K.-H. Li, W. Li, Z.-L. You, *Chinese J. Inorg. Chem.* **2016**, *32*, 369–376;
- (b) K. H. Li, W. Li, Y. Ding, Y. T. Ye, Z. L. You, *Russ. J. Coord. Chem.* **2015**, *41*, 549–554. DOI:10.1134/S1070328415080023
4. (a) H. Kargar, P. Forootan, M. Fallah-Mehrjardi, R. Behjatmanesh-Ardakani, H. A. Rudbari, K. S. Munawar, M. Ashfaq, M. N. Tahir, *Inorg. Chim. Acta* **2021**, *523*, 120414; DOI:10.1016/j.ica.2021.120414
- (b) Y. J. Han, L. Wang, Q. B. Li, L. W. Xue, *Russ. J. Coord. Chem.* **2017**, *43*, 612–618; DOI:10.1134/S1070328417090020
- (c) Y.-Z. Wang, P. Wang, C. Li, Y.-Q. Su, *Synth. React. Inorg. Met.-Org. Nano-Met. Chem.* **2016**, *46*, 927–930; DOI:10.1080/15533174.2014.989605
- (d) G. H. Sheng, X. Han, Z. L. You, H. H. Li, H. L. Zhu, *J. Coord. Chem.* **2014**, *67*, 1760–1770. DOI:10.1080/00958972.2014.916795
5. (a) N. Wang, J. Y. Guo, J. Y. Hu, *Russ. J. Coord. Chem.*, **2013**, *39*, 891–895; DOI:10.1134/S1070328413120087
- (b) M. Sutradhar, T. R. Barman, G. Mukherjee, M. G. B. Drew, S. Ghosh, *Polyhedron* **2012**, *34*, 92–101; DOI:10.1016/j.poly.2011.12.022
- (c) B. Mondal, M. G. B. Drew, R. Banerjee, T. Ghosh, *Polyhedron* **2008**, *27*, 3197–3206; DOI:10.1016/j.poly.2008.07.004
- (d) M. Sutradhar, M. V. Kirillova, M. F. C. G. da Silva, L. M. D. R. S. Martins, A. J. L. Pombeiro, *Inorg. Chem.* **2012**, *51*, 11229–11231; DOI:10.1021/ic3017062
- (e) E. B. Seena, N. Mathew, M. Kuriakose, M. R. P. Kurup, *Polyhedron* **2008**, *27*, 1455–1462; DOI:10.1016/j.poly.2008.01.020
- (f) N. R. Sangeetha, V. Kavita, S. Wocadlo, A. K. Powell, S. Pal, *J. Coord. Chem.* **2000**, *51*, 55–66. DOI:10.1080/00958970008047078
6. (a) S. Gao, Z.-Q. Weng, S.-X. Liu, *Polyhedron* **1998**, *17*, 3595–3606; DOI:10.1016/S0277-5387(98)00154-5
- (b) S. P. Rath, K. K. Rajak, A. Chakravorty, *Inorg. Chem.* **1999**, *38*, 4376–4377; DOI:10.1021/ic990551u
- (c) D. Qu, F. Niu, X. L. Zhao, K.-X. Yan, Y.-T. Ye, J. Wang, M. Zhang, Z. L. You, *Bioorg. Med. Chem.* **2015**, *23*, 1944–1949; DOI:10.1016/j.bmc.2015.03.036
- (d) S. Nica, A. Buchholz, M. Rudolph, A. Schweitzer, A. Wachtler, H. Breitzke, G. Buntkowsky, W. Plass, *Eur. J. Inorg. Chem.* **2008**, 2350–2359. DOI:10.1002/ejic.200800063
7. D. A. Barrio, M. D. Brazianus, S. B. Etcheverry, A. M. Cortizo, *J. Trace Elem. Med. Biol.* **1997**, *11*, 110–115. DOI:10.1016/S0946-672X(97)80035-1
8. Bruker, SMART and SAINT, Bruker AXS Inc., Madison, Wisconsin, USA, **2012**.
9. G. M. Sheldrick, SADABS Program for Empirical Absorption Correction of Area Detector, University of Göttingen, Germany, **1996**.
10. G. M. Sheldrick, *Acta Crystallogr.* **2008**, *A64*, 112–122. DOI:10.1107/S0108767307043930
11. W. J. Geary, *Coord. Chem. Rev.* **1971**, *7*, 81–122. DOI:10.1016/S0010-8545(00)80009-0
12. E.-C. Liu, W. Li, X.-S. Cheng, *Acta Chim. Slov.* **2019**, *66*, 971–977. DOI:10.17344/acsi.2019.5220
13. S. Guo, N. Sun, Y. Ding, A. Li, Y. Jiang, W. Zhai, Z. Li, D. Qu, Z. You, *Z. Anorg. Allg. Chem.* **2018**, *644*, 1172–1176. DOI:10.1002/zaac.201800060
14. H. Yu, S. Guo, J.-Y. Cheng, G. Jiang, Z. Li, W. Zhai, A. Li, Y. Jiang, Z. You, *J. Coord. Chem.* **2018**, *71*, 4164–4179. DOI:10.1080/00958972.2018.1533959
15. H. H. Monfared, R. Bikas, P. Mayer, *Inorg. Chim. Acta* **2010**, *363*, 2574–2583. DOI:10.1016/j.ica.2010.04.046
16. J. H. Jorgensen, J. D. Turnidge, *Manual of Clinical Microbiology*, Washington (DC, USA): American Society for Microbiology, **2003**.

## Povzetek

Dvojedni oksidovanadijev(V) kompleks  $[V_2O_2L_2(OMe)_2]$  (**1**) smo sintetizirali iz *N*'-(2-hidroksi-5-metilbenziden)-4-metilbenzohidrazida in  $VO(acac)_2$  v MeOH. Pri reakciji kompleksa **1** s 3-hidroksi-2-metil-4-pironom (HL) smo dobili enojedni oksidovanadijev(V) kompleks  $[VOLL']$  (**2**). Hidrazon in oba kompleksa smo okarakterizirali z IR, UV in  $^1H$  NMR spektroskopijo ter z rentgensko monokristalo analizo. Komplekse smo analizirali tudi z rentgensko praškovno difrakcijo. Vanadijevi atomi v obeh kompleksih so v oktaedrični koordinaciji. Molekule kompleksa **2** so povezane preko neklasičnih vodikovih vezi tipa C–H...O in tvorijo enodimenzionalne verige vzdolž osi *a*. Biološka evalvacija kaže, da imajo kompleksi učinkovito protimikrobno delovanje na bakterije *P. aeruginosa*, *S. aureus*, *B. subtilis* in *E. coli*.



Except when otherwise noted, articles in this journal are published under the terms and conditions of the Creative Commons Attribution 4.0 International License

Scientific paper

# Copper(II) and Nickel(II) Complexes Derived from Isostructural Bromo- and Fluoro-Containing Bis-Schiff Bases: Syntheses, Crystal Structures and Antimicrobial Activity

Ke-Sheng Cao, Ling-Wei Xue\* and Qiao-Ru Liu

School of Chemical and Environmental Engineering, Pingdingshan University, Pingdingshan Henan 467000, P.R. China

\* Corresponding author: E-mail: pdsuchemistry@163.com

Received: 08-03-2023

## Abstract

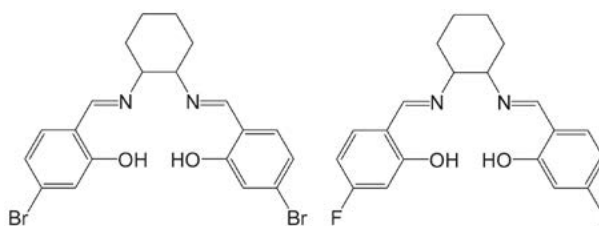
A mononuclear copper(II) complex [CuL<sup>a</sup>] (1), and three mononuclear nickel(II) complexes [NiL<sup>a</sup>] (2), [NiL<sup>a</sup>].CH<sub>3</sub>OH (2·CH<sub>3</sub>OH) and [NiL<sup>b</sup>] (3), where L<sup>a</sup> and L<sup>b</sup> are the dianionic form of *N,N'*-bis(4-bromosalicylidene)-1,2-cyclohexanediamine (H<sub>2</sub>L<sup>a</sup>) and *N,N'*-bis(4-fluorosallylidene)-1,2-cyclohexanediamine (H<sub>2</sub>L<sup>b</sup>), respectively, were prepared and structurally characterized by spectroscopy method and elemental analyses. The detailed structures were determined by X-ray single crystal diffraction. All the copper and nickel complexes are mononuclear compounds. The metal ions in the complexes are in square planar coordination, with the two phenolate oxygens and two imine nitrogens of the Schiff base ligands. The biological effect of the four complexes were assayed on the bacteria strains *Staphylococcus aureus*, *Escherichia coli* and *Candida albicans*, which show that the substituent groups of the ligands and the metal ions can influence the antimicrobial activities. Complexes 1 and 3 have strong activity against *Staphylococcus aureus* and *Escherichia coli*, which are comparable to the reference drug tetracycline.

**Keywords:** Copper complex, Nickel complex, Schiff base, Crystal structure, Antimicrobial activity

## 1. Introduction

Schiff bases containing the functional group –C=N– have received much attention in the fields of inorganic chemistry because of their interesting biological and versatile coordination modes to metal ions.<sup>1</sup> Schiff bases have effective anti-cancer, anti-bacterial, anti-fungal, anti-convulsant, and antioxidant activities.<sup>2</sup> When coordinated to metal ions, the biological activities can be enhanced. A large number of Schiff base complexes have been reported to have remarkable biological activities like antifungal, anti-proliferative, antibacterial and antitumor.<sup>3</sup> Among the complexes of various types of Schiff bases, those with salen type Schiff bases have excellent antimicrobial activities.<sup>4</sup> Copper and nickel complexes have good antimicrobial potential.<sup>5</sup> Recent research indicated that the halide groups can severely increase the antimicrobial activities.<sup>6</sup> Our research group has reported some Schiff base complexes with antimicrobial properties.<sup>7</sup> To explore new antimicrobial agents, herein we report four mononuclear copper(II) and nickel(II) complexes, [CuL<sup>a</sup>] (1), [NiL<sup>a</sup>] (2), [NiL<sup>a</sup>].

CH<sub>3</sub>OH (2·CH<sub>3</sub>OH) and [NiL<sup>b</sup>] (3), where L<sup>a</sup> and L<sup>b</sup> are the dianionic form of *N,N'*-bis(4-bromosalicylidene)-1,2-cyclohexanediamine (H<sub>2</sub>L<sup>a</sup>) and *N,N'*-bis(4-fluorosallylidene)-1,2-cyclohexanediamine (H<sub>2</sub>L<sup>b</sup>; Scheme 1).



Scheme 1. The Schiff base H<sub>2</sub>L<sup>a</sup> (left) and H<sub>2</sub>L<sup>b</sup> (right)

## 2. Experimental

### 2.1. Material and Methods

4-Bromosalicylaldehyde, 4-fluorosallylaldehyde and 1,2-diaminocyclohexane were obtained from Fluka.



The reagents and solvents with AR grade used in the experiment were used as received. The Schiff bases  $H_2L^a$  and  $H_2L^b$  were synthesized with the method as described in literature.<sup>8</sup> C, H and N elemental analyses were performed on a Perkin-Elmer 240B analyzer. Copper and nickel analyses were carried out by EDTA titration method. IR and UV-Vis spectra were recorded on IR-408 Shimadzu 568 and Lambda 900 spectrometers, respectively. Single crystal X-ray determination was done with a Bruker SMART 1000 CCD diffractometer.

## 2. 2. Synthesis of $[CuL^a]$ (1)

$H_2L$  (0.48 g, 1.0 mmol) and copper chloride dihydrate (0.17 g, 1.0 mmol) were dissolved and mixed in 50 mL EtOH. The reaction mixture was heated to reflux and stirred for 30 min. Brown and block like single crystals were formed at the bottom of the vessel by slow evaporation in air for four days. Yield: 0.23 g (43%). Analysis Calcd. for  $C_{20}H_{18}Br_2CuN_2O_2$  (%): C, 44.34; H, 3.35; N, 5.17; Cu, 11.73. Found (%): C, 44.22; H, 3.43; N, 5.05; Cu, 11.91. IR data (KBr,  $cm^{-1}$ ): 1626s, 1585s, 1523s, 1455w, 1417m, 1383m, 1280w, 1191w, 1137m, 1092w, 1064m, 919m, 853w, 790w, 624w, 607m, 517w, 510w, 445w. UV-Vis in MeOH ( $\lambda$ ,  $\epsilon$ ): 232 nm,  $2.53 \times 10^3$  L mol<sup>-1</sup> cm<sup>-1</sup>; 248 nm,  $2.61 \times 10^3$  L mol<sup>-1</sup> cm<sup>-1</sup>; 276 nm,  $1.72 \times 10^3$  L mol<sup>-1</sup> cm<sup>-1</sup>; 355 nm,  $6.72 \times 10^2$  L mol<sup>-1</sup> cm<sup>-1</sup>.

## 2.2. Synthesis of $[NiL^a]$ (2)

According to the same method as described for the synthesis of complex 1, this complex was synthesized from  $H_2L^a$  (0.48 g, 1.0 mmol) with nickel chloride hexahydrate (0.24 g, 1.0 mmol). The product was green single crystals. Yield: 0.29 g (54%). Analysis Calcd. for  $C_{20}H_{18}Br_2NiO_2$  (%): C, 44.74; H, 3.38; N, 5.22; Ni, 10.93. Found (%): C, 44.57; H, 3.32; N, 5.30; Ni, 11.12. IR data (KBr,  $cm^{-1}$ ): 1617s, 1585s, 1517m, 1455m, 1431m, 1385m, 1338w, 1293w, 1245w, 1207w, 1132w, 1060w, 1037w, 1000w, 930m, 917m, 857w, 780m, 633w, 601m, 525w, 458w. UV-Vis in MeOH ( $\lambda$ ,  $\epsilon$ ): 250 nm,  $2.46 \times 10^3$  L mol<sup>-1</sup> cm<sup>-1</sup>; 260 nm,  $2.72 \times 10^3$  L mol<sup>-1</sup> cm<sup>-1</sup>; 313 nm,  $4.92 \times 10^2$  L mol<sup>-1</sup> cm<sup>-1</sup>; 405 nm,  $3.32 \times 10^2$  L mol<sup>-1</sup> cm<sup>-1</sup>.

## 2. 3. Synthesis of $[NiL^a] \cdot CH_3OH$ (2·CH<sub>3</sub>OH)

According to the same method as described for the synthesis of complex 2, this complex was synthesized from MeOH, instead of EtOH. The product was green single crystals. Yield: 0.22 g (39%). Analysis Calcd. for  $C_{21}H_{22}Br_2N_2NiO_3$  (%): C, 44.33; H, 3.90; N, 4.92; Ni, 10.32. Found (%): C, 44.41; H, 3.81; N, 4.84; Ni, 10.55. IR data (KBr,  $cm^{-1}$ ): 3455w, 1618s, 1586s, 1520m, 1477w, 1453w, 1428m, 1383m, 1338w, 1295w, 1254w, 1213w, 1188m, 1131w, 1064w, 1032w, 1002w, 917m, 865w, 733w, 598w, 523w, 487w, 464w, 449w. UV-Vis in MeOH ( $\lambda$ ,  $\epsilon$ ): 250 nm,

$2.38 \times 10^3$  L mol<sup>-1</sup> cm<sup>-1</sup>; 260 nm,  $2.88 \times 10^3$  L mol<sup>-1</sup> cm<sup>-1</sup>; 315 nm,  $5.92 \times 10^2$  L mol<sup>-1</sup> cm<sup>-1</sup>; 405 nm,  $2.75 \times 10^2$  L mol<sup>-1</sup> cm<sup>-1</sup>.

## 2. 4. Synthesis of $[NiL^b]$ (3)

According to the same method as described for the synthesis of complex 2, this complex was synthesized from  $H_2L^b$  (0.36 g, 1.0 mmol), instead of  $H_2L^a$ . The product was green single crystals. Yield: 0.28 g (67%). Analysis Calcd. for  $C_{20}H_{18}F_2N_2NiO_2$  (%): C, 57.87; H, 4.37; N, 6.75; Ni, 14.14. Found (%): C, 57.63; H, 4.45; N, 6.82; Ni, 14.33. IR data (KBr,  $cm^{-1}$ ): 1628s, 1544s, 1479w, 1442m, 1388w, 1312w, 1222m, 1150w, 1115m, 987w, 845w, 778w, 639w, 609w, 526w, 466w, 438w. UV-Vis in MeOH ( $\lambda$ ,  $\epsilon$ ): 240 nm,  $2.23 \times 10^3$  L mol<sup>-1</sup> cm<sup>-1</sup>; 252 nm,  $2.45 \times 10^3$  L mol<sup>-1</sup> cm<sup>-1</sup>; 302 nm,  $4.25 \times 10^2$  L mol<sup>-1</sup> cm<sup>-1</sup>; 390 nm,  $2.87 \times 10^2$  L mol<sup>-1</sup> cm<sup>-1</sup>.

## 2.5. X-Ray Diffraction

Single crystal X-ray data were measured with  $MoK_{\alpha}$  radiation ( $\lambda = 0.71073$  Å) at 298(2) K using a Bruker SMART 1000 CCD diffractometer. The data were reduced with SAINT<sup>9</sup> and corrected for absorption with SADABS.<sup>10</sup> Multi-scan absorption correction was performed with  $\psi$ -scans.<sup>11</sup> Crystal structures of both complexes were solved with SHELXS-97 by direct method and refined by full-matrix least-squares technique on  $F^2$  using anisotropic displacement parameters.<sup>12</sup> All hydrogens of the complexes were placed at the calculated positions. Idealized H atoms were refined with isotropic displacement parameters set to 1.2 (1.5 for O and methyl group) times the equivalent isotropic  $U$  values of the parent carbon atoms. The crystallographic data for the complexes are presented in Table 1.

Supplementary material has been deposited with the Cambridge Crystallographic Data Centre (nos. 2286356 (1), 2286358 (2), 2286595 (3), 2286596 (4)); deposit@ccdc.cam.ac.uk or <http://www.ccdc.cam.ac.uk>.

## 2. 6. Antimicrobial Assay

The assay of antimicrobial activity was performed with the disk diffusion method.<sup>13</sup> The antibacterial activity was tested against *E. coli*, *B. subtilis*, *S. aureus* and *P. fluorescence* using Mueller-Hinton (MH) medium. The minimum inhibitory concentrations (MICs) of the assayed compounds were measured by a colorimetric method using the dye 3-(4,5-dimethylthiazol-2-yl)-2,5-diphenyltetrazolium bromide (MTT). A stock solution of the assayed compound at the concentration of 50  $\mu$ g mL<sup>-1</sup> in DMSO was prepared and quantities of the compound were incorporated in specified quantity of sterilized liquid MH medium. A specified quantity of the medium containing the compound was poured into micro-titration plates. A

**Table 1.** Crystallographic data and experimental details for the complexes

	<b>1</b>	<b>2</b>	<b>2·CH<sub>3</sub>OH</b>	<b>3</b>
Molecular formula	C <sub>20</sub> H <sub>18</sub> Br <sub>2</sub> CuN <sub>2</sub> O <sub>2</sub>	C <sub>20</sub> H <sub>18</sub> Br <sub>2</sub> N <sub>2</sub> NiO <sub>2</sub>	C <sub>21</sub> H <sub>22</sub> Br <sub>2</sub> N <sub>2</sub> NiO <sub>3</sub>	C <sub>20</sub> H <sub>18</sub> F <sub>2</sub> N <sub>2</sub> NiO <sub>2</sub>
Formula weight	541.72	536.89	568.94	415.07
Crystal system	Monoclinic	Orthorhombic	Monoclinic	Monoclinic
Space group	<i>P</i> <sub>2</sub> / <i>n</i>	<i>Pca</i> <sub>2</sub> <sub>1</sub>	<i>P</i> <sub>2</sub> / <i>n</i>	<i>P</i> <sub>2</sub> / <i>c</i>
<i>a</i> , Å	11.2186(12)	13.7957(12)	12.0963(12)	12.0131(12)
<i>b</i> , Å	9.0649(11)	16.7158(13)	14.6857(10)	24.4839(15)
<i>c</i> , Å	19.7670(13)	8.6151(10)	12.8546(11)	12.6104(12)
$\alpha$ , °	90	90	90	90
$\beta$ , °	105.379(1)	90	108.561(1)	107.583(1)
$\gamma$ , °	90	90	90	90
<i>V</i> , Å <sup>3</sup>	1938.2(3)	1986.7(3)	2164.7(3)	3535.8(5)
<i>Z</i>	4	4	4	8
$\rho_{\text{calcd}}$ , g cm <sup>-3</sup>	1.856	1.795	1.746	1.559
<i>F</i> (000)	1068	1064	1136	1712
Absorption coefficient, mm <sup>-1</sup>	5.268	5.016	4.612	1.135
Reflections collected	10047	10187	10617	20485
Independent reflections ( <i>R</i> <sub>int</sub> )	3608 (0.0409)	3538 (0.0631)	3942 (0.0627)	6565 (0.0803)
Reflections [ <i>I</i> > 2 $\sigma$ ( <i>I</i> )]	2469	2419	2029	3629
Data/parameters	3608/244	3538/244	3942/262	6565/487
Restraints	0	1	49	0
Goof on <i>F</i> <sup>2</sup>	1.039	1.048	0.996	1.013
<i>R</i> <sub>1</sub> , <i>wR</i> <sub>2</sub> ( <i>I</i> > 2 $\sigma$ ( <i>I</i> ))	0.0414, 0.0814	0.0444, 0.0883	0.0748, 0.2021	0.0531, 0.1072
<i>R</i> <sub>1</sub> , <i>wR</i> <sub>2</sub> (all data)	0.0754, 0.0926	0.0869, 0.1214	0.1424, 0.2449	0.1197, 0.1326
$\Delta\rho_{\text{max}}/\Delta\rho_{\text{min}}$ , e/Å <sup>3</sup>	0.727, -0.472	0.540, -0.332	1.059, -0.847	0.578, -0.416

suspension of the micro-organism was prepared to contain 10<sup>5</sup> cfu·mL<sup>-1</sup> and applied to micro-titration plates with serially diluted compounds in DMSO to be tested and incubated at 37 °C for 24 h. After the MICs visually determined on each micro-titration plate, 50  $\mu$ L of PBS containing 2 mg MTT per milli-litre was added to each well. Incubation was continued at room temperature for 4–5 hours. The content of each well was removed and 100  $\mu$ L of isopropanol containing hydrochloric acid was added to extract the dye. After 12 hours of incubation at room temperature, the optical density (OD) was measured with a micro-plate reader at 550 nm.

### 3. Results and Discussion

#### 3.1. Chemistry

The two isostructural Schiff bases were readily synthesized from the reaction of 1:2 molar ratio of 1,2-diaminocyclohexane with 4-bromosalicylaldehyde and 4-fluorosalicylaldehyde, respectively in MeOH. The four complexes were prepared by the reaction of 1:1 molar ratio of the Schiff bases with copper chloride and nickel chloride. Complexes **1**, **2** and **3** were prepared with ethanol as solvent, while complex **2·CH<sub>3</sub>OH** was synthesized and crystallized from methanol. When methanol was used for the synthesis and crystallization of complexes **1** and **3**, the same structures can be obtained as those with ethanol. All the complexes are soluble in EtOH, MeOH, DMSO and DMF.

#### 3.2. IR and Electronic Spectra

In the infrared spectra of the complexes, the intense bands at 1617–1628 cm<sup>-1</sup> can be assigned to  $\nu_{\text{C=N}}$ .<sup>14</sup> There is a weak and broad absorption centered at 3455 cm<sup>-1</sup> in the spectrum of complex **2·CH<sub>3</sub>OH**, while no such band in the spectrum of **2**, indicates the presence of O–H bond in **2·CH<sub>3</sub>OH**.

The electronic spectra of the complexes were recorded in MeOH. The charge transfer bands at 230–250 nm and 260–280 nm can be assigned to  $\pi \rightarrow \pi^*$  and  $n \rightarrow \pi^*$  transitions of the Schiff base ligands. The bands at 350–410 nm can be assigned to the metal to ligand charge transfer (MLCT) transition.<sup>15</sup>

#### 3.3. Crystal Structure Description of the Complexes

The bond lengths and bond angles related to the metal ions are given in Table 2. The Schiff bases L<sup>a</sup> and L<sup>b</sup> act as tetradentate ligands. Compound **1** is a mononuclear copper(II) complex with the bis-Schiff base ligand L<sup>a</sup> (Fig. 1). Compounds **2** and **3** are mononuclear nickel(II) complexes with the bis-Schiff base ligand L<sup>a</sup> (Figs. 2 and 3). The difference between the two structures is the presence of methanol solvent in **3**, while absence for **2**. Compound **3** is a mononuclear nickel(II) complex with the bis-Schiff base L<sup>b</sup> (Fig. 4). The metal atoms in the complexes are coordinated by two phenolate oxygens (O1 and O2), and two imine nitrogen atoms (N1 and N2), forming square planar

coordination. The metal atoms deviate from the least-squares planes defined by the  $N_2O_2$  donor atoms by 0.028(2) Å (1), 0.015(2) Å (2), 0.008(2) Å (2- $CH_3OH$ ), and 0.001(2) Å for Ni1 and 0.007(2) Å for Ni2 (3). The dihedral angles between the C1-C6 and C15-C20 benzene rings are 11.0(4)° for 1 and 2, 4.2(5)° for 2- $CH_3OH$ , and 7.2(4) and 11.2(4)° for 3. The Cu–O and Cu–N bond distances of complex 1 are longer than those of the Ni–O and Ni–N bonds in complexes 2, 3 and 4. The bond lengths in the three nickel complexes are similar to each other. All the M–O and M–N bond distances are comparable to those observed in similar copper(II) and nickel(II) complexes with Schiff bases.<sup>12d,16</sup>

The molecules of complex 1 are linked through C–H...O hydrogen bonds (Table 3) to form dimers, which are further linked through weak Br...O interactions to form two dimensional sheets parallel to the  $bc$  plane (Fig. 5). The molecules of complex 2 are linked through C–H...O

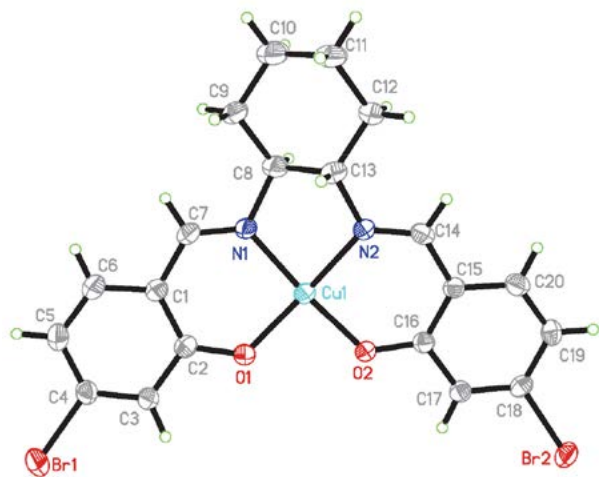


Fig. 1. Molecular structure of complex 1. Thermal ellipsoid is shown at the 30% probability level.

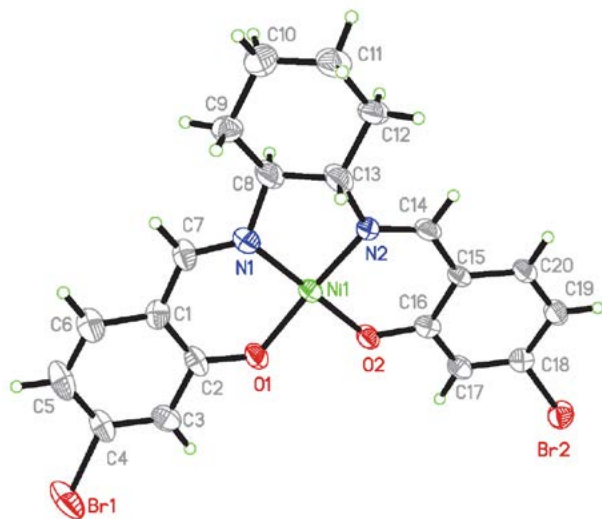


Fig. 2. Molecular structure of complex 2. Thermal ellipsoid is shown at the 30% probability level.

hydrogen bonds (Table 3) to form one dimensional chains running along the  $c$  axis (Fig. 6). The molecules of complex 2- $CH_3OH$  are linked through C–H...O, O–H...O and C–H...Br hydrogen bonds (Table 3) to form two dimensional planes parallel to the  $ab$  plane (Fig. 7). The molecules of complex 3 are linked through C–H...O hydrogen bonds (Table 3) to form dimers (Fig. 8).

### 3. 4. Antimicrobial Activity

The MIC values of the antimicrobial assay are listed in Table 4. In general, all the copper and nickel complexes have higher activity against *Staphylococcus aureus*, *Escherichia coli* and *Candida albicans* than the free Schiff bases  $H_2L^a$  and  $H_2L^b$ . This is caused by the greater lipophilic nature of the complexes than the Schiff base ligands, which can be explained with the chelating theory.<sup>21</sup> The fluoro-containing Schiff base  $H_2L^b$  has better activities

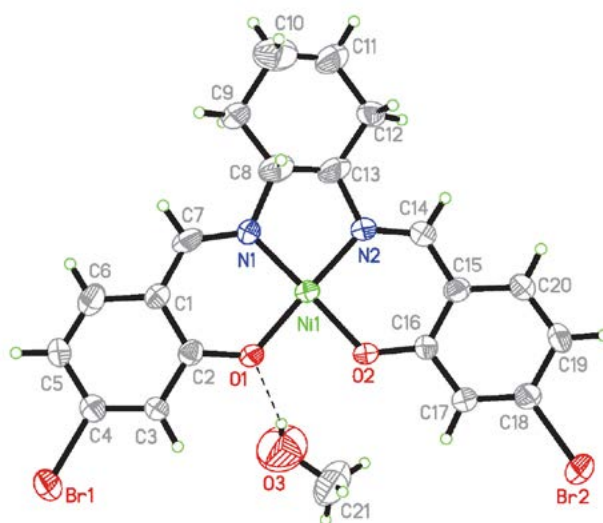


Fig. 3. Molecular structure of complex 2- $CH_3OH$ . Thermal ellipsoid is shown at the 30% probability level.

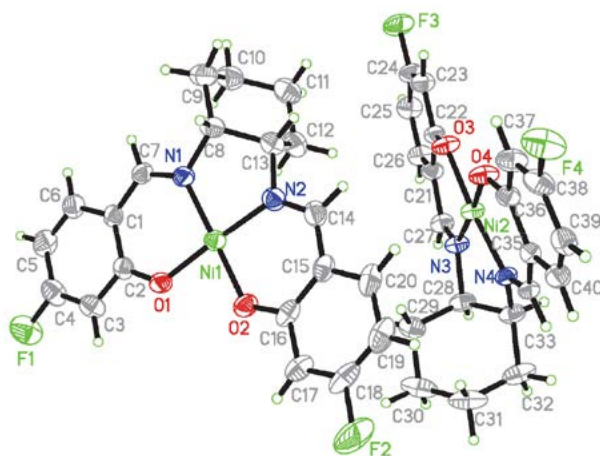


Fig. 4. Molecular structure of complex 3. Thermal ellipsoid is shown at the 30% probability level.

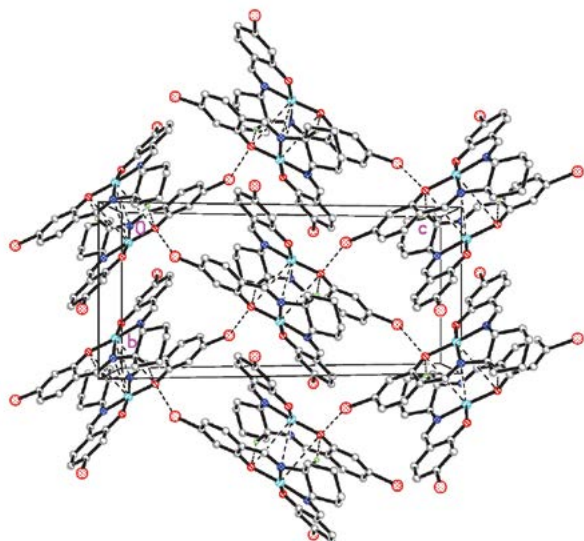


Fig. 5. Molecular packing structure of complex 1, viewed along the *b* axis. Hydrogen bonds are shown as dashed lines.

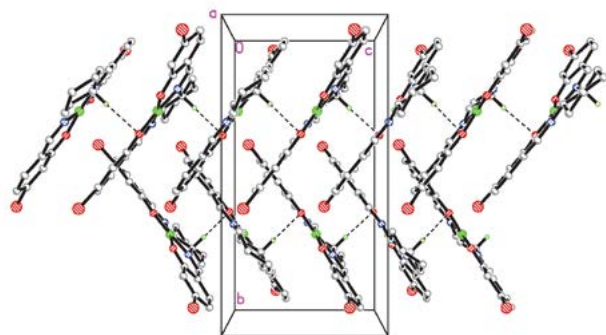


Fig. 6. Molecular packing structure of complex 2, viewed along the *b* axis. Hydrogen bonds are shown as dashed lines.

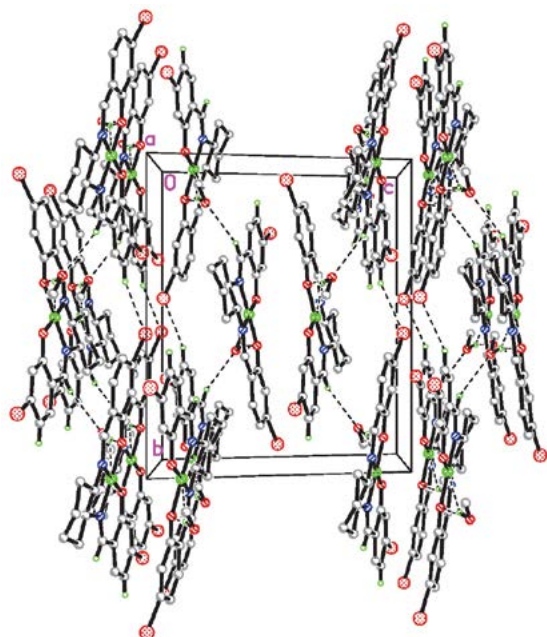


Fig. 7. Molecular packing structure of complex 2-CH<sub>3</sub>OH, viewed along the *b* axis. Hydrogen bonds are shown as dashed lines.

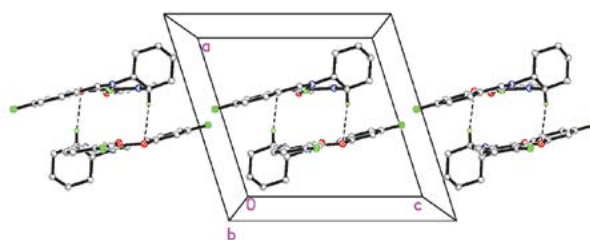


Fig. 8. Molecular packing structure of complex 3, viewed along the *b* axis. Hydrogen bonds are shown as dashed lines.

Table 2. Selected bond distances (Å) and angles (°) for the complexes

1			
Cu1–O1	1.916(3)	Cu1–O2	1.898(3)
Cu1–N1	1.934(4)	Cu1–N2	1.957(4)
O2–Cu1–O1	89.81(14)	O2–Cu1–N1	173.53(16)
O1–Cu1–N1	93.98(15)	O2–Cu1–N2	93.20(15)
O1–Cu1–N2	170.86(16)	N1–Cu1–N2	83.85(16)
2			
Ni1–O1	1.851(5)	Ni1–O2	1.825(5)
Ni1–N1	1.855(7)	Ni1–N2	1.838(6)
O2–Ni1–N2	95.7(3)	O2–Ni1–O1	84.1(2)
N2–Ni1–O1	174.2(3)	O2–Ni1–N1	175.8(3)
N2–Ni1–N1	86.0(3)	O1–Ni1–N1	94.6(3)
2-CH <sub>3</sub> OH			
Ni1–O1	1.843(6)	Ni1–O2	1.855(6)
Ni1–N1	1.821(8)	Ni1–N2	1.841(8)
N1–Ni1–N2	86.2(3)	N1–Ni1–O1	94.9(3)
N2–Ni1–O1	178.2(3)	N1–Ni1–O2	177.2(4)
N2–Ni1–O2	95.3(3)	O1–Ni1–O2	83.6(3)
3			
Ni1–O1	1.831(3)	Ni1–O2	1.830(3)
Ni1–N1	1.856(4)	Ni1–N2	1.843(4)
Ni2–O3	1.847(3)	Ni2–O4	1.841(3)
Ni2–N3	1.829(4)	Ni2–N4	1.846(4)
O2–Ni1–O1	84.69(14)	O2–Ni1–N2	93.71(17)
O1–Ni1–N2	176.94(16)	O2–Ni1–N1	178.60(15)
O1–Ni1–N1	94.95(17)	N2–Ni1–N1	86.71(19)
N3–Ni2–O4	175.70(16)	N3–Ni2–N4	85.81(16)
O4–Ni2–N4	95.12(15)	N3–Ni2–O3	94.25(15)
O4–Ni2–O3	85.19(13)	N4–Ni2–O3	174.91(15)

against *Staphylococcus aureus* and *Escherichia coli* than the bromo-containing Schiff base H<sub>2</sub>L<sup>a</sup>. The same pattern can be observed for the complexes 2 and 3. Complex 3 with the fluoro-containing Schiff base ligand has stronger antimicrobial activities than complex 2 with the bromo-containing Schiff base ligand. Interestingly, the copper complex 1 has better activities than the nickel complex 2. Thus, the substituent groups of the ligands and the metal ions can influence the antimicrobial activities. The copper complex 1 and the nickel complex 3 have strong activity against *Staphylococcus aureus* and *Escherichia coli*, and weak activ-

Table 3. Hydrogen bonding parameters for the complexes

D–H...A	d(D–H) (Å)	d(H...A) (Å)	d(D...A) (Å)	∠(D–H...A) (°)
<b>1</b>				
C13–H13...O2 <sup>i</sup>	0.98	2.49(3)	3.318(5)	143(5)
<b>2</b>				
C8–H8...O2 <sup>ii</sup>	0.98	2.46(4)	1.372(5)	154(5)
<b>2-CH<sub>3</sub>OH</b>				
O3–H3A...O1 <sup>iii</sup>	0.82	1.98(3)	2.767(5)	160(4)
C14–H14...O3	0.93	2.48(4)	3.288(6)	145(5)
C19–H19...Br1 <sup>iv</sup>	0.93	2.92(5)	3.640(6)	135(6)
<b>3</b>				
C8–H8...O2 <sup>v</sup>	0.98	2.57(3)	3.507(5)	160(7)

Symmetry transformation used to generate equivalent atoms: (i)  $-x, 2-y, -z$ ; (ii)  $3/2-x, y, 1/2+z$ ; (iii)  $1/2-x, -1/2+y, 1/2-z$ ; (iv)  $x, -1+y, z$ ; (v)  $1-x, -y, -z$ .

ity against *Candida albicans*. The activities of both complexes are comparable to the reference drug tetracycline. While for *Candida albicans*, all the three complexes have stronger activities than tetracycline.

Table 4. Antimicrobial activities with MIC values ( $\mu\text{g mL}^{-1}$ )

Compound	<i>Staphylococcus aureus</i>	<i>Escherichia coli</i>	<i>Candida albicans</i>
H <sub>2</sub> L <sup>a</sup>	64	128	> 1024
H <sub>2</sub> L <sup>b</sup>	32	32	> 1024
<b>1</b>	0.5	4.0	64
<b>2</b>	4.0	16	256
<b>3</b>	1.0	4.0	32
tetracycline	0.25	2.0	> 1024

## 4. Conclusion

Four new mononuclear copper(II) and nickel(II) complexes derived from the tetradentate Schiff base ligands *N,N'*-bis(4-bromosalicylidene)-1,2-cyclohexanediamine and *N,N'*-bis(4-fluorosalicylidene)-1,2-cyclohexanediamine have been synthesized. All the complexes were characterized by physical-chemical methods. The detailed structures of the complexes were determined by X-ray single crystal diffraction. All the metal ions in the complexes are in square planar geometry. The complexes show effective antibacterial activities on *Staphylococcus aureus* and *Escherichia coli*. The copper complex has the most activity against *Staphylococcus aureus* with MIC value of 0.5  $\mu\text{g mL}^{-1}$ .

## Acknowledgments

This research was supported by the National Science Foundation of China (nos. 20676057 and 20877036)

and Top-class foundation of Pingdingshan University (no. 2008010).

## 5. References

- (a) M. Karmakar, W. Sk, R. M. Gomila, M. G. B. Drew, A. Frontera, S. Chattopadhyay, *RSC Advances* **2023**, *13*, 21211–21224; DOI:10.1039/D3RA04044E  
(b) D. S. Shankar, A. Rambabu, Shivaraj, *Chem. Biodivers.* **2023**, DOI: 10.1002/cbdv.202300030; DOI:10.1002/cbdv.202300030  
(c) Q. U. Sandhu, M. Pervaiz, S. Jelani, *J. Coord. Chem.* **2023**, DOI:10.1080/00958972.2023.2226794  
(d) H. R. Sonawane, B. T. Vibhute, S. K. Patil, *Eur. J. Med. Chem.* **2023**, *258*, 115549; DOI:10.1016/j.ejmech.2023.115549  
(e) M. Kumar, A. K. Singh, A. K. Singh, R. K. Yadav, S. Singh, A. P. Singh, A. Chauhan, *Coord. Chem. Rev.* **2023**, *488*, 215176; DOI:10.1016/j.ccr.2023.215176  
(f) R. Kumar, A. A. Singh, U. Kumar, P. Jain, A. K. Sharma, C. Kant, M. S. H. Faizi, *J. Mol. Struct.* **2023**, *1294*, 136346. DOI:10.1016/j.molstruc.2023.136346
- (a) S. D. Pradeep, A. K. Gopalakrishnan, D. K. Manoharan, R. S. Soumya, R. K. Gopalan, P. V. Mohanan, *J. Mol. Struct.* **2023**, *1271*, 134121; DOI:10.1016/j.molstruc.2022.134121  
(b) N. A. A. Elkanzi, H. Hrichi, R. B. Bakr, *Lett. Drug Des. Discov.* **2022**, *19*, 654–673; DOI:10.2174/1570180819666211228091055  
(c) S. H. Sumrra, W. Zafar, S. A. Malik, K. Mahmood, S. S. Shafiqat, S. Arif, *Acta Chim. Slov.* **2022**, *69*, 200–216;  
(d) B. Li, Z. Zhang, J.-F. Zhang, J. Liu, X.-Y. Zuo, F. Chen, G.-Y. Zhang, H.-Q. Fang, Z. Jin, Y.-Z. Tang, *Eur. J. Med. Chem.* **2021**, *223*, 113624. DOI:10.1016/j.ejmech.2021.113624
- (a) L. Korte-Real, V. Posa, I. Correia, *Inorg. Chem.* **2023**, DOI: 10.1021/acs.inorgchem.3c01066;  
(b) S. El-Kalyoubi, S. A. El-Sebaey, S. M. Elfeky, *J. Enzyme Inhib. Med. Chem.* **2023**, *38*, 2232125; DOI:10.1080/14756366.2023.2198163

- (c) S. Biswas, A. Wasai, M. Ghosh, C. Rizzoli, A. Roy, S. Saha, S. Mandal, *J. Inorg. Biochem.* **2023**, *247*, 112314; DOI:10.1016/j.jinorgbio.2023.112314
- (d) R. Kumar, K. Seema, D. K. Singh, P. Jain, N. Manav, B. Gautam, S. N. Kumar, *J. Coord. Chem.* **2023**, DOI:10.1080/00958972.2023.2231608
- (e) S. Nayab, A. Alam, N. Ahmad, S. W. Khan, W. Khan, D. F. Shams, M. I. A. Shah, M. Ateeq, S. K. Shah, H. Lee, *ACS Omega* **2023**, *8*, 17620–17633; DOI:10.1021/acsomega.2c08266
- (f) S. Feizpour, S. A. Hosseini-Yazdi, E. Safarzadeh, B. Baradaran, M. Dusek, M. Poupon, *J. Biol. Inorg. Chem.* **2023**, DOI:10.1007/s00775-023-02001-5
4. (a) S. Ali, T. Ara, M. Danish, S. Shujah, A. M. Z. Slawin, *Russ. J. Coord. Chem.* **2019**, *45*, 889–898; DOI:10.1134/S1070328419120017
- (b) P. Middy, A. Saha, S. Chattopadhyay, *Inorg. Chim. Acta* **2023**, *545*, 121246; DOI:10.1016/j.ica.2022.121246
- (c) S. Kumar, M. Choudhary, *Indian J. Chem.* **2023**, *62*, 472–497; DOI:10.1007/978-981-19-7997-2\_19
- (d) V. Sharma, E. K. Arora, S. Cardoza, *Chem. Papers* **2016**, *70*, 1493–1502; DOI:10.1515/chempap-2016-0083
- (e) N. Mahlooji, M. Behzad, H. A. Rudbari, G. Bruno, B. Ghanbari, *Inorg. Chim. Acta* **2016**, *445*, 124–128. DOI:10.1016/j.ica.2016.02.040
5. (a) A. Climova, E. Pivovarov, M. I. Szczesio, K. Gobis, D. Ziembicka, A. Korga-Plewko, J. Kubik, M. Iwan, M. Antos-Bielska, M. Krzyzowska, A. Czylkowska, *J. Inorg. Biochem.* **2023**, *240*, 112108; DOI:10.1016/j.jinorgbio.2022.112108
- (b) Y. Tan, Y. Lei, *Polyhedron* **2023**, *231*, 116270; DOI:10.1016/j.poly.2022.116270
- (c) K. Preinerova, M. Puchonova, M. Schoeller, V. Kuchtanin, N. Molnarova, S. Krystofova, M. Mazur, I. Ilko, V. Peterkova, J. Moncol, *Polyhedron* **2022**, *227*, 116146; DOI:10.1016/j.poly.2022.116146
- (d) L. Zhang, X.-Y. Qiu, S.-J. Liu, *Acta Chim. Slov.* **2023**, *70*, 12–20; DOI:10.17344/acsi.2022.10.17344/acsi.2022.7737
- (e) A. Das, A. Rajeev, S. Bhunia, M. Arunkumar, N. Chari, M. Sankaralingam, *Inorg. Chim. Acta* **2021**, *526*, 120515. DOI:10.1016/j.ica.2021.120515
6. M. Zhang, D.-M. Xian, H.-H. Li, J.-C. Zhang, Z.-L. You, *Aust. J. Chem.* **2012**, *65*, 343–350. DOI:10.1071/CH11424
7. (a) L.-W. Xue, H.-J. Zhang, P.-P. Wang, *Acta Chim. Slov.* **2019**, *66*, 190–195; DOI:10.17344/acsi.2018.4773
- (b) G.-X. He, L.-W. Xue, Q.-L. Peng, P.-P. Wang, H.-J. Zhang, *Acta Chim. Slov.* **2019**, *66*, 570–575; DOI:10.17344/acsi.2018.4868
- (c) L.-W. Xue, Y.-J. Han, X.-Q. Luo, *Acta Chim. Slov.* **2019**, *66*, 622–628. DOI:10.17344/acsi.2019.5039
8. Y. Luo, J. Wang, X. Ding, R. Ni, M. Li, T. Yang, J. Wang, C. Jing, Z. You, *Inorg. Chim. Acta* **2021**, *516*, 120146. DOI:10.1016/j.ica.2020.120146
9. Bruker, SMART and SAINT, *Area Detector Control and Integration Software*, Madison (WI, USA): Bruker Analytical X-ray Instruments Inc., 1997.
10. G. M. Sheldrick, SADABS, *Program for Empirical Absorption Correction of Area Detector Data*, Göttingen (Germany): Univ. of Göttingen, 1997.
11. A. C. T. North, D. C. Phillips, F. S. Mathews, *Acta Crystallogr. A* **1968**, *24*, 351–359. DOI:10.1107/S0567739468000707
12. G. M. Sheldrick, SHELXL-97, *Program for the Refinement of Crystal Structures*, Göttingen (Germany): Univ. of Göttingen, 1997.
13. (a) A. Barry, *Procedures and Theoretical Considerations for Testing Antimicrobial Agents in Agar Media*, In: *Antibiotics in Laboratory Medicine*, Lorian, V., Ed., Baltimore: Williams and Wilkins, 1991;
- (b) T. Rosu, M. Negoitu, S. Pasculescu, E. Pahontu, D. Poirier, A. Gulea, *Eur. J. Med. Chem.* **2010**, *45*, 774–781. DOI:10.1016/j.ejmech.2009.10.034
14. A. Ray, D. Sadhukhan, G. M. Rosair, C. J. Gomez-Garcia, S. Mitra, *Polyhedron* **2009**, *28*, 3542–3550. DOI:10.1016/j.poly.2009.07.017
15. M. Enamullah, M. A. Quddus, M. A. Halim, M. K. Islam, V. Vasylyeva, C. Janiak, *Inorg. Chim. Acta* **2015**, 103–111. DOI:10.1016/j.ica.2014.11.020
16. (a) K. Jayakumar, E. B. Seena, M. R. P. Kurup, S. Kayac, G. Serdaroglu, E. Suresh, R. Marzouki, *J. Mol. Struct.* **2022**, *1253*, 132257; DOI:10.1016/j.molstruc.2021.132257
- (b) J. Jiang, P. Liang, H. Y. Yu, Z. L. You, *Acta Chim. Slov.* **2022**, *69*, 629–637; DOI:10.17344/acsi.2022.7513
- (c) I. Al-Qadsy, A. B. Al-Odayni, W. S. Saeed, A. Alrabie, A. Al-Adhrai, L. A. S. Al-Faqeh, P. Lama, A. A. Alghamdi, M. Farooqui, *Crystals* **2021**, *11*, 110; DOI:10.3390/cryst11020110
- (d) S. Mandal, M. Layek, R. Saha, C. Rizzoli, D. Bandyopadhyay, *Transition Met. Chem.* **2021**, *46*, 9–16; DOI:10.1007/s11243-020-00416-6
- (e) B. Mohan, A. Jana, N. Das, S. Bharti, M. Choudhary, S. Muhammad, S. Kumar, A. G. Al-Sehemi, H. Algarni, *Inorg. Chim. Acta* **2019**, *484*, 148–159. DOI:10.1016/j.ica.2018.09.037

## Povzetek

Sintetizirali smo enojedrni bakrov(II) kompleks  $[\text{CuL}^{\text{a}}]$  (**1**) in tri enojedrne nikljeve(II) komplekse  $[\text{NiL}^{\text{a}}]$  (**2**),  $[\text{NiL}^{\text{a}}]\cdot\text{CH}_3\text{OH}$  (**2-CH}\_3\text{OH}**) in  $[\text{NiL}^{\text{b}}]$  (**3**), kjer sta  $\text{L}^{\text{a}}$  in  $\text{L}^{\text{b}}$  dianionski obliki *N,N'*-bis(4-bromosaliciliden)-1,2-cikloheksandiamina ( $\text{H}_2\text{L}^{\text{a}}$ ) in *N,N'*-bis(4-fluorosaliciliden)-1,2-cikloheksandiamina ( $\text{H}_2\text{L}^{\text{b}}$ ). Spojine smo okarakterizirali s spektroskopskimi metodami, elementno analizo in rentgensko strukturno analizo. Bakrov in vsi nikljevi kompleksi so enojedrne spojine. Kovinski ioni v kompleksih so v kvadratno planarni koordinaciji z dvema fenolnima kisikovima atomoma in dvema iminskima dušikovima atomoma Schiffovih ligandov. Biološki učinek štirih kompleksov je bil preverjen na sevih bakterij *Staphylococcus aureus*, *Escherichia coli* in *Candida albicans*. Substituente na ligandu in kovinski ion vplivajo na protimikrobno delovanje. Kompleksa **1** in **3** imata močno aktivnost proti *Staphylococcus aureus* in *Escherichia coli*, ki je primerljiva z referenčnim zdravilom tetraciklinom.



Except when otherwise noted, articles in this journal are published under the terms and conditions of the Creative Commons Attribution 4.0 International License

Scientific paper

# Syntheses, Characterization, Crystal Structures and Xanthine Oxidase Inhibitory Activity of Hydrazones

Xiao-Jun Zhao, Ling-Wei Xue\* and Qiao-Ru Liu

School of Chemical and Environmental Engineering, Pingdingshan University, Pingdingshan Henan 467000, P.R. China

\* Corresponding author: E-mail: pdschemistry@163.com

Received: 08-06-2023

## Abstract

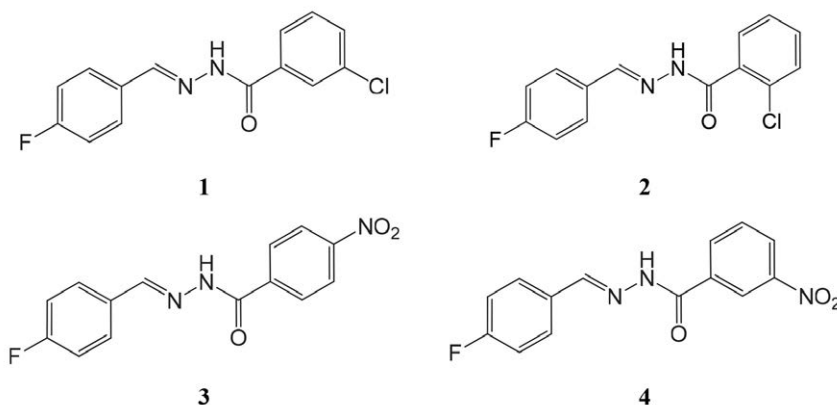
Four new fluoro-containing hydrazones were synthesized from 4-fluorobenzaldehyde with chloro- and nitro-substituted benzohydrazides. They are 3-chloro-*N'*-(4-fluorobenzylidene)benzohydrazide (1), 2-chloro-*N'*-(4-fluorobenzylidene)benzohydrazide (2), *N'*-(4-fluorobenzylidene)-4-nitrobenzohydrazide (3), and *N'*-(4-fluorobenzylidene)-3-nitrobenzohydrazide (4). The compounds have been characterized by IR and <sup>1</sup>H NMR spectroscopy, as well as X-ray single crystal determination. Xanthine oxidase (XO) inhibitory activity indicated that the nitro substituted compounds 3 and 4 have effective activity. Docking simulation was performed to insert the compounds into the crystal structure of xanthine oxidase at the active site to investigate the probable binding modes.

**Keywords:** Hydrazone; xanthine oxidase; inhibition; crystal structure; molecular docking study.

## 1. Introduction

Xanthine oxidase (XO; Enzyme Code 1.17.3.2) is a molybdenum hydroxylase, which catalyzes hypoxanthine and xanthine to form superoxide anions and uric acid. The superoxide anions are responsible for post ischaemic tissue injury and vascular permeability.<sup>1</sup> Xanthine oxidase has many negative effects. It can oxidize the purine drug antileukaemic 6-mercaptopurine to lose its pharmacological activity. Moreover, it can lead to hepatic and kidney damage, atherosclerosis, chronic heart failure, hypertension and sickle-cell disease.<sup>2</sup> Thus, it is necessary to control the activ-

ity of xanthine oxidase. Allopurinol is a well known XO inhibitor, which has been used as medicine to treat the gout.<sup>3</sup> However, it has obvious side effects like toxicity, and inability to prevent the formation of free radicals by the enzyme.<sup>4</sup> So, it is urgent to explore new xanthine oxidase inhibitors. To date, a large number of compounds like pyrimidines and carboxylic acids,<sup>5</sup> 3-cyanoindoles and pyrimidinones,<sup>6</sup> hydrozingerones,<sup>7</sup> amides,<sup>8</sup> pyrazoles,<sup>9</sup> thiobarbiturates,<sup>10</sup> have been reported to have xanthine oxidase inhibitory activity. Schiff bases with C=N functional group have received much attention in the fields of biological chemistry.<sup>11</sup> Leigh has reported a few Schiff bases with



Scheme 1. The hydrazone compounds.



potential xanthine oxidase inhibitory activity.<sup>12</sup> Hydrazones are a special kind of Schiff base which possess the functional group C=N-NH-C(O). These compounds have interesting biological activities.<sup>13</sup> Moreover, the electronic withdrawing groups like F, Cl and NO<sub>2</sub> can improve the biological activities.<sup>14</sup> Recently, we have reported a series of hydrazones, and found that *N*'-(3-methoxybenzylidene)-4-nitrobenzohydrazide and 2-cyano-*N*'-(4-diethylamino-2-hydroxybenzylidene)acetohydrazide have effective activity on xanthine oxidase.<sup>15</sup> However, the xanthine oxidase inhibition of hydrazones has rarely been studied so far. Aiming at obtaining new xanthine oxidase inhibitors, we report herein four new hydrazones (Scheme 1), 3-chloro-*N*'-(4-fluorobenzylidene)benzohydrazide (1), 2-chloro-*N*'-(4-fluorobenzylidene)benzohydrazide (2), *N*'-(4-fluorobenzylidene)-4-nitrobenzohydrazide (3), and *N*'-(4-fluorobenzylidene)-3-nitrobenzohydrazide (4). were synthesized and characterized. Their xanthine oxidase inhibitory activity was studied.

## 2. Experimental

### 2.1. Materials and Methods

4-Fluorobenzaldehyde, 3-chlorobenzohydrazide, 2-chlorobenzohydrazide, 4-nitrobenzohydrazide, 3-nitrobenzohydrazide and solvents were obtained from commercial suppliers and used as received. Elemental analyses for C, H and N were performed on a Perkin-Elmer 240C elemental analyzer. IR spectra were recorded on a Jasco FT/IR-4000 spectrometer as KBr pellets in the 4000–400 cm<sup>-1</sup> region. <sup>1</sup>H NMR data were performed on a Bruker 300 MHz instrument. X-ray single crystal diffraction was determined on a Bruker SMART 1000 CCD diffractometer.

### 2.2. Synthesis of the Compounds

The four compounds were synthesized with the same method as described. 4-Fluorobenzaldehyde (0.12 g, 1.0 mmol) and 1.0 mmol benzohydrazide were respectively dissolved in 20 mL methanol. Then, the two precursors were mixed and stirred at room temperature for 30 min to give clear solution. The solution was stand still in air, and slow evaporate for a few days to obtain X-ray quality single crystals.

#### 3-Chloro-*N*'-(4-fluorobenzylidene)benzohydrazide (1)

The benzohydrazide is 3-chlorobenzohydrazide (0.17 g). Block colorless single crystals. Yield: 0.26 g (93%). Anal. Calc. for C<sub>14</sub>H<sub>12</sub>ClFN<sub>2</sub>O<sub>2</sub> (%): C, 57.06; H, 4.10; N, 9.51. Found (%): C, 57.23; H, 3.97; N, 9.40. IR data (cm<sup>-1</sup>): 3217w (NH), 1665s (C=O), 1600m (C=N). <sup>1</sup>H NMR (300 MHz, *d*<sub>6</sub>-DMSO): δ 11.96 (s, 1H, NH), 8.46 (s, 1H, CH=N), 7.97 (s, 1H, ArH), 7.88 (d, 1H, ArH), 7.82 (d, 2H, ArH), 7.70 (d, 1H, ArH), 7.60 (t, 1H, ArH), 7.32 (t, 2H, ArH).

#### 2-chloro-*N*'-(4-fluorobenzylidene)benzohydrazide (2)

The benzohydrazide is 2-chlorobenzohydrazide (0.17 g). Block colorless single crystals. Yield: 2.4 g (87%). Anal. Calc. for C<sub>14</sub>H<sub>10</sub>ClFN<sub>2</sub>O (%): C, 60.77; H, 3.64; N, 10.12. Found (%): C, 60.61; H, 3.72; N, 10.21. IR data (cm<sup>-1</sup>): 3235w (NH), 1666s (C=O), 1602m (C=N). <sup>1</sup>H NMR (300 MHz, *d*<sub>6</sub>-DMSO): δ 11.90 (s, 1H, NH), 8.28 (s, 1H, CH=N), 7.82 (d, 2H, ArH), 7.55–7.60 (m, 2H, ArH), 7.50 (m, 2H, ArH), 7.30 (d, 1H, ArH), 7.17 (t, 1H, ArH).

#### *N*'-(4-fluorobenzylidene)-4-nitrobenzohydrazide (3)

The benzohydrazide is 4-nitrobenzohydrazide (0.18 g). Prism yellow single crystals. Yield: 2.6 g (91%). Anal. Calc. for C<sub>14</sub>H<sub>10</sub>FN<sub>3</sub>O<sub>3</sub> (%): C, 58.54; H, 3.51; N, 14.63. Found (%): C, 58.37; H, 3.62; N, 14.47. IR data (cm<sup>-1</sup>): 3226w (NH), 1653s (C=O), 1604m (C=N), 1522s and 1345s (NO<sub>2</sub>). <sup>1</sup>H NMR (300 MHz, *d*<sub>6</sub>-DMSO): δ 12.17 (s, 1H, NH), 8.49 (s, 1H, CH=N), 8.40 (d, 2H, ArH), 8.18 (d, 2H, ArH), 7.85 (d, 2H, ArH), 7.35 (d, 2H, ArH).

#### *N*'-(4-fluorobenzylidene)-3-nitrobenzohydrazide (4)

The benzohydrazide is 4-nitrobenzohydrazide (0.18 g). Block yellow single crystals. Yield: 2.5 g (87%). Anal. Calc. for C<sub>14</sub>H<sub>10</sub>FN<sub>3</sub>O<sub>3</sub> (%): C, 58.54; H, 3.51; N, 14.63. Found (%): C, 58.41; H, 3.45; N, 14.50. IR data (cm<sup>-1</sup>): 3227w (NH), 1649s (C=O), 1608m (C=N), 1532s and 1350s (NO<sub>2</sub>). <sup>1</sup>H NMR (300 MHz, *d*<sub>6</sub>-DMSO): δ 12.20 (s, 1H, NH), 8.78 (s, 1H, ArH), 8.51 (s, 1H, CH=N), 8.48 (d, 1H, ArH), 8.38 (d, 1H, ArH), 7.89–7.82 (m, 3H, ArH), 7.35 (d, 2H, ArH).

### 2.3. Xanthine Oxidase Inhibition Assay

The xanthine oxidase activity with xanthine as substrate was measured according to the method reported by Kong and co-workers with modification.<sup>16</sup> The activity of xanthine oxidase was measured by uric acid formation monitored at 295 nm. The assay was performed in K<sub>2</sub>HPO<sub>4</sub> (1.0 mL, 50 mmol L<sup>-1</sup>) in a quartz cuvette. The reaction mixture contains xanthine (200 μL, 84.8 μg mL<sup>-1</sup>) in the solution of K<sub>2</sub>HPO<sub>4</sub>, and various concentrations of tested compounds (50 μL). The reaction was started by addition of xanthine oxidase (66 μL, 37.7 mU mL<sup>-1</sup>), and monitored for 6 min at 295 nm and the product was expressed as μmol uric acid per minute. The reactions kinetic were linear during these 6 min of monitoring.

### 2.4. Docking Simulations

Molecular docking study of the molecules of the hydrazones into the three-dimensional structure of xanthine oxidase (1FIQ in the Protein Data Bank) was carried out by using AutoDock 4.2. AutoGrid component of the program calculates a three-dimensional grid of interaction energies based on the macromolecular target using AMBER force field. The cubic grid box of 60 × 60 × 60 Å<sup>3</sup>

points in  $x$ ,  $y$ , and  $z$  direction with a spacing of 0.375 Å and grid maps were created representing the catalytic active target site region where the native ligand was embedded. Then automated docking studies were carried out to evaluate the binding free energy of the inhibitor within the macromolecules. The GALS search algorithm (genetic algorithm with local search) was chosen to search for the best conformers. The parameters were set using ADT (AutoDockTools 1.5.4) on PC which is associated with AutoDock 4.2. Default settings were used with an initial population of 100 randomly placed individuals, a maximum number of  $2.5 \times 10^6$  energy evaluations, and a maximum number of  $2.7 \times 10^4$  generations. A mutation rate of 0.02 and a crossover rate of 0.8 were chosen. Give overall consideration of the most favorable free energy of binding and the majority cluster, the results were selected as the most probable complex structures.

## 2. 5. Data Collection, Structural Determination and Refinement

The collected data were reduced with SAINT,<sup>17</sup> and multi-scan absorption correction was performed with SADABS.<sup>18</sup> The structures of the compounds were solved by direct method and refined against  $F^2$  by full-matrix least-squares method using SHELXTL.<sup>19</sup> All non-hydrogen atoms were refined anisotropically. The water H atoms

in **1**, and all amino H atoms in the four compounds were located from difference Fourier maps and refined isotropically, with O–H, N–H and H...H distances restrained to 0.85(1), 0.90(1) and 1.37(2) Å, respectively. The remaining H atoms were placed in calculated positions and constrained to ride on their parent atoms. The crystallographic data for the compounds are summarized in Table 1.

## 3. Results and Discussion

### 3. 1. Chemistry

The hydrazones were facile prepared by reaction of 4-fluorobenzaldehyde with 3-chlorobenzohydrazide, 2-chlorobenzohydrazide, 4-nitrobenzohydrazide, and 3-nitrobenzohydrazide, respectively in 1:1 molar ratio in MeOH. X-ray diffraction quality single crystals were obtained by slow evaporation method. All the compounds are soluble in MeOH, EtOH, MeCN, DMF and DMSO.

### 3. 2. Structure Description of the Compounds

The molecular structures of the hydrazones **1–4** are shown in Figs. 1–4, respectively. Selected bond lengths and angles are listed in Table 2. Compound **1** contains one hydrazone molecule and a water molecule of crystallization.

Table 1. Crystallographic and experimental data for the compounds.

Compound	1	2	3	4
Formula	C <sub>14</sub> H <sub>12</sub> ClFN <sub>2</sub> O <sub>2</sub>	C <sub>14</sub> H <sub>10</sub> ClFN <sub>2</sub> O	C <sub>14</sub> H <sub>10</sub> FN <sub>3</sub> O <sub>3</sub>	C <sub>14</sub> H <sub>10</sub> FN <sub>3</sub> O <sub>3</sub>
$M_r$	294.71	276.69	287.25	287.25
$T$ (K)	298(2)	298(2)	298(2)	298(2)
Crystal system	Monoclinic	Triclinic	Monoclinic	Orthorhombic
Space group	$P2_1/n$	$P-1$	$P2_1/c$	$Pbca$
$a$ (Å)	4.7433(8)	5.0121(11)	13.8257(15)	14.9204(13)
$b$ (Å)	12.7365(12)	10.8580(13)	12.6853(13)	15.1431(13)
$c$ (Å)	23.1503(15)	12.3750(13)	7.6638(11)	23.7602(15)
$\alpha$ (°)	90	97.413(1)	90	90
$\beta$ (°)	94.576(1)	93.367(1)	101.447(1)	90
$\gamma$ (°)	90	96.951(1)	90	90
$V$ (Å <sup>3</sup> )	1394.1(3)	661.03(18)	1317.4(3)	5368.4(7)
$Z$	4	2	4	16
$D_c$ (g cm <sup>-3</sup> )	1.404	1.390	1.448	1.422
$\mu$ (Mo-K $\alpha$ ) (mm <sup>-1</sup> )	0.288	0.293	0.114	0.112
$F(000)$	608	284	592	2368
Reflections collected	5057	3475	5358	49187
Unique reflections	1658	2427	1790	4816
Observed reflections [ $I \geq 2\sigma(I)$ ]	1291	1979	1411	2517
Parameters	190	175	193	385
Restraints	4	1	1	2
Goof on $F^2$	1.031	1.048	1.039	1.050
$R_1, wR_2$ [ $I \geq 2\sigma(I)$ ] <sup>a</sup>	0.0360, 0.0803	0.0421, 0.1097	0.0339, 0.0813	0.0508, 0.0863
$R_1, wR_2$ (all data) <sup>a</sup>	0.0515, 0.0878	0.0519, 0.1179	0.0476, 0.0892	0.1397, 0.1122
$\Delta\rho_{\max}/\Delta\rho_{\min}$ (eÅ <sup>-3</sup> )	0.214, -0.227	0.246, -0.286	0.133, -0.150	0.150, -0.190

$$^a R_1 = F_o - F_c/F_o, wR_2 = [\sum w(F_o^2 - F_c^2)/\sum w(F_o^2)]^{1/2}$$

Compound **4** contains two independent hydrazone molecules. All the hydrazone molecules of the compounds adopt *E* configuration with respect to the methyldene units. The distances of the methyldene bonds, ranging from 1.26 to 1.28 Å, confirm them as typical double bonds. The shorter distances of the C–N bonds and the longer distances of the C=O bonds for the –C(O)–NH– units than usual, suggest the presence of conjugation effects in the molecules. All bond lengths in the compounds are comparable to each other, and within normal values.<sup>20</sup> The dihedral angles formed by the two benzene rings of the hydrazone molecules are 9.9(4)° for **1**, 8.1(5)° for **2**, 75.0(5)° for **3**, and 26.8(4)° and 19.3(4)° for **4**.

The hydrogen bonds information is summarized in Table 3. In the crystal structure of compound **1**, the hydrazone and water molecules are linked through O–H...O, N–H...O and C–H...O hydrogen bonds, to form two-dimensional sheets parallel to the *ab* plane. The sheets are further linked through C–H...F hydrogen bonds along the *c* axis, to form three-dimensional network (Fig. 5). In the crystal structure of compound **2**, the hydrazone molecules are linked through N–H...O and C–H...O hydrogen bonds, to form one-dimensional chains running along the *a* axis (Fig. 6). In the crystal structure of compound **3**, the hydrazone molecules are linked through N–H...O hydrogen bonds, to form one-dimensional chains along the *c* axis. The chains are further linked by C–H...F hydrogen bonds, to form two-dimensional sheets parallel to the *ac* plane (Fig. 7). In the crystal structure of compound **4**, the hydrazone molecules are linked through N–H...O, C–H...O and C–H...F hydrogen bonds, to form two-dimensional sheets parallel to the *ac* plane (Fig. 8). In addition, the weak  $\pi\cdots\pi$  interactions among the benzene rings with centroid to centroid distances of 3.6–4.0 Å are observed in **3** and **4** (Table 4).

**Table 2.** Selected bond lengths (Å) and angles (°) for the compounds.

	<b>1</b>	<b>2</b>	<b>3</b>	<b>4</b>
C7–N1	1.275(3)	1.272(2)	1.273(2)	1.271(4)
N1–N2	1.381(3)	1.382(2)	1.391(2)	1.382(4)
N2–C8	1.340(3)	1.348(2)	1.343(2)	1.345(4)
C8–O1	1.235(3)	1.219(2)	1.234(2)	1.234(4)
C22–N4				1.275(4)
N4–N5				1.386(3)
N5–C23				1.343(4)
C23–O4				1.231(4)
C7–N1–N2	115.6(2)	115.5(2)	114.1(2)	115.8(2)
N1–N2–C8	118.5(2)	120.2(2)	120.3(2)	117.9(2)
N2–C8–C9	117.4(2)	114.1(2)	113.5(2)	117.1(2)
N2–C8–O1	122.1(2)	123.0(2)	124.1(2)	122.7(2)
C22–N4–N5				114.6(3)
N4–N5–C23				118.8(3)
N5–C23–C24				116.6(3)
N5–C23–O4				122.6(3)

**Table 3.** Hydrogen bond distances (Å) and bond angles (°) for the compounds.

<i>D</i> –H... <i>A</i>	<i>d</i> ( <i>D</i> –H)	<i>d</i> (H... <i>A</i> )	<i>d</i> ( <i>D</i> ... <i>A</i> )	Angle ( <i>D</i> –H... <i>A</i> )
<b>1</b>				
O2–H2B...O1 <sup>#1</sup>	0.85(1)	1.95(1)	2.800(3)	174(3)
O2–H2A...O1 <sup>#2</sup>	0.85(1)	2.00(1)	2.817(3)	162(3)
N2–H2...O2 <sup>#3</sup>	0.90(1)	1.98(1)	2.865(3)	168(3)
C12–H12...F1 <sup>#4</sup>	0.93	2.51(2)	3.441(3)	176(3)
<b>2</b>				
N2–H2A...O1 <sup>#5</sup>	0.89(1)	2.04(2)	2.862(2)	153(2)
C7–H7...O1 <sup>#5</sup>	0.93	2.52(2)	3.194(3)	130(3)
<b>3</b>				
N2–H2...O1 <sup>#6</sup>	0.90(1)	1.99(1)	2.871(2)	165(2)
C11–H11...F1 <sup>#7</sup>	0.93	2.50(2)	3.275(3)	141(3)
<b>4</b>				
N2–H2...O4 <sup>#8</sup>	0.90(1)	2.13(2)	2.970(3)	154(2)
N5–H5...O1 <sup>#9</sup>	0.90(1)	2.06(1)	2.953(3)	172(3)
C5–H5A...F2 <sup>#10</sup>	0.93	2.38(2)	3.276(3)	161(3)
C10–H10...O4 <sup>#8</sup>	0.93	2.49(2)	3.400(3)	165(3)

Symmetry codes: #1: 1 + *x*, –1 + *y*, *z*; #2: *x*, –1 + *y*, *z*; #3: –*x*, –*y*, 1 – *z*; #4: 5/2 + *x*, 1/2 – *y*, 1/2 + *z*; #5: –1 + *x*, *y*, *z*; #6: *x*, 1/2 – *y*, 1/2 + *z*; #7: 1 + *x*, 1/2 – *y*, 1/2 + *z*; #8: –1/2 + *x*, *y*, 1/2 – *z*; #9: *x*, 1/2 – *y*, 1/2 + *z*; #10: 1 – *x*, –*y*, 1 – *z*.

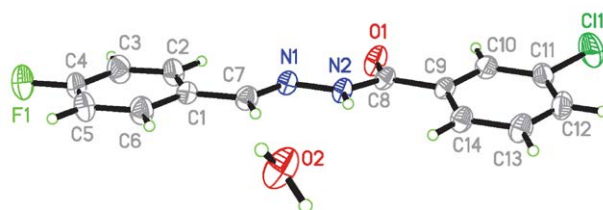


**Fig. 1.** A perspective view of the molecular structure of **1** with the atom labeling scheme. Thermal ellipsoids are drawn at the 30% probability level.

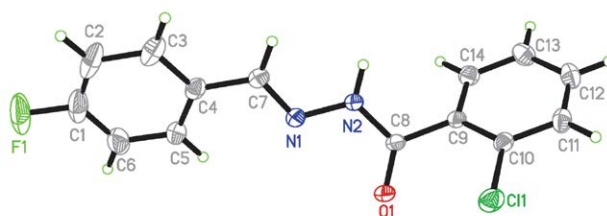


**Fig. 2.** A perspective view of the molecular structure of **2** with the atom labeling scheme. Thermal ellipsoids are drawn at the 30% probability level.

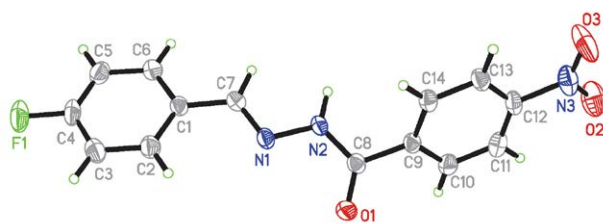


**Fig. 3.** A perspective view of the molecular structure of **3** with the atom labeling scheme. Thermal ellipsoids are drawn at the 30% probability level.

Table 4. Parameters between the planes for compounds 3 and 4.

Cg	Distance between ring centroids (Å)	Dihedral angle (°)	Perpendicular distance of Cg(I) on Cg(J) (Å)	Beta angle (°)	Gamma angle (°)	Perpendicular distance of Cg(J) on Cg(I) (Å)
<b>3</b>						
Cg1–Cg1 <sup>#11</sup>	3.6099	0	–3.3962	19.81	19.81	–3.3962
Cg2–Cg2 <sup>#12</sup>	3.9006	0	–3.5234	25.41	25.41	–3.5234
<b>4</b>						
Cg3–Cg4 <sup>#13</sup>	3.9169	19.287	–3.4087	10.85	29.51	–3.8469
Cg3–Cg5 <sup>#14</sup>	3.7954	5.865	–3.4527	25.86	24.54	3.4155
Cg4–Cg3 <sup>#15</sup>	3.9169	19.287	–3.8469	29.51	10.85	–3.4087
Cg4–Cg4 <sup>#16</sup>	3.9285	0	3.4687	28.00	28.00	3.4687
Cg5–Cg3 <sup>#14</sup>	3.7954	5.865	3.4155	24.54	25.86	3.4155

Cg1 and Cg2 are the centroids of C1–C2–C3–C4–C5–C6 and C9–C10–C11–C12–C13–C14 in 3, respectively. Cg3, Cg4 and Cg5 are the centroids of C1–C2–C3–C4–C5–C6, C9–C10–C11–C12–C13–C14 and C24–C25–C26–C27–C28–C29 in 4, respectively. Symmetry codes: #11:  $-x, 1-y, -z$ ; #12:  $1-x, -y, 1-z$ ; #13:  $\frac{1}{2}+x, \frac{1}{2}-y, -z$ ; #14:  $x, y, z$ ; #15:  $-\frac{1}{2}+x, \frac{1}{2}-y, -z$ ; #16:  $-x, 1-y, -z$ .

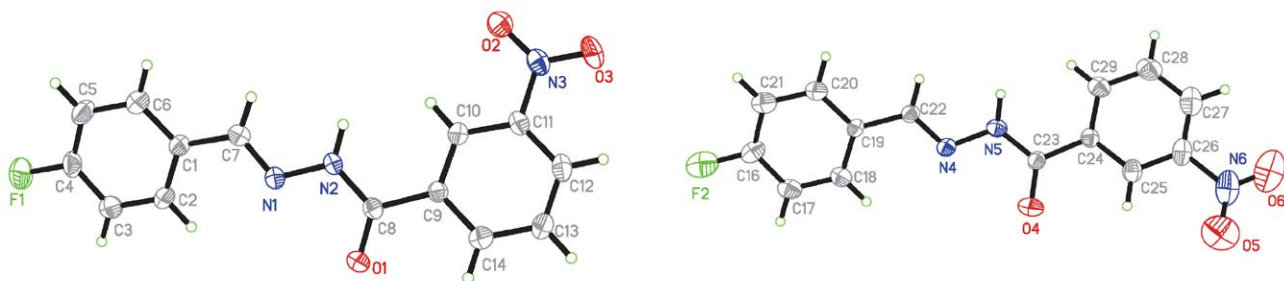


Fig. 4. A perspective view of the molecular structure of 4 with the atom labeling scheme. Thermal ellipsoids are drawn at the 30% probability level.

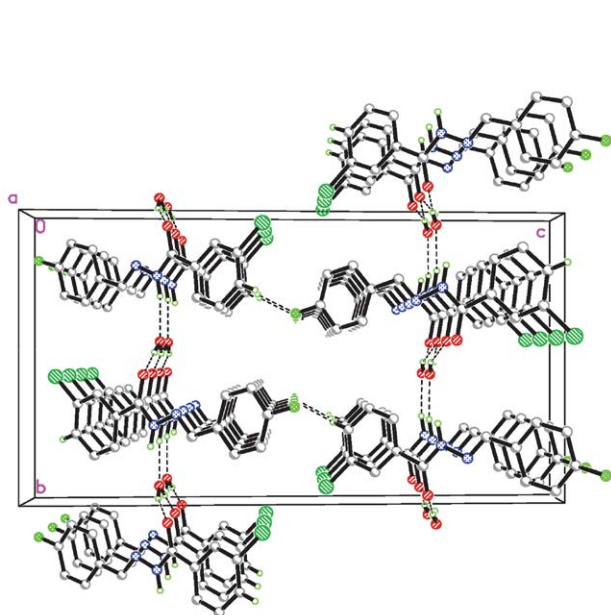


Fig. 5. The packing diagram of 1. Dashed lines represent O–H...O, N–H...O and C–H...F interactions. C: silver; H: the smallest green; F: middle green; Cl: the largest green; N: blue; O: red.

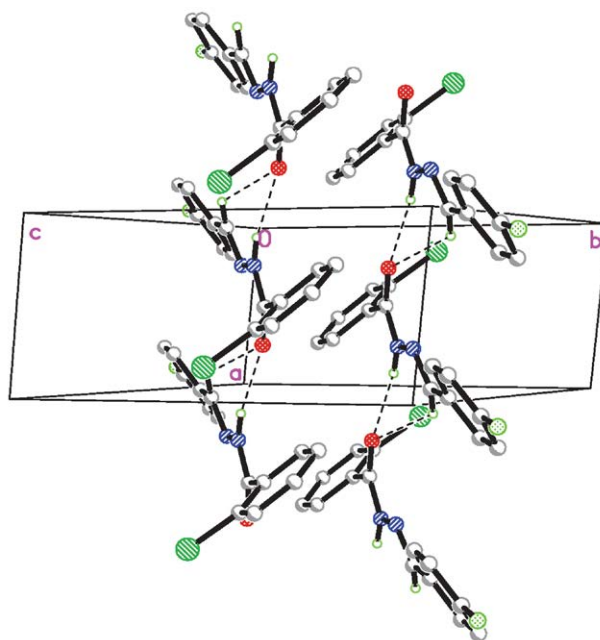


Fig. 6. The packing diagram of 2. Dashed lines represent N–H...O and C–H...O interactions. C: silver; H: the smallest green; F: middle green; Cl: the largest green; N: blue; O: red.

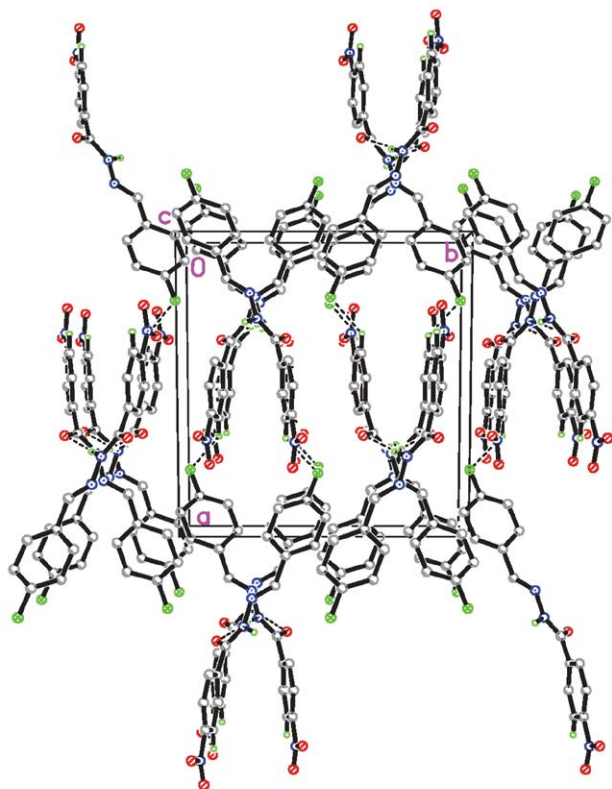


Fig. 7. The packing diagram of 3. Dashed lines represent N-H...O and C-H...F interactions. C: silver; H: the smallest green; F: the largest green; N: blue; O: red.

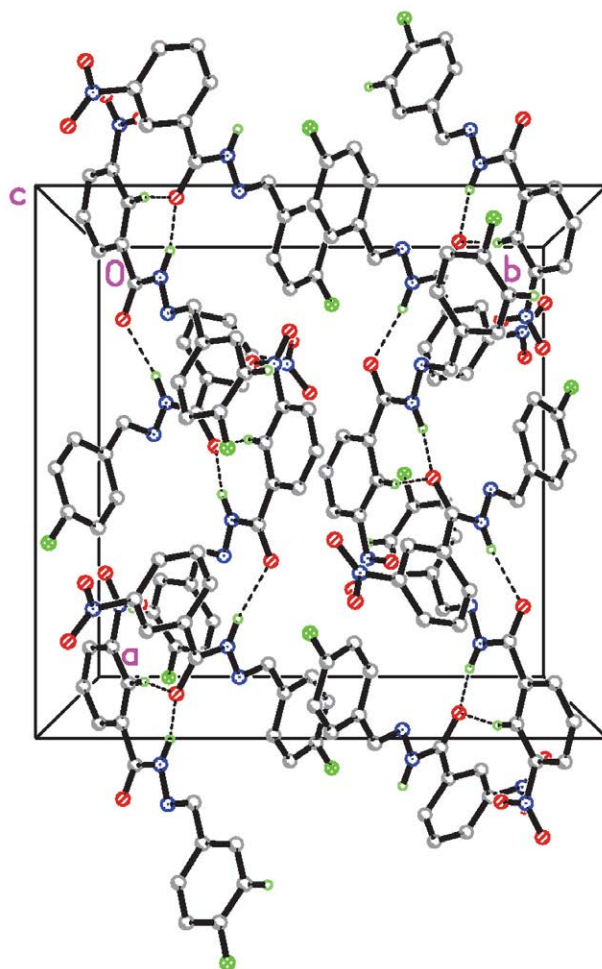


Fig. 8. The packing diagram of 4. Dashed lines represent N-H...O, C-H...O and C-H...F interactions. C: silver; H: the smallest green; F: the largest green; N: blue; O: red.

### 3. 4. IR and $^1\text{H}$ NMR Spectra

In the IR spectra of the compounds, the weak and sharp bands at  $3217\text{ cm}^{-1}$  (1),  $3235\text{ cm}^{-1}$  (2),  $3226\text{ cm}^{-1}$  (3) and  $3227\text{ cm}^{-1}$  (4) are due to the N-H stretching vibrations. The compounds exhibit intense absorptions at  $1649\text{--}1666\text{ cm}^{-1}$ , which can be attributed to the C=O vibrations. The strong absorptions at  $1600\text{--}1608\text{ cm}^{-1}$  can be attributed to the C=N vibrations.<sup>21</sup> The bands indicative of the  $\nu_{as}(\text{NO}_2)$  and  $\nu_s(\text{NO}_2)$  vibrations are observed at  $1522$  and  $1345\text{ cm}^{-1}$  for 1, and  $1532$  and  $1350\text{ cm}^{-1}$  for 2.<sup>21</sup>

In the  $^1\text{H}$  NMR spectra of the compounds, the absence of  $\text{NH}_2$  signals and the appearance of peaks for NH protons in the region  $\delta = 11.96\text{--}12.20$  ppm and imine CH protons in the region  $\delta = 8.30\text{--}8.51$  ppm confirms the synthesis of the hydrazones. The aromatic proton signals were found in their respective regions with different multiplicities, confirming their relevant substitution pattern.

### 3. 5. Pharmacology

The assay of xanthine oxidase inhibition was performed for three parallel times. The results are given in

Table 5. Allopurinol is a commercial xanthine oxidase inhibitor, which was used as a control drug. The percent of inhibition for the drug is  $81.3 \pm 2.8\%$  at the concentration of  $100\text{ }\mu\text{mol L}^{-1}$ , and the  $\text{IC}_{50}$  value is  $8.5 \pm 2.1\text{ }\mu\text{mol L}^{-1}$ . Compounds 1 and 2 have similar activities, with the percent of inhibition in the range of 67–73% and with  $\text{IC}_{50}$  value of  $14\text{--}16\text{ }\mu\text{mol L}^{-1}$ . Compounds 3 and 4 also have similar activities, with the percent of inhibition in the range of 85–90% and with  $\text{IC}_{50}$  value of  $6\text{--}7\text{ }\mu\text{mol L}^{-1}$ . Compounds 3 and 4 have better activities than allopurinol. The merely difference between compounds 1, 2 and 3, 4 are the Cl and  $\text{NO}_2$  substituent groups. Thus, it is not difficult to conclude that  $\text{NO}_2$  group contributes to the inhibition. This agrees well with our previously reported paper that  $\text{NO}_2$  is a preferred group for the inhibition process.<sup>15b</sup> These findings are also coherent with the results reported in the literature that the existence of electron-withdrawing groups in the benzene rings can enhance the activities.<sup>22</sup>

**Table 5.** Inhibition of xanthine oxidase by the assayed compounds.

Tested materials	Percent of Inhibition <sup>a</sup>	IC <sub>50</sub> (μmol L <sup>-1</sup> )
1	67.5 ± 2.6	15.2 ± 1.3
2	72.3 ± 2.5	14.3 ± 1.7
3	89.7 ± 2.3	6.1 ± 1.5
4	85.6 ± 3.0	6.3 ± 1.6
Allopurinol	81.3 ± 2.8	8.5 ± 2.1

<sup>a</sup>The concentration of the tested material is 100 μmol L<sup>-1</sup>.

### 3. 6. Molecular Docking Study

Molecular docking technique was carried out to study the binding mode between the compounds and the active sites of xanthine oxidase (1FIQ in the Protein Data Bank). Allopurinol was used to verify the model of docking, with docking score of  $-6.27$ . Figs. 9–12 are the binding model for the four compounds, which show that the compounds can enter into the active pocket of the enzyme. The docking scores are  $-8.04$  (1),  $-8.09$  (2),  $-9.02$  (3), and  $-9.21$  (4), which are lower than allopurinol. The molecules of 1 and 2 bind with the enzyme through N–H...N hydrogen bonds with ALA1079. The molecules of 3 and 4 bind with the enzyme through N–H...O hydrogen bonds with ARG880 and THR1010.

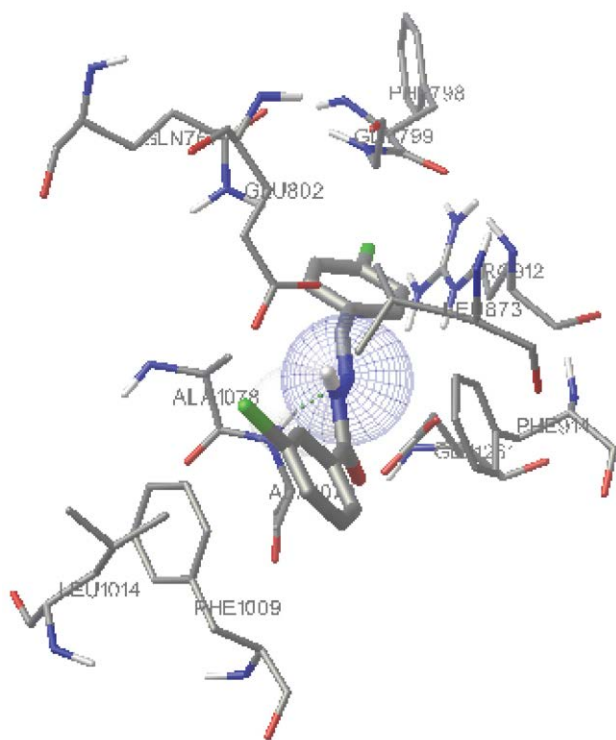


**Fig. 9.** 2D binding mode of 1 with the active site of xanthine oxidase. Dashed lines represent N–H...N interactions.

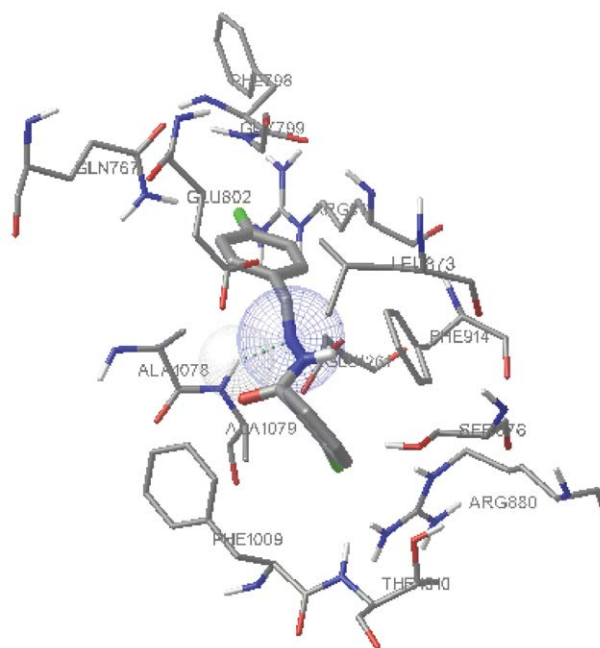


**Fig. 10.** 2D binding mode of 2 with the active site of xanthine oxidase. Dashed lines represent N–H...N interactions.

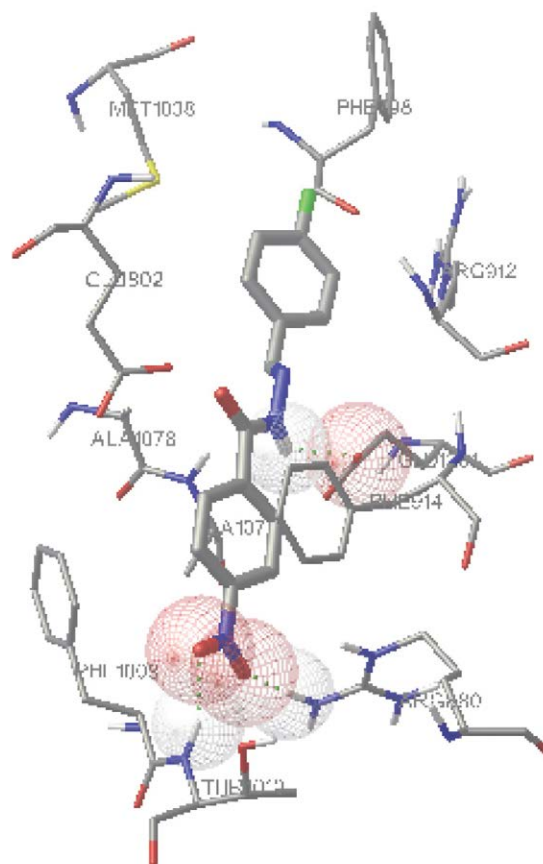


**Fig. 11.** 2D binding mode of 3 with the active site of xanthine oxidase. Dashed lines represent N–H...O interactions.



9. A. Alsayari, M. Z. Hassan, Y. I. Asiri, A. Bin Muhsinah, M. Kamal, M. S. Akhtar, *Indian J. Heterocycl. Chem.* **2021**, *31*, 635–640.
10. J. L. Serrano, D. Lopes, M. J. A. Reis, R. E. F. Boto, S. Silvestre, P. Almeida, *Biomedicines* **2021**, *9*, 1443.  
DOI:10.3390/biomedicines9101443
11. (a) G.-X. He, L.-W. Xue, Q.-L. Peng, P.-P. Wang, H.-J. Zhang, *Acta Chim. Slov.* **2019**, *66*, 570–575;  
DOI:10.17344/acsi.2018.4868  
(b) C.-L. Zhang, X.-Y. Qiu, S.-J. Liu, *Acta Chim. Slov.* **2019**, *66*, 484–489; DOI:10.17344/acsi.2019.5019  
(c) J. Qin, Q. Yin, S.-S. Zhao, J.-Z. Wang, S.-S. Qian, *Acta Chim. Slov.* **2016**, *53*, 55–61; DOI:10.17344/acsi.2015.1918  
(d) F. Qureshi, M. Y. Khuhawar, T. M. Jahangir, A. H. Channar, *Acta Chim. Slov.* **2016**, *63*, 113–120;  
DOI:10.17344/acsi.2015.1994  
(e) X.-Q. Luo, Q.-R. Liu, Y.-J. Han, L.-W. Xue, *Acta Chim. Slov.* **2020**, *67*, 159–166; DOI:10.17344/acsi.2019.5303  
(f) K. M. El-Mahdy, A. M. E.-Kazak, M. Abdel-Megid, M. Seada, O. Farouk, *Acta Chim. Slov.* **2016**, *67*, 18–25;  
DOI:10.17344/acsi.2015.1555  
(g) M. Kaur, S. Kumar, M. Yusuf, J. Lee, R. J. C. Brown, K. H. Kim, A. K. Malik, *Coord. Chem. Rev.* **2021**, *449*, 214214.  
DOI:10.1016/j.ccr.2021.214214
12. (a) N. Choudhary, D. L. Hughes, U. Kleinkes, L. F. Larkworthy, G. J. Leigh, M. Maiwald, C. J. Marmion, J. R. Sanders, G. W. Smith, C. Sudbrake, *Polyhedron* **1997**, *16*, 1517–1528;  
DOI:10.1016/S0277-5387(96)00436-6  
(b) M. Leigh, C. E. Castillo, D. J. Raines, A. K. Duhme-Klair, *ChemMedChem* **2011**, *6*, 612–616.  
DOI:10.1002/cmdc.201000429
13. (a) S. Rollas, S.G. Kucukguzel, *Molecules* **2007**, *12*, 1910–1939; DOI:10.3390/12081910  
(b) S. Omid, A. Kakanejadifard, *RSC Adv.* **2020**, *10*, 30186–30202; DOI:10.1039/D0RA05720G  
(c) D. Blanot, J. Lee, S.E. Girardin, *Chem. Biol. Drug Des.* **2012**, *79*, 2–8; DOI:10.1111/j.1747-0285.2011.01204.x  
(d) Z.A. Kaplancikli, M.D. Altintop, A. Ozdemir, G. Turan-Zitouni, S.I. Khan, N. Tabanca, *Lett. Drug Des. Discov.* **2012**, *9*, 310–315; DOI:10.2174/157018012799129828  
(e) K. Akdag, F. Tok, S. Karakus, O. Erdogan, O. Cevik, B. Kocyigit-Kaymakcioglu, *Acta Chim. Slov.* **2022**, *69*, 863–875;  
DOI:10.17344/acsi.2022.7614
- (f) G.-X. He, L.-W. Xue, *Acta Chim. Slov.* **2021**, *68*, 567–574.  
DOI:10.17344/acsi.2020.6333
14. (a) L. C. Felton, J.H. Brewer, *Science* **1947**, *105*, 409–410;  
DOI:10.1126/science.105.2729.409  
(b) M. Gopalakrishnan, J. Thanusu, V. Kanagarajan, R. Govindaraju, *J. Enzym. Inhib. Med. Ch.* **2009**, *24*, 52–58;  
DOI:10.1080/14756360801906632  
(c) L. Shi, H.-M. Ge, S.-H. Tan, H.-Q. Li, Y.-C. Song, H.-L. Zhu, R.-X. Tan, *Eur. J. Med. Chem.* **2007**, *42*, 558–564.  
DOI:10.1016/j.ejmech.2006.11.010
15. (a) L.-W. Xue, S.-T. Li, Y.-J. Han, X.-Q. Luo, *Acta Chim. Slov.* **2022**, *69*, 385–392; DOI:10.17344/acsi.2021.7252  
(b) Y.-J. Han, X.-Y. Guo, L.-W. Xue, *Acta Chim. Slov.* **2022**, *69*, 928–936. DOI:10.17344/acsi.2022.7817
16. L. D. Kong, Y. Zhang, X. Pan, R. X. Tan, C. H. K. Cheng, *Cell Mol. Life Sci.* **2000**, *57*, 500–505. DOI:10.1007/PL00000710
17. Bruker, SMART and SAINT. Bruker AXS Inc., Madison, Wisconsin, USA (2002).
18. G. M. Sheldrick, SADABS. Program for Empirical Absorption Correction of Area Detector, University of Göttingen, Germany (1996).
19. G. M. Sheldrick, *Acta Crystallogr.* **2008**, *A64*, 112–122.  
DOI:10.1107/S0108767307043930
20. (a) F. H. Allen, O. Kennard, D. G. Watson, L. Brammer, A.G. Orpen, R. Taylor, *J. Chem. Soc. Perkin Trans. 2*, S1, (1987);  
(b) L.-W. Xue, S.-T. Li, Y.-J. Han, X.-Q. Luo, *Acta Chim. Slov.* **2022**, *69*, 385–392; DOI:10.17344/acsi.2021.7252  
(c) F.-M. Wang, L.-J. Li, G.-W. Zang, T.-T. Deng, Z.-L. You, *Acta Chim. Slov.* **2021**, *68*, 541–547;  
DOI:10.17344/acsi.2020.6051  
(d) H.-Y. Zhu, *Acta Chim. Slov.* **2021**, *68*, 65–71;  
(e) C.R. Bhimapaka, N.R. Rayala, R. Kommera, D. Cherupally, R.M. Thampunuri, V.K. Shasi, *Acta Chim. Slov.* **2018**, *65*, 34–49. DOI:10.17344/acsi.2017.3453
21. M. Zhang, D.-M. Xian, H.-H. Li, J.-C. Zhang, Z.-L. You, *Aust. J. Chem.* **2012**, *65*, 343–350. DOI:10.1071/CH11424
22. S. Gupta, L.M. Rodrigues, A.P. Esteves, A.M.F. Oliveira-Campos, M.S.J. Nascimento, N. Nazareth, H. Cidade, M.P. Neves, E. Fernandes, M. Pinto, N.M.F.S.A. Cerqueira, N. Bras, *Eur. J. Med. Chem.* **2008**, *43*, 771–780.  
DOI:10.1016/j.ejmech.2007.06.002

## Povzetek

Štiri nove fluor vsebujoče hidrazone smo sintetizirali iz 4-fluorobenzaldehida s kloro- in nitro-substituiranimi benzohidrazidi. To so 3-kloro-*N*′-(4-fluorobenziliden)benzohidrazid (**1**), 2-kloro-*N*′-(4-fluorobenziliden)benzohidrazid (**2**), *N*′-(4-fluorobenziliden)-4-nitrobenzohidrazid (**3**) in *N*′-(4-fluorobenziliden)-3-nitrobenzohidrazid (**4**). Spojine smo okarakterizirali z IR in <sup>1</sup>H NMR spektroskopijo ter z rentgenskih monokristalno struktarno analizo. Inhibitorna aktivnost ksantin oksidaze (XO) je pokazala, da sta nitro-substituirani spojini **3** in **4** aktivni. Izvedli smo docking simulacijo z vstavitvijo molekul spojin v aktivno mesto v kristalni strukturi ksantin oksidaze, da bi raziskali možne načine vezave.



Except when otherwise noted, articles in this journal are published under the terms and conditions of the Creative Commons Attribution 4.0 International License



Scientific paper

# Comparison of Deep Eutectic Solvent-based Ultrasound- and Heat-assisted Extraction of Bioactive Compounds from *Withania somnifera* and Process Optimization Using Response Surface Methodology

Faizan Sohail and Dildar Ahmed\*

Department of Chemistry, Forman Christian College, Lahore, Pakistan.

\* Corresponding author: E-mail: dildarahmed@gmail.com

Received: 08-26-2023

## Abstract

Extraction of bioactive compounds from *Withania somnifera* roots was studied using sodium acetate-glycerol deep eutectic solvent (DES) and two techniques of extraction: ultrasound-assisted extraction (UAE) and heat-assisted extraction (HAE) under response surface methodology (RSM). For UAE and HAE, total phenolic content (TPC, mg gallic acid equivalents per g dry weight (mg GAE g<sup>-1</sup> DW)), total flavonoid content (TFC, mg rutin equivalents g<sup>-1</sup> DW (mg RE g<sup>-1</sup> DW)), radical scavenging activity (RSA, mg AAE (ascorbic acid equivalents) g<sup>-1</sup> DW), and iron chelating activity (ICA, mg EDTAE (ethylenediaminetetraacetate equivalents) g<sup>-1</sup> DW) were 6.51, 6.08, 12.56, and 3.57, respectively, and 3.33, 3.98, 6.57, and 2.48, respectively. For UAE, the optimal conditions were a DES concentration of 50%, temperature of 60 °C, and time of 20 min, and for HAE, a DES concentration of 60%, temperature of 60 °C, and time of 75 min. The discovered models were strongly supported by the validation experiments. UAE was more efficient and less time-consuming for extracting phytoconstituents of the *W. somnifera* than HAE.

**Keywords:** *Withania somnifera*, phenols and flavonoids, antioxidant activity, deep eutectic solvent, ultrasound-assisted extraction, response surface methodology

## 1. Introduction

*Withania somnifera* is a shrub belonging to the family Solanaceae. It is locally known as “Ashwagandha” (lit., horse smell) in South Asia due to the horse-like smell of its root powder.<sup>1</sup> Other names include “Asghand” in Urdu and “Winter Cherry” in English.<sup>2</sup> It is found in drier parts of Pakistan, the Middle East, South Asia, and Europe.<sup>3</sup> *W. somnifera* is said to promote male fertility, reduce stress levels, and increase overall health.<sup>4</sup> *W. somnifera* is rich in natural products which include phenolics, flavonoids, and steroidal lactones.<sup>5</sup> It has many therapeutic properties including antioxidant and anti-inflammatory effects.<sup>6</sup> Commercially, *W. somnifera* is also used as a dietary supplement and is available on the market as tablets, capsules, and syrups. Due to its high demand, there is a need to find a green extraction technique that can reduce manufacturing costs and waste and give a high yield.<sup>7,8</sup>

Commonly, natural products are extracted using organic solvents including methanol, ethanol, and acetone.<sup>9</sup> However, their use has several drawbacks such as high tox-

icity, volatility, and poor biodegradability. It is, therefore, important to find safer and more sustainable extractants.<sup>10</sup> One possible solution is the use of deep eutectic solvents (DESs) for the extraction of bioactive natural products from plants. The efficacy of the DESs for this purpose is demonstrated by a rapidly growing number of studies. For instance, recently, tartaric acid-glycerol and tartaric acid-ethylene glycol have been shown very effective solvents to extract antioxidant compounds from *Rosa canina* L.<sup>11</sup> In several studies, glycerol-based DES exhibited higher efficiency in extracting phenolics and antioxidants as compared to organic solvents.<sup>12</sup> DESs can be easily tailored for extracting the compound of interest from the plant material. Sodium acetate-glycerol DES proved to be a promising solvent for the extraction of polyphenols from the plant matrices.<sup>13</sup> It is prepared by the interaction of sodium acetate as hydrogen bond acceptor (HBA) and glycerol as hydrogen bond donor (HBD).<sup>14</sup> Recently, the sodium acetate-glycerol DES at a molar ratio of 1:3 has been proven to be more efficient to extract polyphenols from raw

mango peels than any other DESs.<sup>15</sup> It is also effective in extracting antioxidants from the agri-food waste biomass.<sup>16</sup>

Extraction techniques are generally classified into two broad categories, namely, conventional techniques and modern techniques. Conventional techniques include maceration, percolation, infusion, and refluxing which are solvent specific and require prolonged extraction time. On the other hand, modern techniques include supercritical fluid extraction (SFE), microwave-assisted extraction (MAE), and ultrasound-assisted extraction which are less time consuming and, generally, require lesser amounts of solvents.<sup>17</sup> Heat-assisted extraction (HAE) is commonly employed due to the ease of its use and availability. It, however, also has certain disadvantages including a long extraction period and high energy consumption. Prolonged extraction at a certain temperature can also cause thermal degradation of bioactive compounds.<sup>18</sup> On the other hand, ultrasound-assisted extraction (UAE), can show a better extraction efficiency as compared to conventional extraction techniques (maceration, stirring-assisted extraction, refluxing).<sup>19</sup> The mechanism behind ultrasound-assisted extraction involves acoustic cavitation. When ultrasound waves pass through a solvent, the compression and rarefaction in the solvent medium form a vacuum that produces cavitation bubbles. When the cavitation bubbles collide with the plant surface, produce the shear effect and break the plant cell wall.<sup>20</sup> The interaction between the two phases increases and bioactive constituents are transferred into the extracting medium. The phenomenon is known as mass transfer. In UAE, several parameters influence the extraction process which includes ultrasound frequency, power, treatment time, temperature, solvent-to-solid ratio, and type of solvent used.<sup>21</sup>

The current research aimed to find the efficiency of UAE to recover bioactive compounds from *W. somnifera* dried roots in comparison to HAE. For this purpose, preliminary single-factor extractions were carried out to find out the most effective levels of the independent factors both for UAE and HAE. Based on the results of the preliminary study, extraction optimization of both techniques was done according to the Box–Behnken design (BBD) of response surface methodology. The results of this study will contribute to the advancement of extraction technology and provide valuable insights for the nutraceutical industries, leading to the development of standardized extracts from *W. somnifera* for therapeutic applications. To the best of our knowledge, optimization of the extraction of bioactive compounds from *W. somnifera* using DES has not been performed so far. With the growing realization of environmental safety, exploring green industrial processes is highly desirable. The industrial process must be environmentally sustainable. In this context, the research embodied in the article is an important contribution to the field.

## 2. Materials and Methods

### 2.1. Plant Material

A sample of *Withania somnifera* roots was collected from the Akbari market, Lahore. The roots were converted into fine powder in a high-speed multi-function comminutor (RRH-250A). The pulverized powder went through an 80-sized mesh sieve. The plant powder was then placed in a polyethylene zip-locked bag and then refrigerated at 5 °C until further use.

### 2.2. Chemicals

Sodium acetate trihydrate and glycerol were acquired from Duksan (Seoul, Korea). Folin–Ciocâlțeu reagent was from Scharlab (Spain). Sodium carbonate and aluminum chloride were obtained from Merck (Darmstadt, Germany). Sodium nitrite was from Honeywell (Charlotte, USA). Sodium hydroxide, ferrozine, methanol, DPPH, gallic acid, rutin, ascorbic acid, and EDTA were obtained from Sigma-Aldrich (Steinheim, Germany).

### 2.3. Extraction Procedure

HAE was carried out in a shaking incubator (Vision Scientific-VS-8480SN, Korea) at the constant shaking speed of 200 rpm and the solvent-to-solid ratio was also kept constant (30 mL g<sup>-1</sup>). A measured amount (1 g) of dried plant material was mixed with 30 mL of solvent in a 100 mL Erlenmeyer flask. The temperature was varied from 40–60 °C, DES concentration varied from 30–70 (%v/v), and extraction time varied from 30–150 min. The extract was filtered through Whatman filter paper no. 42 and stored in a refrigerator in a glass vial at 5 °C.

UAE was conducted in a sonication bath (Fischer Scientific-FS60, Mexico) at the frequency of 42 kHz and power of 110 W. One gram (1 g) of dried plant material was mixed with 30 mL of solvent in a 100 mL Erlenmeyer flask. The temperature was varied from 30–70 °C, DES concentration varied from 30–70 (%v/v), and extraction time varied from 10–50 min. The extract was filtered through Whatman filter paper no. 42 and stored in the refrigerator in a glass vial at 5 °C.

### 2.4. Single-factor Experiments

The preliminary single-factor experiments were carried out before the HAE and UAE- optimization study to find the factor levels. The effect of DES concentration, temperature, and extraction time on total phenolic content (TPC) from the *W. somnifera* roots was investigated. The single-factor results are shown in Figure 1 and 2.

### 2.5. Total Phenolic Content (TPC)

TPC was assessed using a previously stated method with some slight modifications.<sup>22</sup> The assay was based on

Folin–Ciocâlteu reagent (FC reagent). Briefly, test tubes were covered from the sides with aluminum foil, 100  $\mu\text{L}$  extract of *W. somnifera* roots was taken and diluted with 8 mL of DI water. Afterward, 300  $\mu\text{L}$  of FC reagent was added and incubated for 8 min. Afterward, 1.5 mL of 20%  $\text{Na}_2\text{CO}_3$  solution was added. The mixture was heated in the dark at 40  $^\circ\text{C}$  for 1 hour in an oven. The absorbance was recorded at 765 nm. A calibration curve of gallic acid was drawn at different concentrations (50–400  $\text{mg L}^{-1}$ ,  $R^2 = 0.9982$ ) and TPC was estimated in terms of its equivalents.

## 2. 6. Total Flavonoid Content (TFC)

A reported method was used to estimate the TFC with some slight modifications.<sup>23</sup> The assay is based on the complexation of flavonoids with aluminum. In a test tube, 300 mL extract of *W. somnifera* roots was pipetted out. Then, 3 mL of aqueous methanol (70% DI water: 30% methanol) was added. Afterward, 150  $\mu\text{L}$  of  $\text{NaNO}_2$  solution and then 150  $\mu\text{L}$  of  $\text{AlCl}_3$  solution were added to the solution, which was then left to rest for 5 min. Then, 1 mL of  $\text{NaOH}$  solution was added. The absorption was recorded at 506 nm wavelength. A calibration curve of rutin was obtained with different concentrations (50–400  $\text{mg L}^{-1}$ ,  $R^2 = 0.9987$ ) and TFC was calculated as its equivalents.

## 2. 7. Radical Scavenging Activity (RSA)

RSA was estimated as per a previously reported method based on DPPH radical assay.<sup>24</sup> Test tubes were covered with aluminium foil and 500  $\mu\text{L}$  of the root extract

was put in them. Then, 1 mL of DPPH solution which was prepared earlier was added and then 5 mL of DI water was added. The test tubes were incubated at 37  $^\circ\text{C}$  for the completion of the reaction in the oven. After incubation, absorbance was taken at 517 nm wavelength. A calibration curve of ascorbic acid was obtained with different concentrations (10–50  $\text{mg L}^{-1}$ ,  $R^2 = 0.9975$ ) and antioxidant activity was measured in terms of ascorbic acid equivalents.

## 2. 8. Iron Chelating Activity (ICA)

With some slight modifications, the ICA was estimated as per a reported protocol.<sup>25</sup> In an aluminum foil-wrapped test tube, 100  $\mu\text{L}$  plant extract was taken in test tubes. 3 mL of DI water was added, then, 100  $\mu\text{L}$  of  $\text{FeSO}_4$  solution was added. After that, 50  $\mu\text{L}$  of ferrozine was added and incubated for 15 min in the dark. Then, absorbance was taken at 562 nm wavelength. A calibration curve of EDTA was obtained with different concentrations (10–50  $\text{mg L}^{-1}$ ,  $R^2 = 0.9839$ ) and ICA was expressed as EDTA equivalents.

## 2. 9. Experimental Design

The optimization parameters for both HAE and UAE were kept the same to the sake of comparison of the two techniques. Three-factor-three-level BBD was used for modelling and optimization. The coded levels of each factor were  $-1$ ,  $0$ ,  $+1$  (lower, middle, high). The designs of experiments for HAE and UAE are shown in Table 1 along with the experimental results. Each design had 15 runs including 3 central points.

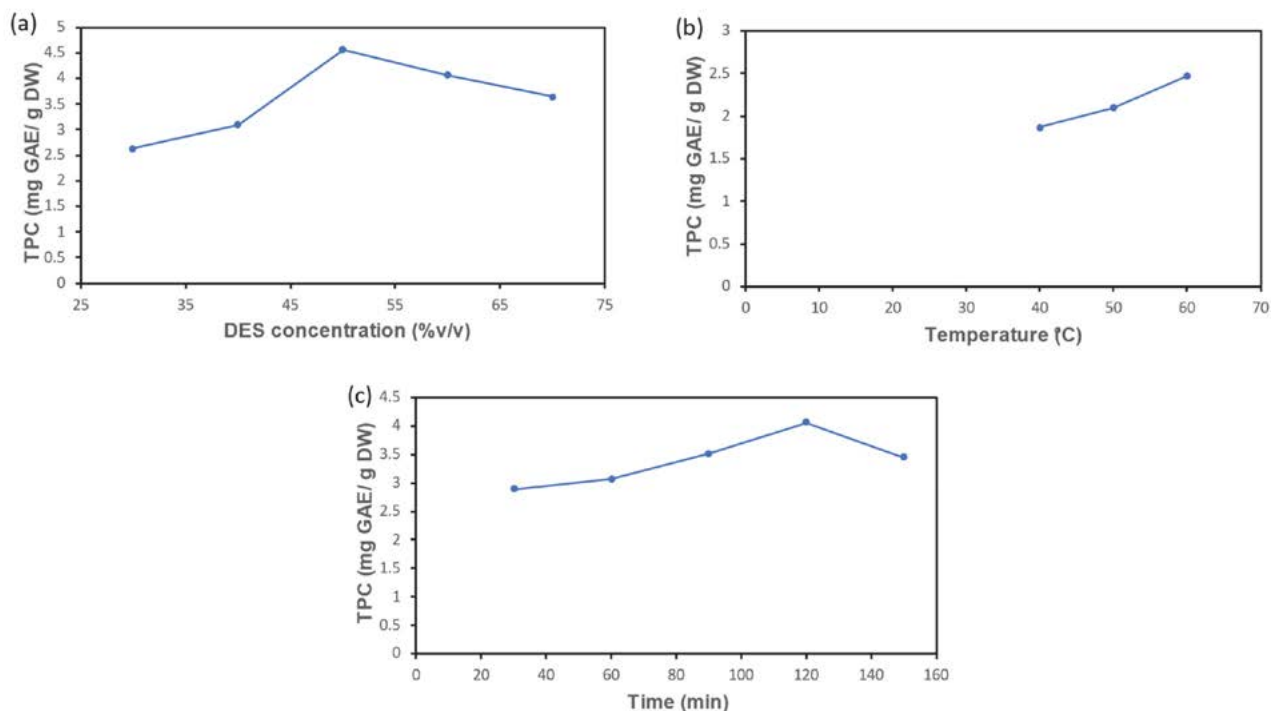


Figure 1. Single-factor experiments showing the effect of HAE parameters on TPC.

The analysis of variance (ANOVA) was performed to determine the interaction between the independent variables and their influence on the observed responses. Co-efficient of determination ( $R^2$ ) was used to determine the adequacy of the model, and  $p$ -values determined the significance of the model. The  $p$ -values  $< 0.05$  were considered significant statistically. Lack of fit represents the failure of the model to describe the relationship between variables and the responses.

### 3. Results and Discussion

#### 3.1. HAE Single-factor Experiments

The single-factor experiments were conducted to discover the effective factors and their levels on the extraction of phenolics. The outcomes of these experiments are shown in Figure 1. Shaking speed (200 rpm) and solvent-to-solid ratio ( $30 \text{ mg L}^{-1}$ ) were kept constant.

Figure 1a shows that as the concentration of the DES increased from 30% to 50%, there was a corresponding increase in TPC. A further increase in DES concentration, however, resulted in a decrease of TPC. Figure 1b displays the effect of temperature on TPC while keeping the other factors (DES concentration and time) constant. There was an increase in TPC as the temperature increased from  $40^\circ\text{C}$  to  $60^\circ\text{C}$ . Figure 1c exhibits the effect of time on TPC while keeping all other factors constant. As the time increased to 120 min, there was a corresponding increase in TPC.

The single-factor experiments were very useful for designing the optimization experiments for HAE as well as UAE. Figure 1a shows the increase in TPC was due to the decrease in polarity with the increasing DES concentration, which enabled moderately polar polyphenols to be extracted into the solvent.<sup>26</sup> However, as the DES concentration increased beyond 50%, TPC started to decrease. This may be because of the increased viscosity of the solvent, which made the solvent less able to penetrate into the plant biomass.<sup>27</sup> Figure 1b shows an increase in TPC can be attributed to the mass transfer. Kinetic energy of the system increases with the increase in temperature resulting in a stronger interaction between the solvent and the plant biomass. Moreover, increase in temperature also results in a decrease in the solvent viscosity. As a result, the solvent penetrates more effectively into the plant biomass extracting a higher amount of phenolics.<sup>28</sup> Figure 1c shows an increase in TPC with solvent, it can be attributed to an effective exposure of the plant biomass to the solvent, allowing the release of phenolic compounds from the biomass. However, an extended exposure of the plant material to the solvent can cause a breakdown of the phenolic compounds. That may lead to a decrease in TPC.<sup>29</sup>

#### 3.2. UAE Single-factor Experiments

The results of the UAE single-factor experiments are shown in Figure 2. Power (110 W), frequency (42 kHz), and solvent-to-solid ratio ( $30 \text{ mg L}^{-1}$ ) were kept constant.

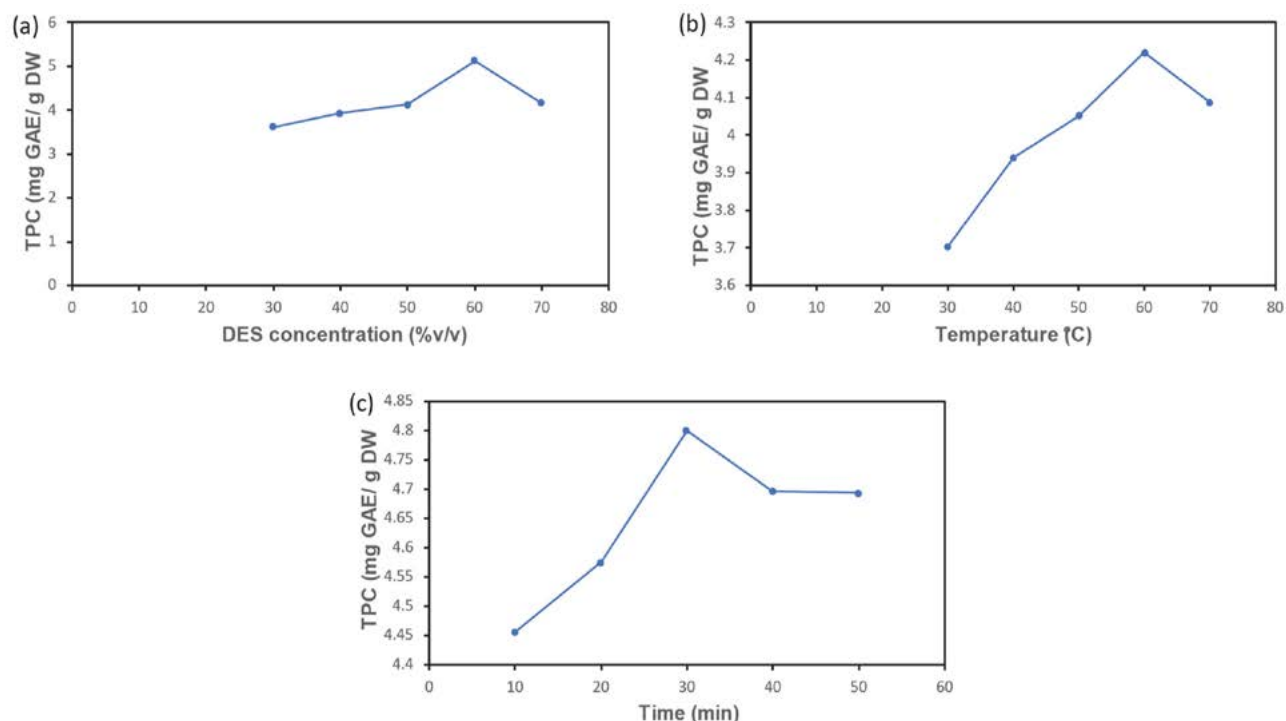


Figure 2. Single-factor experiments showing the effect of UAE parameters on TPC.

Figure 2a shows that there is a considerable effect of DES concentration on TPC. It was noted that as the DES concentration increased from 30% to 60%, TPC also increased. However, after reaching 60% concentration, the TPC started decreasing with any further increase in the DES concentration. Figure 2b demonstrates that TPC increases with the temperature until 60 °C, however, beyond that it starts decreasing. Figure 2c displays the effect of ultrasound treatment time on TPC. With time TPC shows an increase and reaches a maximum at 30 min after which TPC decreases.

Figure 2a shows that, due to the DES being more viscous than water, increased DES concentration led to a corresponding increase in the viscosity of the solution. With the high viscosity of the solvent, it was difficult for it to penetrate the plant biomass. This effect might be responsi-

ble for the decrease in TPC at higher DES concentration.<sup>26</sup> Figure 2b shows that the high temperature might be damaging heat-sensitive phenolics that undergo chemical degradation at elevated temperatures.<sup>30</sup> Figure 2c shows that cavitation effect produced through various mechanisms causes ultrasound waves to promote release of chemical compounds from the cell matrix. However, ultrasound treatment for a certain threshold duration of time may cause breakdown of the chemicals and thus show a lower TPC. Many studies have shown this trend.<sup>31</sup>

### 3. 3. HAE Optimization

The results of HAE optimization experiments as per the Box–Behnken design of experiment are shown in Table 1.

Table 1. Box–Behnken designs of experiments for HAE and UAE and results.

Heat-assisted extraction (HAE)							
Independent variables				Responses			
Run order	A: DES concentration (%v/v)	B: Temperature (°C)	C: Time (min)	TFC mg RE g <sup>-1</sup> DW	TPC mg GAE g <sup>-1</sup> DW	RSA mg AAE g <sup>-1</sup> DW	ICA mg EDTAE g <sup>-1</sup> DW
1	40	50	75	3.10	2.81	5.38	2.20
2	50	50	120	3.75	3.16	5.89	2.47
3	30	50	120	2.96	2.71	5.32	1.33
4	50	40	75	2.88	2.76	5.56	2.66
5	40	60	120	3.81	3.23	6.35	1.83
6	40	50	75	3.55	2.87	5.88	1.78
7	30	60	75	3.72	2.64	6.45	1.51
8	40	40	30	2.65	2.79	5.15	2.25
9	50	50	30	3.19	3.22	5.95	2.36
10	50	60	75	3.81	3.23	6.72	2.70
11	30	50	30	2.58	2.55	5.52	1.63
12	40	60	30	3.50	3.13	6.36	1.95
13	40	50	75	3.66	2.77	5.64	1.99
14	40	40	120	3.04	2.74	5.26	2.04
15	30	40	75	2.25	2.32	5.16	1.53
Ultrasound-assisted extraction (UAE)							
1	30	30	20	3.38	4.86	10.18	2.16
2	45	45	20	4.05	5.72	11.81	2.88
3	45	30	30	4.95	5.42	10.63	2.78
4	60	45	10	5.20	6.34	12.35	3.35
5	45	60	30	5.53	5.61	10.95	3.04
6	45	45	20	4.39	5.33	11.25	3.19
7	30	45	30	5.02	5.48	10.24	2.35
8	45	60	10	4.03	6.32	11.50	3.06
9	45	45	20	4.57	5.67	11.83	2.87
10	45	30	10	3.73	5.35	10.97	2.98
11	60	45	30	6.57	6.27	11.87	3.45
12	60	30	20	4.75	5.68	12.15	3.53
13	60	60	20	6.66	6.70	13.10	3.47
14	30	60	20	4.70	5.30	10.56	2.55
15	30	45	10	3.61	5.41	10.97	2.21

Table 2. Predicted models and their regression equations based on significant terms.

Heat-assisted extraction (HAE)			
Response	Model	Model equation	Eq. No.
TPC	Linear	HAE-TPC = 2.86 + 0.2687A + 0.2025B	Eq. 1
TFC	Linear	HAE-TFC = 3.23 + 0.2650A + 0.5025B + 0.2050C	Eq. 2
RSA	Linear	HAE-RSA = 5.77 + 0.2087A + 0.5937B	Eq. 3
ICA	Linear	HAE-ICA = 2.92 + 0.5238A	Eq. 4
Ultrasound-assisted extraction (UAE)			
TPC	Linear	UAE-TPC = 5.70 + 0.3275A + 0.4925B	Eq. 5
TFC	Linear	UAE-TFC = 4.74 + 0.5137A + 0.8087B + 0.6875C	Eq. 6
RSA	Linear	UAE-RSA = 11.36 + 0.2725A + 0.9400B	Eq. 7
ICA	Linear	UAE-ICA = 2.92 + 0.5662B	Eq. 8

The data was fitted in the 2<sup>nd</sup> order polynomial equation to obtain mathematical models for the responses. ANOVA was carried out to determine the significance of the predicted model and the terms. The model equations including only the significant terms are shown in Table 2.

For each response, a linear model was predicted. Based on the *p*-values and lack of fit *p*-values of the models, the significance of the predicted models was determined. The models were regarded significant if their *p*-values were less than 0.050 and lack of fit *p*-values were higher than 0.050. Similarly, the terms of a model were considered as significant if their *p*-values were less than 0.050. The ANOVA details are given in Table 3 while the coefficients are shown in Table 4. The predicted models were further supported by *R*<sup>2</sup>, adjusted *R*<sup>2</sup> and predicted *R*<sup>2</sup> values (Tables 3 and 4).

### 3. 3. 1. Effects of HAE Parameters on Responses

In HAE, the term A (DES concentration) has a significant positive effect on all the responses. Term B (temperature) also significantly affected all the responses, except ICA. Term C (time) has significant effect only on TFC.

All the factors affected the responses positively. It means that within the experimental ranges of the factors, an increase in them resulted in an increase in the responses. Figures 3a and 3b show that for HAE, DES concentration affects the responses positively. The DES as such is a viscous liquid. Water as a diluent lowers the DES viscosity and, therefore, increases its ability to diffuse into the plant biomass and extract its chemical constituents more effectively.<sup>32</sup>

Figure 3a shows that the temperature has been demonstrated in studies to facilitate the extraction of phenolics from plant roots. It increases the kinetic energy of the system creating strong interaction between the solvent and the plant biomass being extracted. Temperature also decreases the viscosity of the solvent enabling it to penetrate the plant biomass more effectively. Both these effects result in an enhanced extraction of chemical constituents of the biomass.

Figures 3c and 3d show that temperature is more significant as compared to the other factors. An elevated temperature

lowered the viscosity of the extracting solvent, resulting in increased movement of phytochemicals from the plant cell wall into the solvent. As a result, more flavonoids were extracted from the plant material.

Interestingly, time was not a significant factor in TPC, RSA, and ICA. This may be because the extraction rate is initially high and becomes gradually slower as time passes, resulting in little change in the overall extraction efficiency over time.<sup>33</sup> However, time was a significant factor in TFC indicating that a change in time significantly affects the extraction of TFC.

Furthermore, the dilution of DES also played a role in TFC extraction. As the ratio of the DES concentration increases, the extracting solvent becomes less polar. This change in polarity allowed flavonoids with moderate polarity to be extracted more efficiently into the extracting solvent.<sup>34</sup>

Figures 3e and 3f show a drastic increase in RSA with increasing temperature demonstrating that temperature-tolerant phytochemicals are extracted into the solvent which is responsible for the radical scavenging activity. A slight increase of RSA with an increase in DES concentration shows to reduce the polarity of DES which makes it possible for moderately polar phytochemicals to transfer into the extracting solvent. Longer exposure may adversely affect the antioxidant activity of the extracted polyphenols. This may be due to the degradation of the extracted antioxidants over time.<sup>35</sup>

In the current study, temperature and time did not have significant effect on ICA as shown in Figures 3f and 3g. Elevated temperatures for longer extraction time can cause the degradation of the phytochemicals which shows the iron chelating activity. On the other hand, the DES concentration had a significant effect on the ICA. As the DES concentration increases the extracting medium becomes less polar, resulting in better extraction of natural products having similar polarity, such as vitamins, proteins, and carbohydrates that can influence the metal chelating activity. Polyphenols are not the only bioactive compounds that show ICA. Other compounds, such as vitamins and proteins, can also contribute to the overall metal-chelating activity of the extracted compounds.<sup>36</sup>

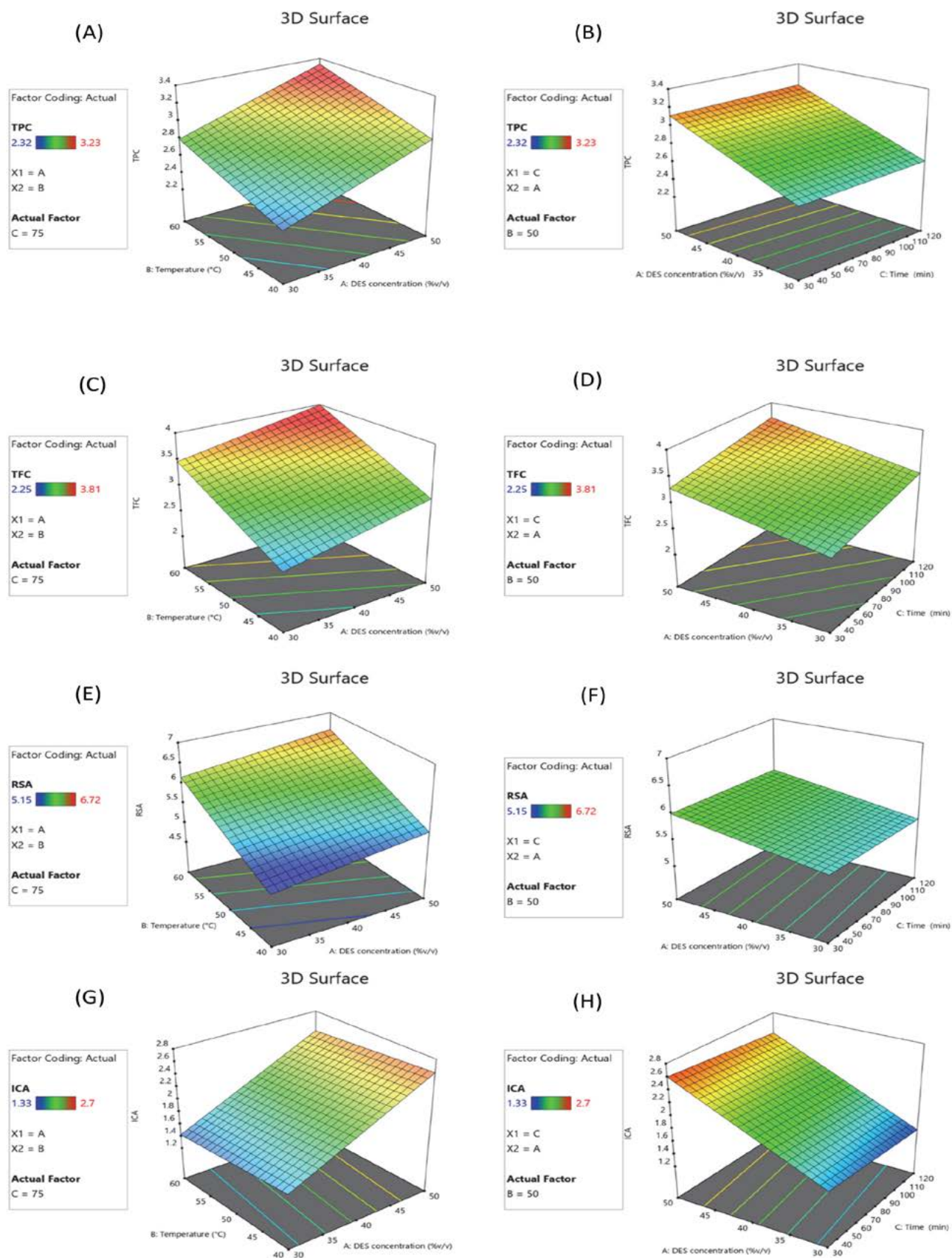


Figure 3. HAE-3D surface plots show combined effect of any two factors on the responses.

Table 3. HAE ANOVA table for all responses.

Source	TPC (mg GAE g <sup>-1</sup> DW)		TFC (mg RE g <sup>-1</sup> DW)		RSA (mg AAE g <sup>-1</sup> DW)		ICA (mg EDTAE g <sup>-1</sup> DW)	
	<i>p</i> -value	<i>F</i> -value	<i>p</i> -value	<i>F</i> -value	<i>p</i> -value	<i>F</i> -value	<i>p</i> -value	<i>F</i> -value
Model	<0.0001	21.34	0.0001	17.99	<0.0001	27	<0.0001	33.79
A	<0.0001	40.7	0.0081	10.39	0.0124	8.9	<0.0001	98.51
B	0.0005	23.11	<0.0001	37.36	<0.0001	72.02	0.2703	1.35
C	0.6649	0.1981	0.0298	6.22	0.7803	0.0817	0.2473	1.52
Lack of fit	0.1379	6.63	0.7939	0.5284	0.7863	0.5432	0.8657	0.3952
<i>R</i> <sup>2</sup>	0.8533		0.8307		0.8804		0.9021	
Adjusted <i>R</i> <sup>2</sup>	0.8133		0.7845		0.8478		0.8761	
Predicted <i>R</i> <sup>2</sup>	0.6964		0.7235		0.7945		0.8261	

Table 4. Coefficient table for HAE and UAE.

Heat-assisted extraction (HAE)				
Model	TPC Linear	TFC Linear	DPPH Linear	ICA Linear
Intercept	2.86	3.23	5.75	2.02
A	<b>0.2687</b>	<b>0.2650</b>	<b>0.2085</b>	0.5238
B	<b>0.2025</b>	<b>0.5025</b>	<b>0.5937</b>	<b>-0.0613</b>
C	0.0188	<b>0.2050</b>	-0.0200	-0.0650
<i>p</i> -value	<0.0001	0.0001	<0.0001	<0.0001
Lack of fit <i>p</i> -value	0.1379	0.7939	0.7863	0.8657
<i>R</i> <sup>2</sup>	0.8533	0.8307	0.8804	0.9021
Adjusted <i>R</i> <sup>2</sup>	0.8133	0.7845	0.8478	0.8754
Predicted <i>R</i> <sup>2</sup>	0.6964	0.7235	0.7945	0.8261
Ultrasound-assisted extraction (UAE)				
Model	Linear	Linear	Linear	Linear
Intercept	5.70	4.74	11.36	2.92
A	<b>0.3275</b>	<b>0.5137</b>	<b>0.2725</b>	0.0837
B	<b>0.4925</b>	<b>0.8087</b>	<b>0.9400</b>	<b>0.5662</b>
C	-0.0800	<b>0.6975</b>	-0.2625	0.0025
<i>p</i> -value	0.0002	0.0001	<0.0001	<0.0001
Lack of fit <i>p</i> -value	0.5097	0.2607	0.5242	0.8426
<i>R</i> <sup>2</sup>	0.8225	0.8382	0.8522	0.9303
Adjusted <i>R</i> <sup>2</sup>	0.7741	0.7940	0.8119	0.9112
Predicted <i>R</i> <sup>2</sup>	<b>0.6590</b>	<b>0.7009</b>	<b>0.7288</b>	<b>0.8772</b>

### 3. 4. UAE Optimization

The UAE results are shown in Table 1 and regression equations based on only significant terms are given in Table 2. The coefficients are given in Table 3 while ANOVA details are given in Table 5.

For all the responses, linear models were predicted which were well fitted based on the significant *p*-values and nonsignificant lack of fit *p*-values. The models were further supported by *R*<sup>2</sup>, adjusted *R*<sup>2</sup> and predicted *R*<sup>2</sup> values.

#### 3. 4. 1. Effects of UAE Parameters on Responses

Like in HAE, TPC and RSA in UAE were affected by the terms A and B, and TFC was affected by A, B and C.

However, in UAE, ICA was not affected by A or C, but only by B. All the factors affected the responses positively. It means that within the experimental ranges of the factors, an increase in them resulted in an increase in the responses.

For UAE, temperature imparts a crucial role in extracting phenolics from plant biomass. The effect can be seen in Figures 4a and 4b. This is because higher temperatures lower the viscosity of the liquids, which in turn speeds up the transfer of the bioactive molecules into the solvent. Thus, the polyphenols can be extracted efficiently by increasing the temperature. DES was diluted with water to lower the viscosity of the DES, making it easier for the extracting medium to penetrate plant tissues and extract the desired phenolic compounds. This method is beneficial in increasing the phenolic content extracted. However, it is important to note that an increase in water content in DES increases the solvent polarity resulting in poor phenolics. Therefore, a balance must be maintained between the water content and the DES for optimal extraction. Prolonged exposure to elevated temperatures can cause phenolic compounds to decompose, reducing their concentration and bioactivity. Therefore, optimization helps to achieve maximum extraction efficiency while preserving the integrity of the polyphenols extracted.<sup>37</sup>

Interestingly, both TPC and TFC have similar *R*<sup>2</sup> values. Since the *R*<sup>2</sup> value represents a goodness of fit of a regression model, it indicates how well the data points fit the regression line. A similar *R*<sup>2</sup> value for TPC and TFC suggests that the relationship between the two variables is similar in strength and direction.

Figures 4c and 4d show that temperature, DES concentration, and time have a considerable impact on TFC. However, when comparing these three factors, it becomes obvious that temperature imparts a less crucial role in the TFC. The probable reason behind this is that as the temperature increases, the vapor pressure difference between the inside and outside of the collapsing bubbles decreases, leading to a decrease in the intensity of the collapsing bubbles. As we know, the collapse of bubbles produced by cavitation is responsible for the extraction process. The force created by these collapsing bubbles damages the plant cell,



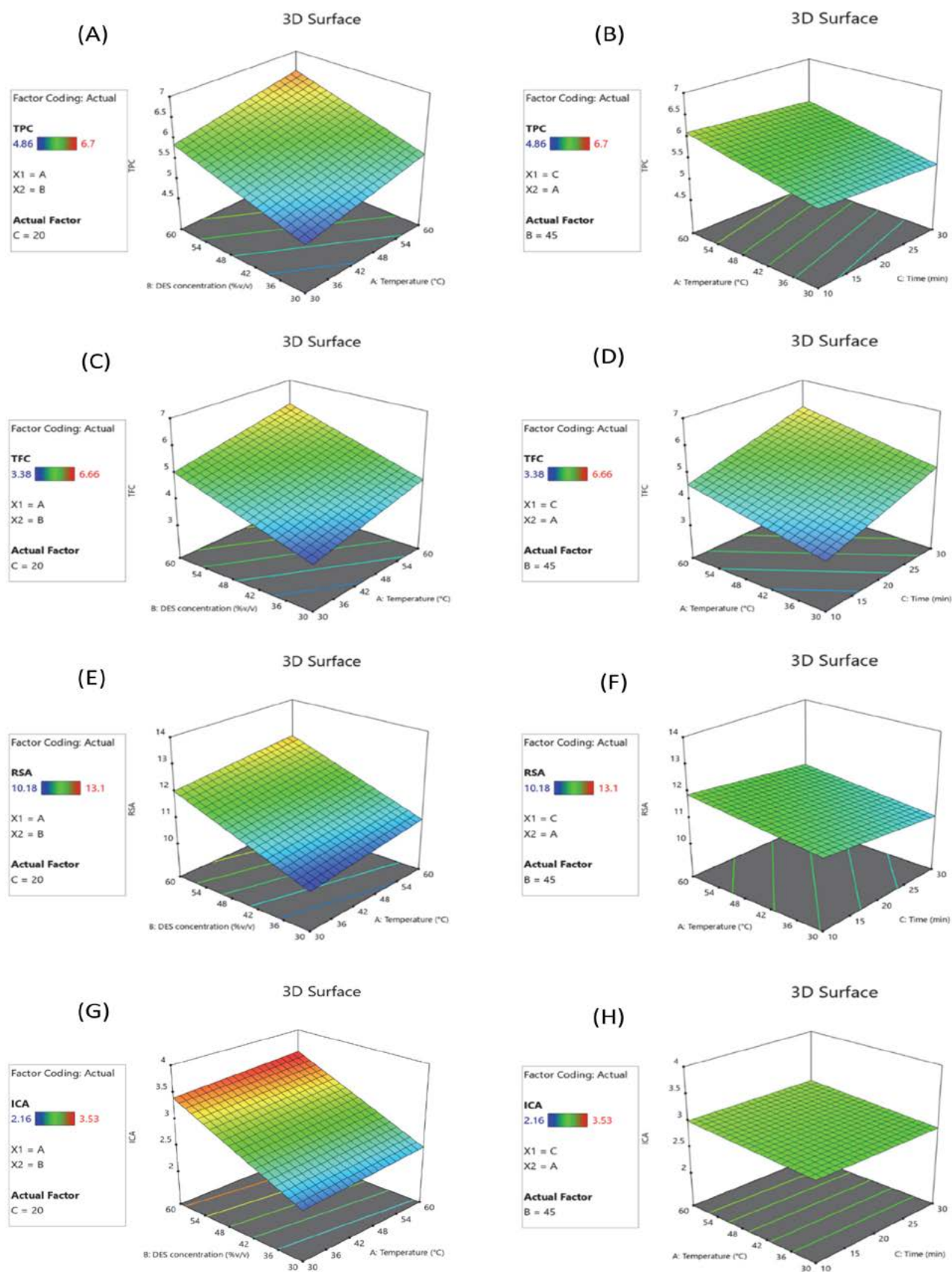


Figure 4. UAE-3D surface plots show combined effect of any two factors on the responses.

Table 5. UAE ANOVA for all responses.

Source	TPC (mg GAE g <sup>-1</sup> DW)		TFC (mg RE g <sup>-1</sup> DW)		RSA (mg AAE g <sup>-1</sup> DW)		ICA (mg EDTAE g <sup>-1</sup> DW)	
	<i>p</i> -value	<i>F</i> -value	<i>p</i> -value	<i>F</i> -value	<i>p</i> -value	<i>F</i> -value	<i>p</i> -value	<i>F</i> -value
<b>Model</b>	0.0002	17	0.0001	18.99	<0.0001	21.14	<0.0001	48.91
<b>A</b>	0.0024	15.35	0.0072	10.81	0.0555	4.59	0.1040	3.14
<b>B</b>	0.0001	34.72	0.0003	26.8	<0.0001	54.57	<0.0001	143.6
<b>C</b>	0.3591	0.9161	0.0011	19.36	0.0635	4.26	0.9588	0.0028
<b>Lack of fit</b>	0.5097	1.29	0.2607	3.20	0.5242	1.24	0.8426	0.4374
<b>R<sup>2</sup></b>	0.8225		0.8382		0.8522		0.9303	
<b>Adjusted R<sup>2</sup></b>	0.7741		0.7940		0.8119		0.9112	
<b>Predicted R<sup>2</sup></b>	0.6590		0.7009		0.7288		0.8772	

thereby releasing the phytochemicals into the extracting solvent. On the other hand, time plays a crucial part in the extraction process. A longer extraction period can increase the chance of the collapsing bubbles produced by cavitation. These collapsing bubbles can then disrupt the plant cell wall, causing the phytochemicals to diffuse into the extracting solvent more efficiently.<sup>38</sup>

Figures 4e and 4f show the slight increases in RSA observed with increasing temperature suggesting that antioxidants are more easily hydrolysed at elevated temperatures. As the concentration of DES increases, more antioxidants are solubilized in the solvent, leading to an increase in radical scavenging activity. This finding highlights the advantages of utilizing DESs as solvents in the extraction of antioxidants. Prolonged exposure to high temperature does not impact the extraction of antioxidants, likely due to the decomposition over time.<sup>39</sup>

Figures 4f and 4g show that the ICA is favoured by an increase in DES concentration, but not by the tempera-

ture or longer extraction process. Specifically, the results suggest that the solvent's polarity decreases as DES concentration is increased, which facilitates the extraction of moderately polar bioactive substances responsible for the iron chelating activity. However, elevated temperatures and prolonged exposure to solvents do not have a significant effect on iron chelating activity which can lead to the degradation of heat-sensitive iron chelating agents.

### 3. 5. Process Optimization and Experimental Verification

Numerical optimization was conducted to discover a single model of all the responses. For HAE and UAE, numerical optimization was done by keeping the independent factors at 'in range' option while the responses at 'maximize'. Under these constraints, the desirability factors for HAE and UAE were 0.935 and 0.882, respectively, which were close to 1 and, thus, a strong indication of the signifi-

Table 6. HAE and UAE predicted and experimental values of the responses obtained at optimal conditions.

Heat-assisted extraction (HAE)				
Input and output parameters	Goal values	Predicted	Experimental values	Percentage error %
DES concentration (%v/v)	in range			
Temperature (°C)	in range			
Time (min)	in range			
TPC (mg GAE g <sup>-1</sup> DW)	Maximize	3.33	3.24 ± 0.14	-2.70
TFC (mg RE g <sup>-1</sup> DW)	Maximize	3.98	3.81 ± 0.10	-4.27
RSA (mg AAE g <sup>-1</sup> DW)	Maximize	6.57	6.38 ± 0.19	-2.89
ICA (mg EDTAE g <sup>-1</sup> DW)	Maximize	2.48	2.61 ± 0.08	5.24
Ultrasound-assisted extraction (UAE)				
DES concentration (%v/v)	in range			
Temperature (°C)	in range			
Time (min)	in range			
TPC (mg GAE g <sup>-1</sup> DW)	Maximize	6.51	6.34 ± 0.17	-2.61
TFC (mg RE g <sup>-1</sup> DW)	Maximize	6.08	5.78 ± 0.17	-4.93
RSA (mg AAE g <sup>-1</sup> DW)	Maximize	12.56	12.78 ± 0.16	1.75
ICA (mg EDTAE g <sup>-1</sup> DW)	Maximize	3.57	3.64 ± 0.04	-2.24

icance of the models. For HAE, the optimal conditions were DES concentration 50%, temperature 60 °C, and time 75 min, and for UAE, DES concentration 60%, temperature 60 °C, and time 20 min. Validation experiments were performed under these conditions and the predicted and experimental values of the responses are given in Table 6.

The minimal percentage errors ranging from 1.75 to 5.24% given in Table 6 indicate a good correlation between the predicted and experimental values of the given responses and fitted well. This leads to the conclusion that within the experimental domain under study, polynomial equations are valid, and they may be employed for point prediction.

The efficacy of both HAE and UAE were tested in terms of response TPC, TFC, RSA, and ICA for both techniques. As Table 6 shows, UAE was more effective than HAE in all the responses at the optimum conditions. UAE also required much less time (only 20 min) as compared to 75 min of HAE. This is an important advantage of UAE over HAE. Many studies have shown similar results when compared to conventional technologies for extraction. Extraction of antioxidants from *Limonium sinuatum* was carried out by UAE at the optimal extraction time 9.8 min showing higher antioxidant activity as compared to maceration and Soxhlet extraction. UAE remarkably reduces the extraction period while enhancing the extraction yield and antioxidant activity.<sup>40</sup> In another study, polyphenolics extraction was carried out using UAE from *Thymus serpyllum*. L. herb compared to HAE and maceration was found to be more effective in all responses, while HAE and maceration do not have a significant difference among responses.<sup>33</sup> Finally, UAE has also been shown to be very efficient in extracting polyphenolics from *Adansonia digitata* which proved to be significant in terms of TPC, TFC, and antioxidant activity, when compared to HAE and maceration at the optimal time of 20 min.<sup>41</sup>

## 4. Conclusions

Extraction optimization of phenolics including flavonoids, radical scavengers, and iron-chelators from *W. somnifera* roots was successfully done using UAE and HAE and glycerol-sodium acetate DES. Well-fitted linear models were obtained for all the responses in both techniques. DES concentration and temperature were the most influential factors in both of the techniques. Optimum conditions suggested by numerical optimization for UAE and HAE were almost the same, except time which was much less in the case of UAE as compared to HAE. Response values were also much higher in UAE than in HAE. TPC, TFC, RSA and ICA of UAE were 6.51, 6.08, 12.56, and 3.57, respectively, which were much higher than for HAE being 3.33, 3.98, 6.57, and 2.48, respectively.

Thus, UAE was not only more efficient but also less time demanding. The optimized models were strongly

supported by the validation study with minimal % errors. The current study can be used for the development of processes that can be applied on an industrial scale for the extraction of bioactive compounds from *W. somnifera*.

## Acknowledgement

The research presented in this paper was done in the labs of the Department of Chemistry, Forman Christian College, Lahore, Pakistan, which the authors thankfully acknowledge.

## Competing interest statement

The authors declare no competing interest of any type.

## 5. References

1. P. K. Mukherjee, S. Banerjee, S. Biswas, B. Das, A. Kar, C. Katiyar, *J. Ethnopharmacol.* **2021**, *264*, 113157. DOI:10.1016/j.jep.2020.113157
2. S. Paul, S. Chakraborty, U. Anand, S. Dey, S. Nandy, M. Ghorai, S. C. Saha, M. T. Patil, R. Kandimalla, J. Proćków, A. Dey, *Biomed. Pharmacother.* **2021**, *143*, 112175. DOI:10.1016/j.biopha.2021.112175
3. S. Aslam, N. I. Raja, M. Hussain, M. Iqbal, M. Ejaz, D. Ashfaq, H. Fatima, M. A. Shah, M. Ehsan, *Am. J. Plant Sci.* **2017**, *8*, 1159–1169. DOI:10.4236/ajps.2017.85076
4. S. Rayees, F. Malik: *Withania somnifera*: From Traditional Use to Evidence Based Medicinal Prominence. In: S. Kaul, R. Wadhwa (Eds.) *Science of Ashwagandha: Preventive and Therapeutic Potentials.* **2017**, Springer, Cham.. DOI:10.1007/978-3-319-59192-6\_4
5. N. Alam, M. Hossain, M. I. Khalil, M. Moniruzzaman, S. A. Sulaiman, S. H. Gan, *BMC Complement. Altern. Med.* **2011**, *11*, 65. DOI:10.1186/1472-6882-11-65
6. L. Cornara, M. Biagi, J. Xiao, B. Burlando, *Front. Pharmacol.* **2017**, *8*, 412. DOI:10.3389/fphar.2017.00412
7. F. Chemat, M. Abert-Vian, A. S. Fabiano-Tixier, J. Strube, L. Uhlenbrock, V. Gunjevic, G. Cravotto, *Trends Anal. Chem.* **2019**, *118*, 248–263. DOI:10.1016/j.trac.2019.05.037
8. N. Rombaut, A. S. Tixier, A. Bily, F. Chemat, *Biofuels, Bioprod. Biorefin.* **2014**, *8*, 530–544. DOI:10.1002/bbb.1486
9. K. Papoutsis, P. Pristijono, J. B. Golding, C. E. Stathopoulos, M. C. Bowyer, C. J. Scarlett, Q. V. Vuong, *Eur. Food Res. Technol.* **2018**, *244*, 1353–1365. DOI:10.1007/s00217-018-3049-9
10. L. Panzella, F. Moccia, R. Nasti, S. Marzorati, L. Verotta, A. Napolitano, *Front. Nutr.* **2020**, *7*, 60. DOI:10.3389/fnut.2020.00060
11. H. Koraqi, B. Qazimi, C. Česko, A. T. Petkoska, *Acta Chim. Slov.* **2022**, *69*, 430–436. DOI:10.17344/acsi.2021.7332
12. A. S. Dheyab, M. F. Abu Bakar, M. AlOmar, S. F. Sabran, A. F. Muhamad Hanafi, A. Mohamad, *Separations.* **2021**, *8*, 176. DOI:10.3390/separations8100176

13. C. B. T. Pal, G. C. Jadeja, *Food Sci. Technol.* **2020**, *26*, 78–92. DOI:10.1177/1082013219870010
14. E. Mouratoglou, V. Malliou, D. P. Makris, *Waste Biomass Valori.* **2016**, *7*, 1377–1387. DOI:10.1007/s12649-016-9539-8
15. C. B. T. Pal, G. C. Jadeja, *Biomass Convers. Biorefin.* **2022**, 1–13. DOI:10.1007/s13399-022-02550-w
16. P. Gullón, B. Gullón, A. Romani, G. Rocchetti, J. M. Lorenzo, *Trends Food Sci. Technol.* **2020**, *101*, 182–197. DOI:10.1016/j.tifs.2020.05.007
17. D. Danjoll-Hashani, Ş. Selen-Işbilir, *Acta Chim. Slov.* **2022**, *69*, 665–673. DOI:10.17344/acsi.2022.7559
18. S. Rodríguez-Rojo, A. Visentin, D. Maestri, M. J. Cocero, *J. Food Eng.* **2012**, *109*, 98–103. DOI:10.1016/j.jfoodeng.2011.09.029
19. H. Guo, S. Liu, S. Li, Q. Feng, C. Ma, J. Zhao, Z. Xiong, *J. Pharm. Biomed. Anal.* **2020**, *185*, 113228. DOI:10.1016/j.jpba.2020.113228
20. C. Wen, J. Zhang, H. Zhang, C. S. Dzah, M. Zandile, Y. Duan, H. Ma, X. Luo, *Ultrason. Sonochem.* **2018**, *48*, 538–549. DOI:10.1016/j.ultsonch.2018.07.018
21. C. S. Dzah, Y. Duan, H. Zhang, C. Wen, J. Zhang, G. Chen, H. Ma, *Food Biosci.* **2020**, *35*, 100547. DOI:10.1016/j.fbio.2020.100547
22. S. Iftikhar, M. T. Qamar, A. Y. Aydar, D. Ahmed, *Folia Horti.* **2022**, *34*, 163–171. DOI:10.2478/fhort-2022-0013
23. S. Ihsan, D. Ahmed, H. Khalid, *J. Medicinal Plants By-products* **2022**, *11*, 119–127. DOI: 10.22092/JMPB.2021.355098.1374.
24. D. Ahmed, M. M. Khan, R. Saeed, *Antioxidants* **2015**, *4*, 394–409. DOI:10.3390/antiox4020394
25. R. Sudan, M. Bhagat, S. Gupta, J. Singh, A. Koul, *BioMed. Res. Int.* **2014**, *2014*, 179865. DOI:10.1155/2014/179865
26. J. B. Barbieri, C. Goltz, F. Batistão Cavalheiro, A. Theodoro Toci, L. Igarashi-Mafra, M. R. Mafra, *Ind. Crops Prod.* **2020**, *144*, 112049. DOI:10.1016/j.indcrop.2019.112049
27. B. Ozturk, C. Parkinson, M. Gonzalez-Miquel, *Sep. Purif. Technol.* **2018**, *206*, 1–13. DOI:10.1016/j.seppur.2018.05.052
28. R.-E. Ghitescu, I. Volf, C. Carausu, A.-M. Bühlmann, I. A. Gilca, V. I. Popa, *Ultrason. Sonochem.* **2015**, *22*, 535–541. DOI:10.1016/j.ultsonch.2014.07.013
29. H. Hosseini, S. Bolourian, E. Yaghoubi Hamgini, E. Ghanuni Mahababadi, *J. Food Process. Preserv.* **2018**, *42*, e13778. DOI:10.1111/jfpp.13778
30. A. Antony, M. Farid, *Appl. Sci.* **2022**, *12*, 2107. DOI:10.3390/app12042107
31. B. Sik, Z. Ajtony, E. Lakatos, R. Szekelyhidi, *Heliyon* **2022**, *8*, e12048. DOI:10.1016/j.heliyon.2022.e12048
32. S. K. Saha, S. Dey, R. Chakraborty, *J. Mol. Liq.* **2019**, *287*, 110956. DOI:10.1016/j.molliq.2019.110956
33. A. A. Jovanović, V. B. Đorđević, G. M. Zdunić, D. S. Pljevljakušić, K. P. Šavikin, D. M. Godevac, B. M. Bugarski, *Sep. Purif. Technol.* **2017**, *179*, 369–380. DOI:10.1016/j.seppur.2017.01.055
34. Z.-L. Sheng, P.-F. Wan, C.-L. Dong, Y.-H. Li, *Ind. Crops Prod.* **2013**, *43*, 778–786. DOI:10.1016/j.indcrop.2012.08.020
35. G. A. Nayik, B. N. Dar, V. Nanda, *Int. J. Food Prop.* **2016**, *19*, 1738–1748. DOI:10.1080/10942912.2015.1107733
36. Í. Gulcin, S. H. Alwasel, *Processes* **2022**, *10*, 132. DOI:10.3390/pr10010132
37. B. Zheng, Y. Yuan, J. Xiang, W. Jin, J. B. Johnson, Z. Li, C. Wang, D. Luo, *LWT* **2022**, *154*, 112740. DOI:10.1016/j.lwt.2021.112740
38. T. P. Vo, L. N. H. Nguyen, N. P. T. Le, T. P. Mai, D. Q. Nguyen, *Curr. Res. Food Sci.* **2022**, *5*, 2013–2021. DOI:10.1016/j.crfs.2022.09.021
39. I. A. Almusallam, I. A. M. Ahmed, E. E. Babiker, F. Y. Al Juhaimi, G. J. Fadimu, M. A. Osman, S. A. Al Maiman, K. Ghafoor, H. A. Alqah, *LWT* **2021**, *140*, 110816. DOI:10.1016/j.lwt.2020.110816
40. D.-P. Xu, J. Zheng, Y. Zhou, Y. Li, S. Li, H. B. Li, *Food Chem.* **2017**, *217*, 552–559. DOI:10.1016/j.foodchem.2016.09.013
41. B. B. Ismail, M. Guo, Y. Pu, W. Wang, X. Ye, D. Liu, *Ultrason. Sonochem.* **2019**, *52*, 257–267. DOI:10.1016/j.ultsonch.2018.11.023

## Povzetek

Raziskovali smo ekstrakcijo bioaktivnih spojin iz korenin rastline *Withania somnifera* pod vplivom ultrazvoka (UAE) ali pa ob uporabi segrevanja (HAE), kjer smo kot topilo uporabili evtektično zmes (DES) natrijevega acetata in glicerola. Ekstrakcije smo študirali s pomočjo metodologije površin odgovora (RSM). Določali smo celokupno vsebnost fenolov (TPC) v mg galne kisline (in njej ekvivalentnih snovi) na g suhe snovi (mg GAE g<sup>-1</sup> DW), celokupno vsebnost flavonoidov (TFC) v mg rutina (in njemu ekvivalentnih snovi) na g suhe snovi (mg RE g<sup>-1</sup> DW), aktivnost lovljenja radikalov (RSA) v mg askorbinske kisline (in njej ekvivalentnih snovi) na g suhe snovi (mg AAE g<sup>-1</sup> DW) ter aktivnost keliranja železovih ionov (ICA) v mg etilendiamintetraacetatnih ekvivalentov na g suhe snovi (mg EDTAE g<sup>-1</sup> DW). Če smo ekstrakcijo izvedli ob uporabi ultrazvoka, smo dobili naslednje vrednosti: 6,51 za TPC, 6,08 za TFC, 12,56 za RSA in 3,57 za ICA; v primeru termične ekstrakcije pa so bile vrednosti sledeče: 3,33 za TPC, 3,98 za TFC, 6,57 za RSA in 2,48 za ICA. Za izvedbo ekstrakcije pod vplivom ultrazvoka so bili optimalni naslednji parametri: koncentracija DES 50 %, temperatura 60 °C in čas 20 min; za termično ekstrakcijo pa se je najbolje izkazala koncentracija DES 60 %, temperatura 60 °C in čas 75 min. Razviti modeli so bili temeljito potrjeni z validacijskimi eksperimenti. Izkazalo se je, da je ekstrakcija rastlinskih snovi iz *W. somnifera* pod vplivom ultrazvoka bolj učinkovita in časovno hitrejša kot pa pri uporabi termične ekstrakcije.



Except when otherwise noted, articles in this journal are published under the terms and conditions of the Creative Commons Attribution 4.0 International License

Scientific paper

# Synthesis and Cholinesterase Inhibitory Activity of Selected Indole-Based Compounds

Marija Gršič,<sup>1</sup> Anže Meden,<sup>2</sup> Damijan Knez,<sup>2</sup> Marko Jukič,<sup>3</sup> Jurij Svete,<sup>1</sup>  
Stanislav Gobec<sup>2</sup> and Uroš Grošelj<sup>\*,1</sup>

<sup>1</sup> University of Ljubljana, Faculty of Chemistry and Chemical Technology, Večna pot 113, SI-1000 Ljubljana, Slovenia.

<sup>2</sup> University of Ljubljana, Faculty of Pharmacy, Aškerčeva 7, SI-1000 Ljubljana, Slovenia.

<sup>3</sup> University of Maribor, Faculty of Chemistry and Chemical Engineering, Smetanova ulica 17, SI-2000 Maribor, Slovenia.

\* Corresponding author: E-mail: uros.groselj@fkkt.uni-lj.si

Received: 09-20-2023

## Abstract

Synthesis and anticholinesterase activity of 18 previously unpublished indole- and tryptophan-derived compounds are disclosed. These compounds containing an indole structural unit exhibit selective submicromolar inhibition of human butyrylcholinesterase (hBChE). The structures of the newly synthesized compounds were confirmed by <sup>1</sup>H and <sup>13</sup>C NMR, IR spectroscopy, and high-resolution mass spectrometry.

**Keywords:** Indole derivatives, Tryptophan derivatives, Amidations, Cholinesterase (ChE) inhibitors, 1,1'-Carbonyldiimidazole (CDI), Rearrangements, Catalytic hydrogenation

## 1. Introduction

Indole is a privileged scaffold found in countless natural products that have diverse biological activities and functions.<sup>1–6</sup> In addition to the well-known skatole (3-methylindole), serotonin, *L*-tryptophan, tryptamine, the plant growth hormone 3-indoleacetic acid, and others, indole-containing alkaloids represent one of the most important alkaloid subgroups.<sup>7,8</sup> Indoles exhibit diverse biological activities ranging from antitumor to antibacterial activity.<sup>9–12</sup> Commercially available drugs with indole moiety include ajmaline<sup>13</sup> (antiarrhythmic agent), physostigmine<sup>14</sup> (for the treatment of glaucoma and anticholinergic poisoning), and vincristine<sup>15</sup> (antitumor agent), among others.<sup>1,16,17</sup>

Dementia is a serious neurological condition that severely affects patient's quality of life. It is estimated that Alzheimer's disease (AD), the most common form of dementia, affects more than 50 million people worldwide, and this number is expected to triple by 2050, mainly due to the aging of the population.<sup>18</sup> Selective human butyrylcholinesterase (hBChE) inhibitors improved cognitive functions, memory, and learning ability in a scopolamine mice model of cognitive deficit with-

out causing peripheral cholinergic side effects typical of acetylcholinesterase (AChE) inhibitors.<sup>19,20</sup> These data suggest that hBChE may be considered a promising therapeutic target to improve cognitive functions in late-stages of AD.<sup>21</sup> Recently, we have disclosed a hit-to-lead development of a new series of tryptophan-derived selective hBChE inhibitors with nanomolar inhibitory potencies, which were developed from (+)-isocampholenic acid-derived tryptophan amide hit **A**<sup>22</sup> by a medicinal chemistry-based approach (Figure 1).<sup>23,24</sup> Lead compounds **B** and **C** inhibited hBChE in the low nanomolar range with high selectivity over AChE, and possessed advantageous physicochemical properties for high blood-brain barrier permeability. Furthermore, compound **B** showed beneficial effects on fear-motivated long-term memory and spatial long-term memory retrieval in a scopolamine AD mouse model, with no adverse peripheral cholinergic side effects.<sup>23–25</sup>

While the structure-activity relationships (SAR) has been explored, several of the indole products were not included in our earlier reports. Therefore, we report here the synthesis and cholinesterase inhibitory activity of those unpublished indole-based compounds.

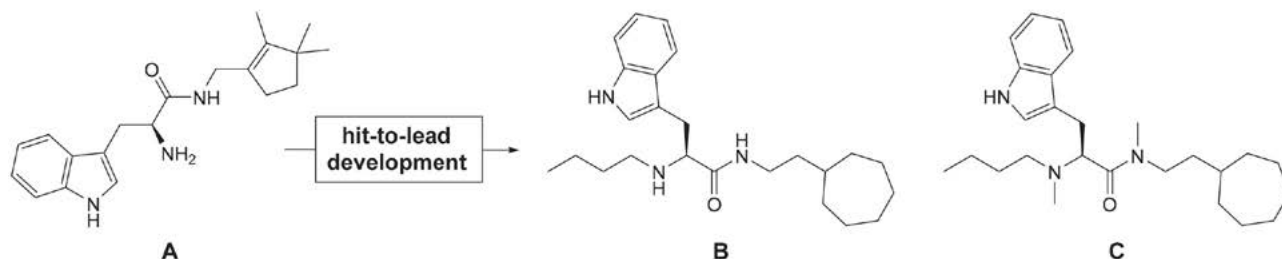


Figure 1. Hit compound A and selected lead compounds B and C.

## 2. Experimental

### 2.1. Materials and Measurements

Solvents for extractions and chromatography were of technical grade and were distilled prior to use. Extracts were dried over technical grade anhydrous  $\text{Na}_2\text{SO}_4$ . Melting points were determined on a Kofler micro hot stage and using the SRS OptiMelt MPA100 – Automated Melting Point System (Stanford Research Systems, Sunnyvale, CA, USA). NMR spectra were recorded on a Bruker UltraShield 500 plus (Bruker, Billerica, MA, USA) at 500 MHz for the  $^1\text{H}$  nucleus and 126 MHz for the  $^{13}\text{C}$  nucleus, using  $\text{CDCl}_3$  with TMS as the internal standard, as solvents. Mass spectra were recorded using an Agilent 6224 Accurate Mass TOF LC/MS (Agilent Technologies, Santa Clara, CA, USA), IR spectra using a Perkin-Elmer Spectrum BX FTIR spectrophotometer (Perkin-Elmer, Waltham, MA, USA). Column chromatography was performed on silica gel (silica gel 60, particle size: 0.035–0.070 mm (Sigma-Aldrich, St. Louis, MO, USA)). All commercial chemicals used were purchased from Sigma-Aldrich (St. Louis, MO, USA). Catalytic hydrogenation was performed in a Parr Pressure Reaction Hydrogenation Apparatus (Moline, IL, USA). Microanalyses were performed by combustion analysis on a Perkin-Elmer Series II CHNS/O Analyser (Perkin-Elmer, Waltham, MA, USA).

**General procedure 1 (GP1) – amide formation.** To a solution/suspension of acid (1 equivalent) in anhydrous MeCN under argon at room temperature was added CDI (1.20 equivalents). The resulting reaction mixture was stirred at room temperature for 1 h, then amine (1.13 equivalents) was added. After stirring the reaction mixture at room temperature for 16 h, the volatile components were evaporated *in vacuo* and the residue was purified by column chromatography on silica gel 60. The fractions containing the pure product (amide) were combined and the volatiles were evaporated *in vacuo*.

**General procedure 2 (GP2) – Boc-deprotection and double bond isomerization.** To a solution of the starting compound in anhydrous  $\text{CH}_2\text{Cl}_2$  at 0 °C was added trifluoroacetic acid (TFA). The resulting reaction mixture was stirred at 0 °C for 30 minutes and then stirred at room temperature for 2 h. Volatile components were evap-

orated *in vacuo*. The residual trifluoroacetic acid was removed by azeotropic evaporation with anhydrous toluene.

**General procedure 3 (GP3) – acetamidation.** To a solution of the trifluoroacetate salt in anhydrous  $\text{CH}_2\text{Cl}_2$  under argon at room temperature was added *N,N*-diisopropylethylamine (DIPEA) followed by  $\text{CH}_3\text{COCl}$ . After stirring the reaction mixture at room temperature for 12 h, the volatiles were evaporated *in vacuo*. The residue was dissolved in EtOAc (50 mL) and washed with  $\text{NaHSO}_4$  (1 M in  $\text{H}_2\text{O}$ , 2×5 mL),  $\text{NaHCO}_3$  (aq. sat, 2 × 5 mL), and NaCl (aq. sat, 2 × 5 mL). The organic phase was dried under anhydrous  $\text{Na}_2\text{SO}_4$ , filtered, and the volatiles were evaporated *in vacuo*. The residue was purified by column chromatography on silica gel 60. The fractions containing the pure product were combined and the volatiles were evaporated *in vacuo*.

**General procedure 4 (GP4) – amine N-Boc protection.** To a solution of the trifluoroacetate salt in anhydrous  $\text{CH}_2\text{Cl}_2$  under argon at room temperature were added  $\text{Et}_3\text{N}$  and  $\text{Boc}_2\text{O}$ . After stirring the reaction mixture at room temperature for 16 h, the volatile components were evaporated *in vacuo*. The residue was purified by column chromatography on silica gel 60. The fractions containing the pure product were combined and the volatiles were evaporated *in vacuo*.

**General procedure 5 (GP5) – alkene hydrogenation.** To a solution of alkene in MeOH, Pd-C (10% Pd on C; 20% by mass reagent was used) was added under argon. The resulting reaction mixture was thoroughly purged with hydrogen and shaken on a Parr apparatus under  $\text{H}_2$  (4 bar) at room temperature. The reaction mixture was filtered through a short pad of Celite® on a ceramic frit and Celite® was washed with MeOH. The volatiles were evaporated *in vacuo*. If necessary, the product was additionally purified by column chromatography on silica gel 60. The fractions containing the pure product were combined and the volatiles were evaporated *in vacuo*.

#### *N*-(Cycloheptylmethyl)-3-(1*H*-indol-3-yl)propanamide (8)

Following GP1. Prepared from 3-(1*H*-indol-3-yl)propanoic acid (1) (283 mg, 1.50 mmol), MeCN (3 mL), CDI (280 mg, 1.73 mmol), cycloheptylmethanamine (5

(250  $\mu\text{L}$ , 1.74 mmol); column chromatography (EtOAc/petroleum ether = 1:1). Yield: 348 mg (1.17 mmol, 78%) of white solid; mp 80.9–85.0  $^{\circ}\text{C}$ . Anal. Calcd for  $\text{C}_{19}\text{H}_{26}\text{N}_2\text{O}$ : C, 76.47; H, 8.78; N, 9.39. Found: C, 76.38; H, 8.85; N, 9.31. ESI-HRMS Calcd for  $\text{C}_{19}\text{H}_{27}\text{N}_2\text{O}$ :  $m/z$  299.2118 ( $\text{MH}^+$ ). Found:  $m/z$  299.2119 ( $\text{MH}^+$ ). IR  $\nu_{\text{max}}$  3258, 3087, 2914, 2848, 1612, 1564, 1492, 1455, 1429, 1350, 1274, 1217, 1181, 1102, 1065, 1008, 979, 790, 767, 733, 698  $\text{cm}^{-1}$ .  $^1\text{H}$  NMR (500 MHz,  $\text{DMSO}-d_6$ ):  $\delta$  1.00–1.11 (m, 2H), 1.28–1.64 (m, 11H), 2.44 (dd,  $J = 6.9, 8.4$  Hz, 2H), 2.84–2.96 (m, 4H), 6.93–6.99 (m, 1H), 7.02–7.09 (m, 2H), 7.32 (dt,  $J = 0.9, 8.1$  Hz, 1H), 7.52 (dd,  $J = 1.0, 7.9$  Hz, 1H), 7.79 (t,  $J = 5.8$  Hz, 1H), 10.73 (s, 1H).  $^{13}\text{C}$  NMR (126 MHz,  $\text{DMSO}-d_6$ ):  $\delta$  21.15, 25.87, 27.99, 31.63, 36.36, 45.11, 111.28, 113.89, 118.09, 118.37, 120.85, 122.08, 127.07, 136.25, 171.87 (one signal missing).

**tert-Butyl (R)-1-((2-Cyclohexylethyl)amino)-3-(1H-indol-3-yl)-1-oxopropan-2-yl)carbamate (9)**

Following *GPI*. Prepared from (*tert*-butoxycarbonyl)-*D*-tryptophan (**2**) (182 mg, 0.598 mmol), MeCN (2 mL), CDI (112 mg, 0.691 mmol), 2-cyclohexylethan-1-amine (**6**) (100  $\mu\text{L}$ , 0.677 mmol); column chromatography (EtOAc). Yield: 221 mg (0.534 mmol, 89%) of white solid; mp 103.9–106.2  $^{\circ}\text{C}$ . Anal. Calcd for  $\text{C}_{24}\text{H}_{35}\text{N}_3\text{O}_3$ : C, 69.70; H, 8.53; N, 10.16. Found: C, 69.77; H, 8.60; N, 10.08. ESI-HRMS Calcd for  $\text{C}_{24}\text{H}_{36}\text{N}_3\text{O}_3$ :  $m/z$  414.2751 ( $\text{MH}^+$ ). Found:  $m/z$  414.2762 ( $\text{MH}^+$ ). IR  $\nu_{\text{max}}$  3413, 3324, 2920, 2849, 1682, 1650, 1521, 1455, 1390, 1366, 1247, 1166, 1090, 1065, 1046, 1011, 857, 795, 736  $\text{cm}^{-1}$ .  $[\alpha]_{\text{D}}^{25} = -14.4$  ( $c = 1.1$  mg/mL,  $\text{CH}_2\text{Cl}_2$ ).  $^1\text{H}$  NMR (500 MHz,  $\text{CDCl}_3$ ):  $\delta$  0.71–0.85 (m, 2H), 0.99–1.21 (m, 6H), 1.43 (s, 9H), 1.51–1.68 (m, 5H), 3.04–3.20 (m, 3H), 3.31 (dd,  $J = 5.0, 14.3$  Hz, 1H), 4.38 (s, 1H), 5.19 (s, 1H), 5.55 (s, 1H), 7.05 (d,  $J = 2.3$  Hz, 1H), 7.11–7.16 (m, 1H), 7.18–7.23 (m, 1H), 7.36 (d,  $J = 8.1$  Hz, 1H), 7.67 (d,  $J = 7.9$  Hz, 1H), 8.15 (s, 1H, NH).  $^{13}\text{C}$  NMR (126 MHz,  $\text{CDCl}_3$ ):  $\delta$  26.26, 26.60, 28.47, 28.78, 33.12, 33.18, 35.23, 36.80, 37.36, 55.43, 80.08, 111.17, 111.30, 119.14, 119.95, 122.47, 123.18, 127.56, 136.37, 155.60, 171.47.

**tert-Butyl (S)-1-((2-Cyclohexylethyl)amino)-3-(1-methyl-1H-indol-3-yl)-1-oxopropan-2-yl)carbamate (10)**

Following *GPI*. Prepared from  $N^{\alpha}$ -(*tert*-butoxycarbonyl)-1-methyl-*L*-tryptophan (**3**) (159 mg, 0.499 mmol), MeCN (2 mL), CDI (99.6 mg, 0.614 mmol), 2-cyclohexylethan-1-amine (**6**) (83.3  $\mu\text{L}$ , 0.564 mmol); column chromatography (EtOAc/petroleum ether = 1:1). Yield: 198 mg (0.463 mmol, 93%) of white solid; mp 118.2–123.8  $^{\circ}\text{C}$ . Anal. Calcd for  $\text{C}_{25}\text{H}_{37}\text{N}_3\text{O}_3$ : C, 70.23; H, 8.72; N, 9.83. Found: C, 70.15; H, 8.89; N, 9.76. ESI-HRMS Calcd for  $\text{C}_{25}\text{H}_{38}\text{N}_3\text{O}_3$ :  $m/z$  428.2908 ( $\text{MH}^+$ ). Found:  $m/z$  428.2910 ( $\text{MH}^+$ ). IR  $\nu_{\text{max}}$  3341, 3320, 2921, 2852, 1679, 1655, 1543, 1514, 1486, 1463, 1452, 1420, 1391, 1369, 1321, 1291, 1238, 1206, 1165, 1123, 1093, 1062, 1045, 1024, 1001, 963, 924, 887, 867, 783, 767, 734 737  $\text{cm}^{-1}$ .  $[\alpha]_{\text{D}}^{25} = -1.03$  ( $c = 2.8$

mg/mL,  $\text{CH}_2\text{Cl}_2$ ).  $^1\text{H}$  NMR (500 MHz,  $\text{CDCl}_3$ ):  $\delta$  0.73–0.85 (m, 2H), 0.98–1.21 (m, 6H), 1.43 (s, 9H), 1.51–1.70 (m, 5H), 3.03–3.23 (m, 3H), 3.30 (dd,  $J = 5.2, 14.5$  Hz, 1H), 3.74 (s, 3H), 4.37 (s, 1H), 5.18 (s, 1H), 5.59 (s, 1H), 6.90 (s, 1H), 7.10–7.14 (m, 1H), 7.21–7.25 (m, 1H), 7.29 (dt,  $J = 0.9, 8.3$  Hz, 1H), 7.64 (d,  $J = 8.0$  Hz, 1H).  $^{13}\text{C}$  NMR (126 MHz,  $\text{CDCl}_3$ ):  $\delta$  26.24, 26.57, 28.45, 28.61, 32.81, 33.12, 33.18, 35.27, 36.86, 37.33, 55.41, 80.04, 109.36, 119.20, 119.38, 121.96, 127.99, 137.07, 155.61, 171.49 (one signal missing).

**tert-Butyl ((S)-1-((R)-2,2-Dimethyl-3-methylenecyclopentyl)ethyl)amino)-3-(1-methyl-1H-indol-3-yl)-1-oxopropan-2-yl)carbamate (11)**

Following *GPI*. Prepared from  $N^{\alpha}$ -(*tert*-butoxycarbonyl)-1-methyl-*L*-tryptophan (**3**) (318 mg, 0.999 mmol), MeCN (3 mL), CDI (188 mg, 1.16 mmol), (*R*)-2-(2,2-dimethyl-3-methylenecyclopentyl)ethan-1-amine (**7**)<sup>22</sup> (182  $\mu\text{L}$ , 1.13 mmol); column chromatography (EtOAc/petroleum ether = 1:2). Yield: 183 mg (0.403 mmol, 40%) of yellow oil. ESI-HRMS Calcd for  $\text{C}_{27}\text{H}_{40}\text{N}_3\text{O}_3$ :  $m/z$  454.3064 ( $\text{MH}^+$ ). Found:  $m/z$  = 454.3068 ( $\text{MH}^+$ ). IR  $\nu_{\text{max}}$  3306, 3068, 2958, 2932, 2867, 1651, 1524, 1473, 1436, 1390, 1365, 1325, 1240, 1166, 1046, 1013, 878, 780, 737  $\text{cm}^{-1}$ .  $[\alpha]_{\text{D}}^{25} = +5.40$  ( $c = 1.8$  mg/mL,  $\text{CH}_2\text{Cl}_2$ ).  $^1\text{H}$  NMR (500 MHz,  $\text{CDCl}_3$ ):  $\delta$  0.72 (s, 3H), 0.95 (s, 3H), 1.00–1.08 (m, 1H), 1.10–1.20 (m, 1H), 1.21–1.31 (m, 1H), 1.31–1.39 (m, 1H), 1.43 (s, 9H), 1.64–1.79 (m, 1H), 2.16–2.28 (m, 1H), 2.35–2.45 (m, 1H), 3.03–3.22 (m, 3H), 3.30 (dd,  $J = 5.2, 14.5$  Hz, 1H), 3.73 (s, 3H), 4.38 (s, 1H), 4.72 (t,  $J = 2.5$  Hz, 1H), 4.74 (t,  $J = 2.2$  Hz, 1H), 5.18 (s, 1H), 5.67 (s, 1H), 6.91 (s, 1H), 7.09–7.14 (m, 1H), 7.20–7.25 (m, 1H), 7.28 (d,  $J = 8.2$  Hz, 1H), 7.64 (d,  $J = 8.0$  Hz, 1H).  $^{13}\text{C}$  NMR (126 MHz,  $\text{CDCl}_3$ ):  $\delta$  23.43, 26.51, 28.04, 28.45, 28.57, 29.71, 30.68, 32.82, 38.94, 44.00, 47.92, 55.43, 80.13, 103.20, 109.38, 119.19, 119.40, 122.01, 127.96, 128.00, 137.08, 155.64, 162.07, 171.54 (one signal missing).

**tert-Butyl ((R)-1-((R)-2,2-Dimethyl-3-methylenecyclopentyl)ethyl)amino)-3-(1-methyl-1H-indol-3-yl)-1-oxopropan-2-yl)carbamate (12)**

Following *GPI*. Prepared from  $N^{\alpha}$ -(*tert*-butoxycarbonyl)-1-methyl-*D*-tryptophan (**4**) (200 mg, 0.628 mmol), MeCN (3 mL), CDI (123 mg, 0.759 mmol), (*R*)-2-(2,2-dimethyl-3-methylenecyclopentyl)ethan-1-amine (**7**)<sup>22</sup> (114  $\mu\text{L}$ , 0.707 mmol); column chromatography (EtOAc/petroleum ether = 1:1). Yield: 140 mg (0.309 mmol, 49%) of orange oil. ESI-HRMS Calcd for  $\text{C}_{27}\text{H}_{40}\text{N}_3\text{O}_3$ :  $m/z$  454.3064 ( $\text{MH}^+$ ). Found:  $m/z$  454.3048 ( $\text{MH}^+$ ). IR  $\nu_{\text{max}}$  3307, 2958, 1651, 1523, 1474, 1365, 1325, 1240, 1166, 1046, 1013, 877, 781, 737  $\text{cm}^{-1}$ .  $[\alpha]_{\text{D}}^{25} = +4.21$  ( $c = 1.4$  mg/mL,  $\text{CH}_2\text{Cl}_2$ ).  $^1\text{H}$  NMR (500 MHz,  $\text{CDCl}_3$ ):  $\delta$  0.73 (s, 3H), 0.96 (s, 3H), 0.99–1.10 (m, 1H), 1.13–1.22 (m, 1H), 1.28–1.37 (m, 2H), 1.43 (s, 9H), 1.70–1.78 (m, 1H), 2.19–2.29 (m, 1H), 2.37–2.45 (m, 1H), 3.01–3.25 (m, 3H), 3.31 (dd,  $J = 5.2, 14.3$  Hz, 1H), 3.74 (s, 3H), 4.37 (s, 1H), 4.73 (t,  $J = 2.5$  Hz, 1H), 4.75

(t,  $J = 2.3$  Hz, 1H), 5.17 (s, 1H), 5.66 (s, 1H), 6.92 (s, 1H), 7.10–7.14 (m, 1H), 7.21–7.25 (m, 1H), 7.29 (dt,  $J = 0.9, 8.3$  Hz, 1H), 7.64 (d,  $J = 7.9$  Hz, 1H).  $^{13}\text{C}$  NMR (126 MHz,  $\text{CDCl}_3$ ):  $\delta$  23.47, 26.54, 28.06, 28.51, 28.45, 29.71, 30.70, 32.84, 39.03, 44.01, 47.97, 55.49, 80.14, 103.21, 109.37, 119.20, 119.41, 122.00, 127.98, 128.04, 137.08, 155.61, 162.09, 171.53 (one signal missing).

**(R)-1-((2-Cyclohexylethyl)amino)-3-(1H-indol-3-yl)-1-oxopropan-2-aminium 2,2,2-Trifluoroacetate (13)**

Following GP2. Prepared from Boc-amine **9** (199 mg, 0.481 mmol),  $\text{CH}_2\text{Cl}_2$  (2 mL), TFA (1.8 mL); the product **13** was thoroughly dried in high vacuum. Yield: 187 mg (0.437 mmol, 91%) of orange oil. ESI-HRMS Calcd for  $\text{C}_{19}\text{H}_{28}\text{N}_3\text{O}$ :  $m/z$  314.2227 ( $\text{MH}^+$ ). Found:  $m/z = 314.2242$  ( $\text{MH}^+$ ). IR  $\nu_{\text{max}}$  3293, 2923, 2851, 1448, 1661, 1341, 1180, 1135, 1011, 838, 799, 741, 722  $\text{cm}^{-1}$ .  $[\alpha]_{\text{D}}^{\text{rt}} = -36.4$  ( $c = 1.8$  mg/mL,  $\text{CH}_2\text{Cl}_2$ ).  $^1\text{H}$  NMR (500 MHz,  $\text{DMSO}-d_6$ ):  $\delta$  0.75–0.87 (m, 2H), 1.04–1.25 (m, 6H), 1.52–1.69 (m, 5H), 2.97–3.22 (m, 4H), 3.84–3.97 (m, 1H), 6.98–7.03 (m, 1H), 7.07–7.11 (m, 1H), 7.19 (d,  $J = 2.5$  Hz, 1H), 7.37 (d,  $J = 8.1$  Hz, 1H), 7.62 (d,  $J = 7.8$  Hz, 1H), 8.15 (s, 3H), 8.38 (t,  $J = 5.6$  Hz, 1H), 11.05 (d,  $J = 2.5$  Hz, 1H).  $^{13}\text{C}$  NMR (126 MHz,  $\text{DMSO}-d_6$ ):  $\delta$  25.67, 26.09, 27.43, 32.52, 32.56, 34.31, 36.13, 36.45, 52.90, 107.00, 111.47, 118.39, 121.11, 124.73, 127.07, 136.27, 158.13 (q,  $J = 31.9$  Hz), 168.08 (one signal missing).

**(S)-3-(1-Methyl-1H-indol-3-yl)-1-oxo-1-((2-(2,3,3-trimethylcyclopent-1-en-1-yl)ethyl)amino)propan-2-aminium 2,2,2-Trifluoroacetate (14)**

Following GP2. Prepared from Boc-amine **11** (98.5 mg, 0.217 mmol),  $\text{CH}_2\text{Cl}_2$  (2 mL), TFA (1 mL); the product **14** was thoroughly dried in high vacuum. Yield: 92.9 mg (0.199 mmol, 92%) of dark brown oil. ESI-HRMS Calcd for  $\text{C}_{22}\text{H}_{32}\text{N}_3\text{O}$ :  $m/z$  354.2540 ( $\text{MH}^+$ ). Found:  $m/z = 354.2541$  ( $\text{MH}^+$ ). IR  $\nu_{\text{max}}$  3056, 2951, 2934, 2862, 1779, 1662, 1549, 1474, 1435, 1378, 1359, 1330, 1199, 1175, 1134, 1014, 965, 837, 798, 739, 722  $\text{cm}^{-1}$ .  $[\alpha]_{\text{D}}^{\text{rt}} = +6.52$  ( $c = 2.3$  mg/mL,  $\text{CH}_2\text{Cl}_2$ ).  $^1\text{H}$  NMR (500 MHz,  $\text{CDCl}_3$ ):  $\delta$  0.86 (s, 3H), 0.89 (s, 3H), 1.34–1.36 (m, 3H), 1.43–1.56 (m, 2H), 1.88–2.06 (m, 4H), 2.95–3.11 (m, 2H), 3.24 (d,  $J = 7.2$  Hz, 2H), 3.70 (s, 3H), 4.16 (t,  $J = 7.3$  Hz, 1H), 6.71 (t,  $J = 5.5$  Hz, 1H), 7.00–7.07 (m, 2H), 7.11–7.20 (m, 1H), 7.22–7.30 (m, 1H), 7.51 (d,  $J = 7.9$  Hz, 1H), 7.94 (s, 3H).  $^{13}\text{C}$  NMR (126 MHz,  $\text{CDCl}_3$ ):  $\delta$  9.26, 26.44, 26.47, 27.72, 27.99, 32.06, 32.78, 38.36, 38.76, 46.92, 54.42, 106.28, 109.75, 118.54, 119.65, 122.26, 127.41, 129.05, 129.30, 138.02, 142.05, 161.69 (q,  $J = 36.9$  Hz), 168.64 (one signal missing).

**(R)-3-(1-Methyl-1H-indol-3-yl)-1-oxo-1-((2-(2,3,3-trimethylcyclopent-1-en-1-yl)ethyl)amino)propan-2-aminium 2,2,2-Trifluoroacetate (15)**

Following GP2. Prepared from Boc-amine **12** (99.7 mg, 0.220 mmol),  $\text{CH}_2\text{Cl}_2$  (2 mL), TFA (1 mL); the product **15** was thoroughly dried in high vacuum. Yield: 89.2 mg

(0.191 mmol, 87%) of dark orange oil. ESI-HRMS Calcd for  $\text{C}_{22}\text{H}_{32}\text{N}_3\text{O}$ :  $m/z$  354.2540 ( $\text{MH}^+$ ). Found:  $m/z = 354.2535$  ( $\text{MH}^+$ ). IR  $\nu_{\text{max}}$  3061, 2951, 2862, 1779, 1663, 1550, 1473, 1435, 1378, 1359, 1330, 1251, 1172, 1135, 1013, 960, 836, 798, 739  $\text{cm}^{-1}$ .  $[\alpha]_{\text{D}}^{\text{rt}} = -9.0$  ( $c = 1.9$  mg/mL,  $\text{CH}_2\text{Cl}_2$ ).  $^1\text{H}$  NMR (500 MHz,  $\text{CDCl}_3$ ):  $\delta$  0.86 (s, 3H), 0.89 (s, 3H), 1.36 (t,  $J = 2.2$  Hz, 3H), 1.44–1.57 (m, 2H), 1.89–2.07 (m, 4H), 2.96–3.13 (m, 2H), 3.24 (d,  $J = 7.3$  Hz, 2H), 3.71 (s, 3H), 4.18 (t,  $J = 7.3$  Hz, 1H), 6.64 (t,  $J = 5.5$  Hz, 1H), 7.02 (s, 1H), 7.03–7.07 (m, 1H), 7.13–7.19 (m, 1H), 7.23–7.28 (m, 1H), 7.50 (d,  $J = 7.9$  Hz, 1H), 7.85 (s, 3H).  $^{13}\text{C}$  NMR (126 MHz,  $\text{CDCl}_3$ ):  $\delta$  9.27, 26.44, 26.47, 27.76, 27.97, 32.05, 32.81, 38.39, 38.76, 46.94, 54.43, 106.13, 109.80, 118.47, 119.71, 122.33, 127.34, 129.05, 129.24, 138.02, 142.18, 161.60 (q,  $J = 37.6$  Hz), 168.61 (one signal missing).

**(R)-2-Acetamido-N-(2-cyclohexylethyl)-3-(1H-indol-3-yl)propanamide (19)**

Following GP3. Prepared from trifluoroacetate salt **13** (160 mg, 0.374 mmol),  $\text{CH}_2\text{Cl}_2$  (2 mL), DIPEA (196  $\mu\text{L}$ , 1.13 mmol),  $\text{CH}_3\text{COCl}$  (32.1  $\mu\text{L}$ , 0.450 mmol); column chromatography (EtOAc/petroleum ether = 1:1). Yield: 78 mg (0.219 mmol, 59%) of white solid; mp 195.7–198.6 °C. ESI-HRMS Calcd for  $\text{C}_{21}\text{H}_{30}\text{N}_3\text{O}_2$ :  $m/z$  356.2333 ( $\text{MH}^+$ ). Found:  $m/z = 356.2347$  ( $\text{MH}^+$ ). IR  $\nu_{\text{max}}$  3407, 3287, 2914, 2849, 1636, 1561, 1539, 1455, 1370, 1287, 1243, 1091, 1023, 1012, 813, 779, 741  $\text{cm}^{-1}$ .  $[\alpha]_{\text{D}}^{\text{rt}} = -15.3$  ( $c = 1.2$  mg/mL,  $\text{CH}_2\text{Cl}_2$ ).  $^1\text{H}$  NMR (500 MHz,  $\text{DMSO}-d_6$ ):  $\delta$  0.74–0.88 (m, 2H), 1.04–1.25 (m, 6H), 1.54–1.67 (m, 5H), 1.78 (s, 3H), 2.87 (dd,  $J = 8.5, 14.5$  Hz, 1H), 2.96–3.11 (m, 3H), 4.42–4.50 (m, 1H), 6.94–6.98 (m, 1H), 7.02–7.07 (m, 1H), 7.10 (d,  $J = 2.3$  Hz, 1H), 7.31 (dt,  $J = 0.9, 8.1$  Hz, 1H), 7.57 (d,  $J = 7.8$  Hz, 1H), 7.84 (t,  $J = 5.6$  Hz, 1H), 7.99 (d,  $J = 8.4$  Hz, 1H), 10.77 (s, 1H, NH).  $^{13}\text{C}$  NMR (126 MHz,  $\text{DMSO}-d_6$ ):  $\delta$  22.57, 25.72, 26.09, 28.07, 32.60, 34.50, 36.24, 36.41, 53.47, 110.26, 111.19, 118.09, 118.42, 120.76, 123.36, 127.32, 136.00, 168.88, 171.25.

**(R)-2-Acetamido-3-(1H-indol-3-yl)-N-(2-(2,3,3-trimethylcyclopent-1-en-1-yl)ethyl)propanamide (20)**

Following GP3. Prepared from trifluoroacetate salt **16**<sup>23</sup> (267 mg, 0.589 mmol),  $\text{CH}_2\text{Cl}_2$  (3.5 mL), DIPEA (307  $\mu\text{L}$ , 1.76 mmol),  $\text{CH}_3\text{COCl}$  (50.3  $\mu\text{L}$ , 0.705 mmol); column chromatography (EtOAc/petroleum ether = 1:1). Yield: 148.6 mg (0.389 mmol, 66%) of yellowish solid; mp 78.2–83.8 °C. ESI-HRMS Calcd for  $\text{C}_{23}\text{H}_{32}\text{N}_3\text{O}_2$ :  $m/z$  382.2489 ( $\text{MH}^+$ ). Found:  $m/z = 382.2489$  ( $\text{MH}^+$ ). IR  $\nu_{\text{max}}$  3282, 3079, 2951, 2861, 1636, 1533, 1457, 1435, 1372, 1358, 1287, 1234, 1204, 1138, 1043, 1011, 908, 838, 801, 732  $\text{cm}^{-1}$ .  $[\alpha]_{\text{D}}^{\text{rt}} = -4.9$  ( $c = 2.3$  mg/mL,  $\text{CH}_2\text{Cl}_2$ ).  $^1\text{H}$  NMR (500 MHz,  $\text{CDCl}_3$ ):  $\delta$  0.86 (s, 3H), 0.87 (s, 3H), 1.33 (t,  $J = 2.1$  Hz, 3H), 1.44–1.54 (m, 2H), 1.91 (s, 3H), 1.94–2.02 (m, 4H), 3.05–3.17 (m, 3H), 3.23 (dd,  $J = 5.9, 14.5$  Hz, 1H), 4.68 (q,  $J = 7.3$  Hz, 1H), 6.02 (t,  $J = 5.6$  Hz, 1H), 6.79 (d,  $J = 7.8$  Hz, 1H), 6.98 (d,  $J = 2.4$  Hz, 1H), 7.05–7.10 (m, 1H), 7.12–7.19 (m, 1H), 7.31 (d,  $J = 8.1$  Hz, 1H), 7.61 (d,  $J = 7.8$  Hz, 1H),



8.61 (s, 1H, NH).  $^{13}\text{C}$  NMR (126 MHz,  $\text{CDCl}_3$ ):  $\delta$  9.30, 23.14, 26.42, 26.46, 28.27, 28.62, 32.10, 37.94, 38.73, 46.86, 54.35, 110.60, 111.41, 118.70, 119.68, 122.19, 123.22, 127.51, 129.58, 136.28, 141.83, 170.52, 171.47.

**tert-Butyl (R)-(3-(1H-Indol-3-yl)-1-oxo-1-((2-(2,3,3-trimethylcyclopent-1-en-1-yl)ethyl)amino)propan-2-yl)carbamate (21)**

Following GP4. Prepared from trifluoroacetate salt **17**<sup>23</sup> (382 mg, 0.842 mmol),  $\text{CH}_2\text{Cl}_2$  (5 mL),  $\text{Et}_3\text{N}$  (500  $\mu\text{L}$ , 3.59 mmol),  $\text{Boc}_2\text{O}$  (377 mg, 1.73 mmol); column chromatography (EtOAc/petroleum ether = 1:2). Yield: 245 mg (0.557 mmol, 66%) of colorless oil. ESI-HRMS Calcd for  $\text{C}_{26}\text{H}_{38}\text{N}_3\text{O}_3$ :  $m/z$  440.2908 ( $\text{MH}^+$ ). Found:  $m/z$  440.2903 ( $\text{MH}^+$ ). IR  $\nu_{\text{max}}$  3307, 2931, 2861, 1698, 1654, 1493, 1457, 1436, 1391, 1365, 1246, 1163, 1102, 1065, 1046, 1011, 909, 857, 780, 735  $\text{cm}^{-1}$ .  $[\alpha]_{\text{D}}^{25} = -11.1$  ( $c = 2.2$  mg/mL,  $\text{CH}_2\text{Cl}_2$ ).  $^1\text{H}$  NMR (500 MHz,  $\text{CDCl}_3$ ):  $\delta$  0.84 (s, 3H), 0.88 (s, 3H), 1.32 (s, 3H), 1.42 (s, 9H), 1.46–1.52 (m, 2H), 1.92–2.02 (m, 4H), 3.05–3.20 (m, 3H), 3.34 (d,  $J = 14.7$  Hz, 1H), 4.39 (s, 1H), 5.06 (s, 1H), 5.63 (s, 1H), 7.04 (d,  $J = 2.5$  Hz, 1H), 7.10–7.15 (m, 1H), 7.17–7.22 (m, 1H), 7.36 (d,  $J = 8.0$  Hz, 1H), 7.63 (d,  $J = 7.9$  Hz, 1H), 8.24 (s, 1H, NH).  $^{13}\text{C}$  NMR (126 MHz,  $\text{CDCl}_3$ ):  $\delta$  9.32, 26.42, 26.55, 28.23, 28.43, 28.64, 32.07, 37.68, 38.78, 46.93, 55.37, 80.14, 110.89, 111.30, 119.08, 119.91, 122.45, 123.21, 127.63, 129.72, 136.36, 142.12, 155.52, 171.47.

**tert-Butyl (R)-(3-(1H-Indol-3-yl)-1-oxo-1-((2,3,3-trimethylcyclopent-1-en-1-yl)methyl)amino)propan-2-yl)carbamate (22)**

Following GP4. Prepared from trifluoroacetate salt **18**<sup>22</sup> (216 mg, 0.491 mmol),  $\text{CH}_2\text{Cl}_2$  (5 mL),  $\text{Et}_3\text{N}$  (386  $\mu\text{L}$ , 2.77 mmol),  $\text{Boc}_2\text{O}$  (350 mg, 1.60 mmol); column chromatography (EtOAc/petroleum ether = 1:2). Yield: 109 mg (0.256 mmol, 52%) of colorless oil. ESI-HRMS Calcd for  $\text{C}_{25}\text{H}_{36}\text{N}_3\text{O}_3$ :  $m/z$  426.2751 ( $\text{MH}^+$ ). Found:  $m/z$  426.2751 ( $\text{MH}^+$ ). IR  $\nu_{\text{max}}$  3303, 2929, 2860, 1691, 1655, 1492, 1457, 1437, 1390, 1365, 1246, 1163, 1099, 1056, 1011, 859, 739  $\text{cm}^{-1}$ .  $[\alpha]_{\text{D}}^{25} = +1.92$  ( $c = 1.9$  mg/mL,  $\text{CH}_2\text{Cl}_2$ ).  $^1\text{H}$  NMR (500 MHz,  $\text{CDCl}_3$ ):  $\delta$  0.89 (s, 3H), 0.90 (s, 3H), 1.34–1.46 (m, 12H), 1.47–1.57 (m, 2H), 1.84–2.02 (m, 2H), 3.09–3.22 (m, 1H), 3.23–3.36 (m, 1H), 3.73 (s, 2H), 4.33–4.49 (m, 1H), 5.05–5.28 (m, 1H), 5.54–5.75 (m, 1H), 7.03 (d,  $J = 2.5$  Hz, 1H), 7.09–7.15 (m, 1H), 7.17–7.21 (m, 1H), 7.35 (d,  $J = 8.1$  Hz, 1H), 7.65 (d,  $J = 7.9$  Hz, 1H), 8.41 (s, 1H, NH).  $^{13}\text{C}$  NMR (126 MHz,  $\text{CDCl}_3$ ):  $\delta$  9.45, 26.31, 28.41, 28.63, 31.07, 37.93, 38.61, 47.08, 55.34, 80.11, 110.81, 111.35, 118.98, 119.79, 122.31, 123.26, 127.49, 128.86, 136.39, 143.51, 155.59, 171.63 (one signal missing).

**tert-Butyl (S)-(3-(1-Methyl-1H-indol-3-yl)-1-oxo-1-((2-(2,3,3-trimethylcyclopent-1-en-1-yl)ethyl)amino)propan-2-yl)carbamate (23)**

Following GP4. Prepared from trifluoroacetate salt **14** (62.9 mg, 0.134 mmol),  $\text{CH}_2\text{Cl}_2$  (3 mL),  $\text{Et}_3\text{N}$  (170  $\mu\text{L}$ ,

1.22 mmol),  $\text{Boc}_2\text{O}$  (203 mg, 0.930 mmol); column chromatography (EtOAc/petroleum ether = 1:4). Yield: 45.2 mg (0.0996 mmol, 74%) of yellow oil. ESI-HRMS Calcd for  $\text{C}_{27}\text{H}_{40}\text{N}_3\text{O}_3$ :  $m/z$  454.3064 ( $\text{MH}^+$ ). Found:  $m/z = 454.3068$  ( $\text{MH}^+$ ). IR  $\nu_{\text{max}}$  3305, 2950, 2931, 2861, 1652, 1523, 1474, 1365, 1325, 1241, 1166, 1121, 1045, 1013, 859, 779, 737  $\text{cm}^{-1}$ .  $[\alpha]_{\text{D}}^{25} = +6.95$  ( $c = 1.7$  mg/mL,  $\text{CH}_2\text{Cl}_2$ ).  $^1\text{H}$  NMR (500 MHz,  $\text{CDCl}_3$ ):  $\delta$  0.82 (s, 3H), 0.87 (s, 3H), 1.31 (s, 3H); 1.42 (s, 9H), 1.44–1.51 (m, 2H), 1.90–1.97 (m, 2H), 2.00 (t,  $J = 6.9$  Hz, 2H), 3.04–3.22 (m, 3H), 3.33 (d,  $J = 11.9$  Hz, 1H), 3.74 (s, 3H), 4.37 (s, 1H), 5.04 (s, 1H), 5.63 (s, 1H), 6.91 (s, 1H), 7.09–7.13 (m, 1H), 7.20–7.25 (m, 1H), 7.28 (dt,  $J = 1.0, 8.3$  Hz, 1H), 7.61 (d,  $J = 7.9$  Hz, 1H).  $^{13}\text{C}$  NMR (126 MHz,  $\text{CDCl}_3$ ):  $\delta$  9.28, 26.36, 26.51, 28.16, 28.42, 31.98, 32.79, 37.62, 38.76, 46.91, 55.48, 80.13, 109.24, 109.34, 119.17, 119.39, 122.00, 127.91, 128.14, 129.74, 137.08, 142.11, 155.51, 171.48.

**tert-Butyl (R)-(3-(1-Methyl-1H-indol-3-yl)-1-oxo-1-((2-(2,3,3-trimethylcyclopent-1-en-1-yl)ethyl)amino)propan-2-yl)carbamate (24)**

Following GP4. Prepared from trifluoroacetate salt **15** (61.8 mg, 0.132 mmol),  $\text{CH}_2\text{Cl}_2$  (3 mL),  $\text{Et}_3\text{N}$  (97.6  $\mu\text{L}$ , 0.700 mmol),  $\text{Boc}_2\text{O}$  (110 mg, 0.504 mmol); column chromatography (EtOAc/petroleum ether = 1:3). Yield: 45.7 mg (0.101 mmol, 76%) of orange oil. ESI-HRMS Calcd for  $\text{C}_{27}\text{H}_{40}\text{N}_3\text{O}_3$ :  $m/z$  454.3064 ( $\text{MH}^+$ ). Found:  $m/z$  454.3067 ( $\text{MH}^+$ ). IR  $\nu_{\text{max}}$  3305, 3052, 2950, 2931, 2861, 1652, 1522, 1474, 1365, 1325, 1242, 1165, 1046, 1013, 923, 860, 778, 734  $\text{cm}^{-1}$ .  $[\alpha]_{\text{D}}^{25} = +28.7$  ( $c = 1.7$  mg/mL,  $\text{CH}_2\text{Cl}_2$ ).  $^1\text{H}$  NMR (500 MHz,  $\text{CDCl}_3$ ):  $\delta$  0.82 (s, 3H), 0.87 (s, 3H), 1.32 (t,  $J = 2.1$  Hz, 3H), 1.42 (s, 9H), 1.45–1.52 (m, 2H), 1.88–1.97 (m, 2H), 2.00 (t,  $J = 7.0$  Hz, 2H), 3.04–3.22 (m, 3H), 3.34 (d,  $J = 14.8$  Hz, 1H), 3.74 (s, 3H), 4.36 (s, 1H), 5.03 (s, 1H), 5.62 (s, 1H), 6.91 (s, 1H), 7.10–7.14 (m, 1H), 7.20–7.25 (m, 1H), 7.28 (dt,  $J = 1.0, 8.3$  Hz, 1H), 7.61 (d,  $J = 7.9$  Hz, 1H).  $^{13}\text{C}$  NMR (126 MHz,  $\text{CDCl}_3$ ):  $\delta$  9.29, 26.36, 26.52, 28.17, 28.43, 31.99, 32.80, 37.62, 38.77, 46.92, 55.47, 80.11, 109.25, 109.34, 119.18, 119.40, 122.01, 127.91, 128.15, 129.74, 137.09, 142.12, 155.53, 171.49.

**2-(1H-Indol-3-yl)-N-(2-((1R,3R)-2,2,3-trimethylcyclopentyl)ethyl)acetamide (cis-27) and 2-(1H-Indol-3-yl)-N-(2-((1R,3S)-2,2,3-trimethylcyclopentyl)ethyl)acetamide (trans-27)**

Following GP5 Prepared from alkene **25**<sup>23</sup> (126 mg, 0.406 mmol), MeOH (20 mL), Pd-C (29 mg); column chromatography (EtOAc/petroleum ether = 1:2). The product was isolated and characterized as a diastereomer mixture of **cis-27:trans-27** = 86:14. Yield: 83.9 mg (0.268 mmol, 66%) of orange oil. ESI-HRMS Calcd for  $\text{C}_{20}\text{H}_{29}\text{N}_2\text{O}$ :  $m/z$  313.2274 ( $\text{MH}^+$ ). Found:  $m/z$  313.2277 ( $\text{MH}^+$ ). IR  $\nu_{\text{max}}$  3407, 3273, 2949, 2867, 1639, 1526, 1456, 1435, 1365, 1339, 1252, 1227, 1186, 1126, 1099, 1009, 925, 878, 778, 738  $\text{cm}^{-1}$ .  $[\alpha]_{\text{D}}^{25} = +9.78$  ( $c = 1.7$  mg/mL,  $\text{CH}_2\text{Cl}_2$ ).  $^1\text{H}$  NMR (500 MHz,  $\text{CDCl}_3$ ) for **cis-27**:  $\delta$  0.41 (s,

3H), 0.71 (s, 3H), 0.78 (d,  $J = 6.8$  Hz, 3H), 0.99–1.21 (m, 4H), 1.33–1.47 (m, 2H), 1.62–1.68 (m, 2H), 3.08–3.24 (m, 2H), 3.74 (s, 2H), 5.66 (t,  $J = 5.9$  Hz, 1H), 7.13–7.18 (m, 2H), 7.22–7.26 (m, 1H), 7.41 (dt,  $J = 0.9, 8.3$  Hz, 1H), 7.56 (d,  $J = 7.9$  Hz, 1H), 8.45 (s, 1H, NH).  $^1\text{H}$  NMR (500 MHz,  $\text{CDCl}_3$ ) for **trans-27**:  $\delta$  0.76 (d,  $J = 7.2$  Hz, 1H).  $^{13}\text{C}$  NMR (126 MHz,  $\text{CDCl}_3$ ) for **cis-27**:  $\delta$  13.95, 14.45, 25.53, 28.06, 30.24, 30.53, 33.61, 39.20, 42.39, 45.02, 48.37, 109.30, 111.53, 118.93, 120.22, 122.76, 123.88, 127.17, 136.58, 171.45.

**tert-Butyl ((S)-3-(1-Methyl-1H-indol-3-yl)-1-oxo-1-((2,3,3-trimethylcyclopentyl)ethyl)-amino)propan-2-yl carbamate (28)**

Following GP5 Prepared from alkene **23** (55.0 mg, 0.121 mmol), MeOH (20 mL), Pd-C (19.7 mg); column chromatography (EtOAc/petroleum ether = 1:2). The product was isolated and characterized as a diastereomer mixture in a ratio of 89:11. Yield: 38.4 mg (0.0843 mmol, 70%) of yellow oil. ESI-HRMS Calcd for  $\text{C}_{27}\text{H}_{42}\text{N}_3\text{O}_3$ ;  $m/z$  456.3221 ( $\text{MH}^+$ ). Found:  $m/z$  456.3222 ( $\text{MH}^+$ ). IR  $\nu_{\text{max}}$  3429, 3305, 2950, 2868, 2243, 1651, 1523, 1501, 1472, 1365, 1325, 1244, 1166, 1047, 1013, 908, 860, 779, 734  $\text{cm}^{-1}$ .  $[\alpha]_{\text{D}}^{25} = +7.6$  ( $c = 2.4$  mg/mL,  $\text{CH}_2\text{Cl}_2$ ).  $^1\text{H}$  NMR (500 MHz,  $\text{CDCl}_3$ ) for the major diastereomer:  $\delta$  0.41 (s, 3H), 0.75 (s, 3H), 0.80 (d,  $J = 6.9$  Hz, 3H), 0.91–1.05 (m, 2H), 1.06–1.18 (m, 2H), 1.28–1.38 (m, 2H), 1.43 (s, 9H), 1.57–1.89 (m, 2H), 2.96–3.17 (m, 3H), 3.30 (dd,  $J = 5.2, 14.6$  Hz, 1H), 3.74 (s, 3H), 4.39 (s, 1H), 5.19 (s, 1H), 5.61 (s, 1H), 6.92 (s, 1H), 7.10–7.14 (m, 1H), 7.20–7.25 (m, 1H), 7.29 (d,  $J = 8.2$  Hz, 1H), 7.65 (d,  $J = 7.9$  Hz, 1H).  $^{13}\text{C}$  NMR (126 MHz,  $\text{CDCl}_3$ ) for the major diastereomer:  $\delta$  13.94, 14.47, 25.59, 28.03, 28.46, 28.65, 30.26, 30.36, 32.83, 39.18, 42.39, 44.98, 48.39, 55.42, 80.07, 109.36, 119.21, 119.41, 121.99, 127.97, 137.09, 155.57, 171.47 (two signals missing).

**N-(2-((1R,3R)-2,2,3-Trimethylcyclopentyl)ethyl)-4,5,6,7-tetrahydro-1H-indole-2-carboxamide (cis-29)**, **N-(2-((1R,3S)-2,2,3-Trimethylcyclopentyl)ethyl)-4,5,6,7-tetrahydro-1H-indole-2-carboxamide (trans-29)** and **N-(2-((1R,3R)-2,2,3-Trimethylcyclopentyl)ethyl)octahydro-1H-indole-2-carboxamide (cis-30)**, **N-(2-((1R,3S)-2,2,3-Trimethylcyclopentyl)ethyl)octahydro-1H-indole-2-carboxamide (trans-30)**

Following GP5 Prepared from alkene **26**<sup>23</sup> (148 mg, 0.499 mmol), MeOH (20 mL), Pd-C (45 mg); column chromatography (1. EtOAc/petroleum ether = 1:1 for the elution of the **cis-29/trans-29** mixture; 2. EtOAc/MeOH = 1:1 for the elution of the **cis-30/trans-30** mixture).

The mixture **cis-29/trans-29** = 88:12 elutes first from the column. The aniline was isolated and characterized as a mixture of two diastereomers. Yield: 14.8 mg (0.0489 mmol, 10%) of dark orange oil. ESI-HRMS Calcd for  $\text{C}_{19}\text{H}_{31}\text{N}_2\text{O}$ ;  $m/z$  303.2431 ( $\text{MH}^+$ ). Found:  $m/z$  303.2429 ( $\text{MH}^+$ ). IR  $\nu_{\text{max}}$  3231, 2930, 2865, 1614, 1585, 1539, 1465, 1411, 1365, 1322, 1266, 1246, 1148, 1132, 1058, 981, 929,

835, 816, 761, 711  $\text{cm}^{-1}$ .  $[\alpha]_{\text{D}}^{25} = +15.1$  ( $c = 1.1$  mg/mL,  $\text{CH}_2\text{Cl}_2$ ).  $^1\text{H}$  NMR (500 MHz,  $\text{CDCl}_3$ ) for **cis-29**:  $\delta$  0.51 (s, 3H), 0.83 (d,  $J = 6.8$  Hz, 3H), 0.86 (s, 3H), 1.13–1.36 (m, 4H), 1.38–1.55 (m, 2H), 1.63–1.92 (m, 6H), 2.49 (t,  $J = 6.0$  Hz, 2H), 2.60 (t,  $J = 6.1$  Hz, 2H), 3.27–3.48 (m, 2H), 5.72 (s, 1H), 6.26 (d,  $J = 2.4$  Hz, 1H), 9.15 (s, 1H).  $^{13}\text{C}$  NMR (126 MHz,  $\text{CDCl}_3$ ) for **cis-29**:  $\delta$  14.00, 14.56, 22.89, 22.92, 23.19, 23.72, 25.72, 28.33, 30.36, 31.15, 39.06, 42.56, 45.14, 48.67, 107.42, 118.90, 123.97, 131.53, 161.45.

The mixture **cis-30/trans-30** = 90:10 elutes second from the column. The product pyrrolidine was isolated and characterized as a mixture of diastereomers. Yield: 58.0 mg (0.189 mmol, 38%) of dark orange oil. ESI-HRMS Calcd for  $\text{C}_{19}\text{H}_{35}\text{N}_2\text{O}$ ;  $m/z$  307.2744 ( $\text{MH}^+$ ). Found:  $m/z$  307.2751 ( $\text{MH}^+$ ). IR  $\nu_{\text{max}}$  3210, 3064, 2929, 2865, 2675, 1672, 1559, 1449, 1366, 1300, 1270, 1249, 1186, 1136, 1079, 1031, 981, 944, 917, 903, 844, 811, 729  $\text{cm}^{-1}$ .  $[\alpha]_{\text{D}}^{25} = +25.8$  ( $c = 1.9$  mg/mL,  $\text{CH}_2\text{Cl}_2$ ).  $^1\text{H}$  NMR (500 MHz,  $\text{CDCl}_3$ ) for the mixture of diastereomers:  $\delta$  0.51 (s, 3H), 0.83 (d,  $J = 6.8$  Hz, 3H), 0.86 (d,  $J = 2.6$  Hz, 3H), 1.13–1.54 (m, 9H), 1.55–1.94 (m, 8H), 2.27–2.38 (m, 1H), 2.55–2.66 (m, 1H), 3.12–3.25 (m, 1H), 3.27–3.40 (m, 1H), 3.61–3.76 (m, 1H), 4.49 (s, 1H), 8.50 (s, 1H).  $^{13}\text{C}$  NMR (126 MHz,  $\text{CDCl}_3$ ) for the mixture of diastereomers:  $\delta$  13.99, 14.58, 22.00, 22.09, 25.73, 25.76, 26.06, 26.52, 28.09, 28.16, 30.31, 30.37, 30.51, 34.74, 37.79, 37.81, 39.70, 42.51, 42.53, 45.19, 45.22, 48.49, 48.59, 58.68, 58.72, 58.84, 58.86, 170.59.

## 2. 2. Biological Evaluation – Inhibition of Cholinesterases

The inhibitory potencies of the compounds against the ChEs were determined using the method of Ellman following the procedure described previously.<sup>19</sup> Briefly, compound stock solutions in DMSO were incubated with Ellman's reagent and the ChEs (final concentrations: 370  $\mu\text{M}$  Ellman's reagent, 1 nM or 50 pM hBChE or murine (m) AChE, respectively) in 0.1 M phosphate buffer pH 8.0 for 5 min at 20 °C. mAChE was chosen as the surrogate for hAChE as they are structurally highly conserved in the composition of active site amino acid residues.<sup>26</sup> The reactions were started by the addition of the substrate (final concentration, 500  $\mu\text{M}$  butyrylthiocholine iodide or acetylthiocholine iodide for hBChE and mAChE, respectively). The final content of DMSO was always 1%. The increase in absorbance at 412 nm was monitored for 2 min using a 96-well microplate reader (Synergy H4, BioTek Instruments, VT, USA). The initial velocities in the presence ( $v_i$ ) and absence ( $v_o$ ) of the test compounds were calculated. The inhibitory potencies were expressed as the residual activities, according to  $\text{RA} = (v_i - b) / (v_o - b)$ , where  $b$  is the blank value using phosphate buffer without ChEs. For  $\text{IC}_{50}$  determinations, at least seven different concentrations of each compound were used. The  $\text{IC}_{50}$  values were obtained by plotting the residual ChE activities against the applied inhibitor concentrations, with the experimental data fitted

to a four-parameter logistic function (GraphPad Prism 8.0, GraphPad Software, Boston, MA, USA). Tacrine and donepezil were used as positive controls.

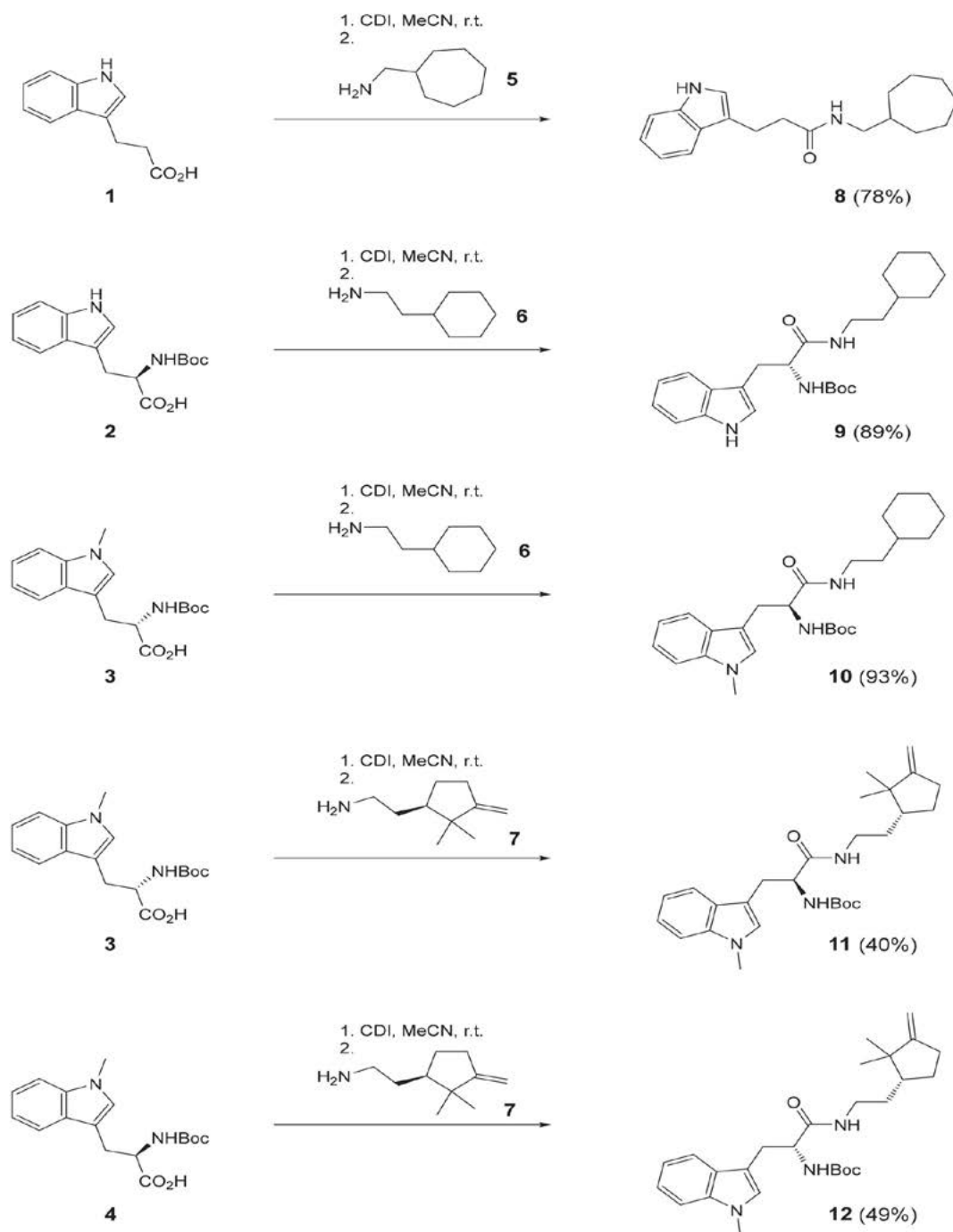
### 3. Results and Discussion

#### 3.1. Synthesis and ChE Inhibitory Activity

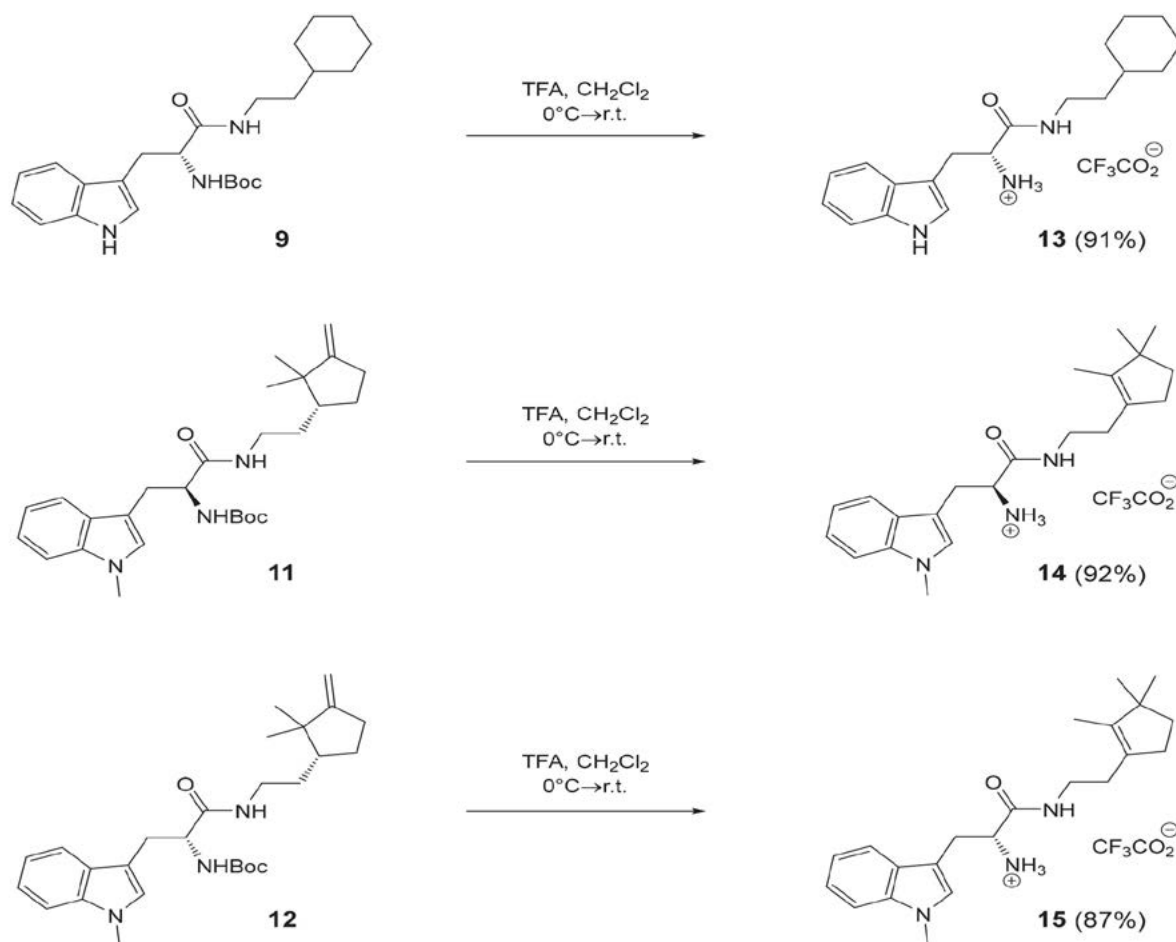
The synthesis of the products is not presented in a linear fashion, as the individual sequences range from one

to four steps. Instead, the synthesis is divided into amidations with 1,1'-carbonyldiimidazole (CDI), *N*-Boc deprotection and isomerization with trifluoroacetic acid (TFA), *N*-Boc protection and acetylation, and catalytic hydrogenation (Schemes 1–4).

3-(1*H*-Indol-3-yl)propanoic acid (**1**) and tryptophan derivatives **2–4** were activated with CDI activating reagent before coupling with cycloalkyl-alkane-amines **5–7**. Amides **8–12** were obtained in 40–93% yields after isolation by column chromatography (Scheme 1).



Scheme 1. Synthesis of amides **8–12**.



Scheme 2. N-Boc deprotection – synthesis of ammonium salts 13–15.

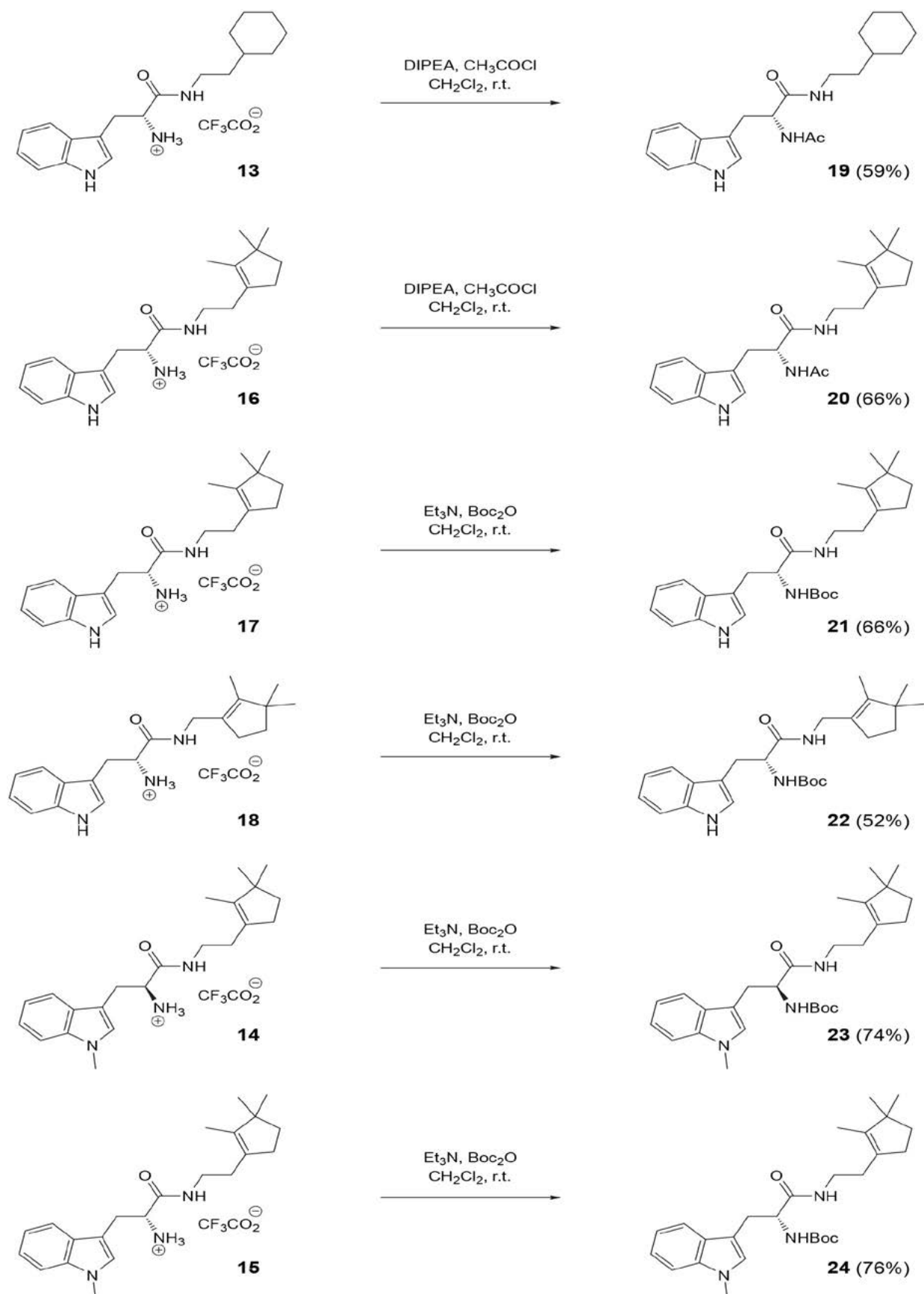
TFA was used for the N-Boc protecting group cleavage of carbamates **9**, **11**, and **12**, and the corresponding trifluoroacetate salts **13–15** were obtained in 87–92% yields (Scheme 2). The Boc protecting group cleavage of carbamates **11** and **12** was accompanied by isomerization of the exocyclic double bond<sup>22</sup> by initial protonation of the double bond, 1,2-methyl shift, followed by deprotonation, giving cyclopentenes **14** and **15**.

Treatment of trifluoroacetate salts **13** and **16** with acetyl chloride in the presence of DIPEA gave acetamides **19** and **20** in 59% and 66% yield, respectively. Similarly, treatment of **14**, **15**, **17**, and **18** with Boc<sub>2</sub>O in the presence of Et<sub>3</sub>N in dichloromethane gave Boc-protected amines **21–24** in 52–76% yield (Scheme 3).

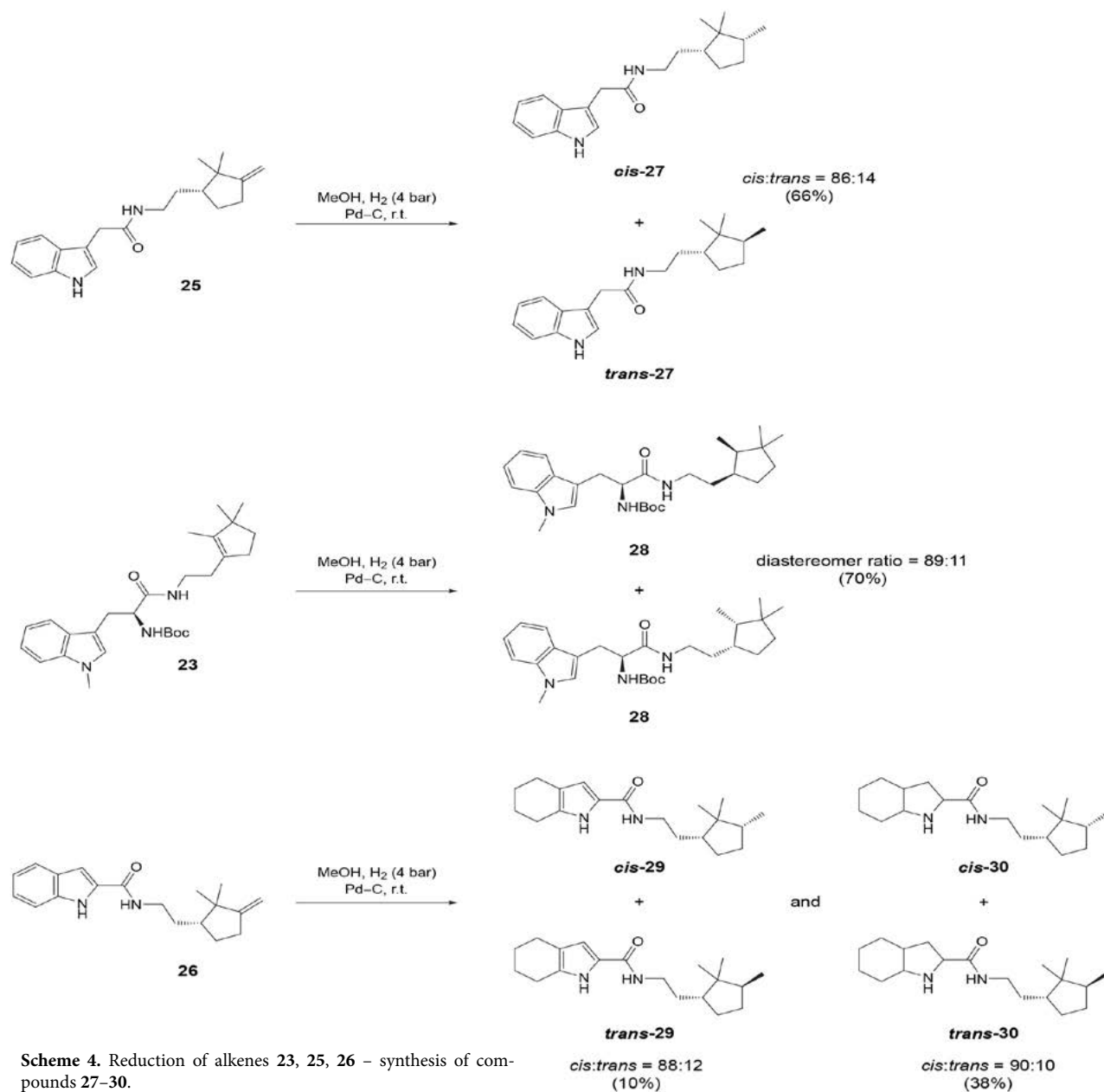
Finally, catalytic hydrogenation of alkene **25** with Pd–C in methanol gave an inseparable mixture of cyclopentanes *cis*-**27** and *trans*-**27** in an 86:14 ratio and 66% yield (Scheme 4). The formation of the major cyclopentane *cis*-**27** was explained by the approach of the reagent from the less hindered side of the exocyclic double bond. Similarly, reduction of the endocyclic alkene **23** afforded an inseparable mixture of two diastereomers of product **28** in the relative ratio 89:11 in 70% yield. The absolute configuration of the newly formed stereocentres could not be determined; a rel-

ative *cis*-configuration on cyclopentane is shown for both isomers. Catalytic hydrogenation of the indole-2-carboxylic acid-derived amide **26** was not chemoselective and afforded a separable mixture of pyrrole derivatives *cis*-**29**/*trans*-**29** and pyrrolidine derivatives *cis*-**30**/*trans*-**30**. The pyrroles *cis*-**29**/*trans*-**29** were isolated in 10% yield as an inseparable mixture of geometric isomers in the ratio 88:12. Similarly, the pyrrolidines *cis*-**30**/*trans*-**30** were isolated in 38% yield as an inseparable mixture of several isomers, with a *cis/trans* cyclopentanes ratio of 90:10 (Scheme 4).

The structures of novel compounds were confirmed by spectroscopic methods (<sup>1</sup>H and <sup>13</sup>C NMR, IR, and high-resolution mass spectrometry) and by elemental analyses for C, H, and N. Figure 2 shows the most typical proton shifts and multiplicities of compounds with substituted cyclopentene or cyclopentane structural motif. The germinal protons of the exocyclic alkene of compound **11** appear at 4.72 and 4.74 ppm as two triplets with a coupling constant of 2.2 and 2.5 Hz. The methyl groups of the cyclopentene moiety appear as singlet at 0.72 and 0.95 ppm. After acid-catalyzed rearrangement of the double bond and methyl group migration, a tetrasubstituted endocyclic bond is formed as shown in compound **20**. The two germinal methyl groups appear as singlet at 0.86 and 0.87 ppm,



**Scheme 3.** N-Boc protection and acetylation – synthesis of compounds 19–24.



**Scheme 4.** Reduction of alkenes **23**, **25**, **26** – synthesis of compounds **27–30**.

while the methyl group on the endocyclic double bond appears as triplet at 1.33 ppm ( $J = 2.1$  Hz). Similar chemical shifts and multiplicities are found for the related compounds **14**, **15**, **21–24**. Finally, catalytic hydrogenation of either the exocyclic or endocyclic double bond leads to substituted cyclopentane, yielding two diastereomers (see Scheme 4). As in compound *cis*-**29** (the major diastereomer), the two germinal methyl groups appear as singlet at 0.51 and 0.86 ppm, while the third methyl group appears as doublet at 0.83 ppm ( $J = 6.8$  Hz). A very similar pattern of methyl groups is also observed for compound *cis*-**27** (Figure 2). The proton spectra of the compounds containing a substituted cyclopentene/cyclopentane structural motif are consistent with the previously reported compounds containing the same structural elements.<sup>22</sup>

All synthesized compounds were tested for inhibitory activity on human (h)BChE and murine (m)AChE (Table 1). Compounds **13**, **20**, **21**, and **24** showed selective submicromolar inhibition of hBChE, with compounds **13** ( $IC_{50} = 617$  nM) and **21** ( $IC_{50} = 501$  nM) being the most potent inhibitors of the series.

## 4. Conclusion

We report on 18 new compounds with indole structural motif that were synthesized and fully characterized. Additionally, inhibitory potencies of the synthesized compounds against hBChE (human butyrylcholinesterase) and mAChE (murine acetylcholinesterase)

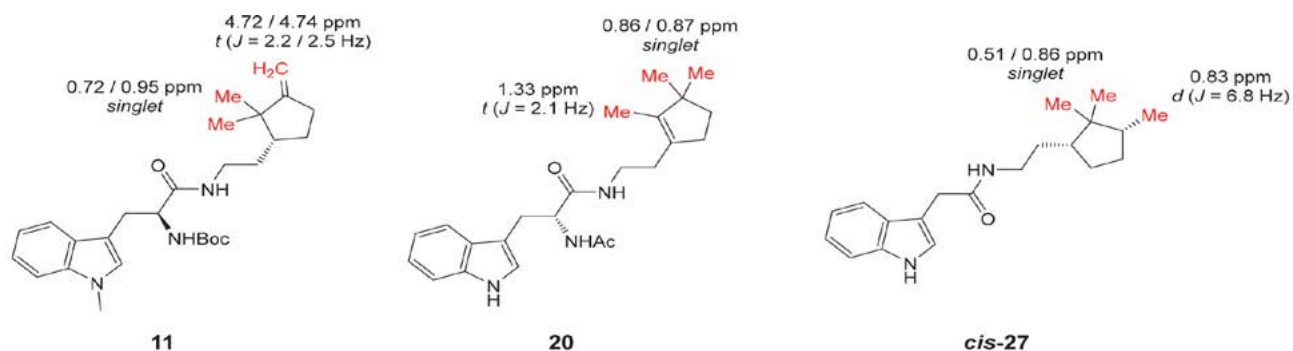
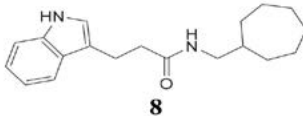
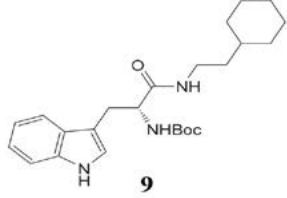
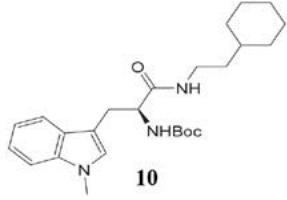
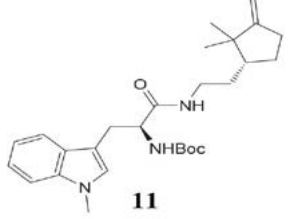
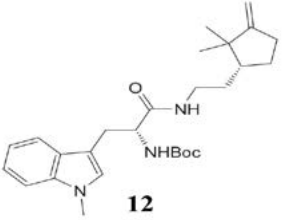


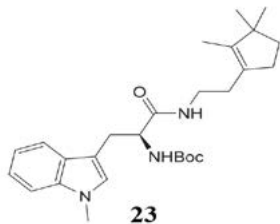
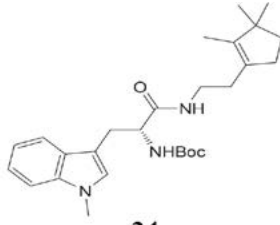
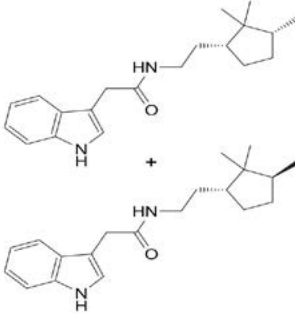
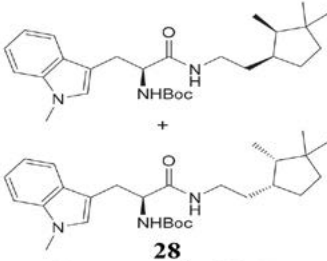
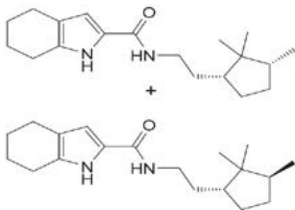
Figure 2. Representative proton shifts and multiplicities of products with substituted cyclopentene and cyclopentane motif.

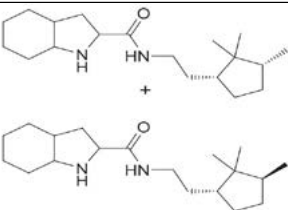
Table 1. *In vitro* ChE inhibition.

Entry	Compound	hBChE RA at 100 $\mu$ M [% $\pm$ SD] or IC <sub>50</sub> [nM] $\pm$ SEM <sup>a</sup>	mAChE RA at 100 $\mu$ M [% $\pm$ SD] or IC <sub>50</sub> [nM] $\pm$ SEM <sup>a</sup>
1	 <b>8</b>	1687.6 $\pm$ 126.7	71.3 $\pm$ 8.7% Not active
2	 <b>9</b>	7653.3 $\pm$ 1141.1	87.4 $\pm$ 18.0% Not active
3	 <b>10</b>	54.8 $\pm$ 8.5% Not active	40981.3 $\pm$ 14812.5
4	 <b>11</b>	50.8 $\pm$ 2.7% Not active	11512.1 $\pm$ 2469.4
5	 <b>12</b>	9733.3 $\pm$ 2037.7	52.9 $\pm$ 8.5% Not active





Entry	Compound	hBChE RA at 100 $\mu$ M [% $\pm$ SD] or IC <sub>50</sub> [nM] $\pm$ SEM <sup>a</sup>	mAChE
13	 <p><b>23</b></p>	42.6 $\pm$ 11.7% Not active	53.5 $\pm$ 0.6% Not active
14	 <p><b>24</b></p>	952.5 $\pm$ 228.5	67.6 $\pm$ 13.7% Not active
15 <sup>b</sup>	 <p><i>cis</i>-27 / <i>trans</i>-27 Isomers ratio: 85:15</p>	1888.7 $\pm$ 123.2	7479.9 $\pm$ 2297.0
16 <sup>b</sup>	 <p><b>28</b> Isomers ratio: 89:11</p>	49.3 $\pm$ 13.5% Not active	12625.0 $\pm$ 3926.5
17 <sup>b</sup>	 <p><i>cis</i>-29 / <i>trans</i>-29 Isomers ratio: 88:12</p>	2948.9 $\pm$ 653.3	21002.0 $\pm$ 4815.0

Entry	Compound	hBChE RA at 100 $\mu\text{M}$ [% $\pm$ SD] or $\text{IC}_{50}$ [nM] $\pm$ SEM <sup>a</sup>	mAChE RA at 100 $\mu\text{M}$ [% $\pm$ SD] or $\text{IC}_{50}$ [nM] $\pm$ SEM <sup>a</sup>
18 <sup>b,c</sup>	 <p><b>cis-30 / trans-30</b> Mixture of stereoisomers</p>	16179.7 $\pm$ 1108.0	84.7 $\pm$ 1.5% Not active

<sup>a</sup> RA – residual activity expressed as percentage  $\pm$  standard deviation (SD) of one independent measurement performed in triplicate, SEM – standard error of the mean,  $\text{IC}_{50}$  values are average of two independent measurements; <sup>b</sup> prepared as an inseparable *cis/trans*-mixture; <sup>c</sup> obtained as a mixture of diastereomers.

was determined by the method of Ellman. The highest selective submicromolar inhibition of hBChE was achieved with compounds **13** ( $\text{IC}_{50}$  = 617 nM) and **21** ( $\text{IC}_{50}$  = 501 nM).

### Supplementary Material

Copies of <sup>1</sup>H and <sup>13</sup>C NMR and MS spectra of the products are presented in the supporting information.

### Acknowledgement

This research was funded by the Slovenian Research and Innovation Agency (ARIS), Research Core Funding No. P1-0179, P1-0208 and L1-8157.

### Conflicts of interest

There are no conflicts to declare.

## 5. References

- G. W. Gribble, *Indole Ring Synthesis: From Natural Products to Drug Discovery*, John Wiley & Sons Ltd., **2016**, Print. ISBN:9780470512180, Online ISBN:9781118695692. DOI:10.1002/9781118695692
- Z. Li, Y. Liang, Y. Zhu, H. Tan, X. Li, W. Wang, Z. Zhang, N. Jiao, *Pyrroles and Their Benzo Derivatives: Reactivity in Comprehensive Heterocyclic Chemistry IV*, Eds.: D. StC Black, J. Cossy, C. V. Stevens, Elsevier, **2022**, 68–155, ISBN 9780128186565. DOI:10.1016/B978-0-12-409547-2.14853-X
- U. Pindur, T. Lemster, *Curr. Med. Chem.* **2001**, *8*, 1681–1698. DOI:10.2174/0929867013371941
- A. Aygun, U. Pindur, *Curr. Med. Chem.* **2003**, *10*, 1113–1127. DOI:10.2174/0929867033457511
- C.-G. Yang, H. Huang, B. Jiang, *Curr. Org. Chem.* **2004**, *8*, 1691–1720. DOI:10.2174/1385272043369656
- W. Gul, M. T. Hamann, *Life Sci.* **2005**, *78*, 442–453. DOI:10.1016/j.lfs.2005.09.007
- D. S. Seigler, *Plant Secondary Metabolism*; Springer: New York, NY, USA, **2001**; p. 628.
- S. M. Umer, M. Solangi, K. M. Khan, R. S. Z. Saleem, *Molecules* **2022**, *27*, 7586. DOI:10.3390/molecules27217586
- V. Sharma, P. Kumar, D. Pathak, *J. Heterocycl. Chem.* **2010**, *47*, 491–502. DOI:10.1002/jhet.349
- S. Kumar, *Future J. Pharm. Sci.* **2020**, *6*, 1–19. DOI:10.1186/s43094-020-00141-y
- A. Dorababu, *RSC Med. Chem.* **2020**, *11*, 1335–1353. DOI:10.1039/D0MD00288G
- Y. Wan, Y. Li, C. Yan, M. Yan, Z. Tang, *Eur. J. Med. Chem.* **2019**, *183*, 111691. DOI:10.1016/j.ejmech.2019.111691
- W. Yin, M. S. Kabir, Z. Wang, S. K. Rallapalli, J. Ma, J. M. Cook, *J. Org. Chem.* **2010**, *75*, 3339–3349. DOI:10.1021/jo100279w
- T. Matsuura, L. E. Overman, D. J. Poon, *J. Am. Chem. Soc.* **1998**, *120*, 6500–6503. DOI:10.1021/ja980788+
- C. Sherer, T. J. Snape, *Eur. J. Med. Chem.* **2015**, *97*, 552–560. DOI:10.1016/j.ejmech.2014.11.007
- https://go.drugbank.com/categories/DBCAT000528.
- Z. Solárová, M. Kello, P. Solár, *Acta Chim. Slov.* **2021**, *68*, 151–158. DOI:10.17344/acsi.2020.6281
- Alzheimer's Disease International, World Alzheimer Report 2019: Attitudes to Dementia, **2019**.
- U. Košak, B. Brus, D. Knez, R. Šink, S. Žakelj, J. Trontelj, A. Pišlar, J. Šlenc, M. Gobec, M. Živin, L. Tratnjek, M. Perše, K. Sašat, A. Podkova, B. Filipek, F. Nachon, X. Brazzolotto, A. Więckowska, B. Malawska, J. Stojan, I. M. Raščan, J. Kos, N. Coquelle, J.-P. Colletier, S. Gobec, *Sci. Rep.* **2016**, *6*, 39495. DOI:10.1038/srep39495
- U. Košak, B. Brus, D. Knez, S. Žakelj, J. Trontelj, A. Pišlar, R. Šink, M. Jukič, M. Živin, A. Podkova, F. Nachon, X. Brazzolotto, J. Stojan, J. Kos, N. Coquelle, K. Sašat, J.-P. Colletier, S. Gobec, *J. Med. Chem.* **2018**, *61*, 119–139. DOI:10.1021/acs.jmedchem.7b01086
- S. Darvesh, *Curr. Alzheimer Res.* **2016**, *13*, 1173–1177.

- DOI:10.2174/1567205013666160404120542
22. U. Grošelj, A. Golobič, D. Knez, M. Hrast, S. Gobec, S. Ričko and J. Svete, *Mol. Divers.* **2016**, *20*, 667–676.  
DOI:10.1007/s11030-016-9668-9
23. A. Meden, D. Knez, M. Jukič, X. Brazzolotto, M. Gršič, A. Pišlar, A. Zahirović, J. Kos, F. Nachon, J. Svete, S. Gobec, U. Grošelj, *Chem. Commun.* **2019**, *55*, 3765–3768.  
DOI:10.1039/C9CC01330J
24. A. Meden, D. Knez, N. Malikowska-Racia, X. Brazzolotto, F. Nachon, J. Svete, K. Sałat, U. Grošelj, S. Gobec, *Eur. J. Med. Chem.* **2020**, *208*, 112766.  
DOI:10.1016/j.ejmech.2020.112766
25. A. Meden, D. Knez, X. Brazzolotto, F. Nachon, J. Dias, J. Svete, J. Stojan, U. Grošelj, S. Gobec, *Eur. J. Med. Chem.* **2022**, *234*, 114248. DOI:10.1016/j.ejmech.2022.114248
26. G. Kryger, M. Harel, K. Giles, L. Toker, B. Velan, A. Lazar, C. Kronman, D. Barak, N. Ariel, A. Shafferman, *Acta Crystallogr. Sect. D* **2000**, *56*, 1385–1394.  
DOI:10.1107/S0907444900010659

## Povzetek

V članku je opisana sinteza in antiholinesterazna aktivnost 18 doslej neobjavljenih spojin, derivatov indola in triptofana. Spojine, ki vsebujejo indolni strukturni fragment, izkazujejo selektivno submikromolarno zaviranje človeške butirilholin esteraze (hBChE). Strukture na novo sintetiziranih spojin so bile potrjene z  $^1\text{H}$  in  $^{13}\text{C}$  NMR, IR spektroskopijo in masno spektrometrijo visoke ločljivosti.



Except when otherwise noted, articles in this journal are published under the terms and conditions of the Creative Commons Attribution 4.0 International License

Scientific paper

# Synthesis and Characterization of Multicolor Luminescent and Thermally Stable Thioureas and Polythioamides

Farah Qureshi\*, Muhammad Yar Khuhawar, Taj Muhammad Jahangir and Abdul Hamid Channar

Institute of Advanced Research Studies in Chemical Sciences, University of Sindh, Jamshoro, Sindh-Pakistan

\* Corresponding author: E-mail: farahqureshi94@yahoo.com

Tel: +92-3313534844

Received: 07-06-2022

## Abstract

Two new polythioamides were prepared through the polycondensation reaction between thiourea monomers and terephthaloyl dichloride, while the thiourea monomers were synthesized by the interaction of aromatic (4,4'-diaminophenylsulfone) or alicyclic (1,2-cyclohexanediamine) diamine with ammonium thiocyanate. The elemental composition of polythioamides was confirmed through CHN microanalysis. The structure and properties of thiourea monomers and polythioamides were determined through proton NMR, UV-Vis, FT-IR spectroscopy, fluorescence, TGA/DTA and SEM. The polythioamides indicated high thermal stabilities which were assessed from their  $T_{\max}$  (temperature indicating highest rate of weight loss) values (670 °C and 346 °C) observed in their DTG graphs. The thioureas and polythioamides were fluorescent and showed multicolor (violet, green, yellow, orange and red) emissions at different excitation wavelengths. All the synthesized compounds were also tested for their antifungal and antibacterial functions and showed antibacterial activity against *Salmonella typhi*, *Bacillus subtilis* and *Staphylococcus aureus*, and antifungal activity against *Candida albicans*.

**Keywords:** polythioamides, thioureas, thermal stability, multicolor fluorescence emissions, antimicrobial functions

## 1. Introduction

In comparison to the wide literature on sulfur containing polymers, the work on the polymers containing thioamide functional group called polythioamides is limited.<sup>1</sup> The polythioamides are analogous to polyamides in which oxygen of the carbonyl group (C=O) is replaced by the sulfur (C=S). The stability of polythioamides is also similar to polyamides, however their melting points and glass transition temperatures are lower as compared to their homologous polyamides.<sup>2–4</sup> The thiocarbonyl group in polythioamides decreases hydrogen bonding which may increase their solubility in common solvents such as chloroform.<sup>5</sup> In recent years, interest in the synthesis of polythioamides has been increasing because of their unique qualities such as high refractive index and luminescence behavior.<sup>6,7</sup> The polythioamides have an ability to selectively adsorb valuable metals such as platinum(IV), gold(III) and palladium(II),<sup>8,9</sup> and toxic metals like mercury(II), lead(II) and chromium(III) from wastewater systems.<sup>10–12</sup> The interest of researchers is increasing to-

wards the preparation and applications of antifungal, antibacterial and antiviral polymeric food packaging after Covid-19 pandemic for reducing the harmful effects of various microorganisms on human health.<sup>13</sup> A number of polythioamide antibiotics have been designed and studied based on Closthioamide (the first polythioamide antibiotic from a strictly anaerobic bacterium *Clostridium cellulolyticum*) architecture.<sup>14–17</sup> Different methods have been adopted for the synthesis of polythioamides, one of them being the condensation reaction between bis(dithioesters) or dithioesters with diamines, but the formation of harmful methanethiol during the synthesis of bis(dithioesters) or dithioesters restricts the employment of this method.<sup>4,18</sup> The conversion of polyamides to polythioamides (thionation reaction) through Lawesson reagent is an alternative technique, however this reaction is usually carried out in toluene at 100 °C and suffers from incomplete conversion and hydrolytic degradation.<sup>1,5</sup> Multi-component polymerization (MCP) is a new and powerful technique for the preparation of functional polymers due to its operational simplicity and high efficiency.<sup>19</sup> The

Willgerodt-Kindler reaction is a useful procedure for the preparation of polythioamides which involves polycondensation of dialdehydes and diamines in attendance of elemental sulfur.<sup>20–22</sup> The corresponding polythioamides were obtained in high yield through polycondensation using isophthalaldehyde and terephthalaldehyde, while polymerization was not achieved with phthalaldehyde due to steric effect. The polycondensation with the use of aliphatic primary diamines and cyclic secondary diamines resulted in good yields of polythioamides, while no polymeric product was obtained with acyclic secondary diamines, whereas aromatic diamines provided insoluble polymers.<sup>21</sup> A catalyst free MCP of aliphatic diamines, aromatic diynes, dicarboxylic acids and elemental sulfur have been reported which resulted in high molecular weight luminescent polythioamides.<sup>7,23</sup> Recently, a series of high refractive index polythioamides were prepared through straight polymerization of primary aliphatic diamines with elemental sulfur at 110 °C without using catalyst, the yield and molecular weight of the resulted polymer was high and they also indicated good thermal stability.<sup>6</sup>

In the present work two (one new) thiourea monomers were synthesized by the interaction of aromatic or aliphatic diamine with ammonium thiocyanate, and two new polythioamides were prepared through polycondensation between thiourea monomers with terephthaloyl dichloride. The monomers and polymers were obtained in good yield (70–92%). The structural design of one of the synthesized polythioamides contains aromatic rings of dapson while other contains aliphatic rings of cyclohexane, the purpose of these structural changes was to study their influence on the properties (solubility, fluorescence, antimicrobial activities and thermal stability) of polythioamides.

## 2. Experimental

### 2.1. Chemicals

4,4'-diaminodiphenyl sulfone (97%, Sigma-Aldrich, USA), ammonium thiocyanate ( $\geq 97.5\%$ , Sigma-Aldrich, USA), 1,2-cyclohexanediamine (99%, Merck, Darmstadt, Germany), chloroform (anhydrous,  $\geq 99\%$ , Merck, Darmstadt, Germany), ethanol (95%, Merck, Darmstadt, Germany), tetrahydrofuran (anhydrous,  $\geq 99\%$ , Merck, Darmstadt, Germany), sodium bicarbonate (ACS reagent,  $\geq 99.7\%$ , Merck, Darmstadt, Germany), activated charcoal (powder extra pure, Merck, Germany), hydrochloric acid (ACS reagent, 37%, Merck, Germany), sodium hydroxide (reagent grade,  $\geq 98\%$ , pellets (anhydrous), Sigma-Aldrich, Seelze), terephthaloyl chloride (99%, Alfa-Aesar, Germany), acetone (ACS reagent,  $\geq 99.5\%$ , Sigma-Aldrich, Germany), N,N-Dimethylformamide ( $\geq 99.8\%$ , AnalaR BDH, England), dimethyl sulfoxide ( $\geq 99.9\%$ , AnalaR BDH, England), and distilled water were used.

### 2.2. Equipment

The melting points of the synthesized thioureas and polythioamides were measured on Gallenkamp Apparatus (U.K.) with build-in thermometer. The solubility of thiourea monomers and polythioamides was tested in different solvents by adding 5 mg of each compound in 2 mL of solvent and mixed well. If precipitates were observed at the bottom of the tube, the contents were heated at 60–70 °C for 5 min. A change in the contents of solid mass in the solvent was noted. The E.I. mass spectra of thiourea monomers were obtained on mass spectrometer JEOL JMS-600H (Japan) at HEJ Research Institute of Chemistry, Karachi University, Sindh, Pakistan. The CHN analysis of the polythioamides was carried out on elemental analyzer EA1110 at Elemental Microanalysis Ltd, Devon, EX20 1UB(UK). The <sup>1</sup>H NMR spectra of thioureas and polythioamides were documented on spectrometer BRUKER AVANCE-NMR 400 MHz. Tetramethylsilane was employed as internal standard and dimethylsulfoxide-*d*<sub>6</sub> (DMSO-*d*<sub>6</sub>) as deuterated solvent. The FT-IR spectroscopy of thioureas and polythioamides was performed on FT-IR spectrometer Thermo Scientific™ Nicolet™ iS10 equipped with ATR (attenuated total reflectance) and Software OMNIC™ within 4000–600 cm<sup>-1</sup>. The UV-Vis spectra of thioureas and polythioamides were performed in solvent DMSO within 190–800 nm, with 1 cm<sup>3</sup> quartz cuvettes on UV-1800 Shimadzu double beam spectrophotometer with software UV Probe. The emission spectra of thioureas and polythioamides were recorded on Shimadzu RF-5301PC Series (Japan) spectrofluorometer, using 1cm quartz cuvette and the solvent was DMSO. The surface morphologies of the thiourea and polythioamides were recorded at Center of Pure and Applied Geology, Sindh University, Jamshoro, Pakistan on Scanning Electron Microscope JEOL JSM-6490 LV or on JEOL JSM-5910 with accelerating voltage 15 kV at Centralized Resource Laboratory (CRL), Peshawar University, Pakistan. The were measured through the SEM images of the synthesized thiourea monomers and polythioamides by using ImageJ software. The TGA (thermogravimetric analysis) and DTA (Differential thermal analysis) graphs of thioureas and polythioamides were recorded in the nitrogen atmosphere with flow rate 20 mL/min on Perkin Elmer Pyris Diamond Series (USA) thermal analyzer particle area, diameter and pore surface area. The sample (3.10–8.26 mg) was placed on ceramic pan and then heated from 40–800 °C with 20 °C/min heating rate and the reference material was alumina. Antibacterial functions of thioureas and polythioamides were examined against various species of bacteria (*Escherichia coli*, *Salmonella typhi*, *Staphylococcus aureus*, *Bacillus subtilis* and *Pseudomonas aeruginosa*) by microplate alamar blue assay through 96 well plate method and using Ofloxacin as standard drug, 2 to 4 mg of compound

(thioureas and polythioamides) was dispersed in DM-SO solvent to make concentration 50 or 200  $\mu\text{g/mL}$ . The Mueller-Hinton Agar (MHA) was utilized as medium for bacterial growth and incubation time was 18 to 20 hrs. The % inhibition by the compound (thioureas and polythioamides) against bacterial strains was estimated from reported procedure and the formula is given as Eq. 1.<sup>24–27</sup>

$$\% \text{ inhibition} = \frac{(\varepsilon_{ox})\lambda_2 A \lambda_1 - (\varepsilon_{ox})\lambda_1 A \lambda_2}{(\varepsilon_{red})\lambda_1 A' \lambda_2 - (\varepsilon_{red})\lambda_2 A' \lambda_1} \times 100 \quad (1)$$

Where  $\varepsilon_{ox}$  is the molar extinction coefficients of dye Alamar blue in its oxidized (blue) form,  $\varepsilon_{red}$  is the molar extinction coefficients of dye Alamar blue in its reduced (pink) form, A is the test well absorbance, A' is negative control well absorbance,  $\lambda_1$  is 570 nm and  $\lambda_2$  is 600 nm. The antifungal functions of thioureas and polythioamides were evaluated by agar tube dilution method against various species of fungi (*Aspergillus niger*, *Candida albicans*, *Fusarium lini*, *Trichophyton rubrum* and *Microsporum canis*), drug Amphotericin B was employed as standard for *Aspergillus niger* and drug Miconazole as standard for other strains. For fungal growth SDA (Sabouraud dextrose agar) medium was utilized, 12 mg of the compound (thioureas and polythioamides) was dispersed in DMSO solvent to make 200  $\mu\text{g/mL}$  concentration. The period of the incubation was seven days at a temperature of 27 °C. The % inhibition by the compounds (thioureas and polythioamides) against fungal strains was calculated through the formula given as Eq. 2.<sup>25–27</sup>

$$\% \text{ Inhibition} = 100 - \frac{\text{linear growth in test (mm)}}{\text{linear growth in control (mm)}} \times 100 \quad (2)$$

### 2. 3. Synthesis of Thiourea Monomers

The monomers 1,2-cyclohexanebis(thiourea) (CBT) and 4,4'-diphenylsulfonebis(thiourea) (SBT) were synthesized by following a literature procedure.<sup>28</sup> The thiourea

monomer CBT is new while thiourea SBT is already reported.<sup>29</sup>

In a typical synthesis, 4,4'-diaminodiphenyl sulfone (dapson) or 1,2-cyclohexanediamine (0.01 mol), 45 ml of deaerated water, pinch of activated charcoal and 10 ml of concentrated. HCl were added to a 250 ml round-bottom flask assembled with magnetic agitator. The mixture was heated at 50 °C under consistent stirring for 20 minutes. Then the contents were filtered and relocated to another 250 ml round-bottom flask assembled with a thermometer, magnetic agitator and condenser, ammonium thiocyanate (0.04 mol) was also added into it. The reaction mixture was refluxed at 90 °C for 48 hours. The resulting granular product was allowed to cool naturally until it reached room temperature, filtered and then washed with hot water. The product was recrystallized with 50 ml of DMSO/water (1:1 by volume) and then dried. In case of thiourea monomer (CBT) derived from 1,2-cyclohexanediamine, the product was not precipitated in the reaction flask, therefore the contents of the flask were transferred in a 250 ml beaker having cold water and permitted for precipitates formation. The resultant compound was filtered and washed with hot water, but it dissolved in the hot water during washing, therefore few drops of 0.1 N sodium hydroxide were added to the product solution in water and as a result precipitates were reappeared. The resulting amount was filtered and then dried. The synthetic reactions for thiourea monomers are given in Figure 1.

#### 2. 3. 1. 4,4'-diphenylsulfonebis(thiourea) (SBT)

Melting point, m.p. mp 80–100 °C, yield = 72%,  $\text{C}_{14}\text{H}_{14}\text{N}_4\text{O}_2\text{S}_3$ , MS  $m/z$  (relative intensity %) 291(12.2), 151(1.0), 75(1.4), 60(1.0). <sup>1</sup>HNMR (400 MHz, DMSO- $d_6$ )  $\delta$  ppm 10.39 (t,  $J$  22.4 Hz, 2H, NH), 7.86 (qu,  $J$  8.8 Hz, 2H, Ph), 7.74 (qu,  $J$  8.8 Hz, 1H, Ph), 7.66 (d,  $J$  8.4 Hz, 1H, Ph), 7.59 (d,  $J$  8.4 Hz, 1H, Ph), 7.50 (t,  $J$  8.8 Hz, 1H, Ph), 7.42 (d,  $J$  8.4 Hz, 1H, Ph), 6.58 (m,  $J$  8.8 Hz, 1H, Ph), 6.10 (d,  $J$  15.6 Hz, 2H, NH<sub>2</sub>), 5.94 (s, 2H, NH<sub>2</sub>). <sup>1</sup>HNMR of this compound is also reported in literature.<sup>28,29</sup> FT-IR,  $\text{cm}^{-1}$  (rela-

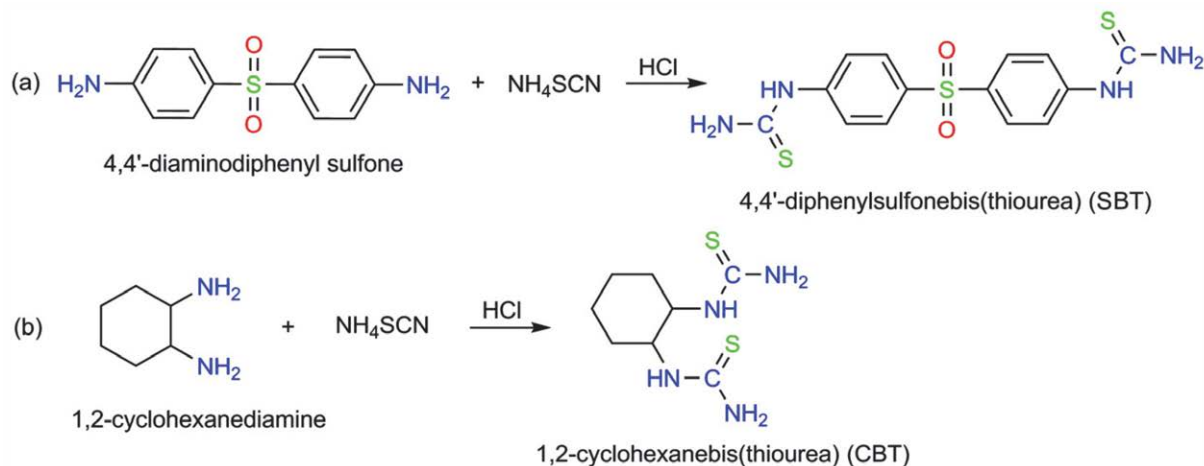


Figure 1. Reactions for the preparation of thiourea monomers: a SBT and b CBT.

tive magnitude) 3333(w), 2050(w), 1624(w), 1588(s), 1526(m), 1493(m), 1402(w), 1289(m), 1249(m), 1182(w), 1142(s), 1102(s), 1071(w), 1011(m), 949(w), 829(m), 716(m), 679(m). UV (DMSO),  $\lambda_{\max}$  ( $\epsilon$ , L mole<sup>-1</sup> cm<sup>-1</sup>) 258 (185767), 294 (148613), 311 nm (191695).

### 2.3.2. 1,2-cyclohexanebis(thiourea) (CBT)

Melting point mp 110 °C, yield = 70%, C<sub>8</sub>H<sub>16</sub>N<sub>4</sub>S<sub>2</sub>, <sup>1</sup>HNMR (400 MHz, DMSO-*d*<sub>6</sub>),  $\delta$  ppm 8.53 (s, 2H, NH), 6.09 (s, 2H, NH<sub>2</sub>), 5.38 (s, 2H, NH<sub>2</sub>), 1.98 (t, *J* 6 Hz, 2H, CH), 1.74 (t, *J* 12 Hz, 4H, CH<sub>2</sub>), 1.59 (d, *J* 6.4 Hz, 2H, CH<sub>2</sub>), 1.37-1.05 (m, 2H, CH<sub>2</sub>). FT-IR, cm<sup>-1</sup> (relative magnitude) 3315(w), 2930(m), 2857(w), 2058(m), 1568(s), 1470(m), 1380(m), 1338(m), 1311(w), 1288(w), 1261(w), 1154(w), 1076(w), 1039(w), 1007(w), 934(w), 820(w), 707(w). UV (DMSO),  $\lambda_{\max}$  ( $\epsilon$ , L mole<sup>-1</sup> cm<sup>-1</sup>) 283 (178.8), 307 nm (145.4).

## 2.4. Synthesis of Polythioamides

Two novel polythioamides poly-4,4'-diphenylsulfonebis(carbamothioyl)benzamide (PSB) and poly-1,2-cy-

clohexanebis(carbamothioyl)benzamide (PCB) were prepared by following a slightly modified literature procedure.<sup>30</sup>

Thiourea monomer (SBT or CBT) (0.01 mol) was dissolved to make concentrated solution in DMF, and 1 M aqueous sodium hydroxide solution (approx. 5–10 ml) was combined slowly until the solution remained clear, then the solution was transferred to 250 ml round-bottom flask assembled with magnetic agitator and ice bath. Terephthaloyl dichloride (0.01 mol) was dispersed alone in DMF and then combined with the help of dropping funnel to the flask containing thiourea solution with constant stirring. The constituents of the flask were stirred continuously for 2 h in ice bath. The mixture was then poured to a 500 ml beaker having cold distilled water for the production of precipitates. The resulting compound was filtered and then dried at room temperature. In case of polythioamide (PCB) derived from thiourea CBT, the product was not precipitated in water, therefore few drops of 0.1 N sodium bicarbonate solution was added into it, but precipitates were not formed, then polymer-water solution was concentrated up to half of its original volume, which resulted to precipitates formation. The product was gathered

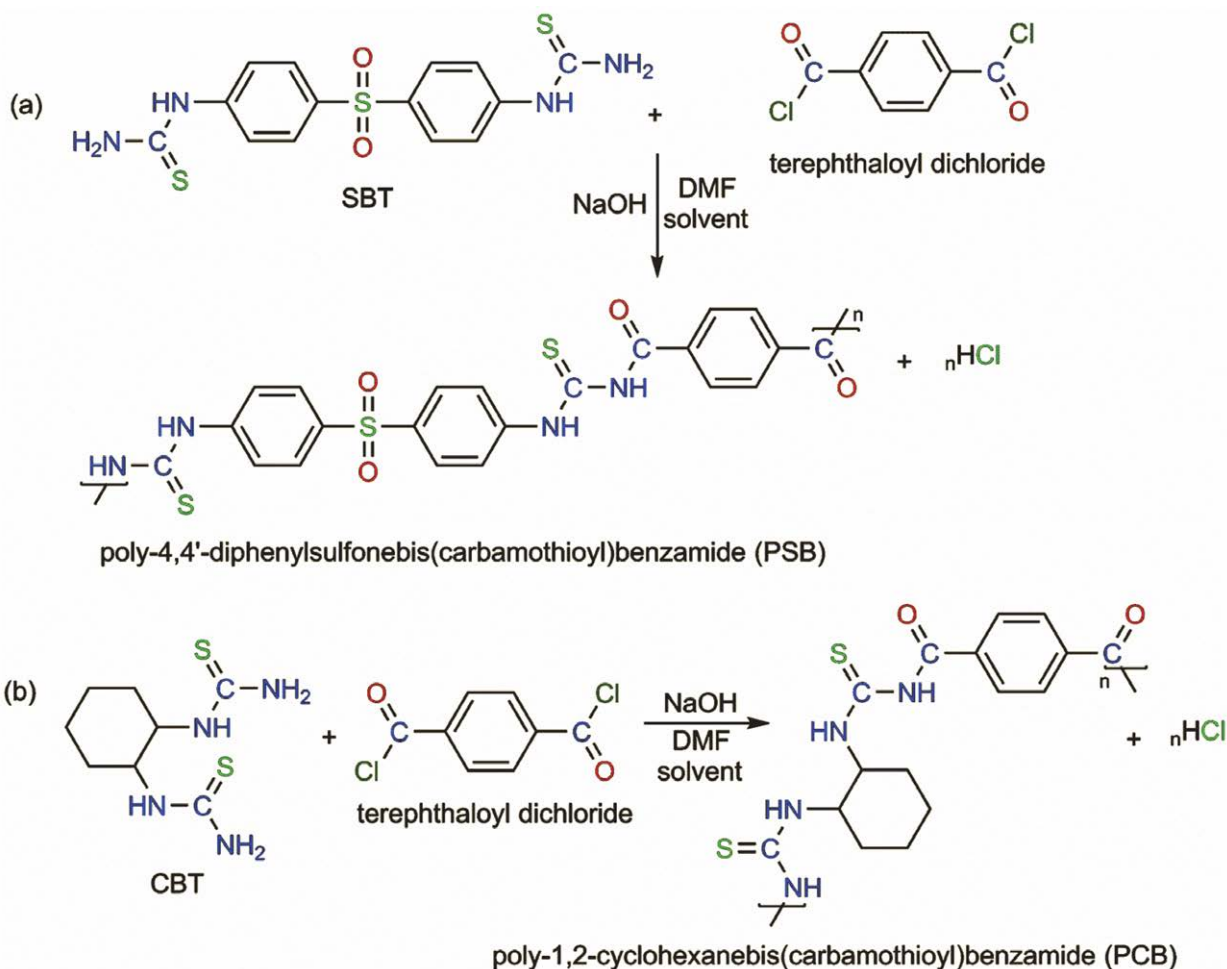


Figure 2. Reactions for the preparation of polythioamides: a PSB and b PCB.

through filtration and dried up at room temperature. The reactions for the preparation of polythioamides are given in Figure 2.

#### 2. 4. 1. poly-4,4'-diphenylsulfonebis(carbamothioyl)benzamide (PSB)

Melting point. mp 275–300 °C, yield 92%, Anal. Calcd for  $(C_{22}H_{16}N_4O_4S_3)_n$ : % C 53.22, H 3.22, N 11.29. Found: % C 52.87, H 3.56, N 11.06.  $^1\text{H NMR}$  (400 MHz, DMSO- $d_6$ ),  $\delta$  ppm 13.18 (t,  $J$  6.2 Hz, 1H, NH), 10.66 (t,  $J$  36 Hz, 1H, NH), 8.03 (s, 8H, Ph), 7.94 (s, 2H, Ph), 7.85 (q,  $J$  8.8 Hz, 2H, Ph), 7.76 (d,  $J$  8.4 Hz, 2H, Ph), 7.71 (t,  $J$  4.0 Hz, 2H, Ph), 7.51 (t,  $J$  8.8 Hz, 2H, Ph), 7.43 (d,  $J$  8.4 Hz, 1H, Ph), 7.33 (d,  $J$  8.0 Hz, 1H, Ph), 6.59 (sext,  $J$  4.4 Hz, 2H, Ph), 6.11 (s, 2H, Ph), 2.88 (s, 1H, CHO end on), 2.70 (s, 1H, CHO end on). FT-IR,  $\text{cm}^{-1}$  (relative magnitude) 3344(w), 2819(w), 2544(w), 1660(s), 1590(m), 1529(w), 1509(w), 1494(w), 1423(w), 1387(w), 1282(s), 1252(m), 1182(w), 1142(s), 1102(s), 1071(w), 1019(w), 934(w), 880(w), 831(w), 782(w), 729(m), 681(w). UV (DMSO),  $\lambda_{\text{max}}$  (1% absorptivity) 294 (3120), 309 nm (3455).

#### 2. 4. 2. poly-1,2-cyclohexanebis(carbamothioyl)benzamide (PCB)

mp > 360 °C, yield 74%, Anal. Calcd for  $(C_{16}H_{18}N_4O_2S_2)_n$ : % C 53.03, H 4.97, N 15.46. Found: % C 52.43, H 4.62, N 14.87.  $^1\text{H NMR}$  (400 MHz, DMSO- $d_6$ )  $\delta$  ppm 13.26 (s, 2H, NH), 8.03 (s, 4H, Ph), 2.89 (s, 1H, CH), 2.72 (s, 1H, CH). FT-IR,  $\text{cm}^{-1}$  (relative magnitude) 3100(w), 3060(w), 2812(w), 2536(w), 1673(s), 1574(m), 1509(m), 1422(m), 1279(s), 1136(w), 1112(m), 1019(w), 930(m), 879(m), 780(m), 727(s) 672(w). UV (DMSO),  $\lambda_{\text{max}}$  (1% absorptivity) 285 nm (92.8).

## 3. Results and Discussion

### 3. 1. Melting Point

The melting points of polythioamides PSB (275–300 °C) and PCB (above 360 °C) were higher than their corresponding thiourea monomers SBT (80–100 °C) and CBT (110 °C) respectively, which indicates their formation, because melting points of the polymers are generally higher than their corresponding monomers due to their high molecular weights.

### 3. 2. Synthesis

The synthetic reactions for the synthesis of thiourea monomers (SBT and CBT) and polythioamides (PSB and PCB) with their structures are given in Figure 1 and Figure 2 respectively. Two (one new) thiourea monomers SBT and CBT were synthesized by the reaction of ammonium thiocyanate with 4,4'-diaminodiphenyl sulfone (also called

dapsone) or 1,2-diaminocyclohexane respectively. The yield of thiourea monomers was SBT = 72% and CBT = 70%. Two new polythioamides PSB and PCB were prepared through polycondensation reaction of thiourea monomers SBT or CBT with terephthaloyl dichloride respectively. The resulting polythioamides were acquired in high yield (PSB = 92% and PCB = 74%). The structures of thioureas (SBT and CBT) and polythioamides (PSB and PCB) were confirmed through different characterization methods, and all the results supported the formation of these compounds.

### 3. 3. E.I Mass Spectrum

The E.I mass spectrum of thiourea monomer SBT recorded fragment ion peak at  $m/z$  291 for  $[\text{NH}_2\cdot\text{CS}\cdot\text{NH}\cdot\text{C}_6\text{H}_4\cdot\text{SO}_2\cdot\text{C}_6\text{H}_4]^+$  with a loss of fragment corresponding to  $[\text{NH}_2\cdot\text{CS}\cdot\text{NH}]^+$  from molecular ion peak ( $M^+$ ) and also indicated fragment ion peaks at  $m/z$  151, 75 and 60 for  $[\text{NH}_2\cdot\text{CS}\cdot\text{NH}\cdot\text{C}_6\text{H}_4]^+$ ,  $[\text{NH}_2\cdot\text{CS}\cdot\text{NH}]^+$  and  $[\text{NH}_2\cdot\text{CS}]^+$  respectively (supplementary Figs. S1a, b).

### 3. 4. Solubility

The solubility of thioureas (SBT and CBT) and polythioamides (PSB and PCB) was tested in DMSO, DMF, THF, chloroform, acetone, ethanol and water. All the compounds were not soluble in water. The thiourea monomer SBT was soluble in all the organic solvents except ethanol while thiourea CBT was fully soluble in DMSO and DMF at room temperature, soluble on heating in ethanol and partially soluble in acetone, chloroform and THF. The polythioamides PSB and PCB were fully soluble in DMSO and DMF without heating, while insoluble in other solvents.

### 3. 5. $^1\text{H NMR}$ Spectroscopy

The  $^1\text{H NMR}$  spectra of thiourea monomers (SBT and CBT) and polythioamides (PSB and PCB) were recorded in DMSO- $d_6$  solvent and all the compounds showed two strong residual protons signals at  $\delta$  ppm 3.3 and 2.49 due to solvent impurities. The thiourea monomer SBT showed triplet at  $\delta$  ppm 10.39 for  $-\text{NH}$ , doublets and multiplets within  $\delta$  ppm 7.86–6.58 for C–H aromatic protons, while doublet and singlet at  $\delta$  ppm 6.10 and 5.94 respectively were for  $\text{NH}_2$  protons (supplementary Fig. S2). The thiourea monomer CBT indicated proton signal at  $\delta$  ppm 8.53 for  $-\text{NH}$ , proton signals at  $\delta$  ppm 6.09 and 5.38 for  $-\text{NH}_2$ , and range of signals within  $\delta$  ppm 1.05–1.98 for aliphatic  $-\text{CH}_2$  protons due to cyclohexane. The polythioamide PSB indicated  $-\text{NH}$  proton signals at  $\delta$  ppm 13.18 and 10.66, range of proton signals within  $\delta$  ppm 8.03–6.11 for C–H aromatic protons and signals at  $\delta$  ppm 2.88 and 2.70 for  $-\text{CHO}$  end on groups. (Figure 3). The polythioamide PCB showed  $-\text{NH}$  proton signal at  $\delta$  ppm 13.26, and



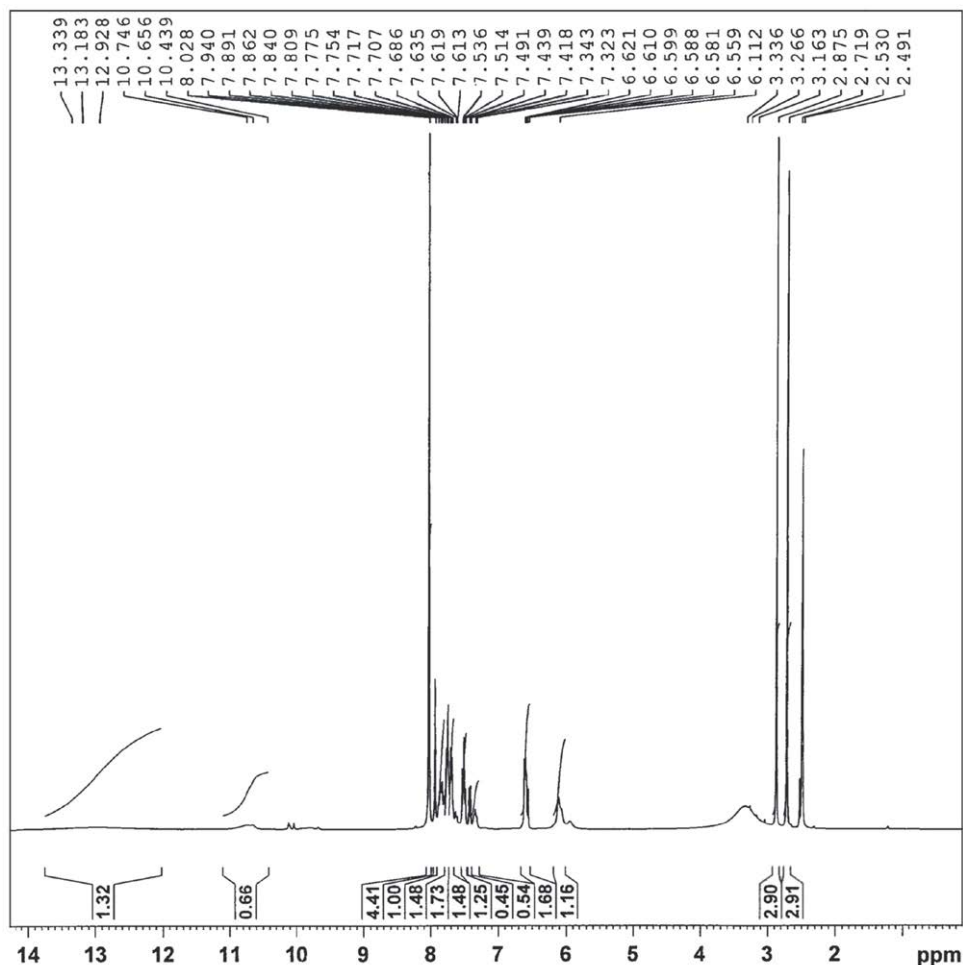


Figure 3.  $^1\text{H}$ NMR spectrum of polythioamide PSB.

$-\text{CH}_2$  aliphatic proton signals at  $\delta$  ppm 2.89 and 2.72 due to cyclohexane. These results supported the formation of thioureas and polythioamides. Similar  $^1\text{H}$ NMR assignments are reported for related thioureas and polythioamides.<sup>12,28,29</sup>

### 3. 6. FTIR Spectroscopy

The FTIR spectra of thiourea monomers SBT and CBT indicated bands of medium intensity at 3333 and 3311  $\text{cm}^{-1}$  respectively for  $\nu$  N-H, thiourea CBT indicated two peaks at 2930  $\text{cm}^{-1}$  and 2858  $\text{cm}^{-1}$  for aliphatic  $\nu$   $\text{CH}_2$  due to cyclohexane, thiourea SBT indicated bands at 1624, 1588 and 1526  $\text{cm}^{-1}$  due to  $\nu$  C=C of aromatic rings and bending vibration of N-H while CBT showed band at 1568  $\text{cm}^{-1}$  due to bending vibration of N-H, both SBT and CBT indicated one weak band at 1071 and 1076  $\text{cm}^{-1}$  for  $\nu$  C=S respectively (Figure 4a and supplementary Fig. S3a). The FT-IR spectra of polythioamide PSB indicated one feeble band at 3344  $\text{cm}^{-1}$  while polythioamide PCB indicated two feeble bands at 3100 and 3060  $\text{cm}^{-1}$  for  $\nu$  N-H, polythioamide PCB indicated band at 2812 for  $\nu$   $\text{CH}_2$  aliphatic owing to cyclohexane, both PSB and PCB indicated

one strong band at 1660 and 1673  $\text{cm}^{-1}$  for  $\nu$  C=O respectively, PSB indicated four bands within 1590–1494  $\text{cm}^{-1}$  while PCB displayed two bands at 1574 and 1509  $\text{cm}^{-1}$  due to  $\nu$  C=C in aromatic rings (Figure 4b and supplementary Fig. S3b). Similar FT-IR assignments are described for related thioureas and polythioamides.<sup>12,28</sup>

### 3. 7. UV-Vis Spectroscopy

The UV-Visible spectra of thiourea monomers and polythioamides were recorded in DMSO solvent. Molar absorptivity ( $\epsilon$ ) ( $\text{L mole}^{-1} \text{cm}^{-1}$ ) was calculated for thiourea monomers, while 1% absorptivity was calculated for polythioamides because molecular weights of polythioamides were unknown. The UV-Vis spectra of thiourea SBT indicated three absorption bands, the first two bands at 258 and 294 nm with molar absorptivity 185767 and 148613  $\text{L mole}^{-1} \text{cm}^{-1}$  respectively were for  $\pi - \pi^*$  transitions within aromatic rings of dapsone while the third band at 311 nm with molar absorptivity 191695  $\text{L mole}^{-1} \text{cm}^{-1}$  was for  $\pi - \pi^*$  transition involving C=S pi-bond and lone pair of nitrogen (Figure 5a). The thiourea CBT indicated two bands, the first at 283 nm with molar absorptivity 178.8  $\text{L mole}^{-1}$

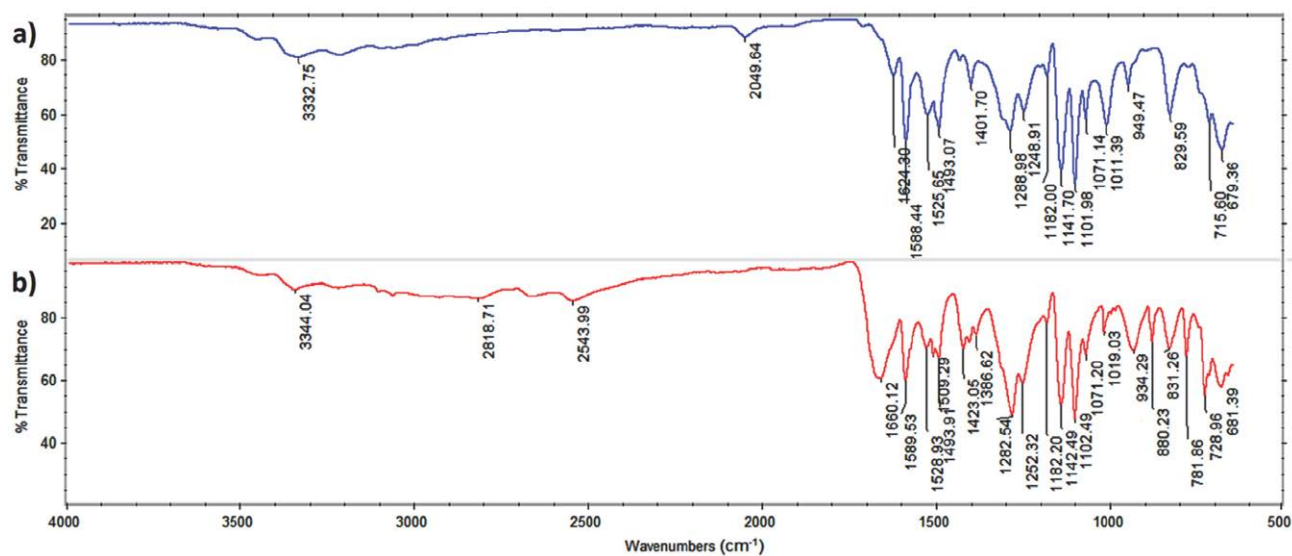


Figure 4. FT-IR spectra of **a** thiourea monomer SBT and **b** its corresponding polythioamide PSB.

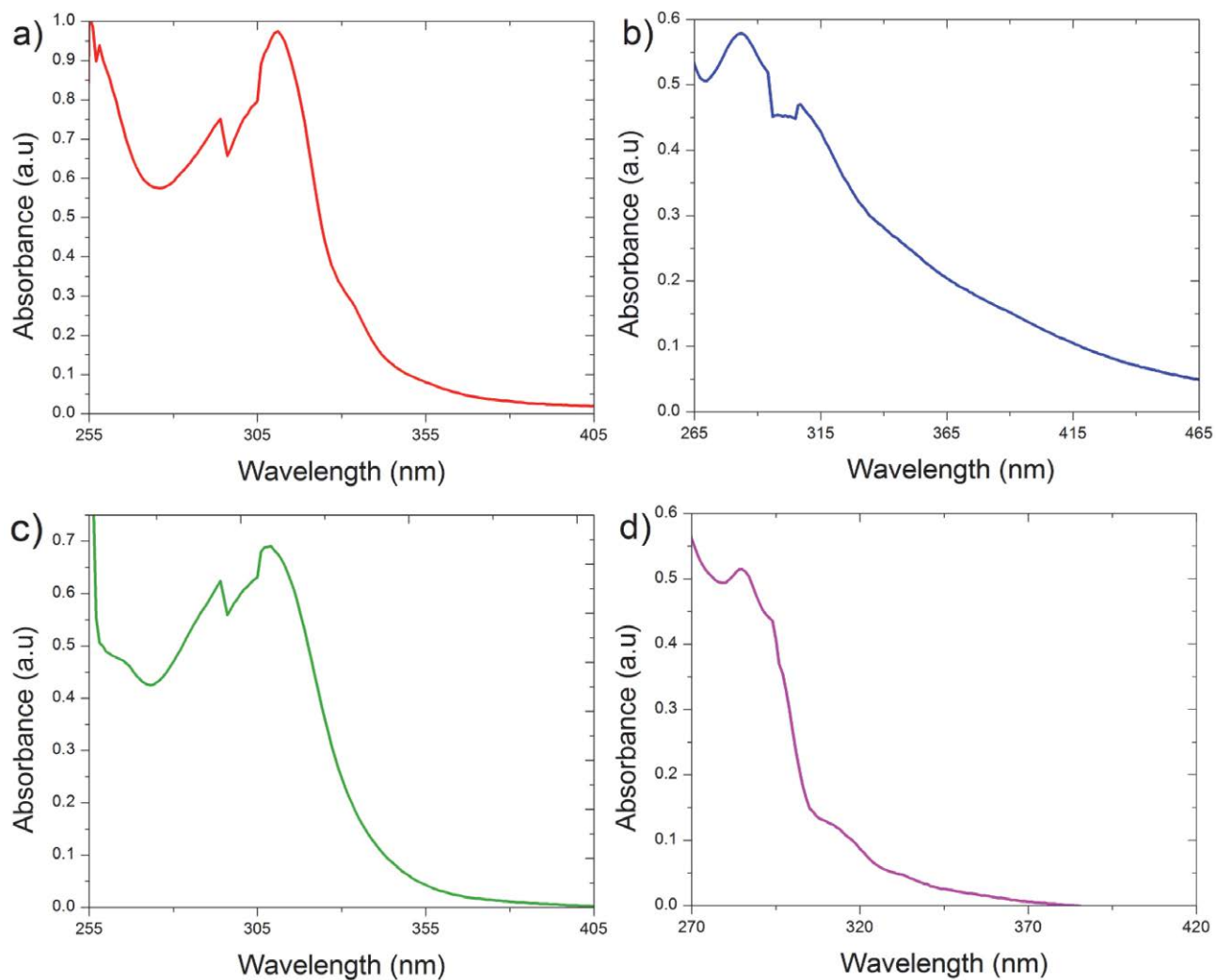


Figure 5. UV-Vis spectra of **a** thiourea SBT, **b** thiourea CBT, **c** polythioamide PSB and **d** polythioamide PCB.

$\text{cm}^{-1}$  was for  $\pi - \pi^*$  transitions within nitrogen lone pair and C=S pi-bond, while second band at 307 nm with molar absorptivity  $145.4 \text{ L mole}^{-1} \text{ cm}^{-1}$  was for  $n - \pi^*$  transition within non-conjugated C=S group and lone pair of sulfur (Figure 5b). The polythioamide PSB indicated two bands, the first band at 294 nm with 1% absorptivity 3120 was for  $\pi - \pi^*$  transitions within aromatic rings of dapsone and the next band at 309 nm with 1% absorptivity 3455 was for  $\pi - \pi^*$  transition engaged in aromatic ring and amide group (Figure 5c). The polythioamide PCB indicated only single band at 285 nm with 1% absorptivity 92.8 for  $\pi - \pi^*$  transition within aromatic ring and amide group (Figure 5d). Similar UV-Vis specifications are described for related compounds.<sup>5,29</sup>

### 3. 8. Fluorescence Spectroscopy

The emission spectra of thiourea monomers (SBT and CBT) and polythioamides (PSB and PCB) were recorded in DMSO solvent and all the compounds showed fluorescence color emissions. The Stokes shifts ( $\lambda_{\text{em}} - \lambda_{\text{ex}}$ ) were also estimated for their emission in visible region, which is the wavelength difference between positions of  $\lambda_{\text{max}}$  (band maxima) in emission and  $\lambda_{\text{max}}$  in absorption spectra. The results of spectrofluorometric measurements are provided in Table 1. The thiourea monomer SBT indicated violet (408 nm) and red (686 nm) light emissions at

excitation 258 nm, violet light (411 nm) emission at excitation 294 nm, and violet (414 nm) and green (532 nm) light emissions at excitation 311 nm (Figure 6a-c). The thiourea CBT indicated violet (417 nm), yellow (565 nm) and red (659 nm and 677 nm) light emissions at excitation 283 nm, and violet (417 nm), orange (616 nm) and red (683 nm) light emission at excitation 307 nm (Figure 6d, e). The polythioamide PSB indicated violet light (416 nm) emissions at excitations 309 and 294 nm (Figure 7a, b), while polythioamide PCB indicated yellow (571 nm) and red light (660 nm) emissions at excitation 285 nm (Figure 7c). The thiourea monomer SBT, polythioamide PSB and polythioamide PCB indicated fluorescence emissions due to the presence of aromatic rings in conjugation with the hetero atoms (nitrogen, oxygen and sulfur) in their structures.<sup>25,26,31–33</sup> However, thiourea monomer CBT indicated multi-color fluorescence emissions, despite the absence of aromatic rings in its structure, these unexpected fluorescence emissions were observed due to the presence of closely assembled hetero atoms (nitrogen and sulfur) containing lone pair of electrons. The emission maxima of the compounds depends upon the formation of molecular aggregates through hydrogen bonding and  $n \rightarrow \pi^*$  interaction between thioamide groups.<sup>1,7,33</sup> The polythioamide PSB showed smaller Stokes shifts (107 and 122 nm) as compared to polythioamide PCB (286 and 375 nm), which indicates its lower vibrational relaxations and strong inter-

**Table 1.** Spectrofluorometric studies of thiourea monomers (SBT and CBT) and polythioamides (PSB and PCB) in DMSO solvent.

S. No	Compound	Concentration ( $\mu\text{g/ml}$ )	$\lambda_{\text{ex}}$ (nm)	$\lambda_{\text{em}}$ (nm)	Relative emission intensity	Color of emission	Stokes shift (nm) ( $\lambda_{\text{em}} - \lambda_{\text{ex}}$ ) of visible region	
1	SBT	166.6	258	408	24	violet	150	
				686	0.9	red	428	
				294	23.12	violet	117	
				311	20	violet	103	
				532	2.22	green	221	
2	PSB	166.6	294	416	15.3	violet	107	
				309	16	violet	122	
3	CBT	416.6	283	350	1016	–	–	
				417	167	violet	134	
				565	66	yellow	282	
				659	118	red	376	
				677	119	red	394	
				307	344	463	–	–
					417	211	violet	110
					616	39	orange	309
					683	41.5	red	376
4	PCB	166.6	285	340	642	–	–	
				571	6.9	yellow	286	
				660	57.5	red	375	

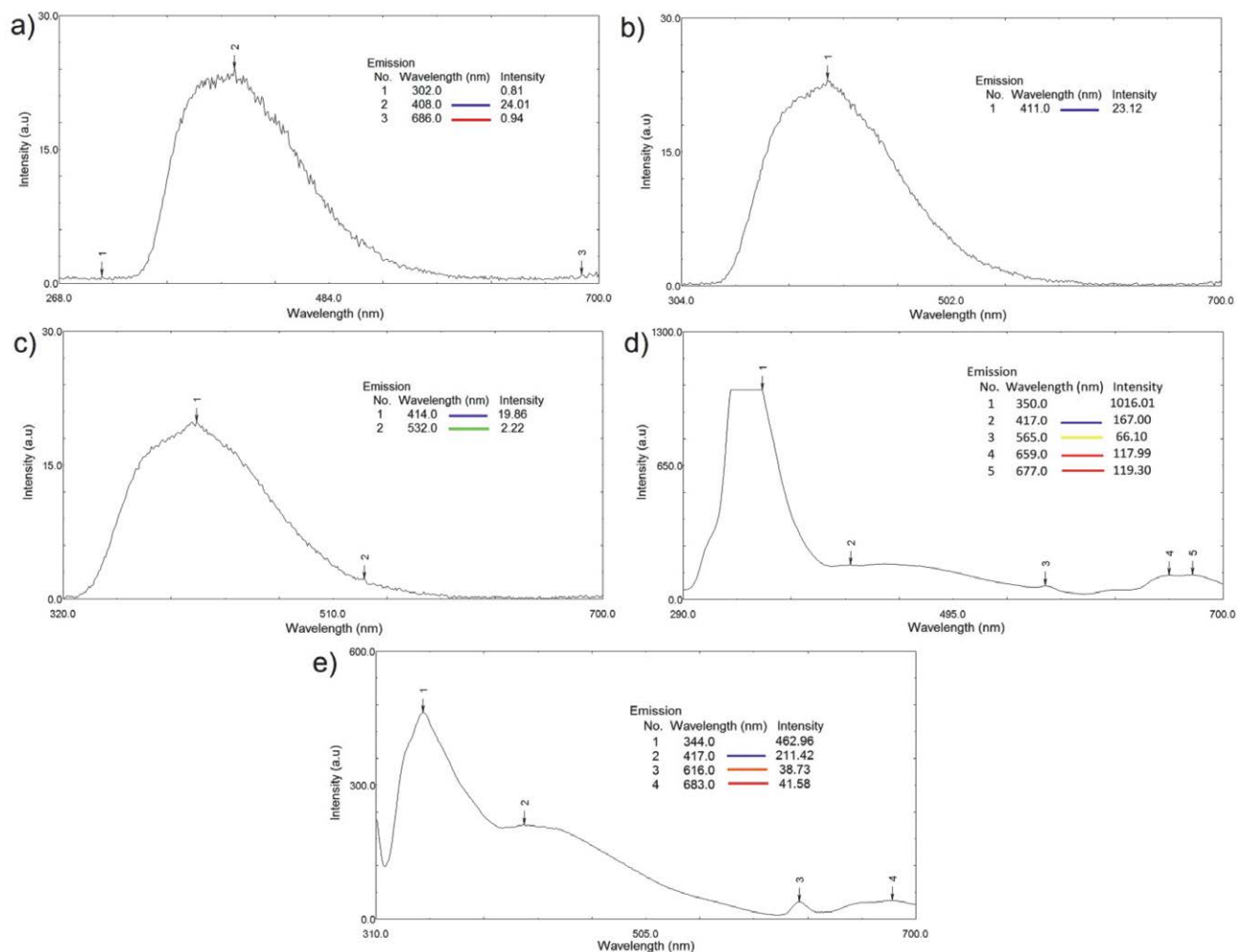


**Figure 6.** Emission spectra of thiourea monomers SBT and CBT: **a** SBT at excitation 258 nm **b** SBT at excitation 294 nm **c** SBT at excitation 311 nm **d** CBT at excitation 283 nm and **e** CBT at excitation 307 nm.

molecular packing due to the existence of large number of rigid aromatic rings in PSB structure,<sup>34,35</sup> while polythioamide PCB contains flexible rings of cyclohexane in addition to aromatic rings, the presence of cyclohexane rings makes its structure less rigid.

### 3. 9. Scanning Electron Microscopy

The SEM image of thiourea monomer SBT noted at 500  $\mu\text{m}$  indicated rugged surface morphology (Figure 8a) and the SEM image of its corresponding polythioamide PSB recorded at 20  $\mu\text{m}$  also revealed rugged surface with intermittent gaps. The average area covered by these gaps was 19.8  $\mu\text{m}^2$  (Figure 8b). Polythioamide PSB can be employed as an adsorbent material because of the presence of these gaps. The SEM images of thiourea CBT recorded from 10  $\mu\text{m}$  to 1  $\mu\text{m}$  showed clusters of needle shaped crystalline particles of different lengths. The average length of these particles was 3.12  $\mu\text{m}$ , the mean diameter of these particles was 0.21  $\mu\text{m}$  and the average area of the interparticle voids

(empty spaces between particles) was 1.15  $\mu\text{m}^2$  (Figure 9a, b). The SEM images of its resulting polythioamide PCB recorded from 10  $\mu\text{m}$  to 1  $\mu\text{m}$  displayed irregular shaped non-porous particles. The average length of these particles was 23.16  $\mu\text{m}$ , the average area of these particles was 314  $\mu\text{m}^2$  and the average area of the interparticle voids was 31  $\mu\text{m}^2$  (Figure 9c, d). The existence of interparticle voids in thiourea CBT and polythioamide PCB makes them potentially effective adsorbent materials by providing greater surface area for adsorption and by facilitating the accessibility of adsorbates to the active sites within the material. The surface morphology of the polythioamide PSB showed larger interparticle voids as compared to its corresponding monomer CBT. The variations between the surface morphology of thiourea monomers (SBT and CBT) and their derived polythioamides (PSB and PCB) were due to the inclusion of  $-\text{COC}_6\text{H}_5\text{CO}-$  moiety in the structures of polythioamides. The synthesized polythioamides can be applied as adsorbents due to the presence of interparticle voids.

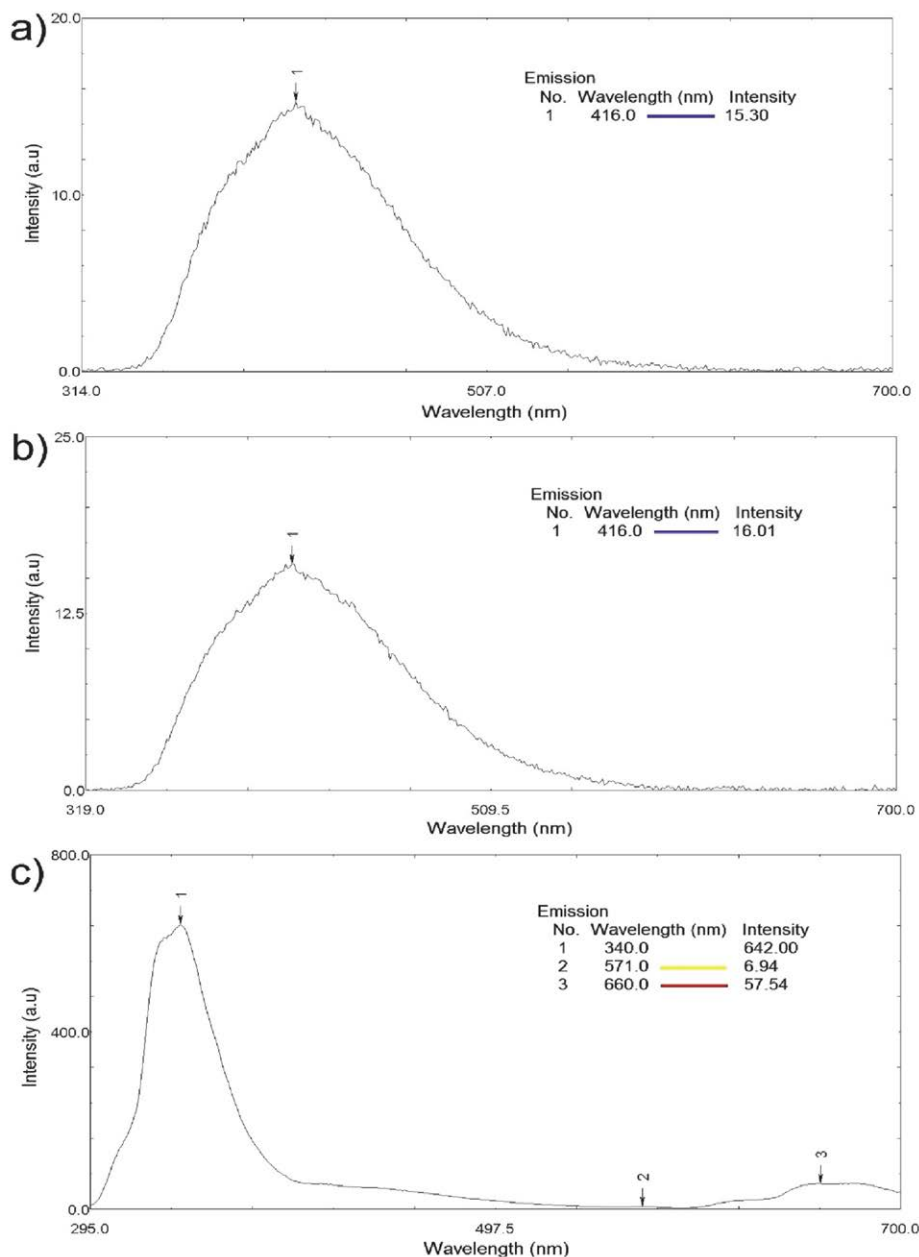


Figure 7. Emission spectra of polythioamides PSB and PCB: a) PSB at excitation 294 nm b) PSB at excitation 309 nm and c) PCB at excitation 285 nm.

### 3. 10. Thermal Analysis

The TGA/DTA graphs of the compounds were recorded in nitrogen atmosphere and all the results are given in Table 2. The thermal stability of the compounds was estimated from the  $T_{\max}$  (temperature indicating highest rate of weight loss) value obtained from their DTG graphs. TGA of thiourea SBT recorded four stages of wt. loss (weight loss) with 5% wt. loss within 38–190 °C due to the loss of water and volatile organic solvents, 13% wt. loss within 191–311 °C was due a thioamide ( $\text{NH}_2\text{C}=\text{S}$ ) group, 36% wt. loss within 312–475 °C owing to loss of thioamide groups, leaving behind  $\text{C}_6\text{H}_5\text{SO}_2\text{C}_6\text{H}_5$  and 46% wt. loss within 476–770 °C due to complete loss in weight. DTG

indicated  $T_{\text{onset}}$  at 188 °C and  $T_{\max}$  was noted at 448 °C. DTA of SBT indicated an endotherm at 221 °C for vaporization/decomposition, exotherm at 367 °C for vaporization/decomposition, endotherm at 510 °C for vaporization/decomposition and a large exotherm at 687 °C for decomposition (Figure 10a). TGA of polythioamide PSB showed three stages of wt. loss, 24% wt. loss indicated within 132–325 °C may be due to decomposition of  $\text{HN}-\text{C}(=\text{S})\text{NH}-/\text{C}(=\text{O})\text{C}_6\text{H}_5\text{C}(=\text{O})$  groups, 28% wt. loss within 326–513 °C may be attributed to the decomposition of  $-\text{C}_6\text{H}_5-(\text{O}=\text{S}=\text{O})-\text{C}_6\text{H}_5-/\text{HN}-\text{C}(=\text{S})\text{NH}-\text{C}(=\text{O})\text{C}_6\text{H}_5\text{C}(=\text{O})-$  and 39% wt. loss within 514–689 °C due to complete decomposition. DTG indicated  $T_{\text{onset}}$  at 132

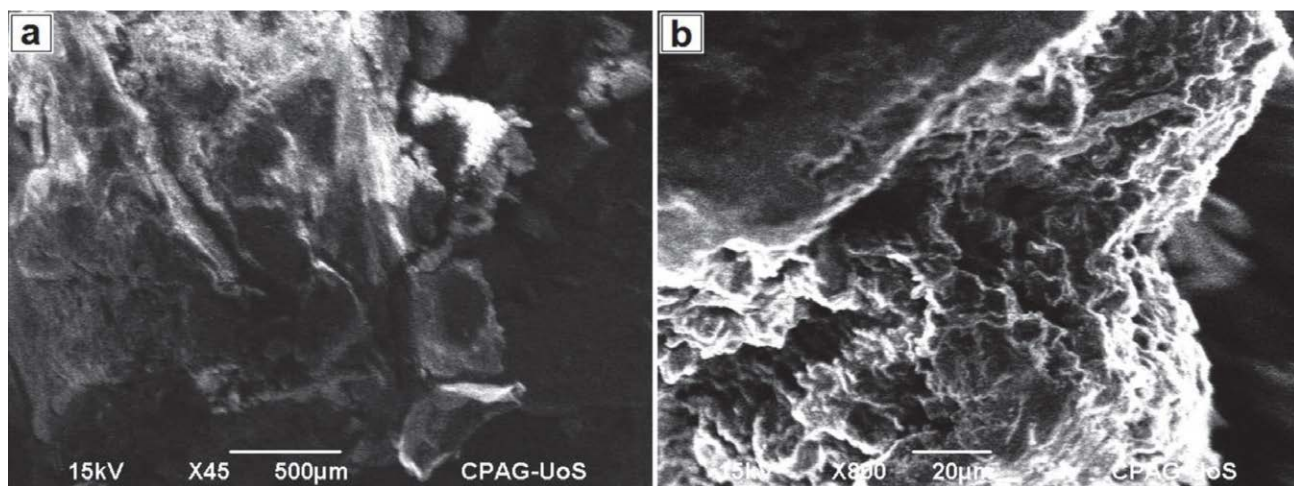


Figure 8. SEM images of thiourea monomer SBT and its corresponding polythioamide PSB: a SBT at 500  $\mu\text{m}$  and b PSB at 20  $\mu\text{m}$ .

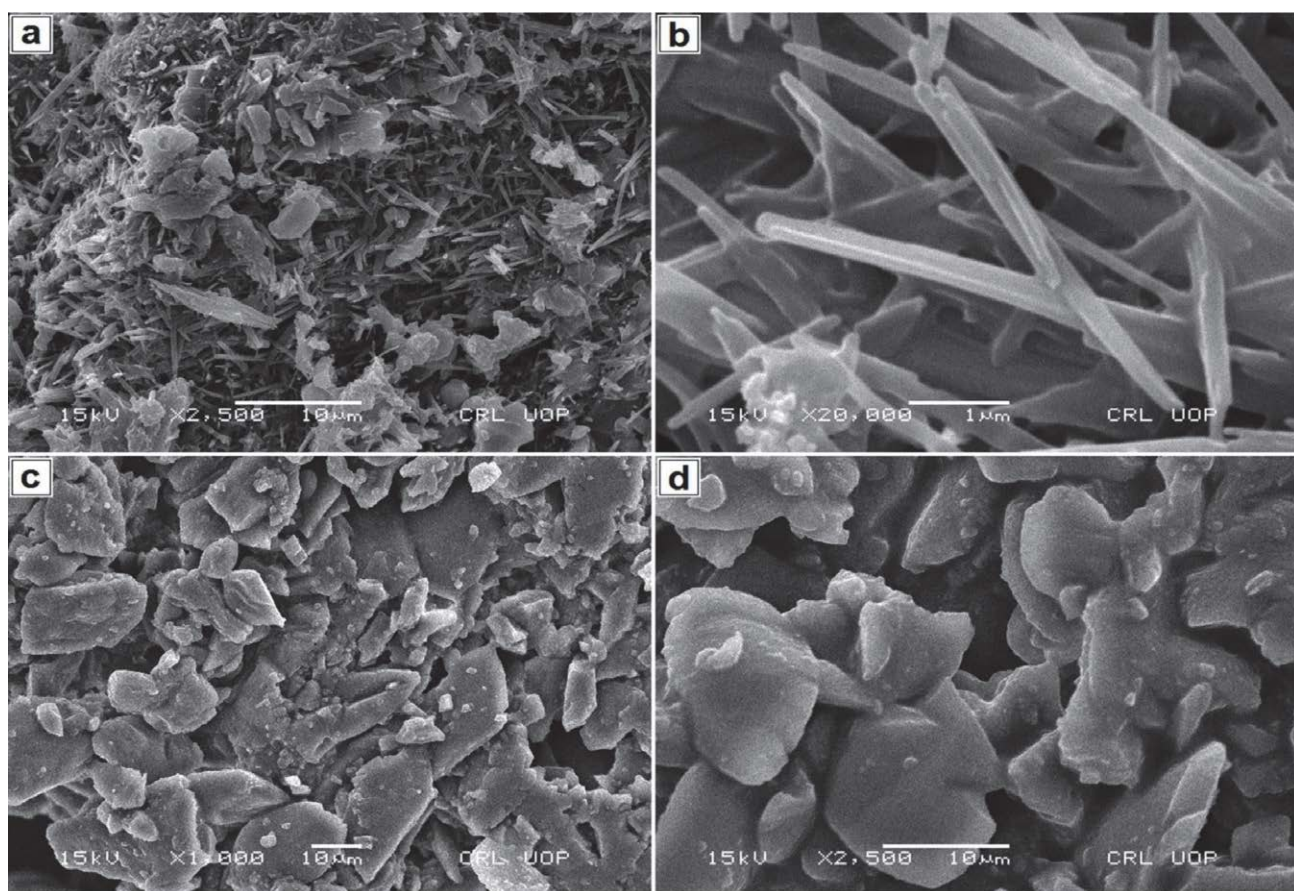


Figure 9 SEM images of thiourea monomer CBT and its derived polythioamide PCB: a CBT at 10  $\mu\text{m}$ , b CBT at 1  $\mu\text{m}$  and c, d PCB at 10  $\mu\text{m}$ .

Table 2. Thermal analysis results of polythioamides (PSB and PCB).

Compound	TGA			DTG		DTA	
	Stages of weight loss			$T_{\text{onset}} \text{ } ^\circ\text{C}$	$T_{\text{max}} \text{ } ^\circ\text{C}$	Endo $^\circ\text{C}$	Exo $^\circ\text{C}$
	I	II	III	Weight loss % (temperature range $^\circ\text{C}$ )			
PSB	24 (138–325)	28 (326–513)	39(514–689)	132	670	296	449, 660
PCB	65 (205–353)	5 (354–498)	–	262	346	345, 427	209, 368, 470

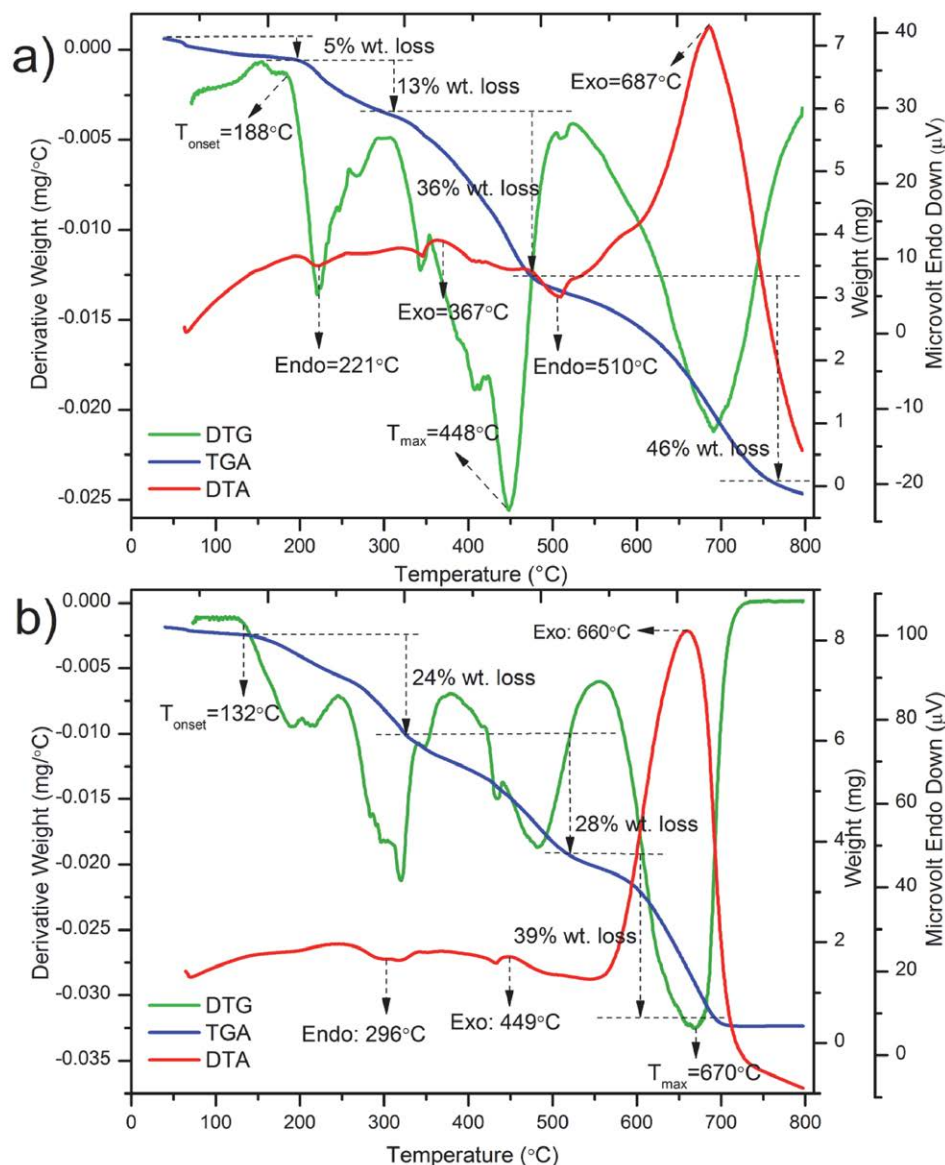


Figure 10. TGA/DTG/DTA graphs of **a** thiourea SBT and **b** polythioamide PSB.

$^\circ\text{C}$  and  $T_{\text{max}}$  was found at  $670^\circ\text{C}$ . The  $T_{\text{max}}$  value of polymer PSB was higher than the monomer SBT. DTA of polythioamide PSB displayed small endotherm at  $296^\circ\text{C}$  for melting, exotherm at  $449^\circ\text{C}$  for vaporization/decomposition and one large decomposition exotherm at  $660^\circ\text{C}$  (Figure 10b). TGA of polythioamide PCB recorded two stages of wt. loss with 65% wt. loss within  $205\text{--}353^\circ\text{C}$  due to decomposition of  $-\text{C}_6\text{H}_5\text{--}/\text{--HN--C(=S)NH--C(=O)C}_6\text{H}_5\text{C(=O)}$  and 5% wt. loss within  $354\text{--}498^\circ\text{C}$  due to complete decomposition. DTG showed  $T_{\text{onset}}$  at  $262^\circ\text{C}$  and  $T_{\text{max}}$  at  $346^\circ\text{C}$ . DTA of PCB indicated an exotherm at  $209^\circ\text{C}$  for vaporization, endotherm at  $345^\circ\text{C}$  for vaporization/decomposition, exotherm at  $368^\circ\text{C}$  owing to vaporization/decomposition, endotherm at  $427^\circ\text{C}$  because of melting, and an exotherm at  $470^\circ\text{C}$  due to decomposition (supplementary Fig. S4).

### 3. 11. Antimicrobial Activities

The synthesized thiourea monomers (SBT and CBT) and polythioamides (PSB and PCB) were tested for their antibacterial and antifungal functions against various strains of bacteria and fungi. All the compounds showed antibacterial function against *Salmonella typhi*, *Bacillus subtilis* and *Staphylococcus aureus*, while no activity was reported for *Escherichia coli* and *Pseudomonas aeruginosa*. The results of antibacterial assay are presented in Table 3. All the compounds showed antifungal activity against *Candida albicans*. The thiourea SBT, polythioamide PSB, thiourea CBT and polythioamide PCB indicated 20%, 15%, 15% and 20% inhibition against *Candida albicans* respectively. The polythioamide PCB showed 20% inhibition against *Fusarium lini*, while others (SBT, PSB and CBT)

did not indicate inhibition against *Fusarium lini*. The synthesized compounds did not show inhibition against *Aspergillus niger*, *Trichophyton rubrum* and *Microsporium canis*.

**Table 3.** Results of antibacterial functions of thiourea monomers and polythioamides.

Compound	% inhibition of thioureas (SBT and CBT) and polythioamides (PSB and PCB) against bacterial strains compared with Ofloxacin (standard drug)		
	<i>Salmonella typhi</i>	<i>Bacillus subtilis</i>	<i>Staphylococcus aureus</i>
SBT	7.5%	18.5%	3.7%
PSB	7.4%	13%	11%
CBT	12%	9.6%	27.5%
PCB	1.85%	7.4%	10%
Ofloxacin	94.09%	92.57%	83.01%

## 4. Conclusion

Two new polythioamides (PSB and PCB) were synthesized through polycondensation reaction of thiourea monomers (SBT and CBT) with terephthaloyl dichloride. The synthesized compounds were achieved in high yield (70–92%). The polythioamides PSB and PCB were completely soluble in DMSO and DMF without heating. The structures of thiourea monomers and polythioamides were analyzed and confirmed by different characterization techniques. All the synthesized thioureas and polythioamides were thermally stable and indicated multicolor fluorescence emission, therefore they can be employed as heat-resistant and fluorescent materials in different industrial and engineering fields. The antibacterial activities of the synthesized thioureas and polythioamides were found within the range of 1.85–27.5% against *Salmonella typhi*, *Bacillus subtilis* and *Staphylococcus aureus*. All the synthesized compounds indicated 15 or 20% antifungal activity against *Candida albicans* and the polythioamide PCB also indicated 20% antifungal activity against *Fusarium lini*.

## 5. References

- H. Mutlu, E. B. Ceper, X. Li, J. Yang, W. Dong, M. M. Ozmen and P. Theato, *Macromol. Rapid Commun.* **2019**, *40*, 1800650. DOI:10.1002/marc.201800650
- G. Levesque, J. C. Gressier, *J. polym. sci., Polym. Lett. Ed.* **1979**, *17*, 281–285. DOI:10.1002/pol.1979.130170506
- J. Gressier, G. Levesque, *Eur. Polym. J.* **1980**, *16*, 1167–1173. DOI:10.1016/0014-3057(80)90021-X
- I. Delfanne and G. Levesque, *Macromolecules* **1989**, *22*, 2589–2592. DOI:10.1021/ma00196a007

- M. Deletre and G. Levesque, *Macromolecules* **1990**, *23*, 4876–4878. DOI:10.1021/ma00224a019
- Z. Sun, H. Huang, L. Li, L. Liu, Y. Chen, *Macromolecules* **2017**, *50*, 8505–8511. DOI:10.1021/acs.macromol.7b01788
- W. Li, X. Wu, Z. Zhao, A. Qin, R. Hu, B. Z. Tang, *Macromolecules* **2015**, *48*, 7747–7754. DOI:10.1021/acs.macromol.5b02193
- S. Kagaya, E. Sato, I. Masore, K. Hasegawa, T. Kanbara, *Chem. Lett.* **2003**, *32*, 622–623. DOI:10.1246/cl.2003.622
- S. Kagaya, E. Tanaka, N. Kawai, I. Masore, E. Sato, K. Hasegawa, M. Kishi, T. Kanbara, *J. Inorg. Organomet. Polym. Mater.* **2009**, *19*, 67–73. DOI:10.1007/s10904-008-9250-8
- S. Kagaya, H. Miyazaki, M. Ito, K. Tohda, T. Kanbara, *J. Hazard. Mater.* **2010**, *175*, 1113–1115. DOI:10.1016/j.jhazmat.2009.10.099
- A. Yasin, Y. Chen, Y. Liu, L. Zhang, X. Zan, Y. Zhang, *Polym. Chem.* **2020**, *11*, 810–819. DOI:10.1039/C9PY01544B
- L. Ravikumar, S. Kalaivani, A. Murugesan, T. Vidhyadevi, G. Karthik, S. D. Kirupha, S. Sivanesan, *J. Appl. Polym. Sci.* **2011**, *122*, 1634–1642. DOI:10.1002/app.33968
- A. Srisa, K. Promhuad, H. San, Y. Laorenza, P. Wongphan, K. Wadaugsorn, J. Sodsai, T. Kaewpetch, K. Tansin, N. Harnkarnsujarit, *Polymers* **2022**, *14*, 4042. DOI:10.3390/polym14194042
- T. Lincke, S. Behnken, K. Ishida, M. Roth, C. Hertweck, *Angew. Chem., Int. Ed. Engl.* **2010**, *122*, 2055–2057. DOI:10.1002/ange.200906114
- F. Kloss, A. I. Chiriac, C. Hertweck, *Chem. Eur. J.* **2014**, *20*, 15451–15458. DOI:10.1002/chem.201403836
- S. Behnken, T. Lincke, F. Kloss, K. Ishida, C. Hertweck, *Angew. Chem., Int. Ed. Engl.* **2012**, *124*, 2475–2478. DOI:10.1002/ange.201108214
- K. L. Dunbar, M. Dell, F. Gude, C. Hertweck, *Proc. Natl. Acad. Sci. U. S. A.* **2020**, *117*, 8850–8858. DOI:10.1073/pnas.1918759117
- G. Tabak, T.-N. Pham, G. Levesque, *Polymer* **1998**, *39*, 5561–5566. DOI:10.1016/S0032-3861(97)10166-5
- P. Theato, *Multi-Component and Sequential Reactions in Polymer Synthesis*, Springer, Switzerland, **2015**. DOI:10.1007/978-3-319-20720-9
- Y. Kawai, T. Kanbara, K. Hasegawa, *J. Polym. Sci. Part A: Polym. Chem.* **1999**, *37*, 1737–1740. DOI:10.1002/(SICI)1099-0518(19990615)37:12<1737::AID-POLA2>3.0.CO;2-5
- T. Kanbara, Y. Kawai, K. Hasegawa, H. Morita, T. Yamamoto, *J. Polym. Sci. Part A: Polym. Chem.* **2001**, *39*, 3739–3750. DOI:10.1002/pola.10019
- A. Shah, M. Y. Khuhawar, A. A. Shah, *Iran. Polym. J. (Engl. Ed.)* **2009**, *18*, 217–225. <https://www.sid.ir/en/journal/ViewPaper.aspx?id=133598>
- W. Cao, F. Dai, R. Hu, B. Z. Tang, *J. Am. Chem. Soc.* **2020**, *142*, 978–986. DOI:10.1021/jacs.9b11066
- R. K. Pettit, C. A. Weber, M. J. Kean, H. Hoffmann, G. R. Pettit, R. Tan, K. S. Franks, M. L. Horton, *Antimicrob. Agents Chemother.* **2005**, *49*, 2612–2617. DOI:10.1128/AAC.49.7.2612-2617.2005



25. F. Qureshi, M. Y. Khuhawar, T. M. Jahangir, *Acta Chim. Slov.* **2019**, *66*, 899–912. DOI:10.17344/acsi.2019.5100
26. F. Qureshi, S. Q. Memon, M. Y. Khuhawar, T. M. Jahangir, *Polym. Bull.* **2021**, *78*, 1505–1533. DOI:10.1007/s00289-020-03170-y
27. F. Qureshi, S. Q. Memon, M. Y. Khuhawar, T. M. Jahangir, A. H. Channar, *J. Polym. Res.* **2021**, *28*, 259. DOI:10.1007/s10965-021-02582-2
28. L. Ravikumar, S. Kalaivani, T. Vidhyadevi, A. Murugasen, S. D. Kirupha, S. Sivanesan, *Open J. Polym. Chem.* **2014**, *4*, 1–11. DOI:10.4236/ojpcem.2014.41001
29. M. Sivadhyanithy, L. Ravikumar, T. Ramachandran, *J. Chil. Chem. Soc.* **2007**, *52*, 1230–1234. DOI:10.4067/S0717-97072007000300007
30. V. D. Bhatt, A. Ray, *Synth. Met.* **1998**, *92*, 115–120. DOI:10.1016/S0379-6779(98)80100-8
31. F. Qureshi, M. Y. Khuhawar, T. M. Jahangir, *Acta Chim. Slov.* **2018**, *65*, 718–729. DOI:10.17344/acsi.2018.4419
32. F. Qureshi, M. Y. Khuhawar, T. M. Jahangir, A. H. Channar, *Acta Chim. Slov.* **2016**, *63*, 113–120. DOI:10.17344/acsi.2015.1994
33. Y. Huang, J. J. Ferrie, X. Chen, Y. Zhang, D. M. Szantai-Kis, D. M. Chenoweth, E. J. Petersson, *ChemComm* **2016**, *52*, 7798–7801. DOI:10.1039/C6CC00105J
34. Y. C. Choi, M. S. Kim, K. M. Ryu, S. H. Lee, Y. G. Jeong, *Fibers Polym.* **2020**, *21*, 238–244. DOI:10.1007/s12221-020-9690-5
35. F. Qureshi, M. Y. Khuhawar, T. M. Jahangir, A. H. Channar, *Polym. Bull.* **2021**, *78*, 5055–5074. DOI:10.1007/s00289-020-03357-3

## Povzetek

Pripravili smo dva nova politioamida s polikondenzacijsko reakcijo med monomeri tiosečnine in tereftaloil dikloridom. Monomere tiosečnine smo sintetizirali z reakcijo med aromatskim (4,4'-diaminofenilsulfona) ali alicikličnim (1,2-cikloheksandiamin) diaminom z amonijevim tiocianatom. Elementno sestavo politioamidov smo potrdili z mikroanalizo CHN. Struktura in lastnosti monomerov tiosečnine in politioamidov so bile določene s protonsko NMR, UV-VIS, FT-IR spektroskopijo, fluorescenco, TGA/DTA in SEM. Politioamidi so pokazali visoko toplotno stabilnost, ki je bila ocenjena na podlagi njihovih vrednosti  $T_{\max}$  (temperatura, ki kaže najvišjo stopnjo izgube teže; 670 °C in 346 °C), opaženih v DTG grafih (derivativne termogravimetrije). Tiousečnine in politioamidi so fluorescirali in pokazali večbarvne (vijolične, zelene, rumene, oranžne in rdeče) emisije pri različnih valovnih dolžinah vzbujanja. Vse sintetizirane spojine so bile testirane tudi na podlagi njihovih protiglivičnih in antibakterijskih funkcij in so pokazale antibakterijsko delovanje proti *Salmonella typhi*, *Bacillus subtilis* in *Staphylococcus aureus* ter protiglivično delovanje proti *Candida albicans*.



Except when otherwise noted, articles in this journal are published under the terms and conditions of the Creative Commons Attribution 4.0 International License

*Scientific paper*

# Glycoprotein Levels and Oxidative Stomach Damage in Diabetes and Prostate Cancer Model: Protective Effect of Metformin

Onur Ertik<sup>\*,1</sup>, Pınar Koroglu Aydin<sup>2</sup>, Omur Karabulut Bulan<sup>3</sup>  
and Refiye Yanardag<sup>1</sup>

<sup>1</sup> Istanbul University-Cerrahpaşa, Faculty of Engineering, Department of Chemistry, Istanbul, Turkey.

<sup>2</sup> Halic University, Faculty of Medicine, Department of Histology and Embryology, Istanbul, Turkey.

<sup>3</sup> Istanbul University, Faculty of Science, Department of Biology, Istanbul, Turkey.

\* Corresponding author: E-mail: onur.ertik@btu.edu.tr  
+ 90 224 300 3701; +90 539 930 00 87

Received: 04-11-2023

## Abstract

People with diabetes have a higher risk of prostate cancer and people with prostate cancer are prone to stomach metastases. Therefore, researchers continue to search for new approaches in the treatment of individuals with all the above diseases at the same time. The protective effect of metformin (which is used in the treatment of diabetes) on cancer continues to be supported by studies. In this study, it was determined that the biochemical parameters showed a protective effect on stomach tissues with the administration of metformin to cancer and group with both cancer and diabetes groups. With the principal component analysis, it was determined that the biochemical parameters studied in the stomach tissue showed a correlation.

**Keywords:** Dunning Prostate Cancer, Diabetes, Metformin, Stomach Damage, Oxidative Stress.

## 1. Introduction

Diabetes mellitus (DM) is induced by many factors such as genetic, dietary and environmental factors. It is mainly divided into two groups; while type 1 diabetes occurs due to insufficient secretion of the hormone insulin, type 2 diabetes occurs due to insulin resistance, with high blood glucose levels observed in both cases.<sup>1</sup> Its incidence is increasing daily depending on the factors. Cancer, a disease that occurs due to the abnormal proliferation of cells requires intensive treatment. It can result in death unless diagnosed at an early stage.<sup>2</sup> The increasing incidence of cancer, high mortality rates, and the fact that a treatment has not been found yet, and for that reason, cancer research remains important scientific.

The incidence of diabetes and many types of cancer has risen especially in recent years owing to changing dietary habits, and external and genetic factors. It is predicted that the incidence of these diseases will increase in the coming years. The prostate cancer is shown common type

of cancer in men, having important social and economic consequences. It accounts for nearly 25 per cent of all new male cancer diagnoses in the UK.<sup>3</sup> Prostate cancer incidence varies regionally and it is known that the highest rates are in Western and the lowest rates are in Asia countries.<sup>4</sup> In addition to this, epidemiological evidence suggests that people with diabetes are at higher risk for cancer<sup>5</sup> and hence, it is essential to find new approaches to the treatment of people with both diseases using existing or newly discovered drugs.

Investigation of the effects of known and currently used drugs on different diseases provides importance for the discovery of more than one targeted drug. Knowing the side effects of these drugs, which will be investigated, and proven by scientific research accelerates their use in the treatment of different diseases. One of them, metformin (1,1-Dimethylbiguanide) is a lipophilic biguanide drug that inhibits hepatic gluconeogenesis and improves peripheral utilisation of glucose. However, in recent studies,

the approach to this molecule has changed, considering that it has anti-tumour properties directly and indirectly, in addition to type 2 diabetes. A potential anti-tumorigenic effect of metformin directly is thought to be exerted by activating AMP-kinase, which inhibits the mammalian target of rapamycin (mTOR).<sup>6</sup> The indirect antitumor effect of metformin is presumed to be by inhibiting hepatic gluconeogenesis. AMPK activation in the liver causes hepatic gluconeogenesis inhibition by acting on gluconeogenesis genes. Inhibited gluconeogenesis genes stimulate the entrance of glucose into the muscles. As a result of this stimulation, blood glucose and insulin levels decrease.<sup>7</sup> Tumour cells have been found to express high levels of insulin receptors. Therefore, this is accepted as an unfavourable prognostic factor for prostate, breast, and colon cancer.<sup>8</sup> In one study, metformin was found to reduce the risk of prostate cancer as well as diabetes in a dose-dependent manner.<sup>9</sup> Considering the effects of metformin on cancer, it is very important to examine the effects of metformin on many tissues, especially in animal models of prostate cancer and diabetes.

The presented study aimed to examine the effects of prostate cancer and diabetic rats on stomach tissue through biochemical parameters.

## 2. Experimental

### 2.1. Prostate Cancer Cell Protocol

Mat-LyLu cells were used according to instructions in our prior investigation.<sup>10</sup> Cell culture and functional assays. Mat-LyLu were grown in a 37 °C/5% CO<sub>2</sub> incubator in RPMI (RPMI-1640; Gibco; Life Technologies, Waltham, MA, USA) culture medium supplemented with 1% fetal bovine serum (FBS) (Gibco; Life Technologies).

### 2.2. Experimental Protocol

In this research, Copenhagen rats were employed. Tubitak MAM Genetic Engineering and Biotechnology Institute produced the rats. The present study was carried out within the framework of the rules determined by the Istanbul University Animal Care and Use Committee (Protocol no: 2014/28- 27.02.2014 the ethics committee decision number and date).

Table 1. Application for the experimental groups.

Groups	n	Application
The control	5	0.9% PS was given for 14 days.
The diabetic	7	65 mg/kg STZ was given to the group with a single injection.
The cancer	8	2.10 <sup>4</sup> MATLyLu cells were given subcutaneously (s.c) inoculated with only one injection.
The cancer+metformin (CM)	8	250 mg/kg metformin was given to the group for 14 days after Mat-LyLu cells inoculation.
The diabetic+cancer (DC)	8	2.10 <sup>4</sup> MAT-LyLu cells and STZ were injected.
The diabetic+cancer+metformin (DCM)	8	Metformin was given for 14 days to treat of STZ and Mat-LyLu cells.

### 2.3. Pharmacological Application and Experimental Groups

Rats, 150–220 g, were housed individually in a light and temperature-controlled room on a 12 h/12 h light-dark cycle and fed a standard pellet lab chow. Streptozotocin (STZ) was given intraperitoneally (i.p.) to the diabetes groups to induce diabetes. At the end of the 72nd hour of the experimental process, blood glucose levels were measured and the rats were considered diabetic if the values were above 200 mg/dL. Rats were given 250 mg/kg of metformin (Sigma, D150959) orally and Table 1 shows the applications to the experimental groups.

At the end of the experimental process, all animals were dissected under ketamine hydrochloride (Ketalar®, Eczacıbaşı) and xylazine HCl (Alfazyne®, Holland) anaesthesia. After that, stomach tissues were taken for biochemical analyses. Stomach tissue was not examined histologically and only biochemical parameters were determined in this study. Also, no other organs, apart from the stomach, were not included in the study.

### 2.4. Biochemical Analyses

#### 2.4.1. Preparation of Stomach Tissues for Biochemical Analyses

Stomach tissues taken for use in biochemical parameters were first washed in cold physiological saline (0.9% NaCl) and then 1 g of stomach tissue was homogenized in 10 mL of saline solution using a glass homogenizer (Tenbroeck glass tissue homogenizer). After homogenization, it was centrifuged and the supernatants were stored at –20 °C to be used for experiments. All chemicals used in the experiments were obtained from Sigma-Aldrich.

#### 2.4.2. Determination of Lipid Peroxidation (LPO) Levels and Myeloperoxidase (MPO) Activities

Lipid peroxidation (LPO) levels of stomach tissues were determined spectrophotometrically by measurement of the LPO products reacted with thiobarbituric (TBA) acid at high temperature and low pH.<sup>11</sup> 0.25 mL of homogenized tissue was mixed with 1.22 M trichloroacetic acid (TCA) and left at room temperature for 15 minutes. Then,

0.375 mL TBA (0.047 M) was added and kept in a boiling water bath for 30 minutes. After cooling, 1 mL n-butanol was added to each tube and centrifuged at 4000 rpm for 10 minutes. Absorbance values of the organic phase were read against the blank at 532 nm. Results were reported as nmol MDA/mg protein.

Myeloperoxidase (MPO) activities were determined by the reaction of 0.13 mL 4-aminoantipyrine (25 mM), 0.13 mL phenol (2%) and 0.26 mL H<sub>2</sub>O<sub>2</sub> (1.7 mM) with 0.4 mL homogenized. The resulting colour change was read at 510 nm in the spectrophotometer.<sup>12</sup> The results were defined as mU/g protein.<sup>12</sup>

#### 2.4.3. Determination of Superoxide Dismutase (SOD) and Catalase (CAT) Activities

130 µL phosphate buffer (50 mM, pH:7.8, 0.1 mM EDTA), 5 µL o-dianisidine (0.19%), 5 µL sample and 10 µL riboflavin (0.2 mM) were placed in a tube and the absorbance values at 0 and 8 minutes were read at 460 nm for the determination of superoxide dismutase (SOD) activities.<sup>13</sup> The results were expressed as U/mg protein.

The activity of the catalase (CAT) of stomach tissues was determined by converting H<sub>2</sub>O<sub>2</sub> to H<sub>2</sub>O and measuring the decreasing absorbance value due to H<sub>2</sub>O<sub>2</sub> consumption at 240 nm in the spectrophotometer.<sup>14</sup> 0.1 mL sample and 0.4 mL H<sub>2</sub>O<sub>2</sub> (30 mM) were added to the same tube and the absorbance values were read at 240 nm. The results were defined as U/mg protein.

#### 2.4.4. Determination of Glutathione Reductase (GR), Glutathione Peroxidase (GPx), and Glutathione-S-Transferase (GST) Activities

NADPH and oxidized glutathione (GSSG) with glutathione reductase (GR) cause a decrease in absorbance due to the consumption of NADPH in the test tube.<sup>15</sup> 870 µL tris-HCl buffer (50 mM, pH:8.0 and 1 mM EDTA), 50 µL NADPH (2 mM) and 50 µL GSSG (20 mM) were added to the same tube. Then, 30 mL samples were placed in the same tube and the absorbance changes were determined at 340 nm. GR activity was expressed as U/g protein.

Glutathione peroxidase (GPx) provides GSSG by oxidation of GSH in the presence of H<sub>2</sub>O<sub>2</sub>. The resulting GSSG is converted to GSH by the oxidation of NADPH to NADP. 400 µL phosphate buffer (0.25 M, pH:7.0, 2.5 mM EDTA, 2.5 mM NaN<sub>3</sub>), 100 µL GSH (10 mM), 100 µL NADPH (2.5 mM), 100 µL GR (6U/mL) and 100 µL H<sub>2</sub>O<sub>2</sub> (12 mM) were added the tube and then sample 200 µL sample also added the same tube. Finally, the absorbance changes were read spectrophotometrically at 340 nm.<sup>16</sup> GPx activity was expressed as U/mg protein.

Glutathione-S-transferase (GST) activity was determined according to the spectrophotometric evaluation of the absorbance at 340 nm of the product formed by the

conjugation of GSH and 1-chloro-2,4-dinitrobenzene (cDNB).<sup>17</sup> For this experiment, 400 µL phosphate buffer (0.2 M, pH: 6.6), 10 µL GSH (60 mM), 10 µL cDNB, 180 µL water and 100 µL sample were reacted in the same tube and absorbance changes were watched at 340 nm. GST activity was expressed as U/g protein.

#### 2.4.5. Determination of Reactive Oxygen Species (ROS), Protein Carbonyl (PC), and Homocysteine (HCy) Levels

Reactive oxygen species (ROS) levels were determined by the reaction of 2000 µM 2',7'-dichlorofluorescein diacetate (DCF) compound dissolved in 20 mM HEPES (4-(2-hydroxyethyl)-1-piperazinetsulfonic acid) buffer.<sup>18</sup> 5 µL sample, 55 µL HEPES buffer and 90 µL DCF were added in the same tube and the first read was observed fluorometrically at Ex. 480 nm/Em. 535 nm. The second read was recorded after incubation at 30 min and 37°C. The results were given as ΔRFU/mg protein.

Protein carbonyl (PC) levels are determined with 2,4-dinitrophenylhydrazine, which is formed by the reaction of carbonyl groups in proteins with 2,4-dinitrophenylhydrazine (DNPH).<sup>19</sup> 0.5 mL sample, and 2 mL DNPH (10 mM, in 2.5 M HCl) were added same tube and the incubation was performed at room temperature. After 2.5 mL TCA (20%) was added to each tube, and the tubes were washed with ethyl alcohol and ethyl acetate mixture (1:1). In every washing, the tubes were centrifuged at 300 rpm and 10 min. Then, 1 mL guanidine-HCl (6 M) was put into each tube and the incubation was formed at 30 min and 37°C. Finally, the absorbance values were taken by using a spectrophotometer at 370 nm. The results were given in nmol PC /mg protein.

Homocysteine (HCy) levels of the stomach tissues were measured according to the manufacturer's procedure via an ELISA kit. The homocysteine levels were given in nmol HCy/mg protein.

#### 2.4.6. Determination of Xanthine Oxidase (XO) and Lactate Dehydrogenase (LDH) Activities

Xanthine oxidase (XO) is the enzyme that converts xanthine to uric acid. For this purpose, 870 µL phosphate buffer (50 mM, pH: 7.4), 33 µL EDTA (3 mM), 33 µL xanthine (2 mM) and 10 µL sample were kept in the same environment and the first reading was taken on the spectrophotometer. Second absorbance values were taken after 10 minutes of incubation at room temperature and at 286 nm in the spectrophotometer.<sup>20</sup> XO activity was expressed as U/mg protein.

Lactate dehydrogenase (LDH) catalyses the conversion of pyruvate to lactate in the presence of NADH. LDH activity was calculated by measuring the oxidation of NADH to NAD<sup>+</sup>.<sup>21</sup> 2 mL NADH (170 µM) and 50 µL sample

was incubated at 5 min and 37 °C. After incubation, 250 µL pyruvate solution (14 mM) was added to each tube and the decreasing absorbances of each tube were recorded at 340 nm. LDH activity was defined as U/mg protein.

#### 2.4.7. Determination of Sodium-Potassium ATPase (Na<sup>+</sup>/K<sup>+</sup>-ATPase) and Histone Deacetylase (HDAC) Activities

Ridderstap and Bonting methods were used for the determination of sodium-potassium ATPase (Na<sup>+</sup>/K<sup>+</sup>-ATPase) activity in stomach tissue with the help of the determination of Mg<sup>2+</sup> ATPase in the presence of 20 mM ouabain and 11 mM ATP in acidic medium.<sup>22</sup> Na<sup>+</sup>/K<sup>+</sup>-ATPase activity was given in nmol Pi/mg protein/h.

Histone deacetylase (HDAC) activities of the stomach tissues were measured according to the manufacturer's procedure by using an ELISA kit. HDAC activity was given in U/mg protein.

#### 2.4.8. Determination of Sialic Acid (SA), Hexose, Hexosamine and Fucose Levels

The method for determining the sialic acid (SA) levels of gastric tissues is based on reading the absorbance at 546 nm of the coloured compound formed by the reaction of 2-formyl pyruvic acid, which is formed as a result of the oxidation of periodic acid, with two moles of thiobarbituric acid.<sup>23</sup> 10 µL sample were added to the tube. Then, 100 µL NaCl (155 mM) and 300 µL H<sub>2</sub>SO<sub>4</sub> (6.7 mM) were added to all tubes, respectively. It was incubated at 80 °C for one hour. After cooling, 100 µL sodium meta periodate (0.2 M) was added to all tubes and kept at room temperature for 20 minutes. Then, 400 µL sodium meta arsenite (1.54 M) was added and the tubes were shaken until the colour of the iodine disappeared. 1 mL of thiobarbituric acid (7.102%) was added to all tubes and kept at 90 °C for 15 minutes. After cooling, 2 mL of cyclohexanone was added and centrifuged for 10 minutes. SA was absorbed into the cyclohexanone phase and absorbance values were read on the spectrophotometer at 546 nm. The results were given as µmol SA/g protein.

In order to determine hexose compounds of the stomach tissues, spectrophotometrically, this method creates the colour reaction method of carbohydrates with orcinol in the presence of concentrated sulphuric acid.<sup>24</sup> 0.25 mL orcinol solution (1.6%) and 2 mL H<sub>2</sub>SO<sub>4</sub> (60%) were added to 0.25 mL of the sample, respectively. After the mixture was boiled in a boiling water bath for 10 minutes and cooled, the absorbances were read on a spectrophotometer at 425 nm. The results were defined as µg hexose / mg protein.

The method used is based on measuring the absorbance of the pink colour formed as a result of the reaction of hexosamine compounds in the tissue with acetylacetone

and p-dimethylaminobenzaldehyde in a spectrophotometer at 530 nm.<sup>24</sup> The results were defined as µg hexosamine /mg protein.

1 mL of sample was mixed with 1 mL of acetylacetone (0.5% in 0.5 Na<sub>2</sub>CO<sub>3</sub>) and then kept in a boiling water bath for 15 minutes. At the end of this period, 5 mL ethyl alcohol (96%) and 1 mL Ehrlich reagent were added to all tubes and the tubes were incubated at room temperature for 1 hour. At the end of this period, absorbance values were taken at 530 nm. The basis determination of fucose in stomach tissue is based on the colour reaction of carbohydrates with thiol groups in a sulfuric acid medium.<sup>25</sup> The results were expressed as µg fucose /mg protein.<sup>25</sup>

#### 2.4.9. Determination of Protein Levels

The amount of protein in the stomach tissue is determined on the basis of the method of measuring the intensity of the blue-violet colour, which is formed as a result of the reduction of proteins reacted with copper ions in an alkaline medium with Folin reagent (phosphomolybdotungstic acid), spectrophotometrically at 500 nm.<sup>26</sup>

### 2.5. Statistical Analysis

Graph-Pad Prism 3.0 (GraphPad Software, San Diego, CA, USA) program was used to interpret the experimental results statistically. Tukey's test was applied to determine the significance between groups and/or parameters, and the obtained data were expressed as mean ± standard deviation (SD). Tukey's test is ANOVA post hoc test, meaning that ANOVA was first performed. p values of less than 0.05 were accepted as a statistically significant difference. Principal component analysis (PCA) was also used to visualize the biomarker's responses for all exposure conditions. PCA was performed using GraphPad Prism Software, version 9 (San Diego, USA).

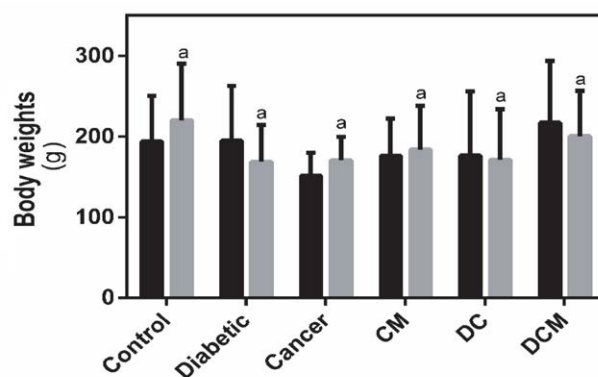


**Figure 1.** The body weights of all groups of rats. The black columns represent the first body weight of the groups. The grey columns represent the final body weight of the groups. CM: cancer+metformin; DC; diabetic+cancer; DCM: diabetic+cancer+metformin. The groups show off mean ±SD. <sup>a</sup>p < 0.05 vs the control group.

### 3. Results

#### 3.1. Body Weights and Blood Glucose Levels

The body weights of all groups are shown in Figure 1. The first and last body weights of all groups were measured. It was observed that the first and last body weights of all groups except the DC group changed significantly ( $^a p < 0.05$ ) and the significance of the body weights and blood glucose levels were determined by using Tukey's test.

The levels of blood glucose of all groups were measured during the experiment and are shown in Figure 2. The blood glucose values measured after 72 hours in the groups given STZ to create diabetes showed an important increase and exceeded 200 mg/dL. All experiment groups were found to be significantly changed when compared with the control group at the end of the experiment ( $^a p < 0.01$ ). In addition, blood glucose levels were measured again at the end of the experiment (14 days later) and an increase was observed in

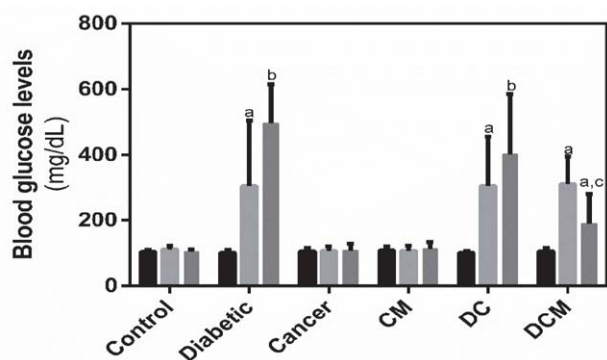


**Figure 2.** The blood glucose levels of all groups of rats. The black columns represent the blood glucose level at the beginning of the experiment of the groups. The light grey columns represent the 72nd h blood glucose level of the groups. The dark grey columns represent the blood glucose level at the end of the experiment of the groups. CM: cancer+metformin; DC; diabetic+cancer; DCM: diabetic+cancer+metformin. The groups show off mean  $\pm$ SD.  $^a p < 0.05$  vs control group;  $^b p < 0.001$  vs control group;  $^c p < 0.05$  vs DC group.

the diabetic, DC, and DCM groups when compared to the control group, but it was observed that the blood glucose level measured at the end of the experiment in the DCM group decreased when compared to the 72nd-hour blood glucose level ( $^b p < 0.05$ ). When the blood glucose levels of the DC group and the DCM group were compared, a decrease was observed in the DCM group ( $^c p < 0.05$ ).

#### 3.2. Biochemical Results

##### 3.2.1. Lipid Peroxidation (LPO) Levels and Myeloperoxidase (MPO) Activities

LPO levels and MPO activities of stomach tissues are presented in Figure 3(A-B) and it was found that the levels of LPO and activities of MPO incremented in the group of the diabetic ( $p < 0.05$ ;  $p < 0.0001$ ), cancer ( $p < 0.05$ ;  $p < 0.0001$ ) and DC ( $p < 0.05$ ;  $p < 0.0001$ ) when compared to the control group. Metformin reduced LPO levels and MPO activities in cancer and DC groups when compared to CM ( $p < 0.05$ ;  $p < 0.05$ ) and DCM ( $p < 0.05$ ;  $p < 0.0001$ ) groups respectively.

##### 3.2.2. Superoxide Dismutase (SOD) and Catalase (CAT) Activities

SOD and CAT activities presented in Figure 4(A-B) indicated that their activities decreased in the diabetic ( $p < 0.01$ ;  $p < 0.0001$ ), cancer ( $p < 0.0001$ ;  $p < 0.0001$ ) and DC ( $p < 0.001$ ;  $p < 0.0001$ ) groups. At the end of the treatment with metformin, SOD and CAT activities were advanced in CM ( $p < 0.001$ ;  $p < 0.01$ ) and DCM ( $p < 0.0001$ ;  $p < 0.0001$ ) groups.

##### 3.2.3. Glutathione Reductase (GR), Glutathione Peroxidase (GPx), and Glutathione-S-Transferase (GST) Activities

GR, GPx and GST activities of all groups were given in Figure 5(A-C) and it was determined that the GR, GPx

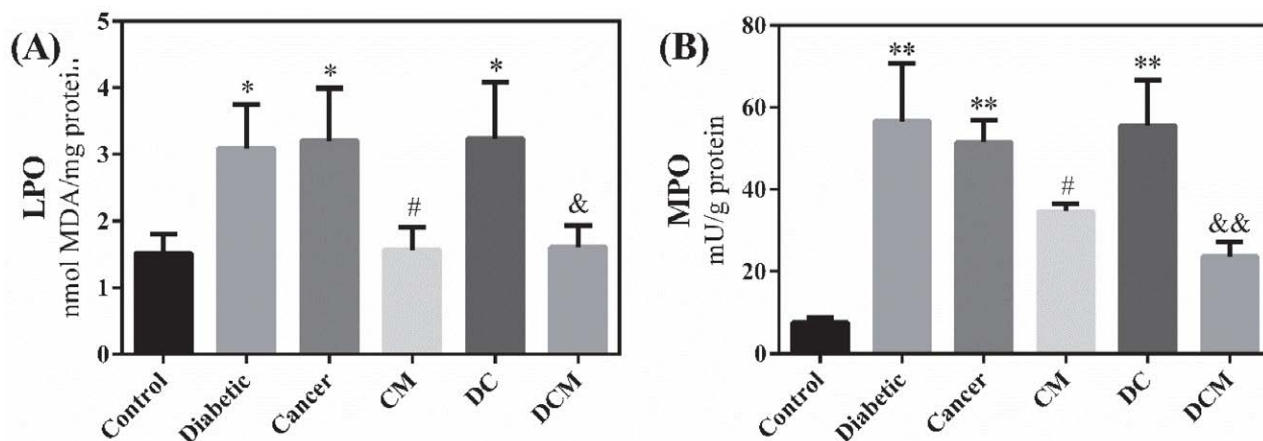


**Figure 3.** (A) Lipid peroxidation (LPO) levels and (B) myeloperoxidase (MPO) activities of all groups of rats. CM: cancer+metformin; DC; diabetic+cancer; DCM: diabetic+cancer+metformin. The groups show off mean  $\pm$ SD.  $^* p < 0.05$  vs control group;  $^{**} p < 0.0001$  vs control group;  $^{\#} p < 0.05$  vs cancer group;  $^{\&} p < 0.05$  vs DC group;  $^{\&\&} p < 0.0001$  vs DC group.

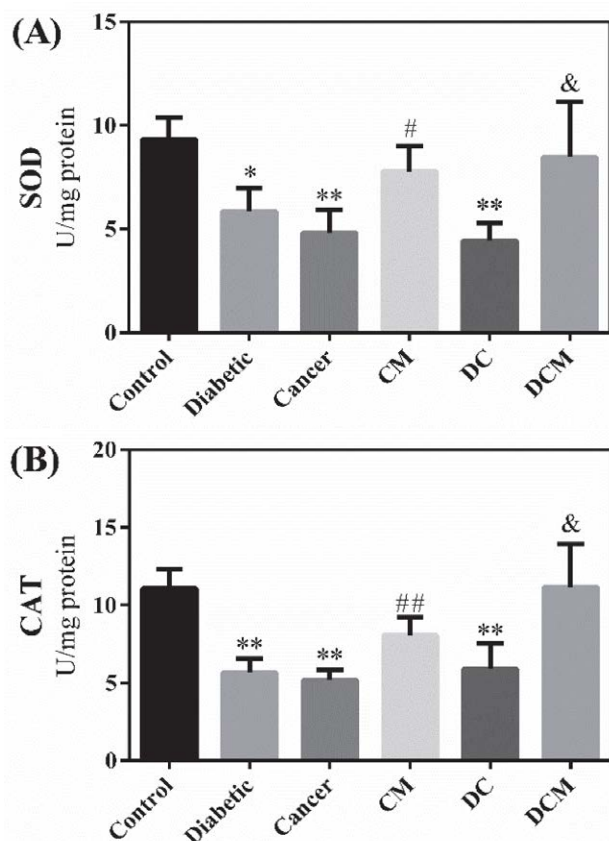


**Figure 4.** (A) Superoxide dismutase (SOD) and (B) catalase (CAT) activities of all groups of rats. CM: cancer+metformin; DC; diabetic+cancer; DCM: diabetic+cancer+metformin. The groups show off mean  $\pm$ SD. \* $p < 0.01$  vs control group; \*\* $p < 0.0001$  vs control group; # $p < 0.001$  vs cancer group; ## $p < 0.01$  vs cancer group; & $p < 0.0001$  vs DC group.

and GST activities of the diabetic ( $p < 0.05$ ;  $p < 0.0001$ ;  $p < 0.0001$ ), cancer ( $p < 0.001$ ;  $p < 0.001$ ;  $p < 0.0001$ ) and DC ( $p < 0.05$ ;  $p < 0.0001$ ;  $p < 0.0001$ ) groups were decreased meaningfully when compared to the control group. Administration of metformin reversed GR, GPx and GST activities of CM ( $p < 0.0001$ ;  $p < 0.0001$ ;  $p < 0.0001$ ) and DCM ( $p < 0.01$ ;  $p < 0.0001$ ;  $p < 0.01$ ) groups.

### 3.2.4. Reactive Oxygen Species (ROS), Protein Carbonyl (PC), and Homocysteine (HCy) Levels

ROS, PC, and HCy levels of stomach tissues are presented in Figure 6(A-C) and it was found that ROS, PC and HCys levels of diabetic ( $p < 0.001$ ;  $p < 0.0001$ ;  $p < 0.0001$ ), cancer ( $p < 0.0001$ ;  $p < 0.0001$ ;  $p < 0.0001$ ) and DC ( $p < 0.0001$ ;  $p < 0.05$ ;  $p < 0.0001$ ) increased when compared to the control groups. Metformin changed the levels of ROS, PC, and HCy. The CM ( $p < 0.0001$ ;  $p < 0.0001$ ;  $p < 0.0001$ ) and DCM ( $p < 0.0001$ ;  $p < 0.0001$ ;  $p < 0.0001$ ) groups showed decreasing ROS, PC and HCy levels when compared to cancer and DC groups respectively.

### 3.2.5. Xanthine Oxidase (XO) and Lactate Dehydrogenase (LDH) Activities

XO and LDH activities of stomach tissues were presented in Figure 7(A-B). It was found that the activities of XO and LDH were meaningfully increased in the diabetic ( $p < 0.0001$ ;  $p < 0.05$ ), cancer ( $p < 0.0001$ ;  $p < 0.0001$ ) and DC ( $p < 0.0001$ ;  $p < 0.0001$ ) groups. These increases in activities were reversed by metformin administration, by de-

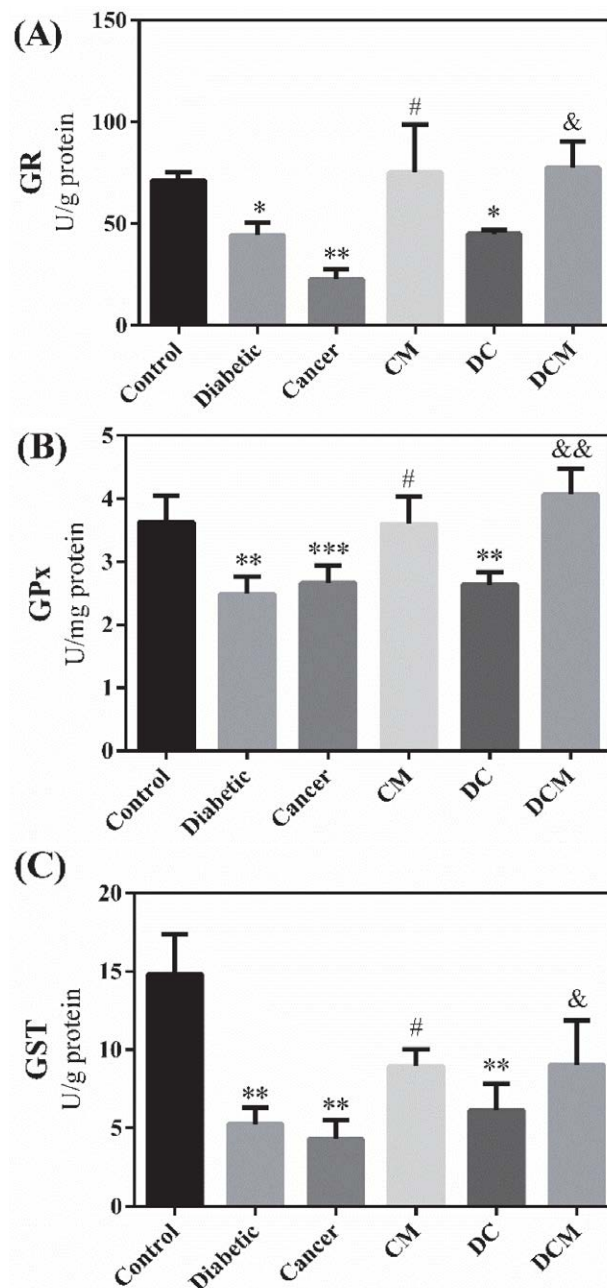


**Figure 5.** (A) Glutathione reductase (GR), (B) glutathione peroxidase (GPx) and (C) glutathione-S-transferase (GST) activities of all groups of rats. CM: cancer+metformin; DC; diabetic+cancer; DCM: diabetic+cancer+metformin. The groups show off mean  $\pm$ SD. \* $p < 0.05$  vs control group; \*\* $p < 0.0001$  vs control group; \*\*\* $p < 0.001$  vs control group; # $p < 0.0001$  vs cancer group; & $p < 0.01$  vs DC group; && $p < 0.0001$  vs DC group.

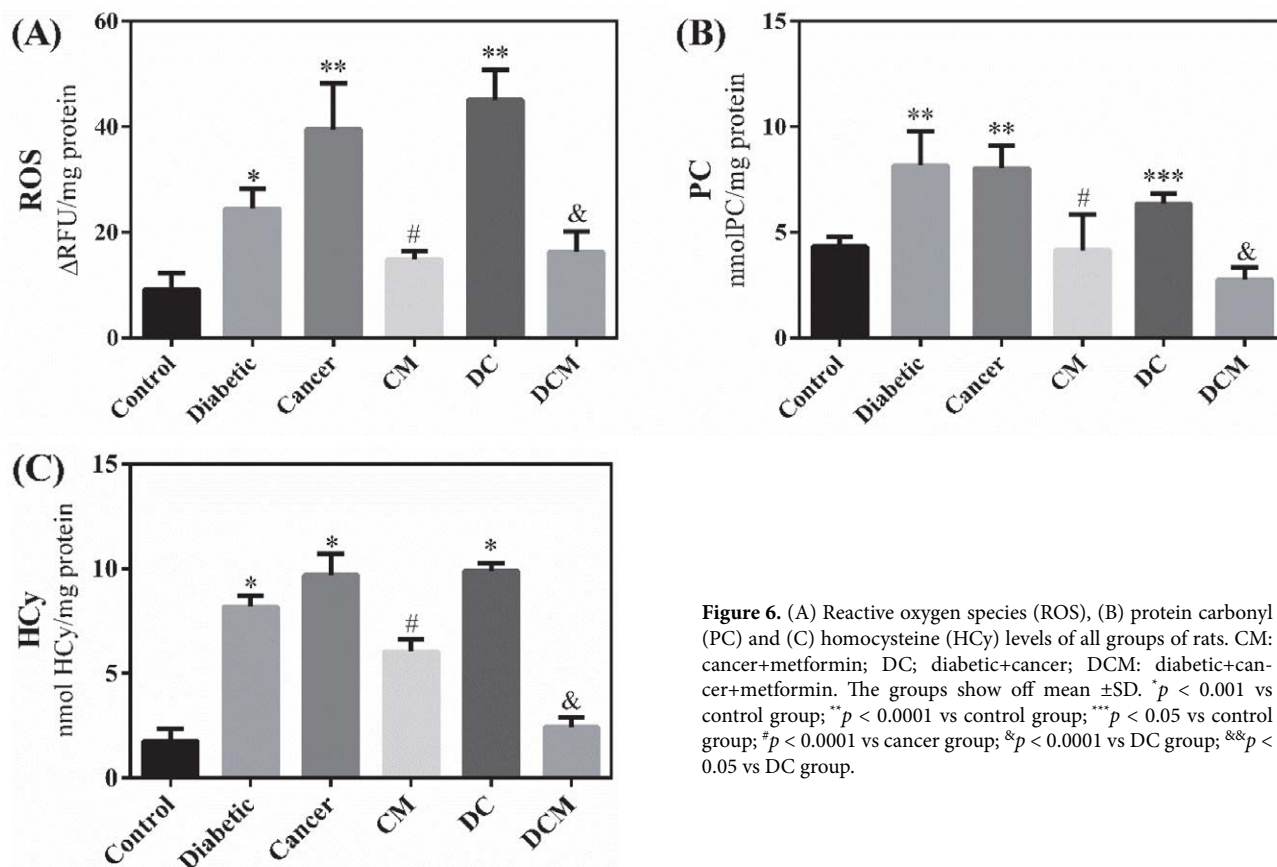


**Figure 6.** (A) Reactive oxygen species (ROS), (B) protein carbonyl (PC) and (C) homocysteine (Hcy) levels of all groups of rats. CM: cancer+metformin; DC: diabetic+cancer; DCM: diabetic+cancer+metformin. The groups show off mean  $\pm$ SD. \* $p$  < 0.001 vs control group; \*\* $p$  < 0.0001 vs control group; \*\*\* $p$  < 0.05 vs control group; # $p$  < 0.0001 vs cancer group; & $p$  < 0.0001 vs DC group; && $p$  < 0.05 vs DC group.

creasing the activities of XO and LDH in CM ( $p$  < 0.0001;  $p$  < 0.05) and DCM ( $p$  < 0.0001;  $p$  < 0.0001) groups.

### 3.2.6. Sodium-Potassium ATPase ( $\text{Na}^+/\text{K}^+$ -ATPase) and Histone Deacetylase (HDAC) Activities

$\text{Na}^+/\text{K}^+$ -ATPase and HDAC activities of stomach tissues were shown in Figure 8 and the results showed

that the activity of  $\text{Na}^+/\text{K}^+$ -ATPase diminished in diabetic, cancer and DC ( $p$  < 0.01;  $p$  < 0.0001;  $p$  < 0.0001 respectively) groups, while HDAC activities were raised in diabetic, cancer and DC ( $p$  < 0.05;  $p$  < 0.0001;  $p$  < 0.001) groups. Metformin supplementation resulted in significantly raised  $\text{Na}^+/\text{K}^+$ -ATPase activity in CM and DCM ( $p$  < 0.0001), while HDAC activity significantly diminished in CM and DCM ( $p$  < 0.0001;  $p$  < 0.001).

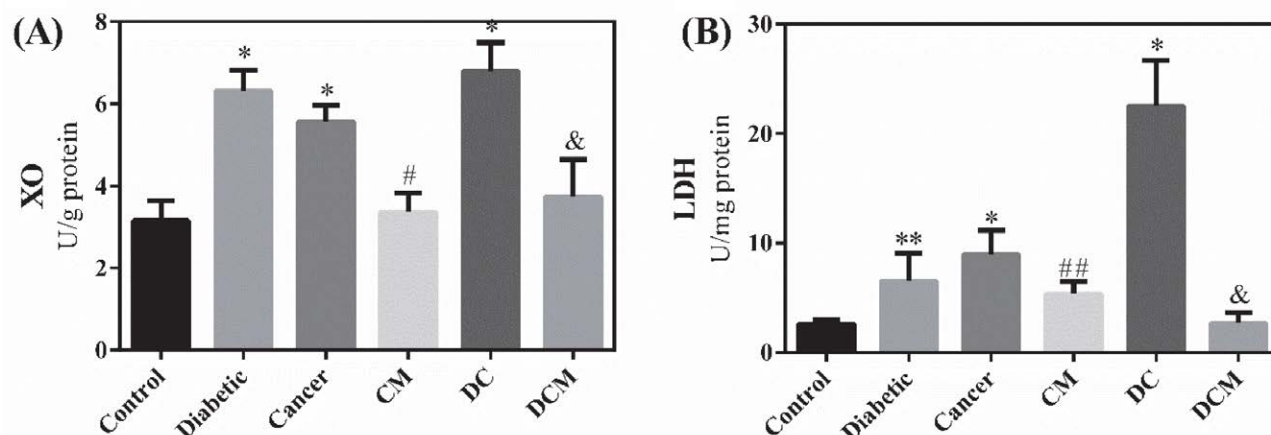


**Figure 7.** (A) Xanthine oxidase (XO) and (B) lactate dehydrogenase (LDH) activities activities of all groups of rats. CM: cancer+metformin; DC: diabetic+cancer; DCM: diabetic+cancer+metformin. The groups show off mean  $\pm$ SD. \* $p$  < 0.0001 vs control group; \*\* $p$  < 0.05 vs control group; # $p$  < 0.0001 vs cancer group; ## $p$  < 0.05 vs cancer group; & $p$  < 0.0001 vs DC group.



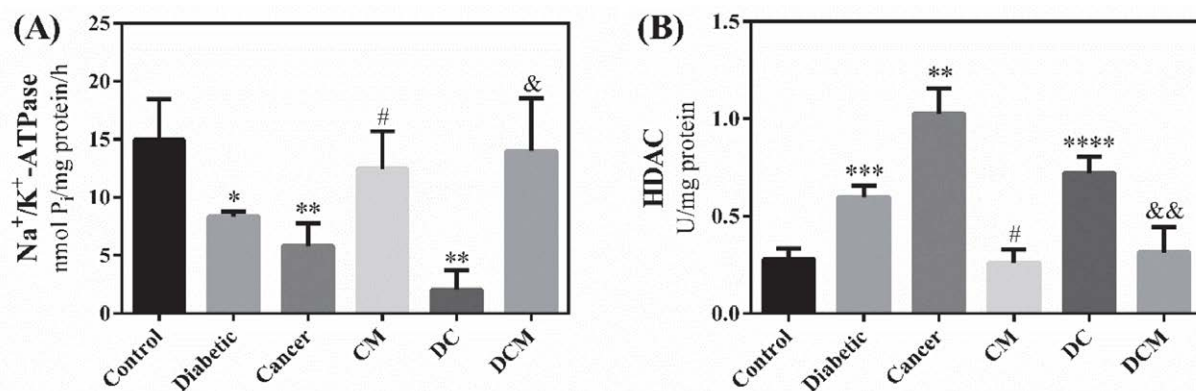


**Figure 8.** (A) Sodium/potassium ATPase ( $\text{Na}^+/\text{K}^+$ -ATPase) and (B) histone deacetylase (HDAC) activities of all groups of rats. CM: cancer+metformin; DC: diabetic+cancer; DCM: diabetic+cancer+metformin. The groups show off mean  $\pm$ SD. \* $p < 0.01$  vs control group; \*\* $p < 0.0001$  vs control group; \*\*\* $p < 0.05$  vs control group; \*\*\*\* $p < 0.001$  vs control group; # $p < 0.0001$  vs cancer group; & $p < 0.0001$  vs DC group; && $p < 0.001$  vs DC group.

### 3.2.7. Sialic Acid (SA), Hexose, Hexosamine and Fucose Levels

Glycoprotein parameters which are SA, hexose, hexosamine and fucose levels are given in Figure 9. Determining glycosylation patterns in diabetes and cancer is of significant importance in both fields of research and clinical applications. Glycosylation refers to the process by which

carbohydrates are added to proteins and lipids, and it plays a crucial role in various biological processes. They can help predict the risk of complications, such as diabetic nephropathy in diabetes. Also, altered glycosylation can differentiate between different cancer subtypes, helping to tailor treatment strategies. Therefore, the determination of glycosylation provides biochemical information about the status of both diseases. Determination of the results

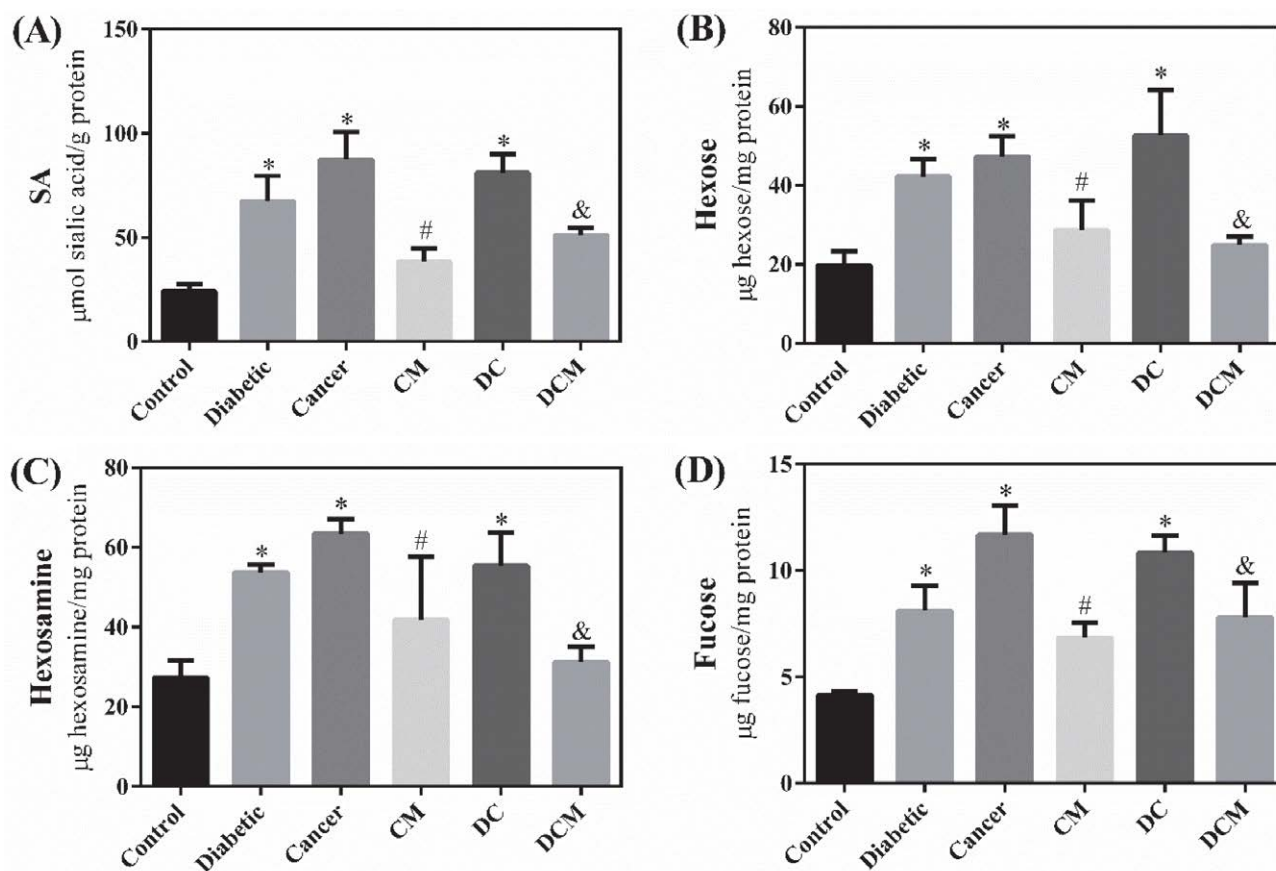


**Figure 9.** (A) Sialic acid (SA), (B) hexose, (C) hexosamine and (D) fucose levels of all groups of rats. CM: cancer+metformin; DC: diabetic+cancer; DCM: diabetic+cancer+metformin. The groups show off mean  $\pm$ SD. \* $p < 0.0001$  vs control group; # $p < 0.0001$  vs cancer group; & $p < 0.0001$  vs DC group.

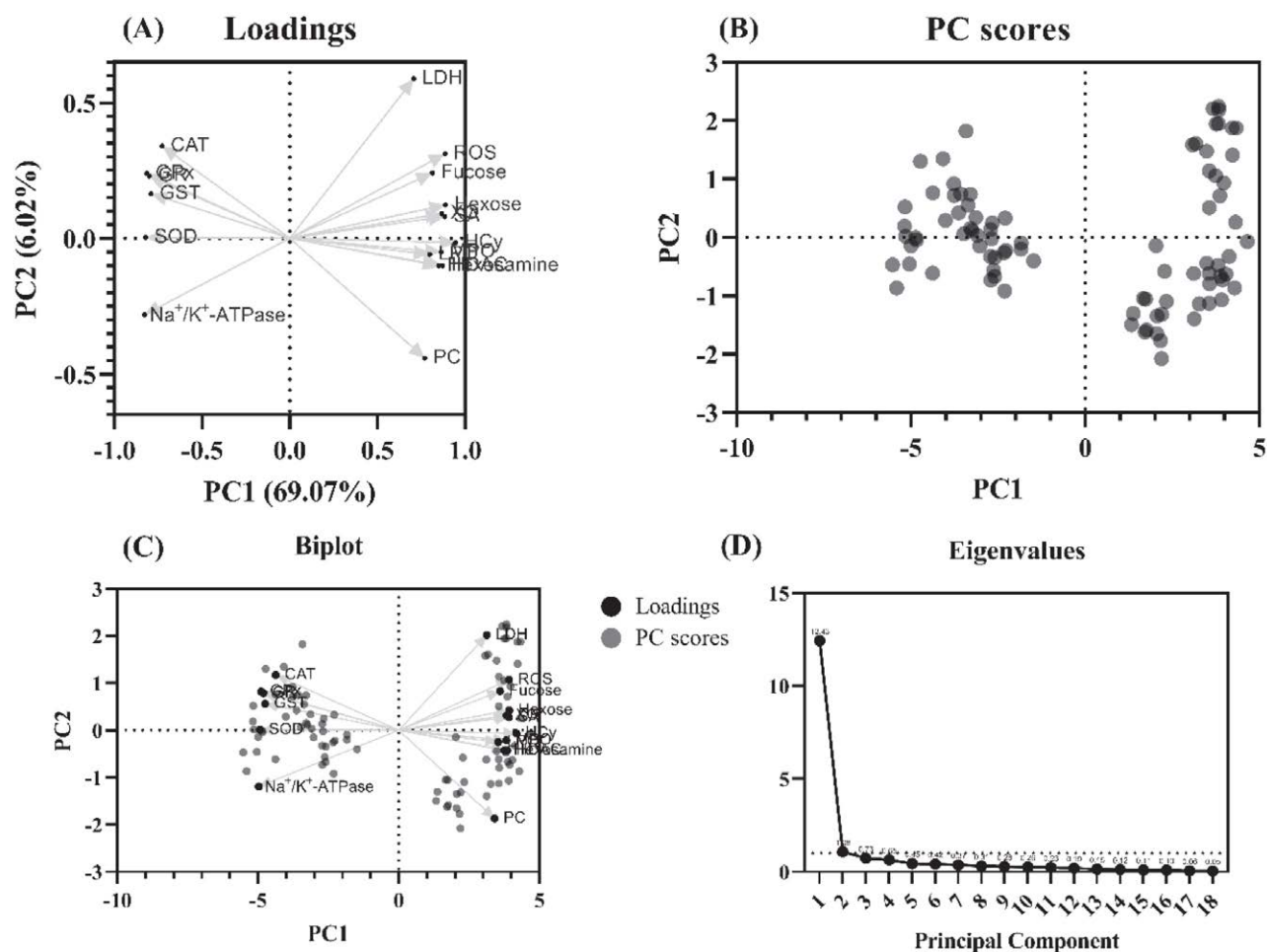


**Figure 10.** Principal component analysis of stomach biochemical parameters plots. (A) Loadings plot, (B) PC Scores, (C) Biplot and (D) Eigenvalues plots.

showed that SA, hexose, hexosamine and fucose levels were raised in the diabetic ( $p < 0.0001$ ), cancer ( $p < 0.0001$ ) and DC ( $p < 0.0001$ ) groups. Treatment with metformin to cancer and DC groups resulted in significantly diminished SA, hexose, hexosamine and fucose levels in CM ( $p < 0.0001$ ) and DCM ( $p < 0.0001$ ) groups.

### 3. 3. Principal Component Analysis

Loadings, PC Scores, Biplot and Eigenvalues graphs of principal component analysis (PCA) of stomach tissues are presented in Figure 10(A-D), respectively. The purpose of the PCA method is to assist in the general interpretation of data and to simplify the complexity of high-dimensional data. It does this by converting the data into fewer dimensions that act like a summary of the properties. In the PCA method, it combines highly correlated variables to create a smaller set of artificial variables called principal components. That's why analysts use PCA as a tool for data analysis and building predictive models. Each PC is a linear combination of the variables that went into it and principal component 1 (PC1) is the one that extracts the max-

imum variance, and principal component 2 (PC2) is the one that extracts the maximum variance from what is left. It aims to show that there is a correlation between the results obtained and the parameters by performing PCA analysis for biochemical experiments in stomach tissue, and the obtained analysis results prove this accuracy.

PCA was used to prove the relationship between the biochemical results of gastric tissues and the analysis results showed that it details approximately 75.09% of the total variation (PC1: 69.07%, PC2: 6.02%). CAT, GR, GPx, GST, SOD, ROS, fucose, hexose, XO and SA are clustered together in the first component and these are negatively correlated with Hcy, LPO, MPO, HDAC, hexosamine, PC and Na<sup>+</sup>/K<sup>+</sup>-ATPase (Figure 10A and 10C).

## 4. Discussion

Patients with diabetes have a very high risk of developing prostate cancer depending on age. Prostate cancer is usually associated with bones and lymph nodes metastasizing, but it has been reported that it metastasizes to the

stomach, albeit rarely.<sup>27–30</sup> Therefore, examining the effects of prostate cancer on stomach tissue is important because the subject is still controversial.

Although metformin is used in treating type 2 diabetes, its limited side effects make it easier to use. The most important of its side effects is that it increases the amount of lactic acid in the blood. Metformin exerts its antioxidant and anti-inflammatory effects with the activation of adenosine monophosphate protein kinase (AMPK). This activation by metformin causes inhibition of nuclear factor kappa light-chain-enhancer of activated B-cells (NF- $\kappa$ B) transcription. In addition, metformin inhibits Poly [ADP ribose] polymerase 1 (PARP-1), which acts as a cofactor of NF- $\kappa$ B. These inhibitions reduce reactive oxygen species (ROS) production, inflammatory pathways and pro-inflammatory cytokines. In addition, metformin increases the amount of NO, which antagonizes inflammation and ROS production, and this increase is due to its activation effect on AMPK.<sup>31,32</sup> On the other hand, metformin inhibits the complex I (NADH: ubiquinone oxidoreductase) of the electron transport chain, thereby helping decrease mitochondrial reactive oxygen species.<sup>33</sup>

Oxidative stress is a condition that arises due to the insufficiency of the organism's own defence system and insufficient antioxidant molecule intake, due to metabolic diseases such as diabetes and cancer. Therefore, studying antioxidant systems gives information about the status of oxidative stress in these diseases. Organism fights against free radicals in two ways. Via antioxidant enzyme systems and antioxidant molecules.<sup>34</sup> Cell defence mechanisms under oxidative stress work to correct this condition and minimise its effects. The enzymatic antioxidant system consists of SOD, CAT, GR, GPx, and GST enzymes, while nonenzymatic antioxidants consist of vitamin E, beta carotene, vitamin C, and GSH molecules. In addition, to understand the oxidative state, not only antioxidant systems, but also some other enzyme activities and biomarkers (LPO, MPO, ROS, PC etc.) are investigated.<sup>35</sup>

The reactive oxygen species levels increase in the case of oxidative stress. This increase affects the functionality of antioxidant systems of organisms. The enzymatic antioxidant system is involved in the removal of reactive oxygen species formed during oxidative stress. However, the decrease in the activity of this enzyme system contributes to the formation of oxidative stress. The superoxide radical is responsible for converting to  $H_2O_2$  by SOD catalysis, and the CAT enzyme converts  $H_2O_2$  to  $H_2O$ , forming a defence system against the harmful effects of the superoxide radical. During these reactions, the enzyme GPx reduces  $H_2O_2$  to  $H_2O$  with the natural antioxidant molecule GSH. The organism reduces GSSG to GSH with the GR enzyme to provide a concentration of GSH for this reaction, and thus the continuity of the antioxidant enzyme system is ensured. Due to the decrease in the activity of this enzyme system, an increase in the amount of ROS is likely to be observed due to the

effects of the antioxidant enzyme system, as well as Fenton reactions.<sup>36</sup> In addition, oxidative stress causes an increase in some biomarkers which are directly related to oxidative stress such as LPO and MPO. Increasing LPO levels in tissues can affect membrane fluidity and decrease the activity of membrane-bound enzymes. Due to the increased activity of MPO, the amount of hypochlorous acid (HOCl) and other strong oxidant substances increases.<sup>37</sup> The increase in LPO levels and MPO activities are biochemical parameters that are often used to provide information about the oxidative states of metabolic diseases, as they are parameters that prove the presence of oxidative stress.

In diabetes and cancer diseases, the antioxidant/oxidant balance of the organism is disrupted and oxidative stress occurs due to the increase in oxidant molecules. In a study by Chukwunonso Obi et al., it was reported that diabetic rats were given the diabetes drugs metformin, glibenclamide (GLI), and repaglinide (REP). They found that metformin increased serum SOD, CAT activity, and GSH amount compared to the diabetes group.<sup>38</sup> Ahmed Amar et al. investigated the activity of antioxidant enzymes and LPO levels in patients with prostate cancer. SOD, CAT activity, and GSH levels decreased in prostate cancer patients, while LPO levels increased.<sup>39</sup> Ozel et al. found that MPO activity increased in diabetes, cancer and diabetes+cancer groups and decreased with metformin administration.<sup>40</sup> In our study, it was found that the activities of antioxidant enzymes SOD, CAT, GR, GPx, and GST decreased in diabetic, cancer, and diabetes+cancer groups, while the levels of LPO and MPO, which are biomarkers of oxidative stress, increased. It was observed that these parameters were reversed upon treatment of these groups with metformin. It can be suggested that these effects occur due to the fact that metformin acts in the direct reduction of ROS concentrations in organisms.

Oxidative stress causes the amount of ROS to increase. Increased amount of ROS has many dangerous effects, such as disruption of the cell membrane structure and DNA damage.<sup>41</sup> The mitochondrial effects of metformin include decreased endogenous ROS production, oxidative stress, decreased DNA damage, and decreased mutagenesis in normal somatic cells.<sup>42</sup> Metformin also inhibits Ras-induced ROS production and DNA damage. PC, another oxidative stress parameter, is a very important early marker of oxidative stress due to its high stability. The high levels of protein carbonyl (CO) groups have been observed in some metabolic diseases such as diabetes, and Alzheimer's.<sup>43</sup> In addition, ROS activates p38 MAPK phosphorylation and inflammation which enhances protein modification by carbonylation.<sup>44</sup> In the present study, it was found that the amount of ROS and PC increased in the damage groups (diabetes, cancer and DC), and the levels of ROS and PC decreased with the administration of metformin. These indicate that metformin might have reduced the formation of ROS in mitochondria.

Homocysteine (HCy) derived from the metabolism of methionine is a sulphur-containing amino acid. Its uncontrolled level in patients is associated with the incidence of stroke. Additionally, HCy level in plasma is a biomarker for metabolic diseases such as diabetes, neural tube defects, Down syndrome, megaloblastic and neurodegeneration. Also, the HCy level is a biomarker of cancer. Hence, the determination of HCy levels in plasma and tissues is correlated to the status of diseases biochemically. Methionine metabolites homocysteine, cystathionine and cysteine are accepted as metastatic risk factors for prostate cancer. The high serum levels of these methionine metabolites have been used to predict the risk of early biochemical relapse and the aggressiveness of the disease.<sup>45</sup> Sannigrahi et al. showed that HCy levels of men with prostate cancer increased significantly when compared to healthy men.<sup>46</sup> The effect of metformin on serum HCy level is upward, but studies show that this effect occurs in the absence of B group vitamins or folic acid supplementation.<sup>47</sup> This may be the reason why the CM and DCM groups showed an increase of HCy levels compared to the control group. In our previous study, it was shown that HCy levels in heart tissue increased in diabetes, cancer, and DC groups<sup>48</sup>, and similar results were seen in the present study.

XO is a purine metabolism enzyme that converts xanthine and hypoxanthine to uric acid. The reaction of XO may cause oxidative stress due to the formation of  $H_2O_2$ . Hence, the activity of XO in tissues is important in determining tissue damage. The activity of XO might increase in various diseases, especially cancer and diabetes.<sup>49</sup> The changes in oxidative stress may alter p53 protein's function and affect many cellular pathways such as; DNA repair. In addition to being a genome protector, p53 protein is involved in the regulation of DNA repair, apoptosis, and cellular responses to oxidative stresses. Due to the antioxidant property of metformin, a decrease in ROS levels is observed. This effect of metformin prevents p53 from showing antioxidant properties and prevents damage to cells by preventing DNA damage.<sup>42</sup> It has been reported that p53 protein also decreases due to the decrease in oxidative stress, and this decrease is thought to be due to the antioxidant property of metformin.<sup>50</sup> Depending on the increase in DNA damage, it is possible to see an increase in the activity of enzymes in purine catabolism. XO is an enzyme involved in both purine metabolism and oxidative stress formation. It has been reported that metformin prevents oxidative stress by reducing ROS levels in addition to its protective effect on DNA.<sup>51</sup> It was observed that XO activity increased in diabetic, cancer and DC groups, but decreased with metformin administration to cancer and DC groups in the study. It can be argued that this decrease is due to the effect of metformin on both DNA repair and the prevention of oxidative stress formation.

LDH is located in cytoplasmic and catalyses the reversible conversion of lactate to pyruvate by reduction of  $NAD^+$  to NADH. Increased LDH activity is seen in many

diseases, but especially pernicious anaemia and haemolytic disorders, liver disorders, skeletal muscle disorders, and some leukaemias.<sup>52</sup> In addition, patients with cancer and/or diabetes have increasing LDH activity and lactate amounts due to anaerobic glycolysis.<sup>53</sup> Bayrak et al. found that increased LDH activity in heart tissues of diabetes, cancer and diabetes+cancer group when compared to the control group. Metformin reversed LDH activities.<sup>48</sup> Similarly, the present study found that LDH activity increased in diabetes, cancer, and diabetes+cancer groups, while metformin treatment reduced LDH activity in all these groups. It can be said that metformin may cause an effect on the protective LDH activity against oxidative stress.

$Na^+/K^+$ -ATPase is an enzyme located on the surface of the cell membrane. It has an effect on energy metabolism and helps maintain osmotic balance and membrane potential. Changes in its activity are quite significant, as they have many effects.<sup>54</sup> In a study conducted on diabetic rats, it was found that metformin increased  $Na^+/K^+$ -ATPase activity.<sup>55</sup> In the present study, it was found that  $Na^+/K^+$ -ATPase activity decreased in diabetes, cancer and diabetes+cancer groups. Metformin increased the activity of  $Na^+/K^+$ -ATPase when given compared to the experimental groups. It can be suggested that these changes may be due to both the antioxidant properties of metformin and the fact that AMPK activation increases  $Na^+/K^+$ -ATPase activity.<sup>56</sup>

Histone deacetylases (HDACs) are a parameter used in the development of inhibitors for use in the treatment of cancer. The purpose of the development and administration of HDAC inhibitors is to increase histone acetylation and transcription of tumour suppressor genes. In addition, HDAC inhibitors induce apoptosis and do so by increasing histone acetylation, expression of p21 and proapoptotic genes. Also, AMPK activation is known to increase histone acetylation. The fact that metformin stops ROS production allows it to be evaluated as a potential inhibitor of HDAC, since it performs it through this pathway.<sup>57</sup> In addition, it has been established that metformin increases histone acetylation by activation of AMPK in prostate and ovarian cancer cells.<sup>58</sup> Interleukin- $1\beta$  is involved in the formation of insulin resistance and  $\beta$ -cell insufficiency in diabetes, and the use of HDAC inhibitors is effective in the development of  $\beta$ -cells. These two connections mean that histone acetylation decreases in diabetes, and HDAC activity decreases. Considering that metformin increases histone acetylation by HDAC inhibition, it is thought that it may be useful in the treatment approach.<sup>59</sup> In the present study, it was found that HDAC activities decreased in diabetes, cancer, and diabetes+cancer groups. The treatment of these groups with metformin increased HDAC activities. It can be suggested that metformin carries out this change in HDAC activities by promoting the activation of the AMPK pathway.

Glycoproteins are important macromolecules with many metabolic effects, their levels can change in many

diseases. Glycoproteins have many functions such as cell differentiation and recognition, membrane transport, structural components of enzymes, hormones, and act as blood group substances. Alterations in glycoprotein levels have been shown to correlate with the development and/or progression of cancer, diabetes and other disease states.<sup>60</sup> Since they have many metabolic effects, it is very important to determine glycoprotein levels, and determine their connections with diseases. In diabetic individuals, increased glycation can be seen due to increased blood glucose levels. Similarly, changes in glycoprotein levels can be observed in cancer patients due to the deterioration of energy metabolism depending on the type of cancer. Similar to the findings of the present study, Chinnannavar et al. found that patients with oral squamous cell carcinoma had increased SA and fucose levels.<sup>61</sup> The outcome of the present investigation indicates that SA, hexose, hexosamine and fucose levels increased in diabetic, cancer and DC groups. All the glycoprotein parameters were reversed in metformin-treated groups. This indicates that metformin both has a protective effect against oxidative stress and lowers blood sugar levels, thereby resulting in a decrease in glycoprotein parameters.

Other publications of our study have been made on the heart, brain, kidney, testicular, and liver.<sup>40,48,62–64</sup> In all studies, it was determined that metformin had a protective effect on the damage groups diabetic, cancer, and group with both cancer and diabetes. Both studies determined that the damage caused by oxidative stress resulting from diabetes was reduced by metformin treatment, based on the relevant parameters. The data obtained in this study showed parallelism with other related studies and It has been determined that oxidative stress caused by diabetes and cancer is reduced by metformin treatment.

PCA is a method of size reduction often used to reduce the dimensionality of large datasets by converting a large set of variables into a smaller variable that still contains most of the information in the large set. PCA analysis is important in terms of making the results more understandable due to the multiplicity of biochemical parameters studied. The correlation between the obtained data and the PCA results reflects the consistency of the results. The PCA analysis applied as a result of the biochemical parameters in the stomach tissue showed a correlation between the biochemical parameters studied.

## 5. Conclusion

Men with diabetes have a higher risk of prostate cancer than healthy individuals, and it is a type of cancer that occurs especially at later ages. Prostate cancer especially metastasizes to the lymph nodes and bone, but rarely metastasizes to the stomach. Although metformin is an old drug, its popularity has increased as a result of research in recent years and it is preferred in research especially be-

cause of its effect on oxidative stress and cancer. In this study, the protective effect of metformin on the gastric tissues of diabetic rats with prostate cancer was investigated within the framework of biochemical parameters. In rats with cancer and/or diabetes, the decrease in oxidative damage after metformin treatment was determined through the studied biochemical parameters. The findings show that oxidative stress as well as alteration of glycoprotein contents are stopped by metformin treatment. Therefore, it can be said that metformin has a protective effect on the gastric tissue of diabetic and prostate cancer rats.

## Authors' Contributions

Onur Ertik: formal analysis; investigation; data curation; writing – original draft. Pinar Koroglu Aydin: formal analysis; investigation; data curation; writing – original draft. Omur Karabulut Bulan: methodology; project administration; resources; supervision; writing – review & editing. Refiye Yanardag: Conceptualisation; project administration; resources; supervision; writing – review & editing.

## Conflict of Interest

The authors declare no conflict of interest

## 6. References

1. M. Blair. *Urol. Nurs.* **2016**, *36*, 27–36. DOI:10.7257/1053-816X.2016.36.1.27
2. G. Mathur, S. Nain, P. K. Sharma. *Academic J. Cancer Res.* **2022**, *8*, 1–9. DOI: 10.5829/idosi.ajcr.2015.8.1.9336
3. B. Turner, L. Drudge-Coates. *Cancer Nurs. Pract.* **2010**, *9*, 29–36. DOI:10.7748/cnp2010.12.9.10.29.c8126
4. D. M. Parkin, F. Bray, J. Ferlay, P. Pisani. *CA Cancer J. Clin.* **2005**, *55*, 77–108. DOI:10.3322/canjclin.55.2.74
5. E. Giovannucci, D. M. Harlan, M. C. Archer, R. M. Bergenstal, S. M. Gapstur, L. A. Habel, M. Pollak, J. G. Regensteiner, D. Yee. *Diabetes Care.* **2010**, *33*, 1674–85. DOI:10.2337/dc10-0666
6. R. Mallik, T. A. Chowdhury. *Diabetes Res. Clin. Pract.* **2018**, *143*, 409–19. DOI:10.1016/j.diabres.2018.05.023
7. R. J. Shaw, K. A. Lamia, D. Vasquez, S. H. Koo, N. Bardeesy, R. A. Depinho, M. Montminy, L. C. Cantley. *Science.* **2005**, *310*, 1642–46. DOI:10.1126/science.1120781
8. J. Whitburn, C. M. Edwards, P. Sooriakumaran. *Curr. Urol. Rep.* **2017**, *18*, 46. DOI:10.1007/s11934-017-0693-8
9. A. Haring, T. J. Murtola, K. Talala, K. Taari, T. L. J. Tammela, A. Auvinen. *Scand. J. Urol.* **2017**, *51*, 5–12. DOI:10.1080/21681805.2016.1271353
10. I. Bugan, Z. Karagoz, S. Altun, M. B. Djamgoz. *Basic Clin. Pharmacol. Toxicol.* **2016**, *118*, 200–07. DOI:10.1111/bcpt.12484
11. A. Ledwozyw, J. Michalak, A. Stepień, A. Kałdziołka. *Clin.*

- Chim. Acta.* **1986**, *155*, 275–83.  
DOI:10.1016/0009-8981(86)90247-0
12. H. Wei, K. Frenkel. *Cancer Res.* **1991**, *51*, 4443–49.
13. A. A. Mylroie, H. Collins, C. Umbles, J. Kyle. *Toxicol. Appl. Pharmacol.* **1986**, *82*, 512–20.  
DOI:10.1016/0041-008X(86)90286-3
14. H. Aebi. *Methods Enzymol.* **1984**, *105*, 121–26.  
DOI:10.1016/S0076-6879(84)05016-3
15. E. Beutler. Red cell metabolism: A manual of biochemical methods, Vol. 12, Grune & Stratton, **1971**.
16. D. E. Paglia, W. N. Valentine. *J. Lab. Clin. Med.* **1967**, *70*, 158–69.
17. W. H. Habig, W. B. Jakoby. *Methods Enzymol.* **1981**, *77*, 398–405. DOI:10.1016/S0076-6879(81)77053-8
18. Y. Zhang, J. Chen, H. Ji, Z. G. Xiao, P. Shen, L. H. Xu. *BMC Complement. Altern. Med.* **2018**, *18*, 343.  
DOI:10.1186/s12906-018-2414-3
19. R. L. Levine, D. Garland, C. N. Oliver, A. Amici, I. Climent, A. G. Lenz, B. W. Ahn, S. Shaltiel, E.R. Stadtman. *Methods Enzymol.* **1990**, *186*, 464–78.  
DOI:10.1016/0076-6879(90)86141-H
20. E. D. Corte, F. Stirpe. *Biochem. J.* **1968**, *108*, 349–51.  
DOI:10.1042/bj1080349
21. R. Bais, M. Philcox. *Eur. J. Clin. Chem. Clin. Biochem.* **1994**, *32*, 639–55.
22. A. Ridderstap, S. Bonting. *Am. J. Physiol.* **1969**, *217*, 1721–27.  
DOI:10.1152/ajplegacy.1969.217.6.1721
23. K. Lorentz, T. Weiß, E. Kraas. *J. Clin. Chem. Clin. Biochem.* **1986**, *24*, 189–98. DOI:10.1515/cclm.1986.24.3.189
24. R. J. Winzler. *Methods Biochem. Anal.* **1955**, *2*, 279–311.  
DOI:10.1002/9780470110188.ch10
25. Z. Dische, L. B. Shettles. *J. Biol. Chem.* **1948**, *175*, 595–603.  
DOI:10.1016/S0021-9258(18)57178-7
26. O. H. Lowry, N. J. Rosebrough, A. L. Farr, R. J. Randall. *J. Biol. Chem.* **1951**, *193*, 265–75.  
DOI:10.1016/S0021-9258(19)52451-6
27. F. Christoph, M. Grünbaum, F. Wolkers, M. Müller, K. Miller. *Urology.* **2004**, *63*, 778–79.  
DOI:10.1016/j.urology.2003.12.009
28. W. H. Holderman, J. M. Jacques, M. O. Blackstone, T. A. Brasitus. *J. Clin. Gastroenterol.* **1992**, *14*, 251–54.  
DOI:10.1097/00004836-199204000-00012
29. K. P. Hong, S. J. Lee, G. S. Hong, H. Yoon, B. S. Shim. *Korean J. Urol.* **2010**, *51*, 431–33. DOI:10.4111/kju.2010.51.6.431
30. A. A. Onitilo, J. M. Engel, J. M. Resnick. *Clin. Med. Res.* **2010**, *8*, 18–21. DOI:10.3121/cmr.2010.855
31. A. Chakraborty, S. Chowdhury, M. Bhattacharyya. *Diabetes Res. Clin. Pract.* **2011**, *93*, 56–62.  
DOI:10.1016/j.diabres.2010.11.030
32. C. Wang, C. Liu, K. Gao, H. Zhao, Z. Zhou, Z. Shen, Y. Guo, Z. Li, T. Yao, X. Mei. *Biochem. Biophys. Res. Commun.* **2016**, *477*, 534–540. DOI:10.1016/j.bbrc.2016.05.148
33. D. Diniz Vilela, L. Gomes Peixoto, R. R. Teixeira, N. Belele Baptista, D. Carvalho Caixeta, A. Vieira de Souza, H. L. Machado, M. N. Pereira, R. Sabino-Silva, F. S. Espindola. *Oxid. Med. Cell Longev.* **2016**, *2016*, 1–9. DOI:10.1155/2016/6978625
34. C. K. Roberts, K. K. Sindhu. *Life Sci.* **2009**, *84*, 705–12.  
DOI:10.1016/j.lfs.2009.02.026
35. E. Birben, U. M. Sahiner, C. Sackesen, S. Erzurum, O. Kalayci. *World Allergy Organ. J.* **2012**, *5*, 9–19.  
DOI:10.1097/WOX.0b013e3182439613
36. Z. Haida, M. Hakiman. *Food Sci. Nutr.* **2019**, *7*, 1555–63.  
DOI:10.1002/fsn3.1012
37. M. J. Davies, C. L. Hawkins. *Antioxid. Redox Signal.* **2020**, *32*, 957–81. DOI:10.1089/ars.2020.8030
38. B. Chukwunonso Obi, T. Chinwuba Okoye, V. E. Okpashi, C. Nonye Igwe, E. Olisah Alumanah. *J Diabetes Res.* **2016**, *2016*, 1635361. DOI:10.1155/2016/1635361
39. S. A. Ahmed Amar, R. Eryilmaz, H. Demir, S. Aykan. *Aging Male.* **2019**, *22*, 198–206. DOI:10.1080/13685538.2018.1488955
40. A. B. Ozel, E. Dagsuyu, P. K. Aydin, I. Bugan, O. K. Bulan, R. Yanardag, A. Yarat. *Biol. Trace Elem. Res.* **2022**, *200*, 1164–70.  
DOI:10.1007/s12011-021-02708-z
41. S. Hebbbar, E. Knust. *Bioessays.* **2021**, *43*, e2100096.  
DOI:10.1002/bies.202100096
42. C. Algire, O. Moiseeva, X. Deschênes-Simard, L. Amrein, L. Petruccielli, E. Birman, B. Viollet, G. Ferbeyre, M. N. Pollak. *Cancer Prev. Res.* **2012**, *5*, 536–43.  
DOI:10.1158/1940-6207.CAPR-11-0536
43. N. Fernando, S. Wickremesinghe, R. Niloofa, C. Rodrigo, L. Karunanayake, H. J. de Silva, A. R. Wickremesinghe, S. Premawansa, S. Rajapakse, S. M. Handunnetti. *PLoS One.* **2016**, *11*, e0156085. DOI:10.1371/journal.pone.0156085
44. N. Nokkaew, P. Mongkolpathumrat, R. Junsiri, S. Jindaluang, N. Tualamun, N. Manphatthanakan, N. Saleese, M. Intasang, J. Sanit, P. Adulyarittikhul, K. Kongpol, S. Kumphune, N. Nernpermpisooth. *Indian J. Clin. Biochem.* **2021**, *36*, 228–34.  
DOI:10.1007/s12291-019-0815-9
45. S. Stabler, T. Koyama, Z. Zhao, M. Martinez-Ferrer, R. H. Allen, Z. Luka, L. Loukachevitch, P. E. Clark, C. Wagner, N. A. Bhowmick. *Plos One.* **2011**, *6*, e22486.  
DOI:10.1371/journal.pone.0022486
46. S. Sannigrahi, D. K. Pal, M. Mukhopadhyay. *JCDR.* **2020**, *14*, XCO1–XCO4. DOI:10.7860/JCDR/2020/42790.13541
47. Q. Zhang, S. Li, L. Li, Q. Li, K. Ren, X. Sun, J. Li. *Nutrients.* **2016**, *8*, 798. DOI:10.3390/nu8120798
48. B. Bayrak, P. Koroglu, O. Karabulut Bulan, R. Yanardag. *Hum. Exp. Toxicol.* **2021**, *40*, 297–309.  
DOI:10.1177/0960327120947452
49. M. G. Battelli, L. Polito, M. Bortolotti, A. Bolognesi. *Cancer Med.* **2016**, *5*, 546–557. DOI:10.1002/cam4.601
50. L. E. Nelson, R. J. Valentine, J. M. Cacicedo, M. S. Gauthier, Y. Ido, N. B. Ruderman. *Am. J. Physiol. Cell Physiol.* **2012**, *303*, C4–C13. DOI:10.1152/ajpcell.00296.2011
51. I. Dogan Turacli, T. Candar, E. B. Yuksel, S. Kalay, A. K. Oguz, S. Demirtas. *Biochimie.* **2018**, *154*, 62–68.  
DOI:10.1016/j.biochi.2018.08.002
52. R. Klein, O. Nagy, C. Tóthová, F. Chovanová. *Vet. Med. Int.* **2020**, *2020*, 5346483. DOI:10.1155/2020/5346483
53. Y. Wu, Y. Dong, M. Atefi, Y. Liu, Y. Elshimali, J. V. Vadgama. *Mediat. Inflamm.* **2016**, *2016*, 1–12.  
DOI:10.1155/2016/6456018

54. W. Kopec, B. Loubet, H. Poulsen, H. Khandelia. *Biochem.* **2014**, *53*, 746–54. DOI:10.1021/bi401425g
55. A. A. Safriyua, I. Semuyaba, S. K. Lawal, M. O. Buhari, E. A. Tiyo, M. Kalange, A. O. Okpanachi, M. Nansunga. *J. Biomed. Eng.* **2018**, *11*, 254–62. DOI:10.4236/jbise.2018.119021
56. B. Benziante, M. Björnhölm, S. Pirkmajer, R. L. Austin, O. Kotova, B. Viollet, J. R. Zierath, A. V. Chibalin. *J. Biol. Chem.* **2012**, *287*, 23451–63. DOI:10.1074/jbc.M111.331926
57. L. Galdieri, H. Gatla, I. Vancurova, A. Vancura. *J. Biol. Chem.* **2016**, *291*, 25154–66. DOI:10.1074/jbc.M116.742247
58. A. Vancura, I. Vancurova. *Oncotarget.* **2017**, *8*, 39939. DOI:10.18632/oncotarget.17829
59. D. P. Christensen, M. Dahllöf, M. Lundh, D. N. Rasmussen, M. D. Nielsen, N. Billestrup, L. G. Grunnet, T. Mandrup-Poulsen. *Mol. Med.* **2011**, *17*, 378–90. DOI:10.2119/molmed.2011.00021
60. J. Zhao, T. H. Patwa, D. M. Lubman, D. M. Simeone. *Curr. Opin. Mol Ther.* **2008**, *10*, 602–10.
61. S. Chinnannavar, L. Ashok, K. Vidya, S. K. Setty, G. Narasimha, R. Garg. *J. Int. Soc. Prev. Community Dent.* **2015**, *5*, 446–50. DOI:10.4103/2231-0762.169211
62. P. Koroglu Aydın, B. B. Bayrak, O. Karabulut Bulan, R. Yanardag. *Toxicol. Mech. Methods.* **2021**, *31*, 489–500. DOI:10.1080/15376516.2021.1919810
63. P. Koroglu Aydın, O. Karabulut Bulan, I. Bugan, I. B. Turkyilmaz, S. Altun, R. Yanardag. *Cell Biochem. Funct.* **2022**, *40*, 60–70. DOI:10.1002/cbf.3674
64. P. Koroglu Aydın, I. B. Turkyilmaz, I. Bugan Gul, O. Karabulut Bulan, R. Yanardag. *J. Diabetes Metab. Disord.* **2023**, *22*, 225–236. DOI:10.1007/s40200-022-01109-w

## Povzetek

Ljudje s sladkorno boleznijo imajo večje tveganje za nastanek raka prostate, ljudje z rakom prostate pa so nagnjeni k metastazam na želodcu. Zato raziskovalci še naprej iščejo nove pristope k zdravljenju posameznikov z vsemi navedenimi boleznimi hkrati. Zaščitni učinek metformina (ki se uporablja pri zdravljenju sladkorne bolezni) pri raku še naprej potrjujejo številne raziskave. V tej raziskavi je bilo ugotovljeno, da biokemični parametri kažejo zaščitni učinek na tkiva želodca ob dajanju metformina pri skupini z rakom in skupini z rakom ter sladkorno boleznijo. Z analizo glavnih komponent je bilo ugotovljeno, da proučevani biokemični parametri v tkivu želodca kažejo korelacijo.



Except when otherwise noted, articles in this journal are published under the terms and conditions of the Creative Commons Attribution 4.0 International License

# Synergistic, Additive and Antagonistic Interactions of Some Phenolic Compounds and Organic Acids Found in Grapes

Crina Vicol\* and Gheorghe Duca

Laboratory of Physical and Quantum Chemistry, Institute of Chemistry, Moldova State University, Chişinău, MD-2028, Republic of Moldova

\* Corresponding author: E-mail: crina.vicol@ichem.md

Received: 21-04-2023

## Abstract

The antioxidant interactions between several natural phenolic and non-phenolic compounds (catechin, quercetin, rutin, resveratrol, gallic acid and ascorbic acid) and organic acids (tartaric, citric and dihydroxyfumaric acids) were studied using the DPPH method. Main additive and antagonistic interactions have been found for the combinations of catechin, quercetin, resveratrol and gallic acid with tartaric and citric acids; such behavior can be due to the enhanced stability of the phenolic compounds in acidic media. Rutin and ascorbic acid showed good synergistic effects with tartaric and citric organic acids, which could be due to the polymerization processes in the case of rutin and the change in the mechanism of action in the case of ascorbic acid. In combination with dihydroxyfumaric acid, the mixtures showed dose-dependent synergistic, additive, or antagonistic antioxidant interactions. Good synergistic effects were observed for the binary mixtures of dihydroxyfumaric acid with ascorbic acid, catechin, and rutin.

**Keywords:** antioxidant interactions; synergistic interactions; additive interactions; antagonistic interactions; phenolic compounds; organic acids.

## 1. Introduction

Antioxidant interactions (AI) have been investigated more intensively in the last twenty years. The interest in AI is justified by the scientific intention to understand the natural processes, but also by the real need to improve the antioxidant activity of natural compounds used in the food, medical, pharmaceutical and other industries, by finding beneficial combinations between antioxidant and non-antioxidant compounds. Until now, synergistic, additive, and antagonistic AI between natural compounds have been declared.<sup>1</sup> Some explanations and hypotheses on the mechanism of mutual interaction of involved compounds have been offered, and imply (1) the regeneration processes, (2) formation of antioxidants' intermolecular complexes, dimers or adducts, and (3) complementary effects that presume the effect of solvent, pH, concentration and solubility.<sup>1,2</sup>

Organic acids such as tartaric and citric are common acids, non-antioxidant compounds, found in large amounts in many fruits, including grapes.<sup>3,4</sup> Although they are not free radical scavengers,<sup>5,6</sup> their influence on

the antioxidant activity of natural reducing compounds has already been demonstrated. The authors found that the combinations of various natural radical scavengers with organic acids have synergistic AI.<sup>5-9</sup> On the other hand, the interactions between grape phenolic compounds were found to be antagonistic, which is due to the polymerization processes and the decrease in the number of electron donating groups.<sup>10-14</sup>

The compounds' concentrations showed to be equally important for antioxidant activity and AI.<sup>12,14,15</sup> According to the reported data,<sup>15-19</sup> it is generally believed that stronger synergistic effects can be obtained when compounds are used at concentrations found in nature (in this case, in grapes),<sup>7,12,20-25</sup> since multicomponent systems similar in composition and concentration to those found in food have multiple mechanisms of action and can inhibit oxidation at many different stages.<sup>26</sup>

Based on this, the present study aims to investigate the influence of different concentrations of common organic acids, namely tartaric and citric acids, on the antioxidant activity of phenolic and non-phenolic compounds found in



grapes: catechin, quercetin, rutin, resveratrol, gallic acid and ascorbic acid. In addition, the AI of the above compounds was studied with the natural organic acid, dihydroxyfumaric acid, which has potent antioxidant activity,<sup>6,27</sup> and is known to be important for the “glyoxylate scenario”<sup>28,29</sup>. Experimental data were obtained by the DPPH method, readily available and widely used antioxidant assay, so that the results could be easily compared with literature data.

## 2. Experimental

### 2.1. General

Quercetin dihydrate (QUE), (+)-catechin (CAT), (+)-rutin trihydrate (RUT), *trans*-resveratrol (RES), L-ascorbic acid (AA), dihydroxyfumaric acid hydrate (DHF), L-(+)-tartaric acid (TA) and 2,2-diphenyl-1-picrylhydrazyl (DPPH) were purchased from Sigma (Germany), gallic acid (GA), citric acid (CA) and 96% ethanol (EtOH) were purchased from MicTan (Republic of Moldova).

Absorbance measurements were recorded on a Lambda 25 UV/VIS spectrophotometer (Perkin Elmer), at 20 °C, using 10 mm quartz cuvettes.

The pH was measured on a HANNA HI 121 pH-meter, using 96% EtOH as solvent.

### 2.2. Preparation of Standard Solutions and Mixtures of Phenolic Compounds and Organic Acids

Standard solutions of AA (1.4 mM), CAT (1.2 mM), GA (1.4 mM), QUE (1.0 mM), RUT (1.0 mM), RES (0.5 mM), DHF (2.0 mM), TA (40.0 mM) and CA (40.0 mM) were prepared in 96% EtOH. For a better dissolution, some of the samples were sonicated in the ultrasonic bath for 3 – 5 min. For the determination of the Efficient Concentration (EC<sub>50</sub>) of single compounds, different concentrations of CAT, GA, QUE, RUT, RES, AA, and DHF ranging from 50 μM to 1000 μM, and different concentrations of TA and CA ranging from 0.2 mM to a maximum of 20 mM were prepared by dilution from stock solutions, using 96% EtOH.

To study AI, the given concentrations of CAT, GA, QUE, RUT, RES, and AA (ranging from 50 μM to 1000 μM) were mixed with three concentrations of TA or CA, found in grapes and wines (16×10<sup>-4</sup> N, 160×10<sup>-4</sup> N, 800×10<sup>-4</sup> N), and with three concentrations of DHF (2×10<sup>-4</sup> N, 4×10<sup>-4</sup> N, 8×10<sup>-4</sup> N). This approach was described by LoScalzo in an attempt to clarify the influence of some organic acids on the antioxidant activity of ascorbic acid.<sup>5</sup>

### 2.3. DPPH Free Radical Scavenging Activity

The concentration of DPPH in 96% EtOH was verified daily though the calibration line and was around 0.03

g/L (Absorbance = 1.000 ± 0.020 a.u.). The absorption maximum of DPPH was found to be at 517 nm with a molar extinction coefficient ε, of 11858 ± 16 M<sup>-1</sup> cm<sup>-1</sup>.

The antioxidant activity of individual compounds and mixtures was estimated according to procedure described previously.<sup>30</sup> To 3.9 mL of free radicals, 0.1 mL of the prepared samples containing the tested compounds was added. Absorbance at 517 nm was recorded when the reactions reached equilibrium, which was after 30 min for GA, AA, DHF, TA, and CA, and after 60 min for QUE, CAT, RUT, and RES. The blank reference cuvette contained 96% EtOH. All measurements were performed at least in triplicate.

### 2.4. Data Analysis

Following the approach reported by Brand-Williams et al.,<sup>30</sup> the antioxidant activity of the compounds or mixtures of compounds tested was expressed as an EC<sub>50</sub> value, defined as the concentration required to annihilate 50% of the radical and expressed as mole of antioxidant per mole of DPPH\* (mole AOX/mole DPPH). This parameter is inversely related to the antioxidant capacity of the compound studied, with lower EC<sub>50</sub> values indicating higher antioxidant activity.

In order to determine EC<sub>50</sub> parameter, the percentage of remaining DPPH\* (%DPPH rem) at the steady state was calculated according to equation 1, and the results obtained for each sample were plotted against the mole AOX/mole DPPH ratio to determine the EC<sub>50</sub> value.

$$\%DPPH \text{ rem} = \left( \frac{A_{\text{sample}}}{A_{\text{control}}} \right) \times 100 \quad (1)$$

The A<sub>sample</sub> corresponds to the absorbance of the sample at steady state and A<sub>control</sub> corresponds to the absorbance of the sample at time zero. Because the EC<sub>50</sub> is related to the stoichiometry of the reaction, results presented as EC<sub>50</sub> values are more accurate and free of error; in addition, these results are easier to compare with literature data.

The percentage of inhibition (%Inhibition) was obtained using equation 2, and was further used to determine the AI type.

$$\%Inhibition = \left( 1 - \frac{A_{\text{sample}}}{A_{\text{control}}} \right) \times 100 \quad (2)$$

From equation 2, A<sub>sample</sub> is the absorbance of the sample at steady state and A<sub>control</sub> is the absorbance of the sample at time zero.

The AI effect of a mixture was calculated from the ratio between the experimental value of the percent inhibition of the mixture (%I<sub>mixture</sub>) and the theoretical value (%I<sub>theoretical</sub>)<sup>9</sup> (equation 3):

$$AI = \left( \frac{\%I_{\text{mixture}}}{\%I_{\text{theoretical}}} \right) \quad (3)$$

Where

$$\%I_{theoretical} = \%I_A + \%I_O - \left( \frac{\%I_A \times \%I_O}{100} \right) \quad (4)$$

$\%I_A$  and  $\%I_O$  represent the percent inhibition of antioxidants and organic acids, respectively, tested in reaction with DPPH\* alone (equation 4).

Therefore, a synergistic effect is found when the AI > 1; if AI = 1, then the interaction is additive; and an AI < 1 reveals an antagonistic effect.

The data obtained were analyzed with ANOVA and Student's *t* tests to evaluate the statistical significance of the difference between the means using the Microsoft Excel programme. A *p* value of 0.05 was considered significant.

### 3. Results and Discussion

#### 3.1. Determination of the EC<sub>50</sub> Values

The literature frequently reports the use of the DPPH method to study the antioxidant activity of individual compounds and to determine the type of AI between natural compounds.<sup>8,9,13,31</sup> The DPPH\* can be scavenged through both HAT and SET mechanisms,<sup>32</sup> depending on the reaction conditions. This suggests that DPPH\* takes either an electron or an H atom from the antioxidant to be neutralized.

Phenolic compounds possess good antioxidant activity against various free radicals<sup>11–13,31</sup> due to the presence of functional groups and conjugated double bonds. Table 1 shows the EC<sub>50</sub> obtained for individual compounds in the reaction with DPPH\*, as well as the EC<sub>50</sub> values for the combinations of AA, CAT, QUE, RUT, RES and GA with organic acids – DHF, TA and CA. As mentioned earlier, the lower is the EC<sub>50</sub> for a compound, the higher is the antioxidant activity. On this basis, GA is the best radical scavenger under these reaction conditions, followed by the other compounds in the order: QUE < CAT = DHF < AA = RUT < RES.

**Table 1.** EC<sub>50</sub> values for individual antioxidant compounds and for their combinations with organic acids.

		Antioxidant compounds							
		AA 30	CAT 60	QUE 60	RUT 60	RES 60	GA 30	DHF 30	
EC <sub>50</sub> (mole AOX/mole DPPH)	No organic acid	0.24±0.00	0.18±0.02	0.15±0.00	0.24±0.00	1.15±0.03	0.06±0.00	0.18±0.01	
	TA	16×10 <sup>-4</sup> N	0.22±0.01	0.19±0.00	0.16±0.01	0.25±0.01	1.22±0.01	0.06±0.00	
		160×10 <sup>-4</sup> N	0.22±0.01	0.18±0.01	0.18±0.00	0.26±0.00	0.98±0.00	0.06±0.01	
		800×10 <sup>-4</sup> N	0.23±0.00	0.18±0.01	0.18±0.00	0.27±0.01	1.78±0.00	0.06±0.01	
	CA	16×10 <sup>-4</sup> N	0.23±0.00	0.18±0.00	0.17±0.00	0.25±0.00	1.59±0.02	0.06±0.00	
		160×10 <sup>-4</sup> N	0.23±0.00	0.21±0.02	0.18±0.03	0.26±0.00	1.14±0.00	0.05±0.00	
		800×10 <sup>-4</sup> N	0.24±0.01	0.18±0.00	0.18±0.02	0.29±0.01	2.83±0.04	0.06±0.00	
	DHF	2×10 <sup>-4</sup> N	0.20±0.00	0.13±0.00*	0.14±0.01*	0.21±0.00*	1.32±0.01	0.09±0.00	
		4×10 <sup>-4</sup> N	0.17±0.00	0.12±0.00*	0.13±0.00*	0.17±0.00*	2.19±0.04	0.08±0.01	
		8×10 <sup>-4</sup> N	0.09±0.01	0.09±0.00*	0.09±0.00*	0.09±0.02*	1.01±0.01	0.06±0.00	

Data are presented as means ± deviation (n ≥ 3). \* Significant difference (*p* < 0.05) calculated using one-sample Student's *t* test.

Similar results have been reported by several authors;<sup>11,13,31,33</sup> the few differences are attributed to the use of different solvents, which have been shown to have a significant effect on the mechanism of action of antioxidants.<sup>6</sup>

The stilbene RES possesses good antioxidant capacity against reactive oxygen species, especially against superoxide anion.<sup>34</sup> However, in the reaction with DPPH\*, RES demonstrates low antioxidant activity, which is confirmed by previous studies.<sup>11,13,31,33</sup> The compound DHF, which in this study was addressed as an organic acid, possesses good antioxidant activity, with an EC<sub>50</sub> = 0.18, which means that DHF in a multicomponent system can affect the overall antioxidant activity even at low concentration. Contrary to DHF, the organic acids TA and CA showed insignificant radical scavenging activity – even at high concentrations, TA and CA are capable of scavenging only 3% of free radicals. Similar results have been reported by others.<sup>5,8,9</sup>

As expected, the presence of organic acids in the solutions lowers the pH to a more acidic value (Table 2). Such pH values are representative of wines, natural juices or fruits.<sup>4,35</sup>

**Table 2.** pH values for each concentration of organic acids (TA, CA and DHF) used in experiments. EtOH was used as solvent.

	Organic acids			
	TA	CA	DHF	96% EtOH
Concentrations				6.58
	16×10 <sup>-4</sup> N	4.43	4.42	
	160×10 <sup>-4</sup> N	3.75	3.89	
	800×10 <sup>-4</sup> N	3.10	3.58	
	2×10 <sup>-4</sup> N		4.04	
	4×10 <sup>-4</sup> N		3.86	
	8×10 <sup>-4</sup> N		3.64	
Student's <i>t</i> test	*	*	*	*

Significant difference (*p* < 0.05) to value 6.58. *p* values were calculated using one-sample Student's *t* test.

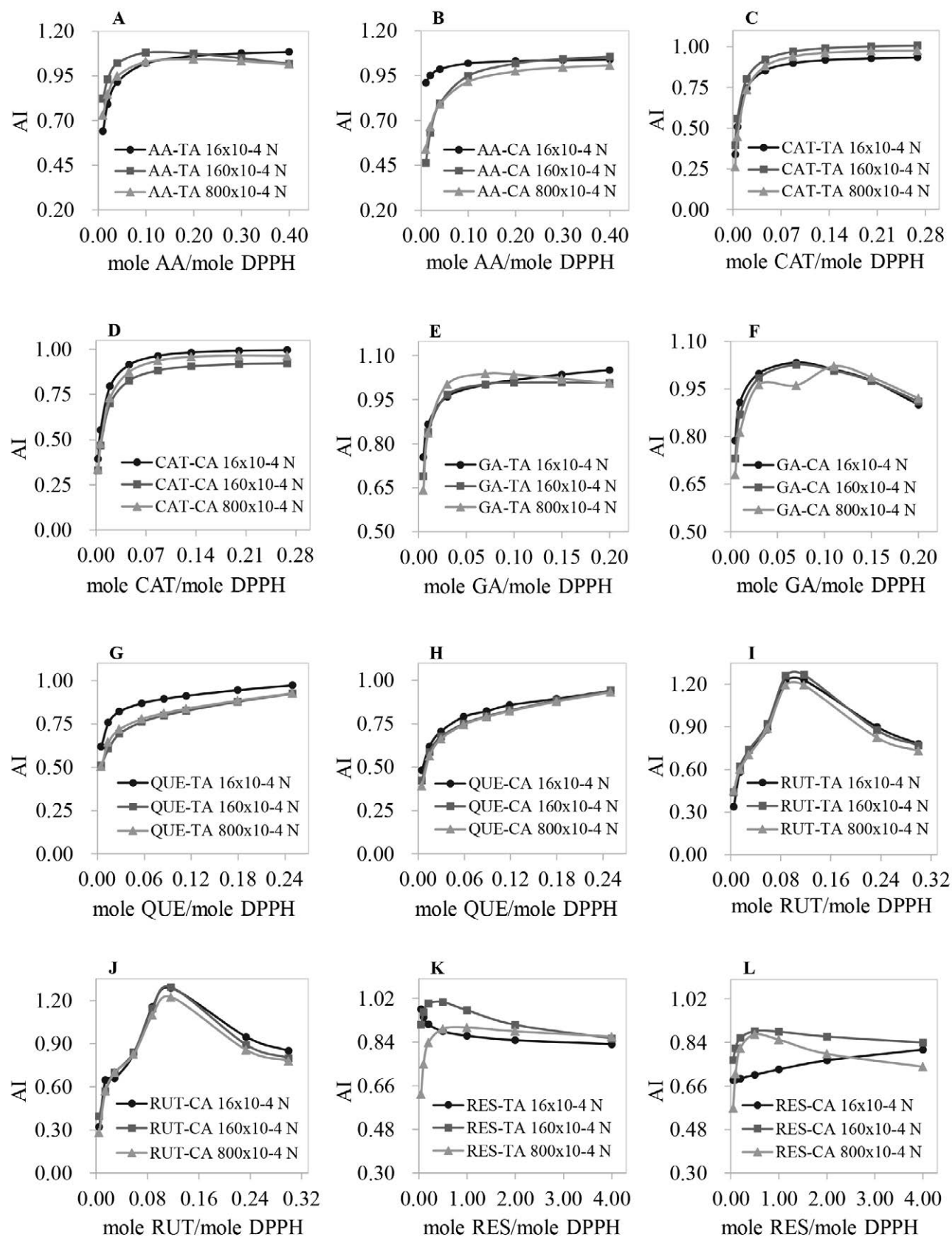


**Figure 1.** AI of AA and phenolic compounds in the combination with different concentrations of TA (A, B, C, D, E, F) and different concentrations of CA (G, H, I, J, K, L). Data are presented as mean values ( $n \geq 3$ ).

Different results were observed by adding organic acids – DHF, TA or CA, to the reaction mixtures between the antioxidant compound and DPPH<sup>•</sup>. The decrease in EC<sub>50</sub> values, which can be interpreted as cooperative activity of two compounds that increases the overall antioxidant activity of the mixture, was registered for combinations of AA – DHF and AA – TA, and for polyphenols CAT, QUE and RUT with DHF. On the contrary, the addition of TA or CA to solutions of phenolic compounds have a negative impact on the EC<sub>50</sub> values of the mixtures and in most cases, leads to an increase in this parameter.

The concentration of organic acids showed to be important for the antioxidant activity of the tested mixtures, however a prevalent tendency cannot be reported at this point. For example, increasing the DHF concentration from  $2 \times 10^{-4}$  N to  $8 \times 10^{-4}$  N the EC<sub>50</sub> for AA, CAT, QUE and RUT decreases, but it becomes higher for RES and GA.

Concerning the other organic acids, the presence of TA or CA in concentrations of  $16 \times 10^{-4}$  N and  $160 \times 10^{-4}$  N has a slightly positive effect on the antioxidant activity of AA, but a negative or no effect in the mixtures with CAT, QUE, RUT and for the majority of the combinations with GA. Except for the presence of  $160 \times 10^{-4}$  N of both TA and CA in the reaction mixtures of RES and DPPH<sup>•</sup>, the other two concentrations of organic acids produce significant increase in the EC<sub>50</sub> values, especially for the combination of RES with  $800 \times 10^{-4}$  N of CA.

The investigation of different concentrations of DHF, TA, and CA shows that the acidic environment in grapes and grape products can positively or negatively affect the antioxidant activity of phenolic and non-phenolic compounds; it also shows that not only the acidic environment is crucial, but also the intrinsic properties are important. Although the variation of EC<sub>50</sub> values shows that the presence of organic acids affects the antioxidant activity of phenolic compounds and AA, these data are insufficient to classify the tested mixtures according to the type of AI – synergistic, additive, or antagonistic; therefore, further calculations are needed.

### 3. 2. AI Between Phenolic Compounds and Organic Acids TA and CA

Among all three types of AI, synergistic interactions are the most advantageous, therefore more intensively investigated. Recently, authors have demonstrated the importance of the non-antioxidant substances such as organic acids, glucose, etc., for the antioxidant activity of naturally occurring bioactive compounds,<sup>5,7–9</sup> and for the quality of the food products.<sup>36–38</sup> The concentrations of the compounds have been shown to be equally important for AI, so that different molar ratios between the same compounds can lead to synergistic, additive, or antagonistic effects.<sup>9,14,15,39–41</sup> In this study, the utilization of three concentrations of organic acids was important for evaluation

of their impact on the antioxidant activity of the phenolic and non-phenolic natural compounds. In addition, the importance of the concentration of the antioxidants tested was evaluated by applying different concentrations of phenolic compounds or AA as depicted in Figure 1.

#### The AI between AA and other organic acids

R. LoScalzo<sup>5</sup> and Piang-Siong et al.,<sup>9</sup> investigated the interaction of AA with organic acids in alcoholic solution, and found significant synergistic effects. Similarly, our results revealed that at certain concentrations, TA and CA ameliorate the antioxidant activity of AA. Data reported in Figure 1 (cases A and G) show that TA has a better influence than CA, being observed six combinations of AA – TA with synergistic effects, and only one combination of AA – CA with the same effect. In both cases, smaller concentrations of organic acids, namely  $16 \times 10^{-4}$  N and  $160 \times 10^{-4}$  N, cause the enhancement of antioxidant activities, being registered synergistic effects of 1.08 for the mixture AA – TA, and 1.06 for AA – CA. Equally important is the concentration of AA. Strong antagonistic effects have been noticed at lower concentrations of AA, and by increasing the AA's content, the AI values rise, reaching the additive and synergistic effects. The notable antagonism, in the range of 0.46 – 0.79, characteristic for lower AA concentrations, and the synergistic effects found at higher AA concentrations, emphasize the importance of the molar ratios in which both natural compounds are mixed.

The enhancement of the antioxidant activity of AA in the presence of organic acids may be due to the action mechanism of this free radical scavenger. The ionization of AA is not supported in this media because of the high amount of ions of TA or CA present in the solution. Consequently, the SPLET (sequential proton loss electron transfer) mechanism is inhibited, and the HAT (hydrogen atom transfer) mechanism becomes operative for DPPH<sup>•</sup> annihilation. The AA is known to be efficient in HAT reaction by donating two H atoms to the radical species.<sup>42</sup> R. LoScalzo suggested that a low pH can contribute to the slow regeneration of AA, thus justifying the enhancement of the antioxidant activity.<sup>5</sup>

#### The AI between CAT and organic acids

In the presence of organic acids, the phenolic compound CAT shows a progressive evolution of the AI values from strong antagonistic effects to additive effects (Figure 1, cases B and H). Samples containing small concentrations of CAT and TA or CA, demonstrated antagonistic interactions in the range of 0.33 – 0.93; the increase of CAT's concentration generated additive AI. Contrary to the example of AA's interactions with organic acids, the change in the TA or CA content does not affect considerably the antioxidant activity of CAT. Similar antagonistic interactions were reported by Zhang et al.,<sup>43</sup> who investi-

gated the influence of organic acids on the antioxidant activity of phenolic compounds from Zhenjiang aromatic vinegar.

The reaction of CAT and DPPH<sup>•</sup> was previously studied in alcohols.<sup>44–47</sup> It was demonstrated that there is the possibility of (1) covalent adduct formation between the free radical and the oxidized form of CAT, and (2) the chance of polymerization reaction, which proved to be less effective for DPPH<sup>•</sup> scavenging.<sup>46</sup> The two pathways depend on the polarity of the solvent and on the flavanol/DPPH<sup>•</sup> ratio.<sup>46</sup> The addition of organic acids to the reaction mixture can affect significantly the reactivity of CAT, and finally the total antioxidant activity. Catechins showed to be more stable at low pH,<sup>48,49</sup> their antioxidant activity being 10 times higher at neutral pH than at acidic pH.<sup>50</sup> In acidic environments like those created by the addition of TA or CA (Table 2), the oxidation rates of the phenolic compounds increase. As a consequence, the ability of CAT to donate electrons and to scavenge DPPH<sup>•</sup> decreases, thus, only additive and antagonistic interactions are registered. A pH dependent change of the antioxidant activity of polyphenols was noticed by others;<sup>51,52</sup> the greater reactivity of phenolic compounds at high pH was attributed to the rapid electron transfer from the phenolate ion to the reactive species.

According to data, polar solvents maintain the SPLET mechanism of antioxidant action of phenolic compounds,<sup>46,53</sup> because these solvents accept protons from the phenol forming the phenolate anion followed by the electron transfer to the reactive species. The presence of the acid ions in the reaction mixture suppresses the deprotonation, and, by this, the SPLET mechanism, so the electron donor will be the parent molecule.<sup>54</sup> At low pH, CAT is expected to be oxidized via the ET-PT (electron transfer – proton transfer) mechanism, which implies the electron abstraction from the neutral molecule followed by the release of a proton.<sup>55</sup>

The diminution of the antioxidant activity of CAT in the presence of TA or CA can also be justified by the fact that low pH conditions might enhance CAT loss on account of its polymerization and condensation.<sup>49</sup> The investigation of the condensed tannins proved that under acidic conditions two competing reactions occur: (1) the polymeric or oligomeric chain can be degraded to their monomers and (2) the flavonoid units can condense.<sup>56</sup> The processes of hydrolysis, condensation and heterocyclic ring opening at low pH are described in the literature as common reactions for tannins.<sup>57</sup> Studies showed that the formation of oligomers of CAT or QUE is due to the cleavage of the interflavonoid bond, and can also be acid-catalyzed.<sup>58,59</sup> Such opposite and competing reactions are characteristic for wine systems, where the presence of organic acids promotes both polymerization and hydrolysis of phenolic compounds.<sup>60</sup>

## The AI between GA and organic acids

The AI of GA with TA or CA is characterized by additive and antagonistic effects (Figure 1, cases C and I). In the presence of TA, the AI values are lower at small concentrations of GA, but augment to additive effects at bigger GA/DPPH molar ratios. The only synergistic effect of 1.05 has been registered for the GA/DPPH molar ratio of 0.20 and the  $16 \times 10^{-4}$  N of TA. The samples containing GA and CA showed an ascending tendency of AI values (maximum AI value of 1.03) followed by a descending one, starting from 0.15 GA/DPPH molar ratio. In this case, no synergistic effects have been noticed. These results are supported by similar AI between GA and organic acids that have been reported by Piang-Siong et al.<sup>9</sup> The fact that the increase of TA or CA concentrations does not cause major variations of the AI values proves that the acidity, regardless of its magnitude, has the same effect on the antioxidant activity of GA. One exception is the situation with the smallest concentration of TA, where the reaction keeps a positive tendency.

According to the EC<sub>50</sub> values (Table 1) and to the AI values of GA with organic acids, it can be inferred that TA or CA have slightly negative or no effect on the GA's antioxidant activity. Therefore, it can be supposed that GA operates efficiently in acidified ethanolic solutions through the HAT mechanism. The carboxyl group of GA along with the phenolic OH tends to deprotonate in ethanol, but the presence of the ions of TA or CA suppresses this process, therefore, likewise the example of CAT, the SPLET mechanism is hindered. Hydrogen transfer mechanism becomes operative for GA in this environment. This assumption is in agreement with the data from DFT calculations,<sup>61–63</sup> which demonstrate that GA is an excellent free radical scavenger by H atom donation.<sup>18,64</sup>

## The AI between QUE and organic acids

The interaction between different concentrations of QUE and TA or CA demonstrated only antagonistic effects in the range of 0.50 – 0.94 and 0.39 – 0.94, respectively, except for one additive interaction of QUE – TA with the value 0.97 (Figure 1, cases D and J). Figure 1D is clearly indicating that at larger TA concentrations the antagonistic effects are stronger. This fact and the persistence of the antagonistic interactions independently of the TA or CA content underline the idea of diminution of the free radical scavenging activity of polyphenols in acidic environments.<sup>46,51,52,54</sup> Similar to catechins,<sup>48,49</sup> QUE is more stable at low pH, and therefore less susceptible to oxidation.

## The AI between RUT and organic acids

The flavonoid RUT manifests a specific behavior in the presence of organic acids. At lowest concentrations of the polyphenol, strong antagonistic effects, in the range of 0.29 – 0.92, can be noticed, (Figure 1, cases E and K). How-

ever, at the 0.09 and 0.12 RUT/DPPH molar ratios, significant synergistic interactions, namely 1.10 – 1.29, are observed, which represent the highest AI values in this series of experiments. The synergistic effects of these two RUT/DPPH molar ratios decrease slightly with the increase of the RUT content. In the same time, the AI between RUT and TA or CA appears to be independent from the concentration of organic acids. These results indicate that, in the case of RUT and TA or CA combinations, the synergistic effect relies mainly on the concentration of polyphenol, being independent of the acid's content. Still, the presence of the organic acids in the reaction mixture is essential for the synergistic effect to occur, as long as the antioxidant activity of RUT is smaller without TA or CA (data not shown).

RUT is the only phenolic compound in this series of experiments to demonstrate such distinctive behavior characterized by a sharp peaking of the AI at 0.09 and 0.12 RUT/DPPH molar ratios. This effect can be caused by the presence of rutinose in the RUT structure, which is absent in the molecule of other tested phenolics. More than that, QUE and RUT have the same aglycon structure, however, QUE in combination with TA or CA manifested only additive and antagonistic effects. Data<sup>45</sup> show that the structural differences in the C ring – the C3 hydroxyl group is present in QUE, but is glycosylated in the case of RUT, affect considerably the antioxidant activity.

Also, the change from antagonistic to synergistic AI may be due to the concentration of reactants, as it has been found for different CAT/AA ratios.<sup>15</sup> The concentration of AA affects CAT's behavior, supporting the formation of different structures, including CAT dimerization to the procyanidin structures.<sup>15</sup> This could also be the situation for the RUT – TA or CA synergistic effect, however, for this example, the concentration of organic acids appears to be insignificant – matters only their presence. This assumption is supported by other findings that describe the formation of dimers and polymers from CAT, QUE and RUT in acidic conditions.<sup>58,59</sup> On the other hand, it should be admitted that some polymerizations and adduct formations may be determined by the flavanol/DPPH<sup>•</sup> ratio, as previously demonstrated,<sup>44–46</sup> along with the formation of new structures with antioxidant properties.

### The AI between RES and organic acids

The combination of stilbene RES with organic acids shows mainly antagonistic effects (Figure 1, cases F and L). The tendencies described by the AI values are different for each concentration of organic acids. The strongest antagonistic interactions are noticed for the concentration of TA or CA of  $16 \times 10^{-4}$  N, and the less antagonistic effect – for the mixtures containing  $160 \times 10^{-4}$  N. The negative effect of organic acids on the RES antioxidant activity is in agreement with the data reported by Shang et al.<sup>54</sup> The authors showed that in acidic media the ioni-

zation of the RES is suppressed, along with the SPLET mechanism of action, therefore, the antioxidant activity is reduced.<sup>54</sup>

Based on data from Figure 1 and on the results described in the literature, it can be concluded that organic acids can influence the antioxidant activity of phenolic compounds by either determining their mechanism of action, or by inducing polymerization or cleavage of the intermolecular bonds of the formed oligomers. Authors<sup>11,13,14,39,65</sup> demonstrated that combination of natural polyphenols shows mainly antagonistic effects, because of their tendency to combine themselves through polymerization, thus decreasing the availability of the hydroxyl groups. We suggest that the addition of organic acids to the reaction mixtures, followed by the increase of acidity, could prevent polymerization by intermolecular bonds break and would maintain a high degree of low complexity structures, and a standing number of electron donating groups. This hypothesis is supported by the fact that the natural environment of the antioxidants from fruits and vegetables is characterized by high content of organic acids and a relatively high acidity, comparable with that created by addition of TA, CA or DHF (Table 2). Also, the antioxidant power of extracts from fruits and vegetables that proved to be stronger than to the sum of the antioxidant activities of individual compounds<sup>11,14</sup> can be argued by the presence of less active compounds from natural sources, like organic acids.

### 3. 3. AI Between Phenolic Compounds and Dihydroxyfumaric Acid

The DHF was for the first time discovered in 1994 by Fenton<sup>66</sup> in his attempt to oxidize TA in the presence of hydrogen peroxide and iron. Lately, the DHF was intensively studied from the perspective of the "glyoxylate scenario".<sup>28,29,67</sup> These investigations have been focused on the propounded idea that DHF could be the central starting materials of chemical constitution for primordial metabolisms – or, the building-blocks for the biogenic molecules.<sup>28,29,67,68</sup>

From the point of view of its occurrence, DHF is widespread in natural products, being a constituent of the reductive citric acid cycle, and therefore a direct precursor of amino acids<sup>67</sup> and a constituent of the cycle of dicarbonic acids – the Baround' cycle of tartaric acid and its intermediate products transformation to oxalic acid.<sup>69,70</sup> DHF is found in wines as reaction product of the TA oxidation by hydroxyl radicals;<sup>71</sup> also, it is added in wines for the enhancement of the quality parameters.<sup>72,73</sup>

### The AI between AA and DHF

The DHF showed to be a strong DPPH<sup>•</sup> scavenger, its antioxidant activity being comparable with and even stronger than that of the AA, in terms of the kinetics and

stoichiometry.<sup>6,27</sup> Starting from this context, we assumed that in combination with phenolic compounds DHF would behave similarly to AA. The synergistic interactions between phenolic compounds and AA have been described in the past few years,<sup>12,15,21,74</sup> authors suggesting that the synergistic effects are due to the regeneration of the polyphenols by the AA. In our attempt to clarify the type of AI between DHF and natural phenolic compounds similar outcomes have been expected.

Previously, we reported data on the synergistic and antagonistic interactions between DHF and AA in 98% EtOH and in wine matrix.<sup>6</sup> This study was performed using the Stopped-flow method, which enabled us to gather data only for the first 2 sec of the reaction. Comparing our results with the data reported in the literature,<sup>27,31</sup> we concluded that, after 2 sec of interaction of AA or DHF alone or in combination against DPPH<sup>•</sup>, the reaction is incomplete and requires further investigations. Figure 2A shows

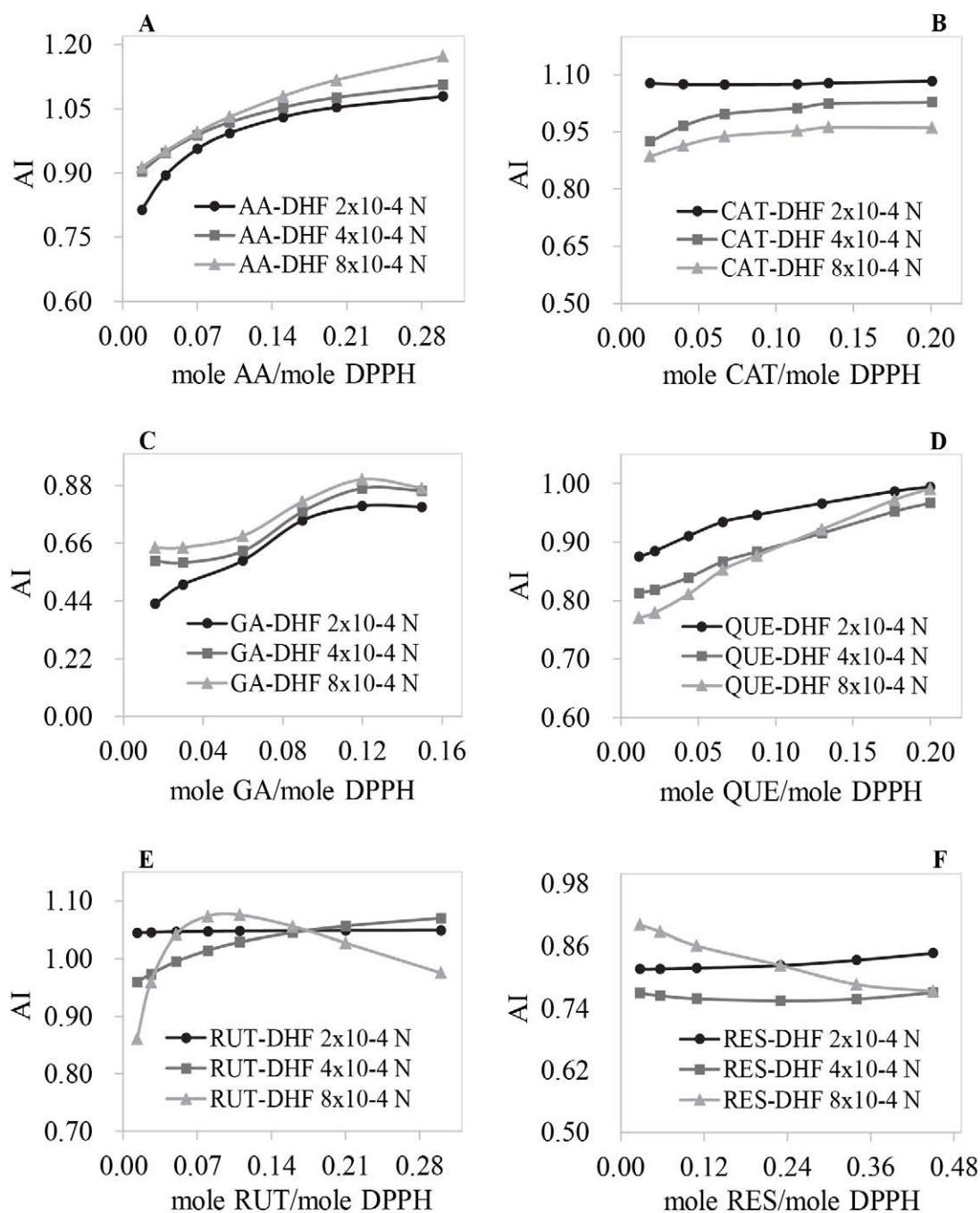


**Figure 2.** AI of AA and phenolic compounds in the combination with different concentrations of DHF. Data are presented as mean values ( $n \geq 3$ ).

that after 30 min of AA – DHF interaction with DPPH<sup>•</sup>, dose – dependent synergistic effects are registered, confirming our suppositions.

The AI values of AA – DHF combinations evolve from antagonistic to synergistic ones as a consequence of the increase of both antioxidants' concentrations. The highest synergistic value of 1.17 was obtained for the mixture of 0.30 AA/DPPH molar ratio with  $8 \times 10^{-4}$  N of DHF (Figure 2A). By using NMR spectroscopy, it was made an attempt to understand the mechanism of synergistic antioxidant action of AA – DHF mixtures in the reaction with DPPH<sup>•</sup>.<sup>75</sup> The hypothesis of a mutual regeneration of antioxidants proved to be valid only in deuterated methanol – chloroform solvents, where partial regeneration of the dehydroascorbic acid by the DHF was established.<sup>75</sup> Therefore, it was admitted that in 96% EtOH some regeneration processes can also occur. On the other hand, the regeneration by AA of the oxidized form of DHF has not been demonstrated. Moreover, the keto groups characteristic to the DHF oxidized form, that were expected to appear in the NMR spectra, have not been detected. Still, the redox reaction between DHF and DPPH<sup>•</sup> did occur as demonstrated by the change in colour of the radical from purple to dark yellow. Previously, it was reported that DHF decomposes spontaneously in aqueous solutions to form carbon dioxide and glycolaldehyde via two consecutive first – order reactions.<sup>68,76</sup> The highest rates of decarboxylation process are in the pH range of 2 – 3.5, because at low pH the keto – enol equilibrium is shifted to the keto form of DHF, which is instable and decomposes.<sup>76–78</sup> In our case, the solutions formed of 96% EtOH, AA and DHF possess relatively high acidity – 3.64 to 4.04 (Table 2), characterized by the prevailing of keto form,<sup>77</sup> that may determine partial decarboxylation of DHF.

### The AI between CAT and DHF

The AI between CAT and DHF (Figure 2B) demonstrate good synergistic effects. The majority of synergistic AI's values (maximum of 1.08) can be noticed in the mixtures with the lowest concentration of DHF ( $2 \times 10^{-4}$  N). Samples containing  $4 \times 10^{-4}$  N and  $8 \times 10^{-4}$  N of DHF demonstrated mostly additive AI, this indicating that the increase of the DHF content is disadvantageous for the total antioxidant activity of the mixtures. The reason behind this effect may be the lowering of the pH caused by higher concentrations of DHF, which negatively affects CAT antioxidant activity. Several authors also reported synergistic interactions between strong antioxidants and phenolic compounds,<sup>12,15,21,74</sup> and suggested as explanation the regeneration mechanism of action. The DHF is a strong and fast antioxidant<sup>6,27</sup> and it will be the first to interact with DPPH<sup>•</sup>, before CAT, thus, the regeneration of CAT by DHF can be excluded. Also, the decarboxylation of oxidized form of DHF in the acidic solution makes impossible its reduction to the initial form by the CAT.

In this case, the operative mechanism of action appears to be the formation of adducts and oligomeric compounds. Similar dose – dependent synergistic behavior of CAT was noticed in combination with AA.<sup>15</sup> Different molar ratios of CAT/AA demonstrated both enhanced antioxidant activity and prooxidant effect.<sup>15</sup> Authors<sup>15,44,46</sup> found the oligomerization of CAT with subsequent formation of procyanidin structures to be a decisive factor influencing the antioxidant – prooxidant balance, and, therefore, the type of AI.

### The AI between GA and DHF

The GA – DHF mixtures show mainly antagonistic effects ranging from 0.43 to 0.82. From Figure 2C it can be noticed that the addition of larger concentrations of DHF slightly improves the total antioxidant activity, however, the majority of the interactions remain in the range of antagonistic values. Unlike the AA – DHF and QUE – DHF (Figure 2D) interactions which follow only antioxidant ascending tendencies, the example of GA – DHF does not respect it. The highest AI value of 0.90 can be observed for 0.12 GA/DPPH molar ratio in combination with  $8 \times 10^{-4}$  N of DHF

Based on the data reported by Piang – Siong et al.<sup>9</sup> on the GA's AI with *trans*-aconitic acid, which have similar structural units as DHF, comparable synergistic effects have been expected from GA – DHF interactions. On the other hand, GA in combination with different concentrations of AA showed strong antagonistic effects.<sup>79</sup> Other antagonistic effects of the mixtures of phenolic compounds and GA have been recently described.<sup>80,81</sup> Authors suggested that the antagonism is a consequence of the weaker antioxidant regeneration by the strongest one – hypothesis that was supported by the analysis of the reduction potentials.<sup>81</sup> Also, the effect of the difference in reaction kinetics between the antioxidant and free radical has been implied.<sup>80</sup>

The oligomerization of GA was also admitted, however, according to the existing data, the polymerization of GA would enhance the antioxidant activity of the reaction products,<sup>82,83</sup> which is in discrepancy with our results.

### The AI between QUE and DHF

The interaction of QUE with DHF shows mainly additive effects which did not exceed the 0.99 value. According to Figure 2D, larger concentrations of DHF affects negatively the total antioxidant activity of the mixtures, and produce antagonistic effects. These outcomes were unforeseen since in the literature are described synergistic regenerative interactions between QUE and AA, AA being a strong antioxidant like DHF.<sup>12,21</sup> Other authors<sup>84,85</sup> also found synergistic interactions of the mixture QUE – AA, and of QUE with other class of compounds.<sup>86,87</sup> The additive effects found in the experiment can be due to the DHF



decarboxylation, which would make impossible the reduction of *o*-quinone to QUE, and by this, excludes the hypothesis of mutual regeneration of QUE and DHF.

### The AI between RUT and DHF

Good antioxidant activity is revealed in the mixtures of RUT and DHF, with a preponderance of synergistic interactions in the range of 1.05 – 1.08 (Figure 2E). The concentration of DHF affects the total antioxidant activity and the AI. The mixtures consisting of different concentrations of RUT and  $2 \times 10^{-4}$  N of DHF possess synergistic effects of 1.05 independently of the change of RUT's content. For the second concentration of DHF –  $4 \times 10^{-4}$  N, the AI start at the value 0.96 and increases till 1.07 once the RUT/DPPH molar ratio is augmented. At  $8 \times 10^{-4}$  N of DHF, the highest synergistic effect of 1.07 can be noticed for the 0.11 RUT/DPPH molar ratio, followed by a significant decrease of the AI.

Similar synergistic results have been obtained by Tavadyan et al.<sup>88</sup> in binary mixtures of bioflavonoids and AA or trolox, using the ORAC method. They observed synergistic interactions of AA with flavonoids RUT and naringin that have O-glucosyl group in the molecular structure; in the same time, AA in combination with QUE and morin showed antagonistic effect. These findings are in accordance with our data on the QUE and RUT antioxidant interaction with DHF (Figure 2, cases D and E). Tavadyan et al.<sup>88</sup> suggested that the enhanced antioxidant activity of RUT – AA mixture is due to the presence of the glycoside in its structure that condition the formation of intramolecular hydrogen bonds between hydrogen atoms and phenolic OH groups responsible for the interaction with radicals and two-electron-donor oxygen atoms of the glucosyl substituent. In the situation of RUT – DHF interactions, the O-glucosyl group can influence positively the stability of DHF, and prevents the decarboxylation process. This idea is supported by recent revelations on the polymerization process involving the DHF, acetone and methanol.<sup>89</sup> Therefore, such situation would enable some regeneration processes between RUT and DHF.

### The AI between RES and DHF

The combination of RES and DHF showed mostly antagonistic effects (0.75 – 0.83) and only few additive interactions (0.85 – 0.90) (Figure 2F). Samples containing RES and the first two concentration of DHF –  $2 \times 10^{-4}$  N and  $4 \times 10^{-4}$  N, demonstrate that the increase in the content of organic acid lead to drastic decrease of AI values. For mixtures with  $8 \times 10^{-4}$  N DHF the AI evolve negatively – from additive to antagonistic effects, with the increase of the RES content.

Other investigations reported both synergistic and antagonistic interactions between RES and various phenolic compounds, with the prevalence of the antagonistic

ones.<sup>11,13,81</sup> In reactions with free radicals, RES yields various oligomers as final products.<sup>54,90,91</sup> The NMR analysis showed that in combination with AA, the oxidation of RES generates viniferins.<sup>92</sup> In this case, the regeneration mechanism of synergistic antioxidant action can be excluded. We assume that in the presence of DHF, the polymerization of RES could be accelerated, this would reduce the number of OH group available for free radicals scavenging, like it was the case of other phenolic compounds.<sup>15,39</sup>

## 4. Conclusions

Organic acids affect the antioxidant activity of phenolic and non-phenolic natural compounds. Their presence can lead to synergistic, additive or antagonistic interactions depending on the antioxidant/organic acid, antioxidant/free radical molar ratio, acidity, mechanism of action, etc. The TA and CA significantly affect the antioxidant activity of CAT, GA, QUE and RES, their combinations mainly causing additive and antagonistic interactions. This can be justified by the fact that phenolic compounds are less susceptible to oxidation and polymerization at high pH. Such behavior is favorable in multi-component phenolic mixtures, where polymerization followed by a decrease in electron donating groups has been observed. Organic acids in combination with RUT enhance the antioxidant activity of polyphenol, showing strong synergistic effects. We assume that some polymerization processes took place and the final products have higher antioxidant activity against DPPH\*. The combination of AA and TA or CA shows good synergistic interactions, which may be due to the suppression of the SPLET mechanism of AA antioxidant activity and the promotion of the HAT mechanism.

The DHF added to phenolic and non-phenolic compounds demonstrates dose-dependent AI, which may be related to the high antioxidant activity of the organic acid. The combinations of CAT or RUT with DHF show good synergistic effects along with additive effects; with QUE, additive and antagonistic AI are observed. The hypothesis of mutual regeneration of polyphenols and DHF is generally discarded since the decarboxylation of DHF in acidic solutions has already been demonstrated. An exception is the combination RUT–DHF, where the O-glucosyl group of RUT may positively affect the stability of DHF and prevent the decarboxylation process. Higher concentrations of AA in combination with DHF show good synergistic effects against DPPH\*, but also additive and antagonistic effects at lower AA and DHF concentrations. The GA and RES mixed with DHF show mainly antagonistic effects. It is suggested that the antagonistic AI is the consequence of the decarboxylation of DHF, together with adverse polymerization processes and the effect of the different reaction kinetics between the antioxidant and DPPH. Further studies and experimental data are needed to confirm these

conclusions and to clarify the mechanisms of antioxidant action.

## Acknowledgements

This work has been performed under the Moldovan National Research Project Nr. 20.80009.5007.27 “Physical-Chemical Mechanisms of the Redox Processes with Electron Transfer in Vital, Technological and Environmental Systems”.

## 5. References

- M. Olszowy-Tomczyk, *Phytochem. Rev.*, **2020**, *19*, 63–103. DOI:10.1007/s11101-019-09658-4
- X. Chen, H. Li, B. Zhang and Z. Deng, *Crit. Rev. Food Sci. Nutr.*, **2022**, *62*, 5658–5677. DOI:10.1080/10408398.2021.1888693
- G. Fia, G. Bucalossi, C. Proserpio and S. Vincenzi, *Aust. J. Grape Wine Res.*, **2022**, *28*, 8–26. DOI:10.1111/ajgw.12522
- V. D. Cotea, C. V. Zănoagă and V. V. Cotea (Ed.): *Tratat de Oenochimie*, Editura Academiei Române, București, **2009**, *1*, 684.
- R. L. Scalzo, *Food Chem.*, **2008**, *107*, 40–43. DOI:10.1016/j.foodchem.2007.07.070
- C. Vicol, C. Cimpoiu and G. Duca, *Studia UBB Chemia*, **2021**, *66*, 49–58. DOI:10.24193/subbchem.2021.02.04
- R. L. Scalzo, *Eur. Food Res. Technol.*, **2021**, *247*, 2253–2265. DOI:10.1007/s00217-021-03785-z
- P. R. Quiroga, V. Nepote and M. T. Baumgartner, *Food Chem.*, **2019**, *277*, 267–272. DOI:10.1016/j.foodchem.2018.10.100
- W. Piang-Siong, P. de Caro, A. Marvilliers, X. Chasseray, B. Payet, A. Shum Cheong Sing and I. Bertrand, *Food Chem.*, **2017**, *214*, 447–452. DOI:10.1016/j.foodchem.2016.07.083
- M. Pinelo, L. Manzocco, M. J. Nunez and M. C. Nicoli, *J. Agric. Food Chem.*, **2004**, *52*, 1177–1180. DOI:10.1021/jf0350515
- P. Iacopini, M. Baldi, P. Storchi and L. Sebastiani, *J. Food Compos. Anal.*, **2008**, *21*, 589–598. DOI:10.1016/j.jfca.2008.03.011
- L. Choueiri, V. Sanda, A. Calokerinos and P. Kefalas, *Food Chem.*, **2012**, *133*, 1039–1044. DOI:10.1016/j.foodchem.2012.01.057
- D. Skroza, I. Generalic Mekinic, S. Svilovic, V. Simat and Visnja Katalinic *J. Food Compos. Anal.*, **2015**, *38*, 13–18.
- D. R. A. Muhammad, D. Praseptianga, D. Van de Walle and K. Dewettinck, *Food Chem.*, **2017**, *231*, 356–364. DOI:10.1016/j.foodchem.2017.03.128
- M. A. A. Mahmoud, V. S. Chedea, A. Detsi and P. Kefalas, *Food Res. Int.*, **2013**, *51*, 907–913. DOI:10.1016/j.foodres.2013.02.023
- B. L. Freeman, D. L. Eggett and T. L. Parker *J. Food Sci.*, **2010**, *75*, C570–C576. DOI:10.1111/j.1750-3841.2010.01717.x
- J. D. Reber, D. L. Eggett and T. L. Parker *Int. J. Food Sci. Nutr.*, **2011**, *62*, 445–452. DOI:10.3109/09637486.2010.549115
- L. M. López-Martínez, H. Santacruz-Ortega, R. E. Navarro, R. R. Sotelo-Mundo and G. A. González-Aguila, *PLoS One*, **2015**, *10*, e0140242. DOI:10.1371/journal.pone.0140242
- H. Palafox-Carlos, J. Gil-Chávez, R. R. Sotelo-Mundo, J. Namiesnik, S. Gorinstein and G. A. González-Aguilar, *Molecules*, **2012**, *17*, 12657–12664. DOI:10.3390/molecules171112657
- T. L. Parker, S. A. Miller, L. E. Myers, F. E. Miguez and N. J. Engeseth, *J. Agric. Food Chem.*, **2010**, *58*, 209–217. DOI:10.1021/jf903080f
- M. Abou Samra, V. S. Chedea, A. Economou, A. Calokerinos and P. Kefalas, *Food Chem.*, **2011**, *125*, 622–629. DOI:10.1016/j.foodchem.2010.08.076
- D. Procházková, I. Bou and N. Wilhelmová, *Fitoterapia*, **2011**, *82*, 513–523. DOI:10.1016/j.fitote.2011.01.018
- M. Carocho and I. C. F. R. Ferreira, *Food Chem. Toxicol.*, **2013**, *51*, 15–25. DOI:10.1016/j.fct.2012.09.021
- D. Ribeiro, M. Freitas, A. M. S. Silva, F. Carvalho and E. Fernandes, *Food Chem. Toxicol.*, **2018**, *120*, 681–699. DOI:10.1016/j.fct.2018.07.060
- R. Sotler, B. Poljšak, R. Dahmane, T. Jukić, D. P. Jukić, C. Rotim, P. Trebše and A. Starc, *Acta Clin. Croat.*, **2019**, *58*, 726–736.
- E. A. Decker, R. J. Elias and D. J. McClements in D. Julian (ed.). *Oxidation in foods and beverages and antioxidant applications: management in different industry sectors*. Elsevier, **2010**, 225–243. DOI:10.1533/9780857090447
- N. Secara, *Chem. J. Mold.*, **2010**, *5*, 83–87. DOI:10.19261/cjm.2010.05(2).11
- V. N. Sagi, V. Punna, F. Hu, G. Meher and R. Krishnamurthy, *J. Am. Chem. Soc.*, **2012**, *134*, 3577–3589. DOI:10.1021/ja211383c
- G. Ward, C. L. Liotta, R. Krishnamurthy and S. France, *J. Org. Chem.*, **2018**, *83*, 14219–14233. DOI:10.1021/acs.joc.8b01867
- W. Brand-Williams, M. E. Cuvelier and C. Berset, *LWT-Food Sci. Technol.*, **1995**, *28*, 25–30. DOI:10.1016/S0023-6438(95)80008-5
- D. Villaño, M. S. Fernández-Pachón, M. L. Moyá, A. M. Troncoso and M. C. García-Parrilla, *Talanta*, **2007**, *71*, 230–235. DOI:10.1016/j.talanta.2006.03.050
- R. L. Prior, X. Wu and K. Schaich, *J. Agric. Food Chem.*, **2005**, *53*, 4290–4302. DOI:10.1021/jf0502698
- M. Gonta, G. Duca and D. Porubin, *Chem. J. Mold.*, **2008**, *3*, 118–126. DOI:10.19261/cjm.2008.03(1).01
- I. Gülçin, *Innov. Food Sci. Emerg. Technol.*, **2010**, *11*, 210–218. DOI:10.1016/j.ifset.2009.07.002
- V. D. Cotea, C. V. Zănoagă and V. V. Cotea (Ed.): *Tratat de Oenochimie*, Editura Academiei Române, București, **2009**, *2*, 750.
- H. Fontoin, C. Saucier, P. L. Teissedre and Y. Glories, *Food Qual. Pref.*, **2008**, *19*, 286–291. DOI:10.1016/j.foodqual.2007.08.004
- W. Li, J. Zhang, S. Tan, Q. Zheng, X. Zhao, X. Gao and Y. Lu, *J. Food Biochem.*, **2019**, *43*, e13046.

38. L. Salaz-Perez, M. J. Gaucin Delgado, P. Preciado-Rangel, J. A. Gonzales Fuentes, A. V. Ayala Garay and M. A. Segura Castruita, *Rev. Mexicana Cien. Agríc.*, **2018**, *9*, 4301–4309.
39. M. Hidalgo, C. Sánchez-Moreno and S. de Pascual-Teresa, *Food Chem.*, **2010**, *121*, 691–696.  
DOI:10.1016/j.foodchem.2009.12.097
40. K. Sak, *Mini Rev. Med. Chem.*, **2014**, *14*, 494–504.  
DOI:10.2174/1389557514666140622204037
41. Y. Pan, Z. Y. Deng, S. L. Zheng, X. Chen, B. Zhang and H. Li, *J. Agric. Food Chem.*, **2018**, *66*, 9107–9120.  
DOI:10.1021/acs.jafc.8b03412
42. H. Boulebd, *J. Mol. Struct.*, **2020**, *1201*, 127210.  
DOI:10.1016/j.molstruc.2019.127210
43. B. Zhang, T. Xia, W. Duan, Z. Zhang, Y. Li, B. Fang, M. Xia and M. Wang, *Molecules*, **2019**, *24*, 3799.  
DOI:10.3390/molecules24203799
44. S. Sang, X. Cheng, R. E. Stark, R. T. Rosen, C. S. Yang and C. T. Ho, *Bioorg. Med. Chem.*, **2005**, *10*, 2233–2237.  
DOI:10.1016/S0968-0896(02)00089-5
45. D. I. Tsimogiannis and V. Oreopoulou, *Innov. Food Sci. Emerg. Technol.*, **2006**, *7*, 140–146.  
DOI:10.1016/j.ifset.2005.09.001
46. A. M. Osman, *Biochem. Biophys. Res. Comm.*, **2011**, *412*, 473–478. DOI:10.1016/j.bbrc.2011.07.123
47. S. M. Ahmadi, R. Farhoosh, A. Sharif and M. Rezaie, *J. Food Sci.*, **2020**, *85*, 298–305. DOI:10.1111/1750-3841.14994
48. M. Friedman and H. S. Jurgens, *J. Agric. Food Chem.*, **2000**, *48*, 2101–2110. DOI:10.1021/jf990489j
49. N. Li, L. S. Taylor, M. G. Ferruzzi and L. J. Mauer, *J. Agric. Food Chem.*, **2012**, *60*, 12531–12539.  
DOI:10.1021/jf304116s
50. F. Nanjo, K. Goto, R. Seto, S. Sakai, M. Miwa and Y. Hara, *Free Radic. Bio. Med.*, **1996**, *21*, 895–902.  
DOI:10.1016/0891-5849(96)00237-7
51. A. Altunkaya, V. Gökmen and L. H. Skibsted, *Food Chem.*, **2016**, *190*, 25–32. DOI:10.1016/j.foodchem.2015.05.069
52. K. Mukai, S. Mitani, K. Ohara and S. I. Nagaoka, *Free Radic. Bio. Med.*, **2005**, *38*, 1243–1256.  
DOI:10.1016/j.freeradbiomed.2005.01.011
53. R. Amorati and L. Valgimigli, *Org. Biomolec. Chem.*, **2012**, *10*, 4147–4158. DOI:10.1039/c2ob25174d
54. Y. J. Shang, Y. P. Qian, X. D. Liu, F. Dai, X. L. Shang, W. Q. Jia, Q. Liu, J. G. Fang and B. Zhou, *J. Org. Chem.*, **2009**, *74*, 5025–5031. DOI:10.1021/jo9007095
55. S. Martinez, L. Valek, Ž. Petrović, M. Metikoš-Huković and J. Piljac, *J. Electroanal. Chem.*, **2005**, *584*, 92–99.  
DOI:10.1016/j.jelechem.2005.07.015
56. D. E. García, W. G. Glasser, A. Pizzi, S. P. Paczkowski and M. P. Laborie, *New J. Chem.*, **2016**, *40*, 36–49.  
DOI:10.1039/C5NJ02131F
57. A. Arbenz and L. Avérous, *Green Chem.*, **2015**, *17*, 2626–2646. DOI:10.1039/C5GC00282F
58. M. Latos-Brozio and A. Masek, *Chem. Biodivers.*, **2019**, *16*, e1900426. DOI:10.1002/cbdv.201900426
59. S. Oliver, J. M. Hook and C. Boyer, *Polym. Chem.*, **2017**, *8*, 2317–2326. DOI:10.1039/C7PY00325K
60. F. Sonni, E. G. Moore, A. C. Clark, F. Chinnici, C. Riponi and G. R. Scollary, *J. Agric. Food Chem.*, **2011**, *59*, 7410–7418.  
DOI:10.1021/jf200968x
61. B. Badhani, N. Sharma and R. Kakkar, *RSC Adv.*, **2015**, *5*, 27540–27557. DOI:10.1039/C5RA01911G
62. T. Marino, A. Galano and N. Russo, *J. Phys. Chem. B*, **2014**, *118*, 10380–10389. DOI:10.1021/jp505589b
63. R. Rohman and R. Kar, *J. Molec. Model.*, **2018**, *24*, 1–10.  
DOI:10.1007/s00894-018-3701-0
64. M. Leopoldini, N. Russo and M. Toscano, *Food Chem.*, **2011**, *125*, 288–306. DOI:10.1016/j.foodchem.2010.08.012
65. M. Pinelo, L. Manzocco, M. J. Nuñez and M. C. Nicoli, *J. Agric. Food Chem.*, **2004**, *52*, 1177–1180.  
DOI:10.1021/jf0350515
66. H. J. H. Fenton, *J. Chem. Soc., Transact.*, **1894**, *65*, 899–910.  
DOI:10.1039/CT8946500899
67. A. Eschenmoser, *Chem. Biodivers.*, **2007**, *4*, 554–573.  
DOI:10.1002/cbdv.200790050
68. C. Richter, F. Berndt, T. Kunde and R. Mahrwald, *Org. Lett.*, **2016**, *18*, 2950–2953. DOI:10.1021/acs.orglett.6b01287
69. G. Duca (Ed.): Homogeneous Catalysis with Metal Complexes: Fundamentals and Applications, Springer Science Business Media, **2012**, *102*, 319–349.  
DOI:10.1007/978-3-642-24629-6\_5
70. N. Bolocan, G. Duca, L. Vlad and F. Macaev, *Chem. J. Mold.*, **2011**, *6*, 29–44. DOI:10.19261/cjm.2011.06(1).14
71. A. C. Clark, *Eur. Food Res. Technol.*, **2008**, *226*, 925–931.  
DOI:10.1007/s00217-007-0615-y
72. B. García, R. Ruiz and J. M. Leal, *J. Phys. Chem. A*, **2008**, *112*, 4921–4928. DOI:10.1021/jp800208s
73. L. Vacarciuc, *Agric.*, **2008**, *57*, 1–8.
74. Y. Sawai and J. H. Moon, *J. Agric. Food Chem.*, **2000**, *48*, 6247–6253. DOI:10.1021/jf000500b
75. C. Vicol, E. Gorincioi, A. Barba and G. Duca, In: National Chemical Conference, Călimănești – Căciulata, Romania, **2021**, *36*, pp. 107.
76. R. W. Hay and J. S. Harvie, *Aust. J. Chem.*, **1965**, *18*, 1197–1209. DOI:10.1071/CH9651197
77. D. Sazou, P. Karabinas and D. Jannakoudakis, *J. Electroanal. Chem. Interfac. Electrochem.*, **1984**, *176*, 225–234.  
DOI:10.1016/S0022-0728(84)80320-4
78. C. J. Butch, J. Wang, J. Gu, R. Vindas, J. Crowe, P. Pollet and C. L. Liotta, *J. Phys. Org. Chem.*, **2016**, *29*, 352–360.  
DOI:10.1002/poc.3542
79. S. Adisakwattana, T. Thilavech, W. Sompong and P. Pasukamonset, *Electr. J. Biotechnol.*, **2017**, *27*, 32–36.  
DOI:10.1016/j.ejbt.2017.03.004
80. M. Olszowy, A. L. Dawidowicz and M. Józwiak-Doleba, *Eur. Food Res. Technol.*, **2019**, *245*, 1473–1485.  
DOI:10.1007/s00217-019-03255-7
81. J. Rúa, D. de Arriaga, M. R. García-Armesto, F. Busto and P. del Valle, *Eur. Food Res. Technol.*, **2017**, *243*, 1211–1217.  
DOI:10.1007/s00217-016-2838-2
82. U. G. Spizzirri, F. Iemma, F. Puoci, G. Cirillo, M. Curcio, O. I. Parisi and N. Picci, *Biomacromolec.*, **2009**, *10*, 1923–1930.  
DOI:10.1021/bm900325t

83. I. J. Kade, D. O. Johnson, V. O. E. Akpambang and J. B. T. Rocha, *Biokem.*, **2012**, *24*, 15–22.
84. G. Fabre, I. Bayach, K. Berka, M. Paloncycova, M. Starok, C. Rossi, J. L. Duroux, M. Otyupke and P. Trouillas, *Chem. Comm.*, **2015**, *51*, 7713–7716. DOI:10.1039/C5CC00636H
85. R. M. L. Colunga Biancatelli, M. Berrill, J. D. Catravas and P. E. Marik, *Front. Immun.*, **2020**, 1451.
86. D. Liu, Y. Li, Y. Qian, Y. Xiao, S. Du and X. Qiu, *ACS Sust. Chem. Engin.*, **2017**, *5*, 8424–8428. DOI:10.1021/acssuschemeng.7b02282
87. D. Tsimogiannis, A. Bimpilas and V. Oreopoulou, *Eur. J. Lip. Sci. Technol.*, **2017**, *119*, 16003473. DOI:10.1002/ejlt.2016003473
88. L. A. Tavadyan and S. H. Minasyan, *J. Chem. Sci.*, **2019**, *131*, 1–11. DOI:10.1007/s12039-019-1618-5
89. E. Gorincioi, C. Vicol, A. Barba and G. Duca, In: The 7th International Conference on Ecological & Environmental Chemistry, **2022**, *48*, pp. 64.
90. Y. Z. Mei, R. X. Liu, D. P. Wang, X. Wang and C. C. Dai, *Bio-technol. Lett.*, **2015**, *37*, 9–18. DOI:10.1007/s10529-014-1651-x
91. Q. Mao, *The synthesis and antioxidant capacities of a range of resveratrol and related phenolic glucosides* (Doctoral dissertation), **2015**.
92. C. Vicol, E. Gorincioi and G. Duca, In: XXIIIrd International Conference “New Cryogenic and Isotope Technologies for Energy and Environment” – EnergEn 2021, **2021**, pp. 312–316.

## Povzetek

Antioksidativne interakcije med več naravnimi fenolnimi in nefenolnimi spojinami (katehin, kvercetin, rutin, resveratrol, galna kislina in askorbinska kislina) ter organskimi kisljinami (vinska, citronska in dihidroksifumarna kislina) smo proučevali z metodo 2,2-difenil-1-pikrilhidrazil (DPPH). Pri kombinacijah katehina, kvercetina, resveratrola in galne kisline z vinsko in citronsko kislino so bile ugotovljene glavne aditivne in antagonistične interakcije; tako vedenje je lahko posledica večje stabilnosti fenolnih spojin v kisljih medijih. Rutin in askorbinska kislina sta pokazala dobre sinergijske učinke z vinsko in citronsko organsko kislino, kar je lahko posledica polimerizacijskih procesov pri rutinu in spremembe mehanizma delovanja pri askorbinski kislini. Mešanice v kombinaciji z dihidroksifumarno kislino so pokazale od odmerka odvisne sinergijske, aditivne ali antagonistične antioksidativne interakcije. Dobri sinergijski učinki so bili opaženi pri binarnih mešanicah dihidroksifumarne kisline z askorbinsko kislino, katehinom in rutinom.



Except when otherwise noted, articles in this journal are published under the terms and conditions of the Creative Commons Attribution 4.0 International License

Feature article

# Chlorination of UV Filters with Antioxidant Shield in Swimming Pool Waters – Products Identification and Toxicity Assessment

Mojca Bavcon Kralj<sup>1</sup>, Albert T. Lebedev<sup>2</sup> and Polonca Trebše<sup>1,2\*</sup><sup>1</sup> Faculty of Health Sciences, University of Ljubljana, Ljubljana, Slovenia<sup>2</sup> Massec, d.o.o. Postojna, Slovenia

\* Corresponding author: E-mail: polonca.trebse@zf.uni-lj.si

Received: 08-24-2023

## Abstract

This work summarizes our research on synthesis, characterization and toxicity of selected UV-A filters and their antioxidant shield in commercial formulation – resveratrol. Benzophenone type of UV filters react under disinfection conditions with chlorine and form different mono- and dichlorinated products, while dibenzoylmethane derivatives, such as avobenzene, react with chlorine and form two main bridge chlorinated products followed by numerous chlorinated species at the advanced stages of the process. Resveratrol showed three main susceptible centers to chlorination, starting from the electrophilic addition to the double bond and continuing with the chlorination of the phenolic moieties. Several experiments conducted under different disinfection conditions (pool/sea water, addition of salts, irradiation) showed basically similar chlorination patterns with some variations in terms of product formation. The results of toxicity assessment using different test organisms (*Vibrio fischeri*, microalgae, daphnids) have shown different sensitivity of testing organisms to the parent UV filters in comparison with chlorinated products as well as different toxicity for specific UV filter in comparison to the others. As the closing loop of all experiments in the laboratory, an up-scaling to the real human skin is presented.

**Keywords:** UV filters, chlorination, disinfection by-products, toxicity

## 1. Introduction

Ultraviolet (UV) light, which comes mainly from the sun, causes damage to materials, which are exposed to it. By the name UV, mainly the light with wavelengths of 290–320 nm (UV-B) and 320–400 nm (UV-A) is meant. Photons of UV light cause breakage of covalent bonds and thus induce various oxidation processes, which are mainly chain-radical oxidation with air oxygen. These processes lead to aging and weathering of different construction materials, coatings, plastics, and rubber. Particularly harmful, however, are these processes in biological systems, where they cause damage to skin cells resulting in skin aging processes, various inflammatory processes, and cancer.

To protect against UV irradiation, various substances are used that either reflect or absorb UV light. Compounds, which absorb UV light, are applied in numerous fields. Especially important are these, where the products

are exposed to solar radiation (coating products, plastic products, and cosmetic products). These compounds absorb UV light and are usually called UV filters. As a result of the growing awareness of the harmful exposure to the sun and in order to reduce the risk for skin cancer they are also widely used as personal care products (e.g. sunscreens, shampoos, hair sprays, lipsticks). They protect human body against the harmful effects of sunlight. In addition to inorganic pigments, which reflect UV light in particular, organic compounds, which absorb UV photons, are also used. UV light is of a broad spectral range, 400–290 nm (UV-A and UV-B), therefore no compound can prevent the exposure to the whole spectrum by itself, since the absorption peaks are much narrower. From that reason, a combination of several compounds covering the whole area, is usually applied. Based on the literature survey about the research on the use and effects of old and new formulations, the list of substances permitted by law is regularly updated. The European Union (EU) currently allows 28

organic substances, while some other compounds are allowed in countries around the world, such as Japan and the U.S., where they are treated as biological agents, available without prescription.<sup>1–3</sup>

The sun protection factor (SPF) depends on the nature and the proportion of UV filter components in the commercial preparation. SPF is an indicator of the effectiveness of a sunscreen. Compounds for protection from the sun are always used in combination, since a single UV filter, which could provide a sufficiently high SPF does not exist. In the final sunscreen products, we observed increased use of inorganic UV filters, especially in sunscreens for children and creams to protect very sensitive skin. The most used is certainly TiO<sub>2</sub>. Organic UV filters are somehow less applicable due to potential instability and, therefore, the reduction is SPF. Moreover, due to photosensitivity and the potential synergistic effects, various international health organizations, e.g. U.S. Food and Drug Agency (FDA), limit the combinations of different UV-A and UV-B organic chemical filters.<sup>4</sup>

Organic chemical filters can be divided into two groups, depending on the spectral range covered. The first consists of the UV-A filters, including benzophenone, antranilates and dibenzoylmethanes, the second one, UV-B filters, includes PABA derivatives, salicylate, cinammates and camphor derivatives. As per the European Community, compounds ranked among the organic UV filters for the protection from the sun express characteristics of persistent organic pollutants (POPs). The common characteristic of all these compounds is the presence of aromatic moiety with a side chain, and various degrees of unsaturation.<sup>5</sup>

When exposed to UV radiation, UV filters must be relatively stable. Sunscreen products are used primarily in special conditions, such as swimming in the sea, swimming pools, on the snow, and in the mountains, where a thorough protection is needed. Considering that the 100% stability to UV radiation of UV filters and other added compounds present in SPF is impossible, natural ROS scavengers are usually included in cosmetics formulations. *Trans*-resveratrol (RES) is one of them. With the two phe-

nol moieties in the chemical structure, it shows antioxidant,<sup>6</sup> anti-inflammatory,<sup>7</sup> and anti-tumor<sup>8</sup> properties. Commercially it is often present in cosmetics, nutraceuticals,<sup>9</sup> and food packaging to increase food stability or/and prevent oxidation.<sup>10</sup> Nevertheless, several recent studies showed that both UV filters and antioxidants are decomposed by light. Mostly, two types of reactions occur: a) direct photolytic reactions, and b) chlorination of aromatic rings or side chains, due to the presence of chlorine and chlorate medium (such as pools, salty seawater).<sup>11–16</sup>

The main environmental concern of UV filters is related to their high lipophilic character ( $\log K_{ow}$  4–8), relative stability against biological decomposition, and organic carbon distribution coefficient ( $\log K_{oc}$  3–4).<sup>13</sup> They were found to accumulate in the aquatic environments, mainly soils and sediments and in the food chain. Some of them have been detected in fish in the range of 25–1800 ng/g, and in the fat of human milk in the range of 16–417 ng/g.<sup>1,2</sup>

When these chemicals are released to the aquatic environment, they can also cause adverse biological effects on aquatic organisms through mechanisms such as toxicity and estrogenic activity. Adverse effects could be expected from original chemicals or their degradation/chlorination intermediates. The existing ecotoxicological data have confirmed their estrogenic hormonal activity and multiple endocrine-disrupting activities such as androgenic, anti-estrogenic, and estrogenic activities.<sup>17–20</sup>

Many reports have shown that the toxicity of chlorinated organic compounds derived from chlorination processes was higher than that of their parent compounds.<sup>21–24</sup> In these studies, it was shown that the toxicity might come from some of the chlorinated products. Beside that it was noticed that different effects of benzophenones chlorination processes might be expressed not only in the significant increase of toxicity, but also decrease or it may remain unchanged.<sup>25</sup> The toxicity of benzophenone type chlorinated products depends on their molecular structure, i.e., the position, number and type of their substituents, and transformation ratios.<sup>25</sup> The transformation activity of precursors presents the intrinsic factor for toxicity changes during chlorination treatment.

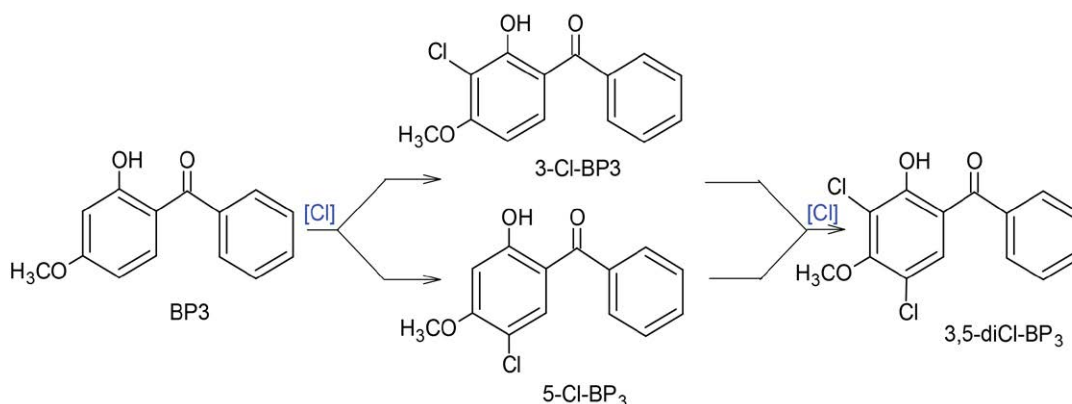


Figure 1. Reaction of BP3 under disinfection conditions.

## 2.1. Reactions of Benzophenone Type UV Filters under Disinfection Conditions

In the case of benzophenone type of UV filters chlorination according to the literature may occur at the aromatic ring or at the side chain. The formation of halogenated byproducts in chlorinated waters is inevitable, especially when filters contain phenolic rings and/or aromatic amines.<sup>12,14–16,26–31</sup> Within our studies we have focused on BP3 (2-hydroxy-4-methoxybenzo-phenone), BP4 (2-hydroxy-4-methoxybenzophenone-5-sulfonic acid), and DHHB (hexyl 2-[4-(diethylamino)-2-hydroxybenzoyl]-benzoate).

In the case of BP3, its diluted aqueous solutions were treated with NaOCl or trichloroisocyanuric acid (TCCA) in the ratio 1:1 at room temperature and after certain period (up to 24 h) reactions were stopped by addition of Na<sub>2</sub>SO<sub>3</sub>. Detailed analysis (HPLC-DAD and independent synthesis of products) proved the formation of 5-chloro-2-hydroxy-4-methoxybenzophenone (5Cl-BP3) and 3,5-dichloro-2-hydroxy-4-methoxybenzophenone (3,5-diCl-BP3) with the small amount of 3-chloro derivative (3-chloro-2-hydroxy-4-methoxybenzophenone, 3-Cl-BP3) in the case of BP3 (Figure 1). After 24 h we did not observe the presence of BP3.<sup>31</sup>

Chlorination of BP4 in neutral aqueous environment resulted in the formation of two products, 5-benzoyl-5-chloro-4-hydroxy-2-methoxybenzenesulfonic acid (5Cl-BP3) and 3,5-diCl-BP3. Interestingly, no 5-benzoyl-3-chloro-4-hydroxy-2-methoxybenzenesulfonic acid (3Cl-BP4) was formed, indicating that in neutral aqueous medium, where sulfonic group is fully ionized, an *ipso* substitution (replacement of sulfonate group by chlorine) is preferred.<sup>31</sup>

In the case of DHHB, HPLC-DAD revealed the formation of several products, which were later identified by

LC-MS/MS as 3-chloro DHHB, 3,5-dichloro DHHB, and the product chlorinated at the aromatic ring with substituted ethyl group.<sup>32</sup> HPLC-ESI-MS and HPLC-ESI-MS/MS experiments of parent compound DHHB undertaken in the positive mode, together with the accurate mass measurements, revealed the detailed fragmentation pathway, which enabled us to elucidate the structure of chlorinated products. According to HPLC-DAD analysis, three products are formed, two of them already in the early stage of reaction of DHHB with NaOCl; the concentration of both increased with time. The presence of ions of *m/z* 404 and 406 in the ratio 3:1 for P1 and *m/z* 432 and 434 for P2 confirms the presence of one chlorine atom in the molecules. Based on MS<sup>2</sup> experiments we concluded that product 1 (Ph-Cl-DHHB) lacked an ethyl group and contained a chlorine atom instead, which is either in positions three or five of the aromatic ring. In the case of product 2, chlorination involved phenolic moiety of DHHB. Collision-induced dissociation (CID) conditions confirmed the formation of 3-substituted product, 3-Cl-DHHB. The structural elucidation of the third by-product was possible using the same procedure as with other ones. It represented a product of introduction of two chlorine atoms into positions three and five of the phenolic ring of DHHB (3,5-diCl-DHHB) (Figure 2).

All identified products were also independently synthesized, fully characterized by spectroscopic methods (NMR, IR, MS), and were employed as chromatographic standards.<sup>31,32</sup>

### 2.1.1 Chloro-Derivatives of BP3 and BP4 in Swimming Pool Water

Swimming pools water disinfection is required to keep its quality and to prevent public health issues, besides it is also highly regulated.<sup>31</sup> On the other hand, being aware

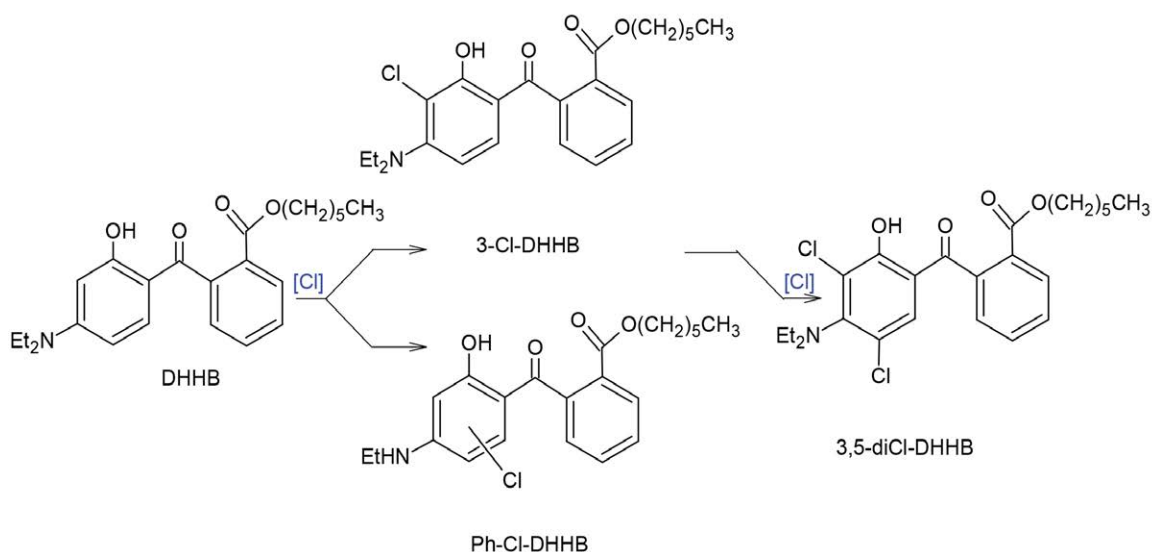


Figure 2. Chlorinated products of DHHB.

of sunburn consequences, people often use SPFs. Therefore, BP3 and BP4 appear in bathing waters as common UV filters. That was the reason to monitor them together with their chloro-derivatives.<sup>31</sup> In summer season of 2011, we undertook a survey by taking samples from 13 bathing areas in Slovenia (swimming pools with fresh and marine water). The presence of BP3 was reliably confirmed at two locations in swimming pools with fresh water in the concentrations of 0.3  $\mu\text{g L}^{-1}$  and 1.7  $\mu\text{g L}^{-1}$ , respectively. 3,5-diCl-BP3 was found only in one swimming pool (6.6  $\mu\text{g L}^{-1}$ ).

## 2. 2. Reactions of Dibenzoylmethane Type of UV Filters under Disinfection Conditions

Besides BP3, BP4, DHHB, avobenzene (4-*tert*-butyl-4'-methoxydibenzoylmethane) is also often present in SPFs. It is an UV-A filter, sold under the trade names Parsol 1789 or Eusolex 9020. It may exist in two tautomeric forms, enol and keto form, but in sunscreen formulations,

avobenzene exists predominantly in the enol one. In the case of avobenzene, we performed several studies under various disinfection conditions and in different matrices. We were able to perform the detailed study to identify products formed under specific conditions. Experimental details with DBPs formed are collected in Table 1.

LC-MS was studied by Santos et al., 2012<sup>13</sup> who reported mono- and dichloro derivatives of avobenzene as primary products of its aqueous chlorination (Figure 3). Since methoxy group is one of the most powerful electron-donating substituents, a logical conclusion was made by Crista et al., 2015<sup>15</sup> that chlorine occupied *ortho* position of the ring to the methoxy group. Nevertheless, detailed study of that reaction with GC-HRMS<sup>33</sup> showed that both aromatic rings did not contain chlorine atoms. Therefore, aqueous chlorination reaction involves double bond of the enol form of avobenzene rather than the activated benzene ring. The primary products 1-(*tert*-butyl)-2-chloro-3-(4-methoxyphenyl)-1,3-dione and 1-(*tert*-butyl)-2,2-dichloro-3-(4-methoxyphenyl)propan-1,3-dione



Figure 3. Chemical structures of main avobenzene chlorinated products (monochloro avobenzene – left and dichloro avobenzene – right).

Table 1. Sum-up of our research (experimental conditions, formation of chlorination products, references).

Disinfectant / medium	Reaction conditions	DBPs	Reference
NaOCl (0 to 2.5 eq) / distilled water	Room temperature – RT, 1 h	monochloro avobenzene dichloroavobenzene <i>p</i> -methoxychloroacetophenone	<i>Journal of Analytical Chemistry</i> <sup>35</sup>
–	UV-C, 1–4 h	4-methoxy-substituted benzaldehyde, benzoic acid, and phenol 4- <i>tert</i> -butyl substituted benzaldehyde, benzoic acid, phenol	<i>Water Research</i> <sup>34</sup>
NaOCl (2 and 20 eq) / distilled water	Experiment in the dark, RT, 30 min	beside previously mentioned mono- and dichloro avobenzene, substituted benzaldehydes, benzoic acid, phenols	<i>Water Research</i> <sup>34</sup>
NaOCl (2 and 20 eq) / distilled water	UV-C, 30 min	25 disinfection by-products; among them substituted benzaldehydes, benzoic acid, phenols, additionally chlorophenols, chloroanhydrides	<i>Water Research</i> <sup>34</sup>
NaOCl (20 eq) / distilled water	addition of inorganic salts (Br <sup>-</sup> , I <sup>-</sup> , Cu <sup>2+</sup> , Fe <sup>3+</sup> )	brominated and iodinated products, such as brominated phenols and acetophenones (even iodinated)	<i>Journal of Analytical Chemistry</i> <sup>35</sup>
KOBr (10 eq) / water	RT, 24 h	several brominated products, including bromoanisol and tribromophenol	<i>Environment International</i> <sup>36</sup>
KOBr (20 eq) / water	addition of Cu <sup>2+</sup>	significant increase of the yields of brominated compounds	<i>Environment International</i> <sup>36</sup>
NaOCl (20 eq) / sea water		40 compounds, including numerous brominated derivatives	<i>Journal of Analytical Chemistry</i> <sup>40</sup>



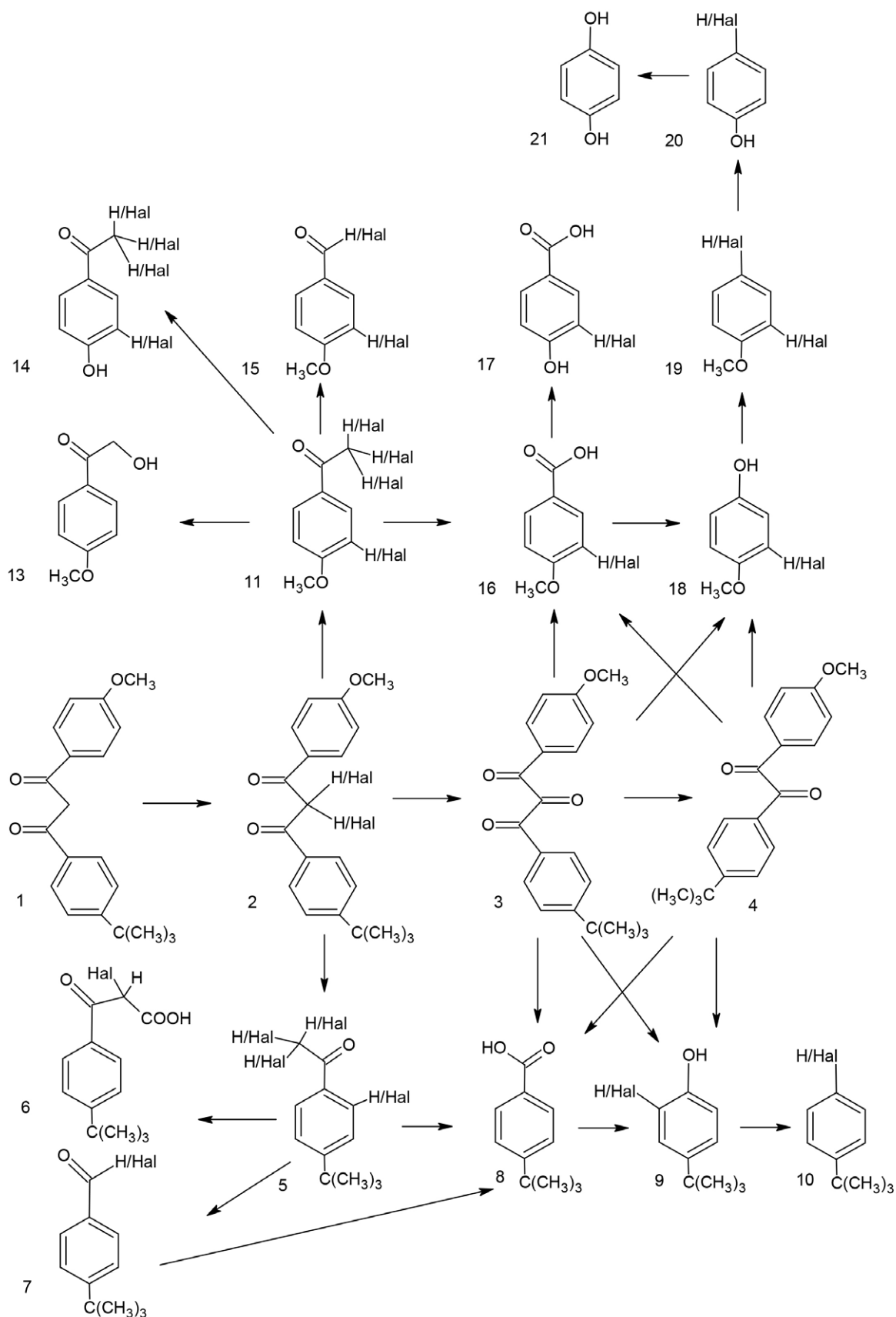


Figure 4. The principal pathways of disinfection process of avobenzone.

were specially synthesized by us.<sup>34</sup> Their mass spectra and retention times repeated those observed during aqueous chlorination of avobenzene. Same reaction with the double bond took place in conditions of aqueous bromination.<sup>35,36</sup>

Then halogen atoms were substituted for oxygen. Further rupture of C-C bonds brought on most various monoaromatic compounds. Figure 4 summarizes the main pathways of the aqueous bromination of avobenzene. Over one hundred DBPs, including substituted aldehydes, acetophenones, acids, and phenols were identified.

Advanced stages of aqueous chlorination and bromination of avobenzene in the fresh and sea water, as well as with the addition of inorganic cations ( $\text{Cu}^{2+}$  and  $\text{Fe}^{3+}$ ) and anions ( $\text{Br}^-$  and  $\text{I}^-$ ) to the tap water were studied in detail.<sup>34–36,40</sup> The experimental conditions dramatically influenced the range and levels of the reaction products. For example, addition of copper ions under aqueous bromination conditions resulted in 100-fold increase in the bromoform yield.<sup>35</sup> Although iodinated organic species easily lose iodine in aqueous chlorination, being substituted by chlorine,<sup>40</sup> two avobenzene iodinated products were still detected upon the addition of iodide anions to the reaction mixture.<sup>35,36</sup> Iodides and iron ions also accelerated the aqueous chlorination reaction.<sup>35</sup>

## 2. 2. 1 Presence of Avobenzene in Swimming Waters

Although avobenzene itself was not detected in bathing waters, it was a precursor of some products. *Tert*-butyl-benzoic acid, being the major product of avobenzene aqueous chlorination in seawater<sup>40</sup> and freshwater<sup>36</sup> in laboratory experiments, appeared to be the major component among the targeted DBPs in the swimming pool water as well. Being rather stable, it may be accumulated in the environment. Acetophenones, being well represented in the laboratory experiments, were also detected in the real bathing waters. Their levels were not high as they are intermediates ending up in acids and phenols.

## 2. 3. Reactions of Resveratrol under Disinfection Conditions

Resveratrol, an antioxidant usually added to sunscreen formulations to prevent oxidation of the UV filters, rapidly reacts with aqueous chlorine both in pure form and in commercial formulations. In the laboratory experiment it disappeared promptly, while 82 transformation products were tentatively identified.<sup>37</sup> GC-MS enabled identifying 95% of semi-volatile resveratrol transformation products, the others were established by UPLC-MS. Unfortunately, toxicity of only few of them is known, all the others are still not classified. There are several principal pathways of transformation, including DBPs coming from the addition to and the rupture of the central double bond,

as well as numerous products of electrophilic substitution in the activated phenolic rings.

In the primary reactions the number of carbon atoms remained equal – fourteen.<sup>37</sup> The first one involved electrophilic addition to the central double bond connecting the two phenol moieties, which resulted in a bunch of transformation products (positional isomers) including hydroxylated or/and chlorinated resveratrol. However, only dichloro resveratrol was reliably identified in the reaction mixture. Since the double bond represents an extremely reactive moiety in aquatic chlorination<sup>38</sup> (Figure 5, reactive center 1), the forming compounds coming from dichloro resveratrol immediately react further by the mechanism of electrophilic substitution in the aromatic ring or with the cleavage of the central aliphatic C–C bond.

The cleavage ended up in transformation products with one benzene ring in the molecule (hydroxybenzaldehyde, mono- and dichloro- hydroxybenzaldehyde, dihydroxybenzaldehyde and their derivatives with chlorine atoms on the ring, hydroquinone, chloro- and dichlorohydroquinone, phenol, and chlorophenols). Not to forget that chlorophenols were included in the list of priority pollutants of US EPA already in 1970.

The second pathway of transformation of resveratrol involved electrophilic substitutions in the aromatic ring. Benzene rings in resveratrol are highly reactive. They have activating *ortho-para*-directing hydroxyl groups in both rings. In the diol ring all positions are very reactive, although the most reactive one is between two hydroxyls (Figure 5, reactive center 2). The main semi-volatile products identified by GC-MS were mono-, di-, and trichloro-substituted resveratrols (two isomeric monochloro- derivatives, one dichloro- derivative, and one trichloro-). A tetrachloro- derivative as well as di-, tri-, tetra-, etc. chlorinated/hydroxylated compounds were identified by UPLC-MS (LC-MS/MS) due to lower volatility. Unfortunately, neither EI nor ESI-MS/MS enabled establishing the exact positions of these groups in the molecules.

Cyclization by *ortho*-positions of the resveratrol aromatic rings may be considered as the third transformation pathway. This cyclization generated phenanthrene-like molecules, which reacted further, similarly as in chlorination of orcinol.<sup>39</sup> After that, some products of substitutions of hydrogens for chlorines and several dicarbonyl products could be formed due to haloform reaction. The most environmentally problematic in the aqueous resveratrol chlorination was the formation of biphenyl-like molecules. Being prohibited for the last 30–40 years, they are highly toxic and unfortunately persistent in the environment.

In summary, it is worth mentioning that only few of 82 identified compounds have the toxicological data available, among them: chlorophenols and hydroxylated polychlorinated biphenyls. It is possible only to predict the toxicity of the others from the similarity to the classified compounds. However, they are too numerous and may be

represented by various isomers. Moreover, they are commercially unavailable and have to be synthesized before.

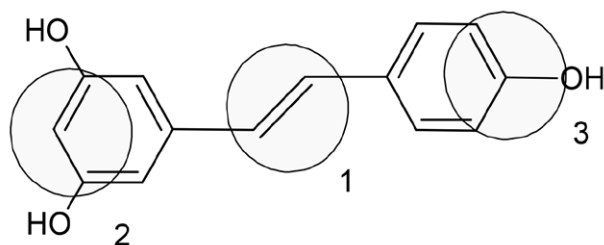


Figure 5. Chemical structure of resveratrol and its reactive centers.

### 3. Stability of Chlorinated Products

Photostability of chlorinated benzophenones and dibenzoylmethanes (3-chloro, 5-chloro, and 3,5-dichloro products) has been performed in a custom-made photoreactor with six UV-A lamps as already described.<sup>28</sup> The experiment revealed different photostability of each compound in the presence of UV-A light after 120 min of irradiation.

In the case of benzophenones, parent benzophenone, 3-chloro, as well as 5-chloro derivatives showed high stability toward UV-A irradiation, while 3,5-dichloro product degraded more than 40% within 120 min of UV-A irradiation.<sup>28</sup>

In the case of avobenzone, dichloroavobenzone exhibited the lowest UV-A stability with a half-life of 22.4 min  $\pm$  0.7 min, while avobenzone and chloro avobenzone were much more stable (half-lives 126  $\pm$  16 min and 128  $\pm$  25 min, respectively). Additional experiments were performed to study pH stability, as well as removal capacity (using TiO<sub>2</sub>/UV-A). They have shown higher stability at neutral pH for all three compounds, whereas the least stable was dichloro avobenzone (half-life 14.1  $\pm$  0.6 min) under photocatalytic conditions.<sup>41</sup>

Our studies on chlorination have been completed with the stability study of three commercial sunscreen products (SPF 30) containing avobenzone under different experimental conditions (UV-A/UV-B, UV-C photostimulation and chlorination). As it was predicted, the degradation of avobenzone as a single compound differs from the degradation of avobenzone in relatively complicated matrix of SCPs. It was shown that commercial products had completely different attitude to protect or promote the degradation of avobenzone when it was treated as analytical standard or as an ingredient in different sunscreens.<sup>36</sup>

### 4. Toxicity of Selected UV Filters And Their Chlorination Products

All our studies have been combined with toxicity experiments. The toxicity of selected UV filters and their

chlorinated by-products was tested with different test organisms (luminescent bacteria *Vibrio fischeri* (LUMISTox, Dr. LANGE), green algae *Pseudokirchneriella subcapitata*, or *Daphnia magna* Straus) based on standard ISO guidelines.<sup>42–44</sup>

The results of toxicity monitoring revealed slightly increased toxicity of BP3 and BP4 to bacteria *Vibrio fischeri*. 30 min IC (inhibitory concentrations) obtained for *Vibrio fischeri* were as follows: IC<sub>20</sub> for BP3 was 33.2 mg/L and 67.3 mg/L for BP4. The 50% inhibition of luminescence was detected at 301 mg/L of BP4 after 30 min of exposure. The reported 16h-EC<sub>50</sub> values were 210 and 250 mg/L obtained for BP4 using *Pseudomonas putida* as a test organism, which confirmed very low toxicity of BP4 to the bacteria.<sup>31</sup> In the case of BP3 and 5-chloro BP3, we had to face with its very low solubility, and from that reason stock solution was prepared in acetone or DMSO. Results revealed BP3 was non-toxic to bacteria at lower concentrations, and in the case of 5-chloro BP3 the concentrations up to 50 mg/L were non-toxic to bacteria.

Toxicity of chlorinated compounds of DHHB tested by marine bacteria *Vibrio fischeri* was found to be in the similar range as that of the starting UV filters.<sup>32</sup> This fact we explained by low transformation ratios of parent compounds and similar toxicity level of chlorinated products compared with their parent compounds. Microalgae *Desmodesmus subspicatus* were more sensitive to DHHB than to its chlorinated by-products.<sup>32</sup> Contrary, crustaceans *Daphnia magna* were affected more by DHHB's chlorinated products. The toxicity of chlorinated DHHB by-product (i.e. 3-chloro DHHB) was significantly higher compared to DHHB when tested on *D. magna*. Similarly, significant toxicity elevation has been shown in the case of BP4 chlorination products in the experiment with *Phospobacterium phosphoricum*.<sup>45</sup> Such toxicity changes could be explained by the nature of substituent or by the reactivity of the molecule. According to literature,<sup>45</sup> the toxicity of benzophenone type UV filters, in general, decreases after the chlorination process.

Toxicity assessment of sunscreens containing avobenzone within chlorination of photodegradation experiments have been performed using marine bacteria *Vibrio fischeri*. It has been shown that within chlorination of avobenzone alone, as well as in sunscreens, in all cases the toxicity increased. We assumed that more toxic products than the original molecule are formed.<sup>36</sup>

The results of toxicity measurements on resveratrol and a sunscreen containing it showed no inhibition effect on *V. fischeri* at the beginning and after 120 min of exposure, whereas it was significantly higher already at the beginning of chlorination experiment and remained almost the same throughout the whole experiment. Active chlorine reacted immediately with resveratrol, no matter was it present as a pure substance or a component of the sunscreen.<sup>37</sup>

## 5. Experiments of Chlorination of Benzophenone and Resveratrol on Human Skin

For this study,<sup>46</sup> a controlled clinical trial was conducted on 38 volunteers (age: 20–60; female: 28; male: 10) to whom an area of the forearm was irradiated with an UV-B light. To conduct the study, the consent of Slovenian National Medical Ethics Committee was obtained (16 May 2018, No. 0120-368/2017/5), as well as written consents from all volunteers. The clinical study was done at the Faculty of Health Sciences, at the University of Ljubljana, in summer 2019 (from June to August). The investigation was oriented to understand the photoprotection role of UV filter (BP3) and two antioxidants (*trans*-resveratrol and  $\beta$ -carotene) under various conditions (including disinfection conditions) on human skin.

For this application, a portable colorimeter (Konica Minolta Chroma Meters CR-410 [Tokyo, Japan]) was used to measure skin redness using the guidelines for skin color measurement and erythema.<sup>47</sup> The skin squares  $3 \times 3$  cm ( $9 \text{ cm}^2$ ) were irradiated over different periods (the 1<sup>st</sup> square uncovered for the entire irradiation period of 8 min, the 2<sup>nd</sup> for 6 min, and the 3<sup>rd</sup> for 4 min). Other squares served to check the effectiveness of the UV filter in the presence of antioxidants and disinfectants.

Descriptive statistics (arithmetic means, standard deviation, *t*-test, one-way repeated-measures ANOVA, Mauchly's test, etc.), were used to describe the skin colours' differences between trials.

The role of antioxidants in sunscreens has previously been reported in a study by Gaspar and Campos,<sup>48</sup> including the combinations of UV filters and vitamins A, C, and E, where the presence of vitamins reduced the skin irritation. Their results are in accordance with the results obtained in our study where we demonstrated the formation of several chlorinated products (5-Cl-BP3, and 3,5-di-Cl-BP3); however, their effect on skin was not tested at that point. Moreover, the formed benzophenone-3 chlorination products were photostable (more than 95% of the initial concentration) during the irradiation periods. The protective role of antioxidants in disinfection conditions was expected also in case of resveratrol and its 82 identified transformation products. In fact, the results proved the resveratrol's protective role and its high potential for acting as a scavenger of reactive oxygen species (ROS) in sunscreens. The addition of antioxidant molecules is beneficial for UV filters by protecting against UV degradation/disinfection processes and other *in vivo* skin effects.<sup>49</sup>

In summary, this clinical study showed that formulations containing antioxidants were more efficient in skin protection than solely UV filters, since they helped to reduce the skin redness. Despite the formation of chlorinated products of BP3 in the presence of chlorinated water, the photoprotection was still effective.

## 6. Conclusions

In our studies we pointed out the importance of identification of chlorinated products, formed in the transformation processes under disinfection conditions in swimming pool waters. Chlorinated products are a very diverse group of compounds. Usually within disinfection processes they are formed very fast. It is highly important to identify them, characterize and then perform toxicity studies since their effects on humans are in many cases still unknown. Mass spectrometry (MS) has proven once again to be the most powerful analytical tool to study environmental issues. Because of its unsurpassed sensitivity, selectivity, and ability to handle complex mixtures of the most various compounds, it is used both in controlling the levels of targeted toxicants in the environment and in research dealing with the discovery of new natural and anthropogenic compounds.<sup>50</sup>

MS is used as a principal method to determine and to quantify disinfection (chlorination) by-products (DBP). Currently, due to applications of both liquid chromatography (LC-MS) and gas chromatography (GC-MS) techniques approximately 700 disinfection by-products are officially listed.<sup>51</sup>

In addition, comparative toxicity studies should be performed for all combinations of parent compounds, as well as for chlorinated products. Our data demonstrated that the toxic potential of benzophenone-like UV filters is related to differences between the type of tested UV filter, the modified effects after chlorination (modification of molecular structure), and species-specific effects (type of organism).

At the end, the closing loop of all efforts of chlorination experiments was the clinical trial, where we have, thanks to volunteers, tested in real environment the photoprotective role of complex mixtures of UV filter, antioxidants during the chlorination process, mimicking in the laboratory the real swimming pool situations.

**FUNDING:** This research was funded by Slovenian Research Agency (ARRS), the research core funding No. P3-0388 (Mechanisms of Health Maintenance).

## 7. References

1. D. L. Giokas, A. Salvador, A. Chisvert, *TrAC* **2007**, *26*, 360–374. DOI:10.1016/j.trac.2007.02.012
2. M. S. Diaz-Cruz, M. Llorca, D. Barcelo, *TrAC* **2008**, *27*, 873–887. DOI:10.1016/j.trac.2008.08.012
3. CosIng – Cosmetics Ingredients [http://ec.europa.eu/consumers/cosmetics/cosing/index.cfm?fuseaction=search.results&annex\\_v2=VI&search](http://ec.europa.eu/consumers/cosmetics/cosing/index.cfm?fuseaction=search.results&annex_v2=VI&search) (assessed: August, 2023)
4. US Food and Drug Administration, **1999**, Sunscreen drug products for over-the-counter human use: Final mono-

- graph. Federal Register, 64(98), 27666–27693.
5. N. A. Shaat, *Photochem. Photobiol. Sci.* **2010**, 9, 464–469. DOI:10.1039/b9pp00174c
  6. V. A. Sakkas, D. L. Giokas, D. A. Lambropoulou, T. A. Albanis, *J. Chromatogr. A* **2003**, 1016, 211–222. DOI:10.1016/S0021-9673(03)01331-1
  7. J. Xiao, J. Song, V. Hodara, A. Ford, X. L. Wang, Q. Shi, J. L. VandeBerg, *J. Diabetes Res.* **2013**, 2013. DOI:10.1155/2013/185172
  8. W. Chao, Z. Xuexin, S. Jun, C. Ming, J. Hua, L. Guofu, X. Wanhai, *Exp. Ther. Med.* **2014**, 7(4), 923–928. DOI:10.3892/etm.2014.1544
  9. D. Rossi, A. Guerrini, R. Bruni, E. Brognara, M. Borgatti, R. Gambari, G. Sacchetti, *Molecules* **2012**, 17(10), 12393–12405. DOI:10.3390/molecules171012393
  10. S. Agustin-Salazar, N. Gamez-Meza, L. À. Medina-Juárez, H. Soto-Valdez, P. Cerruti, *ACS Sustain. Chem. Eng.* **2014**, 2(6), 1534–1542. DOI:10.1021/sc5002337
  11. N. Negreira, P. Canosa, I. Rodriguez, M. Ramil, E. Rubi, R. Cela, *J. Chromatogr. A* **2008**, 1178, 206–214. DOI:10.1016/j.chroma.2007.11.057
  12. M. Nakajima, T. Kawakami, T. Niino, Y. Takahashi, S. Onodera, *J. Health Sci.* **2009**, 55, 363–372. DOI:10.1248/jhs.55.363
  13. A. J. M. Santos, M. S. Miranda, J. C. G. Esteves da Silva, *Water Res.* **2012**, 46, 3167–3176. DOI:10.1016/j.watres.2012.03.057
  14. A. J. M. Santos, D. M. A. Crista, M. S. Miranda, I. F. Almeida, J. P. S. de Silva, P. C. Costa, M. H. Amaral, P. A. L. Lobão, J. M. S. Lobo, J. C. G. E. da Silva, *Environ. Chem.* **2013**, 10, 127–134. DOI:10.1071/EN13012
  15. D. M. A. Crista, M. S. Miranda, J. C. G. Esteves da Silva, *Environ. Technol.* **2015**, 36, 1319–1326. DOI:10.1080/09593330.2014.988184
  16. S. Díaz-Cruz, D. M. Barceló, *TrAC* **2009**, 28, 708–717. DOI:10.1016/j.trac.2009.03.010
  17. K. Fent, P. Y. Kunz, A. Zenker, M. Rapp, *Mar. Environ. Res.* **2010**, 69, S4–S6. DOI:10.1016/j.marenvres.2009.10.010
  18. J. M. Brausch, G. M. Rand, *Chemosphere*, **2011**, 82, 1518–1532. DOI:10.1016/j.chemosphere.2010.11.018
  19. D. Kaiser, A. Sieratowicz, H. Zielke, M. Oetken, H. Hollert, J. Oehlmann, *Environ. Pollut.* **2012**, 163, 84–90. DOI:10.1016/j.envpol.2011.12.014
  20. J. Y. Hu, T. Aizawa, S. Ookubo, *Environ. Sci. Technol.* **2002**, 36, 1980–1987. DOI:10.1021/es011177b
  21. J. Y. Hu, G. H. Xie, T. Aizawa, *Environ. Sci. Technol.* **2002**, 21, 2034–2039. DOI:10.1002/etc.5620211005
  22. J. Y. Hu, S. Cheng, T. Aizawa, Y. Terao, S. Kunikane, *Environ. Sci. Technol.* **2003**, 37, 5665–5670. DOI:10.1021/es034324+
  23. J. Y. Hu, X. Jin, S. Kunikane, Y. Terao, T. Aizawa, *Environ. Sci. Technol.* **2006**, 40, 487–493. DOI:10.1021/es0516108
  24. Q. Liu, Z. Chen, D. Wei, Y. Du, *J. Environ. Sci.* **2014**, 26, 440–447. DOI:10.1016/S1001-0742(13)60411-8
  25. V. A. Sakkas, D. L. Giokas, D. A. Lambropoulou, T. A. Albanis, *J. Chromatogr. A* **2003**, 1016, 211–222. DOI:10.1016/S0021-9673(03)01331-1
  26. A. T. Lebedev, *Eur. J. Mass Spectrom.* **2007**, 13(N1), 51–56. DOI:10.1255/ejms.852
  27. S. E. Duirk, D. R. Bridenstine, D. C. Leslie, *Water Res.* **2013**, 47, 579–587. DOI:10.1016/j.watres.2012.10.021
  28. T. Manasfi, V. Storck, S. Ravier, C. Demelas, B. Coulomb, J.-L. Boudenne, *Environ. Sci. Technol.* **2017**, 51, 13580–13591. DOI:10.1021/acs.est.7b02624
  29. M. Xiao, D. Wei, J. Yin, G. Wei, Y. Du, *Water Res.* **2013**, 47 (16), 6223–6233. DOI:10.1016/j.watres.2013.07.043
  30. N. Negreira, I. Rodriguez, R. Rodil, R. Cela *Anal. Chim. Acta* **2012**, 743, 101–110. DOI:10.1016/j.aca.2012.07.016
  31. R. Zhuang, R. Žabar, G. Grbović, D. Dolenc, J. Yao, T. Tišler, P. Trebše, *Acta Chim. Slov.* **2013**, 60, 826–832.
  32. G. Grbović, P. Trebše, D. Dolenc, A. T. Lebedev, M. Sarakha, *J. Mass Spectrom.* **2013**, 48, 1232–1240. DOI:10.1002/jms.3286
  33. K. Kalister, D. Dolenc, M. Sarakha, O. V. Polyakova, A. T. Lebedev, P. Trebše, *J. Anal. Chem.* **2016**, 71:14, 1289–1293. DOI:10.1134/S1061934816140057
  34. P. Trebše, O. V. Polyakova, M. Baranova, M. Bavcon Kralj, D. Dolenc, M. Sarakha, A. Kutin, A. T. Lebedev, *Water Res.* **2016**, 101, 95–102. DOI:10.1016/j.watres.2016.05.067
  35. E. A. Detenchuk, J. Chen, O. V. Polyakova, P. Trebše, S. A. Pokryshkin, A. T. Lebedev, *J. Anal. Chem.* **2019**, 74, 1271–1276. DOI:10.1134/S1061934819130069
  36. A. T. Lebedev, M. Bavcon Kralj, O. V. Polyakova, E. A. Detenchuk, S. A. Pokryshkin, P. Trebše, *Environ. Int.* **2020**, 137, 105495-1-105495-8. DOI:10.1016/j.envint.2020.105495
  37. E. A. Detenchuk, P. Trebše, A. Marjanović, D. S. Kosyakov, N. V. Ul'yanovskii, M. Bavcon Kralj, A. T. Lebedev, *Chemosphere* **2020**, 260, 127557. DOI:10.1016/j.chemosphere.2020.127557
  38. A. T. Lebedev, *Eur. J. Mass Spectrom.* **2007**, 13(1), 51–56. DOI:10.1255/ejms.852
  39. N. Y. Tretyakova, A. T. Lebedev, V. S. Petrosyan, *Environ. Sci. Technol.* **1994**, 28(4), 606–613. DOI:10.1021/es00053a012
  40. A. A. Chugunova, M. Bavcon Kralj, O. V. Polyakova, V. Artaev, P. Trebše, S. A. Pokryshkin, A. T. Lebedev, *J. Anal. Chem.* **2017**, 72, 1369–1374. DOI:10.1134/S1061934817140039
  41. C. Wang, M. Bavcon Kralj, B. Košmrlj, J. Yao, S. Košenina, O.V. Polyakova, V. Artaev, A. T. Lebedev, P. Trebše, *Chemosphere* **2017**, 182, 238–244. DOI:10.1016/j.chemosphere.2017.04.125
  42. ISO 11348-2, Water quality – Determination of the inhibitory effect of water samples on the light emission of *Vibrio fischeri* (Luminescent bacteria test) – Part 2: Method using liquid-dried bacteria, International Organization for Standardization, Geneva, Switzerland, 2007.
  43. ISO 8692, Water quality – Fresh water algal growth inhibition test with unicellular green algae, International Organization for Standardization, Geneva, Switzerland, 2012.
  44. ISO 6341, Water quality – Determination of the inhibition of the mobility of *Daphnia magna* Straus (Cladocera, Crustacea) – Acute toxicity test, International Organization for Standardization, Geneva, Switzerland, 2012.
  45. G. Grbović, O. Malev, D. Dolenc, R. Sauerborn Klobučar, Ž. Cvetković, B. Cvetković, B. Jovančičević, P. Trebše, *Environ. Chem.* **2016**, 13(1), 119–126. DOI:10.1071/EN15013

46. R. Sotler, M. Adamič, K. Jarni, R. Dahmane, P. Trebše, M. Bavcon Kralj, *Antioxidants* **2021**, *10*(11), 1720. DOI:10.3390/antiox10111720
47. H. Maibach, G. P. Honari: *Applied Dermatotoxicology: Clinical Aspects*, 1<sup>st</sup> ed.; Elsevier Inc.; Academic Press: San Francisco, CA, USA, **2014**, pp.41–56. DOI:10.1016/B978-0-12-420130-9.00003-7
48. L. R. Gaspar, P. M. Campos, *Int. J. Pharm.* **2007**, *343*(1-2), 181–189. DOI:10.1016/j.ijpharm.2007.05.048
49. K. Geoffrey, A. N. Mwangi, S. M. Maru, *SPJ* **2019**, *27*(7), 1009–1018. DOI:10.1016/j.jsps.2019.08.003
50. D. M. Mazur, A. T. Lebedev, *J. Anal. Chem.* **2022**, *77*(14), 1705–1728. DOI:10.1134/S1061934822140052
51. S. D. Richardson, T. A. Ternes, *Anal. Chem.* **2018**, *90*(1), 398–428. DOI:10.1021/acs.analchem.7b04577

## Povzetek

Članek povzema raziskave naše skupine o sintezi, karakterizaciji in toksičnosti izbranih UV-A filtrov in ter vlogo antioksidanta resveratrola kot dodatka v kremah za zaščito pred soncem. UV filtri benzofenonskega tipa reagirajo pod dezinfekcijskimi pogoji s klorom, pri čemer se tvorijo mono- in diklorirani produkti. Derivati dibenzoilmetana, kot je avobenzon, pa reagirajo s klorom tako, da najprej reagira metilenska skupina avobenzona, pri čemer se tvori dva glavna klorirana produkta, v nadaljevanju procesa pa sledi nastanek številnih kloriranih produktov. Resveratrol vsebuje tri skupine, na katerih poteče kloriranje, začenši z elektrofilno adicijo na dvojno vez ter s kloriranjem fenolnih delov. Več poskusov, izvedenih v različnih pogojih dezinfekcije (bazen/morska voda, dodajanje soli, obsevanje s svetlobo), je pokazalo podobne vzorce kloriranja z razlikami pri številu in tipu produktov. Rezultati ugotavljanja toksičnosti z uporabo različnih testnih organizmov (*Vibrio fischeri*, mikroalge, vodne bolhe) so pokazali različno občutljivost testnih organizmov na osnovne UV filtre v primerjavi s kloriranimi produkti ter različno toksičnost posameznih UV filtrov. Nadgradnjo vseh laboratorijskih poskusov predstavlja študija izpostavljenosti pogojem kloriranja in obsevanja, ki je bila izvedena na človeški koži.



Except when otherwise noted, articles in this journal are published under the terms and conditions of the Creative Commons Attribution 4.0 International License

Scientific paper

# Synthesis, Crystal Structure, Hirshfeld Surface Analysis, and DFT Calculations of the New Binuclear Copper(I) Complex Containing 2-Benzimidazolethiole and Triphenylphosphine Ligands

Karwan Omer Ali

Department of General Science, College of Education, University of Halabja, Halabja 46018, Iraq

\* Corresponding author: E-mail: karwan.ali@uoh.edu.iq

Phone No. 009647503849284

Received: 08-26-2023

## Abstract

The reaction of 2-benzimidazolethiole (L) with copper dichloride in the presence of two equivalents of triphenylphosphine led to a binuclear complex of the type  $[\text{Cu}(\text{L})_2(\text{Ph}_3\text{P})_2\text{Cl}_2]$ : dichloridobis( $\mu$ -1,3-dihydro-2H-benzimidazole-2-thione) bis(triphenylphosphine)-di-copper. The Cu(I) compound has been fully identified by elemental analysis, molar conductivity, FT-IR, UV/Vis, and single-crystal X-ray diffraction (XRD). The XRD study reveals that the complex has distorted tetrahedral geometry around the Cu(I) center, which contains two bridge sulfur atoms. The Hirshfeld surface mapped over  $d_{\text{norm}}$ , shape index, and curvature revealed important  $\text{H}\cdots\text{H}$ ,  $\text{H}\cdots\text{C}/\text{C}\cdots\text{H}$ , and  $\text{H}\cdots\text{Cl}/\text{Cl}\cdots\text{H}$  intermolecular interactions as the main contributors to crystal packing. The natural bond orbital (NBO) was applied to understand the strength of nucleophilic and electrophilic attack between ligands and Cu(I) ions. Furthermore, density functional theory (DFT) was employed to demonstrate the molecular reactivity and stability of the ligands and copper complex.

**Keywords:** Copper(I), 2-benzimidazolethiole, distorted tetrahedral geometry, Hirshfeld surface analysis, DFT studies

## 1. Introduction

The extensive study currently conducted in Cu(I) coordination compounds is due to the interactions of this cation in particular chemical redox reactions and can utilize a variety of coordination modes.<sup>1</sup> Cu(I) halides produce complexes with triphenylphosphine as ligands that have copper halide to ligand ratios of 1:2, 2:2, 1:3, 2:3, and 2:4 with the geometry typically being controlled by steric instead of electronic properties of the phosphine ligands.<sup>2,3</sup> Due to their lower toxicity, greater availability, and comparably lower cost compared to third-row transition metal compounds including rhenium, iridium, platinum, and gold, Cu(I) complexes with irregular square planar and tetrahedral geometry are in perpetual interest.<sup>4</sup> For a long time, there is a continuous interest about chelating agents comprising nitrogen and sulfur-donor atoms among with their metal complexes.<sup>5,6</sup> This consideration results from their antimicrobial,<sup>7</sup> antitumour<sup>8,9</sup> activities along with other numerous potential pharmaceutical applications.<sup>10</sup> Several mixed-ligand coordination complexes of Cu(I)

halides with thione compounds and triphenylphosphines were synthesized and structurally determined during our previous study on the interaction of univalent group IB metals with biologically important molecules.<sup>11,12</sup> In such complexes, neutral thione ligands that contained both nitrogen and sulfur as donor atoms regularly adopted the unidentate coordination mode, coordinating with the metal ions via the exocyclic sulfur atom in a bridging or terminal form.<sup>13</sup> However, an incredible variety of complexes, ranging from mononuclear three- or four-coordinate thiones with square planar and tetrahedral Cu(I), respectively, to dimers with distorted tetrahedral geometry, are produced by bridging thione ligands through sulfur atoms.<sup>14,15</sup> For decades, mixed-ligand complexes have pinched a lot of attention as a result of their serious function in biological processes. Numerous studies<sup>16–22</sup> have discussed the production and spectral investigation of mixed-ligand complexes. It was found that the insertion of heterocyclic nitrogen donor ligands, such as nitrogen, oxygen-donors like 8-hydroxyquinoline or nitrogen, nitrogen-donors like 1,10-phenanthroline, significantly en-

hanced the biological and pharmacological actions of the complexes.<sup>16–23</sup> In the current study, a new Cu(I) complex based on a 2-benzimidazolethiole ligand (L) was synthesized and investigated. This complex was characterized using elemental analysis, molar conductivity, FT-IR, UV-Vis, and X-ray analysis. Hirshfeld surface analysis was also used to confirm the crystal structure, which is useful for interpreting the intermolecular forces in crystal packing. DFT simulations were also carried out to forecast the complex's electronic and geometrical structure.

## 2. Experimental

### 2.1. Materials and General Methods

In this study, methanol (99%), dichloromethane (99.7%), and dimethyl sulfoxide (99.8%) were bought from Alfa Aesar and used without further purification. The Sigma-Aldrich product 2-benzimidazolethiole (L) was used directly. At 296 K, a Bruker Kappa Apex II diffractometer was used to measure the single-crystal X-ray structure with a radiation wavelength of ( $\lambda = 0.71073$ ). The EURO EA 300 CHNS analyzer was used to determine the percentages of C, H, N, and S. Infrared spectra in the 4000–400  $\text{cm}^{-1}$  and 600–200  $\text{cm}^{-1}$  range as KBr and CsI discs, respectively, were taken using a Shimadzu FT-IR-8400S spectrophotometer. On the AEUV1609 LTD Shimadzu spectrophotometer, the UV-visible spectra of the compounds in DMSO were measured. On a Meter CON 700 Benchtop Conductivity Meter, the molar conductivities of  $10^{-3}$  M solutions of the complex and ligands in DMSO were measured at 25 °C. The Scientific Stuart SMP3 melting point apparatus was used to determine the melting point of the complex.

### 2.2. Synthesis of $[\text{Cu}(\text{L})_2(\text{Ph}_3\text{P})_2\text{Cl}_2]$

Dropwise under stirring, a solution of  $\text{CuCl}_2 \cdot \text{H}_2\text{O}$  (0.341 g, 2.0 mmol) in methanol (20 mL) was added to a solution mixture of 2-benzimidazolethiole (L) ligand (0.300 g, 2.0 mmol) and triphenylphosphine ligand (0.524 g, 2.0 mmol) in dichloromethane (25 mL). After that, the mixture was stirred for 4 h. at room temperature, resulting in the formation of a clear solution, which was then slowly evaporated at room temperature to produce white crystalline products within two weeks. m.p. 238–239 °C. Yield: 0.947 g (81.60 %). Anal. Calcd. for  $\text{C}_{50}\text{H}_{42}\text{Cl}_2\text{Cu}_2\text{N}_4\text{P}_2\text{S}_2$ : C 58.65, H 4.10, N 5.47, S 6.25. Found: C 58.58, H 4.12, N 5.48, S 6.22. Molar conductivity:  $7.31 \times 10^{-5}$  S  $\text{cm}^2 \text{mol}^{-1}$ . FT-IR (KBr) 3138, 3097, 3055, 1620, 1508, 1458, 1348, 734, 697, 457  $\text{cm}^{-1}$ . UV-Vis data in DMSO [ $\lambda/\text{nm}$ , ( $\text{cm}^{-1}$ ): 316(31645), 247(40485).

### 2.3. X-ray Crystal Structure Determination

A Bruker Kappa Apex II X-ray diffractometer with graphite monochromated Mo-K $\alpha$  radiation ( $\lambda =$

0.71073) at 296 K was used to measure the X-ray diffraction of the Cu(I) complex. The crystallographic software SHELXT-2018 was used to solve the structure using a dual-space algorithm, and SHELXL-2018/3 was used to refine it using least-squares procedures. All C, N, Cl, S, and Cu atoms were anisotropically resolved.<sup>24,25</sup> All of the C, N, Cl, S, and Cu atoms were resolved anisotropically. The hydrogen atoms bound to the C atoms were permitted to rotate geometrically and were treated as a riding model with a C-H distance of 0.93 Å (aromatic), 1.72 Å (C-S group), and 0.84 Å (-NH group).<sup>26</sup> The complex's crystal data and structure refinement details have been collected in Table 1.

Table 1. Crystal data and structure refinement of the complex

Formula	$\text{C}_{50}\text{H}_{42}\text{Cl}_2\text{Cu}_2\text{N}_4\text{P}_2\text{S}_2$
Formula weight	1022.94
Temperature, K	296
Wavelength, Å	0.71073
Crystal system	triclinic
Space group	P-1 (No. 2)
Crystal size, mm	0.18 x 0.43 x 0.47
$a / \text{Å}$	12.4699(7)
$b / \text{Å}$	13.7519(7)
$c / \text{Å}$	14.0572(6)
$\alpha / ^\circ$	95.051(2)
$\beta / ^\circ$	91.866(2)
$\gamma / ^\circ$	103.818(2)
$V / \text{Å}^3$	2328.2(2)
$Z$	2
$D_c / \text{g cm}^{-3}$	1.459
$\mu(\text{Mo-K}\alpha) (\text{mm}^{-1})$	1.227
$\theta$ range for data collection, °	1.5, 28.4
Dataset	-16:16; -18:18; -18:18
$F(000)$	1048
No. of reflections	11605
No. of parameters	575
$R_{\text{int}}$	0.022
$R_1, wR_2$	0.0320, 0.0855
$S$	1.04
$[I > 2\sigma(I)]$	9718
$\Delta\rho_{\text{min}}, \Delta\rho_{\text{max}} / \text{e}\text{Å}^{-3}$	-1.08, 1.02

### 2.4. Computational Details

Density functional theory (DFT) calculations were performed using the Gaussian 09 software program to better understand the structure of the copper complex. The Gauss View 6.0 program at the B3LYP level of theory was helpful in determining the frontier molecular orbitals of the ligand and the Cu(I) complex.<sup>27</sup> In particular, the 6-31G(d) basis set for non-metal elements (C, H, N, S, and Cl) and the LANL2DZ basis set for the copper metal atom were both studied.<sup>28</sup> Using the same level of theory, the complex's neutral bond orbital (NBO) analysis was carried out using the Gaussian 06 program.<sup>29</sup>

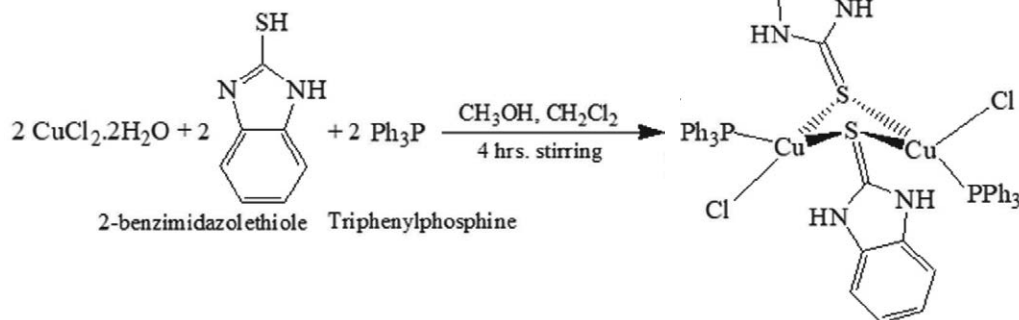


## 2. 5. Hirshfeld Surface

For the Hirshfeld surface visualization of the Cu(I) complex, a crystallographic information file (CIF) obtained from single-crystal X-ray diffraction studies used as the input file. Using the program Crystal Explorer 21.5, the Hirshfeld surface analysis was generated in order to better understand the intermolecular interactions in the complex crystal structure.<sup>30</sup> Using the same program, 2D fingerprint plots with dean  $d_e$  and  $d_i$  distances were calculated, Hirshfeld surface visualization was performed, and results were presented as  $d_{\text{norm}}$ , shape index, and curvedness.<sup>31</sup>

## 3. Results and Discussion

The 2-benzimidazolethiole (L) and triphenylphosphine ligands react with Cu(II) chloride to produce the Cu(I) complex, as illustrated in Scheme 1. In this reaction, Cu(II) is reduced to Cu(I) by triphenylphosphine, which acts as a reducing agent. Under atmospheric conditions, the synthesized Cu(I) compound complex is stable. The metal complex was successfully synthesized as white crystals with a good yield suitable for single-crystal X-ray structure analysis. The complex dissolves in common organic solvents such dimethyl sulfoxide, dimethylformamide, and chloroform at ambient temperature but not in ethanol, acetone, methanol, or water.



Scheme 1. Synthetic route of the Cu(I) complex.

### 3. 1. Description of the Cu(I) Crystal Structure

The main bond lengths and angles for the Cu(I) complex are given in Table 2, and Table 3 shows the details of the hydrogen bonding. Figure 1 display molecular plots that display the atom numbering schemes. The two copper atoms are surrounded by one P and one Cl atom in a distorted tetrahedral coordination, producing a binuclear complex. The two copper atoms are bridged by two sulfur atoms. The largest variation from the ideal tetrahedral geometry is reflected by the Cl1-Cu1-S1, Cl1-Cu1-P2, S1-Cu1-P2, and Cl2-Cu2-S3 bond angles, with values of 113.40(2), 114.65(2), 116.40(2), and 112.67(2),

respectively. These higher bond angles are counterbalanced by the bond angles Cu1-S1-Cu1\_a and Cu2-S3-Cu2\_b, whose values are all less than the ideal tetrahedral value of 109.5°. The bulky triphenylphosphine and the 2-benzimidazolethiole (L) ligands often interact sterically to cause this tetrahedral distortion in a large number of dimeric copper (I) complexes that also contain one heterocyclic thione and two monodentate triphenylphosphine ligands.<sup>32</sup> The bond lengths between Cu1-P2 (2.2379(5)) and Cu2-P4 (2.2371(5)) are shorter than those between Cu1-S1 (2.3256(6)) and Cu2-S3 (2.3580(5)), showing that the interaction between Cu(I) metal center and P donor atom is stronger than that between Cu(I) and S donor atom. The torsional angles of Cl1-Cu1-S1-Cu1\_a, P2-Cu1-S1-C17, and Cl1-Cu1-P2-C211 are 100.94(2)°, 130.32(7)°, and 179.75(7)°, respectively, which results in steric repulsion between triphenylphosphine and thione rings and electron repulsion of chlorine and nitrogen atoms.<sup>33</sup> In the crystal structure of the Cu(I) complex, there are intermolecular N11-H11...Cl1, N12-H12...Cl2, N31-H31...Cl2, N32-H32...Cl1, C212-H212...N11 and C433-H433...Cl1 hydrogen bonds, the nitrogen and carbon atoms of the ligand acts as proton donors, whereas the chlorine acts as proton acceptors.

Table 2. Selected bond lengths (Å) and angles (°) of the complex.

Bond	Distances, Å	Bond	Angle, °
Cu1-Cl1	2.3402(5)	Cl1-Cu1-S1	113.40(2)
Cu1-S1	2.3256(6)	Cl1-Cu1-P2	114.65(2)
Cu1-P2	2.2379(5)	Cl1-Cu1-S1_a	93.49(2)
Cu1-S1_a	2.6203(6)	S1-Cu1-P2	116.40(2)
Cu2-Cl2	2.3563(7)	S1_a-Cu1-S1_a	105.63(2)
Cu2-S3	2.3580(5)	S1_a-Cu1-P2	110.35(2)
Cu2-P4	2.2371(5)	S3-Cu2-S3_b	103.82(2)
Cu2-S3_b	2.4727(5)	S3_b-Cu2-P4	114.30(2)
S1-C17	1.7094(19)	Cl2-Cu2-S3	112.67(2)
P2-C211	1.8237(18)	Cl2-Cu2-P4	107.02(2)
P2-C221	1.8236(19)	Cl2-Cu2-S3_b	101.37(2)
P2-C231	1.822(2)	Cu1-S1-Cu1_a	74.37(2)
S3-C37	1.721(2)	Cu2-S3-Cu2_b	76.18(2)

Table 3. Hydrogen bonding ( $\text{\AA}$ ,  $^\circ$ ) for Cu(I) complex.

D-H...A	$d(\text{D-H}) / \text{\AA}$	$d(\text{H...A}) / \text{\AA}$	$d(\text{D...A}) / \text{\AA}$	$\angle(\text{DHA}) / ^\circ$
N11-H11...Cl1	0.84(2)	2.28(2)	3.1076(17)	166(2)
N12-H12...Cl2	0.840(18)	2.52(2)	3.2323(18)	143(2)
N31-H31...Cl2	0.86(2)	2.24(2)	3.0648(19)	159(2)
N32-H32...Cl1	0.855(19)	2.376(19)	3.2021(19)	163(2)
C212-H212...N11	0.9300	2.5300	3.255(3)	135.00
C433-H433...Cl1	0.9300	2.8200	3.548(3)	136.00

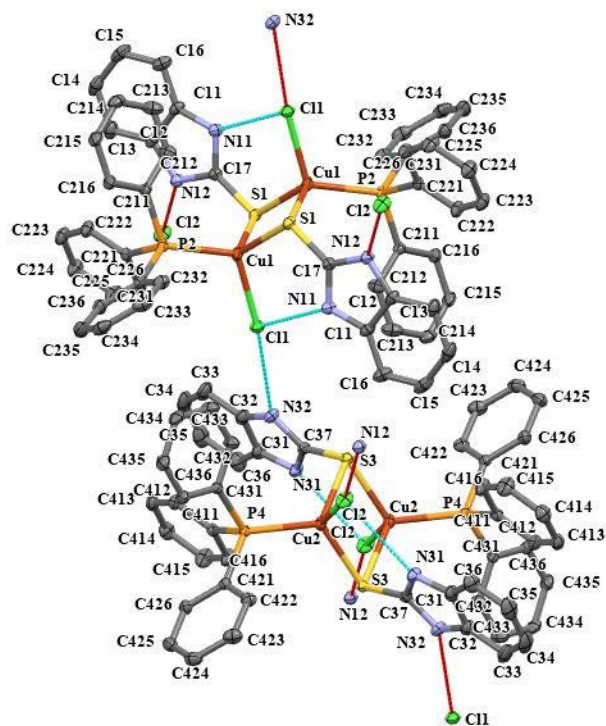


Figure 1. Crystal structure of  $[\text{Cu}(\mu\text{-S-2-BIT})_2(\text{Ph}_3\text{P})_2\text{Cl}_2]$  shown at 20% ellipsoid probability, H atoms are omitted for clarity.

### 3. 2. FT-IR Spectra

The medium intensity peak at  $3155 \text{ cm}^{-1}$  in the IR spectrum of the ligand (2-BIT) can be attributed to the stretching vibration of the NH group, which is shifted by  $17 \text{ cm}^{-1}$  to a lower frequency due to hydrogen bonding because hydrogen bonding weakens the N-H bond, resulting in its absorption frequency being lower.<sup>34</sup> The infrared spectrum of the Cu(I) complex lacked the stretching vibration of the thiol (SH) group at  $2562 \text{ cm}^{-1}$ , indicating that the sulfur atom is coordinated to the metal center and the thione tautomer is more dominant than the thiol tautomer.<sup>35</sup> The strong band at  $1458 \text{ cm}^{-1}$  related to  $\nu(\text{P-C})$  of the triphenylphosphine ligand.<sup>36</sup> The band at  $457 \text{ cm}^{-1}$  in the complex's IR spectrum may be attributed to  $\text{C}=\text{S}-\text{Cu}$  vibrations, whereas the band at  $343 \text{ cm}^{-1}$  is considered to be related to  $\text{Cu}-\text{Cl}$  vibrations.<sup>37</sup> Furthermore, the com-

plex IR spectrum showed a high intensity band at  $697 \text{ cm}^{-1}$  corresponding to  $\nu(\text{Cu-P})$ .<sup>38</sup>

### 3. 3. Electronic Spectra and Conductivity Study

The electronic absorption spectrum of the Cu (I) complex in dimethyl sulfoxide is dominated by two broad bands at 247 and 316 nm.<sup>39</sup> The first one is due to intra-ligand transitions of the triphenylphosphine ligand because uncoordinated triphenylphosphine shows a strong absorption band at 245 nm, which normally stays unshifted upon coordination to Cu(I).<sup>40</sup> The free 2-BIT ligand exhibits a band at 304 nm, whereas the absorption spectrum of the Cu(I) coordination complex is red-shifted by 12 nm, indicating  $\text{C}=\text{S}$  coordination to the Cu(I) center in the LMCT transition.<sup>41</sup> The molar conductivity value in DMSO ( $7.31 \times 10^{-5} \text{ S cm}^2 \text{ mol}^{-1}$ ) of the synthesized complex was found to be very low, suggesting that it is non-ionic in nature.<sup>42</sup>

### 3. 4. DFT Studies

The electronic characteristics of the ligands and Cu(I) complex were investigated using frontier molecular orbitals. The highest occupied molecular orbital ( $E_{\text{HOMO}}$ ) and lowest unoccupied molecular orbital ( $E_{\text{LUMO}}$ ) energies are used to calculate the HOMO-LUMO energy gap ( $\Delta E = E_{\text{LUMO}} - E_{\text{HOMO}}$ ). The energy gaps of the ligands and Cu(I) complex are displayed in Table 4 and Figure 2. One of the most important theories for predicting complex reactivity and stability is the theory of frontier molecular orbitals. A reaction between two chemical compounds is shown by the interaction of one compound's HOMO orbital and another compound's LUMO orbital, according to this idea.<sup>43</sup> The energy gaps ( $\Delta E$ ) of the free 2-BIT and  $\text{Ph}_3\text{P}$  ligands are 6.573 eV and 6.706 eV, respectively, whereas the Cu(I) complex has an ( $\Delta E$ ) of 3.194 eV. Therefore, compared to ligands, the synthesized Cu(I) complex in our study is less stable and more reactive. The 2-BIT ligand appears to be less stable and more reactive than the triphenylphosphine ligand. Table 3 shows the computed NBO atomic charges for the free ligands and their complexes. The Natural Bond Orbitals (NBO) are used to compute electron densities (distributions) in atoms as well as bonds between atoms.<sup>44</sup>

The natural charges of the Cu atom reduce when 2-BIT is connected to Cu by its S atoms, which also become more positive (moved from 0.022e on the ligand alone to 0.226, 0.225e on the ligand coordinated to the Cu complex).

However, the Cu-P complexes have changed slightly (from 0.842e to 0.977e and from 0.842 to 1.000e for P37 and P71), suggesting electron transfer from the  $\text{Ph}_3\text{P}$  ligand to the metal center.<sup>45</sup>

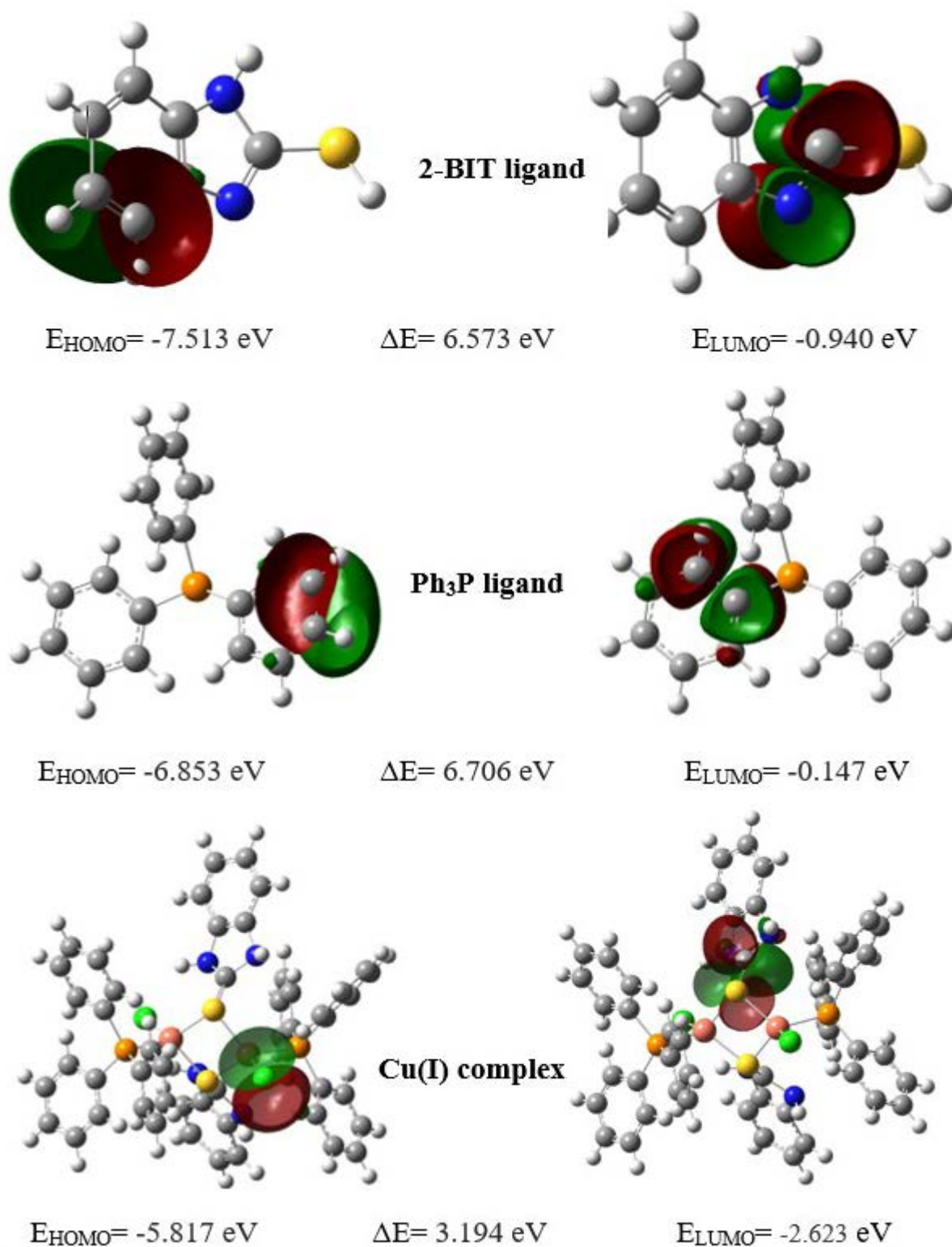


Figure 2. Surface plots of HOMO and LUMO orbitals of ligands and Cu(I) complex

**Table 4.** Energy properties (eV) and NBO Charge (e) of ligands and their Cu(I) complex.

Parameter	Ph <sub>3</sub> P	2-BIT	Cu(I) complex
$E_{\text{HOMO}}^{\text{O}}$	-6.853	-7.513	-5.817
$E_{\text{LUMO}}$	-0.147	-0.940	-2.623
$\Delta E$	6.706	6.573	3.194

The NBO Charge of ligands and Cu(I) complex				
Atom	Ph <sub>3</sub> P	2-BIT	Atom	Cu(I) complex
N12	-	-0.480	Cu1, Cu2	-0.120, -0.166
N13	-	-0.580	S3, S4	0.226, 0.225
S	-	0.022	Cl5, Cl6	-0.553, -0.535
P	0.842	-	P37, P71	0.977, 1.000

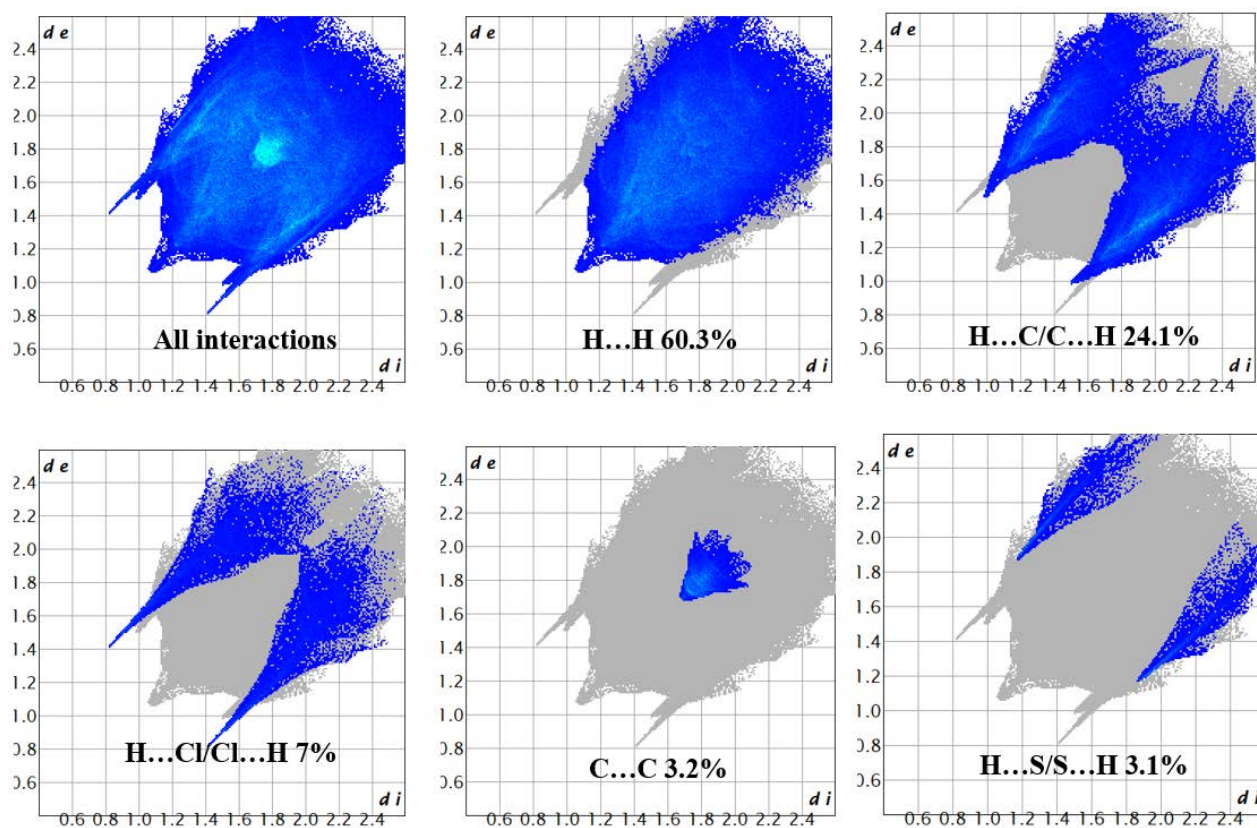
### 3. 5. Hirshfeld Surfaces Analysis (HAS)

The Crystal Explorer 21.5 program was used to create the Hirshfeld surface analyses (HSA) and fingerprints of the Cu(I) complex.<sup>46</sup> The complex's fingerprint plots are shown in Figure 3. In a similar manner, Figure 4 displays the complex's Hirshfeld surface (HS). The  $d_{\text{norm}}$  surfaces are mapped in the range of  $-0.4424$  to  $1.5180$  Å, while the shape index, and curvatures are mapped over ranges  $-1.0$  to  $1.0$  Å, and  $-4.0$  to  $0.4$  Å, respectively. The 2D fin-

gerprint plots of the copper complex show that the major intermolecular interactions are H...H, H...C/C...H, H...Cl/Cl...H, C...C, and H...S/S...H as shown in Figure 4. The largest contribution to the overall Hirshfeld surface is due to H...H close contacts with 60.3%. The percentages of H...H, H...C/C...H, H...Cl/Cl...H, C...C, H...S/S...H, C...N/N...C, H...N/N...H, and Cl...C/C...Cl interactions are 60.3, 24.1, 7.0, 3.2, 3.1, 1.2, 1.0, and 0.1% of the complex surface, respectively. The  $d_{\text{norm}}$  surface detected very close intermolecular interactions, which were displayed as red spots and indicated short C–Cl...H, C–H...Cl, and C–C...H, C...H–C interactions. The stacking interaction can be investigated using the shape index and curvatures of HS, where blue areas represent convex regions of the compound inside the surface and red areas represent concave regions above the surface due to the  $\pi$ ... $\pi$  stacked complex's phenyl groups of triphenylphosphine and 2-benzimidazolethiole (L) ligands. Green flat areas on the curvatures surface also show the presence of  $\pi$ ... $\pi$  interaction in the Cu(I) complex.<sup>47</sup>

## 4. Conclusion

In conclusion, a new copper(I) complex was synthesized using triphenylphosphine and 2-benzimidazolethiole

**Figure 3.** Fingerprint plots for the Cu(I) complex, showing percentages of major contact contributions to the total Hirshfeld surface analysis (HAS).

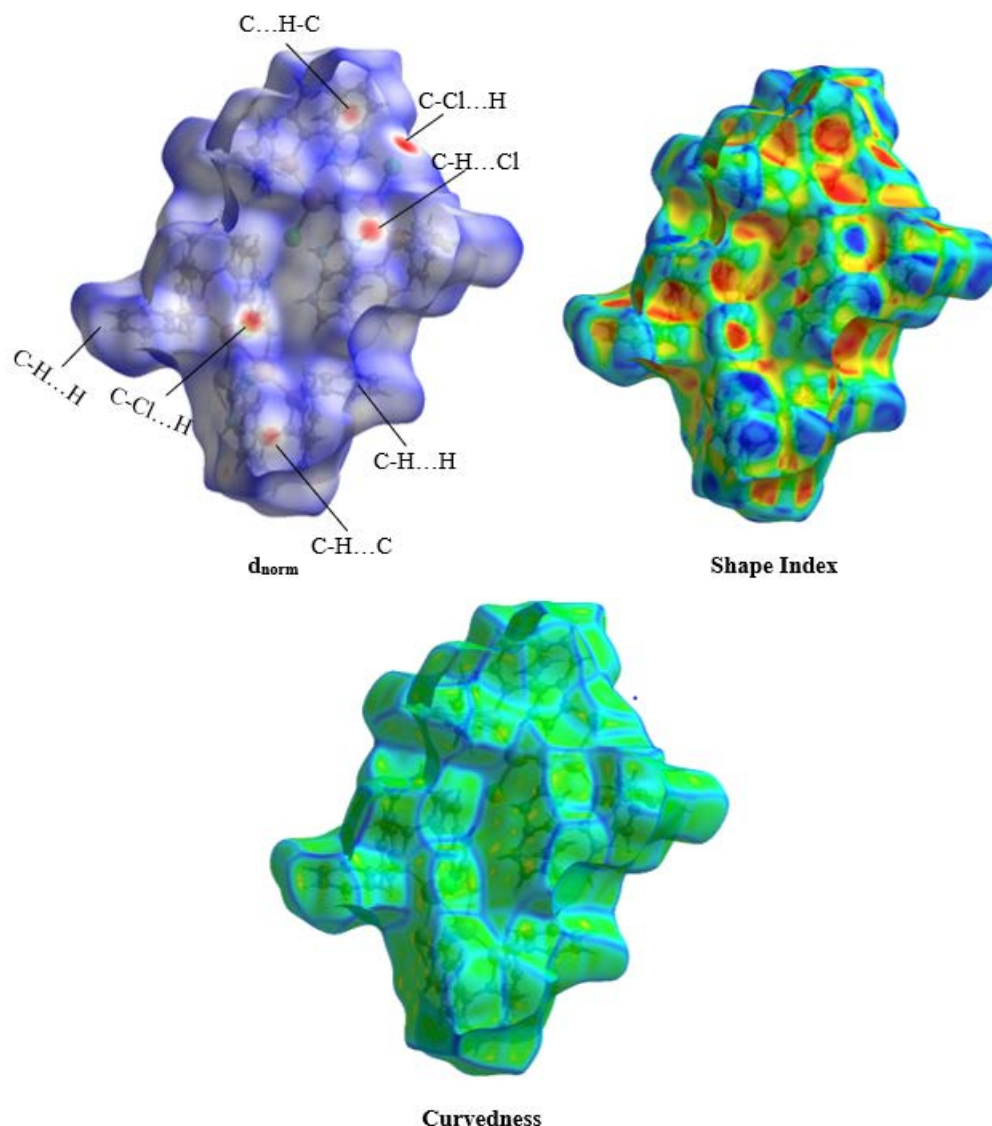


**Figure 4.** Hirshfeld surfaces mapped with  $d_{\text{norm}}$ , shape index, and curvedness of the Cu(I) complex.

(L) ligands in a dichloromethane/methanol mixture. The spectroscopic techniques and X-ray crystallographic data revealed the synthesis of a binuclear copper complex with a 2-benzimidazolethiole ligand acting as a bridging ligand in thione form. The electronic spectrum of the complex displayed a peak at  $31645\text{ cm}^{-1}$ , which corresponded to the ligand-to-metal charge transfer (LMCT) transition. The NBO analysis showed that the charge on the copper metals surrounded by the sulfur and phosphine atoms of the ligands ( $\text{Cu1} = -0.120\text{ e}$ ,  $\text{Cu2} = -0.166\text{ e}$ ) is found to be less than the formal charge of the copper ion (+1) due to the transfer of electrons from the ligands to the metal center. According to the DFT study, the copper complex ( $\Delta E = 3.194\text{ eV}$ ) was less stable and more reactive than ligands. The Hirshfeld surface and 2D fingerprint plots analysis indicated that noncovalent interactions, such as H...H...H

(60.3%), H...C/C...H (24.1%), and H...Cl/Cl...H (7%), constitute the driving force in stable crystal packing.

### Supplementary material

Crystallographic data for the Copper(I) complex have been deposited with the Cambridge Crystallographic Data Center (CCDC), with the deposit number 1991210. The data can be obtained free of charge at <http://www.ccdc.cam.ac.uk/conts/retrieving.html>.

### Acknowledgments

The authors gratefully acknowledge access to the X-ray facilities at Nelson Mandela University, Port Elizabeth, South Africa. We also thank Mr. Mzgin Ayooob for his FT-IR instrumental support.

## Funding

The author would like to acknowledge the college of science at the University of Halabja in Kurdistan Region, Iraq, for providing the financial funding for this study.

## 5. References

- R. Czerwieniec, M. J. Leidl, H. H. Homeier, H. Yersin, *Coord. Chem. Rev.* **2016**, *325*, 2–28. DOI:10.1016/j.ccr.2016.06.016
- B. A. Babgi, *J. Organomet. Chem.* **2021**, *956*, 122124. DOI:10.1016/j.jorganchem.2021.122124
- A. Kobayashi, M. Kato, *Chem. Lett.* **2017**, *46*, 154–162. DOI:10.1246/cl.160794
- H. A. Mohamad, K. O. Ali, E. Hosten, T. Gerber, *Chinese J. Inorg. Chem.* **2021**, *37*, 1106–1112. DOI:10.51380/gujr-37-02-01
- H. S. Seleem, B. A. El-Shetary, M. Shebl, *Heteroat. Chem.* **2007**, *18*, 100–107. DOI:10.1002/hc.20239
- A. K. El-Sawaf, F. El-Essawy, A. A. Nassar, E. A. El-Samanody, *J. Mol. Struct.* **2018**, *1157*, 381–394. DOI:10.1016/j.molstruc.2017.12.075
- O. M. Adly, H. F. El-Shafiy, M. Shebl, *J. Mol. Struct.* **2019**, *1196*, 805–818. DOI:10.1016/j.molstruc.2019.07.010
- A. Fetoh, M. A. Mohammed, M. M. Youssef, G. M. Abu El-Reash, *J. Mol. Liq.* **2019**, *287*, 110958. DOI:10.1016/j.molliq.2019.110958
- M. Shebl, *J. Mol. Struct.* **2017**, *1128*, 79–93. DOI:10.1016/j.molstruc.2016.08.056
- A. Y. Lukmantara, D. S. Kalinowski, N. Kumar, D. R. Richardson, *J. Inorg. Biochem.* **2014**, *141*, 43–54. DOI:10.1016/j.jinorgbio.2014.07.020
- M. Z. M. Zubir, N. S. Jamaludin, S. N. A. Halim, *J. Mol. Struct.* **2019**, *1193*, 141–150. DOI:10.1016/j.molstruc.2019.05.011
- D. Anastasiadou, G. Psomas, M. Lalia-Kantouri, A. G. Hatzidimitriou, P. Aslanidis, *Mater. Sci. Eng. C.* **2016**, *68*, 241–250. DOI:10.1016/j.msec.2016.05.112
- I. I. Ozturk, E. T. Sirinkaya, M. Cakmak, M. Gürgan, D. Ceyhan, N. Panagiotou, A. J. Tasiopoulos, *J. Mol. Struct.* **2021**, *1227*, 129730. DOI:10.1016/j.molstruc.2020.129730
- A. Singh, M. Trivedi, G. Kociok-Köhn, A. K. Singh, M. Mudassir, A. Kumar, *Cryst. Eng. Comm.* **2021**, *23*, 7794–7804. DOI:10.1039/D1CE01147B
- F. Karasmani, A. Tsipis, P. Angaridis, A. G. Hatzidimitriou, P. Aslanidis, *Inorganica Chim. Acta.* **2018**, *471*, 680–690. DOI:10.1016/j.ica.2017.12.002
- H. F. Abd El-Halim, G. G. Mohamed, M. N. Anwar, *Appl. Organometal. Chem.* **2018**, *32*, e3899. DOI:10.1002/aoc.3899
- M. Shebl, S. M. Khalil, A. Taha, M. A. N. Mahdi, *J. Mol. Struct.* **2012**, *1027*, 140–149. DOI:10.1016/j.molstruc.2012.05.067
- O. M. I. Adly, M. Shebl, E. M. Abdelrhman, B. A. El-Shetary, *J. Mol. Struct.* **2020**, *1219*, 128607. DOI:10.1016/j.molstruc.2020.128607
- S. L. Liu, C. L. Wen, S. S. Qi, E. X. Liang, *Spectrochim. Acta A Mol. Biomol. Spectrosc.* **2008**, *69*, 664–669. DOI:10.1016/j.saa.2007.05.019
- M. Shebl, O. M. Adly, A. Taha, N. N. Elabd, *J. Mol. Struct.* **2017**, *1147*, 438–451. DOI:10.1016/j.molstruc.2017.06.085
- S. L. Liu, C. L. Wen, C. Chen, S. S. Qi, E. X. Liang, *Mater. Res. Bull.* **2008**, *43*, 2397–2402. DOI:10.1016/j.materresbull.2007.07.040
- N. Nabil, O. M. I. Adly, M. Shebl, A. Taha, F. Samy, *RSC Adv.* **2022**, *12*, 29939–29958. DOI:10.1039/D2RA03475A
- R. Neelaeni, S. Vasantha, R. Keerthana, S. Sivakolunthu, T. Angelina, *Asian J. Pharm. Clin. Res.* **2016**, *9*, 277–281.
- G. M. Sheldrick, *Acta Cryst. A.* **2015**, *71*, 3–8. DOI:10.1107/S2053229614024218
- C. B. Hübschle, G. M. Sheldrick, B. Dittrich, *J. Appl. Crystallogr.* **2011**, *44*, 1281–1284. DOI:10.1107/S0021889811043202
- L. Krause, R. Herbst-Irmer, G. M. Sheldrick, D. Stalke, *J. appl. Cryst.* **2015**, *48*, 3–10. DOI:10.1107/S1600576714022985
- I. Rajaei, S. N. Mirsattari, *Polyhedron.* **2015**, *102*, 479–489. DOI:10.1016/j.poly.2015.10.019
- B. Rajasekhar, N. Patowary, D. KZ, T. Swu, *Mol. Phys.* **2018**, *116*, 1883–1894. DOI:10.1080/00268976.2018.1460497
- S. L. Chen, Z. Liu, J. Liu, G. C. Han, Y. H. Li, *J. Mol. Struct.* **2012**, *1014*, 110–118. DOI:10.1016/j.molstruc.2012.02.011
- M. Ikram, S. Rehman, I. Feroz, R. Khan, M. O. Sinnokrot, F. Subhan, M. Naeem, C. Schulzke, *Mol. Struct.* **2023**, *1278*, 134960. DOI:10.1016/j.molstruc.2023.134960
- J. Mondal, A. K. Manna, G. K. Patra, *Eur. J. Chem.* **2020**, *11*, 334–341. DOI:10.5155/eurjchem.11.4.334-341.2037
- P. J. Cox, P. Aslanidis, P. Karagiannidis, *Polyhedron.* **2000**, *19*, 1615–1620. DOI:10.1016/S0277-5387(00)00438-1
- V. P. Singh, P. Singh, A. K. Singh, *Inorg. Chim. Acta.* **2011**, *379*, 56–63. DOI:10.1016/j.ica.2011.09.037
- L. H. Wang, X. Y. Qiu, S. J. Liu, *Acta Chim. Slov.* **2019**, *66*, 675–680. DOI:10.17344/acsi.2019.5117
- L. A. Mohammed, N. I. Mahdi, R. A. B. Aldujaili, *Egypt. J. Chem.* **2020**, *63*, 289–300. DOI:10.21608/ejchem.2019.19821.2195
- S. S. Devkule, S. S. Chavan, *Inorganica Chim. Acta.* **2017**, *466*, 122–129. DOI:10.1016/j.ica.2017.05.076
- P. Tyagi, S. Chandra, B. S. Saraswat, D. Yadav, *Spectrochim. Acta – A: Mol. Biomol. Spectrosc.* **2015**, *145*, 155–164. DOI:10.1016/j.saa.2015.03.034
- B. Bal-Demirci, Ş. Güveli, S. Yeşilyurt, N. Özdemir, B. Ülküseven, *Inorganica Chim. Acta.* **2020**, *502*, 119335. DOI:10.1016/j.ica.2019.119335
- L. H. Wang, X. Y. Qiu, S. J. Liu, *J. Coord. Chem.* **2019**, *72*, 962–971. DOI:10.1080/00958972.2019.1590561
- S. M. Khalil, M. Shebl, F. S. Al-Gohani, *Acta Chim. Slov.* **2010**, *57*, 716–725.
- K. J. Koebke, L. Ruckthong, J. L. Meagher, E. Mathieu, J. Harland, A. Deb, N. Lehnert, C. Policar, C. Tard, J. E. Penner-Hahn, J. A. Stuckey, *Inorg. Chem.* **2018**, *57*, 12291–12302. DOI:10.1021/acs.inorgchem.8b01989
- P. Singh, D. P. Singh, K. Tiwari, M. Mishra, A. K. Singh, V. P. Singh, *RSC Adv.* **2015**, *5*, 45217–45230. DOI:10.1080/24701556.2020.1770794 DOI:10.1039/C4RA11929K
- M. Shebl, A. A. Saleh, S. M. Khalil, M. Dawy, A. A. Ali, *Inorg. Nano-Met. Chem.* **2021**, *51*, 195–209.
- L. Saghatforoush, K. Moeini, S. A. Hosseini-Yazdi, Z. Mardani, A. Bakhtiari, A. Hajabbas-Farshchi, S. Honarvar, M. S. Abdelbaky, *Polyhedron.* **2019**, *170*, 312–324. DOI:10.1016/j.poly.2019.05.057
- L. Saghatforoush, K. Moeini, S. A. Hosseini-Yazdi, Z. Mardani, A. Hajabbas-Farshchi, H. T. Jameson, S. G. Telfer, J. D. Woollins, *RSC adv.* **2018**, *8*, 35625–35639. DOI:10.1039/C8RA07463A

46. E. Alaman, A. A. Ađar, M. N. Tahir, M. Ashfaq, E. B. Poyraz, N. Dege, *J. Struct. Chem.* **2023**, *64*, 1314–1328. DOI:10.1134/S0022476623070156
47. Y. Zhang, Y. Q. Pan, M. Yu, X. Xu, W. K. Dong, *Appl. Organomet. Chem.* **2019**, *33*, e5240. DOI:10.1002/aoc.5368

## Povzetek

Z reakcijo med 2-benzimidazoltilom (L) in bakrovim dikloridom v prisotnosti dvakratne množine trifenilfosfina smo sintetizirali nov dvojedrni kompleks  $[\text{Cu}(\text{L})_2(\text{Ph}_3\text{P})_2\text{Cl}_2]$ : dikloridobis( $\mu$ -1,3-dihidro-2H-benzimidazol-2-tion) bis(trifenilfosfin)-di-baker. Spojino bakra(I) smo karakterizirali z elementno analizo, meritvami molske prevodnosti, FT-IR, UV/Vis in monokristalno rentgensko difrakcijo. Strukturna analiza je pokazala, da ima kompleks popačeno tetraedrično geometrijo okoli centralnega Cu(I), z dvema mostovnima atomoma žvepla. Hirschfeldova površinska analiza na  $d_{\text{norm}}$  je pokazala, da so medmolekulske interakcije H...H, H...C/C...H in H...Cl/Cl...H ključne za pakiranje kristalov. Za razumevanje nukleofilnih in elektrofilnih interakcij med ligandom in Cu(I) ioni smo uporabili naravno vezno orbital (NBO). Za prikaz molekularne reaktivnosti oziroma stabilnosti ligandov in kompleksa smo uporabili izračune DFT.



Except when otherwise noted, articles in this journal are published under the terms and conditions of the Creative Commons Attribution 4.0 International License

Scientific paper

# Synthesis, Crystal Structure and In Vitro Cytotoxicity of Novel Cu(II) Complexes Derived from Isatin Hydrazone-Hydrazone Ligands

Cansu Topkaya\*

Muğla Sıtkı Koçman University, Department of Chemistry, 48000 Muğla, Turkey

\* Corresponding author: E-mail: cansutopkaya@mu.edu.tr

Phone: +90 252 2111502, fax: +90 252 2111472

Received: 08-17-2023

## Abstract

In this study, two innovative hydrazine-hydrazone ligands were synthesized through the chemical reaction involving the isatin moiety with 4-hydroxybenzohydrazide and salicyloylhydrazine. Subsequent to the synthesis of these ligands, Cu(II) complexes were meticulously prepared, and their molecular structures were comprehensively analyzed utilizing an array of spectroscopic techniques. Furthermore, the crystallographic investigation was employed to elucidate the precise crystal structure of the Cu(L<sup>2</sup>)<sub>2</sub> complex, incorporating the salicyloylhydrazine moiety. The research focuses on investigating the cytotoxic effects of Cu(II) complexes bearing isatine groups on cancer cells. These complexes were tested against lung carcinoma (A549) and breast carcinoma (MCF-7) cell lines using the MTT assay, with cisplatin as a positive control. Additionally, their effects on human normal cell line 3T3 were assessed. The Cu(L<sup>1</sup>)<sub>2</sub> complex exhibited significant inhibitory effects on tumor cells in a dose-dependent manner, although not as potent as cisplatin. The cytotoxic selectivity indices (SI) indicated acceptable selectivity levels for both cancer cell lines, indicating potential for selective lethality. The crystal structure of one compound was confirmed, revealing van der Waals interactions and hydrogen bonding in the packing.

**Keywords:** Isatin; hydrazone; metal complexes; crystal structure; cytotoxic activity.

## 1. Introduction

Isatin and its derivatives hold significant importance in the field of inorganic chemistry and encompass diverse applications. Isatin serves as a versatile ligand for metal complexes, exerting a profound influence on the synthesis of catalysts, photosensitizers, electrochromic materials, and bioactive compounds. Notably, isatin derivatives have attracted considerable attention in the pharmaceutical industry, showcasing a spectrum of biological activities encompassing anticancer, antiviral, and antimicrobial properties. Moreover, isatin and its derivatives find utility in molecular labeling, sensor technologies, and the realm of biological imaging. Within the domain of inorganic chemistry, the incorporation of isatin and its derivatives as ligands enables investigations into metal complexes, contributing substantially to a broad range of applications.<sup>1,2</sup>

Hydrazone-hydrazone derivatives, distinguished by their unique reactive moiety (CO-NH-N=CH), have

emerged as highly promising candidates in the realm of novel drug development. These compounds have garnered substantial recognition within the field of medicinal chemistry owing to their multifaceted biological properties. Notably, they have exhibited significant potential in various therapeutic areas, encompassing antimicrobial, anti-mycobacterial, anticonvulsant, analgesic, anti-inflammatory, anti-platelet, anti-tubercular, anti-tumoral, anti-cancer, and anti-HIV activities. The remarkable breadth of their potential applications underscores the growing significance and versatility of hydrazone-hydrazone derivatives in the realm of medicinal chemistry.<sup>3-6</sup>

Hydrazone-hydrazone derivatives have demonstrated versatility in coordinating with metal ions, leading to the formation of metal complexes. These complexes exhibit unique properties and biological activities, making them valuable in catalysis, medicinal chemistry, and materials science. The coordination of metal ions with hydrazone-hydrazone derivatives allows for the manipulation of reactivity and stability, expanding their potential applications.



These metal complexes also show promise as antibacterial, antifungal, and anticancer agents, highlighting their potential in therapeutic interventions. Overall, exploring metal complexes of hydrazide-hydrazone offers opportunities for designing novel compounds with enhanced characteristics.<sup>7–9</sup>

Copper holds a pivotal role as an essential bioelement within various biological systems, influencing a wide array of physiological activities and cellular mechanisms. Its significance extends to human metabolism, where it plays a crucial part in enzymatic reactions and cellular processes. Furthermore, copper's importance isn't confined solely to biological functions; it also extends to the development of pharmaceutical agents with therapeutic applications. This dual role, both as a biological necessity and as a key element in pharmaceutical research, underscores the multifaceted importance of copper in the realms of biology and medicine.<sup>10–12</sup>

This study focuses on the synthesis and characterization of new hydrazide-hydrazone derivatives containing isatin groups and their corresponding Cu(II) complexes. The molecular structures of the compounds were investigated using various spectroscopic techniques, and the one of Cu(II) complexes was further characterized by single crystal X-ray diffraction (XRD) analysis. Additionally, the synthesis of a series of hydrazide-hydrazone compounds and the subsequent evaluation of their Cu(II) complexes were carried out with the objective of obtaining novel anticancer agents.

## 2. Experimental

### 2.1. Materials and Measurements

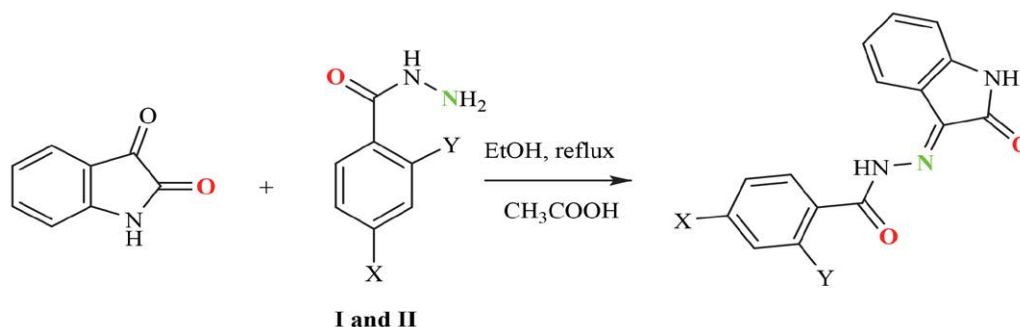
Solvents and chemicals utilized in the laboratory were procured commercially from Merck and Sigma. Solvents employed in the synthesis and measurements were subjected to meticulous purification procedures involving distillation and drying. Microanalysis, specifically carbon (C), nitrogen (N), and hydrogen (H) analysis, was performed using an LECO 932 CHNS analyzer. The copper content was quantified employing atomic absorption spectroscopy on a DV 2000 Perkin Elber ICP-AES instrument.

Thermo-Scientific Nicolet iS10-ATR infrared spectra were acquired using the attenuated total reflectance (ATR) method, spanning the wavenumber range from 4000 to 400  $\text{cm}^{-1}$ . Magnetic susceptibility of powdered materials at ambient temperature was evaluated utilizing a Sherwood Scientific MK1 Model Gouy Magnetic Susceptibility Balance. Electronic spectra were recorded employing a PG Instruments T80+ UV/Vis Spectrophotometer. Notably, the compounds 4-hydroxybenzohydrazide (I)<sup>13</sup> and salicyloylhydrazine (II)<sup>14</sup> were synthesized according to the reported methodology. Crystallographic data were recorded on a Bruker APEX-II CCD diffractometer using  $\text{MoK}\alpha$  radiation ( $\lambda = 0.71073 \text{ \AA}$ ).

### 2.2. Synthesis and Characterization

**Synthesis of Ligands:** The synthesis of these compounds was accomplished by modifying the literature method.<sup>15</sup> A solution of 0.01 mol of 4-hydroxybenzohydrazide ( $\text{HL}^1$ ) and salicyloylhydrazine ( $\text{HL}^2$ ) in 15 mL of ethanol was prepared. Subsequently, a solution containing 0.01 mol of isatin in 10 mL of ethanol was added to the aforementioned solution. Following the completion of the addition, a few drops of acetic acid were introduced as a catalyst, and the reaction mixture was subjected to reflux conditions for approximately 5 hours. Initially, the solution exhibited clarity; however, over time, yellow solid precipitates began to form. The resulting yellow precipitates were isolated by filtration. The purity of the obtained product was assessed using thin-layer chromatography (TLC), and final purification was achieved through crystallization from a 1:1 ethanol-water mixture.

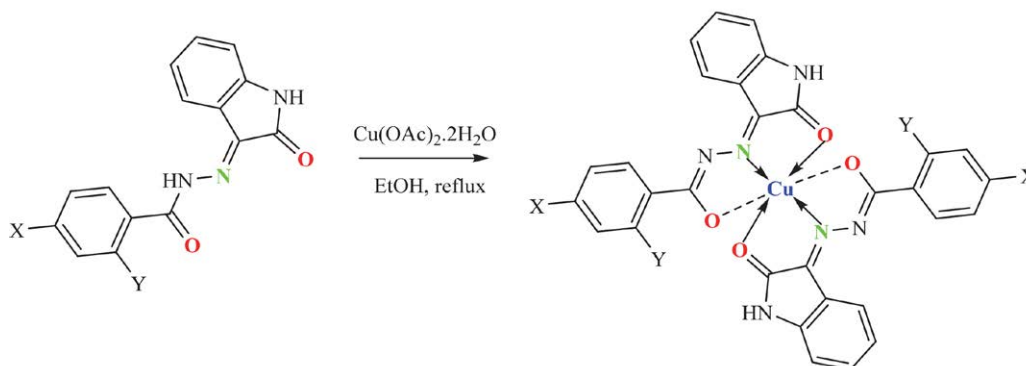
**(E)-4-hydroxy-N'-(2-oxoindolin-3-ylidene)benzohydrazide ( $\text{HL}^1$ ):** Yield: 85 %; m.p. 259–262 °C. FT-IR (ATR,  $\text{cm}^{-1}$ ): 3143  $\nu(\text{N-OH})$ , 1690;1656  $\nu(\text{C=O})$ , 1608  $\nu(\text{C=N})$ , 1265  $\nu(\text{C-O})$ ; UV (EtOH,  $\lambda$ , nm): 220, 250, 274 (sh), 338,5, 404,5 (sh)  $^1\text{H NMR}$  (400 MHz,  $\text{DMSO-}d_6$ , ppm)  $\delta$  13.87 (s, 1H, Ar-OH), 11.37 (s, 1H, NH), 10.31 (s, 1H, NH), 7.77 (t, 2H, Ar-H), 7.60 (t, 1H, Ar-H) 7.39 (q, 1H, Ar-H) 7.12 (q, 1H, Ar-H) 6.95 (m, 3H, Ar-H); Analysis (% calculated/ found) for  $\text{C}_{15}\text{H}_{11}\text{N}_3\text{O}_3$ , C: 64.05/64.10, H: 3.94/3.95, N: 14.94/14.84.



**Scheme 1.** Synthesis and proposed structure of hydrazone ligands (4-hydroxybenzohydrazide ( $\text{HL}^1$ ) and salicyloylhydrazine ( $\text{HL}^2$ )).

(E)-2-hydroxy-N<sup>2</sup>-(2-oxoindolin-3-ylidene)benzohydrazide (**HL<sup>2</sup>**): Yield: 80 %; m.p. 229–229 °C. FT-IR (ATR, cm<sup>-1</sup>): 3156 ν(N-OH), 1740; 1667 ν(C=O), 1607 ν(C=N), 1236 ν(C-O); UV (EtOH, λ, nm): 209,5, 248, 338,5, 403(sh), <sup>1</sup>H NMR (400 MHz, DMSO-*d*<sup>6</sup>, ppm) δ 14.38 (s, 1H, Ar-OH), 12.19 (s, 1H, NH), 10.90 (s, 1H, NH), 8.07 (d, 1H, Ar-H), 7.61 (d, 1H, Ar-H) 7.46 (d, 1H, Ar-H) 7.12 (d, 1H, Ar-H) 7.04 (d, 2H, Ar-H) 6.99 (t, 2H, Ar-H); Analysis (% calculated/found) for C<sub>15</sub>H<sub>11</sub>N<sub>3</sub>O<sub>3</sub>, C: 64.05/64.08, H: 3.94/3.90, N: 14.94/14.97.

**Synthesis of Cu(II) Complexes:** The synthesis procedure proceeded as follows: A suspension of 0.02 mol of the hydrazone ligand in ethanol was prepared, and subsequently, a solution of 0.01 mol of copper(II) acetate dihydrate in ethanol was added dropwise to the suspension. The resulting mixture was subjected to reflux conditions for approximately 2 hours, followed by cooling and filtration. The obtained solid was washed with alcohol and water, and then allowed to dry. Crystallization of the complexes was achieved using a mixture of dimethylformamide (DMF) and ether.



Scheme 2. Synthesis and proposed structure of Cu(II) complexes.

**For Cu(L<sup>1</sup>)<sub>2</sub>:** C<sub>30</sub>H<sub>20</sub>CuN<sub>6</sub>O<sub>6</sub>·2H<sub>2</sub>O, Brown complex; Yield: 65 %; m.p.: >350 °C. μ<sub>eff</sub> = 1.70 B.M.; UV-vis (EtOH, nm) 210,5, 250,0, 276,5 (sh); 363, 398 and 442 (sh). FT-IR (ATR, cm<sup>-1</sup>) 3354 (OH), 1609 m (C=N-N=C), 1214 w (C-O). Analysis (% calculated/found) for C<sub>30</sub>H<sub>20</sub>CuN<sub>6</sub>O<sub>6</sub>, C: 54.59/54.60, H: 3.66/3.59, N: 12.73/12.44, Cu:9.63/9.41.

**For Cu(L<sup>2</sup>)<sub>2</sub>:** C<sub>30</sub>H<sub>20</sub>CuN<sub>6</sub>O<sub>6</sub>·4H<sub>2</sub>O, Dark Brown complex; Yield: 67 %; m.p.: >350 °C. μ<sub>eff</sub> = 1.69 B.M.; UV-vis. (EtOH, nm) 212,5, 250, 291,5, 361,5 (sh), 426,5 (sh). FT-IR (ATR, cm<sup>-1</sup>) 3325 (OH), 1632–1604 m (C=N-N=C), 1213 w (C-O). Analysis (% calculated/found) for C<sub>30</sub>H<sub>20</sub>CuN<sub>6</sub>O<sub>6</sub>, C: 51.76/51.65, H: 4.05/4.07, N: 12.07/12.50, Cu: 9.13/9.25.

### 2. 3. X-ray Crystallography

Suitable crystal of Cu(L<sup>2</sup>)<sub>2</sub> was selected for data collection which was performed on a Bruker diffractometer

equipped with a graphite-monochromatic Mo-Kα radiation at 296 K. The structure was solved by direct methods using SHELXS-2013<sup>16</sup> and refined by full-matrix least-squares methods on F2 using SHELXL-2013.<sup>17</sup> The following procedures were implemented in our analysis: data collection: Bruker APEX2;<sup>18</sup> programs used for molecular graphics were as follow: MERCURY programs;<sup>19</sup> software used to prepare material for publication: WinGX.<sup>20</sup> Crystallographic data for the structure reported herein have been deposited with the Cambridge Crystallographic Data Centre as Supporting Information, CCDC No. **2288219**. Copies of the data can be obtained through application to CCDC, 12 Union Road, Cambridge CB2 1EZ, UK. (fax: +44 1223 336033 or e-mail: deposit@ccdc.cam.ac.uk or at http://www.ccdc.cam.ac.uk).

### 2. 4. Biological studies

#### Cell culture

Human cancer cell lines, breast cancer cell line (MCF-7) and lung carcinoma cell line (A549), human normal cell line [embryonic fibroblast cells (3T3)] were ob-

tained from the European Collection of Cell Cultures (ECACC, UK). The cells were cultured under standard conditions in Dulbeccos' Modified Eagle Medium (DMEM) (Gibco, Invitrogen Inc., Carlsbad, California, USA), supplemented with 10% heat-inactivated fetal bovine serum (FBS) (Gibco, Invitrogen Inc., Carlsbad, California, USA), 100 U/mL of penicilin, and 100 U/ml of streptomycin and 4 mM L-glutamine, incubated in a humidified incubator set at 37 °C with 5% CO<sub>2</sub>. The stock solution of the Cu(II) complexes (10 mM) was prepared in DMF (equivalent to < 0.5% of the final volume), while the clinically-used formulation of cisplatin (Cipintu, 100 mg/100 ml) was used as a stock solution. Further dilutions were made with cell culture medium.

#### Cell viability inhibition assay

3T3, A549 and MCF-7 cells (5x10<sup>3</sup> per well) seeded in 96-well plates to assess cell viability by the 3-[4,5-dimethylthiazol-2-yl]-2,5-diphenyltetrazolium bromide

(MTT) assay for 24 h at 37 °C. Then, cells were treated with Cu(II) complexes at different concentrations (7.5–250  $\mu\text{M}$ ) at 100  $\mu\text{l}$ /well. Under the same settings, the standard anti-cancer drug cisplatin was utilized as a positive control. After 24, 48 and 72 h incubation, 5 mg/ml MTT solution (20  $\mu\text{l}$ /well) was added and cultured for another 4 h. Then, the supernatant was discarded and dimethyl sulfoxide was added (100  $\mu\text{l}$ /well). A Microplate Reader was used to measure the absorbance (A) spectrophotometrically at 540 nm (SpectraMax i3x). The concentrations of the compound were plotted against the percent viability on a graph. Graphs were used to calculate the concentrations of samples that inhibited the growth of 50% of the cells ( $\text{IC}_{50}$  values). All tests were run three times for each concentration level.<sup>21</sup>

### 3. Results and Discussion

#### 3.1. Characterization of the Compounds

According to the  $^1\text{H}$  NMR spectra of the ligands, the proton adjacent to the imine group arising from the two -NH groups in the ligands' structure was observed at chemical shifts of 11.37 ppm and 12.19 ppm, respectively. The -NH group within the isatin ring exhibited signals at 10.31 ppm in the HL<sup>1</sup> ligand and at 10.90 ppm in the HL<sup>2</sup> ligand. The hydroxyl (-OH) peak of the ligand synthesized with 4-hydroxybenzohydrazide appeared at 13.87 ppm, while the -OH peak of the ligand synthesized with salicyloylhydrazine was observed at 14.38 ppm. The downward shift of the phenolic OH proton absorption can be attributed to the presence of strong intramolecular hydrogen bonding in these compounds.<sup>22–24</sup> The other proton resonances of these ligands are given experimental section.

Upon comparison of the FTIR spectra between the derivatives of 4-hydroxybenzohydrazide and salicyloylhydrazone, the stretching vibrations of the  $\nu(\text{C}=\text{O})$  in the HL<sup>1</sup> ligand were observed in the range of 1690–1656  $\text{cm}^{-1}$ , whereas those in the H<sub>2</sub>L<sup>2</sup> ligand appeared in the range of 1740–1667  $\text{cm}^{-1}$ . This observation can be rationalized by the occurrence of intermolecular hydrogen bonding between the carbonyl groups of the salicyloylhydrazone derivatives and the phenolic -OH moiety. The hydroxyl groups within the ligand structure were detected at wavenumbers of 3143  $\text{cm}^{-1}$  and 3156  $\text{cm}^{-1}$ , respectively. Notably, the -NH stretching bands of these compounds could not be discerned in the IR spectra, most likely due to overlap with the -OH stretching frequencies. Additional distinctive IR peaks pertaining to the hydrazide-hydrazone compounds synthesized in this investigation are provided in the experimental section. These results are consistent with the previously reported hydrazone derivatives.<sup>25–27</sup>

The IR spectra of the complexes demonstrate notable distinctions when compared to those of the free ligands. Specifically, the characteristic bands associated with amide I vibrations of  $\nu(\text{C}=\text{O})$ , imine  $\nu(\text{C}=\text{N})$  and amide vibrations of  $\nu(\text{NH})$  are not directly evident in the IR spectra of

the complexes. Instead, the emergence of two new bands within the spectral range of 1609  $\text{cm}^{-1}$  and 1632–1604  $\text{cm}^{-1}$  is observed. These newly observed bands can be ascribed to the presence of  $\text{C}=\text{N}-\text{N}=\text{C}$  and  $\text{C}=\text{O}$  moieties, suggesting a perturbation in the coordination environment.

The absence of the -NH proton resonance in the IR spectra suggests the occurrence of enolization, leading to the relinquishment of the -NH proton. Consequently, the resulting enolic oxygen and azomethine nitrogen actively participate in coordination with the central metal. These findings align with prior investigations.<sup>26,27</sup> The observed upshift in the stretching vibration of the  $\nu(\text{N}=\text{N})$  in the complexes, by approximately 30–35  $\text{cm}^{-1}$  compared to the free ligand, provides additional evidence supporting the involvement of the azomethine nitrogen in coordination. This shift to higher energy suggests a change in the bonding environment around the azomethine nitrogen upon coordination with the metal center. Such alterations in the vibrational frequencies can be indicative of the formation of a coordinate bond between the azomethine nitrogen and the metal atom. This observation further supports the proposition that the azomethine nitrogen actively participates in the coordination process in these complexes. In Cu(II) complexes, the symmetric and asymmetric stretching vibrations of the hydroxyl group  $\nu(-\text{OH})$  in hydrazide-hydrazone derivative ligands are observed, suggesting that they are not engaged in coordination. The IR spectra of these complexes exhibit a broad band around 3300  $\text{cm}^{-1}$  for the 4-hydroxybenzohydrazide derivative and a narrower band for the salicyloylhydrazine derivative. This spectral observation can be attributed to the presence of intramolecular hydrogen bonding involving the phenolic -OH group.

Ligands and Cu(II) complexes exhibit an average of four or five electronic transitions in their electronic spectra. Absorbances occurring around 200–250 nm are presumed to be associated with  $\pi\rightarrow\pi^*$  electronic transitions. The absorptions observed at around 290 nm and 350 nm correspond to  $n\rightarrow\pi^*$  electronic transitions in the compounds. Furthermore, peaks above 400 nm in the complexes' spectra represent the peaks of d-d charge-transfer transitions of the complexes.<sup>28,29</sup>

The Cu(II) complex exhibits paramagnetic behavior at room temperature. The observed magnetic moment values for the mononuclear Cu(II) complexes were measured to be 1.70 BM and 1.69 BM, which falls within the expected range for mononuclear copper(II) complexes (1.73 BM) containing a single Cu(II) cation with a  $d^9$  electronic configuration.<sup>30</sup> The magnetic data analysis reveals that mononuclear copper(II) complexes, which possess an octahedral coordination environment facilitated by the additional axial coordination of ligand molecules, adopt a high-spin configuration.

The thermograms of all Cu(II) complexes were recorded within a temperature range of 30 to 800 °C using a heating rate of 20 °C/min under a nitrogen atmosphere.

Above 900 °C, complete decomposition of the complexes was observed, as depicted in Figure S11–12. The decomposition step occurring around approximately 200 °C with an associated mass loss of about 5% for the  $\text{Cu}(\text{L}^1)_2$  complex corresponds to the removal of two moles of water present in the structure. Furthermore, for the  $\text{Cu}(\text{L}^2)_2$  complex, a similar decomposition stage initiates around 270 °C, indicating an approximate mass loss of 8%. This mass loss, equivalent to four moles of water, occurring at a higher temperature compared to  $\text{Cu}(\text{L}^1)_2$  complex, can be attributed to its encapsulated nature within the crystal structure. The second decomposition stage, which commences at around 300 °C for all complexes, likely signifies the breakdown of all the complexes. This decomposition process culminates at a temperature of around 500 °C.

All spectral data are consistent with those reported for similar compounds.<sup>25–27</sup> Elemental analysis, UV-Vis, IR,  $^1\text{H-NMR}$  and TGA analysis are confirmed the molecular formula.

### 3. 2. X-Ray Structure

The X-ray structural determination of title compound confirms the assignment of its structure from spec-

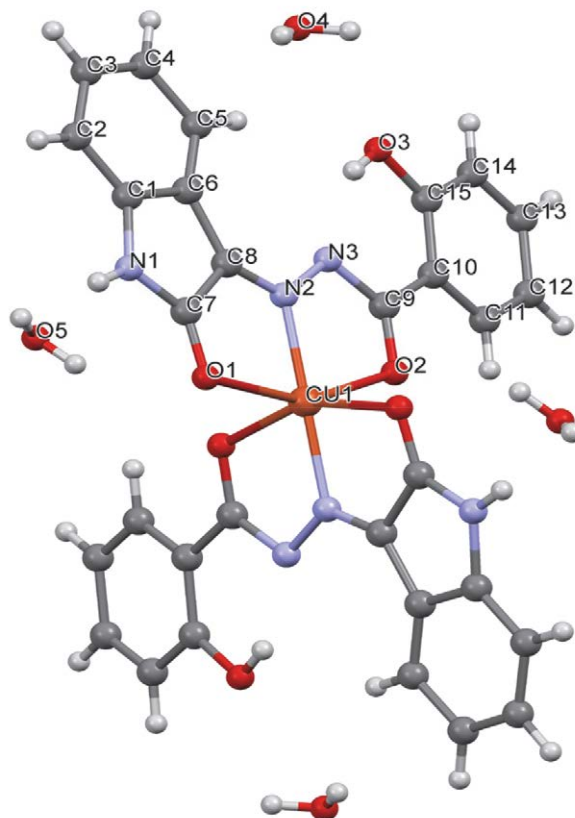


Fig. 1. The asymmetric unit of the title compound with the atom numbering scheme.

Table 1. Experimental details.

Crystal data	
Chemical formula	$\text{C}_{30}\text{H}_{20}\text{CuN}_6\text{O}_6 \cdot 4(\text{H}_2\text{O})$
$M_r$	696.12
Crystal system, space group	Monoclinic, $C2/c$
Temperature (K)	293(2)
$a, b, c$ (Å)	16.820(5), 20.354(7), 9.340(3)
$\beta$ (°)	103.564(9)
$V$ (Å <sup>3</sup> )	3108.5(17) Å <sup>3</sup>
$Z$	4
Radiation type	$\text{MoK}\alpha$
$\mu$ (mm <sup>-1</sup> )	0.77
Crystal size (mm)	0.07 × 0.06 × 0.02
Data collection	
Diffractometer	Bruker APEX-3 CCD
Absorption correction	multi-scan Bruker
No. of measured, independent and observed [ $I > 2\sigma(I)$ ] reflections	22994, 2883, 1448
$R_{\text{int}}$	0.181
$(\sin \theta/\lambda)_{\text{max}}$ (Å <sup>-1</sup> )	0.606
Refinement	
$R[F^2 > 2\sigma(F^2)]$ , $wR(F^2)$ , $S$	0.138, 0.263, 1.25
No. of reflections	2883
No. of parameters	214
H-atom treatment	H atoms treated by a mixture of independent and constrained refinement
$\Delta\rho_{\text{max}}$ , $\Delta\rho_{\text{min}}$ (e Å <sup>-3</sup> )	0.86, -0.49

Computer programs: APEX3 (Bruker, 2013), SAINT (Bruker, 2013), Bruker SAINT, SHELXS (Sheldrick, 2008), SHELXL (Sheldrick, 2015), Mercury (Macrae, 2020), WinGX (Farrugia, 2012).

troscopic datas. As shown in Fig. 1, the compound consists of new hydrazide-hydrazone derivatives containing isatin and salicyloylhydrazine and its  $\text{Cu}(\text{II})$  complexes. The experimental details are given in Table 1. Hydrogen bond

Table 2. Hydrogen-bond geometry (Å, °).

$D\text{—}H\cdots A$	$D\text{—}H$	$H\cdots A$	$D\cdots A$	$D\text{—}H\cdots A$
$\text{N1—H1}\cdots\text{O5}$	0.86	1.94	2.780(15)	166
$\text{O3—H3}\cdots\text{N3}$	0.82	1.82	2.543(11)	146
$\text{O5—H5A}\cdots\text{O4}^{\text{ii}}$	0.90	2.51	3.09(2)	123.4(12)
$\text{O5—H5B}\cdots\text{O4}^{\text{iii}}$	0.85	2.53	3.31(2)	152.5(10)

Symmetry codes: (ii)  $-x + 1/2, y + 1/2, -z + 3/2$ ; (iii)  $x + 1/2, -y + 3/2$ .

Table 3. Selected interatomic distances (Å)

$\text{C7—O1}$	1.241(12)	$\text{Cu1—N2}^{\text{i}}$	1.958(7)
$\text{C9—O2}$	1.263(1)	$\text{Cu1—N2}$	1.958(7)
$\text{C8—N2}$	1.275(11)	$\text{Cu1—O2}$	2.09(7)
$\text{N2—N3}$	1.359(10)	$\text{Cu1—O2}^{\text{i}}$	2.095(7)
$\text{C9—N3}$	1.360(12)	$\text{Cu1—O1}$	2.338(8)
$\text{C7—C8}$	1.495(14)	$\text{Cu1—O1}^{\text{i}}$	2.338(8)
$\text{C7—N1}$	1.346(13)	$\text{N1—H1}$	0.8600
$\text{C9—C10}$	1.465(14)	$\text{O3—H3}$	0.8200

Symmetry code: (i)  $-x + 1, y$ .

geometry is given in Table 2. Selected bond lengths and angles are given in Table 3.

In the crystal structure, the intermolecular C–H...O hydrogen bonds (Table 2) link the copper complex molecules and water anions, in which they may be effective in the stabilization of the structure.

### 3. 3. Stability

The stability of the copper(II) complexes was examined in DMF solution for 24, 48 and 72 hours using a UV-Vis spectroscopy (Figure S9–10). Spectra were recorded at 100  $\mu\text{M}$  concentrations of the complexes. No difference was observed in the spectra of the complexes at the end of 24, 48 and 72 hours. This proves that the complexes are stable in solution.

### 3. 4. MTT Assays

The cytotoxicities of the complexes against human cancer cell lines, namely lung carcinoma cell line (A549) and breast carcinoma cell line (MCF-7), were investigated utilizing the MTT assay. The same conditions were applied for the positive control, involving the traditional anticancer agent cisplatin. Additionally, to facilitate an additional comparison of cytotoxicity between the complex compounds and cisplatin, evaluation was conducted on the human normal cell line 3T3 (embryonic fibroblast cells). The  $\text{IC}_{50}$  values for both the complexes and cisplatin were determined using data derived from MTT assays conducted after 24, 48, and 72 hours of incubation, employing various doses spanning from 7.5 to 250  $\mu\text{M}$ , as illustrated in Fig. 2.

The results have demonstrated that, especially in comparison to cisplatin, the  $\text{Cu}(\text{L}^1)_2$  complex exhibits a visibly inhibitory effect on all tested tumor cells in a dose-dependent manner. Although the complex's inhibitory impact on MCF-7 and A549 cell lines is not as pronounced as that of cisplatin ((with  $\text{IC}_{50}$  values of  $182.67 \pm 0.01$  (24 hours),  $38.53 \pm 0.11$  (48 hours), and  $22.40 \pm 0.13$  (72 hours) for MCF-7; and  $\text{IC}_{50}$  values of  $157.95 \pm 0.49$  (24 hours),  $52.22 \pm 0.46$  (48 hours), and  $26.95 \pm 0.30$  (72 hours) for A549)), it still displays an effect. Dose-response curves for the  $\text{Cu}(\text{L}^2)_2$  complex against MCF-7 and A549

cancer cell lines after 24, 48, and 72 hours of treatment are presented in Fig. 2. The cytotoxic effect of the  $\text{Cu}(\text{L}^1)_2$  complex on cancer cells is higher than that of the  $\text{Cu}(\text{L}^2)_2$  complex. When compared to the positive control of cisplatin, the complexes exhibit limited inhibition on the 3T3 cell lines over the 24, 48, and 72-hour periods. Moreover, the outcomes indicate the capacity of the complexes to dose-dependently and temporally hinder cellular growth.

Furthermore, the analysis of the cytotoxicity of the complexes and cisplatin (control) on the human normal cell line 3T3, as presented in Fig. 2, underscores the toxicity of both compounds towards cells. At 48 and 72 hours, the complexes exhibited comparable effects ( $\text{IC}_{50}$  values of  $38.53 \pm 0.11$ ;  $82.21 \pm 0.22$  and  $52.22 \pm 0.46$ ;  $48.55 \pm 0.27$ , respectively) to those of cisplatin (with  $\text{IC}_{50}$  values of  $32.50 \pm 0.02$  and  $3.65 \pm 0.87$ ), albeit not as potent.

Additionally, the cytotoxic selectivity indices (SI)<sup>31</sup> for both the complexes and cisplatin were determined and compiled in Table 4.

**Table 4.** SI\* Values ( $\mu\text{M}$ ) of Cu(II) complexes obtained with different cell lines for 48 h.

Compounds	3T3/ MCF-7	3T3/A549
$\text{Cu}(\text{L}^1)_2$	3.95	2.92
$\text{Cu}(\text{L}^2)_2$	0.27	0.45
Cisplatin	10.80	96.13

\*SI, cytotoxic selectivity index (the degree of selectivity between healthy cells and cancer cells, expressed as  $\text{SI} = \text{IC}_{50}$  on normal cells/  $\text{IC}_{50}$  on cancer cells).

Some of the other notable findings arising from this in vitro cytotoxicity study encompass the incorporation of SI (Selectivity Index) values. These values were calculated with the purpose of assessing the selective impact of the compounds on cancer cells, achieved by juxtaposing the  $\text{IC}_{50}$  values of the complexes against those exhibited by the normal cell line.<sup>32,33</sup> Despite the fact that the cytotoxic selectivity of the complexes, particularly  $\text{Cu}(\text{L}^1)_2$ , does not attain the level observed with cisplatin, the SI values remain above 2 for both cancer cell lines, thereby warranting consideration as an acceptable level of selectivity:

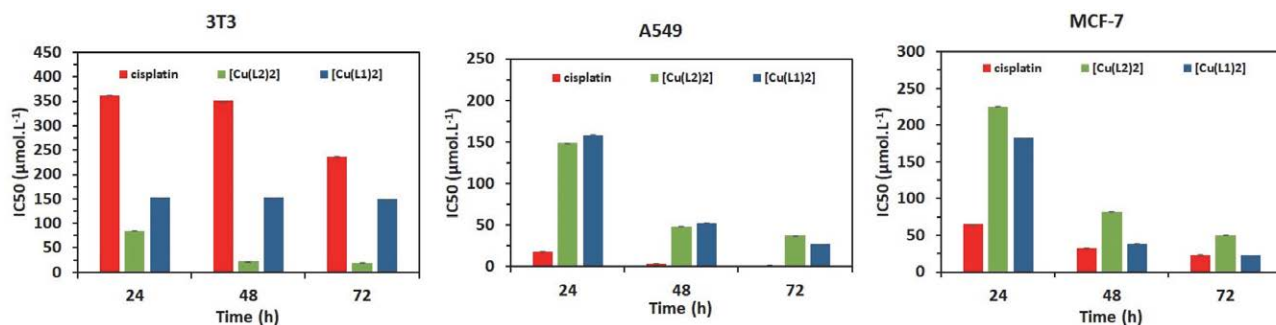


**Fig. 2.** MTT assay results

$SI_{(3T3/A549)} = 2.92$  and  $0.45$ ,  $SI_{(3T3/MCF-7)} = 3.95$  and  $0.27$ . The findings put forth the proposition that the compound's diminished cytotoxicity towards healthy cells, coupled with its moderate cytotoxicity towards cancer cells, augments its viability for the exploration of its potential anticancer effects. Consequently, the compound could potentially induce selective lethality in both cancer cells and healthy cells.<sup>34</sup>

## 4. Conclusions

In this study, two novel hydrazine-hydrazone ligands were synthesized through the reaction of the isatin moiety with 4-hydroxybenzohydrazide and salicyloylhydrazine. Subsequently, Cu(II) complexes of these ligands were prepared and their structures were investigated using various spectroscopic techniques. Additionally, the crystal structure of the  $Cu(L^2)_2$  complex containing the salicyloylhydrazine moiety was elucidated using X-ray crystallography. The cytotoxicities of the obtained complexes against MCF-7 and A549 cancer cells were examined. In studies where cisplatin was utilized as a control, it has been demonstrated that the  $Cu(L^1)_2$  complex with the hydroxyl group in the *-para* position exhibits a superior cytotoxic effect against these cancer cells compared to the  $Cu(L^2)_2$  complex.

The available spectroscopic data have played a significant role in elucidating the chemical properties and structures of  $H_2L^1$  and  $H_2L^2$  ligands, as well as  $Cu(L^1)_2$  and  $Cu(L^2)_2$  complexes. The  $^1H$  NMR spectra have clearly demonstrated the chemical characteristics of the ligands and provided insights into the coordination mechanisms of the Cu(II) complexes. IR spectra have assisted in determining the coordination changes in the Cu(II) complexes, while magnetic moment data have indicated the high-spin configuration of the mononuclear Cu(II) complexes. Thermal analyses have allowed for the examination of the thermal behavior of the complexes. These results succinctly summarize the key findings of this study. In this context, the combination of spectroscopic and structural data comprehensively explains the chemical properties and structures of  $H_2L^1$ ,  $H_2L^2$ ,  $Cu(L^1)_2$  and  $Cu(L^2)_2$ .

The disparity observed in the cytotoxicities of the complexes may potentially stem from the influence of the positioning of the hydroxyl group on the formation of hydrogen bonds within the compounds. The Cu(II) complex with the hydroxyl group in the *-ortho* position could establish stronger hydrogen bonding, whereas *-para* hydroxyl groups might form weaker hydrogen bonds. Consequently, this discrepancy could impact the interaction potential and binding affinities of the compound with target molecules.

In summary, the investigations have evidenced that the  $Cu(L^1)_2$  complex exhibits a substantial, selective, concentration-dependent cytotoxic impact, particularly on

the viability and proliferation of breast cancer cells. Moreover, in order to validate the anticancer benefits of this study, it is essential to conduct *in vivo* research.

## Acknowledgements

The author acknowledges to Scientific and Technological Research Application and Research Center, Sinop University, Turkey, for the use of the Bruker D8 QUEST diffractometer. Also I extend my sincere gratitude to Sevil Dilara Yeniocak for her invaluable contributions and assistance in my cytotoxicity research, which greatly enriched the quality and depth of my study.

## Conflict of interest

The authors declare that they have no conflict of interest.

## 5. References

- S. Mishra, P. Singh. *Eur. J. Med. Chem.* **2016**, 124, 500–536. DOI:10.1016/j.ejmech.2016.09.055
- A. Vaidya, S. Jain, P. Jain, N. Tiwari, R. Jain, R. K. Agrawal. *Mini Rev. Med. Chem.* **2016**, 16, 825–845. DOI:10.2174/1389557516666160211120835
- A. El-Faham, M. Farooq, S. N. Khattab, N. Abutaha, M. A. Wadaan, H. A. Ghabbour, H. K. Fun. *Molecules* **2015**, 20, 14638–14655. DOI:10.3390/molecules200814638
- U. Acar Çevik, B. N. Sağlık, C. M. Ardiç, Y. Özkay, Ö. Ath. *Turk. J. Biochem.* **2018**, 43, 151–158. DOI:10.1515/tjb-2018-0201
- F. Tok, B. N. Sağlık, Y. Özkay, S. Ilgın, Z. A. Kaplancıklı, B. Koçyiğit-Kaymakçioğlu. *Bioorg. Chem.* **2021**, 114, 105038. DOI:10.1016/j.bioorg.2021.105038
- K. Akdağ, F. Tok, S. Karakuş, Ö. Erdoğan, Ö. Çevik, B. Koçyiğit-Kaymakçioğlu. *Acta Chim. Slov.* **2022**, 69. DOI:10.17344/acsi.2022.7614
- G. Verma, A. Marella, M. Shaquiquzzaman, M. Akhtar, M. R. Ali, M. M. Alam. *J. Pharm. Bioallied. Sci.* **2014**, 6, 69–80. DOI:10.4103/0975-7406.129170
- J. de Oliveira Carneiro Brum, T. C. França, S. R. LaPlante, J. D. F. Villar. *Mini Rev. Med. Chem.* **2020**, 20, 342–368. DOI:10.2174/1389557519666191014142448
- S. N. Mali, B. R. Thorat, D. R. Gupta, A. Pandey. *Eng. Proc.* **2021**, 11, 21–29. DOI:10.3390/ASEC2021-11157
- N. Metzler-Nolte, H. B. Kraatz, Concepts and models in bioinorganic chemistry. Wiley-VCH, 2006, 443 p.
- J. M. Berg, Principles of bioinorganic chemistry. 1994, University Science Books.
- J. F. da Silva, R. J. P. Williams, Book The Biological Chemistry of the Elements, 1991, Clarendon/EditorOxford.
- B. Kırkan, R. Güp. *Turk. J. Chem.* **2008**, 32, 9–19.
- R. Güp, B. Kırkan. *Spectrochim. Acta A Mol. Biomol. Spectrosc.* **2005**, 62, 1188–1197. DOI:10.1016/j.saa.2005.04.034

15. N. Dilek, B. Güneş, O. Büyükgüngör, R. Güp. *Crystallography Reports* **2013**, 58, 98–104. DOI:10.1134/S1063774513010173
16. G. M. Sheldrick. *Acta Crystallogr. Sect. A Found. Adv.* **2008**, 64, 112–122. DOI:10.1107/S0108767307043930
17. G. M. Sheldrick, *Acta Crystallographica Section C* **2015**, 71, 3–8. DOI:10.1107/S2053273314026370
18. APEX2, Bruker AXS Inc. Madison Wisconsin, USA **2013**.
19. C. F. Macrae, I. Sovago, S. J. Cottrell, P. T. A. Galek, P. McCabe, E. Pidcock, P. A. Wood, *J. Appl. Crystallogr.* **2020**, 53, 226–235. DOI:10.1107/S1600576719014092
20. L. J. Farrugia, *J. Appl. Crystallogr.* **2012**, 45, 849–854. DOI:10.1107/S0021889812029111
21. T. Mosmann, *J. Immunol. Methods* **1983**, 65, 55–63. DOI:10.1016/0022-1759(83)90303-4
22. R. Gup, B. Kirkan, *Spectrochim. Acta Part A* **2005**, 62, 1188–1195. DOI:10.1016/j.saa.2005.04.015
23. T. Topal, *Acta Chim. Slov.* **2021**, 68, 88–101. DOI:10.17344/acsi.2020.6183
24. T. Topal, H. H. Kart, T. Taslip, E. Karapinar, *Онтика и спектроскопия* **2015**, 118, 897–912. DOI:10.7868/S0030403415060227
25. K. Akdağ, F. Tok, S. Karakuş, Ö. Erdoğan, Ö. Çevik, B. Koçyiğit-Kaymakçıoğlu, *Acta Chim. Slov.* **2022**, 69. DOI:10.17344/acsi.2022.7614
26. R. Gup, C. Gökçe, N. Dilek, *Supramol. Chem.* **2015**, 27, 629–641. DOI:10.1080/10610278.2015.1051978
27. C. Gökçe, N. Dilek, R. Gup, *Inorg. Chim. Acta* **2015**, 432, 213–220. DOI:10.1016/j.ica.2015.03.040
28. Z. C. Liu, B. D. Wang, B. Li, Q. Wang, Z. Y. Yang, T. R. Li, Y. Li, *Eur. J. Med. Chem.* **2010**, 45, 5353–5361. DOI:10.1016/j.ejmech.2010.08.060
29. S. Ramakrishnan, D. Shakhthipriya, E. Suresh, V. S. Periasamy, M. A. Akbarsha, M. Palaniandavar, *Inorg. Chim.* **2011**, 50, 6458–6471. DOI:10.1021/ic1024185
30. A. T. López, M. R. A. Luckie, D. M. Otero, V. S. Mendieta, R. Escudero, F. Morales, *J. Chem. Crystallogr.* **2022**, 1–8. DOI:10.1007/s10870-021-00893-2
31. A. Koch, P. Tamez, J. Pezzuto, D. Soejarto, *J. Ethnopharmacol.* **2005**, 101, 95–99. DOI:10.1016/j.jep.2005.03.011
32. M. Alinaghi, K. Karami, A. Shahpiri, A. A. Momtazi-Borojeni, E. Abdollahi, J. Lipkowski, *J. Mol. Struct.* **2020**, 1219, 128479. DOI:10.1016/j.molstruc.2020.128479
33. Z. Shokohi-Pour, H. Chiniforoshan, M. R. Sabzalian, S. A. Esmaeili, A. A. Momtazi-Borojeni, *J. Biomol. Struct. Dyn.* **2018**, 36, 532–549. DOI:10.1080/07391102.2017.1287006
34. T. D. Pfister, W. C. Reinhold, K. Agama, S. Gupta, S. A. Khin, R. J. Kinders, Y. Pommier *Mol. Cancer Ther.* **2009**, 8, 1878–1884. DOI:10.1158/1535-7163.MCT-09-0016

## Povzetek

V prispevku opisujemo sintezo dveh novih hidrazin-hidrazon ligandov s kemijsko reakcijo med izatinom, 4-hidroksibenzohidrazidom in salicilohidrazinom. V nadaljevanju smo pripravili komplekse bakra(II) z novimi ligandi in jih karakterizirali z različnimi spektroskopskimi metodami. S kristalografskimi metodami smo določili strukturo kompleksa  $\text{Cu}(\text{L}^2)_2$  s salicilohidrazinom. V nadaljevanju smo raziskave posvetili citotoksičnim učinkom  $\text{Cu}(\text{II})$  kompleksov z izatinskimi skupinami. Testirali smo njihovo delovanje na celice pljučnega karcinoma (A549) in raka dojke (MCF-7) z metodo MTT in cisplatinom kot pozitivno kontrolo. Ugotavljali smo tudi njihove učinke na normalne človeške celice 3T3. Kompleks  $\text{Cu}(\text{L}^1)_2$  izkazuje znatno inhibicijo tumorskih celic, vendar šibkejšo kot cisplatin. Meritve citotoksičnosti kažejo da je indeks selektivnosti (SI) ustrezen za obe vrsti rakastih celic, kar kaže na potencial za selektivno letalnost. Določili smo kristalno strukturo enega od kompleksov in potrdili prisotnost van der Waalsovih interakcij in vodikovih vezi v pakiranju.



Except when otherwise noted, articles in this journal are published under the terms and conditions of the Creative Commons Attribution 4.0 International License

Scientific paper

# Synthesis of Novel *cis*-2-Azetidinones from Imines and Chloroacetyl Chloride Using Triethylamine

Handan Can Sakarya<sup>1,\*</sup> and Aslı Ketrez<sup>2</sup><sup>1</sup> Department of Chemistry, Faculty of Arts and Science, Eskişehir Osmangazi University, 26480 Eskişehir, Turkey.<sup>2</sup> Department of Chemistry, Graduate School of Natural and Applied Sciences, Eskişehir Osmangazi University, 26480 Eskişehir, Turkey

\* Corresponding author: E-mail: hsakarya@ogu.edu.tr

Received: 09-20-2023

## Abstract

A synthesis of a novel series of *cis*-2-azetidinones **2a–c** was carried out by the cycloaddition reaction of imine **1a–c** and chloroacetyl chloride in dry dichloromethane at 0–5 °C using triethylamine. The cycloaddition of the Schiff bases with chloroacetyl chloride resulted in the corresponding major product *cis*-2-azetidinone stereoisomers **2a–c**. The synthesized compounds were characterized by analytical and spectral techniques (infrared, <sup>1</sup>H NMR, <sup>13</sup>C NMR, and elemental analysis).

**Keywords:** Benzothiazole, β-lactam, Schiff base, *cis*-2-azetidinone, Staudinger reaction.

## 1. Introduction

2-Azetidinones, known as β-lactams, are well known heterocyclic compounds. The synthesis of heterocyclic compounds has attracted the attention of chemists for many years because of their important biological activities. In particular, 2-azetidinone ring systems are widely found in the construction of broad-spectrum antibiotics containing penicillin cephalosporin. These antibiotics are used as chemotherapeutic agents for the treatment of microbial diseases and bacterial infections.<sup>1–8</sup> Synthesis and antimicrobial properties of 2-azetidinones have been studied by chemists since the 1990s, to obtain pharmacologically active compounds such as cholesterol absorption and inhibitory activity.<sup>9</sup>

Staudinger ketene-imine reaction is the most common method for the synthesis of 2-azetidinones.<sup>10</sup> In this reaction, ketene is formed thermally or photochemically using acid chlorides and triethylamine.<sup>11–12</sup> Although this reaction is generally known as a [2+2] cycloaddition, the reaction is generally described as a stepwise reaction. The first step of the reaction involves the nucleophilic attack of the imine nitrogen on the sp hybridized carbon of a ketene to form the zwitterion intermediate. Then follows the formation of azetidinone ring. The resulting stereochemistry of azetidinone may be *cis*, *trans* or a mixture of both iso-

mers. In the literature, it has been reported that the *cis* product is obtained in higher yield than the *trans* product in this reaction, because of consisting of ketene before the zwitterion intermediate.<sup>13</sup> Also, the group attached to the nitrogen atom in the azetidinone ring determines the stereochemistry of 2-azetidinone. Stereochemistry of 2-azetidinones is important for their biological activity.<sup>3</sup> For example, penicillin and cephalosin antibiotics are *cis* isomer.

In this study, unlike the literature, we designed the synthesis of *cis*-2-azetidinone products by the Staudinger reaction, using electron-donating imine and electron-withdrawing ketene, in apolar solvent environment and adding additives.

## 2. Experimental

### 2.1. General Chemistry Methods

The elemental (C, H, N, S) analysis were carried out using an Elementar VARIO EL III element analysis device. IR spectra were taken by a Perkin Elmer Precisely Spectrum 100 FT-IR Spectrophotometer at Eskişehir Osmangazi University, Faculty of Art and Sciences, Department of Chemistry. <sup>1</sup>H NMR and <sup>13</sup>C NMR spectra were recorded in CDCl<sub>3</sub> and DMSO-*d*<sub>6</sub> using a Bruker DPX FT NMR 500 MHz spectrometer of Anadolu University, Center of



Plants, Drugs and Scientific Studies (AÜBIBAM). Chemical shifts are given as  $\delta$  values in ppm and coupling constants ( $J$ ) are reported in Hertz (Hz) units. Reagents and solvents used for the synthesis were purchased from commercial sources. Solvents were distilled with an appropriate drying agent. Melting points of the synthesized substances were determined by a Gallenkamp device.

## 2. 2. General Procedure for the Synthesis of Schiff Bases 1a–c

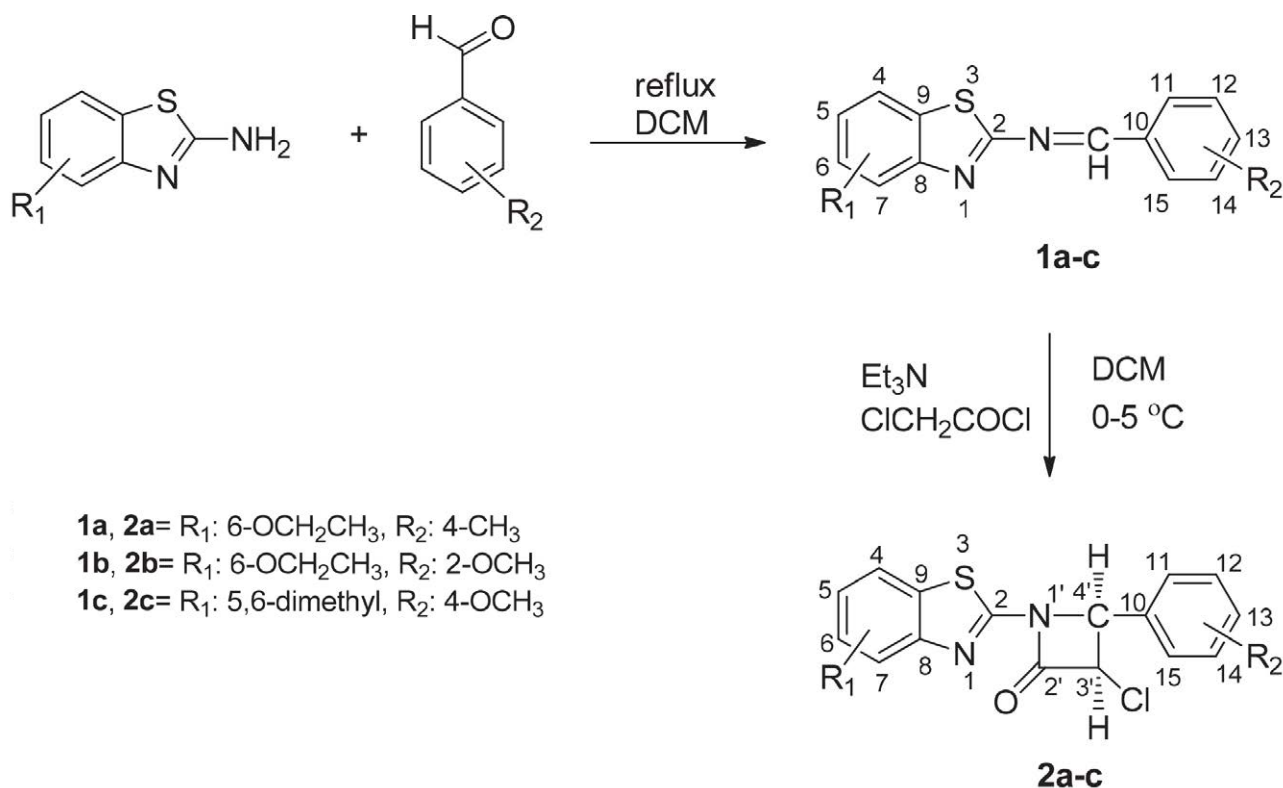
Schiff bases were synthesized by modifying the procedure suggested by Vicini *et al.*<sup>14</sup> The mixture of 6-ethoxy-2-aminobenzothiazole (0.35 g, 1.8 mmol) and *para*-methyl benzaldehyde (0.107 mL, 0.9 mmol) in dichloromethane (40 mL) was refluxed at 70 °C for 6 h. The liquid fraction was evaporated under reduced pressure. The resultant solid **1a** was recrystallized from ethylacetate:hexane (1:3) solvent system (Scheme 1). Compounds **1b** and **1c** were also synthesized by the same method.

## 2. 3. General Procedure for the Synthesis of *cis*-2-Azetidinones 2a–c

*cis*-2-Azetidinones were synthesized by modifying the suggested procedure by Mogilaiah *et al.*<sup>15</sup> Chloroacetyl chloride (0.019 mL, 1.5 mmol) was added dropwise within a period of 30 minute to the dichloromethane solution of Et<sub>3</sub>N (0.066 mL, 3 mmol), at 0–5 °C cooled, and stirred.

Then, the compound **1a** (0.019 g, 0.16 mmol) was added to this well-stirred cold solution. The reaction mixture was then stirred for an additional 9 h at 0–5 °C and left at room temperature for 6 h. The reaction mixture was extracted with, respectively, 10 mL of saturated NaHCO<sub>3</sub> solution, 10 mL of 10% HCl and 10 mL of brine. The organic phase was dried with Na<sub>2</sub>SO<sub>4</sub>. The resultant mixture was concentrated, filtered, and then dried. The product **2a** thus obtained was purified by column chromatography over silica gel using mixture of 20% ethyl acetate, 20% dichloromethane, 60% hexane as the eluent (Scheme 1). Compounds **2b** and **2c** were also synthesized by the same method.

**6-Ethoxybenzothiazol-2-yl-(4-methylbenzylidene) amine (1a)**. This compound was obtained as a yellow solid, yield 0.21 g (79%), m.p. 131–132 °C. FT-IR (KBr)  $\nu_{\max}$  1595 (–CH=N–), 1554, 1481, 1440 cm<sup>-1</sup>. <sup>1</sup>H NMR (DMSO-*d*<sub>6</sub>)  $\delta$  1.40 (t,  $J$  = 6.93 Hz, 3H, OCH<sub>2</sub>CH<sub>3</sub>), 3.03 (s, 3H, PhCH<sub>3</sub>), 4.10 (q,  $J$  = 6.90 Hz, 2H, OCH<sub>2</sub>CH<sub>3</sub>), 7.10 (dd,  $J$  = 2.36, 8.86 Hz, 1H, H-5), 7.40 (d,  $J$  = 7.90 Hz, 2H, H-12 and H-14), 7.64 (d,  $J$  = 2.29 Hz, 1H, H-7), 7.82 (d,  $J$  = 8.89 Hz, 1H, H-4), 8.00 (d,  $J$  = 7.94 Hz, 2H, H-11 and H-15), 9.10 (s, 1H, CH=N) (Fig. S1). <sup>13</sup>C NMR (DMSO-*d*<sub>6</sub>)  $\delta$  15.11, 21.86, 64.21, 106.19, 116.54, 123.70, 130.28, 130.46, 132.60, 135.88, 144.37, 145.98, 157.00, 166.42, 169.40 (Fig. S2) (Spectra of the compounds are given in supplementary materials). Anal. calcd for C<sub>17</sub>H<sub>16</sub>N<sub>2</sub>OS: C, 68.89; H, 5.44; N, 9.45; S, 10.82. Found: C, 68.95; H, 5.53; N, 9.38; S, 10.80.



Scheme 1. Synthesis of Schiff bases **1a–c** and *cis*-2-azetidinones **2a–c**.

**6-Ethoxybenzothiazol-2-yl-(2-methoxybenzylidene)amine (1b).** This compound was obtained as a yellow solid, yield 0.232 g (82%), m.p. 138–139 °C. FT-IR (KBr)  $\nu_{\max}$  1597 (–CH=N–), 1564, 1492, 1440  $\text{cm}^{-1}$ .  $^1\text{H}$  NMR (DMSO- $d_6$ )  $\delta$  1.40 (s, 3H, PhCH<sub>3</sub>), 4.00 (t,  $J$  = 6.92 Hz, 3H, CH<sub>3</sub>CH<sub>2</sub>O), 4.10 (q,  $J$  = 6.89 Hz, 2H, CH<sub>3</sub>CH<sub>2</sub>O), 7.10 (dd,  $J$  = 2.48, 8.86 Hz, 1H, H-5), 7.14 (d,  $J$  = 7.52 Hz, 1H, H-12), 7.25 (d,  $J$  = 8.48 Hz, 1H, H-4), 7.62 (d,  $J$  = 2.45 Hz, 1H, H-7), 7.66 (dt,  $J$  = 7.77 Hz, 1H, H-14), 7.84 (d,  $J$  = 8.87 Hz, 1H, H-15), 8.10 (dd,  $J$  = 2.45, 7.68 Hz, 1H, H-13), 9.50 (s, 1H, CH=N) (Fig. S3).  $^{13}\text{C}$  NMR (DMSO- $d_6$ )  $\delta$  15.10, 59.52, 64.21, 106.16, 112.90, 116.60, 121.48, 122.88, 123.79, 127.93, 135.91, 145.99, 156.98, 160.95, 169.80 (Fig. S4). Anal. calcd for C<sub>17</sub>H<sub>16</sub>N<sub>2</sub>O<sub>2</sub>S: C, 65.36; H, 5.16; N, 8.9; S, 10.26. Found: C, 65.50; H, 5.30; N, 8.95; S, 10.30.

**5,6-Dimethylbenzothiazol-2-yl-(4-methoxybenzylidene)amine (1c).** This compound was obtained as a yellow solid, yield 0.217 (81%), m.p. 142–143 °C.  $^1\text{H}$  NMR (DMSO- $d_6$ )  $\delta$  2.37 (s, 6H, Bzt. CH<sub>3</sub>), 2.43 (s, 3H, PhOCH<sub>3</sub>), 7.41 (d,  $J$  = 7.98 Hz, 2H, H-12 and H-14), 7.73 (s, 1H, H-4), 7.82 (s, 1H, H-7), 7.99 (d,  $J$  = 8.02 Hz, 2H, H-11 and H-15), 9.10 (s, 1H, CH=N).  $^{13}\text{C}$  NMR (DMSO- $d_6$ )  $\delta$  30.15, 30.70, 40.70, 122.46, 123.46, 130.29, 130.54, 131.78, 132.54, 134.95, 135.99, 139.31, 144.49, 150.48, 166.91, 170.84.

**3-Chloro-1-(6-ethoxybenzothiazol-2-yl)-4-*para*-tolylazetidion-2-one (2a).** This compound was obtained as a white solid, yield 0.016 g (65%), m.p. 220–221 °C. FT-IR (KBr)  $\nu_{\max}$  2976, 2925 (C–H), 1666 (C=O), 1595 and 1517  $\text{cm}^{-1}$  (Aryl C–H).  $^1\text{H}$  NMR (DMSO- $d_6$ )  $\delta$  1.35 (t,  $J$  = 5.10 Hz, 3H, CH<sub>3</sub>CH<sub>2</sub>O), 2.30 (s, 3H, PhCH<sub>3</sub>), 4.07 (q,  $J$  = 6.95 Hz, 2H, CH<sub>3</sub>CH<sub>2</sub>O), 5.17 (d,  $J$  = 8.82 Hz, 1H, H-3'), 5.29 (d,  $J_{\text{cis}}$  = 8.8 Hz, 1H, H-4'), 6.93 (dd,  $J$  = 2.41, 9.12 Hz, 1H, H-5), 7.20 (d,  $J$  = 7.96 Hz, 2H, H-12 and H-14), 7.27 (d,  $J$  = 8.09 Hz, 2H, H-11 and H-15), 7.39 (d,  $J$  = 2.4 Hz, 1H, H-7), 8.04 (d,  $J$  = 8.89 Hz, 1H, H-4) (Fig. S5).  $^{13}\text{C}$  NMR (DMSO- $d_6$ )  $\delta$  15.06, 22.22, 29.45, 64.35, 65.48, 109.3, 113.33, 124.48, 127.88, 128.96, 129.64, 132.30, 137.91, 163.09 (Fig. S6). Anal. calcd for C<sub>19</sub>H<sub>17</sub>ClN<sub>2</sub>O<sub>2</sub>S: C, 61.20; H, 4.60; N, 7.51; S, 8.60. Found: C, 61.03; H, 4.62; N, 7.53; S, 8.67.

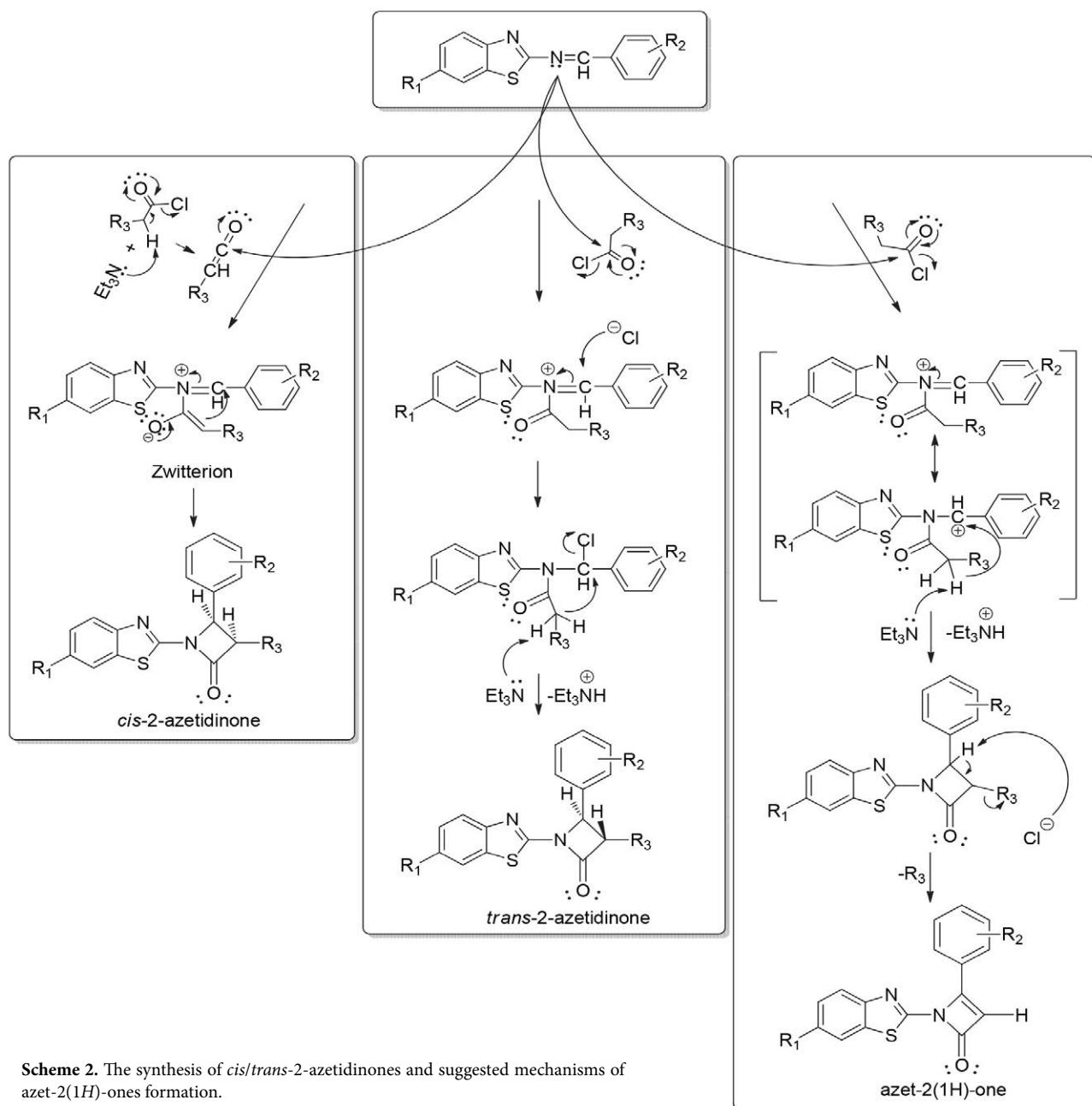
**3-Chloro-1-(6-ethoxybenzothiazol-2-yl)-4-(2-methoxyphenyl)azetidion-2-one (2b).** This compound was obtained as a white solid, yield 0.0731 g (84%), m.p. 228–229 °C. FT-IR (KBr)  $\nu_{\max}$  1658 (C=O), 1593, 1552, 1514, 2925, 2854  $\text{cm}^{-1}$ .  $^1\text{H}$  NMR (DMSO- $d_6$ )  $\delta$  1.35 (t,  $J$  = 6.85 Hz, 3H, CH<sub>3</sub>CH<sub>2</sub>O), 2.90 (s, 3H, OCH<sub>3</sub>), 4.50 (q,  $J$  = 6.95 Hz, 2H, CH<sub>3</sub>CH<sub>2</sub>O), 5.43 (d,  $J_{\text{cis}}$  = 5.24 Hz, 1H, H-3'), 5.10 (d,  $J_{\text{cis}}$  = 5.3 Hz, 1H, H-4'), 6.92 (dd,  $J$  = 2.7, 9.02 Hz, 1H, H-12), 6.97 (t,  $J$  = 7.43 Hz, 1H, H-11), 7.09 (d,  $J$  = 8.12 Hz, 1H, H-4), 7.19 (dd,  $J$  = 1.58, 7.53 Hz, 1H, H-5), 7.36 (dd,  $J$  = 2.35, 8.06 Hz, 1H, H-10), 7.39 (d,  $^4J$  = 0.95 Hz, 1H, H-7), 8.05 (d,  $J$  = 9.02 Hz, 1H, H-13) (Fig. S7).  $^{13}\text{C}$  NMR (DMSO- $d_6$ , ppm):  $\delta$  15.10, 56.52, 64.21, 106.16, 112.90,

116.60, 121.48, 122.88, 123.79, 127.93, 135.91, 145.99, 156.98, 160.95, 160.98, 169.80 (Fig. S8). Anal. calcd for C<sub>19</sub>H<sub>17</sub>ClN<sub>2</sub>O<sub>2</sub>S: C, 58.68; H, 4.41; N, 7.20; S, 8.25. Found: C, 58.70; H, 4.35; N, 7.17; S, 8.31.

**3-Chloro-1-(5,6-dimethylbenzothiazol-2-yl)-4-(4-methoxyphenyl)azetidion-2-one (2c).** This compound was obtained as a white solid, yield 0.103 g (82%), m.p. 274–275 °C. FT-IR (KBr)  $\nu_{\max}$  1651 (C=O), 2854 and 2923  $\text{cm}^{-1}$  (C–H).  $^1\text{H}$  NMR (DMSO- $d_6$ )  $\delta$  2.40 (s, 6H, CH<sub>3</sub>), 3.81 (s, 3H, PhOCH<sub>3</sub>), 4.13 (d,  $J_{\text{cis}}$  = 5.34 Hz, 1H, H-3'), 4.15 (d,  $J_{\text{cis}}$  = 5.51 Hz, 1H, H-4'), 7.20 (d,  $J$  = 8.06 Hz, 2H, H-15 and H-11), 7.7 (d,  $J$  = 8.01 Hz, 2H, H-12 and H-14), 8.20 (s, 1H, H-4), 8.87 (s, 1H, H-7) (Fig. S9). Anal. calcd for C<sub>19</sub>H<sub>17</sub>ClN<sub>2</sub>O<sub>2</sub>S: C, 61.20; H, 4.60; N, 7.51; S, 8.60. Found: C, 61.03; H, 4.85; N, 7.53; S, 8.67.

### 3. Results and Discussion

Azetidionones were prepared via the Staudinger reaction. The Staudinger reaction involves the nucleophilic attack of an imine on a ketene, leading to a zwitterion intermediate, which then undergoes stepwise ring closure to yield the  $\beta$ -lactam ring.<sup>16</sup> Stereoselectivity depends directly on the competition between ring closure and isomerization of the imine moiety in the zwitterion intermediate. In the Staudinger reaction, ketene formation prior to the cyclocondensation results in the formation of the  $\beta$ -lactam product as the major *cis* form. However, the direct reaction of imine with acid chloride gives the exclusive or major product of *trans*- $\beta$ -lactam<sup>17,18</sup> (Scheme 2). The competition between the isomers depends on many factors, such as the electronic effect of the ketene substituents and the steric hindrance of the N substituent of imines. Another factor influencing the Staudinger reaction is solvents, possibly affecting the stability and half-life of the zwitterion intermediate, causing changes in stereoselectivity.<sup>18</sup> In our previous study, the Staudinger reactions were carried out at different temperatures using different equivalents, differently substituted Schiff bases, and different acid chloride derivatives. *cis*-2-Azetidinones were obtained in good yields using the concentration of acid chloride derivatives (1.5–3 eq) and triethylamine (2–3 eq). However, some unexpected azet-2(1*H*)-ones were synthesized by changing the order of addition of the reactants and concentrations of triethylamine (7.4–15 eq) and chloroacetyl chloride (2–3.7 eq) without changing other reaction conditions such as temperature and solvent type.<sup>19</sup> We proposed that the formation of azet-2(1*H*)-ones depends on the concentration of triethylamine, and the suggested mechanism of azet-2(1*H*)-ones formation is given in Scheme 2. In the first step, the novel Schiff bases **1a–c** are synthesized by the reaction of benzaldehyde and the substituted benzothiazole in dichloromethane solution (DCM). The reaction time was 6 hours. These novel Schiff bases **1a–c** were iso-



lated with yields ranging from 79–82% (Scheme 1). Among the Schiff bases prepared **1a–c**, the compound **1b** was isolated with the highest efficiency (82%), which is explained as follows: Electron-donating groups attached to the 2-aminobenzothiazole ring increase the reactivity of the amino group for nucleophiles and accelerate the formation of Schiff bases. The structures of Schiff bases were confirmed by  $^1\text{H}$  NMR,  $^{13}\text{C}$  NMR and FT-IR spectra. In the FT-IR spectrum for compound **1b**, the signal observed at  $1597\text{ cm}^{-1}$  was assigned as the imine ( $-\text{CH}=\text{N}-$ ) group. In the  $^1\text{H}$  NMR spectrum of the same compound, one singlet of the methyl proton was observed at 1.40 ppm and another singlet of the protons of an imine at 9.50 ppm. (The num-

bering of protons is given in Scheme 1). Additionally, the signal observed as a result of the long-range interaction at 7.62 ppm ( $^4J = 2.45\text{ Hz}$ ) was marked as belonging to the H-7 proton. Likewise, at 7.66 ppm, the triplet of the doublet was assigned as belonging to the H-14 proton, while at 7.10 ppm ( $^3J = 8.86\text{ Hz}$ ,  $^4J = 2.48\text{ Hz}$ ) and 8.10 ppm ( $^3J = 7.68\text{ Hz}$ ,  $^4J = 2.45\text{ Hz}$ ) the doublet of the doublet was marked as belonging to the H-5 and H-13 protons, respectively. In the compound **1b**, the other three doublets at 7.14, 7.25, and 7.84 ppm were assigned the protons H-12, H-4, and H-15, respectively. The triplet and a quartet observed at 4.0 and 4.10 ppm belong to the methyl and methylene groups in the ethoxy group, respectively. In the  $^{13}\text{C}$

NMR spectrum of compound **1b**, 17 signals belonging to the carbons of the compound were observed and from these signals, the signal at 169.80 ppm was observed for the C=N carbon in the benzothiazole ring. The signal at 160.98 ppm was marked as belonging to the imine carbon.

Azetidinone was obtained from electron donating novel Schiff bases **1a–c** by Staudinger reaction in the second step as depicted in the Scheme 1. In this reaction, ketene electrophiles and imine molecules can act as a nucleophile. The order of addition of chloroacetyl chloride and imine affects stereoselectivity, so ketene formation was carried out by adding chloroacetyl chloride in the presence of triethylamine before the formation of zwitterion intermediate. Thus, ketene and the resulting zwitterion intermediate were subjected to stepwise ring closure to give the  $\beta$ -lactam ring and produced mostly *cis*-2-azetidiones **2a–c**. Especially depending on the concentrations of triethylamine and chloroacetyl chloride, for example triethylamine 2–3 eq, chloroacetyl chloride 1.5–3 eq and dichloromethane as the solvent, *cis*-2-azetidione compounds were formed in good yield. Based on the reference 18, the *cis*- and *trans*-2-azetidione formation mechanism of the novel synthesized compounds is shown in Scheme 2. By mixing the imine, substituted with electron-donating substituent, and the ketene, having electron-withdrawing substituents, in a nonpolar solvent and with the addition of triethylamine at 0–5 °C in an ice bath for 9 h, almost only the single isomer *cis*-2-azetidione was obtained with 65–84% yield. However, it is declared in the literature that imines having electron-withdrawing substituents and ketenes having electron-donating substituents cause *cis*- $\beta$ -lactam formation.<sup>16</sup> On the contrary, when the concentration of acid chloride and triethylamine is adjusted, *cis*- $\beta$ -lactam stereoisomer can be obtained by the Staudinger reaction from the reaction of the imine having electron-donating substituents and from ketene, having electron-withdrawing substituents (Scheme 1).

The structure of *cis*-2-azetidiones is confirmed by <sup>1</sup>H NMR, <sup>13</sup>C NMR and FT-IR spectra. In the FT-IR spectrum of compound **2b**, the imine signal was not observed at 1597 cm<sup>-1</sup>, while the strong peak observed at 1658 cm<sup>-1</sup> confirmed the presence of a carbonyl group in the *cis*-2-azetidione ring. The peaks at 2976 and 2887 cm<sup>-1</sup> were marked as belonging to the aliphatic CH<sub>3</sub> and CH<sub>2</sub> groups of the imine compound, and the CH signal in the *cis*-2-azetidione ring was also observed as a strong signal in the same region. In the <sup>1</sup>H NMR spectrum of compound **2b**, three doublet doublets at 6.92, 7.19 and 7.36 ppm due to long distance coupling have been marked as belonging to H-12, H-5 and H-10 protons, respectively. (The numbering of protons is given in Scheme 1.) Signals for protons H-11, H-4, and H-13, respectively, have been observed as a triplet at 6.97 ppm and two doublets at 7.09 and 8.05 ppm. Additionally, at 6.97, 7.09 and 8.05 ppm observed a triplet and two doublets, belong to the H-11, H-4, and H-13 protons, respectively. The value of the spin-spin coupling constant of

the protons H-3' and H-4' in the 2-azetidione cyclobutane ring determined whether the product is *cis* or *trans*. The stereoisomer of these compounds is determined by the spin-spin coupling constant of the protons in the azetidione ring, where  $J > 4.0$  Hz for the *cis* isomers,  $J \leq 3.0$  Hz for the *trans* isomers, and the stereoisomer of the synthesized compounds was determined by comparing these values.<sup>19–23</sup> For compound **2b**, while the two doublets observed at 5.43 and 5.10 ppm were marked as belonging to the H-3' and H-4' protons in the azetidione ring, the coupling constant values of these protons were calculated as 5.24 and 5.30 Hz. For compound **2a**, the spin-spin coupling constant of the doublets were observed at 8.82 and 8.86 Hz, respectively (Figure S5). For compound **2b**, the coupling constant of protons in the 2-azetidione ring was found to be 5.24 and 5.30 Hz. Similarly, for compound **2c**, the coupling constant of protons in the 2-azetidione ring was found to be 5.34 and 5.51 Hz. Based on these data, the stereoisomer of the synthesized azetidione was determined to be *cis*-2-azetidione.

## 4. Conclusions

Electron-donating substituents on the phenyl and benzothiazole rings of the Schiff bases increase the nucleophilicity of the imine nitrogen, while the electron withdrawing substituents of the chloroacetyl chloride increase the acidity of  $\alpha$ -hydrogen, and elimination with triethylamine accelerates the formation of ketene. Ketene and imine give the intermediate zwitterion, and the presence of nitrogen and sulfur in the benzothiazole ring ionizes the imine moiety, accelerating ring closure, and *cis*-2-azetidione is formed. As a result, contrary to what is said in the literature, when conditions such as apolar solvent, the amount of triethylamine, the electronic effect of the imine, the cold environment and the addition order of the reagents are adjusted, the ketene with electron-withdrawing substituent and the imine with electron-donating substituent could produce *cis*-2-azetidione. These *cis*-2-azetidione derivatives have been synthesized from the reaction of the ketene source (chloroacetyl chloride) and novel Schiff bases in the presence of triethylamine via Staudinger reaction, in good yields (65–84%). The concentration of chloroacetyl chloride and triethylamine has been found to affect the reaction mechanism of 2-azetidione formation. We concluded that *cis*-2-azetidiones were formed in good yields using 1 eq. of a Schiff base, 3 eq. of Et<sub>3</sub>N and 1.5 eq. of chloroacetyl chloride in dichloromethane solution at 0–5 °C.

## Acknowledgements

The authors would like to thank the Eskişehir Osmangazi University Scientific Research Projects Council for financial support (Project No: 2014/19A208).

## 5. References

1. C. M. L. Delpiccolo, M. A. Fraga, E. G. Mata, *J. Comb. Chem.* **2003**, *5*, 208–210. DOI:10.1021/cc020107d
2. R. B. Pawar, V. V. Mulwad, *Chem. Heterocycl. Compd.* **2004**, *40*, 219–226. DOI:10.1023/B:COHC.0000027896.38910.d1
3. P. D. Mehta, N. P. S. Sengar, A. K. Pathak, *Eur. J. Med. Chem.* **2010**, *45*, 5541–5560. DOI:10.1016/j.ejmech.2010.09.035
4. G. S. Singh, B. J. Mmolotsi, *Il Farmaco*, **2005**, *60*, 727–730. DOI:10.1016/j.farmac.2005.06.008
5. C. D. Risi, G. P. Pollini, A. C. Veronese, V. Bertolasi, *Tetrahedron Lett.* **1999**, *40*, 6995–6998. DOI:10.1016/S0040-4039(99)01421-5
6. The Organic Chemistry of  $\beta$ -Lactams, ed. G. I. Georg, VCH: Weinheim, 1993.
7. R. F. Abdulla, K. H. Fuhr, *J. Med. Chem.* **1975**, *18*, 625–627. DOI:10.1021/jm00240a022
8. W. Dürckheimer, J. Blumbach, R. Lattrell, K. H. Scheunemann, *Angew. Chem. Int. Ed. Engl.* **1985**, *24*, 180–202. DOI:10.1002/anie.198501801
9. P. D. Mehta, N. P. S. Sengar, A. K. Pathak, *Eur. J. Med. Chem.* **2010**, *45*, 5541–5560. DOI:10.1016/j.ejmech.2010.09.035
10. H. Staudinger, *Justus Liebigs Ann. Chem.* **1907**, *356*, 51–123. DOI:10.1002/jlac.19073560106
11. A. K. Bose, M. Jayaraman, A. Okawa, S. S. Bari, E. W. Robb, M. S. Manhas, *Tetrahedron Lett.* **1996**, *37*, 6989–6992. DOI:10.1016/0040-4039(96)01571-7
12. A. K. Bose, B. K. Banik, M. S. Manhas, *Tetrahedron Lett.* **1995**, *36*, 213–216. DOI:10.1016/0040-4039(94)02225-Z
13. A. Arrieta, B. Lecea, F. P. Cossio, *J. Org. Chem.* **1998**, *63*, 5869–5876. DOI:10.1021/jo9804745
14. P. Vicini, A. Geronikaki, M. Incerti, B. Busonera, G. Poni, C. A. Cabras, P. L. Colla, *Bioorg. Med. Chem.* **2003**, *11*, 4785–4789. DOI:10.1016/S0968-0896(03)00493-0
15. K. Mogilaiah, R. B. Rao, K. N. Reddy, *Indian J. Chem.* **1999**, *38B*, 818–822.
16. G. I. Georg, V. T. Ravikumar: Stereocontrolled Ketene-Imine Cycloaddition Reactions, in *The Organic Chemistry of  $\beta$ -Lactams*, ed. G. I. Georg, VCH, Weinheim, 1993, pp. 295–368. DOI:10.1002/chin.199425299
17. L. Jiao, Y. Liang, J. Xu, *J. Am. Chem. Soc.* **2006**, *128*, 6060–6069. DOI:10.1021/ja056711k
18. Y. Wang, Y. Liang, L. Jiao, D.-M. Du, J. Xu, *J. Org. Chem.* **2006**, *71*, 6983–6990. DOI:10.1021/jo0611521
19. H. C. Sakarya, M. Yandimoğlu, *Croat. Chem. Acta*, **2018**, *91*, 533–541. DOI:10.5562/cca3386
20. D. A. Nelson, *J. Org. Chem.* **1972**, *37*, 1447–1449. DOI:10.1021/jo00974a038
21. K. D. Barrow, T. M. Spotswood, *Tetrahedron Lett.* **1965**, *6*, 3325–3335. DOI:10.1016/S0040-4039(01)89203-0
22. J. Decazes, J. L. Luche, H. B. Kagan, *Tetrahedron Lett.* **1970**, *11*, 3665–3668. DOI:10.1016/S0040-4039(01)98556-9
23. D. A. Nelson, *Tetrahedron Lett.* **1971**, *12*, 2543–2546. DOI:10.1016/S0040-4039(01)96914-X

## Povzetek

S pomočjo cikloadicijske reakcije iminov **1a–c** in kloroacetyl klorida v suhem diklorometanu pri 0–5 °C z dodatkom trietilamina smo uspešno pripravili serijo novih *cis*-2-azetidionov **2a–c**. S cikloadicijo Schiffovih baz na kloroacetyl klorid so kot ustrezni glavni stereoizomeri nastali produkti *cis*-2-azetidiononi **2a–c**. Pripravljene spojine smo karakterizirali z analitskim in spektroskopskimi tehnikami (infrardeča spektroskopija, <sup>1</sup>H NMR, <sup>13</sup>C NMR ter elementna analiza).



Except when otherwise noted, articles in this journal are published under the terms and conditions of the Creative Commons Attribution 4.0 International License

Scientific paper

# Development of QSAR Model Based on Monte Carlo Optimization for Predicting GABA<sub>A</sub> Receptor Binding of Newly Emerging Benzodiazepines

Aleksandra Antović<sup>1</sup>, Radovan Karadžić<sup>1</sup>, Jelena V. Živković<sup>2</sup> and Aleksandar M. Veselinović<sup>2,\*</sup>

<sup>1</sup> Institute of Forensic Medicine, Faculty of Medicine, University of Niš, Bulevar Dr Zorana Đinđića 81, 18000 Niš, Serbia

<sup>2</sup> Department of Chemistry, Faculty of Medicine, University of Niš, Bulevar Dr Zorana Đinđića 81, 18000 Niš, Serbia

\* Corresponding author: E-mail: [aveselinovic@medfak.ni.ac.rs](mailto:aveselinovic@medfak.ni.ac.rs)  
Fax: +381 18 4238770; Phone: +381 18 4570029

Received: 09-21-2023

## Abstract

The rising prevalence and appeal of designer benzodiazepines (DBZDs) pose a significant public health concern. To evaluate this threat, the biological activity/potency of DBZDs was examined through *in silico* studies. To gain a deeper understanding of their pharmacology, we employed the Monte Carlo optimization conformation-independent method as a tool for developing QSAR models. These models were built using optimal molecular descriptors derived from both SMILES notation and molecular graph representations. The resulting QSAR model demonstrated robustness and a high degree of predictability, proving to be very reliable. The newly discovered molecular fragments used in the computer-aided design of the new compounds were believed to have caused the increase and decrease of the studied activity. Molecular docking studies were used to make the final assessment of the designed inhibitors and excellent correlation with the results of QSAR modeling was observed. This discovery paves the way for the swift prediction of binding activity for emerging benzodiazepines, offering a faster and more cost-effective alternative to traditional *in vitro/in vivo* analyses.

**Keywords:** Benzodiazepines; QSAR; Monte Carlo optimization; New psychoactive substances; GABA<sub>A</sub> receptor

## 1. Introduction

Everyday prescriptions involve benzodiazepines, as well as their derivatives, in the form of anxiolytic, anti-insomnia and anti-convulsant drugs for the purpose of tackling a multitude of medical conditions by acting on the gamma-aminobutyric acid type A (GABA<sub>A</sub>) receptor.<sup>1</sup> Gamma-aminobutyric acid (GABA) is the endogenous neurotransmitter for the GABA<sub>A</sub> receptor and its binding reduces cell excitability.<sup>2</sup> Much lower cellular excitability is effected by benzodiazepines that potentiates GABA<sub>A</sub> receptor's response to GABA. In physiological terms, this leads to relaxation and sedation.<sup>1</sup> In such instances, the medical benefit of benzodiazepines is visible, since their anxiolytic effects lessen agitation and stress in patients. Nevertheless, owing to the psychoactive effects of the mentioned, there is a long abuse history of benzodiaze-

pines, and they are frequently illegally secured.<sup>1–5</sup> Recently, the black market has had a steady supply of benzodiazepines. They are either licensed as prescription drugs in countries which are not their original home country, or are newly-synthesized and they are called 'new psychoactive substances' (NPS).<sup>6–9</sup> Most of the benzodiazepines that have appeared in this manner have not been subjected to regular pharmaceutical trials. For this reason, their effects can vary greatly and their activity may prove to be extremely hazardous.<sup>10</sup> Even though the use of benzodiazepines is quite safe if they are taken as prescribed, simultaneous use of benzodiazepines and opioids (whether abused or prescribed) can cause respiratory depression and even lead to death.<sup>11,12</sup> Numerous side effects may occur if benzodiazepines are not carefully monitored and if they are not prescribed. Such side-effects include dependency and tolerance in the event that the medication is taken long-

term. Furthermore, sudden withdrawal can lead to medical problems, such as insomnia and anxiety.<sup>13,14</sup> A certain number of overdose cases, driving under the influence of drugs (DUID) and hospital admissions have already been reported with regard to the use of NPS benzodiazepines.<sup>15–17</sup> One of the most prominent issues is that illegal benzodiazepines are not controlled at all and represent a safety hazard. In addition, in the event that the trend of their abuse gets increasingly big, the situation might be even more worrying.

Benzodiazepines represent a diverse group of psychoactive compounds whose central structural component consists of a diazepine ring and a benzene ring. There is a multitude of derivatives, including imidazo-benzodiazepines, thienotriazolobenzodiazepines and triazolobenzodiazepines. Correlating molecular structure to biological activity is attempted through the use of the quantitative structure-activity relationship (QSAR), frequently with the use of a various molecular descriptors, such as electronic, topological, physicochemical and steric properties.<sup>18</sup> Commonly, a set of compounds with a known biological activity is used for the purpose of attaining a ‘training’ dataset and creating a model. Afterwards, the model may be utilized for predicting the unknown biological activity possessed by compounds having a similar structure or for exploring the key structural features for the relevant biological activity in question. There have been numerous reasons for the use of QSAR, such as the pharmacological interpretation of drug-related deaths and developing compounds in the pharmaceutical industry.<sup>19–21</sup> Over the recent years, an approach in which the studied activity is treated as a random event has showed promise in QSAR modeling: the Monte Carlo optimization method. The mentioned method relies on the approach which is of conformation-independent nature, where the optimal descriptors are based on topological molecular features and the molecules in the Simplified Molecular Input Line Entry System (SMILES) notation.<sup>22–24</sup> The simplicity and efficiency of the method described are the primary advantages over more commonly used methods. What is more, molecular fragments (calculated as SMILES notation descriptors) with an impact on studied activity and which can be associated with the studied compounds’ chemical structures can also be determined with the use of this method. When it comes to the applications with regard to new psychoactive substances, the application of QSAR’s predictive power has mainly been aimed at cannabinoid binding to CB1 and CB2 receptors.<sup>25–27</sup> However, its use has also been to examine the biological activity of hallucinogenic phenylalkylamines, as well as the binding of tryptamines, phenylalkylamines and LSD to the 5-HT<sub>2A</sub> receptor and the selectivity of methcathinone for norepinephrine (NAT), dopamine (DAT) and serotonin transporters (SERT).<sup>28–30</sup> At present, a great many novel benzodiazepines have not been analyzed, and their physicochemical and biological properties have not been

determined, since this would entail making a considerable investment, both in terms of money and time. This is precisely why a quick and economical method is desirable for predicting their properties.

Predicting the absorption rate, clearance, bioavailability, half-life and distribution volume for a group of benzodiazepines has previously been the application of QSAR to benzodiazepines. This study included phenazepam, a benzodiazepine which appeared as an NPS in 2007.<sup>31,32</sup> Over the years, after the publication of this study, other benzodiazepines (such as etizolam) appeared solely as new psychoactive substances. Also, QSAR methodology has been applied for the purpose of modeling the post-mortem redistribution of benzodiazepines, in which case a good model was obtained ( $R^2 = 0.98$ ), where energy, ionization and molecular size were discovered to have a significant impact.<sup>33</sup> In an attempt to predict how toxic these compounds are, the toxicity of benzodiazepines to their structure has been correlated with the use of quantitative structure-toxicity relationships (QSTR).<sup>34</sup> In recent years, a study concluded that identifying the structural fragments responsible for toxicity (the presence of hydrazone substitutions and amine, as well as saturated heterocyclic ring systems resulting in greater toxicity) was possible with the use of QSTR, and that the information could potentially be used in order to create new, less toxic benzodiazepines for medical purposes. Correlating the benzodiazepine structure to GABA<sub>A</sub> receptor binding and tearing apart the complex relationship between various substituents, as well as their effect on activity have been achieved with the use of different QSAR models, though no one has specifically attempted to predict the binding values for the benzodiazepines which represent new psychoactive substances.<sup>35,36</sup> The main aim of this study is the development of QSAR models for predicting GABA<sub>A</sub> receptor binding of newly emerging benzodiazepines.

## 2. Materials and Methods

The studied activity is expressed as the logarithm of the reciprocal of concentration ( $\log 1/c$ ), with “c” representing the molar inhibitory concentration (IC<sub>50</sub>) required to displace 50% of [3H]-diazepam from synaptosomal preparations in the cerebral cortex of rats.<sup>37,38</sup> The primary objective of this study is to construct a QSAR model capable of predicting the potential biological activity of newly-appearing benzodiazepines. The ultimate aim is to enhance our comprehension of these substances and consequently reduce their potential harm more rapidly than through traditional *in vitro/in vivo* testing methods.

To establish relevant QSAR models, the initial step involved acquiring molecules from the literature sources.<sup>37,38</sup> These molecules were subsequently rendered as graphical representations using ACD/ChemSketch software v.11.0, and were then transformed into the SMILES

notation using the same software. The Supporting Information section provides the chemical structures of the compounds utilized in QSAR modeling, along with their corresponding SMILES notation. The dependent variable used for QSAR model was the relationship between GABA receptor binding and the structure of characterized benzodiazepines, expressed as the logarithm of the reciprocal of concentration ( $\log 1/c$ ). The numerical values presented in Table S1 of the Supplementary material correspond to these data. After completing the construction of the appropriate database, it was divided into two sets through three different main molecule random splits. The first set was the training set, comprising 63 compounds (75%), while the second set was the test set, containing 21 compounds (25%). Subsequently, the distribution activity normality was assessed using the method outlined in published literature.<sup>23,24</sup> The CORAL (CORrelation and Logic, <http://www.insilico.eu/coral>) software was employed to create conformation-independent QSAR models using the Monte Carlo method and its algorithm, which treats the relevant activity as a random event. Two types of molecular descriptors, based on the SMILES notation and the molecular graph, were considered. Invariants were established as local graph invariants using the molecular graphs, specifically path numbers of length 2 and 3 (p2, p3), Morgan extended connectivity index of increasing order (EC0), the Code of Nearest Neighbors (NNCK) and the valence shells within the range of 2 and 3 (s2, s3). In recent years, the Simplified Molecular Input-Line Entry System (SMILES) notation, particularly in chemoinformatics, since the SMILES notation has emerged as the most convenient representation, especially in the field of chemoinformatics. In the realm of medicinal chemistry this is particularly advantageous, as establishing correlations between molecular fragments and descriptors based on the molecular graph can be quite challenging. In the realm of QSAR modeling, one can establish molecular optimal descriptors (DCW) by utilizing the SMILES notation, and these DCW descriptors can be computed as a result of applying Equation 1 to the SMILES notation.

$$\text{DCW}(T, N_{\text{epoch}})_{\text{SMILES}} = \Sigma \text{CW}(\text{ATOMPAIR}) + \Sigma \text{CW}(\text{NOSP}) + \Sigma \text{CW}(\text{BOND}) + \Sigma \text{CW}(\text{HALO}) + \Sigma \text{CW}(\text{HARD}) + \Sigma \text{CW}(S_k) + \Sigma \text{CW}(\text{SS}_k) + \Sigma \text{CW}(\text{SSS}_k) \quad (1)$$

This research employed SMILES notation-based descriptors, encompassing global, local, and HARD-index descriptors. An essential aspect of the developed QSAR model is the calculation of the correlation weight (CW) for each optimal descriptor used, which is accomplished through the application of the Monte Carlo method.<sup>23,24</sup> This process can be accomplished by generating suitable random numbers and observing how the distribution of these numbers adheres to specific properties or criteria. In this procedure, CW values are assigned randomly to all the optimal descriptors, including both SMILES nota-

tion-based descriptors and molecular graph-based ones, during each independent Monte Carlo run. Subsequently, the Monte Carlo optimization process is employed to compute the numerical data for correlation weights. These weights are instrumental in achieving the highest possible correlation coefficient between the optimal descriptors used and the target activity under study. The Monte Carlo method employs two parameters to attain this objective: the number of epochs (Nepoch) and the threshold (T). For the construction of QSAR models, a range of values was used, specifically 0 to 10 for T and 0 to 70 for Nepoch. The determination of the most effective combination of T and Nepoch, based on predictive performance, was conducted following the methodology outlined in published literature.<sup>23,24</sup>

The primary objective in any QSAR modeling process is to create a robust model capable of accurately, consistently, and objectively predicting the properties of new molecules. The effectiveness of the established QSAR models was assessed using the following methods: internal validation through the training set, external validation using the validation set, and data randomization through the Y-scrambling test. This was accomplished by utilizing various statistical parameters to assess the quality of the models. These parameters include the correlation coefficient ( $r_2$ ), cross-validated correlation coefficient ( $q_2$ ), mean absolute error (MAE), standard error of estimation (s), root-mean-square error (RMSE), the Fischer ratio (F), Rm2, and MAE-based metrics.<sup>39–43</sup> Recently, a new criterion called the Index of Ideality of Correlation (IIC) has been introduced to evaluate the predictive potential of QSAR models. The IIC takes into account both the correlation coefficient and the distribution of data points relative to the diagonal line in the coordinate space of observed versus calculated values of the studied endpoint. The IIC is calculated using Equations 2–5 as the final estimator for the QSAR model's performance.<sup>44–46</sup>

$$\Delta_k = \text{observed}_k - \text{calculated}_k \quad (2)$$

With data available for all  $\Delta_k$  for the test set, in the test set, it is possible to calculate the sum of negative and positive values of  $\Delta_k$  akin to the calculation of the mean absolute error (MAE):

$${}^{-}\text{MAE}_{\text{test}} = \frac{1}{-N} \sum_{k=1}^{-N} |\Delta_k| \quad \Delta_k < 0, \quad (3)$$

$-N$  is the number of  $\Delta_k < 0$

$${}^{+}\text{MAE}_{\text{test}} = \frac{1}{+N} \sum_{k=1}^{+N} |\Delta_k| \quad \Delta_k \geq 0, \quad (4)$$

$+N$  is the number of  $\Delta_k \geq 0$

$$\text{IIC}_{\text{test}} = r_{\text{test}} \times \frac{\min({}^{-}\text{MAE}_{\text{test}}, {}^{+}\text{MAE}_{\text{test}})}{\max({}^{-}\text{MAE}_{\text{test}}, {}^{+}\text{MAE}_{\text{test}})} \quad (5)$$

Molegro Virtual Docker (MVD) software was used to perform molecular docking studies on geometrically



optimized ligands using MMFF94 force field. The target of these docking studies was the CryoEM structure of human full-length alpha1beta3gamma2L GABA(A)R in complex with diazepam (Valium) (PDB: 6HUP). MVD uses a rigid receptor structure and a flexible ligand structure for docking studies. It accounts for both hydrophilic and hydrophobic interactions, with a particular focus on van der Waals and steric interactions. This includes the identification of hydrogen bonds between the amino acids in the studied ligands and the active site. These interactions can be quantified using scoring functions, which are calculated numerical values that correlate with relevant binding energies.<sup>47</sup> As a general rule, for most enzymes, the stronger the interaction between the receptor and the ligand, the higher the inhibition. Therefore, the numerical values obtained for scoring functions can be used to assess the potential inhibitory effect of the studied ligands.<sup>24</sup> To estimate inhibitory potential, the following scoring functions were calculated and used: Pose energy, MolDock, and Re-rank Score. A published methodology was used to validate the entire molecular docking protocol.<sup>48,49</sup> Discovery Studio Client v20.1.0.19 was used to display two-dimensional representations of the interactions between the studied molecules and the amino acids in the dopamine transporter active site.

### 3. Results and Discussion

A pivotal aspect to consider is the applicability domain (AD), which is determined based on the criteria mentioned.<sup>50,51</sup> To establish the AD, we applied the meth-

odology outlined in published literature and found that all the molecules encompassed by this study fell within the defined AD range, with no outliers detected.<sup>23</sup> Table S2 displays the values of statistical metrics used by the authors to assess the quality of the developed QSAR models for the studied activity. The results suggest that the method employed was effective in creating a QSAR model with strong reproducibility, as confirmed by the concordance correlation coefficient. The predictability of the established QSAR model was subsequently assessed using the values provided in Table S2, confirming the model's validity. Additionally, the model's validity was affirmed through the utilization of MAE-based metrics. The ultimate assessment of the developed QSAR models was carried out for both the test set and the training set, utilizing the Ideality of Correlation Index. The resulting values indicate that the developed QSAR models exhibit a strong predictive capability. Figure 1 displays the graphical representation of the best-developed QSAR model, which achieved the highest  $r^2$  value across all three splits and was determined through the best Monte Carlo optimization run. Furthermore, a Y-randomization approach was implemented, involving the randomization of Y values in 1000 trials and across ten distinct runs, to assess the robustness of the developed QSAR models. Additionally, a Y-randomization procedure was employed, involving the randomization of Y values in 1000 trials and across ten separate runs to evaluate the robustness of the developed QSAR models. The values provided in Table S3 demonstrate that there was no chance correlation present in the developed models. In terms of the statistical results, the most favorable QSAR model was derived from the first split.

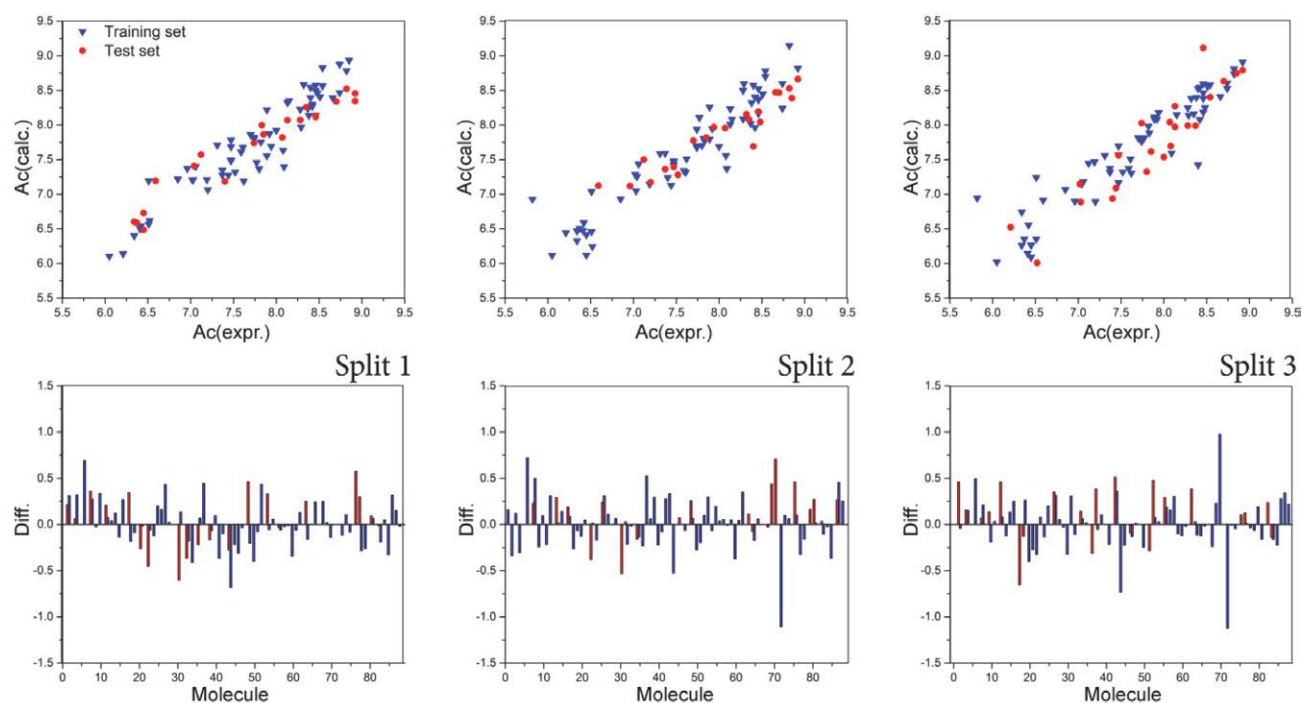


Figure 1. Graphical presentation of the best Monte Carlo optimization runs (the highest value for  $r^2$ ) for the developed QSAR models.

Mathematical expressions for the best QSAR models, as determined by the test set  $r^2$  values across all splits, are provided in Equations 6–8.

$$\text{Split 1: } \log(1/c) = 2.2950(\pm 0.024) + 0.0484(\pm 0.0002) \times \text{DCW}(1,12) \quad (6)$$

$$\text{Split 2: } \log(1/c) = 2.1642(\pm 0.030) + 0.0504(\pm 0.0002) \times \text{DCW}(1,20) \quad (7)$$

$$\text{Split 3: } \log(1/c) = -1.2010(\pm 0.048) + 0.0700(\pm 0.0004) \times \text{DCW}(1,20) \quad (8)$$

Equations 6–8 highlight that the optimal values for T and  $N_{\text{epoch}}$  for Split 1 are 1 and 12, respectively. Similarly, for Split 2, the preferred values for T and  $N_{\text{epoch}}$  are 1 and 20, respectively. Lastly, for Split 3, the recommended values for T and  $N_{\text{epoch}}$  are also 1 and 20, respectively.

The primary objective of this study is to create dependable QSAR models capable of predicting the correlation between GABA<sub>A</sub> receptor binding and the structure of characterized benzodiazepines, represented as the logarithm of the reciprocal of concentration ( $\log 1/c$ ). The quality of predictability is assessed through the application of a range of statistical parameters. The calculations for the conformation-independent models, constructed based on the optimal descriptors derived from SMILES notation invariants and a local graph, were executed using the Monte Carlo optimization method. The utilization of various statistical techniques enabled the evaluation of the resilience and predictive capability of the created QSAR models. The strong applicability of these models is evident from the numerical values employed to validate them. The molecular fragments employed in the QSAR modeling, categorized as SMILES notation fragments with either a positive or negative effect, were successfully identified using the Monte Carlo optimization method. These findings are detailed in Table S4 in the Supplementary material. An illustration

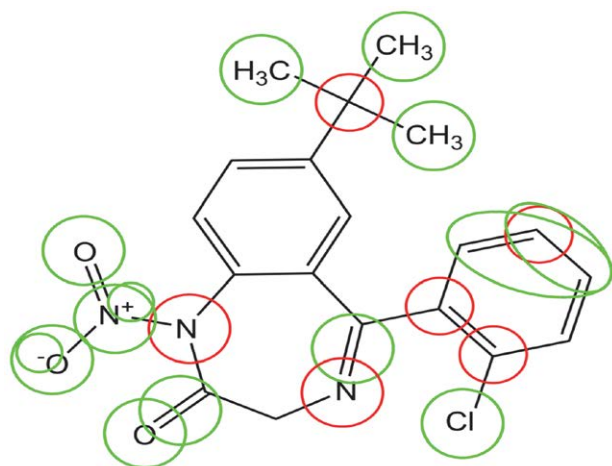


**Figure 2.** Contribution of Molecular Fragments to Benzodiazepines Binding Activity (Green – Increase, Red – Decrease).

of the calculation for both the summarized correlation weight (DCW) and the studied activity ( $\text{pIC}_{50}$ ) of a molecule is provided in Table S5. For ease of interpretation, the molecular graph-based descriptors were excluded. Additionally, a graphical representation of the chosen molecular fragments is depicted in Figure 2.

Based on the results obtained from the QSAR modeling studies, the molecular fragments that exert an influence on the studied activity are: “O.....” and “O...-.....” – both a regular oxygen atom and an oxygen atom carrying a negative charge positively influence the studied activity. Moreover, fragments associated with a negative charge also contribute significantly to this impact, “-.....”, also has positive impact on studied activity; “=.....”, “O...=.....” – the presence of a double bond, as well as a double bond on an oxygen atom, both exert a positive impact on the studied activity, but fragment “N...=.....” associated to double bond on nitrogen atom has negative impact on the studied activity; While a regular nitrogen atom associated with the “N.....” fragment has negative impact but nitrogen with positive charge, “N...+.....” fragment, a nitrogen atom with a positive charge exerts a positive influence on the studied activity – “+.....”; Molecular branching in the form of a simple molecular feature associated with the molecular fragment “(.....” and molecular branching on a nitrogen atom, “N...(.....”, both have a negative impact. However, molecular branching on a carbon atom, “C...(.....”, has a positive impact on the studied activity; Furthermore, additional molecular branching on a carbon atom, defined as “(...C...(.....” and “C...(.....”, has a positive impact. Likewise, a regular carbon atom or a methyl group, defined as “C.....”, and two carbon atoms or an ethyl group, defined as “C...C.....”, also have a positive impact on the studied activity; conversely, a single aromatic carbon atom, defined by the molecular fragment “c.....”, negatively affects the activity. However, the presence of two or three connected aromatic carbon atoms, defined by the molecular fragments “c...c.....” and “c...c...c...”, positively influences the studied activity.

Obtained molecular fragment were further used for the Computer-Aided Design (CAD) of higher/lower activity compounds and summarized results are presented in Figure 3, where conformation-independent results in the CAD process generated the design of six novel potential inhibitors (structures presented in Figure 3). CAD process started with addition of methyl group in ortho and para position which yield molecules A1 and A2, both having additional molecular fragment “C.....”, SMILES notation descriptor, in comparison to molecule A. Additionally, molecules A1 and A2 have molecular branching on benzene ring with carbon atom involved, in comparison to molecule A, defined with molecular fragments – “c...(.....”, “C...(.....”, “c...c...(.....”, “c...C.....” and “c...C...(.....”. These fragments have positive impact on studied activity so calculated values for  $\text{pIC}_{50}$  for molecules A1 and A2 were 7.4308 and 7.5591, respectively, both higher in comparison to

pIC<sub>50</sub> for molecules A (7.2771). Molecules A3, A4, A5 and A6 have added hydroxyl group or chlorine atom in ortho and para position respectively. All molecules have added appropriate molecular fragments “O.....”, “Cl.....”, both with positive impact on studied activity. Like molecules A1 and A2, molecules A3, A4, A5 and A6 have molecular branching on benzene ring defined with “c...(.....”. Addition of above stated fragments yield to the increase of calculated pIC<sub>50</sub> for molecules A3, A4, A5 and A6 in comparison to molecule A.

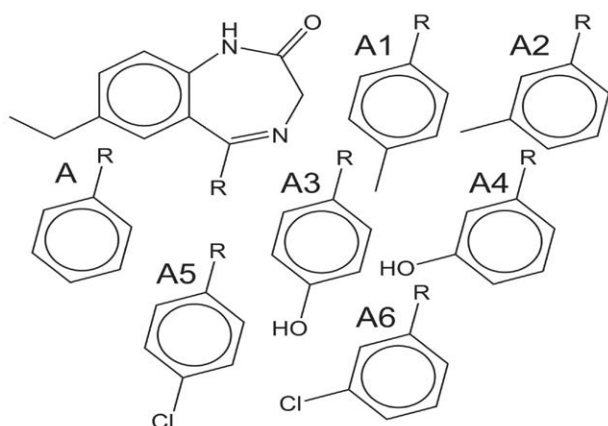


Figure 3. Chemical structures of designed molecules.

Computational studies were performed using molecular docking to evaluate the binding affinities of all designed molecules and the template molecule A to the GABA<sub>A</sub>. This was done to assess the predictive power of the developed QSAR models and to further validate them. Table 1 summarizes the calculated scoring functions for all molecules. Various scoring functions can be used to represent different ligand-amino acid interactions. Therefore, when assessing inhibitory potency, all scoring functions must be considered. The results from the MolDock and Re-Rank scoring functions show that all designed molecules have the potential to be more active than the template molecule A, with molecule A6 having the highest predicted activity. The energy scoring function results show that all designed molecules have higher interaction energies with the amino acids than molecule A, with molecule A6 also hav-

ing the highest energy. Overall, the results from the molecular docking studies, as represented by the scoring function values, correlate well with the QSAR modeling results. The Supplementary Information figures show all the interactions between the amino acids of the GABA<sub>A</sub> active site and the selected molecules. They also depict hydrogen bonds and hydrophilic and hydrophobic interactions within the binding pocket in two dimensions. Figure 3 shows the best-predicted poses of all the designed molecules within the active site of the GABA<sub>A</sub>.

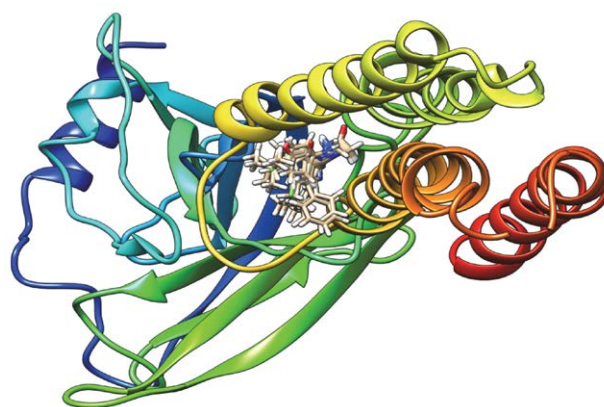


Figure 4. The best calculated poses for all the designed molecules within the active site of GABA<sub>A</sub>.

## 4. Conclusion

The effectiveness of the QSAR methodology, which relies on the Monte Carlo optimization in conjunction with molecular graph and SMILES notation descriptors, has been showcased in this study. It has proven to be a valuable approach for establishing the relationship between GABA<sub>A</sub> receptor binding and the structural characteristics of characterized benzodiazepines. To construct the conformation-independent QSAR models presented here, easily interpretable descriptors with a mechanistic interpretation were employed successfully. Additionally, this methodology has efficiently identified molecular fragments, characterized as SMILES notation fragments in QSAR modeling, that exhibit both positive and negative effects on the studied activity. Subsequently, the developed

Table 1. The list of all the designed molecules with their SMILES notation, calculated activities and score values (kcal/mol) for all computer-aided designed compounds

Molecule	SMILES notation	pIC <sub>50</sub> (calc.)	Energy	MolDock Score	Rerank Score
A0	CCc1ccc2c(c1)C(=NCC(=O)N2)c1ccccc1	7.2771	-96.9452	-93.7531	-69.8862
A1	CCc1ccc2c(c1)C(=NCC(=O)N2)c1ccc(cc1)C	7.4308	-97.3104	-95.8847	-71.252
A2	CCc1ccc2c(c1)C(=NCC(=O)N2)c1cccc(c1)C	7.5591	-97.6046	-97.0659	-72.638
A3	CCc1ccc2c(c1)C(=NCC(=O)N2)c1ccc(cc1)O	7.5996	-97.3448	-95.7188	-71.8375
A4	CCc1ccc2c(c1)C(=NCC(=O)N2)c1cccc(c1)O	7.7038	-98.5056	-99.387	-62.6546
A5	CCc1ccc2c(c1)C(=NCC(=O)N2)c1ccc(cc1)Cl	8.0723	-97.1929	-95.606	-71.5423
A6	CCc1ccc2c(c1)C(=NCC(=O)N2)c1cccc(c1)Cl	8.3195	-100.576	-96.6462	-75.8107

QSAR models were used to design new compounds with higher pIC<sub>50</sub> values. Molecular docking studies were then performed to validate the QSAR models and assess the potential activity of the designed molecules. A good correlation was observed between the calculated pIC<sub>50</sub> values from the QSAR models and the calculated binding energies from the molecular docking studies. Notably, this approach facilitates a swift overview of the dataset without the need for complex calculations of molecular conformations. Consequently, it holds promise for future applications in rapidly and accurately assessing the relationship between GABA<sub>A</sub> receptor binding and the structure of novel benzodiazepines.

We have no conflict of interest to disclose.

## Acknowledgments

This research is made possible through support from the Ministry of Education and Science of the Republic of Serbia (Grant No: 451-03-47/2023-01/200113) and the Faculty of Medicine at the University of Niš, Republic of Serbia (project No. 70).

## 5. References

- M. Lader, *Addiction* **2011**, *106*, 2086–2109. DOI:10.1111/j.1360-0443.2011.03563.x
- E. Engin, *Front. Psychiatry* **2023**, *13*, 1060949. DOI:10.3389/fpsyt.2022.1060949
- J. D. Jones, S. Mogali, S. D. Comer, *Drug Alcohol Depend.* **2012**, *125*, 8–18. DOI:10.1016/j.drugalcdep.2012.07.004
- C. P. O'Brien, *J. Clin. Psychiatry* **2005**, *66*, 28–33. DOI:10.4088/JCP.v66n0104
- C. Stefania, M. Andrea, M. Alessio, P. Mauro, G. Amira, C. J. Martin, M. Giovanni, Di Giannantonio Massimo, S. Fabrizio, *Curr. Neuropharmacol.* **2021**, *19*, 1728–1737. DOI:10.2174/1570159X19666210113151136
- B. Moosmann, P. Bisel, V. Auwärter, *Drug Test. Anal.* **2014**, *6*, 757–763. DOI:10.1002/dta.1628
- X. Yu, H.K. Greenblatt, D. J. Greenblatt, *Expert Rev. Clin. Pharmacol.* **2023**, *16*, 109–117. DOI:10.1080/17512433.2023.2170349
- P. Brunetti, R. Giorgetti, A. Tagliabracchi, M. A. Huestis, F. P. Busardò, *Pharmaceuticals (Basel)* **2021**, *14*, 560. DOI:10.3390/ph14060560
- R. E. Moustafa, F. Tarbah, H. S. Saeed, S. I. Sharif, *Crit. Rev. Toxicol.* **2021**, *51*, 249–263. DOI:10.1080/10408444.2021.1907303
- G. Høiseith, S. S. Tuv, R. Karinen, *Forensic Sci. Int.* **2016**, *268*, 35–38. DOI:10.1016/j.forsciint.2016.09.006
- M. Jann, W. K. Kennedy, G. Lopez, *J. Pharm. Pract.* **2014**, *27*, 5–16. DOI:10.1177/0897190013515001
- J. A. Gudín, S. Mogali, J. D. Jones, S. D. Comer, *Postgrad. Med.* **2013**, *125*, 115–130. DOI:10.3810/pgm.2013.07.2684
- A. Higgitt, P. Fonagy, M. Lader, *Psychol. Med. Monogr.* **1988**, *Suppl. 13*, 1–55. DOI:10.1017/S026418100000412
- H. Pétursson, *Addiction* **1994**, *89*, 1455–1459. DOI:10.1111/j.1360-0443.1994.tb03743.x
- P. Kriikku, L. Wilhelm, J. Rintatalo, J. Hurme, J. Kramer, I. Ojanperä, *Forensic Sci. Int.* **2012**, *220*, 111–117. DOI:10.1016/j.forsciint.2012.02.006
- C.W. O'Connell, C. A. Sadler, V. M. Tolia, B. T. Ly, A. M. Saitman, R. L. Fitzgerald, *Ann. Emerg. Med.* **2014**, *65*, 465–466. DOI:10.1016/j.annemergmed.2014.12.019
- K. Shearer, C. Bryce, M. Parsons, H. Torrance, *Forensic Sci. Int.* **2015**, *254*, 197–204. DOI:10.1016/j.forsciint.2015.07.033
- C. Nantasenamat, C. Isarankura-Na-Ayudhya, V. T. Naenna, A. Prachayasittikul, *EXCLI J.* **2009**, *8*, 74–88.
- A. G. Leach, *Drug Test. Anal.* **2013**, *6*, 739–745. DOI:10.1002/dta.1593
- P. Kawczak, L. Bober, T. Bączek, *Med. Chem. Res.* **2018**, *27*, 2279–2286. DOI:10.1007/s00044-018-2234-5
- A. Bărbulescu, L. Barbe, C-Ş. Dumitriu, *J. Chem.* **2021**, *2021*, 4816970.
- A. P. Toropova, A. A. Toropov, *Mini-Rev. Med. Chem.* **2018**, *18*, 382–391. DOI:10.2174/1389557517666170927154931
- A. M. Veselinović, J. B. Veselinović, J. V. Živković, G. M. Nikolić, *Curr. Top. Med. Chem.* **2015**, *15*, 1768–1779.
- M. Zivkovic, M. Zlatanovic, N. Zlatanovic, M. Golubović, A. M. Veselinović, *Mini-Rev. Med. Chem.* **2020**, *20*, 1389–1402. DOI:10.2174/1389557520666200212111428
- S. Durdagi, A. Kapou, T. Kourouli, T. Andreou, S. P. Nikas, V. R. Nahmias, D. P. Papahatjis, M. G. Papadopoulos, T. Mavroumoustakos, *J. Med. Chem.* **2007**, *50*, 2875–2885. DOI:10.1021/jm0610705
- G. Floresta, O. Apirakkan, A. Rescifina, V. Abbate, *Molecules* **2018**, *23*, 2183. DOI:10.3390/molecules23092183
- P. Kumar, A. Kumar, *Chemometr. Intell. Lab.* **2020**, *200*, 103982. DOI:10.1016/j.chemolab.2020.103982
- Z. Zhang, L. An, W. Hu, Y. Xiang, *J. Comput. Aided Mol. Des.* **2007**, *21*, 145–153. DOI:10.1007/s10822-006-9090-y
- M. Schulze-Alexandru, K.-A. Kovar, A. Vedani, *Mol. Inf.* **1999**, *18*, 548–560. DOI:10.1002/(SICI)1521-3838(199912)18:6<548::AID-QSAR548>3.0.CO;2-B
- S. S. Negus, M. L. Banks, *Curr. Top. Behav. Neurosci.* **2016**, *32*, 119–131.
- A. G. Artemenko, V. E. Kuz'min, E. N. Muratov, P. G. Polishchuk, I. Yu. Borisyuk, N. Ya. Golovenko, *Pharm. Chem. J.* **2009**, *43*, 454–462. DOI:10.1007/s11094-009-0332-x
- P. D. Maskell, G. D. Paoli, L. N. Seetohul, D. J. Pounder, *J. Forensic Legal Med.* **2012**, *19*, 122–125. DOI:10.1016/j.jflm.2011.12.014
- C. Giaginis, A. Tsantili-Kakoulidou, S. Theocharis, *J. Anal. Toxicol.* **2014**, *38*, 242–248. DOI:10.1093/jat/bku025
- S. Funar-Timofei, D. Ionescu, T. Suzuki, *Toxicol. in Vitro* **2010**, *24*, 184–200. DOI:10.1016/j.tiv.2009.09.009
- G. Greco, E. Novellino, C. Silipo, A. Vittoria, *Mol. Inf.* **1993**, *11*, 461–477. DOI:10.1002/qsar.2660110403
- Y. Yang, W. Zhang, J. Cheng, Y. Tang, Y. Peng, Z. Li, *Chem. Biol. Drug. Des.* **2013**, *81*, 583–590. DOI:10.1111/cbdd.12100
- D. Hadjipavlou-Litinat, C. Hansch, *Chem. Rev.* **1994**, *94*,

- 1483–1505. DOI:10.1021/cr00030a002
38. L. Waters, K. R. Manchester, P. D. Maskell, C. Haegeman, S. Haider, *Sci. Justice*. **2018**, *58*, 219–225. DOI:10.1016/j.scijus.2017.12.004
39. P. K. Ojha, K. Roy, *Chemometr. Intell. Lab.* **2011**, *109*, 146–161. DOI:10.1016/j.chemolab.2011.08.007
40. P. K. Ojha, I. Mitra, R. N. Das, K. Roy, *Chemometr. Intell. Lab.* **2011**, *107*, 194–205. DOI:10.1016/j.chemolab.2011.03.011
41. P. P. Roy, J. T. Leonard, K. Roy, *Chemometr. Intell. Lab.* **2008**, *90*, 31–42. DOI:10.1016/j.chemolab.2007.07.004
42. K. Roy, R. N. Das, P. Ambure, R. B. Aher, *Chemometr. Intell. Lab.* **2016**, *152*, 18–33. DOI:10.1016/j.chemolab.2016.01.008
43. L. I. Lin, *Biometrics* **1989**, *45*, 255–268. DOI:10.2307/2532051
44. V. Stoičkov, D. Stojanović, I. Tasić, S. Šarić, D. Radenković, P. Babović, D. Sokolović, A. M. Veselinović, *Struct. Chem.* **2018**, *29*, 441–449. DOI:10.1007/s11224-017-1041-9
45. A. P. Toropova, A. A. Toropov, *Sci. Total Environ.* **2017**, *586*, 466–472. DOI:10.1016/j.scitotenv.2017.01.198
46. A. M. Veselinović, A. Toropov, A. Toropova, D. Stanković-Dordević, J. B. Veselinović, *New J. Chem.* **2018**, *42*, 10976–10982. DOI:10.1039/C8NJ01034J
47. R. Thomsen, M. H. Christensen, *J. Med. Chem.* **2006**, *49*, 3315–3321. DOI:10.1021/jm051197e
48. Manisha, S. Chauhan, P. Kumar, A. Kumar, *SAR QSAR Environ. Res.* **2019**, *30*, 145–159. DOI:10.1080/1062936X.2019.1568299
49. A. Halder, *SAR QSAR Environ. Res.* **2018**, *29*, 911–933. DOI:10.1080/1062936X.2018.1529702
50. D. Gadaleta, G.F. Mangiatordi, M. Catto, A. Carotti, O. Nicolotti, *IJQSPR* **2016**, *1*, 45–63. DOI:10.4018/IJQSPR.2016010102
51. P. Gramatica, *QSAR Comb. Sci.* **2007**, *26*, 694–701. DOI:10.1002/qsar.200610151

## Povzetek

Naraščajoča razširjenost in uporaba benzodiazepinov na črnem trgu predstavlja pomembno javnozdravstveno skrb. V tem delu uporabljamo in silico tehnike, s katereimi ocenjujemo biološko aktivnost takšnih benzodiazepinov. Da bi poglobili razumevanje njihove farmakologije, smo uporabili metodo od konformacij neodvisne Monte Carlo optimizacije kot orodje za razvoj modelov QSAR. Ti modeli so bili zgrajeni z uporabo optimalnih molekularnih deskriptorjev, pridobljenih tako iz notacije SMILES kot tudi iz molekularnih grafov. Izdelani model QSAR je pokazal robustnost in visoko stopnjo napovedljivosti, kar kaže na njegovo zanesljivost. Novi molekularni fragmenti, odkriti pri računalniško podprtem načrtovanju novih spojin, povzročijo povečanje in zmanjšanje aktivnosti. Za končno oceno zasnovanih inhibitorjev smo uporabili orodja molekularnega sidranja, pri čemer smo opazili odlično ujemanje z rezultati modeliranja QSAR. Študija odpira pot hitremu napovedovanju vezavne aktivnosti za nove benzodiazepine ter ponuja hitrejšo in stroškovno učinkovito alternativo tradicionalnim analizam in vitro/in vivo.



Except when otherwise noted, articles in this journal are published under the terms and conditions of the Creative Commons Attribution 4.0 International License

Scientific paper

# The Role of Nitrogen-Rich Moieties in the Selection of Arginine's Tautomeric Form at Different Temperatures

Aned de Leon<sup>1,\*</sup>, José Luis Cabellos<sup>2</sup>, César Castillo-Quevedo<sup>3</sup>,  
Martha Fabiola Martín-del-Campo-Solís<sup>3</sup> and Gerardo Martínez-Guajardo<sup>4</sup>

<sup>1</sup> Departamento de Ciencias Químico-Biológicas, Edificio 5<sup>a</sup>, Universidad de Sonora, Blvd. Luis Encinas y Rosales S/N Centro, Hermosillo, 8300, México

<sup>2</sup> Universidad Politécnica de Tapachula. Carretera a Puerto Madero km 24+300, San Benito, Puerto Madero C.P. 30830 Tapachula, Chiapas.

<sup>3</sup> Departamento de Fundamentos del Conocimiento, Centro Universitario del Norte, Universidad de Guadalajara, Carretera Federal No. 23, Km. 191, C.P., Colotlán 46200, Jalisco, México

<sup>4</sup> Unidad Académica de Ciencias Químicas, Área de Ciencias de la Salud, Universidad Autónoma de Zacatecas, Km. 6 Carretera Zacatecas-Guadalajara S/N, Ejido La Escondida C.P. Zacatecas 98160, Zac, México.

\* Corresponding author: E-mail: aned.deleon@unison.mx

Received: 09-07-2023

## Abstract

It is well known that the guanidinium group in Arginine plays an important role in noncovalent interactions. However, its role is not well documented since the selection of its global minimum structure is still controversial. The main difficulties on obtaining accurate results lie on: neutral Arginine can occur in 3 forms, two of which are canonical and one is zwitterion; each form has degenerate enantiomers D- and L-; its numerous degrees of freedom make it challenging to perform a thorough study; the short-range interactions require higher levels of theory to correctly describe them. Thus, we have performed a meticulous global minimum search. We performed optimizations of the systems at the PBE0 / Def2TZVP level of theory and single point calculations at the DLPNO-CCSD(T)/Def2TZVP level with zero-point corrections at PBE0 / Def2TZVP. We also analyzed Thermal Populations and IR Spectra of the systems to fully understand Arginine's behavior. The results show the energy minima structures strongly rely on its internal nitrogen-rich groups.

**Keywords:** Arginine, canonical forms, zwitterion, theoretical study

## 1. Introduction

L-amino acids are naturally occurring molecules that are essential in several biofunctions<sup>1–4</sup>. D-amino acids are also important in biological systems such as memory and growth<sup>5–10</sup>. D-serine (D-Ser) is an indicator for early-stage tumor growth. Atypical levels of D-serine can induce schizophrenia, Alzheimer's disease, amyotrophic lateral sclerosis<sup>11,12</sup>; low levels of D-aspartic acid (D-Asp) can lead to sexual dysfunction<sup>13</sup>; D-arginine (D-Arg) has a high toxicity for bacteria<sup>14–16</sup>. Unfortunately, the understanding of D-amino acids is still incomplete due to technical limitations for their detection<sup>17</sup>

Amino acids exist as zwitterions in aqueous solution at a specific pH window<sup>18–22</sup>. The structure of amino acids is specially sensitive to protic solvents<sup>23–26</sup> since they release H<sup>+</sup> in the solution, forming hydrogen-bonded networks with them. In the absence of solvent, it has been reported experimentally that not all amino acids exist as zwitterions<sup>27–30</sup>. In the case of Arg in aqueous solution, the formation of zwitterions is led by a protonation of the guanidine side chain<sup>31</sup>. Similarly, in the gas phase, the guanidine side chain acts as a competitive site of protonation compared to the carboxylate group<sup>32</sup>. Whether or not the most stable structure in the gas phase is a zwitterion is still under debate<sup>28, 31–36</sup>. Its extremely basic guanidine side

chain makes arginine perhaps one of the common naturally occurring amino acid most likely to form a stable zwitterion<sup>25</sup>. Arg can form stable charged aggregates intermolecularly bound by salt bridges<sup>29,37–39</sup>. In addition, several studies have shown that zwitterionic states can be induced through different mechanisms such as: adding diffuse proximal charges<sup>40–45</sup>, electrons<sup>46</sup>, noncovalent clustering<sup>29,39</sup> or a few solvent molecules<sup>47–49</sup>.

The determination of the dominant tautomeric form of neutral Arg in the gas phase has been studied experimentally<sup>32,35,29,39–42</sup>. According to the work of Price and coworkers, protonated dimers of arginine are bound in a salt bridge<sup>32</sup>. Their study at BLYP/6-31G\* and MP2/6-31G\* levels of theory implied that the global minimum of arginine is a zwitterion lower by 1 kcal/mol than the lowest canonical tautomer. Anyhow, Maksic and Kovacevic performed MP2 and density functional theory (DFT) calculations<sup>50</sup>, where they reported that the most stable structure was canonical with a energy difference between the lowest zwitterion and canonical structures within 1-3 kcal/mol depending on the level of theory. Skurski and coworkers have extended this work at CCSD/6-31++G(d,p)+5(sp)//MP2/6-31++G(d,p)+5(sp) levels of theory<sup>36</sup> and found the canonical form to be 2.8 kcal/mol lower in energy than the lowest zwitterion. This group performed a more extensive global minimum search at CCSD/6-31++G\*\* level of theory, obtaining the minimum canonical structure was 3.2 kcal/mol lower than the lowest zwitterion. Ling and coworkers have similar results at CCSD/6-31++G(d,p) level of theory, where the most stable canonical conformer is 3.4 kcal/mol lower than the lowest zwitterion<sup>51</sup>.

A conformational search for arginine is the most challenging of the 20 amino acids due to its great number of degrees of freedom<sup>28,33</sup>. Arginine has two kinds of proton donor groups (OH and NH), six proton acceptor sites (N's and O's) and six/seven (depending on the tautomer) bonds that can be rotated. Thus, a meticulous conformational search is required. If not done carefully, it could lead to mistaking local with global minima. Several conformational searches on arginine have been performed in the gas phase<sup>31, 35, 36, 50–53</sup>. Theoretical studies in the presence of water have also been conducted<sup>14,54–58</sup>. Gu et al. performed a theoretical study on the thermal dissociation of singly protonated Arginine<sup>59</sup>. They reported that backbone dissociations and side-chain fragmentations compete during dissociation. The guanidine loss occurred as a consequence of the side-chain dissociation; while CO and H<sub>2</sub>O loss were part of the backbone breakage. The effect of temperature on neutral Arg has been taken into account in the past. However, only a few representative temperatures have been reported<sup>51</sup>.

In this paper, we performed a thorough energy minima search for both D- and L- enantiomers, which has only been done to the best of our knowledge for L-arginine in the gas phase<sup>36,51</sup>. Before the study of the solvation of arginine, it is of primordial importance to understand its

electronic interactions in the gas phase and use them as a reference point for further investigations. The results could help predict its behavior upon solvation in different media. This search was performed at DLPNO-CCSD(T)/Def2-TZVP level of energy. This wider basis set is a correction to those used in previous papers<sup>36,51</sup> to take into account the dispersion forces involved in these systems more accurately.

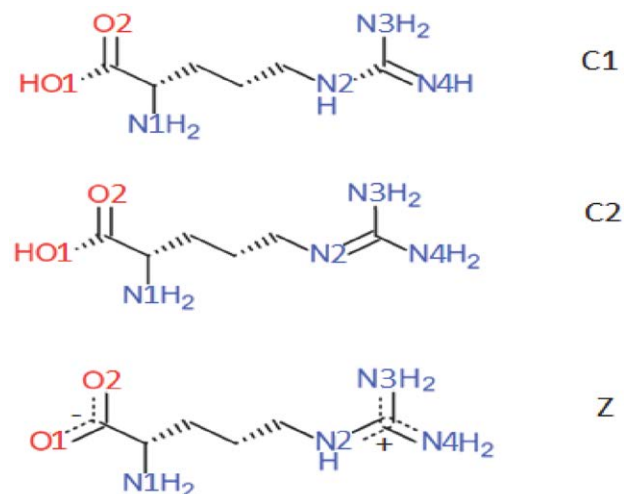


Fig. 1. Structures of canonical 1 (C1), 2 (C2) and zwitterionic arginine considered in this work.

Several works have shown that energy minima structures are temperature-dependent,<sup>60–66</sup>. Thus, we performed a temperature-dependent relative populations analysis in the range of 0–1800 K since enantioselectivity is a function of temperature<sup>60,67</sup>. It is our intention to elucidate if nitrogen-rich moieties such as the guanidinium and amino groups participate in minimizing the energy of Arginine structures, based on reports<sup>22,32</sup> that have affirmed that the guanidine side chain is a competitive site of protonation.

Photodissociation spectra for cationized Arg with Li<sup>+</sup>, K<sup>+</sup>, Na<sup>+</sup> have been experimentally observed in<sup>68</sup>. In this work, we calculate the gas phase temperature dependent Boltzmann weighted IR spectra. These two spectra are not comparable. To the best of our knowledge, Arginine's IR spectra is not reported.

## 2. Theoretical Methods

### 2.1 Computational Details

We employed the ensemble DFT methodology in order to emulate experimental conditions<sup>69</sup>. It has been proven to be valid for finite temperatures<sup>70</sup>. The global minimum search for Arg is complicated due to the amount of degrees of freedom, as mentioned in the Introduction section. To explore the potential free energy surface, we

employed the kick methodology<sup>71</sup>. The global minima search is computationally expensive for medium to large systems. Especially, for Arg with several dihedral angles, the possible configurations rise significantly. We studied it at a higher level of theory than past studies<sup>31,35,36,50–53</sup>, at the domain based local pair natural orbital coupled cluster single, double and perturbative triples DLPNO-CCSD(T)<sup>72,73</sup> level of theory. We employed a two-step approach. The first step was to perform a thorough exploration of the potential energy surface at the PBE0 / Def2TZVP<sup>74,75</sup> level in conjunction with the Grimme dispersion correction GD3<sup>76</sup> coupled to the conformational search code (CSC). It generated 800 conformers with the random variation of dihedral angles of Arg, similarly to other conformational search algorithms<sup>77</sup> applied in Python as a part of global search of the GALGOSON code<sup>60,61</sup>. The second step was to obtain single point calculations of the lowest energy systems at the DLPNO-CCSD(T)/Def2TZVP level with zero-point corrections at the PBE0 / Def2TZVP. The optimizations and single point calculations were all performed using the ORCA software<sup>78</sup>.

## 2. 1. Thermochemical Properties

We used the following equations to calculate thermochemical properties. The partition function  $Q$  assuming ideal gas, a particle in a box, rigid rotor harmonic oscillator (RRHO), and Born Oppenheimer approximation (BOA)<sup>79</sup> is stated on equation (1)

$$Q(T) = \sum_I g_i e^{\Delta E_i/k_B T}, \quad (1)$$

Where  $g_i$  is the degeneracy factor,  $k_B$  is the Boltzmann factor,  $T$  is temperature and  $\Delta E_i$  is the total energy. It should be noted that in order for an accurate comparison between theoretical and experimental results, anharmonicity must be contemplated.

Employing BOA and RRHO approximations,  $Q$  can be expressed by equation (2)

$$Q = q_{trans} q_{rot} q_{vib} q_{elec}. \quad (2)$$

The equations for each component to the canonical ensemble are reported in<sup>80</sup>. The equations for free energy, entropy, enthalpy and internal energy ( $U$ ) depend on the partition function since they can be expressed either in terms of it or its derivatives<sup>80–82</sup>.

## 2. 2. IR Spectra

The IR spectra and vibrational spectra of each isomer were computed employing DFT as implemented in ORCA code<sup>78</sup> under the harmonic approximation. Anharmonic effects are not considered. We scaled harmonic frequencies by a factor of 0.97 and convoluted with a Gaussian line shape of 20 cm<sup>-1</sup> full width at half maximum (FWHM).

At thermal equilibrium all arginine-rotamers are populated according to the Boltzmann distribution. Consequently, the observed properties in a molecule are statistical Boltzmann-averages over the ensemble of geometrical conformations. We employed the thermal population to compute the IR spectra of arginine at temperature  $T$ , we weighted the IR spectrum of each isomer according to the thermal populations and summed them up.

## 3. Results and Discussion

### 3. 1. Energy Minima Structures

Qualitatively, the energy values of all reported geometries at PBE0/def2-TZVP and DLPNO-CCSD(T)/def2-TZVP levels showed the same trend. It is interesting to note that C2 D- geometries were not obtained on previous theoretical studies and therefore we only compare L- geometries. Our results listed in Table 1, confirm L- and D- Arg structures' degeneracy.

Fig. 2 shows the lowest energy structures of arginine for D- and L- enantiomers of C1, C2 and Z at 0K. The global energy minima structures are D- and L- C2. References<sup>36,51</sup> have a very similar L- C2 structure (named C3 and C4 in their papers, respectively) with mild differences. The main hydrogen (H-) bonds are a) between N2 and HO1 and b) two H-bonds form between O2 and the amino group N1H<sub>2</sub>.

Structures 3 and 4 are only at 0.07 kcal/mol higher than geometries 1 and 2. Most noncovalent interactions in arginine are due to the guanidinium group, as Schug and Linder wrote on their Review<sup>8386</sup>. This has incredible variations on entropy and thus on thermal percent shares, which will be discussed further on.

**Table 1.** Relative energies in kcal mol<sup>-1</sup>. DLPNO-CCSD(T) and PBE0 with zero-point energy correction at 0K for structures 1–12.

Arg	CCSD(T)	PBE0
1	0.00	0.00
2	0.00	0.00
3	0.07	0.02
4	0.07	0.02
5	1.47	1.07
6	1.47	1.07
7	1.53	1.14
8	1.53	1.14
9	1.51	1.37
10	1.51	1.37
11	5.04	2.13
12	5.04	2.13

Structures 5 and 6, at a relative energy of 1.47 kcal/mol, differ from the last structures mainly on the loss of a H-bond between O2 and N1H<sub>2</sub>. Structures 7 and 8 have a



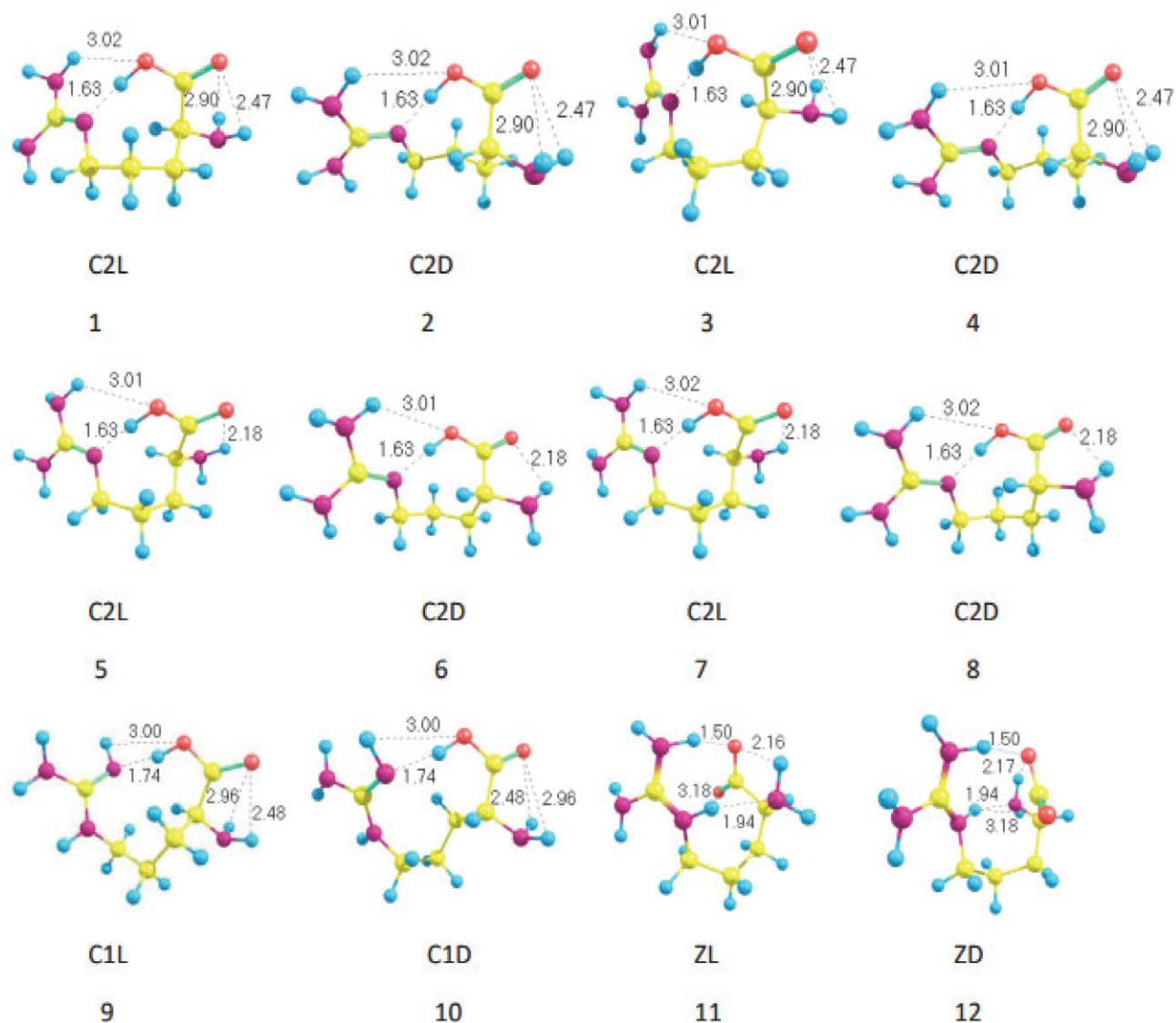


Fig. 2. Selected geometrical parameters in Å for geometries 1–12, where C1, C2 and Z stand for canonical 1, 2 or zwitterion, respectively according to Fig. 1. L or D stand for Levorotatory or Dextrorotatory enantiomers, respectively.

relative energy of 1.53 kcal/mol. They share most H-bond values. Anyhow, positions of the hydrogens on both, the guanidinium and amino groups differ. Structures 5–7 are most similar to structure C5 on ref.<sup>51</sup> There are no similar structures for ref.<sup>36</sup>

At a relative energy of 1.51 kcal/mol the D- and L-enantiomers of C1 Arg were found. These structures also form H-bonds similar to those of Ref<sup>36</sup>. As for Ref.<sup>51</sup>, the most stable C1 geometry is totally different, with a relative energy of 0.65 kcal/mol.

At 5.038 kcal/mol, we found the first zwitterionic arginine enantiomers. The DFT relative energy for the zwitterionic enantiomers was of 2.13 kcal/mol. This notable difference can be accounted for the importance of the methodology used on systems with short-range interactions. The results of<sup>36,51</sup> show that the first zwitterion was 3.2 and 3.4 kcal/mol away from the most stable canonical

structure, respectively. The wider basis set we used (def2-TZVP) models dispersion forces better, which increase on zwitterionic structures. The most stable zwitterion at 0K we found shows half structure facing toward the other half, which increases the van der Waals interactions and even adds a H-bond between N1 and N4H of 1.94 Å (1.96 Å for Ref<sup>51</sup>) in addition to a H-bond between O2 and N3H the carboxylate group and the guanidinium group of 1.50 Å (1.59 Å for Ref<sup>51</sup>). The first zwitterion found on Ref<sup>36</sup> does form this last H-bond at 1.64 Å, yet the amino group lies far apart from the guanidinium group and does not form a H-bond.

### 3. 1. Thermal Populations

At 0K, thermal populations of C2-Arg structures 1 and 2 are immensely different from those of 3 and 4. It is

interesting to note that the main difference between these pairs of structures relies on the position of hydrogen atoms on amino and guanidinium groups.

At low temperatures, the degrees of freedom of the system are minimum. However, at higher temperatures, kinetic energy allows movement. Thus, this implies higher degrees of freedom, positively influencing entropy. At around 335 K, which is a healthy body temperature, structures 1–4 are equiprobable.

Fig. 3 depicts the importance of nitrogen-rich groups in arginine on thermal populations. These groups are responsible for not only the gap at 0K between structures 1–4, but also with the rest of the geometries, which is confirmed by Shug and Linder's review<sup>8386</sup>, where they state that the guanidinium group is accountable for most non-covalent interactions of arginine, as mentioned in the above Results and Discussion section. Structures 5–8 are also C2-Arg, with an important difference, the loss of a hydrogen bond between O2 and HN1. Structures 9 and 10 correspond to C1-Arg, where the main difference with C2-Arg lies on a double bond in the guanidinium group.

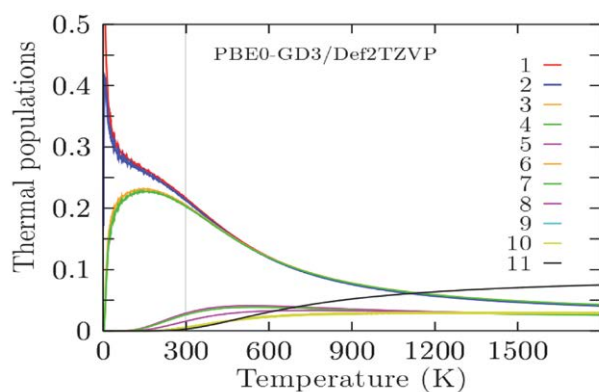


Fig. 3. Relative population for temperature 0–1800 K at the CCSD(T)/Def2-TZVP.

Geometries 11 and 12 pertain to Z D- and L- enantiomers. By around 750 K, their curve has crossed those of structures 5–10 and by around 1100 K, their thermal population is the highest. At higher temperatures, increased kinetic energy could contribute to the migration of a hydrogen from the carboxyl group to the guanidinium one.

### 3. 2. IR Spectra

A direct comparison between experimental IR data and IR spectra is not possible since in most DFT calculations the temperature is not considered. Differences between experimental and calculated IR spectra can be due mainly to finite temperature, anharmonic effects and the fact that IR experiments are essential of multi-photon nature, whereas IR spectra calculations assume single-photon processes and DFT calculations are at 0 K.

According to our DFT calculations, only few low energy structures on the free energy surface strongly dominate the thermal population in temperature range 0 to 900 K and are responsible for the observed IR in Arg. This is displayed in Fig. 3.

Fig. 4 displays the Boltzmann spectrum for Arg. In it there are two main peaks. The first one is located at 1700  $\text{cm}^{-1}$  that pertains to the carbonyl-bending of the carboxylate group. The second peak at 491  $\text{cm}^{-1}$  represents the bending of the hydrogens attached to N3 and N4.

In Fig. 4a we show the IR spectrum of the lowest energy structure of arginine. D-enantiomers at room temperature have a contribution of 21%. We underline the lowest energy conformers of arginine are enantiomers. Fig. 4b portrays the IR spectrum of the lowest energy enantiomers-L. Their contribution to total IR spectrum is similar, with a value of 20.7%. In Fig. 4c,d we show the spectrum of the lowest Arg-enantiomers configurations with just an H with a different orientation in the amine group. Energetically, the isomers located at the same thermal point, but at cold temperature, below 335 K, have a different probability. In summary, the IR spectrum and all molecular properties are strongly dominated by those four structures through the entire temperature range of 20 to 900 K.

## 4. Conclusion

According to our studies, more than 89% of Arg occurrence is attributed to C2. D- and L- enantiomers showed to be equally likely in all the range of temperatures. At 0K, structures 1 and 2 are global energy minima. The difference with structures 3 and 4 lies only in the orientation of hydrogen atoms bonded to N-rich groups such as the amino and guanidinium groups. As temperature rises, at around 335 K, structures 1–4 are equiprobable. This could be explained by the fact that as temperature increases, so does kinetic energy, enabling the movement from one configuration to another. Structures 5–8 have only form 1 hydrogen bond O2-HN1, whereas for structures 1–4, they form 2 hydrogen bonds between these moieties. The first zwitterion appeared at 5.04 kcal/mol higher in energy than the global energy minimum C2 structure. The relative energy at which the first zwitterion appears has been a very controversial subject. We reported energies at the DLPNO-CCSD(T)/Def2TZVP and the PBE0/Def2TZVP level. The greatest difference in them was with the zwitterion, where the predicted energy was of 2.13 kcal/mol. This is more than twice the energy difference. Zwitterions should be studied at a high theory level, since short range interaction such as dispersion forces play a strong role in their interactions. This could be the reason why previous works<sup>36,50,51</sup> differ so much on how far from the most stable canonical structure are they.

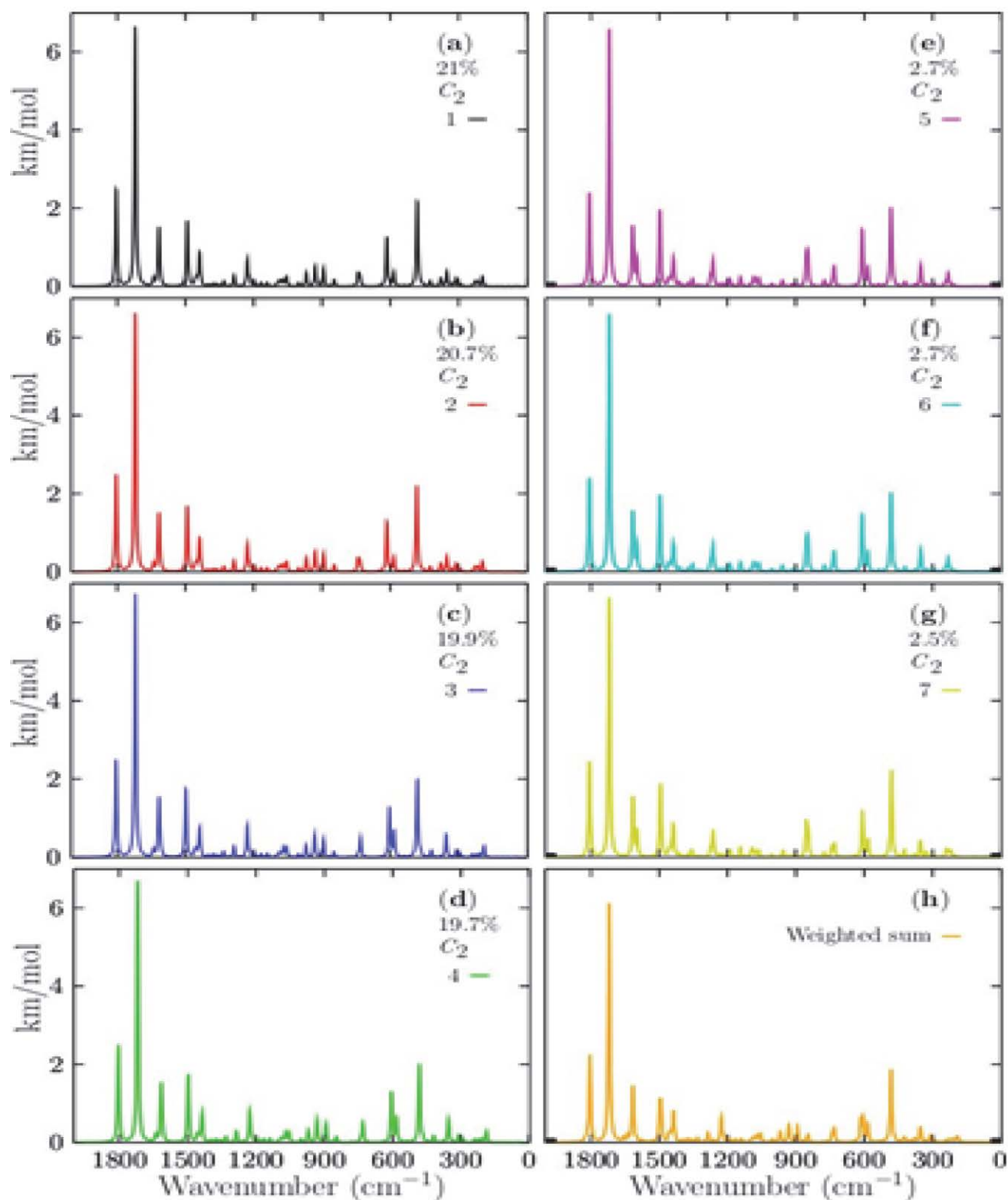


Fig. 4. IR Spectra of most probable structures (1–7). They comprise 89.2% of occurrence.

## Acknowledgements

We thank CONACyT for its support. Also, we are grateful to the High-Performance Computing Area of the University of Sonora (ACARUS).

## 5. References

1. I. Maze, K.-M. Noh, A. A. Soshnev, C. D. Allis, *Nat. Rev. Genet.* **2014**, *15*, 259–271. DOI:10.1038/nrg3673
2. H. Lemos, L. Huang, G. C. Prendergast, A. L. Mellor, *Nat.*

- Rev. Cancer* **2019**, *19*, 162–175.  
DOI:10.1038/s41568-019-0106-z
3. P. J. Murray, *Nat. Immunol.* **2016**, *17*, 132–139.  
DOI:10.1038/ni.3323
4. J. Chen, Y. Ou, Y. Yang, W. Li, Y. Xu, Y. Xie, Y. Liu, *Nature* **2018**, *557*, 585–589. DOI:10.1038/s41586-018-0128-9
5. S. A. Sievers, J. Karanicolas, H. W. Chang, A. Zhao, L. Jiang, O. Zirafi, J. T. Stevens, J. Münch, D. Baker, D. Eisenberg, *Nature* **2011**, *475*, 96–100. DOI:10.1038/nature10154
6. J. Sasabe, Y. Miyoshi, S. Rakoff-Nahoum, T. Zhang, M. Mita, B. M. Davis, K. Hamase, M. K. Waldor, *Nat. Microbiol.* **2016**, *1*, 16125. DOI:10.1038/nmicrobiol.2016.125
7. M. Garton, S. Nim, T. A. Stone, K. E. Wang, C. M. Deber, P. M. Kim, *Proc. Natl. Acad. Sci. U.S.A.* **2018**, *115*, 1505–1510.  
DOI:10.1073/pnas.1711837115
8. X. Dai, E. Zhou, W. Yang, X. Zhang, W. Zhang, Y. Rao, *Nat. Commun.* **2019**, *10*, 1986.  
DOI:10.1038/s41467-019-09544-9
9. S. Beltrán-Castillo, M. J. Olivares, R. A. Contreras, G. Zúñiga, I. Llona, R. Von Bernhardt, J. L. Eugenin, *Nat. Commun.* **2017**, *8*, 838. DOI:10.1038/s41467-017-00960-3
10. C. Henneberger, T. Papouin, S. H. R. Oliet, D. A. Rusakov, *Nature* **2010**, *463*, 232–236. DOI:10.1038/nature08673
11. D. T. Balu, Y. Li, M. D. Puhl, M. A. Benneyworth, A. C. Basu, S. Takagi, V. Y. Bolshakov, J. T. Coyle, *Proc. Natl. Acad. Sci. U.S.A.* **2013**, *110*, 2400–2405.  
DOI:10.1073/pnas.1304308110
12. S. Neame, H. Safory, I. Radziszewsky, A. Touitou, F. Marchesani, M. Marchetti, S. Kellner, S. Berlin, V. N. Foltyn, S. Engelender, *Proc. Natl. Acad. Sci. U.S.A.* **2019**, *116*, 20736–20742. DOI:10.1073/pnas.1909458116
13. A. D'Aniello, *Brain Res. Rev.* **2007**, *53*, 215.  
DOI:10.1016/j.brainresrev.2006.08.005
14. C. L. Chen, S. C. Hsu, T. Y. Chung, C. Y. Chu, H. J. Wang, P. W. Hsiao, S. D. Yeh, D. K. Ann, Y. Yen, H. J. Kung, *Nat. Commun.* **2021**, *12*, 2398. DOI:10.1038/s41467-021-22652-9
15. M. D. Shmueli, L. Levy-Kanfo, E. Haj, A. R. Schoenfeld, E. Gazit, D. Segal, *Oncogene* **2019**, *38*, 1038–1049.  
DOI:10.1038/s41388-018-0491-x
16. L. Alvarez, A. Aliashkevich, M. A. de Pedro, F. Cava, *ISME J.* **2018**, *12*, 438–450. DOI:10.1038/ismej.2017.176
17. X. Yu, B. Zhang, C. Fan, Q. Yan, S. Wang, H. Hu, Q. Dong, G. Du, Y. Gao, C. Zeng, *iScience* **2022**, *25*, 104964.  
DOI:10.1016/j.isci.2022.104964
18. S. Bhunia, S. K. Srivastava, A. Materny, A. K. Ojha, *J. Raman Spectrosc.* **2016**, *47*, 1073–1085. DOI:10.1002/jrs.4918
19. C. Garrido, T. Aguayo, E. Clavijo, S. Gómez-Jeria, M. M. Campos-Vallette, *J. Raman Spectros.* **2013**, *44*, 1105–1110.  
DOI:10.1002/jrs.4331
20. C. A. Fitch, G. Platzer, M. Okon, B. Garcia-Moreno E. Lawrence, L. P. McIntosh, *Prot. Sci.* **2015**, *24*, 752–763.  
DOI:10.1002/pro.2647
21. T. Miyatake, S. Yoshizawa, T. Arakawa, K. Shiraki, *Int. J. Biolog. Macromolec.* **2016**, *87*, 563–570.  
DOI:10.1016/j.ijbiomac.2016.03.015
22. B. Xu, M. I. Jacobs, O. Kostko, M. Ahmed, *Chem. Phys. Chem. Comm.* **2017**, *18*, 1503–1506. DOI:10.1002/cphc.201700197
23. B. Hernández, F. Pflüger, N. Derbel, J. De Coninck, M. Ghomi, *J. Phys. Chem. B* **2010**, *114*, 1077.  
DOI:10.1021/jp909517r
24. A. Barrozo, B. Xu, A. O. Gunina, M. I. Jacobs, K. Wilson, O. Kostko, M. Ahmed, A. I. Krylov, *J. Phys. Chem. Lett.* **2019**, *10*, 1860–1866. DOI:10.1021/acs.jpcclett.9b00494
25. S. Hu, J. Han, H. Liu, J. Qiu, Y. Zhao, Y. Guo, H. Huang, H. He, P. J. Wang, *Chem. & Engin. Data* **2021**, *66*, 2383–2391.  
DOI:10.1021/acs.jced.0c01074
26. J. Vondrášek, P. E. Mason, J. Heyda, K. D. Collins, P. Jungwirth, *J. Phys. Chem. B. Lett.* **2009**, *113*, 9041–9044.  
DOI:10.1021/jp902377q
27. C. J. Chapo, R. A. Provencal, K. Roth, R. J. Saykally, *J. Am. Chem. Soc.* **1997**, *119*, 11988–11994.
28. J. Rak, P. Skurski, J. Simons, M. Gutowski, *J. Am. Chem. Soc.* **2001**, *123*, 11695–11664. DOI:10.1021/ja011357l
29. R. R. Julian, J. L. Beauchamp, W. A. Goddard, *J. Phys. Chem. A*, **2002**, *106*, 32–41. DOI:10.1021/jp013205i
30. R. C. Dunbar, N. C. Polfer, J. Oomens, *J. Am. Chem. Soc.*, **2007**, *129*, 14562–14563. DOI:10.1021/ja076131i
31. S. Schlund, R. Müller, C. Graßmann, B. Engels, *J. Comp. Chem.* **2007**, *29*, 407–419. DOI:10.1002/jcc.20798
32. W. D. Price, R. A. Jockusch, E. R. Williams, *J. Am. Chem. Soc.* **1997**, *119*, 11988–11989. DOI:10.1021/ja9711627
33. M. J. Locke, R. L. Hunter, R. T. McIver, *J. Am. Chem. Soc.* **1979**, *101*, 272–273. DOI:10.1021/ja00495a073
34. J. Bertran, L. Rodriguez-Santiago, M. Sodupe, *J. Phys. Chem. B* **1999**, *103*, 2310–2318. DOI:10.1021/jp984534m
35. C. J. Chapo, J. B. Paul, R. A. Provencal, K. Roth, R. J. Saykally, *J. Am. Chem. Soc.* **1998**, *120*, 12956–12967.  
DOI:10.1021/ja982991a
36. P. Skurski, M. Gutowski, R. Barrios, R. Simons, *Chem. Phys. Lett.* **2001**, *337*, 143–150.  
DOI:10.1016/S0009-2614(01)00166-X
37. J. S. Prell, J. T. O'Brien, J. D. Steill, J. Oomens, E. R. Williams, *J. Am. Chem. Soc.* **2009**, *131*, 11442–11449.  
DOI:10.1021/ja901870d
38. K. D. Walker, T. P. Causgrove, *J. Mol. Model.* **2009**, *15*, 1213.  
DOI:10.1007/s00894-009-0482-5
39. R. R. Julian, R. Hodyss, J. L. Beauchamp, *J. Am. Chem. Soc.* **2001**, *123*, 3577–3583. DOI:10.1021/ja003105a
40. T. Wyttenbach, M. Witt, M. T. Bowers, *J. Am. Chem. Soc.* **2000**, *122*, 3458–3464. DOI:10.1021/ja992546v
41. R. A. Jockusch, P. D. William, E. R. Williams, *J. Phys. Chem. A* **1999**, *103*, 9266–9270. DOI:10.1021/jp9931307
42. B. A. Cerda, C. Wesdemiotis, *Analyst* **2000**, *125*, 657–660.  
DOI:10.1039/a909220j
43. E. F. Strittmatter, E. R. Williams, *J. Phys. Chem. A* **2000**, *104*, 6069–6075. DOI:10.1021/jp000038y
44. T. Wyttenbach, M. Witt, M. T. Bowers, *Int. J. Mass Spectrom.* **1999**, *182–183*, 243–252.  
DOI:10.1016/S1387-3806(98)14255-0
45. A. S. Lemoff, M. F. Bush, E. R. Williams, *J. Am. Chem. Soc.* **2003**, *125*, 13576–13583. DOI:10.1021/ja034544n
46. M. Gutowski, P. Skurski, J. Simons, *J. Am. Chem. Soc.* **2000**,

- 122, 10159–10166. DOI:10.1021/ja001658f
47. S. Xu, J. M. Nilles, K. H. Bowen, *J. Chem. Phys.* **2003**, *119*, 10696–10703. DOI:10.1063/1.1620501
48. J. H. Jensen, M. S. Gordon, *J. Am. Chem. Soc.* **1995**, *117*, 8159–8170. DOI:10.1021/ja00136a013
49. E. Kassab, J. Langlet, E. Evleth, Y. Akacem, *J. Mol. Spectrosc.* **2000**, *531*, 267–282. DOI:10.1016/S0166-1280(00)00451-6
50. Z. B. Maksić, B. Kovačević, *J. Chem. Soc. Perkin Trans.* **1999**, *2*, 2623–2629. DOI:10.1039/a902404b
51. S. Ling, W. Yu, Z. Huang, Z. Lin, M. Harańczyk, M. Gutowski, *J. Phys. Chem. A* **2006**, *110*, 12282–12291. DOI:10.1021/jp0645115
52. S. Schlund, C. Schmuck, B. Engels, *Chem. Europ. J.* **2007**, *13*, 6644–6653. DOI:10.1002/chem.200601741
53. A. E. Aliaga, C. Garrido, P. Leyton, G. Diaz, J. S. Gomez-Jeria, T. Aguayo, E. Clavijo, M.M. Campos-Vallette, S. Sanchez-Cortez, *Spectrochim. Acta Part A: Molec. Biomolec. Spectros.* **2010**, *76*, 458–463. DOI:10.1016/j.saa.2010.01.007
54. M. Remko, D. Fitz, B. M. Rode, *J. Phys. Chem. A* **2008**, *112*, 7652–7657. DOI:10.1021/jp801418h
55. J. Gupta, D. Chand, A. K. Nain, *J. Molec. Liq.* **2020**, *305*, 112848. DOI:10.1016/j.molliq.2020.112848
56. R. Prabhakar, R. Margareta, A. Blomberg, M. A. Siegbahn, *Theor. Chem. Acc.* **2000**, *104*, 461–470. DOI:10.1007/s002140000170
57. B. Gao, T. Wyttenbach, M.T. Bowers, *J. Phys. Chem. B* **2009**, *113*, 9995–10003. DOI:10.1021/jp903307h
58. S. Im, S. W. Jang, S. Lee, Y. Lee, B. Kim, *J. Phys. Chem. A* **2008**, *112*, 9767–9775. DOI:10.1021/jp801933y
59. M. Gu, R. Guo, J. Zhang, Y. Yao, L. Yang, *Chem. Phys.* **2020**, *538*, 110890. DOI:10.1016/j.chemphys.2020.110890
60. C. E. Buelna-García, E. Robles-Chaparro, T. Parra-Arellano, J. M. Quiroz-Castillo, T. del-Castillo-Castro, G. Martínez-Guajardo, C. Castillo-Quevedo, A. de-Leon-Flores, G. Anzueto-Sánchez, M. F. Martín-del-Campo-Solis, A. M. Mendoza-Wilson, A. Vásquez-Espinal, J. L. Cabellos, *Molecules* **2021**, *26*, 3953. DOI:10.3390/molecules26133953
61. C. E. Buelna-García, J. L. Cabellos, J. M. Quiroz-Castillo, G. Martínez-Guajardo, C. Castillo-Quevedo, A. de Leon-Flores, G. Anzueto-Sánchez, M. F. Martín-del-Campo-Solis, *Materials*, **2021**, *14*, 112–138. DOI:10.3390/ma14010112
62. V. G. Grigoryan, M. Springborg, *Phys. Chem. Chem. Phys.* **2019**, *21*, 5646–5654. DOI:10.1039/C9CP00123A
63. Z. Hua-Li, A. W. Jasper, D. G. Truhlar, *J. Am. Chem. Soc.* **2007**, *129*, 14899–14910. DOI:10.1021/ja073129i
64. C. Sutton, S. V. Levchenko, *Front. Chem.*, **2020**, *8*, 757. DOI:10.3389/fchem.2020.00757
65. E. Dzib, J. L. Cabellos, F. Ortiz-Chi, S. Pan, A. Galano, G. Merino, *Int. J. Quant. Chem.* **2019**, *119*, e25686. DOI:10.1002/qua.25686
66. G. Brehm, M. Reiher, B. Le Guennic, M. Leibold, S. Schindler, F. W. Heinemann, S. Schneider, *J. Raman Spect.*, **2006**, *37*, 108–122. DOI:10.1002/jrs.1437
67. P. Oswald, K. Desmet, P. Sandra, J. Krupcik; P. Májek, D. W. Armstrong, *J. Chromatogr. B.* **2002**, *779*, 283–295. DOI:10.1016/S1570-0232(02)00396-3
68. M. F. Bush, J. T. O'Brien, J. S. Prell, R. J. Saykally, E. R. Williams, *J. Am. Chem. Soc.* **2007**, *129*, 1612–1622. DOI:10.1021/ja066335j
69. C. E. Buelna-García, C. Castillo-Quevedo, J. M. Quiroz-Castillo, E. Paredes-Sotelo, M. Cortez-Valadez, M. F. Martín-del-Campo-Solis, T. López-Luke, M. Utrilla-Vázquez, A. M. Mendoza-Wilson, P. L. Rodríguez-Kessler, A. Vásquez-Espinal, S. Pan, A. de Leon-Flores, J. R. Mis-May, A. R. Rodríguez-Domínguez, G. Martínez-Guajardo, J. L. Cabellos, *Frontiers in Chem.* **2022**, *10*, 841964. DOI:10.3389/fchem.2022.841964
70. P. Kratzer, J. Neugebauer, *Frontiers in Chem.*, **2019**, *7*, 106. DOI:10.3389/fchem.2019.00106
71. M. Saunders, *J. Am. Chem. Soc.* **1987**, *109*, 3150–3152. DOI:10.1021/ja00244a051
72. J. Čížek, On the use of the cluster expansion and the technique of diagrams in calculations of correlation effects in atoms and molecules. *J. Adv. Chem. Phys.*, Ed. P. C. Hariharan, Vol. 14 (Wiley Interscience, New York **1969**) 35. DOI:10.1002/9780470143599.ch2
73. C. Riplinger, B. Sandhoefer, A. Hansen, F. Neese, *J. Chem. Phys.* **2013**, *139*, 134101. DOI:10.1063/1.4821834
74. C. Adamo, V. Barone, *J. Chem. Phys.* **1999**, *110*, 6158–6170. DOI:10.1063/1.478522
75. F. Weigend, *Phys. Chem. Chem. Phys.*, **2006**, *8*, 1057–1065. DOI:10.1039/b515623h
76. S. Grimme, J. Antony, S. Ehrlich, H.A. Krieg, *J. Chem. Phys.* **2010**, *132*, 154104. DOI:10.1063/1.3382344
77. S. Schlund, R. Müller, C. Graßmann, B. Engels, *J. Comput. Chem.*, **2008**, *29*, 407–415. DOI:10.1002/jcc.20798
78. Neese, F. The ORCA program system, *Wiley Interdiscip. Rev.: Comput. Mol. Sci.*, **2012**, *2*, 73–78. DOI:10.1002/wcms.81
79. M. Planck, *Annalen der Physik* **1901**, *4*, 553–560. DOI:10.1002/andp.19013090310
80. R. K. Pathria, & P.D. Beale, P.D. (2011). *Statistical Mechanics* (3rd ed.). Elsevier. Chapter 4.
81. Reichl, L.E. (2016). *A Modern Course in Statistical Physics*. Wiley-VCH. DOI:10.1002/9783527690497
82. Lakowicz, J.R. (2006). *Principles of Fluorescence Spectroscopy* (3rd ed.). Springer. DOI:10.1007/978-0-387-46312-4
83. K. A. Schug, W. Lindner, *Chem. Rev.* **2005**, *105*, 67–114. DOI:10.1021/cr040603j

## Povzetek

Dobro je znano, da ima gvanidinska skupina v argininu pomembno vlogo pri nekovalentnih interakcijah. Kljub temu njena vloga ni dobro dokumentirana, saj je določitev strukture v globalnem minimumu energije težka in nezanesljiva. Glavna težava pri pridobivanju natančnih rezultatov je v tem, da lahko nevtralni arginin obstaja v treh oblikah; vsaka oblika ima degenerirani enantiomeri D- in L-. Številne prostostne stopnje arginina otežujejo temeljito študijo; za pravilno opisovanje kratkosežnih interakcij je potrebno uporabiti visoko raven teorije. Zato smo izvedli natančno iskanje globalnega minimuma. Opravili smo optimizacije sistemov na nivoju PBE0/Def2TZVP, ki jim je sledil izračun energije na nivoju DLPNO-CCSD(T)/Def2TZVP s popravki ničelnega vibracijskega nivoja, izračunanimi po metodi PBE0/Def2TZVP. Prav tako smo analizirali termične populacije vibracijskih stanj in infrardeče spektre sistemov, da bi podrobneje razumeli lastnosti molekule arginina. Rezultati kažejo, da so strukture energijskih minimumov močno odvisne od položaja z dušikom bogatih funkcionalnih skupin arginina.



Except when otherwise noted, articles in this journal are published under the terms and conditions of the Creative Commons Attribution 4.0 International License

Scientific paper

# The Role of *Fallopia baldschuanica* Plant Extract in the Regression of Induced Hepatocellular Carcinoma in Rats

Luma Abd Almunim Baker,\* Shaymaa Zuhir Jalal Aldin  
and Hamza N Hameed

Department of Chemistry, College of Education for Pure Sciences, University of Mosul, Al-Majmoa'a Street,  
Mosul 41002, Nineveh, Iraq

\* Corresponding author: E-mail: Lumabaker50@uomosul.edu.iq  
tel.: +9647725380963

Received: 08-10-2023

## Abstract

Liver cancer continues to pose a formidable global health challenge, with its incidence on the rise across the world. Predictions suggest that by 2040, the toll of individuals affected by liver cancer will surpass one million. Consequently, numerous researchers have been motivated to improve therapies and develop new medications with minimal side effects on human health. Plant-derived natural products have offered a variety of pharmacological chemical structures and biologically active substances, which exhibit cytotoxic effects on tumor cells. The current study investigates the potential anti-cancer properties of *Fallopia baldschuanica* flower extract against thioacetamide (TAA) induced cancer. This study pinpointed specific amino acids in the raw extract, with methionine registering the highest percentage, trailed by cysteine, valine, threonine, tyrosine, isoleucine, and lysine. Amino acids have vital activities in various aspects of human health and the condition of diseases. The aim of this study is to evaluate the potential impact of *Fallopia baldschuanica* flower extract on the regression of the experimentally induced HCC in rats. These assessments were conducted through the measurement of liver function, involving aspartate aminotransferase, alanine transaminase, and alkaline phosphatase. Moreover, antioxidant enzyme and tumor marker assays were utilized and the histopathological examination to support the findings.

**Keywords:** Thioacetamide (TAA); *Fallopia baldschuanica* flower; Mitomycin C; Antioxidant; Anticancer.

## 1. Introduction

Cancer continues to pose a substantial global health challenge, affecting millions of individuals, with a mortality rate expected to reach approximately 1.4 million by the year 2040.<sup>1</sup> Worldwide, there were approximately 19.3 million new cases of cancer in 2020, with a projected rise to 28.4 million by 2040.<sup>2,3</sup> Various external factors, including smoking, pollution, UV radiation, and chemicals, significantly contribute to this estimate. Additionally, internal factors encompass immunological disorders, genetic mutations, hormones, and alterations occurring during the body's metabolic processes.<sup>4</sup>

The liver is essential for synthesis of bile acids, metabolism of fat, and detoxification.<sup>5</sup> However, the rising tide of metabolic disorders, including metabolic syndrome, diabetes, obesity, and NAFLD, these expected to make in-

dividuals more susceptible to hepatocellular carcinoma (HCC).<sup>6,7</sup> Accumulation of fats in the liver is associated with NASH characterized by inflammatory reaction and cellular death, also referred to as NAFLD.<sup>8</sup> Conventional management techniques involving either surgical resection and chemotherapy or liver transplantation have exhibited satisfactory results. Nevertheless, minimizing their side effects would significantly enhance their effectiveness. The above problems underscore the need for other methods that will give secure and more suitable medicines for liver tumor patients.<sup>9</sup>

Oxidative stress takes center stage as a significant mechanism for cancer development. This phenomenon unfolds within an environment where the heightened production of Reactive Oxygen Species (ROS) surpasses the cellular antioxidant defense, creating a pivotal imbalance that contributes to the intricate tapestry of cancer pro-

gression. This oxidative onslaught triggers the oxidation of crucial biomolecules—DNA, proteins, and lipid peroxidation. These oxidative events, fueled by ROS, form a fundamental nexus in the intricate web of cancer formation. ROS was believed to have played an essential role in cancer progression hence the need for novel therapies, and new therapeutic targets.<sup>10</sup>

Carcinogenesis, the intricate process of cancer development, hinges on a diverse array of natural chemicals sourced from plants. This has spurred extensive research into the potential anti-cancer properties of these natural products, positioning plant extracts as indispensable resources for potential cancer chemotherapeutics. In various drug development programs, extracts from plants emerge as critical suppliers, contributing to the expansive arsenal of potential anti-cancer agents.<sup>11</sup> Several plants carry bioactive compounds like alkaloids, flavonoids, terpenoids, and phenolics that possess cytotoxic features towards cancer cells.<sup>12</sup> However, structurally related analogs of those natural substances were developed with different pharmaceutical agents expanding, strengthening the anti-cancer arsenal.<sup>13</sup> Remarkably, over 70 percent of current anticancer drugs trace their origins to natural resources or their derivatives.<sup>14</sup> This reliance on nature's diversity underscores its significance as a template for discovering novel molecular scaffolds, paving the way for innovative approaches in the ongoing battle against cancer.<sup>15</sup>

Asian *Fallopia baldschuanica* is an herbaceous perennial plant known for its highly competitive and invasive nature within the Polygonaceae family.<sup>16</sup> Studies have revealed its phytochemical composition, highlighting the substantial presence of various compounds, including: anthraquinones (emodin, citreorosein, fallacinol, physcion, and others), flavonoids (rutin, apigenin, quercetin, quercitrin, isoquercitrin, hyperoside, Stilbenes resveratrol and polydatin, coumarins, lignins with essential oil and a host of compounds.<sup>17,18</sup> The key bioactive compounds can be also found in *Fallopia* plant parts like the stem, leaf, flower, and roots.<sup>19</sup> Extracts obtained from different parts of *Fallopia* species such as roots, rhizome, stems, leaves, and flowers possess promising medicinal properties including antibacterial<sup>20</sup>, antioxidant<sup>21</sup>, anticancer, antiproliferative and apoptotic properties.<sup>22</sup> These findings emphasize the capacity of *Fallopia* species to serve as a rich source of diverse natural compounds with potential therapeutic applications. For instance, a previous study illustrated that *Fallopia japonica* extract exhibited potent inhibition of ABC transporters, significant inhibition of metabolic enzymes, and cell growth.<sup>23</sup> As research continues, natural products may prove to be valuable sources of medication regarding those with cancer, with the ability to offer safer and more effective therapies.<sup>24</sup>

The aim of the present study is to evaluate the potential anticancer effects of *Fallopia baldschuanica* flower extract on thioacetamide D (TAA)-induced cancer. For this purpose, the anticancer potential of plant extract was

examined through biochemical studies of liver function tests and histological examination.

## 2. Experiment

### 2.1. Preparation of the Plant Extracts

Asian *Fallopia baldschuanica* was used in this study, Family: Polygonaceae, Genus: *Fallopia baldschuanica* and Species: *F. baldschuanica*.<sup>25</sup>

Asian *Fallopia baldschuanica* flower (100 g) was taken and homogenized after mixing with distilled water (1:5) weight: volume and then the crude extract was prepared.<sup>26</sup>

### 2.2. Experimental Design

In the present study, male rats (Wister) weighing between 200 and 250 gm of body weight were involved in this study. For the experiments on rats, the study received approval from the University of Mosul College of Veterinary Medicine/ Institutional Animal Care and Use Committee, under reference number UM.VET.2023.029. This rigorous ethical oversight ensures the humane and responsible treatment of the animal subjects involved in the research, upholding the principles of ethical conduct in scientific investigations. To ensure methodological precision and mitigate potential complications, a deliberate decision was made to exclude the influence of the female rat estrus cycle, which could introduce variability in the results. 36 rats were involved in the study, which was divided into 6 groups with 6 animals in each group. All groups were treated as the following:

**Group 1:** Control group (Normal). These rats were given a regular diet with distilled water for 48 days.

**Group 2:** a group that received 23 days of treatment with flower plant extract.

**Group 3:** a group that received a daily LD<sub>50</sub> dose of 100 mg/kg of TAA for 5 days. The 50% Lethal Dose (LD<sub>50</sub>) was determined using the methodology outlined in the study conducted by Enevide *et al.*<sup>27</sup> The specific concentration of TAA was diluted (200, 175, 150, 125, 100, 75, and 50 mg/kg), ten male rats for each concentration. The LD<sub>50</sub> value, a critical measure of lethal dose, is typically derived using a straightforward formula:

$LD_{50} = [M_0 + M_1] / 2$ , where M<sub>0</sub> represents the highest administered dose with no mortality, while M<sub>1</sub> signifies the lowest dose at which mortality is observed.

**Group 4:** a group that received daily doses of TAA for five days and then treated with flower plant extract for a period of 23 days.

**Group 5:** a group that received daily doses of TAA for five days and then treated with mitomycin C (MMC) for a period of 23 days.

**Group 6:** a group that received daily doses of TAA for five days. After that, they were treated with a combination of flower plant extract and MMC for a duration of 23 days.



After the specified period, blood samples were collected from the medial canthus of the eye of male rats to conduct the required tests.<sup>28</sup> Then after a period of 30 days, the rats were dissected to examine the extent of liver damage caused by TAA. Liver samples were extracted, weighed, and then fixed in a 10% formalin solution for further analysis.

### 2. 3. Histology

Liver tissue has been fixed in 10% formalin and then dehydrated using an ethanol gradient. Washing has been done with xylene and embedded in paraffin wax. The tissue blocks were sectioned at a thickness of 5–6 micrometers, deparaffinized, and stained with hematoxylin and eosin to enable microscopic examination.<sup>29</sup>

### 2. 4. Biochemical Parameters Assay

Serum samples were analyzed for various biochemical parameters, including alpha-fetoprotein AFP measured using an ELISA kit (Kamiya Biomedical),<sup>30</sup> alkaline phosphatase ALP measured using an ELISA kit (Mybiosource),<sup>31</sup> Aspartate Transaminase (AST) measured using an ELISA kit (Mybiosource),<sup>26</sup> alanine transaminase (ALT) measured using an ELISA kit (Mybiosource),<sup>32</sup> Malondialdehyde (MDA) levels, which were determined using a modified thiobarbituric acid reaction.<sup>34</sup> The level of glutathione (GSH) was measured using Ellman's reagent/ DTNB,<sup>34</sup> while the total protein levels were determined using the Biuret method at 564nm.<sup>35</sup>

#### 2. 5. Amino Acid Analyzer

Amino acids were extracted from the sample using the Young Lin Amino Acid Analysis System, which employed a ZORBAX Eclipse-AAA column for separation. The column had a dimension of 150 × 4.6 mm with a particle size of 3.5 μm. This system was available at the Ministry of Science and Technology/Department of Environment and Water Laboratories.<sup>36</sup>

### 2. 6. Statistical Analysis

The acquired data underwent meticulous statistical scrutiny employing one-way analysis of variance (ANOVA). To discern specific differences between the groups, the Duncan test was employed, providing a detailed exploration of the dataset. All statistical computations were executed with the aid of IBM SPSS Statistics 22 software. Additionally, Graph Pad Prism v8.0 was used for graphical representation. The significance level for the statistical analysis was set at 5% ( $P < 0.05$ ).

## 3. Results and Discussion

The liver dysfunction is a major health problem. The present study evaluates the potential role of *Fallopia*

*baldschuanica* flower extracts on thioacetamide D (TAA)-induced cancer in rats. TAA has been widely used by researchers as an experimental model to induce liver damage in animals. The toxicity of TAA causes oxidative stress leading to the production of reactive oxygen species, inflammation responses, and apoptosis in Hepatocytes. This ultimately leads to liver injury and failure. Consequently, there is an elevation in serum aminotransferase levels, including aspartate aminotransferase and alanine aminotransferase (ALT).<sup>37</sup>

### 3. 1. The effect of Some Enzymes on Liver Cancer

Liver enzymes are essential for detoxification purposes yet an imbalance in their levels leads to liver damage that causes initiation, progression, and spread of liver cancer. The most sensitive biochemical indicators used to diagnose hepatic impairment are serum AST, ALT, and ALP.<sup>38</sup>

The mean of AST, ALT, and ALP levels in serum were significantly ( $P < 0.05$ ) higher in TAA-treated rats than in the control group 92.75, 61.75, 63.3 to 117.5, 155.75, and 153.69 respectively (Fig. 1; Table 1). There were significantly increased concentrations of AST and ALT in TAA-treated male rats but given extract crude of flower plant when compared to the group given crude extract only. Abnormally high levels of these enzymes denote the presence of liver damage, inflammation, or tumor growth (1, 2). These findings are in agreement with earlier works that showed similarly raised levels of liver enzymes.<sup>37,39,40</sup> The graph depicted in Figure shows a statistically viable reduction ( $P < 0.05$ ) of these mentioned factors for the male rats receiving TAA with MMC, flower plant extract, or MMC + flower plant extract compared to the male rats treated with the TAA group (Fig. 1; Table 1). These results are consistent with Marzouk *et al.* (2011) findings, which demonstrated decreased activities of certain enzymes (AST, ALT, and ALP) associated with liver damage in male rats treated with the hydroalcoholic extract of *Cichorium endivia*.<sup>41</sup> This indicates the potential of the plant extract to alleviate liver damage in TAA-treated rats. Furthermore, the administration of MMC resulted in a decrease in ALT and ALP activities, which indicates an improvement in liver function.<sup>42,43</sup> Many studies demonstrated that certain plant extracts can exhibit synergistic effects when used in combination with conventional chemotherapy drugs. Consequently, their anticancer properties would take effect.<sup>44</sup> Various plant extracts with different structures have demonstrated efficacy in reversing various malignancies.

According to a recent study, the combination of *C. maritimum* ethyl acetate extract and a half-dosage of sorafenib IC<sub>50</sub> reduced the suppression of HCC cell lines (Huh7 and HepG2) growth comparably to a full dose of sorafenib, without causing more cell damage.<sup>45</sup> In contrast, there was a significant ( $P < 0.05$ ) increase in the activity of

AST observed in the TAA male rats group when treated with MMC, as depicted in Figure 1 and Table 1. The reason may be attributed to the rapid destruction of cancer cells during treatment can lead to increased AST levels due to the release of AST from the dying cells.

Notably, the most potent agent in inhibiting the growth of HCC was an ethyl acetate fraction derived from extracts of *Brassica oleracea L.* and *Crithmum maritimum L.* This mechanism resulted in the inhibition of protein synthesis, thereby influencing membrane biosynthesis, and disrupting the lipid equilibrium within HCC cells. All these items played a significant part in enhancing chemotherapy and reducing its side effects.<sup>46–49</sup>

Notably, the protein content demonstrated minimal variation between TAA-treated male rats and the healthy control group. This aligns with a prior study, where no statistical difference in serum total protein levels was observed among patients with oral cancer.<sup>50</sup> Nevertheless, this finding differs from other studies dealing with low levels of total protein in cancer.<sup>51, 52</sup>

There was a statistically significant decrease observed ( $P < 0.05$ ) for the AFP levels among TAA-treated rats with flower plant extract, MMC, or MMC+flower plant extract compared to the TAA group (Fig. 1; Table 2). The decrease can be attributed to some of the components found in the plant flower extract, including antioxidants and essential

**Table 1:** Effects sum of AST, ALT, and ALP in both normal and experimental conditions.

	Control	Crude extract	TAA	TAA + crude extract	TAA + MMC	TAA + MMC + crude extract
AST	92.75 ± 2.50 c	54.25 ± 3.77* b	117.50 ± 2.08* d	94.25 ± 2.5 c	131.50 ± 7.77* e	45.50 ± 7.05* a
ALT	61.75 ± 8.02 a	59.00 ± 9.20 a	155.75 ± 4.35* d	72.75 ± 4.57* b	63.50 ± 4.80 a	90.50 ± 2.08* c
ALP	63.30 ± 4.26 b	71.51 ± 8.89* c	153.69 ± 3.97* d	8.02 ± 0.51* a	5.91 ± 0.89* a	5.63 ± 1.00* a

AST=aspartate aminotransferase; ALT = alanine aminotransferase; ALP = alkaline phosphatase; MMC= Mitomycin C  
Values are given as mean ± SD of 5 replicates; \*P value <0.05 = significant level.

The variables a, b, c, d, and e are represented in multiple comparison settings among groups that were identified using the Duncan test.

### 3. 2. The Effect of Some Biochemical Parameters on Liver Cancer

The findings of this study highlight a significant elevation in serum AFP and MDA levels in TAA-treated male rats, registering at 186.19 and 6.13, respectively, compared to the control group, which exhibited levels of 2.11 for AFP and 1.65 for MDA (Fig. 1; Table 2). This notable surge in oxidative stress is attributed to lipid peroxidation within liver tissue, a consequence of TAA-induced hepatotoxicity.

amino acids that are known to enhance hepatic functionality and may buffer the effects of thioacetamide.<sup>53,54</sup>

The concentration of TP in the TAA-treated rats considerably dropped from 17.56 g/dL to 8.66 g/dL in comparison to the control rats treated with floral plant extract, as evidenced by the results in Fig. 1 and Table 2. This decline is a result of the body's inability to properly digest proteins because of TAA exposure, which might result in hypoalbuminemia. The prevailing cirrhotic state associated with malabsorption is known to contribute to

**Table 2:** Effects sum of biochemical variables in both normal and experimental conditions.

	Control	Crude extract	TAA	TAA + crude extract	TAA + MMC	TAA + MMC + crude extract
AFP ng/ml	2.11 ± 0.35 a	2.94 ± 0.87 a	186.19 ± 6.51* e	144.85 ± 14.53* d	33.46 ± 1.94* b	69.76 ± 6.98* c
T.P g/dL	9.67 ± 0.92 ab	17.42 ± 2.24* e	12.17 ± 0.24 bc	8.66 ± 1.00 a	16.52 ± 1.68* de	14.04 ± 3.61* cd
GSH *10 <sup>-6</sup> μmol/L	3.35 ± 0.49 c	2.55 ± 0.16* b	1.29 ± 0.05* a	2.46 ± 0.38* b	2.50 ± 0.20* b	2.70 ± 0.10* b
MDA * 10 <sup>-5</sup> μM/L	1.71 ± 0.04 a	2.38 ± 0.14* b	6.60 ± 0.51* e	4.83 ± 0.11* c	4.93 ± 0.24* c	5.81 ± 0.10* d

AFP = alpha-fetoprotein; TP= total protein; GSH = glutathione; MDA= malondialdehyde.

Values are given as mean ± SD of 5 replicates; \*P value < 0.05 = significant level.

The variables a, b, c, d, and e are represented in multiple comparison settings among groups that were identified using the Duncan test.

decreased albumin levels.<sup>55</sup> In alignment with this, the study validates a substantial increase in total protein (TP) concentration in TAA-treated rats receiving injections of

MMC, rising significantly from 12.17 g/dL to 16.52 g/dL compared to the TAA-only group. However, the findings revealed a non-significant increase in the concentration

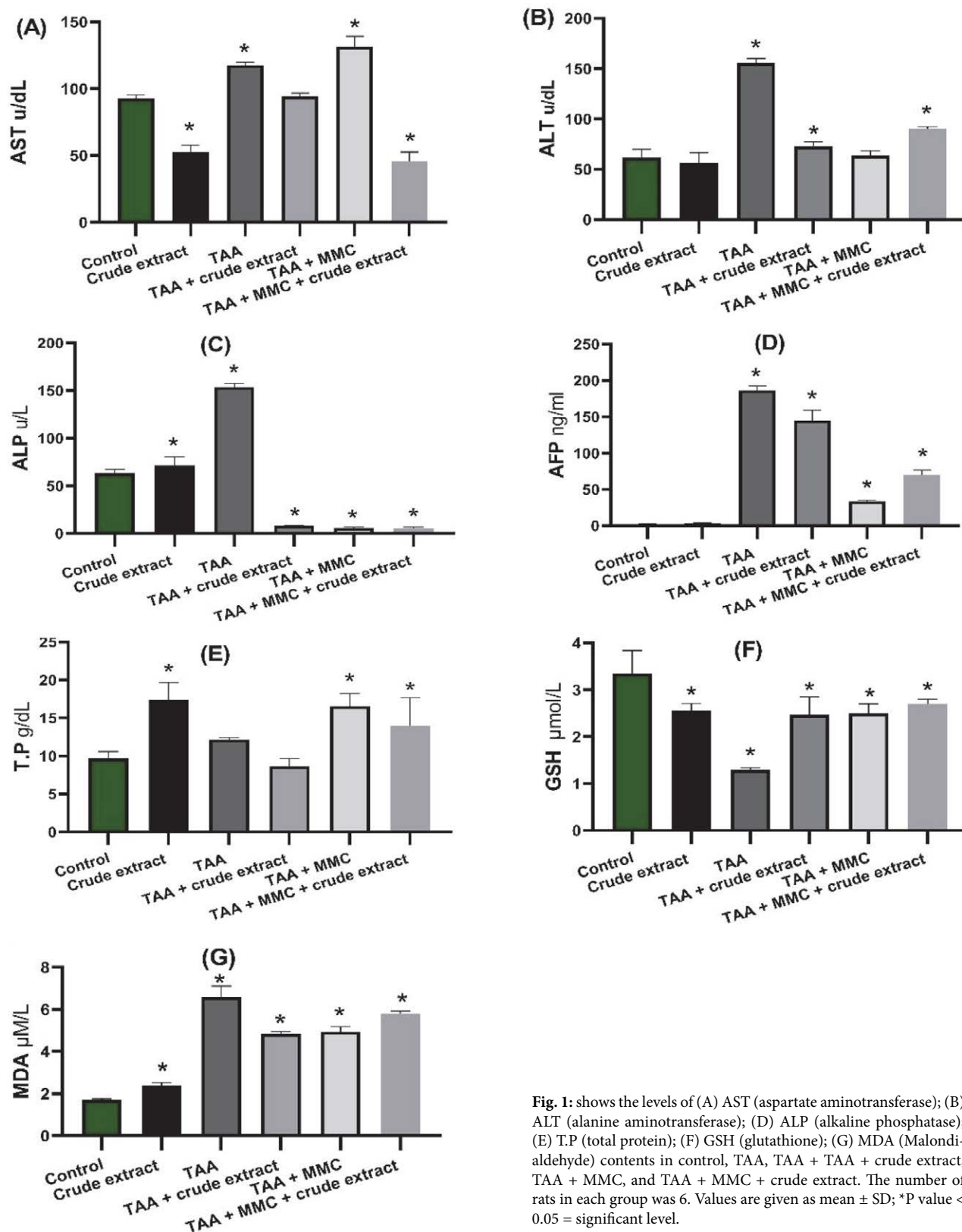


Fig. 1: shows the levels of (A) AST (aspartate aminotransferase); (B) ALT (alanine aminotransferase); (D) ALP (alkaline phosphatase); (E) T.P (total protein); (F) GSH (glutathione); (G) MDA (Malondialdehyde) contents in control, TAA, TAA + TAA + crude extract, TAA + MMC, and TAA + MMC + crude extract. The number of rats in each group was 6. Values are given as mean  $\pm$  SD; \*P value < 0.05 = significant level.

of total protein (TP) following treatment with a combination of MMC and the flower plant extract. The exposure of MMC in cancer cell exposure is known to trigger the DNA damage response (DDR), a cellular mechanism.<sup>56</sup> One protein that can be stimulated by the DDR is p53, a transcription factor controlling the expression of various genes related to DNA repair, cell cycle, and apoptosis. Activation of p53, in turn, can potentially elevate the overall cellular protein levels, presenting a complex interplay of molecular events in response to the treatment.<sup>56</sup>

In contrast, the data showed a significant reduction in total protein (TP) activity among male rats treated with both TAA (thioacetamide) and the flower plant extract, as opposed to the TAA group. Natural products employed in cancer treatment can decrease the proteins associated with tumor growth by lowering their expression levels. This process leads to apoptosis and decreased tumor growth.<sup>57</sup>

According to the data shown in Fig. 1 and Table 2, rats treated with flower plant extract, MMC or a combination of both demonstrated reduced levels of MDA compared to the group that received only TAA. Remarkably, TAA-treated male rats receiving the flower plant extract displayed significantly elevated MDA levels compared to the control group treated solely with the extract. MDA, a widely recognized biomarker of oxidative stress in cancer, and the observed reduction in MDA levels implies a potential protective effect against the oxidative stress induced by TAA.

In Table 2, the data shows serum Glutathione (GSH) levels of the untreated control group exhibited significantly higher GSH levels at 3.34  $\mu\text{mol/L}$  compared to the TAA-treated male rats of 1.29  $\mu\text{mol/L}$ . Interestingly, the GSH levels in the male rats treated with TAA and administered with flower plant extract, as well as the control rats administered with flower plant extract, showed no

significant difference. Furthermore, the GSH data have revealed a significant elevation in TAA-treated rats administered with various treatments of (MMC, MMC + flower plant extract, or flower plant extract) when contrasted with the TAA-treated male rats. GSH is one of the significant antioxidants that assumes a crucial role in shielding cells from the detrimental impact of free radicals. Nevertheless, flower plant extract and MMC increased the activity of GSH indicating a positive effect against oxidative stress.<sup>57</sup>

### 3. 3. Estimation of Amino Acids in the *Fallopia baldschuanica* Crude Extracts

The crude extracts of *Fallopia baldschuanica* flower reveal the presence of various amino acids, including glutamic acid, valine, glycine, threonine, serine, isoleucine, and phenylalanine, that may have antioxidant properties, helping to eliminate harmful free radicals within the body (Fig. 2; Table 3). Notably, methionine constitutes a larger percentage of the sample, playing a pivotal role in bolstering antitumor immunity by enhancing the activity of cyclic GMP-Amp synthases and promoting chromatin dissociation.<sup>58,59</sup> Similarly, cysteine, another amino acid identified in the extract, is recognized as a tumor regression amino acid, that enhances chemotherapy.<sup>60</sup>

### 3. 4. Histological Examination

Hematoxylin and eosin (H&E) staining has been used to examine liver tissue under a microscope. According to the description provided, the control group showed normal architecture of the hepatic lobules. Microscopical examination of liver sections stained with H&E, the control group exhibited a normative architectural profile with

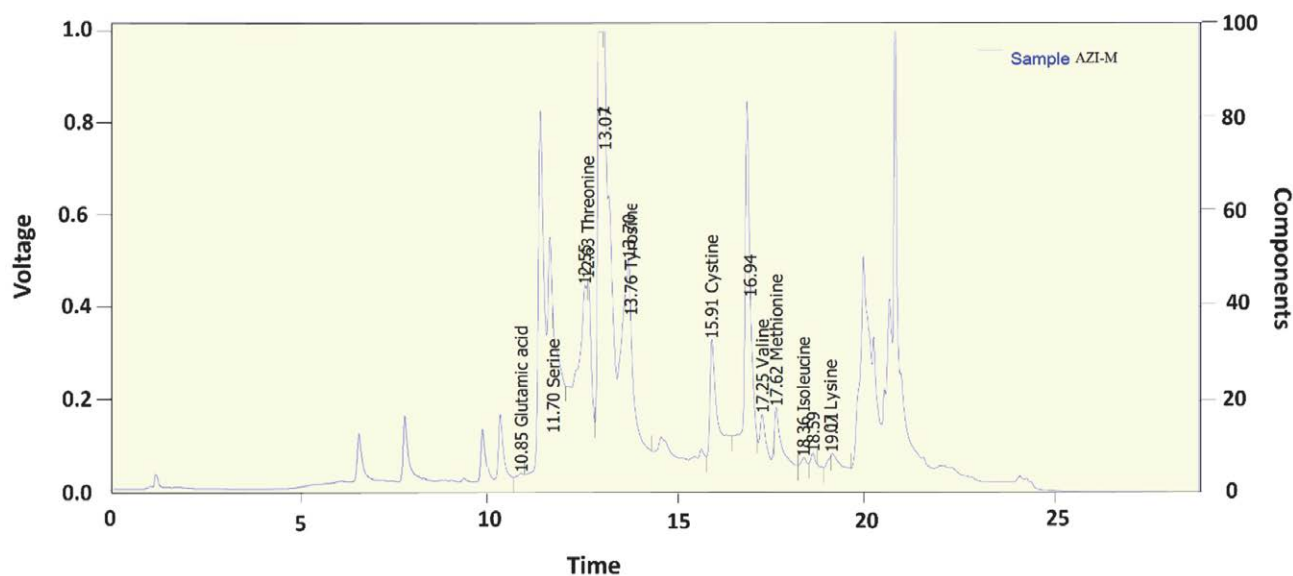


Fig. 2: Amino acids identified in the crude extracts of *Fallopia* flower.

**Table 3:** Percentage of amino acids present in the crude extracts of *Fallopia* flower.

	Reten. Time [min]	Response	Amount [ppm]	Amount [%]	Peak Type	Compound Name
1	10.848	37.642	1.122	0.5	Ordnr	Glutamic acid
2	11.704	207.714	2.125	1.0	Ordnr	Serine
3	12.548	3251.788	0.000	0.0		
4	12.632	1853.310	20.134	9.6	Ordnr	Threonine
5	13.012	7948.690	0.000	0.0		
6	13.072	12747.388	0.000	0.0		
7	13.700	2944.959	0.000	0.0		
8	13.760	1635.572	19.948	9.5	Ordnr	Tyrosine
9	15.912	3528.679	58.573	27.8	Ordnr	Cysteine
10	16.844	6577.316 j	0.000	0.0		
11	16.936	2009.170	0.000	0.0		
12	17.248	1256.845	26.694	12.7	Ordnr	Valine
13	17.616	1308.515	69.785	33.2	Ordnr	Methionine
14	18.356	132.608	6.149	2.9	Ordnr	Iso leucine
15	18.592	161.316	0.000	0.0		
16	19.068	151.532	5.862	2.8	Ordnr	Lysine
17	19.108	365.632 1	0.000	0.0		
	Total		210.392	100.0		

a notable proliferation of Kupffer Cells, signaling the absence of any discernible pathological changes in the tissue (Fig. 3). The microscopic portrayal of the TAA group (100

mg/kg of TAA over 5 days) showed intricate pathological alterations. Hepatocellular carcinoma, sinusoidal dilatation, the penetration of mononuclear cells, degeneration

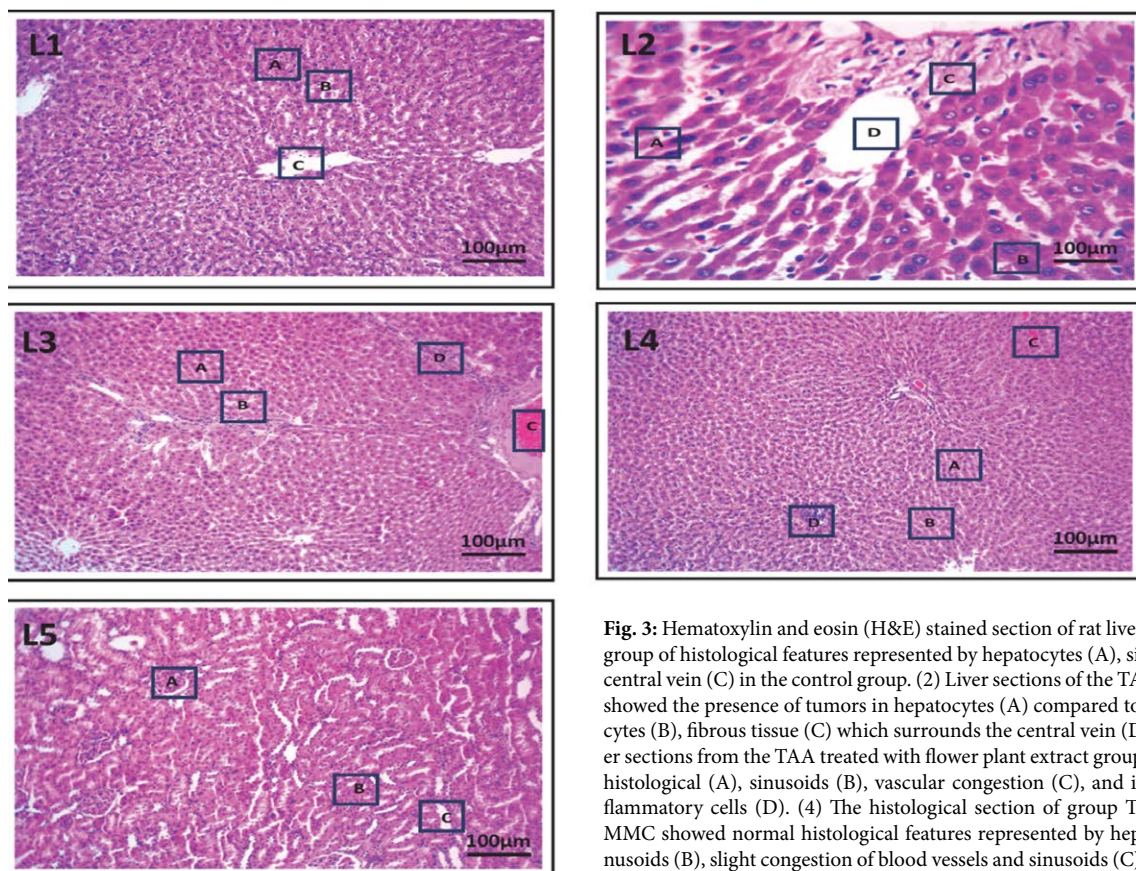


**Fig. 3:** Hematoxylin and eosin (H&E) stained section of rat liver. (1) The control group of histological features represented by hepatocytes (A), sinusoids (B), and central vein (C) in the control group. (2) Liver sections of the TAA-treated group showed the presence of tumors in hepatocytes (A) compared to normal hepatocytes (B), fibrous tissue (C) which surrounds the central vein (D), 400X. (3) Liver sections from the TAA treated with flower plant extract group showed normal histological (A), sinusoids (B), vascular congestion (C), and infiltration of inflammatory cells (D). (4) The histological section of group TAA treated with MMC showed normal histological features represented by hepatocytes (A), sinusoids (B), slight congestion of blood vessels and sinusoids (C), and infiltration of inflammatory cells (D). (5) The histological section of group TAA-treated male rats with flower plant extract and MMC showed the normal histological features represented by the central vein (A), the sinusoids (B), and a slight (cloudy) vacuolar degeneration of the hepatocytes (C).

of hepatocytes, cellular hypertrophy, and vascular congestion are all included (Fig. 3). Moreover, the TAA-induced liver injury precipitated an increase in ROS production, instigating oxidative stress and damage to proteins, lipids, and DNA within the hepatic cellular milieu. This is consistent with previous studies which indicated that the use of the chemical substance TAA caused liver tumors and infiltration of hepatocytes.<sup>61,62</sup>

The lesions were reduced in a TAA group treated with the flower plant extract and only a few tumor cells were present. These findings indicate that the plant extract may have anti-cancer properties that can effectively reduce the development of tumors in liver tissue (Fig. 3).

The histological sections of TAA group treated with MMC at a concentration of 75 mg/kg (which is used as chemotherapy) showed changes in the liver tissue, including the appearance of some tumor cells, nucleus polymorphism and division, and the emergence of congestion in the central vein of the liver, and infiltration of inflammatory cells (Fig. 3). Many studies suggest that MMC can effectively shrink tumors when used as a form of chemotherapy. However, the use of MMC can also lead to various side effects that affect the liver tissue, such as congestion in the central vein and infiltration of hepatocytes.<sup>63</sup>

Histological sections revealed that treatment with both MMC and plant extract induced changes in the liver tissue. These changes included less appearance of tumor cells, the proliferation of Kupffer cells, and sinusoidal obstruction (Fig. 3). These findings suggest that the combination of MMC and plant extract may have an impact on liver health, affecting the liver tissue structure and function. Many studies have revealed that *Annona muricata* plant pulp has several beneficial effects on liver tissue, including anti-cancer properties attributed to the presence of flavonoids and phenols.<sup>64</sup>

#### 4. Conclusion

The findings of the current study have reinforced the idea that *Fallopia baldschuanica* flower crude extracts or combining them with MMC can effectively improve liver damage caused by TAA-treated rats. The data demonstrated that the plant extract improved the reversal of liver damage caused by TAA, through the restoration of liver enzyme levels that approach normal. Furthermore, this study has provided new insights into the potential benefits of this combination therapy. However, further research is required to fully understand the mechanisms behind how these substances work together.

#### Acknowledgments

We would like to extend our heartfelt gratitude and appreciation to Mosul University/College of Education for Pure Science/Department of Chemistry for the unwaver-

ing support and exceptional facilities provided throughout our study period.

The source of funding was provided through self-financing.

#### 5. References

1. WHO, Number of new cases and deaths from liver cancer predicted to rise by more than 55% by 2040 (who.int), (6 October 2022).
2. F. Bray, J. Ferlay, I. Soerjomataram, R. L. Siegel, L. A. Torre, A. Jemal, *Cancer J. Clin.* **2018**, *68*, 3–31. DOI:10.3322/caac.21492
3. H. Sung, J. Ferlay, R. L. Siegel, M. Laversanne, I. Soerjomataram, A. Jemal, F. Bray, *Cancer J. Clin.* **2021**, *71*, 209–249. DOI:10.3322/caac.21660
4. M. Maule, F. Merletti, *Oncology.* **2012**, *13*, 745–746. DOI:10.1016/S1470-2045(12)70268-1
5. E. Trefts, M. Gannon, D. H. Wasserman, *Curr. Biol.* **2017**, *27*, 1147–1151. DOI:10.1016/j.cub.2017.09.019
6. A. Forner, M. Reig, J. Bruix, *Lancet.* **2018**, *391*, 1301–1314. DOI:10.1016/S0140-6736(18)30010-2
7. P. Agosti, C. Sabba, A. Mazzocca, *Bba-Mol. Basis Dis.* **2018**, *1864*, 607–617. DOI:10.1016/j.bbdis.2017.11.026
8. D. Gnocchi, C. Sabbà, M. Massimi, A. Mazzocca, *Int. J. Mol. Sci.* **2023**, *24*, 1–17. DOI:10.3390/ijms24043710
9. C. Y. Liu, K. F. Chen, P. J. Chen, *Csh. Perspect. Med.* **2015**, *5*, 1–16. DOI:10.1101/cshperspect.a021535
10. K. M. Zahra, R. Lefter, A. Ali, H. A. Ech-Cha, T. Constantin, C. Alin, T. Daniel, *Oxid. Med. Cell Longev.* **2021**, *5*, 1–25. DOI:10.1155/2021/9965916
11. B. Orlikova, M. Diederich, *Curr. Med. Chem.* **2012**, *19*, 2061–2087. DOI:10.2174/092986712800228998
12. M. Singh, M. Kaur, O. Silakari, *Eur. J. Med. Chem.* **2014**, *84*, 206–239. DOI:10.1016/j.ejmech.2014.07.013
13. M. Gordaliza, *Clin. Transl. Oncol.* **2007**, *9*, 767–776. DOI:10.1007/s12094-007-0138-9
14. G. A. Karikas, *J. BUON.* **2010**, *15*, 627–638. DOI:10.3390/molecules15020627
15. G. Tan, C. Gyllenhaal, *Curr. Drug Targets.* **2006**, *7*, 265–277. DOI:10.2174/138945006776054942
16. J. Forman, R. V. Kesseli, *Am. J. Bot.* **2003**, *90*, 586–592. DOI:10.3732/ajb.90.4.586
17. J. H. Park, H. K. Moon, C. W. Park, *Korean J. Plant Taxon.* **2011**, *41*, 10–15. DOI:10.11110/kjpt.2011.41.1.010
18. S. Lachowicz, J. Oszmianski, *Molecules.* **2019**, *24*, 1436. DOI:10.3390/molecules24071436
19. V. Metlicar, I. Vovk, A. Albrecht, *Plants.* **2019**, *8*, 1–15. DOI:10.3390/plants8100384
20. I. Nawrot-Hadzik, J. Hadzik, M. Fleischer, A. Choromanska, B. Sterczala, P. Kubasiewicz-Ross, J. Saczko, M. Galczynska-Rusin, T. Gedrange, A. Matkowski, *Med. Sci. Monit.* **2019**, *25*, 3279–3287. DOI:10.12659/MSM.913855
21. C. Chan, R. Gan, H. Corke, *Int. J. Food Sci. Tech.* **2016**, *51*, 565–573. DOI:10.1111/ijfs.13024

22. M. Hong, H. Y. Tan, S. Li, F. Cheung, N. Wang, T. Nagamatsu, Y. Feng, *Int. J. Mol. Sci.* **2016**, *17*, 893. 1–21. DOI:10.3390/ijms17060893
23. S. Y. Eid, M. Z. El-Readi, M. L. Ashour, M. Wink, *Evid-Based Compl. Alt.* **2015**, *2015*, pp. 1–8. DOI:10.1155/2015/868424
24. S. Mishra, S. Ahmad, N. Kumar, B. Sharma, *Glob. J. Pharma Res.* **2013**, *2*, 1613–1618.
25. M. H. Kim, J. H. Park, H. P. Won, W. Chong, *Can. J. Bot.* **2000**, *78*, 1136–1143. DOI:10.1139/b00-079
26. E. Agbai, C. Njoku, C. Nwanegwo, *Afr. J. Pharm. Pharmacol.* **2015**, *9*, 745–755. DOI:10.5897/AJPP2015.4389
27. C. Enegeide, A. David, S. A. Fidelis, *Toxicol. Int.* **2013**, *20*, 224–226. DOI:10.4103/0971-6580.121674
28. D. Stillinger, K. Helland, C. Van Atta, *J. Fluid. Mech.* **1983**, *131*, pp. 91–122. DOI:10.1017/S0022112083001251
29. N. Aljuhani, M. A. Elkablawy, H. M. Elbadawy, A. M. Alahmadi, A. M. Aloufi, S.H. Farsi, B. S. Alhubayshi, S. S. Alhejaili, J. M. Alhejaili, O. B. Abdel-Halim, *J Taibah Univ. Med. Sci.* **2019**, *14*, 553–559. DOI:10.1016/j.jtumed.2019.10.002
30. J. Liang, J. Wang, L. Zhang, S. Wang, C. Yao, Z. Zhang, *Ana-lyst.* **2019**, *144*, 265–273. DOI:10.1039/C8AN01791C
31. M. Tomás, M. Sentí, F. n. García-Faria, J. Vila, A. Torrents, M. Covas, J. Marrugat, *Arterioscl. Throm. Vas.* **2000**, *20*, 2113–2119. DOI:10.1161/01.ATV.20.9.2113
32. I. S. Khan, K. B. Dar, S. A. Ganie, M. N. Ali, *Drug Chem. Toxicol.* **2020**, *45*, 1345–1354. DOI:10.1080/01480545.2020.1825472
33. N. A. Botsoglou, D. J. Fletouris, G. E. Papageorgiou, V. N. Vassilopoulos, A. J. Mantis, A. G. Trakatellis, *J. Agr. Food Chem.* **1994**, *42*, 1931–1937. DOI:10.1021/jf00045a019
34. S. Cao, X. Li, Y. Gao, F. Li, K. Li, X. Cao, Y. Dai, L. Mao, S. Wang, X. Tai, *Dalton T.* **2020**, *49*, 11851–11858. DOI:10.1039/D0DT01742F
35. A. G. Gornall, C. J. Bardawill, M.M. David, *J. Biol. Chem.* **1949**, *177*, 751–766. DOI:10.1016/S0021-9258(18)57021-6
36. R. Dahl-Lassen, J. van Hecke, H. Jørgensen, C. Bukh, B. Andersen, J. K. Schjoerring, *Plant Methods.* **2018**, *14*, 1–9. DOI:10.1186/s13007-018-0277-8
37. S. Y. Nancy, M. H. Amal, A. G. Mohammad, Elmersy, A. M. Heba, *Sci. Rep-UK.* **2021**, *11*, 1–17. DOI:10.1038/s41598-021-91666-6
38. N. Johnkennedy, E. Adamma, A. Austin, N. N. Chukwunyere, *Am. J. Sci.* **2010**, *3*, 317–321.
39. M. Bhadauria, S. K. Nirala, *Food Chem. Toxicol.* **2009**, *27*, 17–25. DOI:10.1016/j.etap.2008.07.003
40. S. H. Shareef, A. S. M. Juma, D. N. F. Agha, A. R. Alzahrani, I. A.A. Ibrahim, M. A. Abdulla, *Appl. Sci.* **2023**, *13*, 5243, 2–19. DOI:10.3390/app13095243
41. M. Marzouk, A. A. Sayed, M. A. Soliman, *J Med.* **2011**, *2*, 1273–1279.
42. C. A. Ukwubile, *Int. J. Pharm. Front.* **2012**, *2*, 9–17. DOI:10.1016/S1995-7645(14)60258-3
43. S. H. Orabi, S. M. Shawky, *Int. J. Sci. Basic Appl. Res.* **2014**, *17*, 137–147.
44. S. Pezzani, I. Vitalini, S. R. Zuñiga, M. Martorell, *Medicina.* **2019**, *55*, p. 110. DOI:10.3390/medicina55040110
45. D. Gnocchi, F. Castellaneta, G. Cesari, G. Fiore, C. Sabbà, A. Mazzocca, *J. Pharm. Pharmacol.* **2012**, *73*, 1369–1376. DOI:10.1093/jpp/rgab070
46. D. Gnocchi, G. Cesari, G. J. Calabrese, R. Capone, C. Sabbà, A. Mazzocca, *Plant Food Hum. Nutr.* **2020**, *75*, pp. 33–40. DOI:10.1007/s11130-019-00781-3
47. D. Gnocchi, L. Del Cocco, C. R. Girelli, F. Castellaneta, G. Cesari, C. Sabbà, F. P. Fanizzi, A. Mazzocca, *Sci. Rep. UK.* **2021**, *11*, p.1259. DOI:10.1038/s41598-020-78867-1
48. D. Gnocchi, C. Sabbà, A. Mazzocca, *Plant Food Hum. Nutr.* **2022**, *77*, 481–483. DOI:10.1007/s11130-022-00986-z
49. D. Gnocchi, C. Sabbà, A. Mazzocca, *Plant Food Hum. Nutr.* **2023**, *78*, 230–232. DOI:10.1007/s11130-022-01037-3
50. N. Abhishek, K. Mubeen, K. R. Vijayalakshmi, B. Suman, H. C. Gayitri, M. Anitha, *Malaysian J. Pathol.* **2012**, *34*, 4–52.
51. M. Rasouli, A. Okhovatian, A. Enderami, *Clin. Chem. Lab. Med.* **2005**, *43*, 913–918. DOI:10.1515/CCLM.2005.156
52. S. AlMuhtaseb, *Oncol. Lett.* **2014**, *8*, 2752–2756. DOI:10.3892/ol.2014.2535
53. A. M. Gowifel, M. G. Khalil, S. A. Nada, S. A. Kenawy, K. A. Ahmed, M. M. Salama, M. M. Safar, *Toxicol. Mech. Method.* **2020**, *30*, 620–633. DOI:10.1080/15376516.2020.1801926
54. R. S. Ali, W. C. Hmood, M. A. Alsirrag, *Mater. Sci. Eng.* **2019**, *571*, 1–12. DOI:10.1088/1757-899X/571/1/012101
55. N. M. Abd-Elrahman, A. S. Farid, K. M. Fararh, *Vet. Med. US.* **2014**, *27*, 456–465.
56. S. X. Xinxin, K. A. Dilly, J. Y. Lee, *Mol. Canc. Res.* **2015**, *13*, 1533–1543. DOI:10.1158/1541-7786.MCR-15-0237
57. C. G. Vijayameena, M. Subhashini, B. R. Loganayagi, *Int. J. Curr. Microbiol.* **2013**, *2*, 1–8.
58. D. Wanders, K. Hobson, X. Ji, *Nutrients.* **2020**, *12*, p.684. DOI:10.3390/nu12030684
59. F. Wei, J. W. Locasale, *Trend. Cancer.* **2023**, *9*, 705–706. DOI:10.1016/j.trecan.2023.07.008
60. J. Y. Min, K. S. Chun, D. H. Kim, *Future Oncol.* **2023**, *12*, p. 997919. DOI:10.3389/fonc.2022.997919
61. C. G. de David, Rodrigues, S. Bona, L. Meurer, J. González-Gallego, M. J. Tuñón, N. P. Marroni, *Toxicol. Pathol.* **2011**, *39*, 949–957. DOI:10.1177/0192623311418680
62. T. Akhtar, N. Sheikh, *Toxin Rev.* **2013**, *32*, 43–46. DOI:10.3109/15569543.2013.805144
63. L. Antonio, L. B. Rafael, M. Roberta, *J. Clin. Pathol.* **2022**, *55*, 641–7. DOI:10.1136/jcp.55.9.641
64. M. Domínguez, M. Luján-Hidalgo, D. González-Mendoza, A. Vargas-Díaz, N. Ruiz-Lau, F. Gutiérrez-Miceli, C. Lecona-Guzmán, *Phyton.* **2019**, *88*, p. 139. DOI:10.32604/phyton.2019.06546

## Povzetek

Rak na jetrih še vedno predstavlja velik globalni zdravstveni izziv, saj njegova pojavnost po vsem svetu narašča. Napovedi kažejo, da bo do leta 2040 število obolelih za rakom na jetrih preseglo milijon. Zato so številni raziskovalci motivirani za izboljšanje terapij in razvoj novih zdravil z minimalnimi stranskimi učinki na zdravje ljudi. Naravni izdelki rastlinskega izvora ponujajo različne farmakološke kemijske strukture in biološko aktivne snovi, ki izkazujejo citotoksične učinke na tumorske celice. Pričujoča študija raziskuje potencialne protirakave lastnosti izvlečka cvetov *Fallopia baldschuanica* proti raku, povzročenemu s tioacetamidom (TAA). Študija je natančno opredelila specifične aminokislino v surovem izvlečku, pri čemer je bil najvišji odstotek metionina, sledili so mu cistein, valin, treonin, tirozin, izolevcin in lizin. Aminokislino so pomembne za različne vidike človekovega zdravja in bolezni. Namen te študije je oceniti potencialni vpliv izvlečka cvetov *Fallopia baldschuanica* na regresijo eksperimentalno povzročene HCC pri podganah. Ocene so bile izvedene z merjenjem delovanja jeter, ki vključuje aspartatno aminotransferazo, alanin-transaminazo in alkalno fosfatazo. Poleg tega so bili uporabljeni testi antioksidativnih encimov in tumorskih označevalcev ter histopatološki pregledi, ki so potrdili ugotovitve.



Except when otherwise noted, articles in this journal are published under the terms and conditions of the Creative Commons Attribution 4.0 International License



Scientific paper

# Zinc Metal-Organic Frameworks- Graphene Quantum Dots Nanocomposite Mediated Highly Sensitive and Selective Fluorescence “On-Off-On” Probe for Sensing of Quercetin

Sopan N. Nangare<sup>1</sup>, Premnath M. Sangare<sup>2</sup>, Ashwini G. Patil<sup>3</sup>  
and Pravin O. Patil<sup>2,\*</sup>

<sup>1</sup> Department of Pharmaceutics, H. R. Patel Institute of Pharmaceutical Education and Research, hirpur 425405, Dist: Dhule (MS), India.

<sup>2</sup> Department of Pharmaceutical Chemistry, H. R. Patel Institute of Pharmaceutical Education and Research, Shirpur 425405, Dist: Dhule (MS), India.

<sup>3</sup> Department of Microbiology, R. C. Patel Arts, Commerce and Science College, Shirpur 425405, Dist: Dhule (MS), India.

\* Corresponding author: E-mail: rxpatilpravin@yahoo.co.in

Received: 11-03-2022

## Abstract

The current study presents a fluorescence-based ‘On-Off-On’ nanoprobe composed of rose petal-derived graphene quantum dots embedded in zinc metal-organic frameworks (RP-GQDs@Zn-MOFs) as a proof of concept for quercetin sensing. The particle size and HR-TEM analysis confirmed the synthesis of a uniformly distributed nanosized probe, while the zeta potential (+33.03 mV) verified its good stability. The fluorescence analysis confirmed that the introduction of copper ions (Cu<sup>2+</sup>) resulted in fluorescence quenches, while the inclusion of quercetin forms quercetin-Cu<sup>2+</sup> complex, leading to recovery of quenched fluorescence in RP-GQDs@Zn-MOFs due to static quenching. The nanoprobe demonstrated a wide concentration range and a low detection limit of 100 ng/mL to 1400 ng/mL ( $R^2 = 0.99$ ) and 37.8 ng/mL, respectively. Selectivity analysis highlighted pronounced specificity for quercetin, attributed to Cu<sup>2+</sup> coordination between carbonyl oxygen atom and the 3-OH group of quercetin. Furthermore, designed probe exhibited excellent stability, repeatability (RSD < 5), and potential for real-time analysis.

**Keywords:** Zinc metal-organic frameworks; graphene quantum dots; copper ions; quercetin; high sensitivity; high selectivity

## 1. Introduction

Metal-organic frameworks (MOFs) are preferred for various applications, including biomedical and environmental uses. This preference stems from their distinctive characteristics, such as their ability to modify surfaces, their large surface area, and their adjustable structure.<sup>1</sup> It provides a highly porous structure through the association of metal ions with carefully selected organic linkers via strong bonding.<sup>2</sup> To date, various types of MOFs have been developed for numerous applications, including drug delivery, biosensing, chemical sensing, gas separation, and more.<sup>3,4</sup> At present, they are widely employed for biosensing purposes, offering low detection limits, high sensitivity,

excellent responsiveness, and good stability, among other benefits.<sup>4</sup> Despite these groundbreaking merits, MOFs suffer from major drawbacks, primarily the collapse of their structure and pore shrinkage.<sup>2</sup> As a result, there is a need for complementary nanoparticles that can help overcome these significant drawbacks while preserving the original features of MOFs.

Currently, significant efforts are underway to develop innovative MOFs-centered composites to address the genuine needs of the scientific community. Encapsulating nanosized components within MOFs represents a novel advancement in the biomedical field.<sup>5,6</sup> In this context, it is worth noting that fluorescence-mediated sensing tech-

niques are widely employed due to their several advantages, including a straightforward process, rapid detection, high sensitivity, and specificity compared to previously existing technologies.<sup>7</sup> Furthermore, MOFs are porous frameworks with numerous unsaturated metal coordination sites and superior surfaces, making them suitable hosts for the integration of fluorescent nanomaterials.<sup>8</sup> In this context, various types of fluorescent nanomaterials have been reported for the development of MOFs-based nanocomposites, including carbon dots,<sup>9</sup> graphene quantum dots (GQDs),<sup>10</sup> molybdenum disulfide quantum dots,<sup>11</sup> black phosphorus quantum dots,<sup>12</sup> and more. Among these, fluorescent GQDs have been extensively reported as the latest carbon-mediated nanomaterial for biomedical applications.<sup>13</sup> Interestingly, they offer good stability, consistent fluorescence, biocompatibility, and excellent aqueous solubility, among other qualities.<sup>14</sup> Furthermore, they have been widely favored for numerous biomedical applications, including drug delivery, biosensing,<sup>15</sup> and chemical sensing.<sup>16</sup> The bare, green-synthesized GQDs were used to detect curcumin.<sup>17</sup> In this case, the selective detection mechanism has been unknown. Additionally, it has been conjugated with various types of nanomaterials to achieve highly sensitive and selective recognition of the target analyte.<sup>18,19</sup> The designed nanoprobe based on GQDs and manganese dioxide nanosheets offers a simple, highly sensitive, and selective fluorescent 'Off-On' configuration.<sup>20</sup> In this situation, the primary focus was to maintain the sufficient fluorescence potential of GQDs and the substantial adsorption capacity of the functional material. Therefore, we aim to synthesize new RP-GQDs@Zn-MOFs nanoprobes by decorating RP-GQDs within Zn-MOFs.

Quercetin is a flavonoid primarily found in medicinal plants.<sup>21</sup> It plays a crucial role in accurate pharmacological response and monitoring of biochemical and biological activities.<sup>22</sup> Various recognition methods have been employed for the analysis of quercetin, including high-performance liquid chromatography,<sup>23</sup> fluorescence-centered sensing,<sup>22</sup> electroanalytical methods, and electrophoresis.<sup>21</sup> Despite the numerous advantages, there are several drawbacks, including the cost factor, and the need for larger equipment, expertise, and solvents. Furthermore, there is a desire to enhance the sensor's sensitivity and selectivity.

In this study, our objective was to design a new RP-GQDs@Zn-MOFs fluorescence-based sensor through a simple method and demonstrate its utility in sensing quercetin as a proof of concept. In brief, this work involved synthesizing Zn-MOFs using zinc ions ( $Zn^{2+}$ ) as the metal source and 2-methyl-1*H*-imidazole as an organic linker. Simultaneously, we focused on synthesizing RP-GQDs using rose petal waste. By combining the desirable fluorescence potential of RP-GQDs and the substantial adsorption capability of Zn-MOFs, we aimed to create new RP-GQDs@Zn-MOFs nanoprobes through the incorporation of RP-GQDs onto Zn-MOFs. To enhance selectivity

for the target analyte, we developed a quenched version of the  $Cu^{2+}$ -RP-GQDs@Zn-MOFs probe, utilizing copper ions ( $Cu^{2+}$ ) to confer specificity. Ultimately, our research aimed to evaluate the performance of the quenched  $Cu^{2+}$ -RP-GQDs@Zn-MOFs probe, prepared by combining RP-GQDs and Zn-MOFs, for the sensitive, specific, simple, rapid, and cost-effective detection.

## 2. Materials and Methods

### 2.1. Materials

Rose petal waste was collected from a local market in Shirpur, Maharashtra, India. Zinc dinitrate hexahydrate (molecular formula:  $H_{12}N_2O_{12}Zn$ ), and 2-methyl-1*H*-imidazole (molecular formula:  $C_4H_6N_2$ ) were purchased from Loba Chemie Pvt. Ltd., Mumbai, India. Copper dinitrate was purchased from Sigma-Aldrich Chemicals Pvt. Ltd., Bangalore, India. Sodium hydroxide (NaOH) was supplied from Merck Specialties Pvt. Ltd., Mumbai, India. Methanol was purchased from Loba Chemie Pvt. Ltd., Mumbai, India. Sulphuric acid was purchased from Merck Specialties Pvt. Ltd., Mumbai, India. Quercetin was obtained from Otto Chemicals in Marine Lines, Mumbai, India. Ethanol was purchased from Anil Cottage Industries, A/31, M.I.D.C., Wardha, India. Also, the HPLC grade deionized water (DI, 0.2  $\mu m$  filtered) and hydrochloric acid (HCl) were purchased from Avantor Performance Materials India Ltd., Thane, India. Quinine sulfate (99%) was purchased from Loba Chemie Pvt. Ltd., Mumbai, India. Phosphate buffer tablets (pH 7.4) were obtained from Loba Chemie Pvt. Ltd., Mumbai, India. All chemicals employed in the research study were analytical grade and pure, as supplied by the distributor.

### 2.2. Methods

#### 2.2.1. Synthesis of RP-GQDs using the Green Approach

At the outset, abandoned rose petals were acquired from a local market and cut into small fragments before being ground into a paste using a mortar and pestle. The creation of RP-GQDs from these discarded rose petals was achieved using a one-pot hydrothermal technique. To summarize, 10 g of the rose petal paste was homogenized with 50 mL of distilled water (DI water) and sonicated for 20 min. The resulting dispersion was then transferred into a Teflon-lined autoclave and heated for 10 h at 200 °C. After the reaction, the slurry was cooled to room temperature. To obtain a uniform dispersion, the resulting dark brown dispersion was ultrasonicated for 10 min. Subsequently, the dispersion was passed through a 0.22  $\mu m$  microporous membrane to remove any insoluble or untreated carbonous elements. The resulting filtrate was retained for 36 h and subjected to rinsing using a dialysis bag (12,000 kDa). Afterwards, the outer dispersion was collected and

processed in a hot air oven (Bio-Technics, India) at 60 °C for 24 h.<sup>4</sup> Finally, the photoluminescence spectrum analysis of the obtained RP-GQDs was conducted.

## 2. 2. 2. Synthesis of Zn-MOFs

We adopted the previously published strategy for the fabrication of Zn-MOFs.<sup>24,25</sup> To begin, 2 g of zinc dinitrate hexahydrate (as the source of metal ions) was evenly mixed in 10 mL of distilled water (DI water) at 50 rpm. Simultaneously, at room temperature, 4 g of 2-methyl-1*H*-imidazole (the organic linker) was dissolved in 10 mL of DI water. The zinc solution was then combined with the 2-methyl-1*H*-imidazole solution while continuously stirring at 100 rpm. All procedures were carried out at 20 °C. Subsequently, a milky precipitate formed, indicating the formation of Zn-MOFs. Afterwards, the Zn-MOFs precipitate was centrifuged and washed three times with DI water. Finally, the drying of Zn-MOFs was achieved using a laboratory hot air oven (Bio-Technics, India) at 60 °C. The photoluminescence spectra of the resulting Zn-MOFs were then analyzed.

## 2. 2. 3. Development of RP-GQDs@Zn-MOFs

In this phase, we employed various diluted concentrations of Zn-MOFs to assess the impact on the strong fluorescence of RP-GQDs. Fluorescence spectra of RP-GQDs were recorded using an excitation wavelength of 330 nm. Subsequently, 10 ppm solutions of Zn-MOFs in phosphate-buffered saline (PBS) at pH 7.4 were prepared for the fabrication of the RP-GQDs@Zn-MOFs probe. Different concentrations of Zn-MOFs were individually added to 1.5 mL of RP-GQDs to optimize the overall fluorescence of the probe. The fluorescence change of RP-GQDs was assessed after 5 min. Finally, the concentration of Zn-MOFs used for constructing the RP-GQDs@Zn-MOFs fluorescence nanoprobe was determined. For this purpose, a physical absorption technique was employed to synthesize the RP-GQDs@Zn-MOFs probe. Specifically, 1.5 mL of RP-GQDs and 0.5 mL of pre-synthesized Zn-MOFs (10 ppm) were combined and magnetically stirred for 15 min. To separate the nanoconjugates, the resulting mixture was centrifuged at 15,000 rpm for 45 min using a refrigerated centrifuge (Etek Overseas Pvt., India), and then washed four times with ethanol to remove unreacted species. To examine the variation in fluorescence intensity, we conducted a photoluminescence spectrum analysis of the resulting RP-GQDs@Zn-MOFs probe.

## 2. 2. 4. Spectroscopical Characterization

Ultraviolet-visible (UV-Vis) spectroscopy was employed to confirm the synthesis of RP-GQDs, Zn-MOFs, and RP-GQDs@Zn-MOFs using a UV-Vis Spectrophotometer (UV 1800 Shimadzu, Japan) with a scanning

wavelength range of 200 nm to 800 nm, utilizing a quartz cuvette (1 cm). The fluorescence behavior of RP-GQDs, Zn-MOFs, and RP-GQDs@Zn-MOFs was observed within a laboratory UV cabinet (Southern Scientific Lab Instruments, Chennai, India) under different lighting conditions, including visible light, short UV (wavelength: 254 nm), and long UV (wavelength: 365 nm). Excitation spectra, emission spectra, and sensing were performed using a Jasco fluorescence spectrophotometer (FP-8200). Subsequently, Fourier transform infrared spectroscopy (FTIR, IR-Affinity-1, Shimadzu) was utilized to investigate the surface functionality of the synthesized RP-GQDs, Zn-MOFs, and RP-GQDs@Zn-MOFs over a scanning wavelength range from 400 cm<sup>-1</sup> to 4000 cm<sup>-1</sup>. Particle size, polydispersity index, and zeta potential analysis were conducted using a Particle size analyzer (Nanoplus 3, Micromeritics, USA). The powder X-ray diffraction (PXRD) analysis of RP-GQDs, Zn-MOFs, and RP-GQDs@Zn-MOFs was conducted using an X-ray diffractometer (D2 PHASER). The dimensions and selected area diffraction (SAED) pattern of RP-GQDs, Zn-MOFs, and RP-GQDs@Zn-MOFs were confirmed through high-resolution transmission electron microscopy (HR-TEM-SAED, Jeol/JEM 2100) utilizing a LaB6 light source at 200kV (STIC Cochin, India).

## 2. 2. 5. Fluorescence Study and Quantum Yield (% QY)

In this case, we measured the fluorescence intensity of the synthesized RP-GQDs, Zn-MOFs, and RP-GQDs@Zn-MOFs probe using a spectrofluorometer (JASCO FP 8200 Spectrofluorometer). Additionally, we assessed the excitation-emission spectrum of the produced RP-GQDs, as well as the photoluminescence behavior of the RP-GQDs at different excitation wavelengths ranging from 300 nm to 350 nm. Following these measurements, we determined the % QY (quantum yield) of RP-GQDs using the previously reported method.<sup>4</sup> In brief, quinine sulfate (with a known quantum yield, QY = 0.54, in 0.1 M sulfuric acid) served as the reference standard. Simultaneously, RP-GQDs were dissolved in deionized (DI) water, and their concentrations were adjusted to achieve a UV absorbance value of less than 0.1. For the analysis, a 10 mm cuvette was utilized, and slit widths were set at 5 nm for both excitation and emission. Finally, the fluorescence emission spectra of the standard and RP-GQDs were measured at an excitation wavelength of 330 nm. The following formula (1) was employed for calculating the % QY.

$$QY_s = QY_r \frac{I(Ar)ns^2}{I_r(As)nr^2} \quad (1)$$

Wherein, 'QY<sub>s</sub>' and 'QY<sub>r</sub>' represent the quantum yields of the sample and the standard reference, respectively. Similarly, 'I<sub>s</sub>' and 'I<sub>r</sub>' denote the unified photoluminescence intensities of the sample and the reference standard. 'Ar' and 'As' correspond to the absorbance values, while

'nr' and 'ns' signify the refractive indices of the reference and the sample, respectively.

## 2. 2. 6. Sensing of Quercetin

In this study, we measured the changes in fluorescence of RP-GQDs, Zn-MOFs, and RP-GQDs@Zn-MOFs using a spectrofluorometer. Subsequently, we executed the detection of quercetin using a fluorescent RP-GQDs@Zn-MOFs probe. In essence, we prepared a stock solution of 5 mg of quercetin (50 µg/mL) by dissolving it in a volumetric flask containing 100 mL of deionized (DI) water (at 18 °C). Using this stock solution, we created different concentrations of quercetin, ranging from 100 ng/mL, 200 ng/mL, 300 ng/mL, 400 ng/mL, 500 ng/mL, 600 ng/mL, 700 ng/mL, 800 ng/mL, 900 ng/mL, 1000 ng/mL, 1100 ng/mL, 1200 ng/mL, 1300 ng/mL and 1400 ng/mL in cleaned volumetric flasks (n = 3). Meanwhile, we dissolved 10 mg of RP-GQDs@Zn-MOFs fluorescent probe in 100 mL of DI water. Next, we assessed the fluorescence intensity of the designed probe at an excitation wavelength of 330 nm (n = 3). For this work, we adopted the Cu<sup>2+</sup>-Zn-MOFs@RP-GQDs probe as a new sensory platform. In this case, we evaluated different concentrations of Cu<sup>2+</sup> (ranging from 0.1 mL, 0.2 mL, 0.3 mL, 0.4 mL, 0.5 mL, 0.6 mL, 0.7 mL, 0.8 mL, 0.9 mL, 1.0 mL, 1.1 mL, and 1.2 mL of a 0.16 mM Cu<sup>2+</sup> solution) as quenching agents to suppress the fluorescent ability of the Zn-MOFs@RP-GQDs, leading to a fluorescent "Turn-Off" effect (n = 3). Following this, the concentration of Cu<sup>2+</sup> ions at which the RP-GQDs@Zn-MOFs probe fluorescence was completely quenched was considered the optimized concentration of Cu<sup>2+</sup> ions. Subsequently, several RP-GQDs@Zn-MOFs probes were designed as a sensory platform for the recognition of quercetin, with fluorescence quenching being ensured for each probe, separately (n = 3). In brief, the probes were prepared in individual test tubes containing 1.2 mL of a 0.16 mM Cu<sup>2+</sup> ion solution and left for 5 min at 25 °C. The first probe was then incubated with a 100 ng/mL concentration of quercetin to initiate complex formation between Cu<sup>2+</sup> ions and quercetin. In this step, the recovery of the quenched fluorescence of RP-GQDs@Zn-MOFs referred to as "Turn-On," was monitored. The fluorescence intensity was measured using optimized parameters at an excitation wavelength of 330 nm. The same procedure was applied to the other prepared quercetin concentrations (samples), each time with a fresh Cu<sup>2+</sup>-RP-GQDs@Zn-MOFs probe. Each experiment was performed in triplicate to confirm their reproducibility. Finally, the linear concentration range was determined by plotting the recovered probe fluorescence against quercetin concentration. Additionally, the limit of detection (LOD) and limit of quantification (LOQ) were computed using previously described methods and formulas (2) and (3).

$$\text{LOD: } 3.3\sigma/m \quad (2)$$

$$\text{LOQ: } 10\sigma/m \quad (3)$$

In this context, 'm' (slope) and 'σ' (standard deviation) were obtained from the calibration curve of quercetin concentration (ng/mL) vs. the recovery of fluorescent intensity of the quenched RP-GQDs@Zn-MOFs probe.

Stability and repeatability are crucial parameters for this sensor. Therefore, the stability of the envisioned RP-GQDs@Zn-MOFs fluorescent probes was assessed. Specifically, the concentration of quercetin at 600 ng/mL for six consecutive days was recorded using a manufactured probe (n = 6) under laboratory-programmed parameters at 25 °C. Subsequently, the efficiency of the sensory system was evaluated and computed the percent relative standard deviation (% RSD). Furthermore, the repeatability of the probe for the detection of quercetin was investigated using the RP-GQDs@Zn-MOFs probe (n = 9), with quercetin concentrations set at 500 ng/mL for assessment. Finally, the percent RSD was calculated based on the collected responses.

## 2. 2. 7. Interference Study and Spiked Sample Analysis

In this study, plasma served as the representative sample. In brief, the various potential interfering agents were selected based on the composition of plasma to evaluate the selectivity of the designed RP-GQDs@Zn-MOFs fluorescence probe. Additionally, other interfering agents were randomly chosen for confirmation. In summary, we tested the selectivity of the RP-GQDs@Zn-MOFs fluorescence probe towards quercetin in the presence of several interfering chemicals, including ascorbic acid, glucose, albumin, potassium (K<sup>+</sup>), magnesium (Mg<sup>2+</sup>), calcium (Ca<sup>2+</sup>), sodium (Na<sup>+</sup>), citric acid, ascorbic acid, glycine, and others. To do this, 2 mL of the Cu<sup>2+</sup>-RP-GQDs@Zn-MOFs probe was incubated with 600 ng/mL of quercetin, while different interfering elements (600 ng/mL) were introduced separately to the Cu<sup>2+</sup>-RP-GQDs@Zn-MOFs probe in individual test tubes. The concentration of interfering agents remained constant to assess their effects at the same concentration as quercetin. Subsequently, we evaluated the fluorescence intensity for each sample using preprogrammed settings. Also, spiked sample analysis of quercetin in artificial plasma was performed using the Cu<sup>2+</sup>-RP-GQDs@Zn-MOFs probe. In this procedure, an artificial plasma sample was prepared using a previously described method.<sup>26</sup> Afterwards, 1000 ng/mL of quercetin was added into a test tube containing 1 mL of artificial plasma sample (n = 3). Simultaneously, a placebo test tube containing only 1 mL of artificial plasma sample was prepared. Then the 500 ng/mL quercetin-containing plasma sample was added to 2 mL of Cu<sup>2+</sup>-RP-GQDs@Zn-MOFs probe. The test tube was allowed to sit for 5 min, after which the fluorescence intensity of the Cu<sup>2+</sup>-RP-GQDs@Zn-MOFs probe was monitored under optimized conditions. Finally, the percent recovery of quercetin and %

RSD was calculated to confirm the real-time applicability of the proposed  $\text{Cu}^{2+}$ -RP-GQDs@Zn-MOFs probe.

## 3. Results and Discussion

### 3.1. UV Cabinet Fluorescence Study

RP-GQDs were initially synthesized from rose petal waste using a hydrothermal technique in a stainless steel Teflon line reactor. Subsequently, the resulting RP-GQDs were analyzed for fluorescence within a UV cabinet. RP-GQDs exhibited a yellow color under visible light (Figure 1A), greenish fluorescence when excited with 254 nm light (Figure 1B), and blue fluorescence when excited with 365 nm light (Figure 1C). This observation supported the successful synthesis of carbon-centered RP-GQDs from rose petal waste. Furthermore, the fluorescence capacity of the Zn-MOFs diminished under various UV lights, indicating that Zn-MOFs lacked fluorescence capabilities. However, the final product of the RP-GQDs@Zn-MOFs probe exhibited fluorescence properties similar to RP-GQDs (Figure 1D). The presence of blue fluorescence under UV light with an excitation wavelength of 365 nm in RP-GQDs@Zn-MOFs confirmed the successful encapsulation of RP-GQDs within Zn-MOFs without compromising the fluorescence behavior of RP-GQDs.

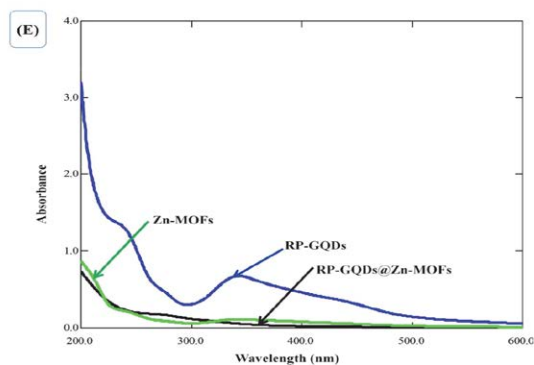
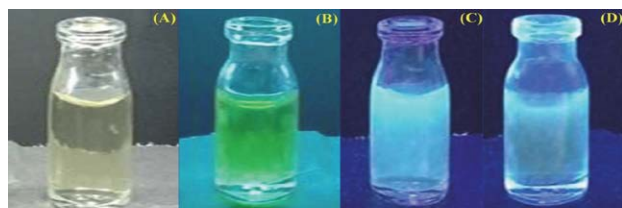


**Figure 1:** Photographs of RP-GQDs under visible light (A), UV light with  $\lambda_{\text{Ex}}$  254 nm (B), and  $\lambda_{\text{Ex}}$  365 nm (C) taken inside a UV cabinet. (D) Photographs of the RP-GQDs@Zn-MOFs probe under UV light with  $\lambda_{\text{Ex}}$  365 nm in the UV cabinet. (E) UV spectral analysis of RP-GQDs, Zn-MOFs, and the RP-GQDs@Zn-MOFs probe.

### 3.2. UV Vis Spectroscopy

The UV-Vis spectra of RP-GQDs, Zn-MOFs, and RP-GQDs@Zn-MOFs are presented in Figure 1E. In these spectra, RP-GQDs exhibit a prominent absorption peak

ranging from 238 nm to 341.50 nm, which supports the  $\pi \rightarrow \pi^*$  transition of  $\text{sp}^2$  C=O bonds and the  $n \rightarrow \pi^*$  transition of C=O bonds, respectively.<sup>27</sup> This observation suggests that RP-GQDs are derived from rose petal waste and possess carboxylic functionality on the surface of RP-GQDs. The UV-Vis absorption spectra of Zn-MOFs exhibit a peak at 239 nm, confirming the successful synthesis of Zn-MOFs, which is consistent with previously reported literature.<sup>24</sup> The final composite, RP-GQDs@Zn-MOFs, displays a broadened absorption spectrum. In this case, the absorption peak intensities of both RP-GQDs and Zn-MOFs were observed to decrease, possibly indicating efficient encapsulation of RP-GQDs within the Zn-MOFs structure.<sup>25</sup> Ultimately, this confirms the successful fabrication of RP-GQDs utilizing Zn-MOFs as a fluorescent detector for precise target measurements as a proof of concept.

### 3.3. Fluorescence Study and % QY Measurement

The excitation and emission spectra of RP-GQDs were measured using a spectrofluorometer at various excitation wavelengths ranging from 290 nm to 360 nm under controlled experimental conditions, including a temperature of 25 °C. The photoluminescence ability of green-synthesized RP-GQDs, dependent on excitation wavelength (ranging from 310 nm to 350 nm), is illustrated in Figure 2A. Initially, excitation wavelengths from 310 nm to 330 nm resulted in a shift of the emission peak towards longer wavelengths (from 429 nm to 492 nm). Additionally, there was an increase in emission peak intensity up to an excitation wavelength of 330 nm. Surprisingly, a strong emission peak at 492 nm was observed with an excitation wavelength of 330 nm. Furthermore, as the excitation wavelength increased, the peak emission intensity decreased from 340 nm to 350 nm. Overall, the photoluminescence of the obtained RP-GQDs was found to be dependent on the excitation wavelength. In this study, the excitation and emission spectra for green-processed GQDs were reported at 288 nm and 492 nm, respectively (Figure 2B). Subsequently, RP-GQD QY were calculated to be 18.20%. In conclusion, the excellent optical properties of RP-GQDs synthesized using the green method were confirmed. Figure 2C depicts a comparison of the fluorescence behavior of RP-GQDs, Zn-MOFs, and RP-GQDs@Zn-MOFs. In this case, Zn-MOFs displayed the absence of fluorescence. Conversely, the obtained RP-GQDs exhibited strong fluorescence at 492 nm. Importantly, the conjugation of Zn-MOFs and RP-GQDs did not significantly alter the fluorescence behavior of RP-GQDs. Hence, it validates the development of the fluorescence-based RP-GQDs@Zn-MOFs probe.

### 3.4. FT-IR Spectroscopy

Figure 3 displays the FT-IR spectrum of RP-GQDs, Zn-MOFs, and RP-GQDs@Zn-MOFs. In this case, the use

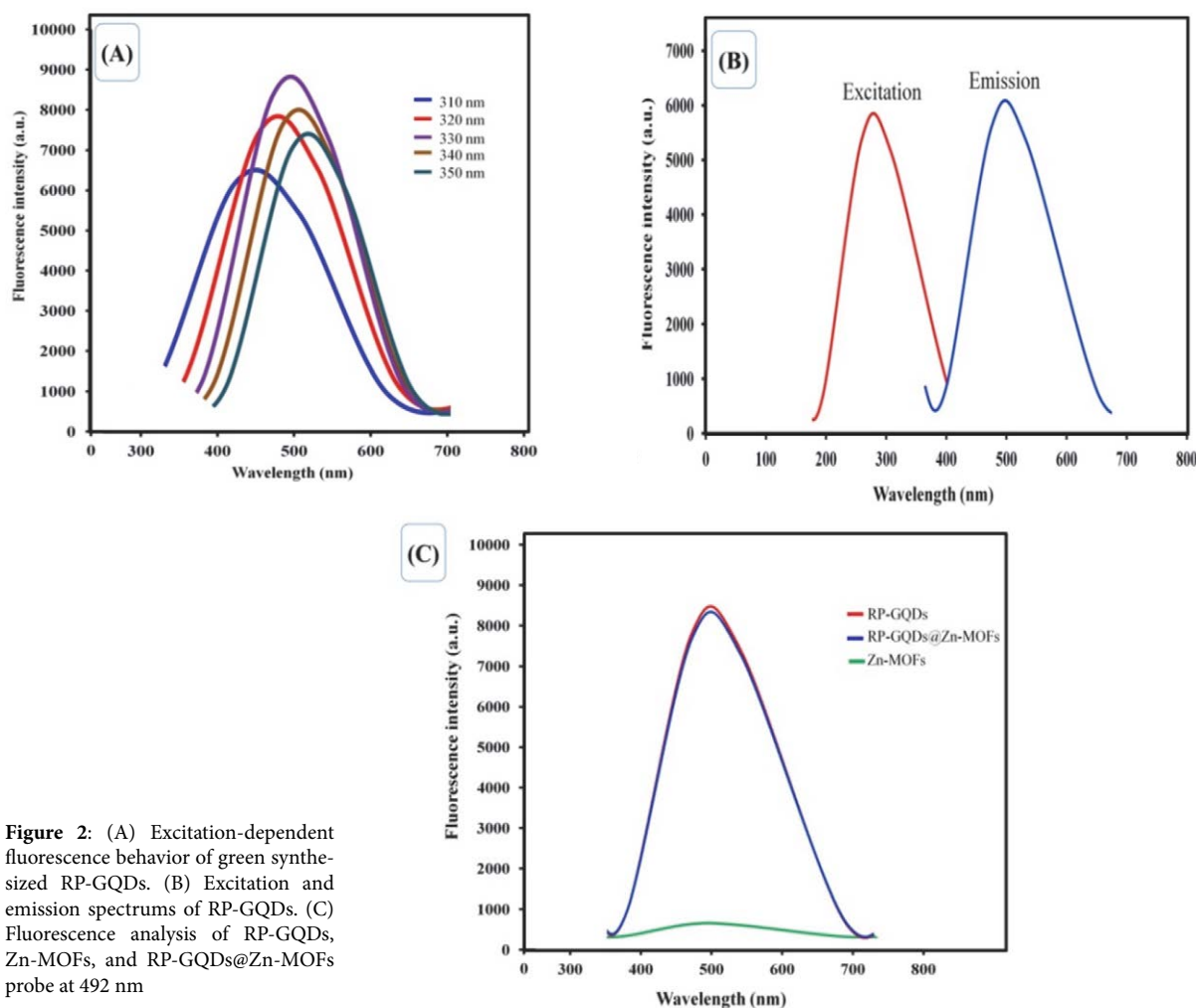


**Figure 2:** (A) Excitation-dependent fluorescence behavior of green synthesized RP-GQDs. (B) Excitation and emission spectrums of RP-GQDs. (C) Fluorescence analysis of RP-GQDs, Zn-MOFs, and RP-GQDs@Zn-MOFs probe at 492 nm

of FT-IR for RP-GQDs and Zn-MOFs aids in the characterization of the RP-GQDs@Zn-MOFs probe. The FT-IR spectrum of RP-GQDs exhibits peaks at  $3403.57\text{ cm}^{-1}$ ,  $1637.6\text{ cm}^{-1}$ , and  $1079.14\text{ cm}^{-1}$ , respectively, indicating the presence of -OH, C=O, and C-O functionalities.<sup>28</sup> This confirms the presence of hydroxylic and carboxylic functionality in RP-GQDs, ensuring good solubility in water. The FT-IR spectrum of Zn-MOFs shows peaks at  $2931\text{ cm}^{-1}$  and  $2864\text{ cm}^{-1}$ , verifying the presence of the C-H stretching mode of the aromatic ring and aliphatic chain present in 2-methyl-1H-imidazole. Additionally, the peaks at  $1089\text{ cm}^{-1}$  and  $1434\text{ cm}^{-1}$  confirm the presence of imidazole ring-related stretching and bending modes. Finally, the peak at  $1600\text{ cm}^{-1}$  assures the existence of the C-N stretching mode in 2-methyl-1H-imidazole, while the broad peak at  $3220\text{ cm}^{-1}$  verifies the presence of -OH stretching in Zn-MOFs, which may be due to the presence of water content. In the case of the RP-GQDs@Zn-MOFs probe, the peak at  $3312\text{ cm}^{-1}$  confirms the presence of OH stretching in RP-GQDs, while the peaks at  $2931\text{ cm}^{-1}$  and  $2864\text{ cm}^{-1}$  verify the presence of the C-H stretching mode of the aromatic ring and aliphatic chain present in the link-

er of Zn-MOFs. Additionally, the peaks at  $1664\text{ cm}^{-1}$  and  $1093\text{ cm}^{-1}$  indicate the presence of C=O and C-O stretching, which are characteristics of RP-GQDs, while the peak

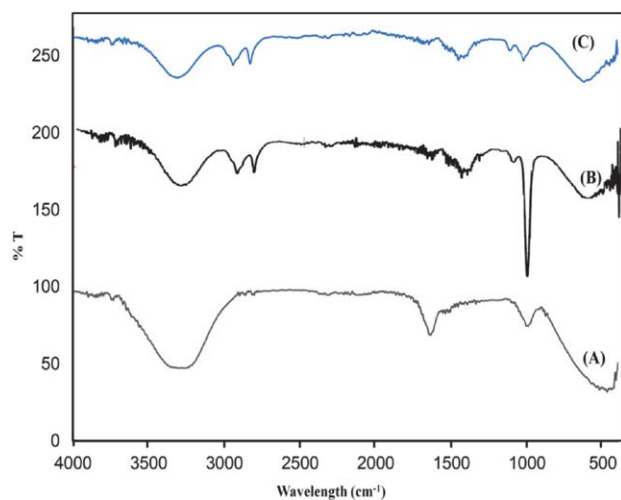


**Figure 3:** FTIR of (A) RP-GQDs, (B) Zn-MOFs, and (C) RP-GQDs@Zn-MOFs probe

at  $1584\text{ cm}^{-1}$  assures the presence of the C-N stretching mode in 2-methyl-1*H*-imidazole. Therefore, this confirms the formation of RP-GQDs embedded in Zn-MOFs, constituting the RP-GQDs@Zn-MOFs probe.

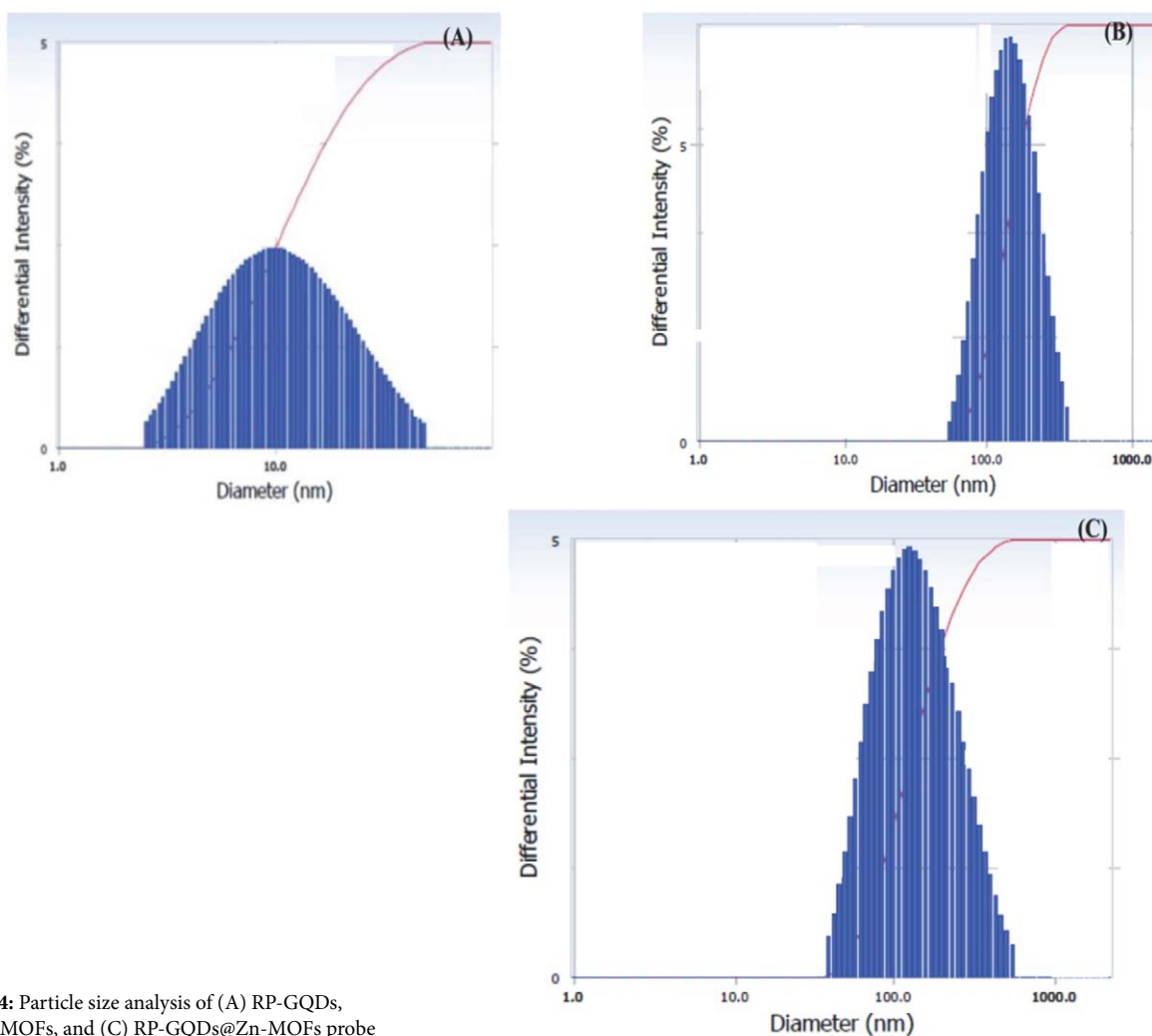
### 3. 4. Particle Size and Zeta Potential Analysis

Figure 4 presents the particle size distribution of RP-GQDs, Zn-MOFs, and the RP-GQDs@Zn-MOFs probe. To summarize, the particle size of the obtained RP-GQDs was estimated to be 10.80 nm, and the polydispersity index (PDI) was found to be 0.32. This confirms the production of nanosized GQDs in water with a uniform distribution in the system. In Figure 4B, the particle size of Zn-MOFs is represented, with the average diameter and PDI confirmed as 141.20 nm and 0.26, respectively. The average diameter and PDI of the final RP-GQDs@Zn-MOFs probe were observed to be 158.23 nm and 0.36, respectively. HR-TEM analysis was conducted to verify the precise dimensions of RP-GQDs, Zn-MOFs, and the RP-GQDs@Zn-MOFs probe. Zeta potential analysis was performed to assess stability. Figure 5 illustrates the zeta potential analysis

of RP-GQDs, Zn-MOFs, and the RP-GQDs@Zn-MOFs probe. Due to the presence of oxygen functionality on the surface of RP-GQDs, the zeta potential was confirmed to be  $-14.82\text{ mV}$ , indicating excellent stability of nanosized RP-GQDs in an aqueous environment and the potential for interaction with  $\text{Zn}^{2+}$  ions from Zn-MOFs.<sup>29</sup> As a result of  $\text{Zn}^{2+}$  ions, the zeta potential of Zn-MOFs was confirmed to be  $+41.32\text{ mV}$ . Finally, the zeta potential of the RP-GQDs@Zn-MOFs probe was reported to be  $+33.03\text{ mV}$ , lower than that of the naked Zn-MOFs in this study, possibly due to interactions between Zn-MOFs and RP-GQDs. In conclusion, this confirms the construction of a stable form of RP-GQDs, Zn-MOFs, and the RP-GQDs@Zn-MOFs probe.

### 3. 5. PXRD Analysis

Figure 6 represents the diffractogram of RP-GQDs, Zn-MOFs, and the RP-GQDs@Zn-MOFs probe. In brief, the diffractogram of RP-GQDs shows a sharp diffraction peak at  $2\theta = 10.59^\circ, 12.83^\circ, 14.84^\circ, 16.73^\circ, 18.12^\circ, 24.75^\circ, 26.74^\circ, 29.92^\circ, 35.08^\circ, 36.65^\circ$ , etc. confirming that the ob-



**Figure 4:** Particle size analysis of (A) RP-GQDs, (B) Zn-MOFs, and (C) RP-GQDs@Zn-MOFs probe

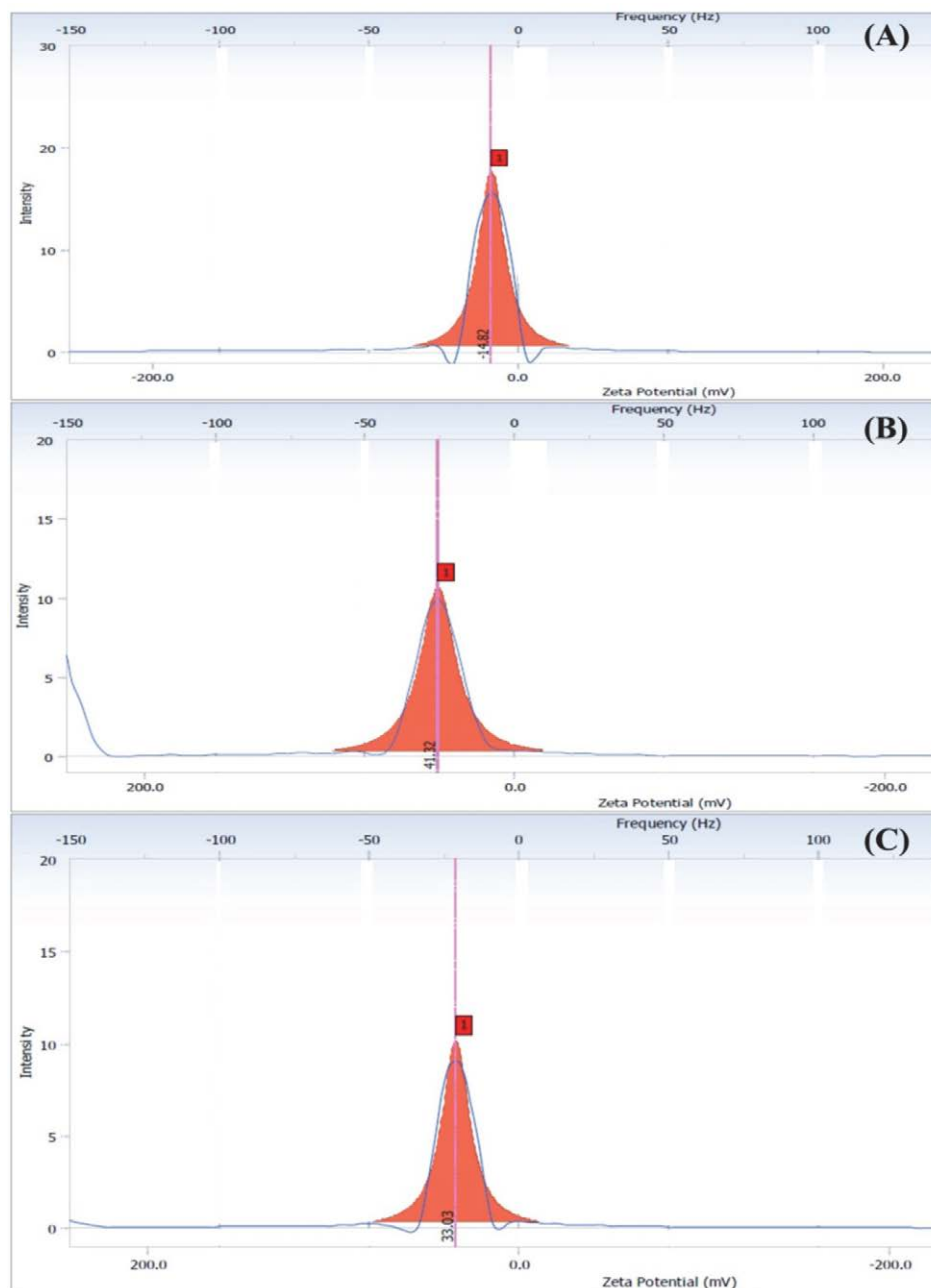


Figure 5: Zeta analysis behavior of (A) RP-GQDs, (B) Zn-MOFs, and (C) RP-GQDs@Zn-MOFs probe

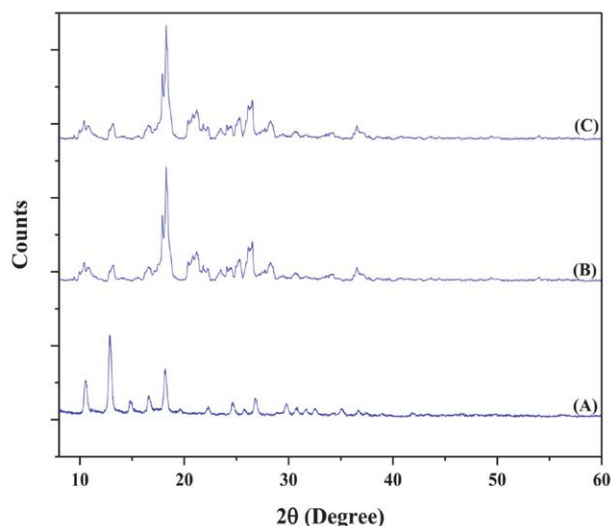
tained RP-GQDs are highly crystalline. Similarly, both the Zn-MOFs and RP-GQDs@Zn-MOFs probe exhibit sharp diffraction peaks at  $2\theta = 10.47^\circ, 13.23^\circ, 16.75^\circ, 18.24^\circ, 21.20^\circ, 23.58^\circ, 25.35^\circ, 26.56^\circ, 28.43^\circ, 30.57^\circ, 33.89^\circ,$  and  $36.54^\circ$  confirming the formation of a crystalline form of Zn-MOFs in both cases. Furthermore, the diffractogram of the RP-GQDs@Zn-MOFs probe only shows characteristic peaks of Zn-MOFs, with no discernible peaks from RP-GQDs.<sup>30</sup> It is possible that the incorporation of RP-GQDs into the framework of Zn-MOFs, where the surface carboxylic functionality of RP-GQDs may interact with the amine functionality of 2-methyl-1*H*-imidazole (the

organic linker).<sup>31</sup> Additionally, the fact that there was no change in the diffractogram of Zn-MOFs after conjugation with RP-GQDs confirms the probe stability.

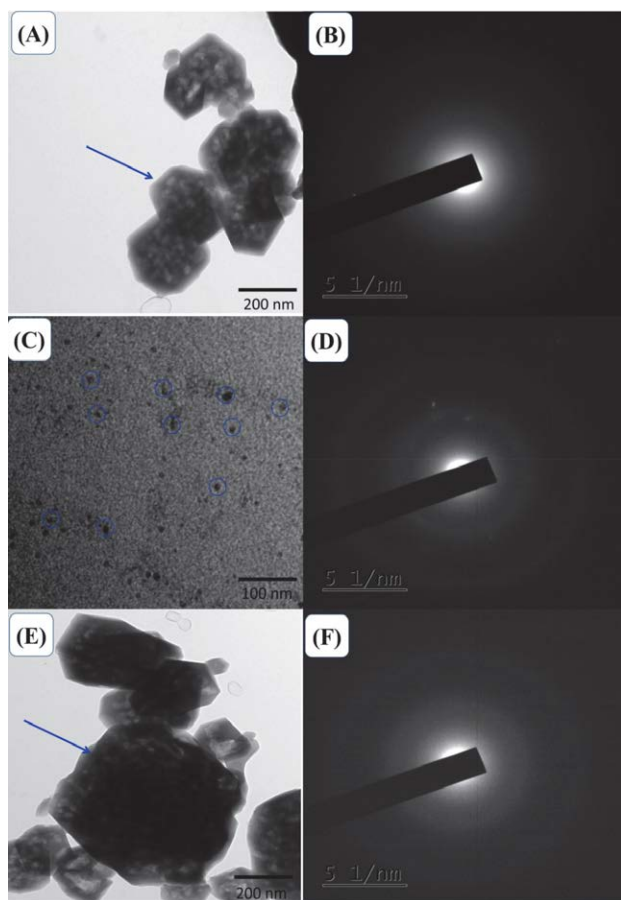
### 3. 6. HR-TEM Analysis

Figure 7 presents the HR-TEM images and SAED patterns of RP-GQDs, Zn-MOFs, and the RP-GQDs@Zn-MOFs probe. In essence, RP-GQDs were found to exhibit a spherical shape with a uniform distribution. The average diameter of RP-GQDs was measured to be 8.68 nm,





**Figure 6:** Diffractogram of (A) RP-GQDs, (B) Zn-MOFs, and (C) RP-GQDs@Zn-MOFs probe



**Figure 7:** HR-TEM images and SAED pattern of (A, B) RP-GQDs, (C, D) Zn-MOFs, and (E, F) RP-GQDs@Zn-MOFs probe, respectively

confirming the synthesis of nanoscale GQDs from a green precursor. The HR-TEM image of Zn-MOFs displayed a hexagonal form, with an average diameter of 210.12 nm.<sup>32</sup>

The surface morphology of the RP-GQDs@Zn-MOFs probe closely resembles that of the Zn-MOFs, with an average diameter of 226.98 nm. This observation is crucial as it confirms the successful assembly of the RP-GQDs@Zn-MOFs probe without any disruption of the Zn-MOF frameworks. Finally, the selected area electron diffraction (SAED) patterns of Zn-MOFs, RP-GQDs, and the RP-GQDs@Zn-MOFs probe indicate their polycrystalline nature.

### 3. 7. Sensing of Quercetin

To detect quercetin, a stable and nanosized RP-GQDs@Zn-MOFs probe was created, wherein zinc ( $Zn^{2+}$ ) ions and carboxylic ions engage in a charge-charge interaction, effectively linking the RP-GQDs and Zn-MOFs. Additionally, hydrogen bonding interactions involving RP-GQDs with carboxyl, epoxy, and hydroxyl groups, as well as Zn-MOFs with amine functionality of 2-methyl-1*H*-imidazole, contribute to the formation of the RP-GQDs@Zn-MOFs probe (Turn-On). In this configuration, the developed probe exhibits fluorescence behavior. This probe was employed for sensing quercetin, with  $Cu^{2+}$  ions chosen as a quenching agent (Figures 8 A and B). In this scenario, the fluorescence property of the RP-GQDs@Zn-MOFs probe was observed to decrease (Turn-Off) upon the addition of  $Cu^{2+}$  ions, likely due to the formation of a complex between  $Cu^{2+}$  ions and RP-GQDs@Zn-MOFs ( $Cu^{2+}$ -RP-GQDs@Zn-MOFs). Subsequently, the introduction of quercetin led to the restoration of fluorescence in the  $Cu^{2+}$ -RP-GQDs@Zn-MOFs complex (Figures 8 C and D), indicating a proportional relationship between quercetin concentration and the recovered probe fluorescence (referred to as “Turn-On”). This provided a linear concentration range of 100 ng/mL to 1400 ng/mL ( $Y = 4.2x + 777.8$ ,  $R^2 = 0.99$ ). Additionally, the LOD and LOQ were determined to be 37.8 ng/mL and 114.7 ng/mL, respectively. Table 1 summarizes various types of sensors for the detection of quercetin. In summary, the utilization of sulfur-doped GQDs as a fluorescent sensor for the detection of quercetin requires a thorough discussion of sensitivity and selectivity.<sup>22</sup> The development of modern electrodes is essential for designing electrochemical sensors, and it is equally important to thoroughly discuss the selectivity study for quercetin. Additionally, a comprehensive exploration of the impact of current/voltage is necessary.<sup>33,34</sup> Similarly, the importance of selecting modified MOFs<sup>35</sup> as well as the use of carbon nanoparticles<sup>36</sup> should not be understated. However, it's crucial to note that the discussion should include specific details about their impact on selectivity and sensitivity analysis for quercetin detection. In the present work, it is confirmed that the designed nanoprobe offers a wide linear range and a low LOD. Interestingly, due to the coordination of quercetin with its 3-OH functionality (B ring) and 4-carbonyl groups (B ring) with  $Cu^{2+}$  ions, the addition of quercetin demonstrates signifi-

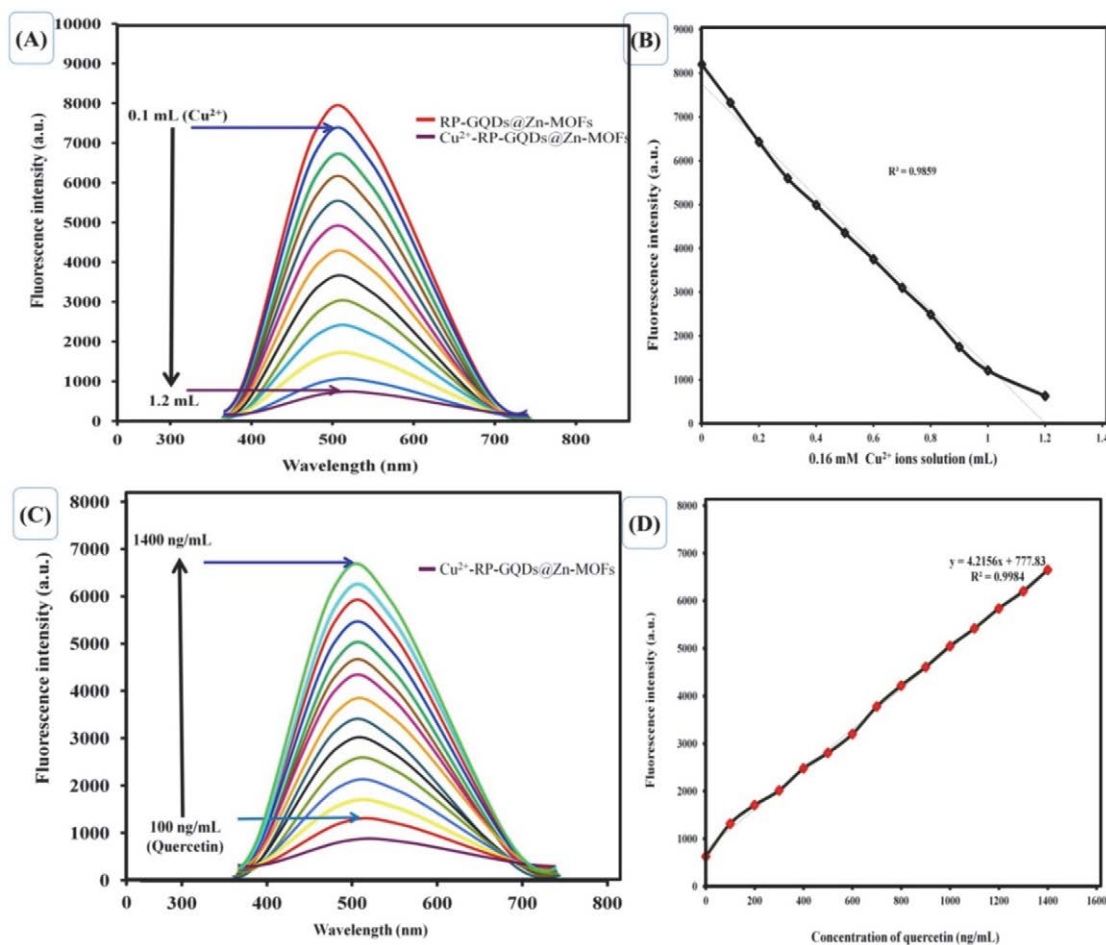


**Figure 8:** (A) Depicts the fluorescence quenching spectra of RP-GQDs@Zn-MOFs in the presence of  $\text{Cu}^{2+}$  ions. (B) Presents a graphical representation of the quenched fluorescence of the RP-GQDs@Zn-MOFs probe plotted against the concentration of  $\text{Cu}^{2+}$  ions. (C) Shows the fluorescence spectra of the  $\text{Cu}^{2+}$ -RP-GQDs@Zn-MOFs probe with varying concentrations of quercetin (ranging from 100 ng/mL to 1400 ng/mL). (D) Provides a graphical representation illustrating the relationship between quercetin concentration and the recovered fluorescence of the RP-GQDs@Zn-MOFs probe.

cant selectivity towards  $\text{Cu}^{2+}$  ions. In this context, 3-OH, with its more acidic proton, and 4-carbonyl groups are the preferred sites for complex formation. On the other hand, the 'C' ring, which contains 3'-OH and 4'-OH functionality, serves as the second site for complex formation. Additionally, the steric barrier of the first choice complex, combined with the lower proton acidity of 5-OH functionality, makes them non-reactive sites in quercetin sensing. Figure

9A illustrates the detection of quercetin using RP-GQDs@Zn-MOFs, followed by the formation of a  $\text{Cu}^{2+}$ -quercetin complex. Altogether, the proposed RP-GQDs@Zn-MOFs-based fluorescence probe, which exhibits a "Turn-On-Off-On" behavior, was found to be highly responsive to quercetin. The stability and reproducibility of the fluorescent RP-GQDs@Zn-MOFs probe were subsequently evaluated. In terms of stability testing, the %RSD was found to

**Table 1:** The summary of different types of sensors reported for detection of quercetin

Sr. No.	Type of sensor	Nanomaterial used	Linearity range	LOD	Ref.
1.	Fluorescent	Sulfur doped GQDs	0 to 50 $\mu\text{M}$	0.006 $\mu\text{g/mL}$	22
2.	Electrochemical	GQDs/Gold nanoparticle nanocomposite	0.01 to 6 $\mu\text{M}$	2 nM	33
3.	Amperometric	Aminated-GQDs/ thiolated $\beta$ -cyclodextrin /gold nanoparticles	1 to 210 nM	285 pM	34
4.	Fluorescent	Carbon nanoparticles	3.3 to 41.2 $\mu\text{M}$	0.175 $\mu\text{M}$	36
5.	Fluorescent	MOFs	0.3 to 80 $\mu\text{M}$	0.14 $\mu\text{M}$	35
6.	Fluorescent	$\text{Cu}^{2+}$ -RP-GQDs@Zn-MOFs	100 ng/mL to 1400 ng/mL	37.8 ng/mL	Present work

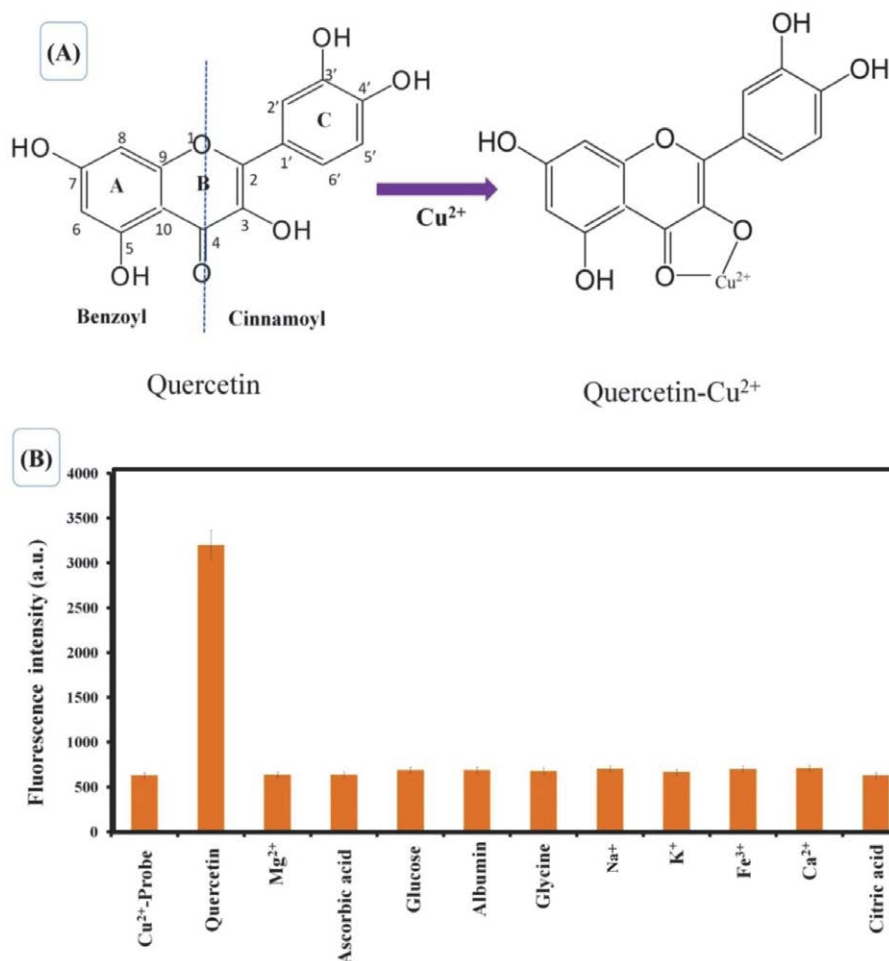


**Figure 9:** (A) Mechanism involved in quercetin detection using proposed design of RP-GQDs@Zn-MOFs nanoprobe and  $\text{Cu}^{2+}$  ions. (B) Interference study of RP-GQDs@Zn-MOFs fluorescence probe for detection of quercetin

be 1.3%, which is well below the 5% threshold, indicating that the probe remains robust under experimental conditions. Furthermore, repeatability testing yielded a %RSD of 1.8%, also meeting the criteria for reproducibility of the proposed sensor for quercetin measurement.

### 3. 8. Study of Selectivity and Real-Time Analysis

In this study, the selectivity of the RP-GQDs@Zn-MOFs fluorescence probe for quercetin was confirmed in the presence of various interfering compounds. Initially, the addition of copper ions to RP-GQDs@Zn-MOFs resulted in the formation of quenched  $\text{Cu}^{2+}$ -RP-GQDs@Zn-MOFs. Subsequently, the introduction of quercetin to this quenched  $\text{Cu}^{2+}$ -RP-GQDs@Zn-MOFs probe led to the recovery of fluorescence, thereby validating quercetin's exceptional selectivity even in the presence of multiple interfering compounds. Figure 9B illustrates the selectivity of quercetin amidst competing substances. The addition of various interfering agents to the quenched

$\text{Cu}^{2+}$ -RP-GQDs@Zn-MOFs probe resulted in the minimal recovery of quenched fluorescence compared to the control  $\text{Cu}^{2+}$ -RP-GQDs@Zn-MOFs quenched probe (absence of quercetin). This lack of significant recovery can be attributed to the absence of interactions between the  $\text{Cu}^{2+}$  ions (the quencher) responsible for quenching and the selected metal ions. Similarly, the use of citric acid, glycine, albumin, glucose, and ascorbic acid as interfering agents to assess the selectivity potential of  $\text{Cu}^{2+}$ -RP-GQDs@Zn-MOFs confirmed the high selectivity of the probe for quercetin alone. This selectivity is likely due to the specific interaction between copper ions and the 3-OH and 4-C=O functionalities of quercetin. Any minor changes in fluorescence recovery may be attributed to weak interactions between copper ions and amino acids, proteins, or other biomolecules, which have no significant impact on the selectivity of  $\text{Cu}^{2+}$ -RP-GQDs@Zn-MOFs. Additionally, the application of quercetin to simulated plasma samples resulted in a 97.42% recovery rate, with LOD and LOQ values of 38.11 ng/mL and 115.64 ng/mL, respectively. This demonstrates the feasibility of using the

Zn-MOFs@RP-GQDs probe for quercetin detection in complex samples. In the future, we intend to validate the RP-GQDs@Zn-MOFs-mediated fluorescence turn "On-Off-On" probe with preclinical blood samples as a proof of concept.

## 4. Conclusion

In this paper, we have presented an exceptionally stable and nanosized RP-GQDs@Zn-MOFs-based fluorescence turn "On-Off-On" nanoprobe. This innovative probe was developed by encapsulating RP-GQDs, synthesized from rose petals, within Zn-MOFs. The interaction between Zn<sup>2+</sup> and carboxylic functionalities was employed to create RP-GQDs@Zn-MOFs, which was confirmed through spectroscopic analysis. Importantly, the encapsulation of RP-GQDs in Zn-MOFs retained the luminescent properties of RP-GQDs. The particle size analysis of the complex demonstrated the stability of Zn-MOFs. The study further showed that the presence of quercetin in the Cu<sup>2+</sup>-RP-GQDs@Zn-MOFs sensing system led to fluorescence recovery. This recovery is attributed to the formation of a complex between Cu<sup>2+</sup> ions and specific functionalities of quercetin, specifically the 3-OH and the carbonyl group (4-C=O) in the 'B' ring. This probe exhibited a low LOD of 37.8 ng/mL, indicating its high sensitivity for quercetin detection. Additionally, the probe's selectivity was assessed through interference testing, confirming its high specificity for quercetin in the presence of various interfering substances. The analytical parameters demonstrated the probe's stability and repeatability, making it a reliable sensing system for quercetin detection. Real-time analysis in artificial plasma validated its practical utility. In conclusion, the developed RP-GQDs@Zn-MOFs-based sensor offers a straightforward process, excellent sensitivity, and selectivity for quercetin detection. This sensor has the potential for applications in measuring quercetin levels in clinical samples and food products.

## Conflict of interest

The author has declared that there are no conflicts of interest related to this research.

## Acknowledgment

The researchers would like to extend their acknowledgments to the Principal of the H. R. Patel Institute of Pharmaceutical Education and Research in Shirpur for providing the essential research facilities. They would also like to express their appreciation to the Sophisticated Test and Instrumentation Centre in Cochin for granting access to HR-TEM analysis facilities. These acknowledgments highlight the importance of institutional support and collaboration in conducting successful research.

## 5. References

1. Y. Zhao, H. Zeng, X.-W. Zhu, W. Lu and D. Li, *Chem Soc Rev* **2021**, *50*, 4484–4513. DOI:10.1039/D0CS00955E
2. A. Mousavi, R. Zare-Dorabei and S. H. Mosavi, *Anal Methods* **2020**, *12*, 5397–5406. DOI:10.1039/D0AY01592J
3. G. L. Yang, X. L. Jiang, H. Xu and B. Zhao, *Small* **2021**, *17*, 2005327. DOI:10.1002/smll.202005327
4. S. N. Nangare, A. G. Patil, S. M. Chandankar and P. O. Patil, *J Nanostruc Chem* **2023**, *13*, 197–242. DOI:10.1007/s40097-022-00479-0
5. G. Lu, S. Li, Z. Guo, O. K. Farha, B. G. Hauser, X. Qi, Y. Wang, X. Wang, S. Han and X. Liu, *Nature chemistry* **2012**, *4*, 310–316. DOI:10.1038/nchem.1272
6. Z. Li and H. C. Zeng, *Chem Mater* **2013**, *25*, 1761–1768. DOI:10.1021/cm400260g
7. S. N. Nangare, P. M. Sangale, A. G. Patil, S. H. Boddu, P. K. Deshmukh, N. R. Jadhav, R. S. Tade, D. R. Patil, A. Pandey and S. Mutalik, *Microchem J* **2021**, *169*, 106567. DOI:10.1016/j.microc.2021.106567
8. Y. Tao, Y. Jiang, Y. Huang, J. Liu, P. Zhang, X. Chen, Y. Fan, L. Wang and J. Xu, *CrystEngComm* **2021**, *23*, 4038–4049. DOI:10.1039/D1CE00392E
9. C. Yao, Y. Xu and Z. Xia, *J Mater Chem C* **2018**, *6*, 4396–4399. DOI:10.1039/C8TC01018H
10. H. Abdolmohammad-Zadeh and F. Ahmadian, *Microchem J* **2021**, *164*, 106001. DOI:10.1016/j.microc.2021.106001
11. G. Kaur, S. Sharma, S. Singh, N. Bhardwaj and A. Deep, *ACS Omega* **2022**, *7*, 17600–17608. DOI:10.1021/acsomega.2c00126
12. X. Jiang, H. Jin, Y. Sun, Z. Sun and R. Gui, *Biosens Bioelectron* **2020**, *152*, 112012. DOI:10.1016/j.bios.2020.112012
13. J. Pantwalawalkar, S. Chandankar, R. Tade, Z. Khan, M. Shaikh, T. Powar, P. Patil, V. Sugandhi and S. Nangare, *Adv Nat Sci: Nanosci Nanotechnol* **2022**, *13*, 013001. DOI:10.1088/2043-6262/ac5e35
14. M. Li, T. Chen, J. J. Gooding and J. Liu, *ACS sensors* **2019**, *4*, 1732–1748. DOI:10.1021/acssensors.9b00514
15. R. S. Tade, S. N. Nangare, A. G. Patil, A. Pandey, P. K. Deshmukh, D. R. Patil, T. N. Agrawal, S. Mutalik, A. M. Patil and M. P. More, *Nanotechnology* **2020**, *31*, 292001. DOI:10.1088/1361-6528/ab803e
16. H. Sun, L. Wu, W. Wei and X. Qu, *Mater Today* **2013**, *16*, 433–442. DOI:10.1016/j.mattod.2013.10.020
17. R. S. Tade and P. O. Patil, *Curr Appl Phy* **2020**, *20*, 1226–1236. DOI:10.1016/j.cap.2020.08.006
18. R. Li, L. Liu, H. Zhu and Z. Li, *Anal Chim Acta* **2018**, *1008*, 38–47. DOI:10.1016/j.aca.2018.01.031
19. S. R. Ahmed, M. Sherazee, S. Srinivasan and A. R. Rajabzadeh, *Food Chem* **2022**, *379*, 132152. DOI:10.1016/j.foodchem.2022.132152
20. S. Nangare, S. Patil, S. Patil, Z. Khan, A. Patil and P. Patil, *Inorg Chem Commun* **2022**, *143*, 109751. DOI:10.1016/j.inoche.2022.109751
21. Y. Zou, F. Yan, T. Zheng, D. Shi, F. Sun, N. Yang and L. Chen, *Talanta* **2015**, *135*, 145–148.

- DOI:10.1016/j.talanta.2014.12.029
22. S. Kadian and G. Manik, *Food Chem* **2020**, *317*, 126457.  
DOI:10.1016/j.foodchem.2020.126457
23. K. Ishii, T. Furuta and Y. Kasuya, *J Chromatogr B* **2003**, *794*, 49–56. DOI:10.1016/S1570-0232(03)00398-2
24. L. R. de Moura Ferraz, A. É. G. A. Tabosa, D. D. S. da Silva Nascimento, A. S. Ferreira, V. de Albuquerque Wanderley Sales, J. Y. R. Silva, S. A. Júnior, L. A. Rolim, J. J. de Souza Pereira and P. J. Rolim-Neto, *Sci Rep* **2020**, *10*, 1–14.  
DOI:10.1038/s41598-020-73848-w
25. H. Kaur, G. C. Mohanta, V. Gupta, D. Kukkar and S. Tyagi, *J Drug Deliv Sci Technol* **2017**, *41*, 106–112.  
DOI:10.1016/j.jddst.2017.07.004
26. M. Basiaga, Z. Paszenda, W. Walke, P. Karasiński and J. Marciniak: Information Technologies in Biomedicine, Volume 4, Springer, **2014**, pp. 411–420.  
DOI: 1007/978-3-319-06596-0\_39
27. S. Zhu, Y. Song, X. Zhao, J. Shao, J. Zhang and B. Yang, *Nano Res* **2015**, *8*, 355–381. DOI:10.1007/s12274-014-0644-3
28. Y. Dong, J. Shao, C. Chen, H. Li, R. Wang, Y. Chi, X. Lin and G. Chen, *Carbon* **2012**, *50*, 4738–4743.  
DOI:10.1016/j.carbon.2012.06.002
29. D. Pan, L. Wang, Z. Li, B. Geng, C. Zhang, J. Zhan, L. Yin and L. Wang, *New J Chem* **2018**, *42*, 5083–5089.  
DOI:10.1039/C7NJ04909A
30. H. Yu, W. Zhu, H. Zhou, J. Liu, Z. Yang, X. Hu and A. Yuan, *RSC Adv* **2019**, *9*, 9577–9583. DOI:10.1039/C9RA01488H
31. Z. Tian, X. Yao, K. Ma, X. Niu, J. Grothe, Q. Xu, L. Liu, S. Kaskel and Y. Zhu, *ACS Omega* **2017**, *2*, 1249–1258.  
DOI:10.1021/acsomega.6b00385
32. X. Fu, H. Li, R. Lv, D. Hong, B. Yang, W. Gu and X. Liu, *J Solid State Chem* **2018**, *264*, 35–41.  
DOI:10.1016/j.jssc.2018.04.021
33. J. Li, J. Qu, R. Yang, L. Qu and P. de B. Harrington, *Electroanalysis* **2016**, *28*, 1322–1330. DOI:10.1002/elan.201500490
34. Z. Zhou, P. Zhao, C. Wang, P. Yang, Y. Xie and J. Fei, *Microchim Acta* **2020**, *187*, 1–9. DOI:10.1007/s00604-019-4106-1
35. P. Wu, Q. Du, L. Chen, M. Yang, Y. Sun, H. Zhi, P. Dramou and H. He, *Microchim Acta* **2021**, *188*, 1–8.  
DOI:10.1007/s00604-020-04664-2
36. P. Zuo, D. Xiao, M. Gao, J. Peng, R. Pan, Y. Xia and H. He, *Microchim Acta* **2014**, *181*, 1309–1316.  
DOI:10.1007/s00604-014-1236-3

## Povzetek

Pričujoča študija predstavlja 'On-Off-On' nanoprobe na osnovi fluorescence kot možnost za zaznavanje kvercetina. Proba je narejena iz grafenskih kvantnih točk, proizvedenih iz vrtničnih cvetnih listov in vključenih v cinkova kovinsko-organska ogrodja (RP-GQDs@Zn-MOF). Z analizo velikosti delcev in HR-TEM smo potrdili sintezo uniformno porazdeljene probe v nanovelikosti, medtem ko je zeta potencial (+33,03 mV) dokazal njeno dobro stabilnost. Fluorescenčna analiza je potrdila, da dodatek bakrovih ionov ( $\text{Cu}^{2+}$ ) povzroči dušenje fluorescence, medtem ko dodatek kvercetina povzroči nastanek kvercetin- $\text{Cu}^{2+}$  kompleksa, kar privede do obnovitve zadušene fluorescence pri RP-GQDs@Zn-MOF zaradi statičnega dušenja. Nanoprobe je izkazala široko koncentracijsko območje od 100 ng/mL do 1400 ng/mL ( $R^2 = 0,99$ ) ter nizko mejo zaznave 37,8 ng/mL. Analiza selektivnosti je pokazala izrazito specifičnost za kvercetin, kar pripisujemo koordinaciji  $\text{Cu}^{2+}$  s karbonilnim kisikovim atomom in 3-OH skupino kvercetina. Nadalje je pripravljena proba pokazala odlično stabilnost, ponovljivost ( $\text{RSD} < 0,05$ ) in potencial za analizo v realnem času.



Except when otherwise noted, articles in this journal are published under the terms and conditions of the Creative Commons Attribution 4.0 International License

Scientific paper

# Synthesis and Characterization of a Nanosilica-Cysteine Composite for Arsenic(III) Ion Removal

Omar Alnasra\* and Fawwaz Khalili

Department of Chemistry, Faculty of Science, The University of Jordan, Amman 11942.

\* Corresponding author: E-mail: amr9170169@ju.edu.jo

Tel.: +962799413977

Received: 03-26-2023

## Abstract

This article describes the synthesis of a nanosilica-cysteine composite (SiO<sub>2</sub>-Cys) and its application as a sorbent and carrier for arsenic(III) using different media. Attenuated total reflectance-Fourier-transform infrared spectroscopy, scanning and transmission electron microscopy, X-ray diffraction, and thermogravimetric analysis were applied to characterize SiO<sub>2</sub>-Cys. Using the batch technique, the sorption of As(III) ions by SiO<sub>2</sub>-Cys was studied, and the effects of pH, sorbent dosage, temperature, initial concentration, and contact time were all taken into consideration. According to kinetic studies, the pseudo-second-order equation adequately described the sorption of the As(III) ion. The spontaneity of the sorption process on SiO<sub>2</sub>-Cys is suggested by the negative values of Gibbs free energy ( $\Delta G^\circ$ ). Positive values of enthalpy ( $\Delta H^\circ$ ) indicate an endothermic adsorption process and positive values of entropy ( $\Delta S^\circ$ ) for the adsorption of As(III) ions mean that adsorption is associated with increasing randomness. The Langmuir model, which has a maximum sorption capacity for SiO<sub>2</sub>-Cys of (66.67 mg/g) at 25 °C, provided a better fit to the sorption isotherm.

**Keywords:** Arsenic; modification; silica nanoparticles; cysteine; sorption; ion uptake

## 1. Introduction

Arsenic, a group 15 metalloid element with an atomic weight of 74.9216 amu and atomic number 33, is considered one of the most common elements in nature.<sup>1,2</sup> Arsenic is an element of concern from both an environmental and human health perspective.<sup>3</sup> Arsenic is in all its features mostly recognized as a poison. Arsenic species can be found in all kinds of environments and can come from both natural and anthropogenic sources.<sup>4</sup> The most toxicologically potent arsenic compounds are in the trivalent oxidation state. This is due to their ability to produce reactive oxygen species and their reactivity with compounds that contain sulfur. Nevertheless, humans are exposed to both trivalent and pentavalent arsenicals.<sup>5</sup> Natural sources of arsenic include weathering, the activity of volcanoes and some biological processes. Anthropogenic sources are diverse from the burning of fossil fuels, smelting, and mining to different types of industrialization (pesticides, desiccants, pigments, and preservatives). However, these are all responsible for the presence of arsenic in water.<sup>6–8</sup> The World Health Organization (WHO, Geneva, Switzerland), Environmental Protection Agency (US-EPA, United States)<sup>9,10</sup> and Central Pollution Control Board (CPCB,

India)<sup>11,12</sup> have established that arsenic in drinking water that is not to exceed a certain level of the range from 0.01 to 0.05 mg L<sup>-1</sup> due to its extreme toxicity.

Arsenic can be eliminated from aqueous solutions using many physical and chemical treatment methods. Over the past few decades, various techniques have been used, inclusive of sorption, ion exchange, chemical precipitation, and electro dialysis.<sup>13</sup> Several variables, including the concentration of arsenic, pH, and the interference with competing ions, affect the effectiveness of each of these techniques. Sometimes, they are suitable for As(V), but not for As(III).<sup>14</sup> The efficiency, affordability, and ease of the technique, all play a role in selecting the best arsenic removal method.<sup>15,16</sup> Adsorption is one of the most promising techniques among all those that are currently in use.<sup>17</sup> Moreover, current infrastructure and technologies for treating wastewater and water are at their capacity to provide water of sufficient quality to meet both environmental and human needs.<sup>18,19</sup> Nanoparticles are good options for water treatment applications due to their many diverse properties involving surface area, specificity, and reactivity.<sup>20,21</sup> In the past ten years, reports on the selective and effective adsorption of arsenic ions by silica that have been functionalized with amino

acids,<sup>22,23</sup> surface ions-imprinted silica,<sup>24</sup> or quaternary amines<sup>25</sup> have all been made. The purpose of this research is to synthesize composite material using cysteine, where the thiol groups play a major role in the process of As(III) adsorption, and to thoroughly investigate the effectiveness of As(III) removal from water and different media. The main goals are to (a) synthesize and characterize the composite nano-material, (b) to determine the kinetics of As(III) adsorption, and (c) to study the impact of temperature, pH, time, and initial concentration on As(III) adsorption. This is the first novel work that deals with nanosilica-cysteine composite (SiO<sub>2</sub>-Cys) and its application as a sorbent and carrier for arsenic(III) using different media.

## 2. Experimental

### 2.1. Materials

Nano powder of SiO<sub>2</sub> (99.5%), L-Cysteine (≥ 98%) from a non-animal source and Luecocrystal violet (4,4',4''-methylidynetris(N,N-dimethylaniline) from Sigma Aldrich, Ninhydrin from Bio Basic Inc. Hydrochloric acid (37%) from VWR Chemicals, Arsenic trioxide (99.5%) from BDH Chemicals, England. NaOH pellets from Merck.

### 2.2. Instruments

The RADWAG® AS 220.R2, Electronic Balance was used for the weighing. A BANTE pH-meter (PHS-25CW) was used to determine the pH of the solutions. The attenuated total reflectance-Fourier transform infrared spectrum was recorded on a Bruker Vertex 70-FT-IR spectrometer at room temperature coupled with a vertex Pt-ATR-FTIR accessory. Centrifugation was done using (DJB Lab Care-AIC PK 130) at 4000 RPM speed. DHP-9052 heating incubator was used to heat the samples. Using a NETZSCH STA 409 PG/PC thermal analyzer with a heating rate of 20 °C/min from (0–1000 °C), thermal gravimetric analysis was performed. The Philips X-Pert PW 3060, running at 45 kV and 40 mA, was used to measure X-Ray Diffraction. The 3D shape was examined using a scanning electron microscope NCF's FEI QUANTA 600 FEG. Shape and size distribution of the nanoparticles were obtained by a Formvar-coated copper grid (Electron Microscopy Sciences, USA) using an FEI Morgagni 268 transmission electron microscopy (Eindhoven, The Netherlands) at a 60 kV accelerating voltage. GRIFFIN (1-150) vacuum oven was used to dry samples at 25 °C and 630 mm Hg. A 1.0 cm quartz cell and a METASH vis-spectrophotometer, model V-5100, were used to measure the As(III) concentration.

### 2.3. Modification of Nanosilica with Cysteine

Dissolving 36 g ± 0.1 mg of the nanosilica powder in 600.0 ± 0.1 mL of deionized water and adjusting the pH to

5.60 ± 0.01. Add 36 g ± 0.1 mg of cysteine to the nanosilica solution and shaking was done using a magnetic stirrer for 48 hrs. Then the mixture was filtered by centrifugation and dried in a vacuum oven at 25 ± 0.5 °C for 5 days (90% yield). The product is labeled as (SiO<sub>2</sub>-Cys).

## 2.4. Characterization

### Attenuated total reflectance-Fourier Transform Infrared (ATR-FTIR) Spectroscopy Analysis

SiO<sub>2</sub>-Cys and SiO<sub>2</sub>-Cys with As(III) (SiO<sub>2</sub>-Cys/ATO) spectra of ATR-FTIR were recorded using a Vertex 70-FT-IR spectrometer (Bruker, Germany) at room temperature coupled with a vertex Pt-ATR-FTIR accessory.

### Thermal Gravimetric Analysis (TGA)

The TGA of SiO<sub>2</sub>-Cys and SiO<sub>2</sub>-Cys/ATO was performed using a Netzsch STA 409 PG/PC thermal analyzer (Selb Bavaria, Germany) in the temperature range (0–1000 °C) at a 20 °C/min heating rate and 50 mL/min flow rate for nitrogen purging.

### X-ray Diffraction (XRD) Analysis

Philips X pert PW 3060 diffractometer (PANalytical, United Kingdom) was used to investigate the crystalline phases of SiO<sub>2</sub>-Cys and SiO<sub>2</sub>-Cys/ATO. The XRD experiments were operated with Cu K $\alpha$ -radiation ( $\lambda = 1.5406 \text{ \AA}$ ) in the 2 $\theta$  range (6.0–60.0°) at 45 kV and 40 mA.

### Scanning Electron Microscope (SEM)

Information about the surface topography and composition of the sample was examined for SiO<sub>2</sub>-Cys and SiO<sub>2</sub>-Cys/ATO using NCF's FEI QUANTA 600 FEG (FEI Ltd, Japan). Disperse 3 mg ± 0.1 mg of the sample on the carbon tape. Samples weren't further coated before being analyzed.

### Transmission Electron Microscopy (TEM)

Shape and size distribution of SiO<sub>2</sub>-Cys and SiO<sub>2</sub>-Cys/ATO were obtained by a Formvar-coated copper grid (Electron Microscopy Sciences, USA). The grid was left to dry overnight, and a FEI Morgagni 268 TEM (Eindhoven, The Netherlands) was used for imaging (60 kV accelerating voltage).

### Point of zero charge (PZC) of SiO<sub>2</sub>-Cys

PZC was determined using two methods: Salt Addition and the pH drift method. PZC values by the salt addition method were determined in 0.1 M NaNO<sub>3</sub> solution at 25 ± 0.5 °C. In the Salt Addition method, SiO<sub>2</sub>-Cys (0.1 g ± 0.1 mg) and 0.1 M NaNO<sub>3</sub> (40 ± 0.1 mL) were mixed in different reaction flasks. The pH of the suspension was then adjusted to an initial pH value of 3, 4, 5, 6, 7, 8, 9, 10, and 11 using either 0.1 M HCl or 0.1 M NaOH solutions. Each flask was then vigorously agitated in a shaker for 24 hr. After settling, the final pH of each suspension

was measured very carefully. In the drift method, 0.1 M HCl or 0.1 M NaOH, was used to change the pH of NaNO<sub>3</sub> solution to a range of 3 to 11. The pH was measured after SiO<sub>2</sub>-Cys (0.1 g ± 0.1 mg) was added to 20 ± 0.1 ml of the pH-adjusted solution and equilibrated for 24 hr then the final pH was measured.

## 2. 5. Removal of As(III) Ions from Water

### Preparation of standard curve of As(III)

The stock solution of arsenic (1000 ppm) was prepared by dissolving an appropriate quantity of arsenic trioxide in 20 ± 0.1 mL of 2 ± 0.1 mg g NaOH, which was neutralized by adding dilute HCl to make acid. The solution was then made up to the mark in a 500 mL volumetric flask by adding deionized water. From the stock solution, a working solution of 100 ppm has been prepared. These two solutions were used to build up an analytical calibration curve with various concentrations (0.75, 1.25, 1.50, 2.50, 3.00, 4.00 and 5.00 ppm).

### Sorption experiments

Sorption experiments of As(III) implying kinetic studies were conducted in the following simple settings to establish the sorption equilibrium time by SiO<sub>2</sub>-Cys using batch technique; 0.05 g ± 0.1 mg of SiO<sub>2</sub>-Cys was shaken with 25.0 ± 0.1 mL of 50 ppm As(III) ion solution, pH 6 is to be assured, the contact time was varied from 12 to 108 hours at 25.0, 37.5 and 45.0 °C. A spectrophotometric method using Luecocrystal violet indicator to quantify the amount of As(III) ions that were still present in the filtrate was applied. The following equations have been used to calculate the sorption capacity ( $q_e$ ) and the percentage uptake of As(III) ions:

$$\text{Uptake (\%)} = \frac{(C_0 - C_e)}{C_0} \times 100\% \quad (1)$$

$$q_e = \frac{(C_0 - C_e)V}{m} \quad (2)$$

where  $C_0$  is the initial As(III) ions concentration (ppm),  $C_e$  is the concentration of As(III) ions left in solution at equilibrium,  $V$  is the volume (L) of As(III) solution, and  $m$  is the mass (g) of SiO<sub>2</sub>-Cys.

### Sorption isotherms and kinetics modelling

The following two models were used in kinetic evaluation to better understand how As(III) ions adsorb to SiO<sub>2</sub>-Cys:

Pseudo-first-order:

$$\ln(q_e - q_t) = \ln q_e - k_1 t \quad (3)$$

and pseudo-second-order:

$$\frac{t}{q_t} = \frac{1}{k_2 q_e^2} + \frac{t}{q_e} \quad (4)$$

where  $k_1$ ,  $k_2$  are the rate constants for pseudo-first-order and pseudo second-order adsorption process, respectively.  $q_e$  and  $q_t$  (mg/g) are the amounts of As(III) ions adsorbed onto SiO<sub>2</sub>-Cys at equilibrium and time  $t$  (min).<sup>26</sup>

The sorption of As(III) ions onto SiO<sub>2</sub>-Cys was investigated using three different isotherm models: Langmuir,<sup>27</sup> Freundlich,<sup>28</sup> and Dubinin–Radushkevich (D-R).<sup>29</sup> The sorption isotherms were carried out by shaking 0.05 g ± 0.1 mg of SiO<sub>2</sub>-Cys with 25.0 ± 0.1 mL of solutions of variable concentrations (50, 100, 150, 200 and 250 ppm) for As(III) at pH 6.0 ± 0.01 and at 25.0, 37.5 and 45.0 °C. Samples were shaken for 96 hours, then centrifuged and the amount of As(III) ions left in solution was determined. The adsorption isotherms are studied using the following formulas:

- Langmuir equation (Form I):

$$\frac{C_e}{q_e} = \frac{1}{q_m K_L} + \left(\frac{1}{q_m}\right) C_e \quad (5)$$

- Freundlich equation:

$$\text{Log } q_e = \text{log } K_F + \frac{1}{n} \text{log } C_e \quad (6)$$

- Dubinin–Radushkevich equations:

$$\ln q_e = \ln q_{max} - \beta \varepsilon^2 \quad (7)$$

where the Polanyi potential  $\varepsilon$ , can be calculated as:

$$\varepsilon = RT \ln \left(1 + \frac{1}{C_e}\right) \quad (8)$$

### Desorption experiments

A 0.05 g ± 0.1 mg of SiO<sub>2</sub>-Cys was dissolved in 25.0 ± 0.1 mL of 50 ppm As(III) at pH 6.0 ± 0.01 and 25.0 ± 0.5 °C, shaken for 96 hours, then centrifuged and dried in a vacuum oven. Adding to vessels containing 50.0 mL media solution (normal saline, dextrose, ringer lactate, water (all at pH = 7.4 ± 0.01), and 0.1 M HCl, then were shaken at 250 rpm for 48 hr and 37.5 ± 0.5 °C. After that an aliquot was taken out for the determination of desorbed As(III) ions. The concentration of As(III) in each sample was determined by comparison with a calibration curve based on the absorption maximum at 590 nm.

## 2. 6. Regeneration and Reusability of SiO<sub>2</sub>-Cys

The regeneration and reusability of SiO<sub>2</sub>-Cys after As(III) adsorption/desorption cycles were investigated. Four cycles were performed. 25 ± 0.1 mL of a 50 ppm As(III) solution at pH 7.4 was contacted with 0.5 g ± 0.1 mg of SiO<sub>2</sub>-Cys with shaking at 37.5 ± 0.5 °C during 24 hr. The suspension was centrifuged, the final solution was measured for As(III) content and the remaining solid was washed with 50 ± 0.1 mL of 0.1 M HCl followed by washing with deionized water. The washed adsorbent was then



dried at  $25 \pm 0.5$  °C in a vacuum oven for 24 hr. The dried solid was weighted, and the process was repeated three more times. The amount of As(III) adsorbed was determined by Equation 2 and the removal % was calculated using Equation 1.

### 3. Results and Discussion

Nanosilica-cysteine composite (SiO<sub>2</sub>-Cys) was prepared successfully. The yield percentage of the reaction was 90% and a well structural characterization of the synthesized nanoparticles using ATR-FTIR, TGA, SEM, TEM and XRD was achieved.

#### 3. 1. ATR-FTIR Analysis

The ATR-FTIR analysis was performed to establish the changes in the functional groups of SiO<sub>2</sub>-Cys to ensure the uptake of As(III). The spectrum of SiO<sub>2</sub>-Cys (Figure 1b) shows distinctive peaks at three main wavenumbers: 1077, 800, and 453 cm<sup>-1</sup> which corresponds to the asymmetric, symmetric modes of Si–O–Si, bending O–Si–O, respectively, and a characteristic peak at 962 cm<sup>-1</sup> for the silanol group stretching vibration.<sup>30</sup> The red shift in asymmetric Si–O–Si band from original 1060 cm<sup>-1</sup> on nanosilica to 1077 cm<sup>-1</sup> on SiO<sub>2</sub>-Cys indicated the interaction of amino acid with surface silanols of nanosilica.<sup>31</sup> Other peaks: 1583 cm<sup>-1</sup> (COO<sup>-</sup> asymmetric stretching), 1486 cm<sup>-1</sup> (N–H bending), and 1406 cm<sup>-1</sup> (COO<sup>-</sup> symmetric

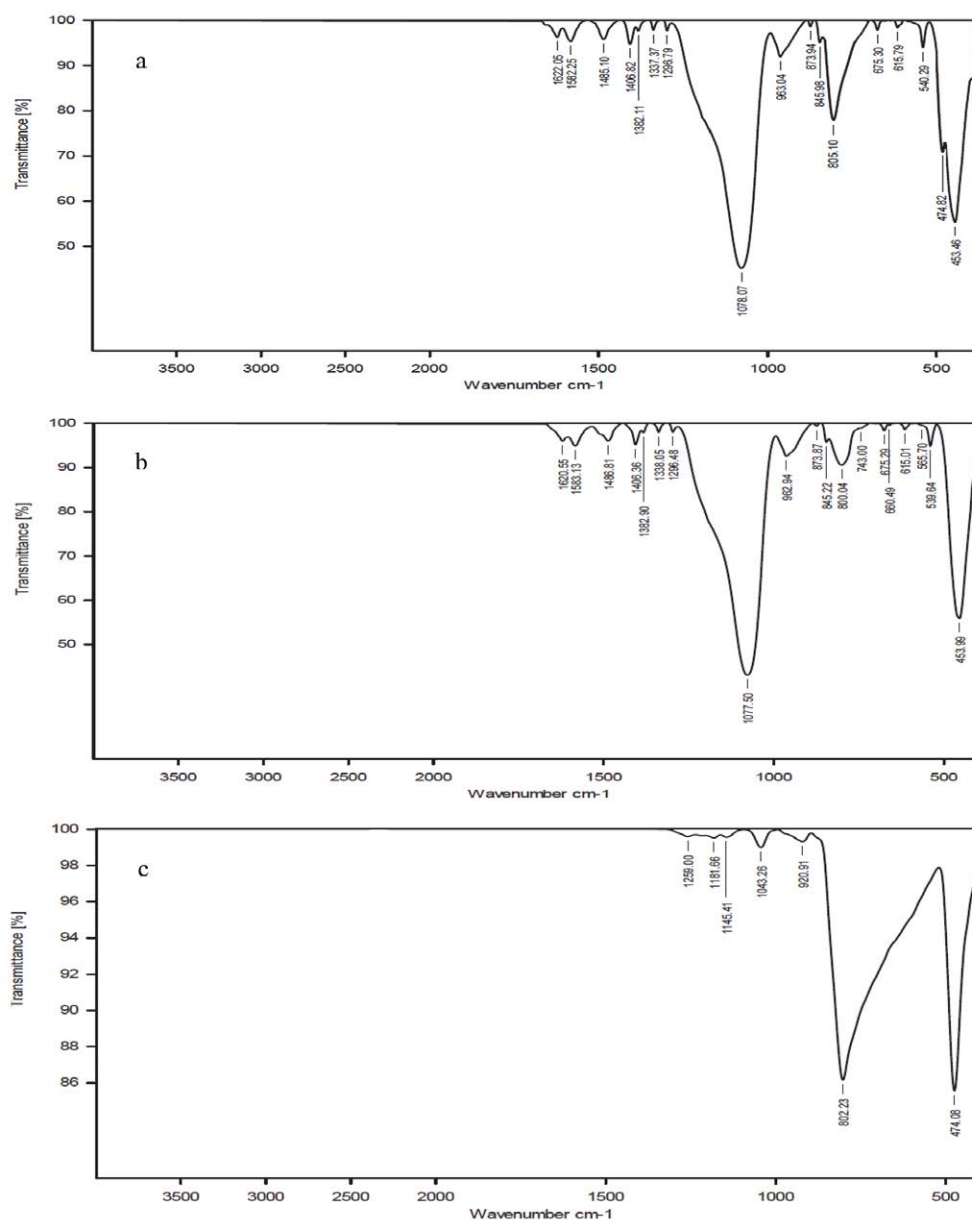


**Figure 1.** ATR-FTIR spectra for a fine powder sample of a) SiO<sub>2</sub>-Cys/ATO, b) SiO<sub>2</sub>-Cys, and c) ATO. The spectra were recorded in the mid-infrared region (4000–400 cm<sup>-1</sup>) and show characteristic absorption bands corresponding to the sample's chemical composition and functional groups.

stretching) were also observed. The existence of  $\text{COO}^-$  and N-H peaks showed that cysteine is present as a zwitterion molecule.<sup>32</sup>

ATR-FTIR spectra of the bare  $\text{As}_2\text{O}_3$  (Figure 1c) shows the prominent peak of As–O stretching vibration at  $802\text{ cm}^{-1}$  and another peak at  $474\text{ cm}^{-1}$  which is related to As–O bending.<sup>33</sup>

### 3. 2. TGA Thermogram

The TGA thermogram of  $\text{SiO}_2$ -Cys in Figure 2 (line 2) consisted of a main gradual weight loss starting at about  $180\text{ }^\circ\text{C}$  attributed to decomposition loss (about 21 wt %) of the organic component, which is in our case is cysteine.<sup>34</sup> The thermogram showed a prior decomposition occurred around  $100\text{ }^\circ\text{C}$ , which has to do with the elimination of water that has been adsorbed (physically).<sup>35</sup> TGA thermogram for  $\text{SiO}_2$ -Cys/ATO which is shown in Figure 2 (line 1) showed two decomposition behaviours; the first

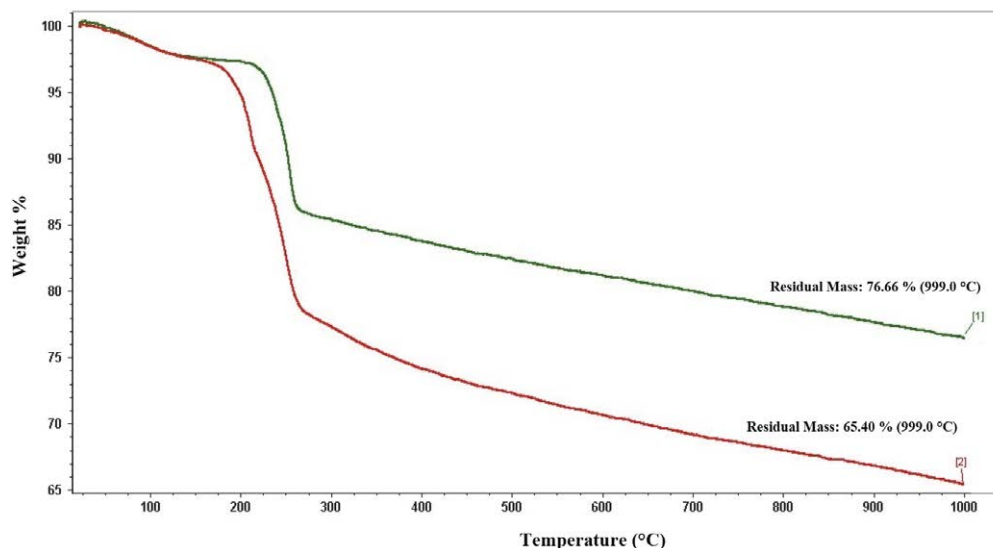


**Figure 2.** TGA thermogram of [1]  $\text{SiO}_2$ -Cys/ATO and [2]  $\text{SiO}_2$ -Cys under a nitrogen atmosphere in the temperature range (0–1000 °C). The thermogram shows the weight loss as a function of temperature, revealing the thermal stability and decomposition behavior of the samples.

occurred around  $100\text{ }^\circ\text{C}$ , which is related to the elimination of water, whereas the second (about 14 wt %) about  $220\text{ }^\circ\text{C}$  related to the loss of cysteine. It is obvious from the residual mass percent that  $\text{SiO}_2$ -Cys/ATO (line 1) retains more mass than  $\text{SiO}_2$ -Cys (line 2) which can be explained by the existence of the arsenic-oxide in addition to the nanosilica.

### 3. 3. XRD Pattern

XRD pattern of  $\text{SiO}_2$ -Cys and  $\text{SiO}_2$ -Cys/ATO (Figure 3) illustrates important solid-state structural data, represented by the degree of crystallinity. Instead of distinct peaks, a broad hump or diffuse scatter-

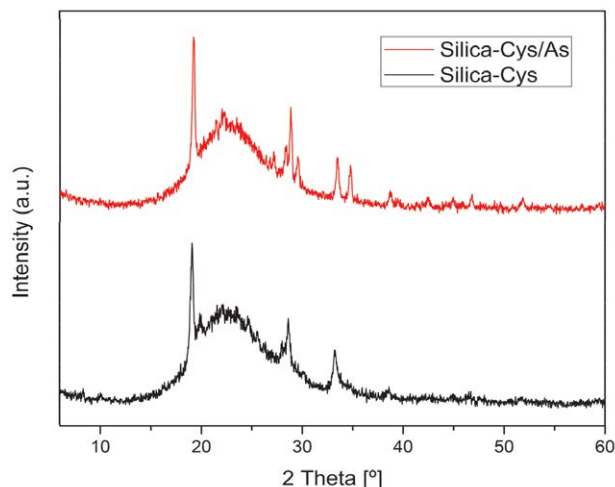


**Figure 3.** XRD pattern of a sample of  $\text{SiO}_2$ -Cys and  $\text{SiO}_2$ -Cys/ATO obtained using a Cu  $K\alpha$  radiation source ( $\lambda = 1.5406\text{ \AA}$ ) in the  $2\theta$  range ( $6.0^\circ - 60.0^\circ$ ).

ing over a range of angles appeared at  $2\theta = 22.50^\circ$  for  $\text{SiO}_2$ -Cys. This indicates the lack of long-range order characteristic of crystalline materials, this has to be a characteristic peak related to the amorphous silica.<sup>36</sup> The presence of three sharp peaks at  $2\theta = 19.22^\circ$ ,  $2\theta = 28.34^\circ$  and  $2\theta = 33.46^\circ$  associated with the monoclinic crystalline cysteine.<sup>37</sup> The XRD pattern of  $\text{SiO}_2$ -Cys/ATO possesses two sharp peaks at  $2\theta = 29.56^\circ$  and  $2\theta = 34.78^\circ$  corresponding to monoclinic crystal of arsenic trioxide in which the intensity of the peaks indicates the abundance of arsenic trioxide in the sample. Higher peak intensity suggests a higher concentration of ATO.<sup>38</sup> This finding confirms the formation of  $\text{SiO}_2$ -Cys/ATO.

### 3. 4. SEM Spectroscopy

Using FEI Quanta SEM, the morphology of SiO<sub>2</sub>-Cys and SiO<sub>2</sub>-Cys/ATO was examined. All of the SEM

images (Figure 4) showed that the ATO particles had spread out over the SiO<sub>2</sub>-Cys system and created a smooth surface.

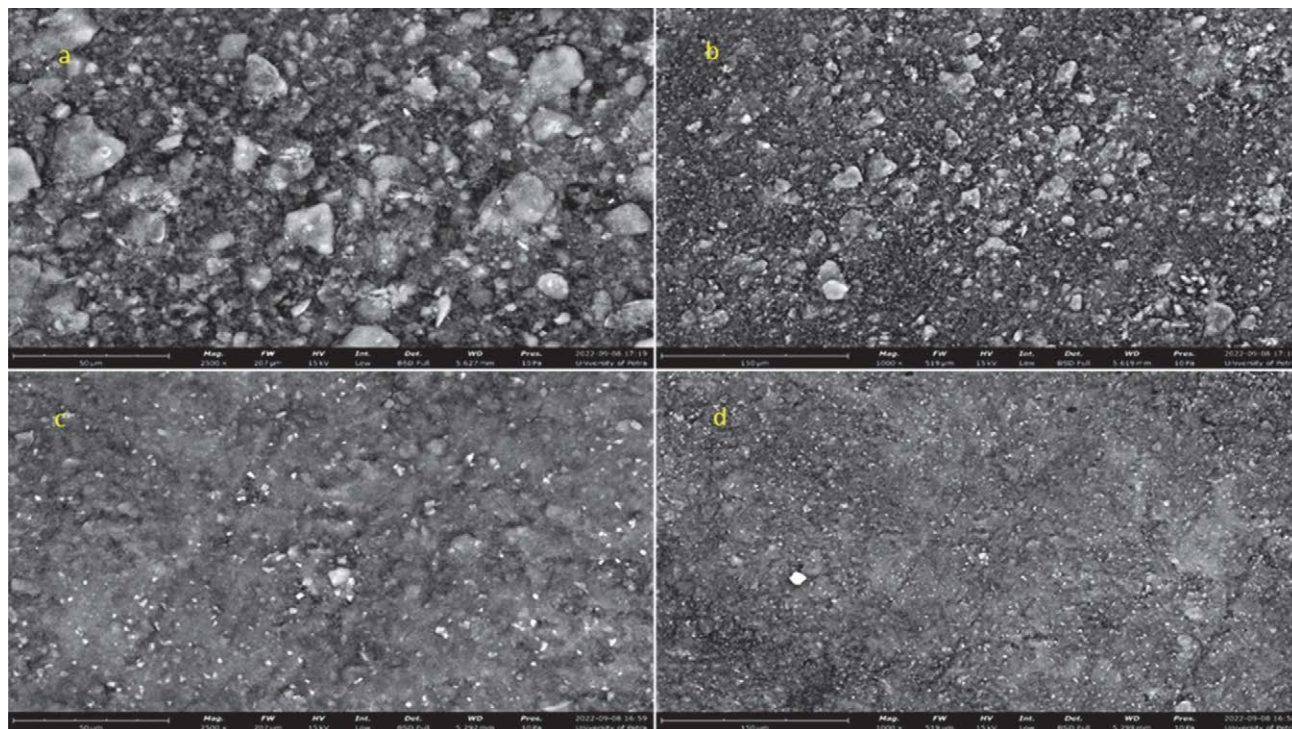


**Figure 4.** SEM micrographs at different magnifications: (a,c) 2500x-magnification image revealing the surface details and microstructure for SiO<sub>2</sub>-Cys and SiO<sub>2</sub>-Cys/ATO, respectively. (b,d) 1000x-magnification image showing the overall morphology of SiO<sub>2</sub>-Cys and SiO<sub>2</sub>-Cys/ATO, respectively.

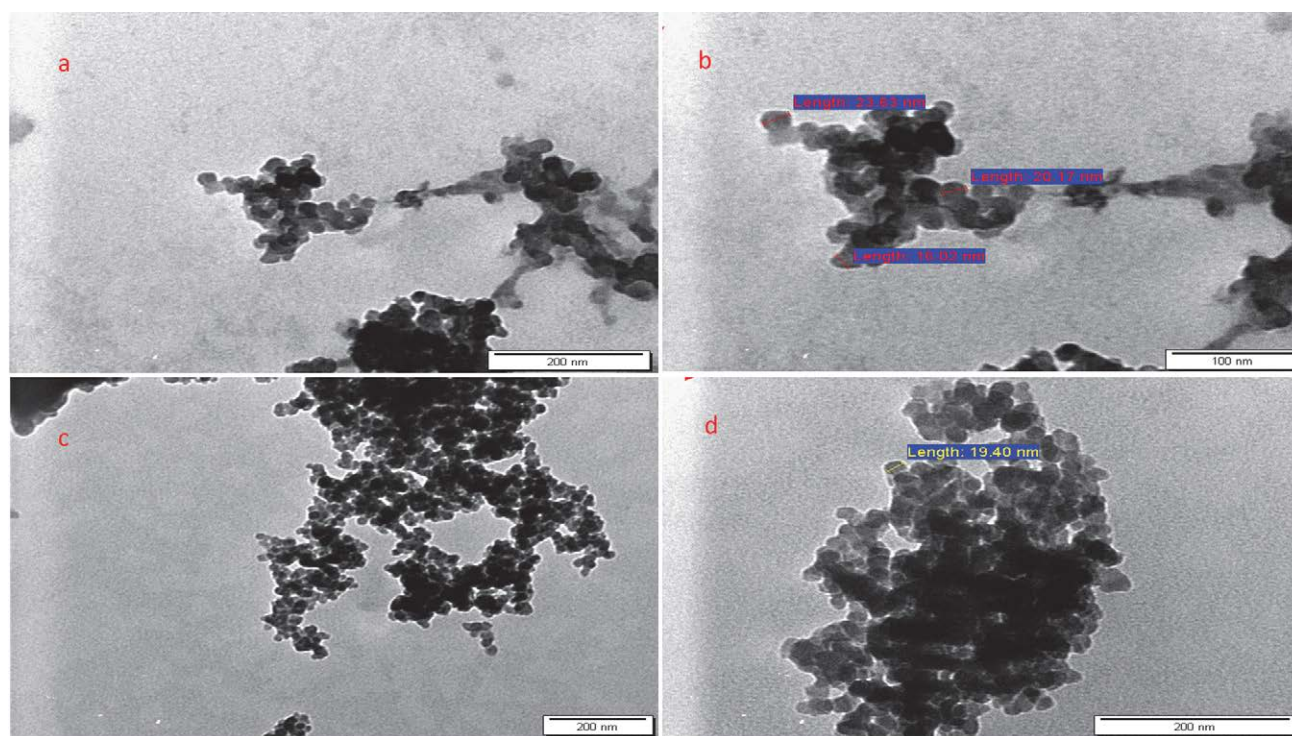


**Figure 5.** TEM images for (a) SiO<sub>2</sub>-Cys, scale bar: 200 nm; (b) SiO<sub>2</sub>-Cys, scale bar: 100 nm; (c,d) SiO<sub>2</sub>-Cys/ATO, scale bar: 200 nm. Images showing the morphology of the samples in the atomic-level.

The adsorption of ATO on nanosilica can involve binding interactions between the ATO molecules and the surface atoms or functional groups of nanosilica (i.e. cysteine). These binding interactions can promote the formation of stable surface species or bridging structures, which can contribute to the smoothness of the surface by reducing surface roughness and promoting surface uniformity. Additionally, ATO adsorption can contribute to surface energy minimization. Adsorbed molecules tend to redistribute and orient themselves to achieve a lower energy state, which can lead to a smoother surface in which the interaction between ATO molecules and the nanosilica surface can facilitate the rearrangement of surface atoms or molecules, reducing height variations and resulting in a more uniform surface.

### 3. 5. TEM Spectroscopy

TEM analysis was carried out to achieve the shape and size distribution of SiO<sub>2</sub>-Cys and SiO<sub>2</sub>-Cys/ATO. Figure 5 shows that the composite was observed to have dense nano-aggregates possessing a (16–24 nm) particle size and a morphology shape that is roughly spherical in appearance.

Nanosilica particles may have a high surface energy, which can drive them to aggregate and minimize their surface area. Additionally, the presence of ATO can also affect the surface properties of the nanosilica particles,

promoting their aggregation. Surface interactions between the nanosilica and ATO, such as van der Waals forces or chemical bonding, can contribute to the formation of the observed dense nano-aggregates.

### 3. 6. PZC of SiO<sub>2</sub>-Cys

PZC is traditionally known as the pH where one or more components of the surface charge vanishes at a specified temperature, pressure, and aqueous solution composition. PZC was obtained using two methods: Salt Addition and the pH drift method.

PZC values using the salt addition method were determined in 0.1 M NaNO<sub>3</sub> solution at 298 K. The pH of the suspension was adjusted to an initial pH value in the range of 3 to 11. The addition of SiO<sub>2</sub>-Cys to the NaNO<sub>3</sub> solution changes the pH. The final pH values were calculated, and the initial pH values were plotted against ΔpH as seen in Figure 6a. The PZC was chosen to represent the initial pH at which pH is zero.<sup>39</sup> In the pH 5 to 11 range, the ΔpH values are positive with a maximum value at pH 10 and the PZC of SiO<sub>2</sub>-Cys is pH = 5.

In the drift method, the pH of the 0.01 M NaNO<sub>3</sub> was adjusted to a value in the range of 3 to 11. The difference between the final and initial pH was measured and plotted. The PZC was determined to be the pH at which the curve crosses the pH<sub>initial</sub> = pH<sub>final</sub> line.<sup>43</sup> The PZC for SiO<sub>2</sub>-Cys using the drift method is given in Figure 6b. There are no

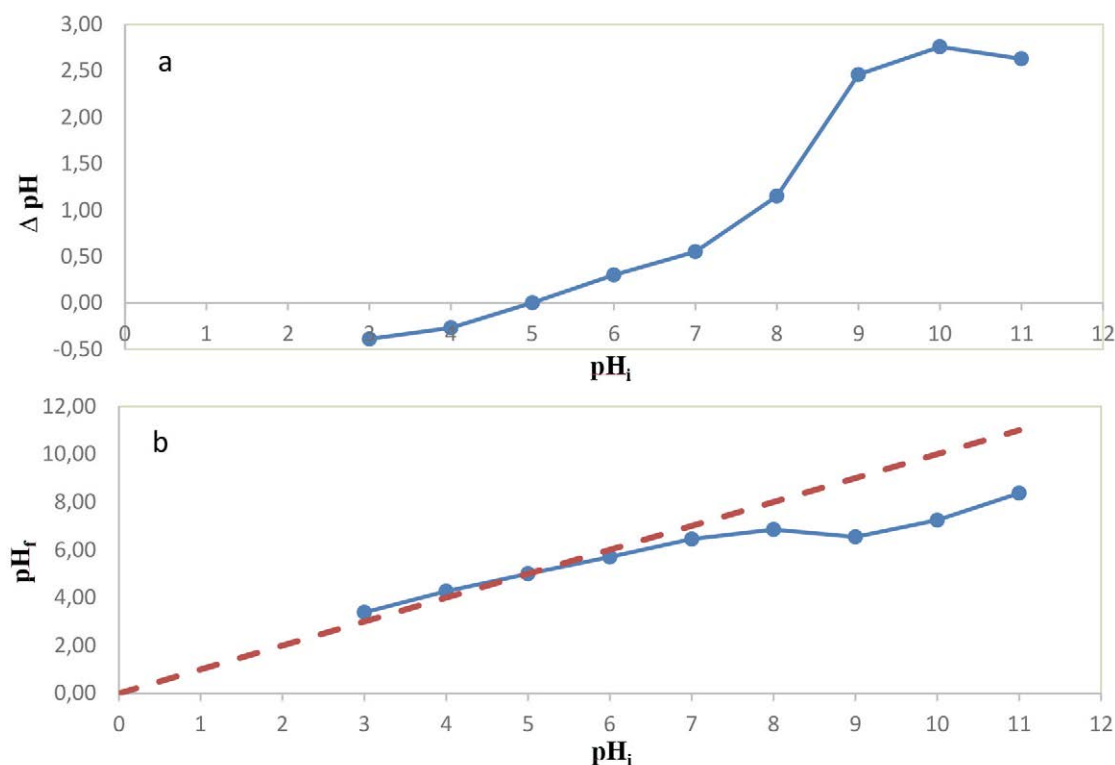


**Figure 6.** PZC diagram for SiO<sub>2</sub>-Cys sample obtained through (a) salt addition method and (b) drift method using 0.1 M NaNO<sub>3</sub> at 25 °C. The diagram illustrates the variation in surface charge as a function of pH, indicating PZC.

ions in the diffuse swarm to neutralize the surface charge at the PZC, so any ions that are adsorbed must be adsorbed in surface complexes.<sup>40</sup> The PZC achieved (pH = 5), showed the existence of perfect charge balance in the acidic region in an aqueous solution.

### 3. 7. Effect of Adsorbent Dose

Adsorption capacity reaches a maximum as adsorbent (i.e. SiO<sub>2</sub>-Cys) dosage rises, while all other parameters remain constant. As(III) uptake decreases with increasing adsorbent dosage, as shown in Figure 8. Since there are more active sites at lower adsorbent concentrations, increasing the dosage of adsorbent causes particle

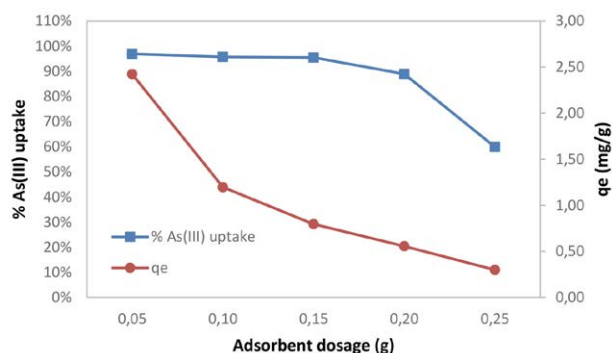
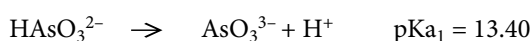
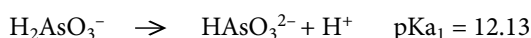


**Figure 7.** Adsorbent dosage effect on the adsorption of As(III) using SiO<sub>2</sub>-Cys at 25 °C. The graph shows the influence of varying SiO<sub>2</sub>-Cys dosage in the range of 0.05–0.25 g on the adsorption efficiency of As(III).

aggregation, which lowers adsorption capacity and As(III) uptake. Figure 8 shows that 0.05 g of nanosilica has the highest adsorption capacity and achieves a 97% uptake.

### 3. 8. Effect of pH

Arsenic existing in different forms, alteration in the oxidation state, and solubility in aqueous solutions are all strongly influenced by pH.<sup>41</sup> According to literature,<sup>42</sup> As(III) species are predominant in nature. Arsenite can be found in water as arsenous acid (H<sub>3</sub>AsO<sub>3</sub>) with pKa values as shown in Scheme 1.



**Scheme 1:** pKa values of arsenous acid

Arsenic can be soluble in water at pH levels between 2 and 11 with the right chemical and physical conditions, but generally, it is soluble at low pH levels (less than 2).<sup>43</sup> Oxidation of the trivalent form of As to pentavalent happens rather slowly; days are needed. Oxidation occurs when air is present between 4 to 9 days. However, it takes 2 to 5 days when pure oxygen is present.<sup>44</sup>

The impact of aqueous solution initial pH values, in the range of pH 3 to 8 on the adsorption behaviour of

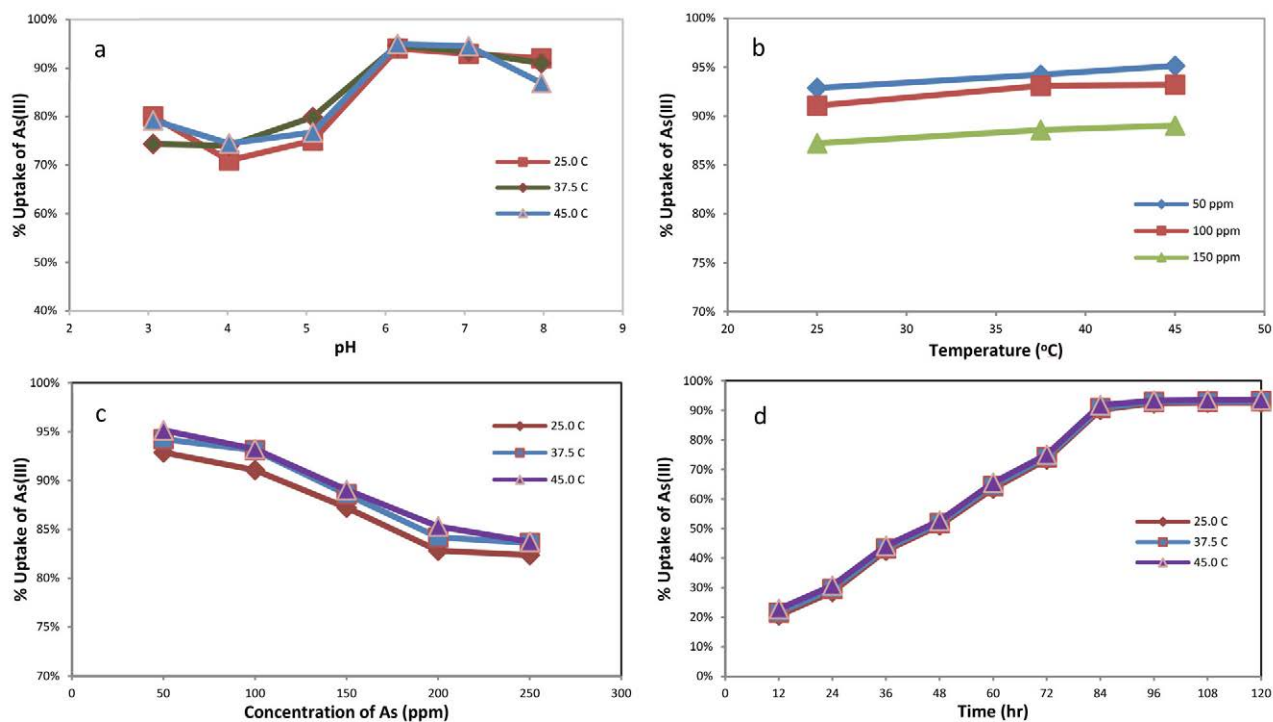


**Figure 8.** % Uptake of As(III) by 0.05 g of SiO<sub>2</sub>-Cys at different (a) pH, (b) temperatures, (c) As(III) concentrations, and (d) contact times. % Uptake experiments were carried out in the range of 25, 37.5, and 45 °C

SiO<sub>2</sub>-Cys for fixed As(III) concentration was investigated at different temperatures. It can be clearly observed from Figure 8a that the % uptake of As(III) was low at pH 3 to 5, indicating the existence of competitive adsorption on SiO<sub>2</sub>-Cys surface between H<sub>3</sub>O<sup>+</sup> and H<sub>4</sub>AsO<sub>3</sub><sup>+</sup> at low pH, and its approach was constrained by the repulsive force that existed between the protonated surface and H<sub>4</sub>AsO<sub>3</sub><sup>+</sup>. After that, the % uptake of As(III) increased from pH 6 to pH 8, where pH 6 produced the highest level of uptake. The positive charges or the negative charges on SiO<sub>2</sub>-Cys may change depending on the H<sup>+</sup> concentration so that H<sub>4</sub>AsO<sub>3</sub><sup>+</sup> ions were more readily absorbed when placed on the silica surface. The percentage of As(I-II) ions that are absorbed increases with increasing solution pH for this reason.<sup>45</sup> The relation between PZC and the pH of high uptake comes into play when examining the uptake of ions onto a surface. The PZC of a particular surface can be used in the adsorption prediction of an ion onto that surface, with a higher PZC increasing the likelihood of adsorption. To complicate the matter further, the pH of a given solution also impacts ion adsorption. In a basic solution (higher pH) or acidic solution (lower pH), the adsorption of a given ion can be significantly altered or even reduced altogether. So in our case, pH = 5 is the point at which a molecule or surface has neither a net positive nor negative charge, making it a neutral surface, with higher numbers indicating a more basic/alkaline surface and lower numbers indicating a more acidic surface.

### 3. 9. Effect of Temperature

For the purpose of determining how temperature affects the adsorption of As(III) by SiO<sub>2</sub>-Cys, experiments were performed at 25, 37.5, and 45 °C. Figure 8b shows a slightly increasing % uptake of As(III) ions as increasing the temperature from 25 to 45 °C, which demonstrated the energy-dependent and endothermic nature of the As(III) ion adsorption mechanism.<sup>46</sup>

### 3. 10. Effect of Initial Concentration

The initial As(III) concentration was varied from 50 to 250 ppm in order to study the sorption of As(III) ions onto SiO<sub>2</sub>-Cys composite. As(III) ions were readily adsorbed at low initial concentrations of As(III) because there are a lot of adsorption sites available and the surface area is relatively large. As(III) ion removal percentages decline at higher initial concentrations due to a limited number of total adsorption sites (Figure 8c).

### 3. 11. Contact Time Effect and Models of Sorption Kinetic

It is evident from the findings in Figure 8d that the As(III) ions adsorption efficiency increases rapidly during the first 84 hours before gradually reaching equilibrium. This phenomenon indicates that, with increasing contact time, these binding sites gradually become fewer until reaching saturation, which resulted in decreased uptake and the ad-

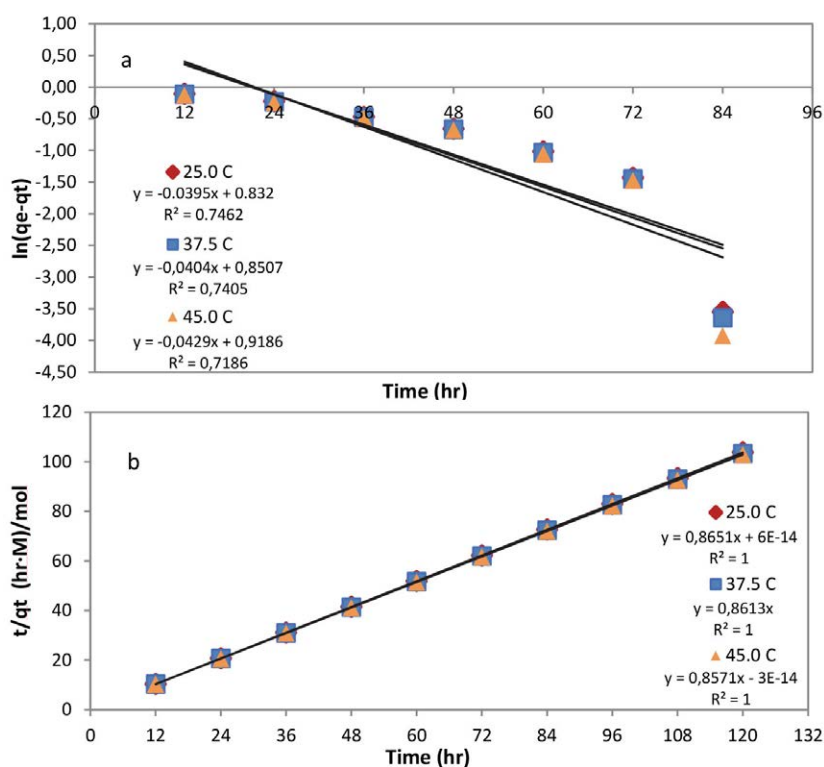


**Figure 9.** (a) Pseudo-first order and (b) Pseudo-second order adsorption kinetics of 50 ppm As(III) on 0.05 g SiO<sub>2</sub>-Cys at pH 6 and different temperatures (25.0, 37.5 and 45.0 °C).

**Table 1.** Kinetic parameters for adsorption of 50 ppm As(III) on 0.05 g SiO<sub>2</sub>-Cys at pH 6 and different temperatures (25.0, 37.5 and 45.0 °C).

Kinetic models	Parameters	T (K)		
		298	310.5	318
Pseudo-first-order model	$k_1$ (L/min)	0.0395	0.0404	0.0429
	$q_e$ (mg/g)	2.298	2.341	2.506
	$R^2$	0.746	0.741	0.719
Pseudo-second-order model	$k_2$ (g/mg.min)	0.748	0.742	0.735
	$q_e$ (mg/g) calculated	1.156	1.161	1.167
	$q_e$ (mg/g) experimental	1.157	1.163	1.168
	$R^2$	1.000	1.000	1.000

sorption reaction reaching equilibrium. The equilibrium time has been taken as 96 hours. The linear plots of  $[\ln(q_e - q_t)]$  vs. *time* and  $[t/q_t]$  vs. *time* were displayed in Figure 9a and Figure 9b for As(III), and the values of  $q_e$ ,  $k_1$ ,  $k_2$ , and correlation coefficient ( $R^2$ ) are given in Table 1. The pseudo-second-order kinetic model was better suited to explain the adsorption process of As(III) by SiO<sub>2</sub>-Cys due to its  $R^2$  values ( $R^2 = 1.00$ ) and its calculated adsorption capacity ( $q_e$ ) was close to the experimental equilibrium adsorption capacity. One could argue that the rate-controlling step is chemisorption.<sup>47</sup>

### 3. 12. Initial Concentrations Effect and Models of Sorption Isotherm

To understand what is occurring in the adsorption process (i.e. the mechanism of interaction) we must deal

with adsorption isotherms. Three distinct isotherm models were employed for the adsorption of As(III) onto SiO<sub>2</sub>-Cys: Langmuir, Freundlich, and D-R.<sup>48</sup> Isotherm models as shown in Figures: 10b, 10c and 10d for As(III). Table 2 displays the isotherm parameter values that were determined. The adsorption of As(III) on SiO<sub>2</sub>-Cys show high correlation coefficients ( $R^2 > 0.97$ ) for both the Langmuir and Freundlich isotherm models. The fact that the adsorption process included both monolayer and multilayer adsorption possibly contributed to that.

Figure 10a shows the effect of adsorption of the initial concentration of As(III) by SiO<sub>2</sub>-Cys. The adsorption capacities ( $q_e$ ) of As(III) were obviously increased as the initial concentration of As(III) increased at pH 6. The process of adsorption may have been enhanced because an increase in the initial concentration of As(III) provided a

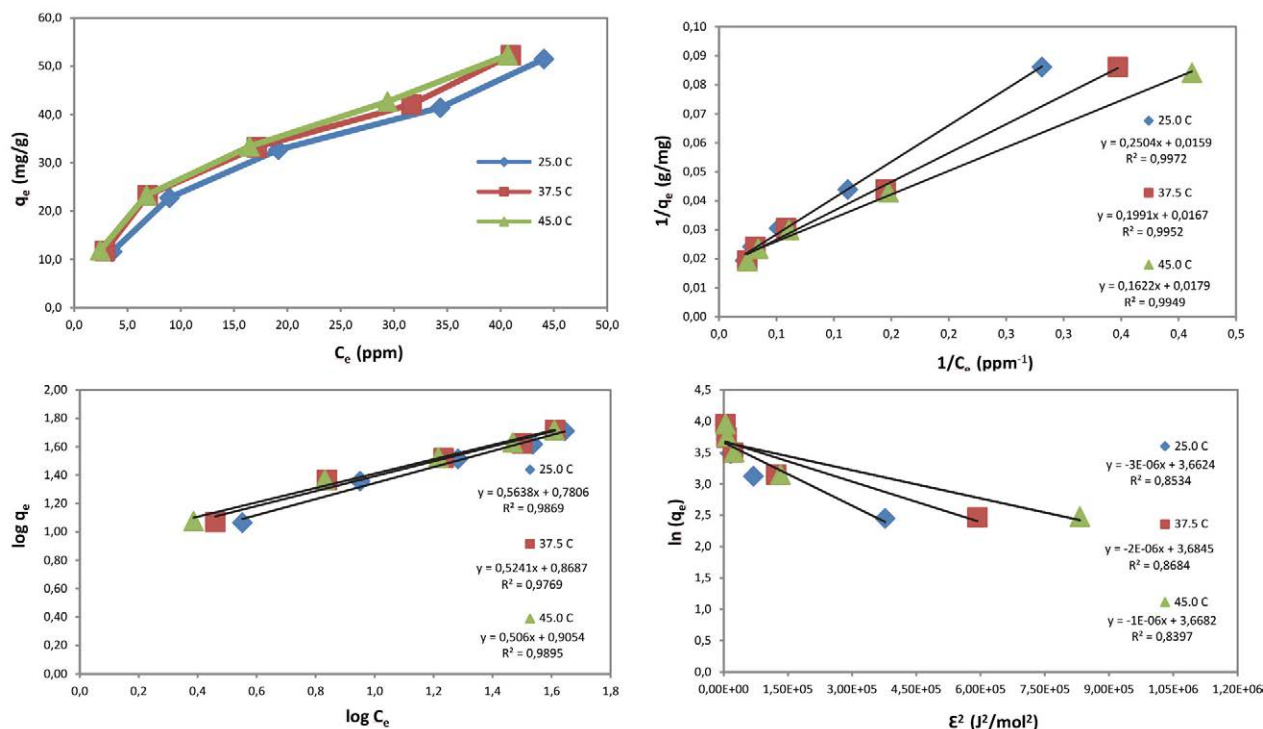


**Figure 10.** Plots of (a) adsorption isotherm of As(III) on SiO<sub>2</sub>-Cys, (b) linearized Langmuir(I), (c) linearized Freundlich, (d) D-R isotherm. The sorption onto 0.05 g SiO<sub>2</sub>-Cys using the three isotherm models was investigated with solutions of variable concentrations (50, 100, 150, 200 and 250 ppm) for As(III) at pH 6.0 and at 25.0, 37.5 and 45.0 °C.

potent impact to overcome the mass transfer resistance between the solid phase and aqueous phase.<sup>49</sup>

With a finite number of identical centers evenly distributed across the surface of the sorbent, Langmuir adsorption distinguishes monolayer adsorption from other types of adsorption. A high level of adsorption capacity (66.67 mg/g) was attained compared with other sorbents used with As(III) (Table 3). The separation factor ( $R_L$ ) and also known as the equilibrium parameter can be calculated using the Langmuir isotherm. As shown in Table 2, it was found that ( $0 < R_L < 1$ ), which can be explained that the adsorption of As(III) on SiO<sub>2</sub>-Cys was favourable.<sup>50</sup> Additionally, despite the unity, which is considered a completely reversible case, the value of  $R_L$  tended toward zero (the completely ideal irreversible case).<sup>51</sup>

Another model, Freundlich isotherm, is used to describe the adsorption on a solid surface. This model describes heterogeneous surface adsorption. Freundlich constant  $K_F$  and  $n$  are distinctive features related to the relative sorption capacity of the sorbent and the intensity of sorption, respectively. The values of  $n$ , represent the degree of favorability of adsorption. As illustrated in Table 2, the values of  $n$  are greater than 1.0, which shows that the adsorption of As(III) on SiO<sub>2</sub>-Cys is a successful process across the entire temperature and concentration range.<sup>52</sup>  $K_F$  (mg/g) for the adsorption of As(III) increased with temperature, demonstrating the endothermic nature of the adsorption process.<sup>53</sup>

To calculate the apparent free energy of adsorption, the D-R isotherm was used.<sup>50</sup> This isotherm model is more general than Langmuir isotherm as it rejects the homogeneous surface or constant adsorption potential. It is possible to get a good idea of the general mechanism of the sorp-

tion process from the amount of free energy of adsorption ( $E$ ). Typical values for  $E$  range from 8 to 16 kJ/mol, if the adsorption follows ion exchange, and  $< 8$  kJ/mol, if physical adsorption dominates. The calculated  $E$  values are reported in Table 2 and indicate that As(III) ion uptake by SiO<sub>2</sub>-Cys follows physical adsorption rather than chemical ion exchange.<sup>54</sup> The same outcomes were observed when examining the values of  $R_L$ ,  $K_F$ , and  $n$ .

### 3. 13. Thermodynamic Studies

The following equations were applied to determine the system's thermodynamic functions, such as changes in Gibbs free energy ( $\Delta G^\circ$ ), enthalpy of adsorption ( $\Delta H^\circ$ ), and entropy of adsorption ( $\Delta S^\circ$ ):

$$\Delta G^\circ = -RT \ln K_d = \Delta H^\circ - T \Delta S^\circ \quad (9)$$

$$\ln K_d = \frac{\Delta S^\circ}{R} - \frac{\Delta H^\circ}{RT} \quad (10)$$

The values of  $K_d$  (distribution coefficient) are shown in Table 4, which were calculated from the intercept of  $\ln(q_e/C_e)$  vs.  $q_e$ . Results revealed that  $K_d$  rises with  $T$ , indicating the endothermic nature<sup>63</sup> of As(III) adsorption on SiO<sub>2</sub>-Cys.

**Table 4.** Distribution coefficient for As(III) SiO<sub>2</sub>-Cys at pH 6.0 at different temperatures.

$T$ (°C)	$K_d$	$\ln K_d$
25.0	3.262	1.182
37.5	4.088	1.408
45.0	4.895	1.588

**Table 2.** Langmuir, Freundlich and D-R isotherm parameters for SiO<sub>2</sub>-Cys towards As(III) at different temperatures (25.0, 37.5 and 45.0 °C).

$T$ (°C)	Langmuir Isotherm				Freundlich Isotherm			D-R Isotherm			
	$R^2$	$q_m$ (mg/g)	$K_L$ (L/mg)	$R_L$	$R^2$	$n$	$K_F$ (mg/g)	$R^2$	$B$ (mol <sup>2</sup> /kJ <sup>2</sup> )	$q_m$ (mg/g)	$E$ (kJ/mol)
25.0	0.997	66.667	0.060	0.250	0.986	1.776	6.026	0.853	$3 \times 10^{-6}$	38.939	0.408
37.5	0.995	62.500	0.080	0.199	0.976	1.908	7.379	0.868	$2 \times 10^{-6}$	39.805	0.500
45.0	0.994	58.824	0.105	0.160	0.989	1.976	8.035	0.839	$1 \times 10^{-6}$	39.173	0.707

**Table 3:** Comparison of adsorption capacities of different adsorbents for the removal of As(III)

	Adsorbent	qm (mg/g)	Year of publication	Reference
1	Waste rice husk	0.02	2006	55
2	Non-immobilized sorghum biomass	2.765	2007	56
3	Immobilized sorghum biomass	2.437		
4	Calix arene-appended functional material	0.412	2012	57
5	Thioglycolated sugarcane carbon	0.085	2013	58
6	Fe-Mn binary oxide impregnated chitosan beads	54.2	2015	59
7	Recombinant E. coli expressing arsR	2.32	2018	60
8	Iron-olivine composite	2.831	2018	61
9	Graphene Oxide and Granular Ferric Hydroxide	0.023	2023	62



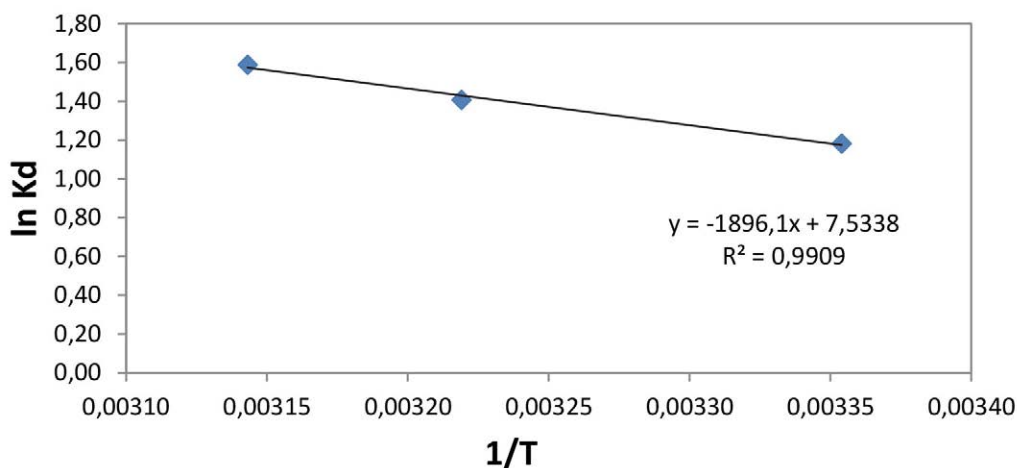


Figure 11. Plot of  $\ln K_d$  vs  $1/T$  for 50 ppm As(III) on 0.05 g SiO<sub>2</sub>-Cys at pH 6.0 and different temperatures (25.0, 37.5 and 45.0°C).

Figure 11 illustrates how  $\Delta H^\circ$  and  $\Delta S^\circ$  were determined from the slope and intercept of the plot of  $\ln K_d$  vs  $1/T$  for As(III) ion, while  $\Delta G^\circ$  values were calculated using equation 9.

$\Delta G^\circ$  measures the degree of the spontaneity of the adsorption process. More negative values of the Gibbs free energy represent adsorption processes that are more energetically advantageous.<sup>64</sup> Results in Table 5 show a negative value of  $\Delta G^\circ$ , which indicated that the adsorption of As(III) onto SiO<sub>2</sub>-Cys is energetically and agreed with  $K_d$  values.

Table 5. Thermodynamic parameters for adsorption of As(III) by SiO<sub>2</sub>-Cys.

$\Delta G^\circ$ (kJ/mol)	$\Delta H^\circ$ (kJ/mol)	$\Delta S^\circ$ (J/mol K)
-2.931	15.763	62.629

The positive values of  $\Delta H^\circ$  (Table 5) demonstrated that As(III) on SiO<sub>2</sub>-Cys is adsorbed through an endothermic process. In addition, the type of adsorption can be accepted as a physical process when the value of  $\Delta H^\circ$  is less than 40 kJ/mol.<sup>65</sup>

Van der Waals force and electrostatic force between adsorbate molecules and atoms that make up the adsorbent surface are the main causes of physical adsorption. The As(III) ions are well solvated, so they must lose some of their hydration to be adsorbed, which is one explanation for  $\Delta H^\circ$  being positive. The energy needed to carry out the ions process of dehydration outweighs the exothermicity of the ions attachment to the surface.<sup>54,66</sup>

The increased randomness at the solid/solution interface during the adsorption process is indicated by the positive value of  $\Delta S^\circ$  for SiO<sub>2</sub>-Cys. Adsorbent affinity for the As(III) ions used is also reflected. The presence of randomness in the system is made possible by the fact that

the adsorbed water molecules, which the adsorbate species displace, gain more translational energy than is lost by the adsorbate ions. Dehydration of As(III) ions also makes the system more random.<sup>66,67</sup>

### 3. 14. Desorption and Stability Experiments

When dealing with aqueous media solutions, various biological media are options that could be used. The most popular ones were chosen as shown in Table 6. The stability of the sorbent is being compared in these different solutions. Based on the % removal of As(III) by SiO<sub>2</sub>-Cys in these solutions, the stability is evaluated. SiO<sub>2</sub>-Cys exhibits the highest stability in Ringer lactate, as indicated by the % removal value of 6.22. This suggests that Ringer lactate is effective as a media when delivering As(III) using SiO<sub>2</sub>-Cys with a relatively low percentage of the substance released. On the other hand, the sorbent shows the lowest stability in 0.1 M HCl (stomach acidic environment), as indicated by the % removal value of 21.70. This implies that the sorbent is less effective at removing As(III) in 0.1 M HCl compared to other media. A higher percentage of As(III) is released after the sorption process in this solution. Based on these findings, it is concluded that SiO<sub>2</sub>-Cys exhibits superior stability and performance in physiological conditions (represented by Ringer lactate), making it more suitable for the desired drug delivery application. It could be further optimized SiO<sub>2</sub>-Cys formulation and drug loading process to enhance its stability in physiological environments, ensuring effective drug release and targeted delivery to cancer cells.

### 3. 15. Regenerability of SiO<sub>2</sub>-Cys in Multiple As(III) Adsorption/ Desorption Cycles

The reuse of a functionalized adsorbent is of paramount importance from economic and synthetic points of view. Because of this, the feasibility of reusing SiO<sub>2</sub>-Cys

**Table 6.** Determination of 5.00 ppm As(III) in presence of nanosilica-cysteine composite from different media at 25 °C

Media	pH	Absorbance of SiO <sub>2</sub> -Cys*	Absorbance of SiO <sub>2</sub> -Cys/ATO*	Amount of As(III) detected (ppm)	% Release
Normal saline	7.4 ± 0.01	0.131	0.361	0.949	18.98
Dextrose	7.4 ± 0.01	0.102	0.236	0.407	8.14
Ringer lactate	7.4 ± 0.01	0.102	0.219	0.311	6.22
Water	7.4 ± 0.01	0.125	0.271	0.475	9.50
0.1 M HCl	1.0 ± 0.01	0.122	0.376	1.085	21.70

\*Mean value of three determinations

after four reuse cycles was assessed in this work. Results (Figure 12) showed that SiO<sub>2</sub>-Cys loses about 35% of the As(III) removal efficiency in the Ringer lactate media (from ~94% to 58%), about 45% in both the Dextrose and water media, and about 50% in the Normal saline media. These results are encouraging in applying this adsorbent for As(III) in drug delivery and biological systems.

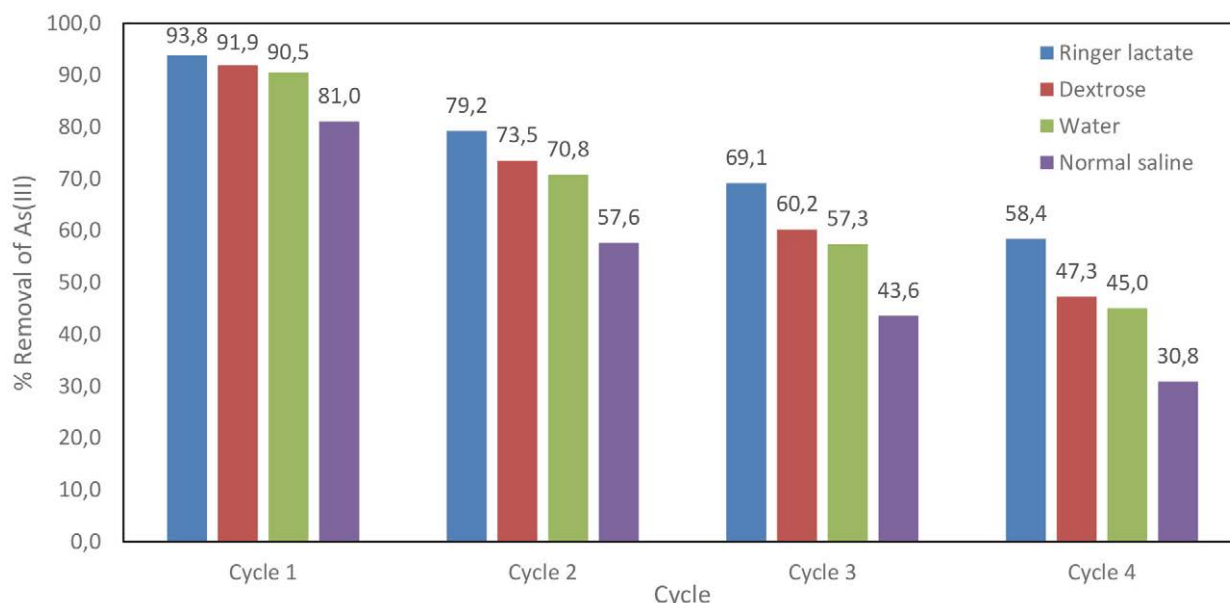
#### 4. Conclusions

The modification of silica nanoparticles with cysteine (SiO<sub>2</sub>-Cys) has been carried out and further characterized by ATR-FTIR, TGA, XRD, SEM, and TEM techniques. Using batch sorption experiments under different experimental conditions, the removal of As(III) ions by SiO<sub>2</sub>-Cys from aqueous solutions was studied. Was found that the As(III) sorption onto SiO<sub>2</sub>-Cys is highly dependent on pH. Kinetic studies indicate that sorption needs 96 hours to reach equilibrium, and its data complied with the pseudo-second-order model well. High correlation coefficients ( $R^2 > 0.97$ ) of the two isotherm models, Langmuir and Freundlich, for the adsorption of As(III) on SiO<sub>2</sub>-

Cys are achieved, which can be explained by the fact that both monolayer and multilayer adsorption is included in the process. Thermodynamic parameters demonstrated the endothermic and spontaneous nature of the sorption process. SiO<sub>2</sub>-Cys represents a featured sorbent in which it works in harmony with the biological environment; this could have a practical application in drug delivery and biological systems (promising candidates for ATO delivery in medical therapy applications). In addition, this sorbent has a high adsorption capacity (66.67 mg/g) and can be reused without significant loss of performance. This characteristic reduces the overall cost and environmental impact associated with using this sorbent. The prepared composite is thus an effective, efficient, and biologically compatible for As(III) adsorption and could be used for ATO delivery in cancer therapy applications.

#### 5. References

1. D. R. Lide (Ed.): *CRC Handbook of Chemistry and Physics*, CRC Press, Boca Raton, Florida, U.S., 2002, pp. 4.4.
2. J. A. Dean (Ed.): *Lange's Handbook of Chemistry*, McGraw-

**Figure 12.** As(III) adsorption/desorption regeneration cycles on SiO<sub>2</sub>-Cys, at pH 7.4 and at 37.5°C.

- Hill Book Company, New York, U.S., 2002, pp. 3.17.
3. J. P. Hughes, L. Polissar, G. Van Belle, Evaluation and synthesis of health effects studies of communities surrounding arsenic producing industries, *Int. J. Epidemiol.* **1988**, *17*, 407–413. DOI:10.1093/ije/17.2.407
  4. National Research Council, *Arsenic in Drinking Water*, The National Academies Press, Washington, DC, U.S., 1999. pp. 15–16.
  5. M. F. Hughes, B. D. Beck, Y. Chen, A. S. Lewis, D. J. Thomas, Arsenic Exposure and Toxicology: A Historical Perspective. *Toxicol Sci.* **2011**, *123*(2), 305–332. DOI:10.1093/toxsci/kfr184
  6. D. Mohan, P. Charles, Arsenic removal from water/wastewater using adsorbents – a critical review, *J. Hazard. Mater.* **2007**, *142*(1), 1–53. DOI:10.1016/j.jhazmat.2007.01.006
  7. Y. S. T. Choong, G. T. Chuah, H.Y. Robia, L. F. G. Koay, I. Azni, Arsenic toxicity, health hazards and removal techniques from water: an overview, *Desalination* **2007**, *217*, 139–166. DOI:10.1016/j.desal.2007.01.015
  8. S. Shevade, R. Ford, Use of synthetic zeolites for arsenate removal from pollutant water, *Water Res.* **2004**, *38*, 3197–3204. DOI:10.1016/j.watres.2004.04.026
  9. WHO, *Exposure to arsenic: a major public health concern*, WHO Document Production Services, Geneva, Switzerland, **2010**, pp. 1–3.
  10. EPA, *Environmental Pollution Control Alternatives*, EPA/625/5-90/025, EPA/625/4-89/023, Cincinnati, US, **1990**, pp.19.
  11. M. J. Maushkar, *Guidelines for water quality monitoring*, Central pollution control board (A Government of India organisation), Delhi, India, **2007**.
  12. BIS, *Indian Standard Drinking Water Specification*, Bureau of Indian Standard Publication, New Delhi, India, **1991**, pp. 3.
  13. T. R. Harper, N. W. Kingham, Removal of arsenic from wastewater using chemical precipitation methods, *Water Environ. Res.* **1992**, *64*, 200. DOI:10.2175/WER.64.3.2
  14. W. H. Ficklin, Separation of arsenic(III) and arsenic(V) in ground waters by ion-exchange, *Talanta* **1983**, *30*, 371. DOI:10.1016/0039-9140(83)80084-8
  15. D. Mohan, C.U. Pittman, Arsenic Removal from Water/Wastewater Using Adsorbents-A Critical Review, *J. Hazard. Mater.* **2007**, *142*, 1–53. DOI:10.1016/j.jhazmat.2007.01.006
  16. A. B. Mukherjee, P. Bhattacharya, Arsenic in groundwater in the Bengal Delta Plain: slow poisoning in Bangladesh, *Environ. Rev.* **2001**, *9*(3), 189–220. DOI:10.1139/a01-007
  17. S. W. Wan Ngah, C. L. Teong, M.K. Hanafiah, Adsorption of dyes and heavy metal ions by chitosan composites a review, *Carbohydr. Polym.* **2011**, *83*, 1446–1456. DOI:10.1016/j.carbpol.2010.11.004
  18. P. Pillewan, S. Mukherjee, T. Roychowdhury, S. Das, A. Bansiwala, S. Rayalu, Removal of As(III) and As(V) from water by copper oxide incorporated mesoporous alumina, *J. Hazard. Mater.* **2011**, *186*, 367–375. DOI:10.1016/j.jhazmat.2010.11.008
  19. X. Qu, P. Alvarez, Q. Li, Applications of nanotechnology in water and wastewater treatment, *Water Res.* **2013**, *47*, 3931–3946. DOI:10.1016/j.watres.2012.09.058
  20. K. Hristovski, A. Baumgardner, P. Westerhoff, Selecting metal oxide nanomaterials for arsenic removal in fixed bed columns: from nanopowders to aggregated nanoparticles media, *J. Hazard. Mater.* **2007**, *147*(1), 265–274. DOI:10.1016/j.jhazmat.2007.01.017
  21. X. Qu, J. Brame, Q. Li, P. Alvarez, Nanotechnology for a safe and sustainable water supply: enabling integrated water treatment and reuse, *Acc. Chem. Res.* **2013**, *46*(3), 834–843. DOI:10.1021/ar300029v
  22. M. S. Angotzi, V. Mameli, C. Cara, K. B. Borchert, C. Steinbach, R. Boldt, D. Schwarz, C. Cannas, Meso- and Macroporous Silica-Based Arsenic Adsorbents: Effect of Pore Size, Nature of the Active Phase, and Silicon Release. *Nanoscale Adv.* **2021**, *3*, 6100–6113. DOI:10.1039/D1NA00487E
  23. J. Dobrynska, Amine- and Thiol-Functionalized SBA-15: Potential Materials for As(V), Cr(VI) And Se(VI) Removal from Water. Comparative Study, *J. Water Proc. Eng.* **2021**, *40*, 101942. DOI:10.1016/j.jwpe.2021.101942
  24. H. T. Fan, X. Fan, J. Li, M. Guo, D. Zhang, F. Yan, T. Sun, Selective Removal of Arsenic(V) from Aqueous Solution Using a Surface-Ion Imprinted Amine-Functionalized Silica Gel Sorbent, *Ind. Eng. Chem. Res.* **2012**, *51*, 5216–5223. DOI:10.1021/ie202655x
  25. O. Valdés, A. Marican, Y. Mirabal-Gallardo, L.S. Santos, Selective and Efficient Arsenic Recovery From Water Through Quaternary Amino-Functionalized Silica, *Polymers (Basel, Switz.)* **2018**, *10*, 626. DOI:10.3390/polym10060626
  26. S. Azizian, Kinetic models of sorption: a theoretical analysis, *J. Colloid Interface Sci.* **2004**, *276*, 47–52. DOI:10.1016/j.jcis.2004.03.048
  27. Langmuir, The sorption of gases on plane surfaces of glass, mica and platinum, *J. Am. Chem. Soc.* **1918**, *40*, 1361–1403. DOI:10.1021/ja02242a004
  28. H. Freundlich, Over the sorption in solution, *J. Phys. Chem.* **1906**, *57*, 385–470. DOI:10.4236/ajac.2013.47A001
  29. M.M. Dubinin, L.V. Radushkevich, Equation of the characteristic curve of activated charcoal, *Chem. Zentralbl.* **1947**, *1*, 875–890.
  30. T. Fan, Y. Liu, B. Feng, G. Zeng, C. Yang, M. Zhou, H. Zhou, X. Wang, Biosorption of cadmium(II), zinc(II) and lead(II) by *Penicillium simplicissimum*: Isotherms, kinetics and thermodynamics, *J. Hazard. Mater.* **2008**, *160*(2), 655–661. DOI:10.1016/j.jhazmat.2008.03.038
  31. M. Du, Y. Zheng, Modification of silica nanoparticles and their application in UDMA dental polymeric composites, *Polym. Compos.* **2007**, *28*, 198–207. DOI:10.1002/pc.20377
  32. A. Khataee, A. Movafeghi, F. Nazari, F. Vafaei, M. Dadpour, Y. Hanifehpour, S. Joo, The toxic effects of L-Cysteine-capped cadmium sulfide nanoparticles on the aquatic plant *Spirodela polyrrhiza*, *J. Nanopart. Res.* **2014**, *16*, 2774–2784. DOI:10.1007/s11051-014-2774-7
  33. V. Jadhav, S. Sachar, S. Chandra, D. Bahadur, P. Bhatt, Synthesis and Characterization of Arsenic Trioxide Nanoparticles and Their In Vitro Cytotoxicity Studies on Mouse Fibroblast and Prostate Cancer Cell Lines, *J. Nanosci. Nanotechnol.* **2016**, *16*, 7599–7605. DOI:10.1166/jnn.2016.11663

34. I. M. Weiss, C. Muth, R. Drumm, H. Kirchner, Thermal decomposition of the amino acids glycine, cysteine, aspartic acid, asparagine, glutamic acid, glutamine, arginine and histidine, *BMC Biophysic.* **2018**, *11*(1), 1–15. DOI:10.1186/s13628-018-0042-4
35. J. Wu, G. Ma, P. Li, L. Ling, B. Wang, Surface modification of nanosilica with acrylsilane-containing tertiary amine structure and their effect on the properties of UV curable coating, *J. Coat. Technol. Res.* **2014**, *11*(3), 387–395. DOI:10.1007/s11998-013-9552-9
36. V. Jafari, A. Allahverdi, Synthesis and Characterization of Colloidal Nanosilica via an Ultrasound Assisted Route Based on Alkali Leaching of Silica Fume, *Int. J. Nanosci. Nanotechnol.* **2014**, *10*(3), 145–152.
37. H. Chen, H. Bian, J. Li, X. Guo, X. Wen, J. Zheng, Molecular Conformations of Crystalline L-Cysteine Determined with Vibrational Cross Angle Measurements, *J. Phys. Chem. B.* **2013**, *117*, 15614–15624. DOI:10.1021/jp406232k
38. H. Longa, X. Huang, Y. Zhenga, Y. Pengb, H. He, Purification of crude As<sub>2</sub>O<sub>3</sub> recovered from antimony smelting arsenic-alkali residue, *Process Saf. Environ. Prot.* **2020**, *139*, 201–209. DOI:10.1016/j.psep.2020.04.015
39. T. Mahmood, M.T. Saddique, A. Naeem, P. Westerhoff, S. Mustafa, A. Alum, Comparison of Different Methods for the Point of Zero Charge Determination of NiO, *Ind. Eng. Chem. Res.* **2011**, *50*, 10017–10023. DOI:10.1021/ie200271d
40. M. Khan, A. Sarwar, Determination of Points of Zero Charge of Natural and Treated Adsorbents, *Surf. Rev. Lett.* **2007**, *14*(3), 461–469. DOI:10.1142/S0218625X07009517
41. W.R. Cullen, K.J. Reimer, Arsenic speciation in the environment, *Chem. Rev.* **1989**, *89*, 713–764. DOI:10.1021/cr00094a002
42. L. Rajakovic, V. Rajakovic-Ognjanovic (Ed.): *Arsenic in Water: Determination and Removal in Arsenic - Analytical and Toxicological Studies*, InTech, 2018. DOI: 10.5772/intechopen.72058. DOI:10.5772/intechopen.72058
43. H. Garelick, A. Dybowska, E. Valsami-Jones, N. Priest, Remediation Technologies for Arsenic Contaminated Drinking Waters, *J. Soils Sediments.* **2005**, *5*, 182–190. DOI:10.1065/jss2005.06.140
44. P. Jana, REMOVAL OF ARSENIC(III) FROM WATER WITH A NEW SOLID-SUPPORTED THIOL, College of Arts and Sciences, University of Kentucky, Lexington, Kentucky, **2012**.
45. F. Khalili, A. Khalifa, G. Al-Banna, Removal of uranium(VI) and thorium(IV) by insolubilized humic acid originated from Azraq soil in Jordan, *J. Radioanal. Nucl. Chem.* **2017**, *311*, 1375–1392. DOI:10.1007/s10967-016-5031-y
46. Y. Huang, Y. Hu, L. Chen, T. Yang, H. Huang, R. Shi, P. Lu, C. Zhong, Selective biosorption of thorium (IV) from aqueous solutions by ginkgo leaf, *PLOS ONE.* **2018**, *13*(3), 0193659. DOI:10.1371/journal.pone.0193659
47. L. Dolatyari, M. Yaftian, S. Rostamnia, Removal of uranium(VI) ions from aqueous solutions using Schiff base functionalized SBA-15 mesoporous silica materials, *J. Environ. Manage.* **2016**, *169*, 8–17. DOI:10.1016/j.jenvman.2015.12.005
48. K. Foo, B. Hameed, Insights into the modeling of adsorption isotherm systems, *Chem. Eng. J.* **2010**, *156*, 2–10. DOI:10.1016/j.cej.2009.09.013
49. Z. Naseem, H. Bhatti, S. Sadaf, S. Noreen, S. Ilyas, Sorption of uranium (VI) by *Trapa bispinosa* from aqueous solution, effect of pretreatments and modeling studies, *Desalin. Water Treat.* **2016**, *57*(24), 11121–11132. DOI:10.1080/19443994.2015.1041059
50. D. Humelnicu, C. Blegescu, D. Ganju, Removal of uranium(VI) and thorium(IV) ions from aqueous solutions by functionalized silica: kinetic and thermodynamic studies, *J. Radioanal. Nucl. Chem.* **2014**, *299*, 1183–1190. DOI:10.1007/s10967-013-2873-4
51. E. Prasetyo, Synthesis of a humic acid-silica gel as a low cost adsorbent for uranium and thorium removal from wastewater, Division of Environmental Science Development, Graduate School of Environmental Science, Hokkaido University, **2016**, pp. 91–92.
52. S. Chegrouche, A. Mellah, M. Barkat, A. Aknoun, Kinetics and Isotherms for Uranium (VI) Adsorption from Aqueous Solutions by Goethite, *Am. J. Mater. Sci.* **2016**, *3*(2), 6–12.
53. U.H. Kaynar, M. Ayvacıklı, U. Hiçsönmez, S.C. Kaynar, Removal of thorium(IV) ions from aqueous solution by a novel nanoporous ZnO: isotherms, kinetic and thermodynamic studies, *J. Environ. Radioact.* **2015**, *150*, 145–151. DOI:10.1016/j.jenvrad.2015.08.014
54. A.S. Singha, A. Guleria, Chemical modification of cellulose biopolymer and its use in removal of heavy metal ions from wastewater, *Int. J. Biol. Macromol.* **2014**, *67*, 409–417. DOI:10.1016/j.ijbiomac.2014.03.046
55. M. Amin, S. Kaneco, T. Kitagawa, A. Begum, H. Katsumata, T. Suzuki, K. Ohta, Removal of arsenic in aqueous solutions by adsorption onto waste rice husk, *Ind. Eng. Chem. Res.* **2006**, *45*, 8105–8110. DOI:10.1021/ie060344j
56. N. Haque, G. Morrison, G. Perrusquia, M. Gutierrez, A. Aguilera, I. Cano-Aguilera, J. Gardea-Torresdey, Characteristics of arsenic adsorption to sorghum biomass, *J. Hazard. Mater.* **2007**, *145*, 30–35. DOI:10.1016/j.jhazmat.2006.10.080
57. I. Qureshi, S. Memon, Synthesis and application of calixarene-based functional material for arsenic removal from water, *Appl. Water Sci.* **2012**, *2*, 177–186. DOI:10.1007/s13201-012-0035-4
58. P. Roy, N. Mondal, S. Bhattacharya, B. Das, K. Das, Removal of arsenic(III) and arsenic(V) on chemically modified low-cost adsorbent: batch and column operations, *Appl. Water Sci.* **2013**, *3*, 293–309. DOI:10.1007/s13201-013-0082-5
59. J. Qi, G. Zhang, H. Li, Efficient removal of arsenic from water using a granular adsorbent: Fe-Mn binary oxide impregnated chitosan bead, *Bioresour. Technol.* **2015**, *193*, 243–249. DOI:10.1016/j.biortech.2015.06.102
60. C. Ke, C. Zhao, C. Rensing, S. Yang, Y. Zhang, Characterization of recombinant *E. coli* expressing *arsR* from *Rhodospseudomonas palustris* CGA009 that displays highly selective arsenic adsorption, *Appl. Microbiol. Biotechnol.* **2018**, *102*, 6247–6255. DOI:10.1016/j.jenvman.2017.12.040
61. P. Ghosal, K. Kattil, M. Yadav, A. Gupta, Adsorptive removal of arsenic by novel iron/olivine composite: Insights into prepa-

- ration and adsorption process by response surface methodology and artificial neural network, *J. Environ. Manage.* **2018**, *209*, 176–187. DOI:10.1016/j.jenvman.2017.12.040
62. A. Tolkou, E. Rada, V. Torretta, M. Xanthopoulou, G. Kyzas, I. Katsoyiannis, Removal of Arsenic(III) from Water with a Combination of Graphene Oxide (GO) and Granular Ferric Hydroxide (GFH) at the Optimum Molecular Ratio, *C.* **2023**, *9*, 10. DOI:10.3390/c9010010
63. T. Sato, S. Motomura, Y. Ohno, Adsorption and desorption of metal ions by systems based on cellulose derivatives that contain amino acid residues, *Textile Society Journal.* **1985**, *41* (6), 235–240. DOI:10.2115/fiber.41.6\_T235
64. L. Xia, K. Tan, X. Wang, W. Zheng, W. Liu, C. Deng, Uranium Removal from Aqueous Solution by Banyan Leaves: Equilibrium, Thermodynamic, Kinetic, and Mechanism Studies, *J. Env. Engin.* **2013**, *139*, 887–895. DOI:10.1061/(ASCE)EE.1943-7870.0000695
65. Z. Talip, M. Eral, U. Hicsonmez, Adsorption of thorium from aqueous solutions by perlite, *J. Environ. Radioact.* **2009**, *100*, 139–143. DOI:10.1016/j.jenvrad.2008.09.004
66. G. Mirzabe, A. Keshtkar, Selective sorption of U(VI) from aqueous solutions using a novel aminated Fe<sub>3</sub>O<sub>4</sub>@SiO<sub>2</sub>/PVA nanofiber adsorbent prepared by electrospinning method, *J. Radioanal. Nucl. Chem.* **2015**, *303*(1), 561–576. DOI:10.1007/s10967-014-3478-2
67. F. Khalili, G. Al-Banna, Adsorption of uranium(VI) and thorium(IV) by insolubilized humic acid from Ajloun soil – Jordan, *J. Environ. Radioact.* **2015**, *146*, 16–26. DOI:10.1016/j.jenvrad.2015.03.035

## Povzetek

Ta članek opisuje sintezo nanosilicijevega dioksida in cisteinskega kompozita (SiO<sub>2</sub>-Cys) ter njegovo uporabo kot sorbenta in nosilca za arzen(III) z uporabo različnih medijev. Za karakterizacijo SiO<sub>2</sub>-Cys so uporabili infrardečo spektroskopijo oslabiljene popolne odbojnosti s Fourierovo transformacijo, vrstično in transmisijsko elektronsko mikroskopijo, rentgensko difrakcijo in termogravimetrično analizo. S šaržno tehniko smo proučevali sorpcijo As(III) iona s SiO<sub>2</sub>-Cys, pri čemer smo upoštevali vplive pH, odmerka sorbenta, temperature, začetne koncentracije in kontaktnega časa. Glede na kinetične študije je enačba psevdodrugerega reda ustrezno opisala sorpcijo iona As(III). Na spontanost sorpcijskega procesa na SiO<sub>2</sub>-Cys nakazujejo negativne vrednosti Gibbsove proste energije ( $\Delta G^\circ$ ). Pozitivne vrednosti entalpije ( $\Delta H^\circ$ ) kažejo na endotermni proces adsorpcije, pozitivne vrednosti entropije ( $\Delta S^\circ$ ) za adsorpcijo ionov As(III) pa pomenijo, da je adsorpcija povezana z naraščajočo naključnostjo. Langmuirjev model, ki ima največjo sorpcijsko kapaciteto za SiO<sub>2</sub>-Cys (66,67 mg/g) pri 25 °C, je zagotovil boljše prilaganje sorpcijski izotermi.



Except when otherwise noted, articles in this journal are published under the terms and conditions of the Creative Commons Attribution 4.0 International License

Scientific paper

# The Comparison of the Speed of Solving Chemistry Calculation Tasks in the Traditional Way and with the use of ICT

Brina Dojer<sup>1,\*</sup>, Matjaž Kristl<sup>2</sup> and Andrej Šorgo<sup>1</sup><sup>1</sup> Faculty of Natural Sciences and Mathematics, University of Maribor, Koroška cesta 160, Maribor SI-2000, Slovenia<sup>2</sup> Faculty of Chemistry and Chemical Engineering, University of Maribor, Smetanova 17, Maribor SI-2000, Slovenia

\* Corresponding author: E-mail: brina.dojer@um.si

Received: 09-29-2023

## Abstract

Efficiency of time use is a key factor in chemistry calculation tasks, affecting both, personal and professional domains. This study is dedicated to finding the fastest methods for accomplishing chemistry tasks. Our investigation delves into the comparative temporal outlays made by students as they engage three different approaches: using an electronic calculator, a basic calculator app on a smartphone, and a desktop computer calculator. As part of our research, we examine a cohort of 52 Slovenian university students, preservice teachers who were actively enrolled in chemistry and related science programs, spanning the academic years of 2019 and 2022. The results from 2019 show that students can solve the chemistry tasks most quickly using electronic calculator and take the most time to calculate the tasks using smartphones ( $\Delta_{mean} = 133$  s;  $\Delta_{SD} = 5$  s;  $\Delta_{min} = 97$  s;  $\Delta_{max} = 131$  s). An even larger difference is observed from the 2022 study year ( $\Delta_{mean} = 189$  s;  $\Delta_{SD} = 129$  s;  $\Delta_{min} = 170$  s;  $\Delta_{max} = 625$  s). In summary, although smartphones are recognised as a multitasking device, replacing traditional single-purpose devices, they have not been able to outperform them.

**Keywords:** Chemistry tasks; chemistry calculations; electronic calculator, smartphones, computer calculators.

## 1. Introduction

Solving chemical equations and calculating quantities of reactants and products, as well as concentrations of solutions, are a traditional part of virtually every secondary and tertiary chemistry class and are skills that extend beyond the chemistry laboratory<sup>1,2</sup> and can be considered a lifelong skill.<sup>3</sup> There are basically two approaches to dealing with chemical equations. The first is algebraic, when one is more interested in proportions, and the second is more "practical", when students are expected to deal with measurable quantities. While the first approach is mainly concerned with the micro level and symbolic level, the second approach is mainly concerned with the macro level and measurable quantities associated with symbolic annotations.<sup>4</sup> Typical examples for the first approach are stoichiometric equations and for the second approach, for example the calculation of quantities used to produce solutions by mixing ingredients. The term chemical calculations is used in the text to refer to these types of chemistry tasks, although in some cases they may be considered

physics, showing the interconnectedness of the scientific disciplines.

Solving chemical calculations is anything but an easy task, because students have to switch between real (measurable) quantities and ratios and their symbolic representations,<sup>4</sup> using different procedures and concepts learned in other subjects (e.g., mathematics). Some difficulties can also be traced to teachers who try to teach their students, usually forgetting that what may be obvious to them was actually developed by some of the most brilliant minds of the past.<sup>5</sup>

Chemistry classes are compulsory for all Slovenian students in lower secondary education (8<sup>th</sup> and 9<sup>th</sup> grade of compulsory school), for students in upper secondary education and for students in many vocational education programmes, which places an additional burden on teachers, as many students lack interest, motivation and various skills to learn chemistry, including solving equations and performing calculations that are expected as learning outcomes of the courses.<sup>6</sup> An additional problem, especially in the early grades, is the need to apply mathematical pro-

cedures and concepts with which students are not familiar, such as negative exponents or logarithms. What does not make the problems easier is the finding that many students are not able to transfer knowledge and skills from mathematics to chemistry.<sup>7</sup>

Thus, to successfully teach chemical calculations to students, teachers should consider several factors at different levels of control. While teachers have very limited, if any, control over students' individual abilities and, at least in the Slovenian context, over the curriculum content prescribed by the authorities, they have almost absolute control over the methods used to teach the prescribed topics and over the application of the technology used for chemical calculations.

Typically, early in their education, students learn how to perform chemical calculations with paper and pencil, with or without the use of an electronic calculator, and later in their education they may also learn how to process data with software (e.g., structural calculations).<sup>8</sup> What makes chemical computing complex is that students need not only chemical knowledge, but also mathematical knowledge (initially algebra), language, graphing and information processing skills.<sup>9</sup> It has long been known that chemical calculations present difficulties for students, especially in molar and stoichiometric calculations<sup>10,11</sup> and that there is only a weak link between students' algorithmic skills and conceptual understanding of topics in chemistry, which is also related to solving chemical problems.<sup>12,13</sup>

In solving chemical calculations we can see two basic steps. The first is the understanding of what to do, associated with symbolic representations of substances, formulas, conventions, units of measurement, and the like, and the second part is a general ability to perform numerical operations (calculations). Both steps can be supported with or without the help of digital technologies.

Nowadays, digital technologies have become everyday companions in the professional and personal lives of teachers and students, sometimes as invisible and sometimes as visible technologies.<sup>14</sup> When teaching and learning chemistry in secondary schools and high schools, teachers and students typically use computers, tablets and smartphones to investigate substances, phenomena and processes at the macroscopic level and explain them at the submicroscopic level, which can improve understanding of chemical concepts.<sup>15,16</sup> It is beyond the scope of this article to list all possible applications of digital technologies, but we would like to highlight some references as examples of such use. For example, Dolničar et al.<sup>17</sup> have developed a molecular editor for constructing and editing molecular models; Tortosa<sup>18</sup> provides an overview of the use of data loggers in chemistry laboratories; and the potential of artificial intelligence for chemistry education has yet to be evaluated.<sup>19</sup> Nevertheless, the question of whether digital technologies are ubiquitous and pervasive is one of the most common questions that arise in schools and to which there is no simple answer.<sup>20</sup> The question that needs to be

answered is, "Is the use of computers, smartphones, or tablets always justified in schools?"

The answer to this question cannot be answered in a blanket manner, and each individual use or context of use should be evaluated and possible side effects should be considered. While the use of desktop calculators and computers is the norm in chemistry labs today, the situation with smartphones is completely different. The use of smartphones is banned in many schools or even entire school systems unless justified. It is hard to imagine someone asking students to put desktop calculators or mobile computers in a locker and punishing them if they do not. The opposite might be true for smartphones. One of the useful uses of smartphones in school could be solving chemistry problems using the smartphone calculator or searching for information about chemicals. Solving a particular task or exchanging information with colleagues while writing exams are usually the cases where the use of smartphones should be prohibited, unless the study regulations or teacher's instructions are different.

Time is a precious commodity in education, and one of the most important tasks of teachers should be time management so that they can focus their efforts on activities where they can expect to make progress in knowledge and skills. In line with Borton's reflective cycle (What?, So what?, What now?)<sup>21</sup> teachers should be able to identify portions of instruction devoted to chemical calculations when time is being wasted on routine procedures or tasks where mastery of the speed and accuracy of calculations cannot be further improved. Since numerical calculations can be performed with or without digital technologies, we were interested in finding out whether the use of different digital technologies can affect the time required to solve a typical chemistry task related to the preparation of solutions. Three standard options were included in the study: a) the standard paper – electronic calculator method; b) paper – smartphone calculator, and; c) paper – desktop computer calculator. In addition to the direct aim of the study, we also had in mind showing students how to use simple research methods that could later be used in their classroom practice in the role of reflective practitioners and researchers of their own work.<sup>22</sup>

The research question was as follows: Are there differences in the time required to solve and present chemical calculation problems between three approaches, namely a) the standard paper – electronic calculator method; b) paper – smartphone calculator; and c) paper – desktop computer calculator.

## 2. Methods

### 2.1. Sample

The sample was 52 two-stream master level preservice teachers of chemistry and other science subject from the Faculty of Natural Sciences and Mathematics, Univer-

sity of Maribor, Slovenia. The sample included 27 females and two males from a population of 29 students (56%) in a 2019 degree programme and 23 students (44%), 8 males and 15 females, from a population of students in 2022. Despite the covid 19 situation, all students in both cohorts were enrolled in an equal number of chemistry subjects in which they gained experience in solving chemical equations and quantity calculations, which was part of the curriculum.

The students were randomly divided into three groups. Each group had a similar task. The time taken to solve the task is shown in Table 1.

Some of the data are missing because some students did not cooperate on all tasks.

## 2. 2. Procedure

1. The students were given three chemistry tasks with similar data. The students had already solved similar tasks on the same level of difficulty during the study process. Each task involved data from inorganic acid (hydrochloric acid, nitric(V) acid and sulphuric(VI) acid): the volume of the acid and volumetric flask, the acid concentration and the density of the newly prepared solution.
2. The students were randomly divided into three groups. Each group had to solve the given task in three different ways 1) using the standard paper – electronic calculator method, 2) using paper – smartphone calculator and 3) using paper – desktop computer calculator. The students who solved the tasks using the standard method (1) were also given the table with specific information about the densities of the acids in different mass fractions. The other two groups were instructed to obtain the information from the Internet (using their smartphone or computer).
3. The students read the task and then began to measure the time it took them to solve the task until they had the correct result.
4. Each group was given a new task once every three weeks. The first group solved the task with hydrochloric acid using basic calculator app on their smartphones.

After three weeks, the same students were given the task with nitric acid to solve using the standard method, etc.

### Text of Task 1:

We add 15 mL of concentrated 38% HCl into a 250 mL volumetric flask already filled with some distilled water (up to 1/3 of the volume) and dilute it to the division mark. Calculate the molar concentration and mass fraction of the newly prepared solution with a density of 1.010 g/mL.

### Text of Task 2:

We add 20 mL of concentrated 65% HNO<sub>3</sub> into a 250 mL volumetric flask already filled with some distilled water (up to 1/3 of the volume) and dilute it to the division mark. Calculate the molar concentration and mass fraction of the newly prepared solution with a density of 1.036 g/mL.

### Text of Task 3:

We add 25 mL of concentrated 96% H<sub>2</sub>SO<sub>4</sub> into a 250 mL volumetric flask already filled with some distilled water (up to 1/3 of the volume) and dilute it to the division mark. Calculate the molar concentration and mass fraction of the newly prepared solution with a density of 1.107 g/mL.

## 2. 3. Statistical analyses

Statistical analyses were performed using the open-source statistical programme Jamovi 2.3.16.<sup>23,24</sup> Research variables were analysed for mean, median, mode, standard deviation (SD), minimum and maximum.

The assumption of normality was tested using the Shapiro Wilk test and visual inspections of Q-Q plots. If the Shapiro-Wilk p-values are  $p < 0.05$ , it means that the assumptions of the normality are violated.

For the analysis comparing differences between years nonparametric Mann-Whitney test was applied. Results with a significance coefficient of less than 0.05 ( $p < 0.05$ ) were marked as statistically significant differences.

Since the assumptions of normal distribution were violated the Spearman's rho test was applied to examine of

**Table 1:** Measures of central tendencies of Tkls = time needed to solve the task with an electronic calculator, Trac = time needed to solve the task with a desktop computer calculator and Tmob = time needed to solve the task with a smartphone calculator.

Descriptives	year	N	Missing	Mean	Median	Mode	SD	Minimum	Maximum	Shapiro-Wilk	
										W	p
Tkls	2019	29	0	558	439	343 <sup>a</sup>	299	322	1436	0.686	<0.001
	2022	22	1	611	557	566 <sup>a</sup>	235	260	1118	0.941	0.210
Trac	2019	29	0	685	597	507	300	401	1564	0.686	<0.001
	2022	20	3	726	705	210 <sup>a</sup>	277	210	1320	0.988	0.993
Tmob	2019	29	0	691	574	419 <sup>a</sup>	304	419	1567	0.750	<0.001
	2022	23	0	800	674	430 <sup>a</sup>	364	430	1743	0.760	<0.001

<sup>a</sup> More than one mode exists, only the first is reported



the similarities or differences between a various approaches to solving chemical calculation problems. Additional insight was gained by applying the paired Wilcoxon signed rank test using data from an entire research sample. The effect size was calculated as Cohen's  $d$  from the value of the Wilcoxon signed rank test and interpreted according to the recommendations provided. Margins were set as follows:  $0 < \text{no effect} < 0.2 < \text{small effect} < 0.5 < \text{medium effect} < 0.8 < \text{large effect}$ .

### 3. Results

As can be seen from Table 1, the chemistry task was solved fastest in 2019 and 2022 when students used an electronic calculator, and they spent the most time solving the task using a smartphone calculator. On the other hand, it is very interesting to see that the least amount of time was spent solving the task when it was calculated using a desktop computer calculator, although this method was not the fastest to solve the task on average.

To test whether the data conformed to the normal distribution, the Shapiro-Wilk test was used. If the Shapiro-Wilk  $p$  values are  $p < 0.05$ , the assumptions for the normality test are violated. The violation is given for most items, except for the  $T_{kls}$  and  $T_{rac}$  cases in 2022.

From the results in Table 1 we can be seen that for all approaches and in all years the median values are much lower than the mean values, and that the differences between minimum and median values are quite small compared to the differences between maximum and median values. This suggests that most students took less or normal amounts of time to solve the tasks, but a few took much more time. Those students who took the most time to solve the task with one approach also took more time to solve the task with other approaches.

The minimum, maximum, median and mean times needed to solve the task increased from the time needed to solve the task with the electronic calculator to the desktop

computer calculator and smartphone calculator. The mean and median times needed for solving tasks by all approaches are longer in 2022.

In Figure 1 we visually inspect the fit of the normal distribution to the data with Q-Q plots.

Since the results of the Shapiro-Wilk test show the assumption of normality was violated, the independent Mann-Whitney test was used. It shows us that there are no statistically significant differences between years at the  $p < 0.05$  level. The results are as follows:  $T_{kls}$ :  $U = 231$ ,  $p = 0.096$ ;  $T_{rac}$ :  $U = 235$ ,  $p = 0.268$ ;  $T_{mob}$ :  $U = 242$ ,  $p = 0.092$ . This test was used because different students solved chemistry tasks in 2019 and 2022.

**Table 2:** Correlation matrix between  $T_{kls}$  = time needed to solve the task with an electronic calculator,  $T_{rac}$  = time needed to solve the task with a desktop computer calculator and  $T_{mob}$  = time needed to solve the task with a smartphone calculator.

		$T_{kls}$	$T_{rac}$	$T_{mob}$
$T_{kls}$	Spearman's rho	–		
$T_{rac}$	Spearman's rho	0.752	–	
$T_{mob}$	Spearman's rho	0.579	0.590	–

Note. All correlations are statistically significant at the  $p < 0.001$  levels.

The values of Spearman's rho in Table 2 show us that the correlation for all approaches is positive and  $p$  is significant at all levels ( $p < 0.01$ ). These results show that the students who calculate the task faster with the specific approach also take less time on average to obtain the result with the other approach. The values of the correlation coefficients can be interpreted to mean that the connections between the methods used for chemical calculations range from moderate to high. We can interpret this to mean that in addition to differences caused by a particular technology, there are other factors at play that are not accounted for in a study design.

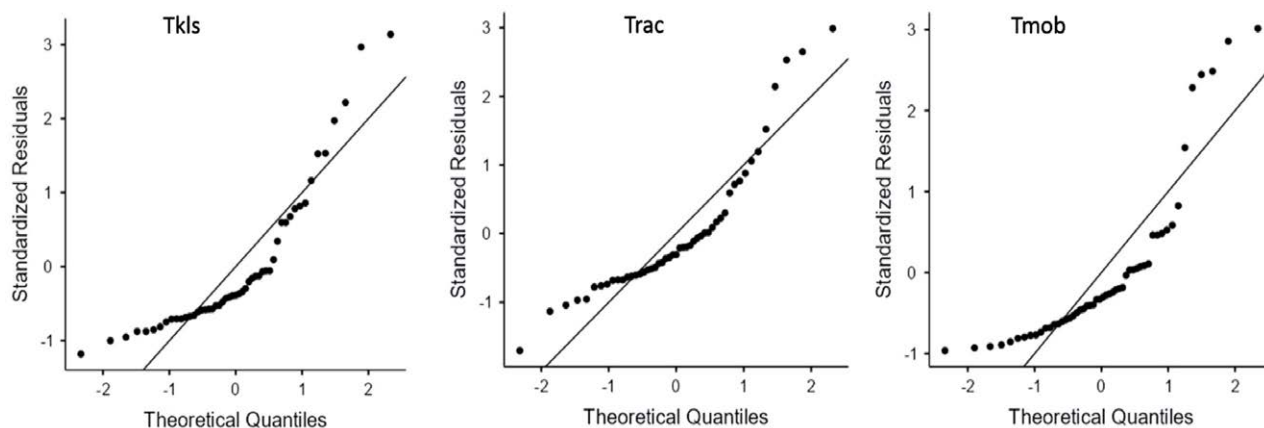


**Figure 1:** The distribution of data for each approach to solving the chemistry task. The data are not normally distributed.

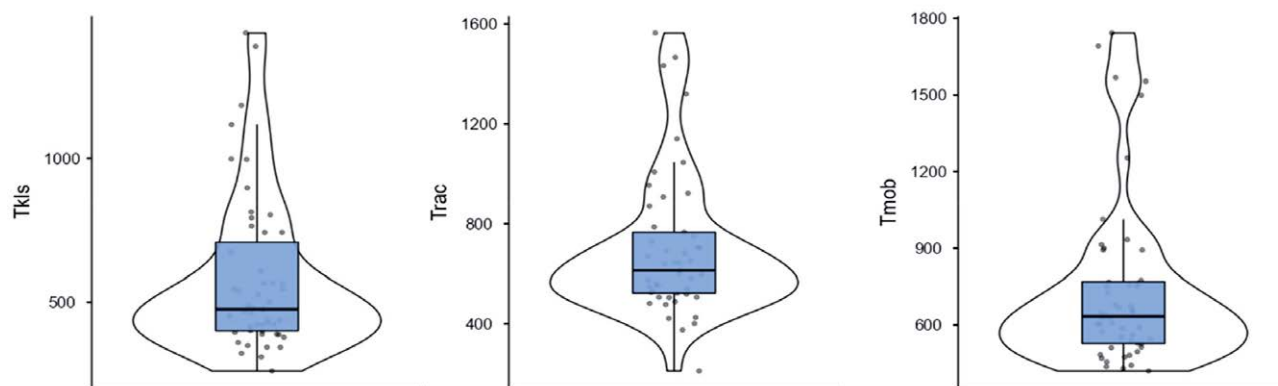


Figure 2: The distribution of the data.

The results are similarly distributed. This confirms that the students who needed more time to solve the chemistry task in one approach also needed more time in the other two approaches.

Figure 3 shows that two students actually took much more time to solve the chemistry task using the smartphone calculator than the electronic calculator and the same students also took much more time using the smartphone calculator compared to using the desktop computer calculator.

Since the comparison between years there was no statistically significant differences, we decided to perform the Paired Sample Wilcoxon signed rank test on a total sample ( $N = 52$ ).

The result of Wilcoxon signed rank test shows that there are no significant differences in the case of  $Trac - Tmob$ ,  $p = 0.901$ ,  $W = 599.5$ . The effect size for this analysis was found to be small ( $d = 0.0212$ ) according to Cohen's convention.

The result shows that there is a significant difference in the  $Tkls - Trac$  ( $p < 0.001$ ,  $W = 89.5$ ) and  $Tkls - Tmob$

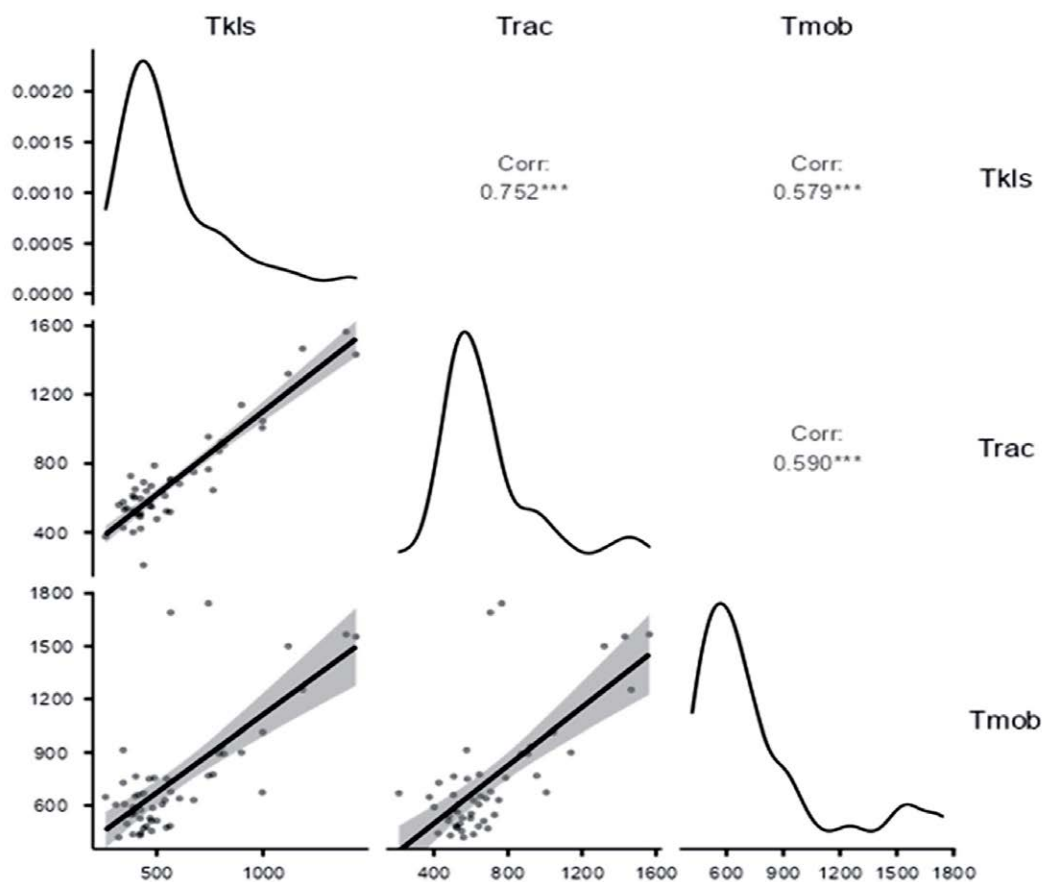


Figure 3: The distribution of the data using results of Spearman's rho.

Table 3: Paired sample T-test.

			Statistic	<i>p</i>	Mean difference	SE difference	Effect Size
Tkls	Trac	Wilcoxon <i>W</i>	89.5	<0.001	-121.45	16.0	-0.8478
Tkls	Tmob	Wilcoxon <i>W</i>	101.0	<0.001	-130.00	33.0	-0.8477
Trac	Tmob	Wilcoxon <i>W</i>	599.5	0.901	-2.50	36.0	-0.0212

( $p < 0.001$ ,  $W = 101.0$ ) cases. The effect size for these analyses was found to exceed the Cohen's convention as large ( $d = 0.848$ ).

The Wilcoxon test shows that using a smartphone and computer while calculating tasks produces similar results while using the calculator produces different results.

The Shapiro-Wilk statistic was calculated to test the assumption of normality for the paired samples t-test. The result of the Shapiro-Wilk test showed that the assumption of normality was violated in the *Tkls* – *Tmob* ( $W = 0.786$ ,  $p < 0.001$ ) cases and *Trac* – *Tmob* ( $W = 0.795$ ,  $p < 0.001$ ) while it was not violated for *Tkls* – *Trac* ( $W = 0.976$ ,  $p = 0.410$ ).

calculated with an electronic calculator, which has been mostly abandoned in private life because the alternative is always the hand as an application of smart devices that become “Swiss Army knives” of digital technologies.<sup>25</sup> Based on the results presented in the previous chapter, we can conclude that students in both cohorts, 2019 and 2022, took more time to solve the tasks when they calculated them using a desktop computer calculator and basic calculator apps on their smartphones. While the small sample limits the extent on which the findings can be generalized, we nevertheless can conclude that for some students, using the smartphone calculator takes much more time also if compared to the desktop computer calculator. It has

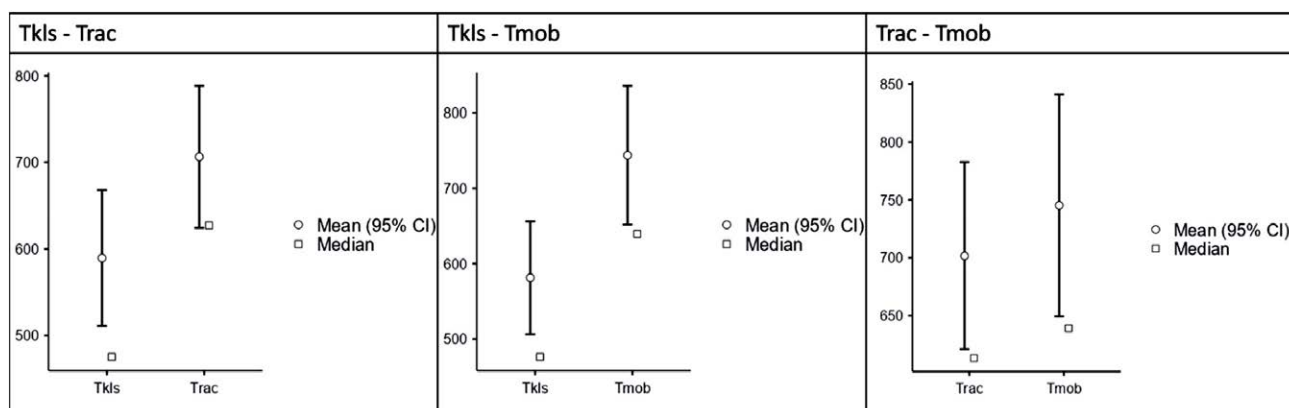


Figure 4: The distribution of the pairs of the data.

In Figure 4 we present the data distribution with the 95% confidence interval, which shows that there are no important differences between the time needed for solving tasks when calculated with a desktop computer calculator and smartphone calculator, but there are important differences when comparing the time needed for solving chemistry tasks with an electronic and a desktop computer calculator or with an electronic and a smartphone calculator. From each plot it is obvious on which approach the students used to solve the task faster.

## 4. Discussion

Calculating chemistry tasks is part of students' daily routine in chemistry classes or in the laboratory when preparing solutions or dilutions. The results of our study indicate that chemistry tasks can be solved most quickly when

been reported in earlier research, that the time spent on task is known to correlate with the results, with unsuccessful students turning to a quick solution while the successful students spending more time while solving the task.<sup>26</sup> However, due to a different experiment design, the conclusions are only partially comparable with the present study.

From our results we can draw some conclusions about the factors that may influence the choice of technology in a classroom. The technology teachers choose to use in the classroom, usually depends on the educational goals they want to achieve and the availability of those technologies. Computers, and especially in the last decade smartphones, are commonly used as educational tools in learning environments. Their integration is believed to have positive effects on student learning expectations and outcomes.<sup>27</sup> The use of computers in chemistry classrooms is common when working with computer-assisted teaching and learning (CATL) methods. These have been around for

years and are mainly used to teach students the basic concepts or principles of a dynamic chemical process.<sup>28,29</sup> Since all desktop stationary and mobile computers have built-in calculators, their use can be approved. However, in line with our findings, computers should be used primarily for explaining and illustrating concepts rather than for calculating the above written tasks. In working practice, the desktop computer calculator is mostly used in chemistry for mathematical calculations such as addition, multiplication, subtraction or division. Therefore, the use of the PC-integrated calculator for the calculation of basic chemistry tasks, although justified, is not an optimal solution.

Since chemistry calculation tasks are usually solved in classrooms or laboratories where students do not have their own laptops or PC-s and the smartphones, because of their omnipresence (if allowed in a classroom), are the next choice of the teachers to be inline with 'digital natives'.<sup>30</sup>

Over the past decade years smartphones have become more and more prevalent in the school day. It has been suggested that they can be a useful tool in chemistry to learn the naming of organic chemical compounds,<sup>31</sup> to use them in analytical chemistry for optical and electrochemical detection and chemometric applications,<sup>32</sup> for quantifying gold-nanoparticle concentrations,<sup>33</sup> for pH determination,<sup>34</sup> many students need the smartphone camera to make videos of demonstrations, to copy complex diagrams from the blackboard<sup>35</sup> etc. In addition, chemistry apps such as Chemdoodle, Periodic Table, Chemistry Helper, Reaction Flash, Learn IUPAC Nomenclature, Chemical Solution Calculator and many others whose target audience is students, chemistry professionals, and teachers, provide them with powerful and compact tools to solve problems conveniently and free themselves from traditional media, heavy books, and bulky computers.<sup>36</sup> Yet, in our study, they were found to be the least effective tool for computation compared to desktop computers and even traditional electronic calculators.

In summary the use of traditional calculators should be encouraged because of their efficiency, not because of arguments against the use of smartphones in a classroom or the lack of stationary or mobile computers in a classroom. Reasoning that in faculties or in a school the use of smartphones should be allowed during the learning process (searching for information, calculating tasks, recording processes, etc.) but should be prohibited when writing exams because of potential cheating is plausible, but efficiency in time management should be a priority. Nevertheless, unintentionally because of this system students have to get used to using electronic calculators to solve the basic chemistry tasks especially those similar to the given ones, which is the least time-consuming approach.

To our knowledge this study is the first to provide information on the time comparison for the fastest way to

calculate basic chemistry tasks similar to the one presented here, using three different approaches. An important limitation of the study was that students self-measured their time rather than using more objective measures. For future studies, it is suggested that an objective supervisor be involved in the measurement.

## 5. Conclusions

Problem-solving ability has been reported to be one of the most important skills and is predicted to be even more important in the future and thus needs to be emphasized during teachers' pre-service education. One of the basic skills for future chemistry teachers is to perform basic chemical calculation, using digital technologies. Three different approaches, using either electronic calculator, smartphone calculator, or desktop computer, were considered in the study. Although our sample size does not allow for generalization, we can draw conclusions about the fastest way to solve chemistry tasks based on the results presented above.

From our everyday experience, we can conclude that electronic calculators are mainly used for arithmetic in chemistry classes, while smartphones and computers are intended for broader use. Therefore, it is not surprising that the presented results of 2019 and 2022 show that the chemistry tasks are on average solved most quickly with the electronic calculator. Unexpectedly, the fastest particular way to obtain the result was with the desktop computer calculator. The research showed that students who took more time to solve a chemistry task using one approach also took more time to solve them using other two approaches, suggesting that students' general problem-solving ability and chemical calculation skills are more important than the choice of the particular digital technology approach.

The results may act as a suggestion to future chemistry teachers' training, showing the need to identify the task and choose the most efficient way to solve it and include those skills later in their classroom practise. The possibilities to further improve future chemistry teachers' skills in chemical calculation, as well as performing correlations between time spent on the calculation and the validity of results, depending on the three calculation approaches, should be the subject of future research.

## Acknowledgements

We thank Slovenian Research Agency P2-0057 (A.Š.) and P2-0006 (M.K.). The content of this article represents the views of the authors only and is their sole responsibility; it cannot be considered to reflect the views of the funding organization. We thank Marjeta Capl for the data from 2019 and Živa Majcen Rošker for useful comments.

## Ethics statement

All participants voluntarily participated in the study. All data were anonymized to ensure participant privacy.

## 6. References

- M. Rusek, K. Vojir, V. Sirotek, M. Klečkova, J. Štrofova, I. Bartova, How well students solve chemistry calculation tasks when starting their university studies, Project documentation: Chemistry calculations – undergraduate chemistry (teacher) students skills, ESERA 2021, Fostering scientific citizenship in an uncertain world. **2021**.
- M. Rusek, K. Vojir, I. Bartova, M. Klečkova, V. Sirotek, J. Štrofova, *Acta Chim. Slov.* **2022**, 69, 371–377. DOI:10.17344/acsi.2021.7250
- K. S. Taber, *Chem. Educ. Res. Pract.* **2016**, 17, 225–228. DOI:10.1039/C6RP90003H
- L. Z. Jaber, S. BouJaoude, *Int. J. Sci. Educ.* **2012**, 34, 973–998. DOI:10.1080/09500693.2011.569959
- A. Laugier, A. Dumon, *Chem. Educ. Res. Pract.* **2004**, 5, 327–342. DOI:10.1039/B4RP90030H
- C. Bolte, S. Streller, A. Hofstein, *How to Motivate Students and Raise Their Interest in Chemistry Education*. In: Eilks, I., Hofstein, A. (eds) *Teaching Chemistry – A Studybook*. SensePublishers, Rotterdam. **2013**, pp. 67–95. DOI:10.1007/978-94-6209-140-5\_3
- N. Jaafar, *Secondary school students' understanding of attributes for solving stoichiometry problems* (Doctoral dissertation, Universiti Teknologi MARA). **2015**. Available at: <https://ir.uitm.edu.my/id/eprint/14627/1/14627.pdf> (Assessed: July 11, 2023)
- E. Castellon, J. F. Ogilvie, *Chem. Teach. Int.* **2019**, 1, 1–6. DOI:10.1515/cti-2018-0007
- H. P. Drummond, M. Selvaratnam, *S. Afr. J. Chem.* **2009**, 62, 179–184. DOI:10.5771/0342-300X-2009-4-179
- D. Gabel, R. D. Sherwood, *J. Res. Sci. Teach.* **1984**, 21, 843–851. DOI:10.1002/tea.3660210808
- S. Novick, J. Menis, *J. Chem. Educ.* **1976**, 53, 720–722. DOI:10.1021/ed053p720
- S. BouJaoude, H. Barakat, *H. Sch. Sci. Rev.* **2000**, 81, 91–98. DOI:10.1097/00005176-200007000-00022
- S. C. Nurrenbern, M. Pickering, *J. Chem. Educ.* **1987**, 64, 508–510. DOI:10.1021/ed064p508
- J. Hallström, C. Klasander, *Int. J. Technol. Des. Educ.* **2017**, 27, 387–405. DOI:10.1007/s10798-016-9356-1
- N. Rizman Herga, D. Dinevski, *Organizacija* **2012**, 45, 108–116. DOI:10.2478/v10051-012-0011-7
- N. Rizman Herga, D. Dinevski, *Anali PAZU* **2016**, 5, 34–43. DOI:10.18690/analipazu.5.1-2.34-43.2015
- D. Dolničar, B. Boh Podgornik, V. Ferik Savec, *Acta Chim. Slov.* **2022**, 69, 167–186. DOI:10.17344/acsi.2021.7181
- M. Tortosa, *Chem. Educ. Res. Pract.* **2012**, 13, 161–171. DOI:10.1039/C2RP00019A
- M. E. Emenike, B. U. Emenike, *J. Chem. Educ.* **2023**, 100, 1413–1418. DOI:10.1021/acs.jchemed.3c00063
- M. Danet, *J. Child. Fam. Stud.* **2020**, 29, 2890–2904. DOI:10.1007/s10826-020-01760-y
- M. Skinner, D. Mitchell, *Health Soc. Care Chaplain.* **2016**, 4, 10–19. DOI:10.1558/hsc.v4i1.28972
- A. Šorgo, J. Heric, *Cent. Educ. Policy Stud. J.* **2020**, 10, 77–97. DOI:10.26529/cepsj.869
- R Core Team. *R: A Language and environment for statistical computing*. (Version 4.1) [Computer software]. **2021**. Retrieved from <https://cran.r-project.org>. (R packages retrieved from MRAN snapshot 2022-01-01).
- The jamovi project (2022). *jamovi*. (Version 2.3) [Computer Software], **2022**. Retrieved from <https://www.jamovi.org>.
- A. Livingston, *Educ. Q.* **2004**, 27, 46–52. DOI:10.1111/j.1467-9205.2004.00213.x
- M. Tothova, M. Rusek, *Front. Educ.* **2022**, 7, 1051098. DOI:10.3389/educ.2022.1051098
- K. C. Costley, The positive effect of technology on teaching and student learning. **2014** Available at: <https://files.eric.ed.gov/fulltext/ED554557.pdf> (Assessed: August 4, 2023).
- J. B. Bharathy, *Sci. J. Edu.* **2015**, 3, 11–16. DOI:10.11648/j.sjedu.s.2015030401.13
- K. A. Burke, T. J. Greenbowe, M. A. Windschitl, *J. Chem. Educ.* **1998**, 75, 1658–1661. DOI:10.1021/ed075p1658
- a) M. Prensky, *Horiz.* **2001**, 9(5), 1–6. DOI:10.1108/10748120110424816  
b) M. Prensky, *Horiz.* **2001**, 9(6), 1–9. DOI:10.1108/10748120110424843
- N. Zan, *US-China Education Review A*, **2015**, 5, 105–113. DOI:10.17265/2161-623X/2015.02.003
- M. Rezazadeh, S. Seidi, M. Lid, S. Pedersen-Bjergaard, Y. Yamini, *Trends Analyt. Chem.* **2019**, 118, 548–555. DOI:10.1016/j.trac.2019.06.019
- A. R. Campos, C. M. Knutson, T. R. Knutson, A. R. Mozzetti, C. L. Haynes, R. L. Penn, *J. Chem. Educ.* **2016**, 93, 318–321. DOI:10.1021/acs.jchemed.5b00385
- N. Lopez-Ruiz, V. F. Curto, M. M. Erenas, F. Benito-Lopez, D. Diamond, A. J. Palma, L. F. Capitan-Vallvey, *Anal. Chem.* **2014**, 86, 9554–9562. DOI:10.1021/ac5019205
- H. E. Pence, *Educ. Sci.* **2020**, 10, 34. DOI:10.3390/educsci10020034
- D. Libman, L. Huang, *J. Chem. Educ.* **2013**, 90, 320–325. DOI:10.1021/ed300329e

## Povzetek

Učinkovitost porabe časa je ključni dejavnik pri računanju kemijskih nalog, ki vpliva tako na osebno kot poklicno področje. Študija je namenjena iskanju najhitrejše metode za reševanje kemijskih računskih nalog. V raziskavi smo primerjali čas, ki ga študentje porabijo, ko pri reševanju računske naloge uporabijo tri različne načine: računanje z običajnim kalkulatorjem, računanje z aplikacijo kalkulator na pametnem telefonu in računanje s kalkulatorjem namiznega računalnika. V raziskavo smo vključili 52 slovenskih študentov, predmetnih učiteljev, ki so bili aktivno vključeni v programe kemije in sorodnih naravoslovnih programov v študijskih letih 2019 in 2022. Rezultati iz leta 2019 kažejo, da študentje rešijo kemijske naloge najhitreje z uporabo običajnega kalkulatorja in porabijo največ časa za izračun nalog ob uporabi aplikacije kalkulatorja na pametnih telefonih ( $\Delta_{mean} = 133$  s;  $\Delta_{SD} = 5$  s;  $\Delta_{min} = 97$  s;  $\Delta_{max} = 131$  s). Še večja razlika je opazena v podatkih iz študijskega leta 2022 ( $\Delta_{povprečje} = 189$  s;  $\Delta_{SD} = 129$  s;  $\Delta_{min} = 170$  s;  $\Delta_{max} = 625$  s). Če povzamemo: čeprav so pametni telefoni večopravilne naprave, ki nadomeščajo tradicionalne enonamenske naprave, so bile naloge hitreje rešene z običajnimi kalkulatorji.



Except when otherwise noted, articles in this journal are published under the terms and conditions of the Creative Commons Attribution 4.0 International License

## AUTHOR INDEX

Acta Chimica Slovenica  
Year 2023, Vol. 69 No. 1–4

Abbas Samir .....	500	Castillo-Quevedo Cesar.....	642
Abdallah Amira E. M. ....	261	Channar Abdul Hamid.....	560
Abdelaziz Mahmoud Ali .....	398	Charde Manoj S. ....	204
Ahmed Dildar .....	533	Chen Ruo-nan.....	1
Aksoy Lacine .....	218	Cheng Chil-Hung.....	44
Al -Obaidi Faisal Naji .....	21	Choudhury Chirantan Roy .....	479
Aldin Shaymaa Jalal .....	651	Chowdhury Manas.....	479
Al-Harbi Reem A. K.....	380	Chowdhury Shakhawat.....	173
Al-Harbi Reem.....	500	Civaner Mehmet Ulas .....	196
Ali Akbar .....	281	Cristea Ramona Maria (Iancu) .....	345
Ali Chin Hung .....	281		
Ali Karwan Omer .....	611	Demchyna Oksana .....	316
Aliabad Shahrzad Mahdavi.....	101	Dojer Brina.....	690
Al-Khafaji Ali Hussein Demin .....	173	Doruk Tugrul .....	29
Alnasra Omar Alaa.....	674	Duan Meng-Meng.....	509
Amin Muhammad.....	86	Duca Gheorghe.....	588
Aned de Leon.....	642		
Anshar Andi Muhammad .....	173	Elkader Mariam M. Abd .....	261
Antović Aleksandra.....	634	El-Sharief Marwa.....	500
Apostolescu George Florian.....	231	El-Sharkawy Karam Ahmed .....	398
Ashfaq Muhammad .....	281	Ergin Murat Altuner .....	247
Atabey Hasan .....	21	Eroglu Pelin.....	196
Ayaz Muhammad .....	173	Erol İbrahim.....	218
Aydin Pinar Koroglu .....	574	Ertik Onur .....	574
		Esmaili Enis.....	44
Bagheri Fatemeh Hassani.....	101		
Baker Luma .....	651	Feng Ge.....	1
Balkır Şehnaz .....	218	Florjančič Urška.....	91
Barboza-Arenas Luis Andres .....	173		
Bavcon Kralj Mojca .....	601	Gadžurić Slobodan.....	59
Bektas Necla .....	440	Garbuz Olga .....	122
Biletskaya Elena .....	226	Ghaith Alabed Ibrayke Elefkhakry .....	247
Binzet Riza .....	196	Ghobadi Shahin .....	44
Biswas Niladri .....	479	Ghonchepour Ehsan .....	101
Boroon Niloofar Bakhshi .....	449	Gligorić Emilia.....	59
Boševski Igor.....	65	Gobec Stanislav.....	545
Botoran Oana.....	231	Golubović Mlađan .....	318
Bourosh Pavlina.....	122	Gouasmia Abdelkrim.....	111
Bourougaa Lotfi .....	333	Graur Vasilii .....	122
Bulan Omur Karabulut.....	574	Grošelj Uroš.....	545
		Gršič Marija.....	545
Cabellos Jose Luis .....	642	Grujić-Letić Nevena.....	59
Cai Zhi-qiang.....	1	Gulea Aurelian .....	122
Cakir Oguz .....	218	Guo Xue-Yao .....	148
Calhan Selda Dogan .....	196		
Cao Ke-Sheng.....	516	Habiddin Habiddin .....	184
		Hadžalić Selma.....	74

Halit Muğlu .....	247	Makota Oksana .....	316
Hamza Hameed .....	651	Marah Sarmad .....	29
Han Yuxin.....	353	Mardari Anastasia .....	122
Hao Yu-Mei .....	327	Marinković Marija .....	318
Harkati Brahim .....	111	Marinšek Marjan .....	371
Hasan Yakan.....	247	Markoski Mile.....	488
Hazman Omer .....	218	Martin-del-Campo-Solis	
He Guo-Xu .....	148	Martha Fabiola.....	642
Helal Maher H. E. ....	261	Martínez-Guajardo Gerardo.....	642
Honmane Sandip M. ....	204	Meden Anton .....	371
Huang Qiu-chen.....	1	Meden Anže .....	545
Hussain Muhammad Sher Muhammad		Mladenović Sara .....	318
Ajaz.....	86	Mohareb Rafat M. ....	261, 398
Idrizi Hirijete.....	488	Mukhtar Sayeed .....	398
Islami Mohammad Reza.....	101	Munawar Khurram Shahzad.....	281
Jahangir Taj Muhammad.....	560	Musa Bulkis.....	173
Jiang Jian .....	139, 353	Mustafa Yasser Fakri .....	173
Jin Ke-yun.....	1	Nadjem Abdelkader .....	111
Jukič Marko.....	545	Naeem-ul-Hassan Muhammad .....	86
Kahrović Emira.....	74	Najdoski Metodija .....	488
Kara Recep.....	218	Nangare Sopan.....	661
Karadžić Radovan .....	634	Neamtu Johny .....	231
Kasim Syahrudin.....	173	Nejadshafiee Vajihe .....	101
Ketrez Asli .....	628	Nikolić Nemanja .....	318
Khabazzadeh Hojatollah.....	101	Nikolić Tamara .....	318
Khalili Behzad.....	449	Nikonov Anatolij.....	91
Khalili Fawwaz Izzat .....	674	Onul Nihal.....	440
Khan Hafeezullah .....	86	Osmani Riyaz Ali M. ....	204
Khan Shafi Ullah .....	333	Osmanković Inesa.....	74
Khan Shahzad Hassan.....	86	Osmanović Amar .....	74
Khuhawar Muhammad Yar.....	560	Otašević Biljana .....	385
Knez Damijan .....	545	Ouassaf Mebarka .....	333
Kočar Drago .....	274	Ozen Tevfik .....	29
Kostić Tomislav .....	318	Ozturk Seyhan .....	29
Kravtsov Victor.....	122	Page Elizabeth Mary.....	184
Kristl Matjaž.....	690	Parveen Humaira.....	398
Kutuk Halil.....	29	Patil Ashwini .....	661
Kuzmanovski Igor .....	488	Patil Pravin Onkar.....	661
Lebedev Albert T. ....	601	Pattnaik Satyanarayan.....	467
Lei Yan .....	303	Pavlin Anže .....	274
Lekova Vanya .....	295	Perić Velimir .....	318
Levitt Stephen R.....	430	Pliuta Konstantin.....	163
Li Wei.....	1, 240, 509	Pompe Matevž.....	274
Liang Peng.....	353	Popescu Diana Ionela (Stegarus).....	231
Liao Wen-Ming.....	310	Qiu Cheng .....	303
Liu Bo.....	139	Qiu Xiao-Yang .....	12
Liu Qiao-Ru.....	516, 524	Qureshi Farah .....	560
Liu Shu-Juan.....	12	Ramirez-Coronel Andres Alexis, .....	173
Liu Yao .....	139	Rao Bojja Rajeshwar.....	281
M. Serdar Cavuş .....	247	Rašević Marija.....	385
Magoda Amina .....	74	Raya Indah .....	173
		Romero-Parra Mireya Rosario .....	173



Saha Sandeepa .....	479	Vraneš Milan .....	59
Sakarya Handan Can .....	628	Wang Yijin .....	139
Salkić Alma.....	385	Xiao Xiuchan .....	303
Samiey Babak.....	44	Xiong Zhongduo .....	155
Sandru Daniela .....	231, 345	Xue Ling-Wei .....	148, 516, 524
Sangale Premnath.....	661	Yakan Hasan.....	29
Sari Hayati .....	21	Yanardag Refiye .....	574
Sepay Nayim.....	479	Yanev Pavel.....	295
Shahid Irshad Ali.....	281	Yang Kun-Zhong .....	310
Snigur Denys.....	163	Yenigun Semiha .....	29
Sohail Faizan .....	533	Yevchuk Iryna .....	316
Soudani Asma .....	111	Yi Xiu-Guang.....	310
Stojnova Kirila .....	295	Yılmaz Mustafa Abdullah .....	218
Sun Tao .....	1	You Zhonglu.....	139, 240, 353, 509
Şuğan Nicoleta Anca .....	231	Zabibah Rahman S. ....	173
Sutormina Elena .....	371	Zahirović Adnan.....	74
Svete Jurij.....	545	Zangrando Ennio .....	479
Swain Kalpana.....	467	Zečević Mira.....	385
Šorgo Andrej.....	690	Zhang Hui.....	353
Tahir Muhammad Nawaz.....	281	Zhang Jin-Bing.....	310
Tan Xue-Rong .....	509	Zhang Li.....	12
Teofilović Branislava .....	59	Zhang Ping .....	155
Thalluri Chandrashekar .....	467	Zhang Wei .....	1
Tolgay Elvan Uyar.....	29	Zhang Wei-Guang.....	421
Topkaya Cansu .....	620	Zhao Xiao-Jun.....	524
Trebše Polonca .....	601	Zhao Yi.....	1
Turkyılmaz Ismet Burcu.....	131	Zhou Yi-Xuan .....	240
Ulchina Ianina .....	122	Zhou Zheng .....	303
Ulger Mahmut .....	196	Zhyhailo Mariia .....	316
Usataia Irina .....	122	Zinchuk Victor .....	226
Veselinović Aleksandar M. ....	318, 634	Zou Rong.....	310
Vicol Crina .....	588	Žgajnar Gotvajn Andreja.....	65
Višnjevac Aleksandar.....	74	Živković Jelena.....	634



**DRUŠTVENE VESTI IN DRUGE AKTIVNOSTI**  
**SOCIETY NEWS, ANNOUNCEMENTS, ACTIVITIES**

**Vsebina**

Koledar važnejših znanstvenih srečanj s področja kemije in kemijske tehnologije .....	S119
Navodila za avtorje .....	S120

**Contents**

Scientific meetings – Chemistry and chemical engineering.....	S119
Instructions for authors .....	S120



# KOLENDAR VAŽNEJŠIH ZNANSTVENIH SREČANJ S PODROČJA KEMIJE IN KEMIJSKE TEHNOLOGIJE

## SCIENTIFIC MEETINGS – CHEMISTRY AND CHEMICAL ENGINEERING

### 2024

#### January 2024

---

- 24 – 26 SCF CHEMICAL BIOLOGY SYMPOSIUM 2024  
Orsay, France  
Information: <https://scf-chembio2024.com/>
- 24 – 26 1ST FRENCH - ITALIAN COORDINATION CHEMISTRY DAYS (JCC 2024)  
Strasbourg, France  
Information: <https://jcc2024.sciencesconf.org/>

#### February 2024

---

- 22 – 23 XV MEETING OF YOUNG CHEMICAL ENGINEERS (SMLKI)  
Zagreb, Croatia  
Information: <https://pierre.fkit.hr/smlki/en/index.html>
- 27 GWB2024 – CATALYZING DIVERSITY IN SCIENCE  
Online Virtual  
Information: <https://www.nice-conference.com>

#### May 2024

---

- 19 – 22 INTERNATIONAL CONFERENCE ON BIOMASS – ICONBM2024  
Palermo, Italy  
Information: <https://www.aidic.it/iconbm2024/>
- 26 – 29 INTERNATIONAL SCHOOL OF PROCESS CHEMISTRY 2024 (ISPROCHEM 2024)  
Gargnano, Italy  
Information: <http://www.isprochem.unimi.it/>
- 27 – 31 POLY-CHAR 2024 – POLYMERS FOR OUR FUTURE  
Madrid, Spain  
Information: <https://www.poly-char2024.org>

# Acta Chimica Slovenica

## Author Guidelines

### Submissions

Submission to ACSi is made with the implicit understanding that neither the manuscript nor the essence of its content has been published in whole or in part and that it is not being considered for publication elsewhere. All the listed authors should have agreed on the content and the corresponding (submitting) author is responsible for having ensured that this agreement has been reached. The acceptance of an article is based entirely on its scientific merit, as judged by peer review. There are no page charges for publishing articles in ACSi. The authors are asked to read the Author Guidelines carefully to gain an overview and assess if their manuscript is suitable for ACSi.

### Additional information

- Citing spectral and analytical data
- Depositing X-ray data

### Submission material

Typical submission consists of:

- full manuscript (PDF file, with title, authors, abstract, keywords, figures and tables embedded, and references)
- supplementary files
  - **Full manuscript** (original Word file)
  - **Statement of novelty** (Word file)
  - **List of suggested reviewers** (Word file)
  - **ZIP file containing graphics** (figures, illustrations, images, photographs)
  - **Graphical abstract** (single graphics file)
  - **Proposed cover picture** (optional, single graphics file)
  - **Appendices** (optional, Word files, graphics files)

Incomplete or not properly prepared submissions will be rejected.

### Submission process

Before submission, authors should go through the checklist at the bottom of the page and prepare for submission.

Submission process consists of 5 steps.

#### Step 1: Starting the submission

- Choose one of the journal sections.
- Confirm all the requirements of the **checklist**.
- Additional plain text comments for the editor can be provided in the relevant text field.

#### Step 2: Upload submission

- Upload full manuscript in the form of a Word file (with title, authors, abstract, keywords, figures and tables embedded, and references).

#### Step 3: Enter metadata

- First name, last name, contact email and affiliation for all authors, in relevant order, must be provided. Corresponding author has to be selected. Full postal address and phone number of the corresponding author has to be provided.

- **Title and abstract** must be provided in plain text.
- Keywords must be provided (max. 6, separated by semicolons).
- Data about contributors and supporting agencies may be entered.
- **References** in plain text must be provided in the relevant text field.

#### Step 4: Upload supplementary files

- Original Word file (original of the PDF uploaded in the step 2)
- **List of suggested reviewers** with at least five reviewers with two recent references from the field of submitted manuscript must be uploaded as a Word file. At the same time, authors should declare (i) that they have no conflict of interest with suggested reviewers and (ii) that suggested reviewers are experts in the field of the submitted manuscript.
- All **graphics** have to be uploaded in a single ZIP file. Graphics should be named Figure 1.jpg, Figure 2.eps, etc.
- **Graphical abstract image** must be uploaded separately
- **Proposed cover picture** (optional) should be uploaded separately.
- Any additional **appendices** (optional) to the paper may be uploaded. Appendices may be published as a supplementary material to the paper, if accepted.
- For each uploaded file the author is asked for additional metadata which may be provided. Depending of the type of the file please provide the relevant title (Statement of novelty, List of suggested reviewers, Figures, Graphical abstract, Proposed cover picture, Appendix).

#### Step 5: Confirmation

- Final confirmation is required.

### Article Types

**Feature Articles** are contributions that are written on Editor's invitation. They should be clear and concise summaries of the author's most recent work written with the broad scope of ACSi in mind. They are intended to be general overviews of the authors' subfield of research but should be written in a way that engages and informs scientists in other areas. They should contain the following (see also general guidelines for article structure below): (1) an introduction that acquaints readers with the authors' research field and outlines the important questions for which answers are being sought; (2) interesting, novel, and recent contributions of the author(s) to the field; and (3) a summary that presents possible future directions. Manuscripts should normally not exceed 40 pages of one column format (font size 12, 33 lines per page). Generally, experts who have made an important contribution to a specific field in recent years will be invited by the Editor to contribute a **Feature Article**. Individuals may, however, send a proposal (of no more than one page) for a **Feature Article** to the Editor-in-Chief for consideration.

**Scientific articles** should report significant and innovative achievements in chemistry and related sciences and should exhibit a high level of originality. They should have the following structure:

1. Title (max. 150 characters),
2. Authors and affiliations,
3. Abstract (max. 1000 characters),
4. Keywords (max. 6),
5. Introduction,
6. Experimental,
7. Results and Discussion,
8. Conclusions,
9. Acknowledgements,
10. References.

The sections should be arranged in the sequence generally accepted for publications in the respective fields and should be successively numbered.

**Short communications** generally follow the same order of sections as Scientific articles, but should be short (max. 2500 words) and report a significant aspect of research work meriting separate publication. Editors may decide that a Scientific paper is categorized as a Short Communication if its length is short.

**Technical articles** report applications of an already described innovation. Typically, technical articles are not based on new experiments.

## Preparation of Submissions

**Text** of the submitted articles must be prepared with Microsoft Word. Normal style set to single column, 1.5 line spacing, and 12 pt Times New Roman font is recommended. Line numbering (continuous, for the whole document) must be enabled to simplify the reviewing process. For any other format, please consult the editor. Articles should be written in English. Correct spelling and grammar are the sole responsibility of the author(s). Papers should be written in a concise and succinct manner. The authors shall respect the ISO 80000 standard [1], and IUPAC Green Book [2] rules on the names and symbols of quantities and units. The Système International d'Unités (SI) must be used for all dimensional quantities.

**Graphics** (figures, graphs, illustrations, digital images, photographs) should be inserted in the text where appropriate. The captions should be self-explanatory. Lettering should be readable (suggested 8 point Arial font) with equal size in all figures. Use common programs such as MS Excel or similar to prepare figures (graphs) and ChemDraw to prepare structures in their final size. Width of graphs in the manuscript should be 8 cm. Only in special cases (in case of numerous data, visibility issues) graphs can be 17 cm wide. All graphs in the manuscript should be inserted in relevant places and **aligned left**. The same graphs should be provided separately as images of appropriate resolution (see below) and submitted together in a ZIP file (Graphics ZIP). Please do not submit figures as a Word file. In **graphs**, only the graph area determined by both axes should be in the frame, while a frame around the whole graph should be omitted. The graph area should be white. The legend should be inside the graph area. The style of all graphs should be the same. **Figures and illustrations** should be of sufficient quality for the printed version, i.e. 300 dpi minimum. **Digital images and photographs** should be of high quality (minimum

250 dpi resolution). On submission, figures should be of good enough resolution to be assessed by the referees, ideally as JPEGs. High-resolution figures (in JPEG, TIFF, or EPS format) might be required if the paper is accepted for publication.

**Tables** should be prepared in the Word file of the paper as usual Word tables. The captions should appear above the table and should be self-explanatory.

**References** should be numbered and ordered sequentially as they appear in the text, likewise methods, tables, figure captions. When cited in the text, reference numbers should be superscripted, following punctuation marks. It is the sole responsibility of authors to cite articles that have been submitted to a journal or were in print at the time of submission to ACSi. Formatting of references to published work should follow the journal style; please also consult a recent issue:

1. J. W. Smith, A. G. White, *Acta Chim. Slov.* **2008**, *55*, 1055–1059.
2. M. F. Kemmere, T. F. Keurentjes, in: S. P. Nunes, K. V. Peinemann (Ed.): *Membrane Technology in the Chemical Industry*, Wiley-VCH, Weinheim, Germany, **2008**, pp. 229–255.
3. J. Levec, Arrangement and process for oxidizing an aqueous medium, US Patent Number 5,928,521, date of patent July 27, **1999**.
4. L. A. Bursill, J. M. Thomas, in: R. Sersale, C. Collola, R. Aiello (Eds.), *Recent Progress Report and Discussions: 5th International Zeolite Conference*, Naples, Italy, 1980, Gianini, Naples, **1981**, pp. 25–30.
5. J. Szegezdi, F. Csizmadia, Prediction of dissociation constant using microconstants, [http://www.chemaxon.com/conf/Prediction\\_of\\_dissociation\\_constant\\_using\\_microconstants.pdf](http://www.chemaxon.com/conf/Prediction_of_dissociation_constant_using_microconstants.pdf), (assessed: March 31, 2008)

Titles of journals should be abbreviated according to Chemical Abstracts Service Source Index (CASSI).

## Special Notes

- Complete characterization, **including crystal structure**, should be given when the synthesis of new compounds in crystal form is reported.
- Numerical **data should be reported with the number of significant digits corresponding to the magnitude** of experimental uncertainty.
- **The SI system of units and IUPAC recommendations** for nomenclature, symbols and abbreviations should be followed closely. Additionally, the authors should follow the general guidelines when citing spectral and analytical data, and depositing crystallographic data.
- **Characters** should be correctly represented throughout the manuscript: for example, 1 (one) and l (ell), 0 (zero) and O (oh), x (ex), D7 (times sign), B0 (degree sign). Use Symbol font for all Greek letters and mathematical symbols.
- The rules and recommendations of the **IUBMB** and the **International Union of Pure and Applied Chemistry (IUPAC)** should be used for abbreviation of chemical names, nomenclature of chemical compounds, enzyme nomenclature, isotopic compounds, optically active isomers, and spectroscopic data.
- **A conflict of interest** occurs when an individual (author, reviewer, editor) or its organization is in-

volved in multiple interests, one of which could possibly corrupt the motivation for an act in the other. Financial relationships are the most easily identifiable conflicts of interest, while conflicts can occur also as personal relationships, academic competition, etc. **The Editors** will make effort to ensure that conflicts of interest will not compromise the evaluation process; potential editors and reviewers will be asked to exempt themselves from review process when such conflict of interest exists. When the manuscript is submitted for publication, **the authors** are expected to disclose any relationships that might pose potential conflict of interest with respect to results reported in that manuscript. In the Acknowledgement section the source of funding support should be mentioned. The statement of disclosure must be provided as Comments to Editor during the submission process.

- **Published statement of Informed Consent.** Research described in papers submitted to ACSi must adhere to the principles of the Declaration of Helsinki (<http://www.wma.net/e/policy/b3.htm>). These studies must be approved by an appropriate institutional review board or committee, and informed consent must be obtained from subjects. The Methods section of the paper must include: 1) a statement of protocol approval from an institutional review board or committee and 2), a statement that informed consent was obtained from the human subjects or their representatives.
- **Published Statement of Human and Animal Rights.** When reporting experiments on human subjects, authors should indicate whether the procedures followed were in accordance with the ethical standards of the responsible committee on human experimentation (institutional and national) and with the Helsinki Declaration of 1975, as revised in 2008. If doubt exists whether the research was conducted in accordance with the Helsinki Declaration, the authors must explain the rationale for their approach and demonstrate that the institutional review body explicitly approved the doubtful aspects of the study. When reporting experiments on animals, authors should indicate whether the institutional and national guide for the care and use of laboratory animals was followed.
- To avoid conflict of interest between authors and referees we expect that not more than one referee is from the same country as the corresponding author(s), however, not from the same institution.
- Contributions authored by **Slovenian scientists** are evaluated by non-Slovenian referees.
- Papers describing **microwave-assisted reactions** performed in domestic microwave ovens are not considered for publication in *Acta Chimica Slovenica*.
- *Manuscripts that are **not prepared and submitted** in accord with the instructions for authors are not considered for publication.*

## Appendices

Authors are encouraged to make use of supporting information for publication, which is supplementary material (appendices) that is submitted at the same time as the manuscript. It is made available on the Journal's

web site and is linked to the article in the Journal's Web edition. The use of supporting information is particularly appropriate for presenting additional graphs, spectra, tables and discussion and is more likely to be of interest to specialists than to general readers. When preparing supporting information, authors should keep in mind that the supporting information files will not be edited by the editorial staff. In addition, the files should be not too large (upper limit 10 MB) and should be provided in common widely known file formats to be accessible to readers without difficulty. All files of supplementary materials are loaded separately during the submission process as supplementary files.

## Proposed Cover Picture and Graphical Abstract Image

**Graphical content:** an ideally full-colour illustration of resolution 300 dpi from the manuscript must be proposed with the submission. Graphical abstract pictures are printed in size 6.5 x 4 cm (hence minimal resolution of 770 x 470 pixels). Cover picture is printed in size 11 x 9.5 cm (hence minimal resolution of 1300 x 1130 pixels)

Authors are encouraged to submit illustrations as candidates for the journal Cover Picture\*. The illustration must be related to the subject matter of the paper. Usually both proposed cover picture and graphical abstract are the same, but authors may provide different pictures as well.

\* The authors will be asked to contribute to the costs of the cover picture production.

### Statement of novelty

Statement of novelty is provided in a Word file and submitted as a supplementary file in step 4 of submission process. Authors should in no more than 100 words emphasize the scientific novelty of the presented research. Do not repeat for this purpose the content of your abstract.

### List of suggested reviewers

List of suggested reviewers is a Word file submitted as a supplementary file in step 4 of submission process. Authors should propose the names, full affiliation (department, institution, city and country) and e-mail addresses of five potential referees. Field of expertise and at least two references relevant to the scientific field of the submitted manuscript must be provided for each of the suggested reviewers. The referees should be knowledgeable about the subject but have no close connection with any of the authors. In addition, referees should be from institutions other than (and countries other than) those of any of the authors. Authors declare no conflict of interest with suggested reviewers. Authors declare that suggested reviewers are experts in the field of submitted manuscript.

## How to Submit

Users registered in the role of author can start submission by choosing USER HOME link on the top of the page, then choosing the role of the Author and follow the relevant link for starting the submission process.

Prior to submission we strongly recommend that you familiarize yourself with the ACSi style by browsing the journal, particularly if you have not submitted to the ACSi before or recently.



## Correspondence

All correspondence with the ACSi editor regarding the paper goes through this web site and emails. Emails are sent and recorded in the web site database. In the correspondence with the editorial office please provide ID number of your manuscript. All emails you receive from the system contain relevant links. **Please do not answer the emails directly but use the embedded links in the emails for carrying out relevant actions.** Alternatively, you can carry out all the actions and correspondence through the online system by logging in and selecting relevant options.

## Proofs

Proofs will be dispatched via e-mail and corrections should be returned to the editor by e-mail as quickly as possible, normally within 48 hours of receipt. Typing errors should be corrected; other changes of contents will be treated as new submissions.

## Submission Preparation Checklist

As part of the submission process, authors are required to check off their submission's compliance with all of the following items, and submissions may be returned to authors that do not adhere to these guidelines.

1. The submission has not been previously published, nor is it under consideration for publication in any other journal (or an explanation has been provided in Comments to the Editor).
2. All the listed authors have agreed on the content and the corresponding (submitting) author is responsible for having ensured that this agreement has been reached.
3. The submission files are in the correct format: manuscript is created in MS Word but will be **submitted in PDF** (for reviewers) as well as in original MS Word format (as a supplementary file for technical editing); diagrams and graphs are created in Excel and saved in one of the file formats: TIFF, EPS or JPG; illustrations are also saved in one of these formats. The preferred position of graphic files in a document is to embed them close to the place where they are mentioned in the text (See **Author guidelines** for details).
4. The manuscript has been examined for spelling and grammar (spell checked).
5. The **title** (maximum 150 characters) briefly explains the contents of the manuscript.
6. Full names (first and last) of all authors together with the affiliation address are provided. Name of author(s) denoted as the corresponding author(s), together with their e-mail address, full postal address and telephone/fax numbers are given.
7. The **abstract** states the objective and conclusions of the research concisely in no more than 150 words.
8. Keywords (minimum three, maximum six) are provided.
9. **Statement of novelty** (maximum 100 words) clearly explaining new findings reported in the manuscript should be prepared as a separate Word file.
10. The text adheres to the stylistic and bibliographic requirements outlined in the **Author guidelines**.
11. Text in normal style is set to single column, 1.5 line spacing, and 12 pt. Times New Roman font is

recommended. All tables, figures and illustrations have appropriate captions and are placed within the text at the appropriate points.

12. Mathematical and chemical equations are provided in separate lines and numbered (Arabic numbers) consecutively in parenthesis at the end of the line. All equation numbers are (if necessary) appropriately included in the text. Corresponding numbers are checked.
13. Tables, Figures, illustrations, are prepared in correct format and resolution (see **Author guidelines**).
14. The lettering used in the figures and graphs do not vary greatly in size. The recommended lettering size is 8 point Arial.
15. Separate files for each figure and illustration are prepared. The names (numbers) of the separate files are the same as they appear in the text. All the figure files are packed for uploading in a single ZIP file.
16. Authors have read **special notes** and have accordingly prepared their manuscript (if necessary).
17. References in the text and in the References are correctly cited. (see **Author guidelines**). All references mentioned in the Reference list are cited in the text, and vice versa.
18. Permission has been obtained for use of copyrighted material from other sources (including the Web).
19. The names, full affiliation (department, institution, city and country), e-mail addresses and references of five potential referees from institutions other than (and countries other than) those of any of the authors are prepared in the word file. At least two relevant references (important recent papers with high impact factor, head positions of departments, labs, research groups, etc.) for each suggested reviewer must be provided. Authors declare no conflict of interest with suggested reviewers. Authors declare that suggested reviewers are experts in the field of submitted manuscript.
20. Full-colour illustration or graph from the manuscript is proposed for graphical abstract.
21. **Appendices** (if appropriate) as supplementary material are prepared and will be submitted at the same time as the manuscript.

## Privacy Statement

The names and email addresses entered in this journal site will be used exclusively for the stated purposes of this journal and will not be made available for any other purpose or to any other party.

ISSN: 1580-3155

---

## Koristni naslovi

---

Slovensko kemijsko društvo  
Slovenian Chemical Society



**Slovensko kemijsko društvo**

[www.chem-soc.si](http://www.chem-soc.si)

e-mail: [chem.soc@ki.si](mailto:chem.soc@ki.si)

---



**Wessex Institute of Technology**

[www.wessex.ac.uk](http://www.wessex.ac.uk)

---



**SETAC**

[www.setac.org](http://www.setac.org)

---



**European Water Association**

<http://www.ewa-online.eu/>

---



**European Science Foundation**

[www.esf.org](http://www.esf.org)

---



**European Federation of Chemical Engineering**

<https://efce.info/>

---



**I U P A C**

INTERNATIONAL UNION OF  
PURE AND APPLIED CHEMISTRY

**International Union of Pure and Applied Chemistry**

<https://iupac.org/>

---

---

## Novice evropske zveze kemijskih društev EuChemS najdete na:

---

 **EuChemS**  
European Chemical Society

**Brussels News Updates**

<http://www.euchems.eu/newsletters/>

---



## Sušenje z uporabo organskih topil

V kombinaciji z aparatom Inert Loop S-395 Mini Spray Dryer S-300 ponuja varno delo z vzorci, ki vsebujejo organska topila. Nivo kisika in pretoka plina je zaradi varnosti kontinuirno spremljan.

## Oddaljen dostop

Aplikacija na katerih koli mobilnih napravah ali računalnikih omogoča popolno kontrolo nad uporabniškim vmesnikom aparata.

## Auto način

Omogoča programiranje aparata Mini Spray Dryer S-300 Advanced in avtomatski potek metode.

## Prevlečen zbiralni ciklon

Zmanjšuje izgubo vzorca med procesom.

## SI enote

Vsi parametri, kot so npr. razpršilni in sušilni plin ter hitrost črpalke so na voljo v SI enotah in so avtomatsko regulirani.

## Zaščita vzorca

Aparat omogoča tako monitoring izhodne temperature, kot tudi končne temperature produkta.

## Programiranje metod

Programirajte sekvenco vzorcev za izvedbo enega vzorca za drugim, za kar največjo priročnost.

## Poročila

Vsi eksperimenti se na aparatu Mini Spray Dryer S-300 beležijo in shranjujejo v pomnilnik. Na voljo so kot PDF poročilo ali kot .csv datoteka.

### Tipične aplikacije:

Aktivne farmacevtske učinkovine, dostava zdravila, cepiva, zdravila za inhalacijo, nanotehnologija, keramika, UV absorberji, gorivne celice, baterije, sušenje, mikronizacija, enkapsulacija aditivov, kontrolirano sproščanje, nutracevtiki, funkcionalna hrana, arome, vitamini, proteini, probiotične bakterije, koncentri sokov, mleko v prahu, enkapsulacija bakterij in proteinov, transplantacija celic, kozmetika.



# Razvoj in inovacije za globalno uspešnost

Znanje, kreativnost zaposlenih in inovacije so ključnega pomena v okolju, kjer nastajajo pametni premazi skupine KANSAI HELIOS. Z rešitvami, ki zadostijo široki paleti potreb, kontinuiranim razvojem ter s kakovostnimi izdelki, Helios predstavlja evropski center za inovacije in poslovni razvoj skupine Kansai Paint.



Part of  **KANSAI  
PAINT**



[www.helios-group.eu](http://www.helios-group.eu)

 **KANSAI  
HELIOS**  
Designing Excellence





*May your wishes be sincere,  
your thoughts creative and your actions decisive.*

***Happy New Year 2024!***







NATIONAL INSTITUTE OF CHEMISTRY

Hajdrihova 19,  
1000 Ljubljana  
Slovenia  
[www.ki.si](http://www.ki.si)



**research**  
**EXCELENCE**

Basic and applied research in materials, life sciences, biotechnology, chemical engineering, structural and theoretical chemistry, analytical chemistry and environmental protection.

In line with EU research and innovation priorities: nanotechnology, genomics and biotechnology for health, sustainable development, climate change, energy efficiency and food quality and safety.

We expand knowledge and technology transfer to domestic and foreign chemical, automotive and nanobiotechnology industries.

We are aware of the power of youth, so we transfer our knowledge to younger generations and offer many opportunities for cooperation.

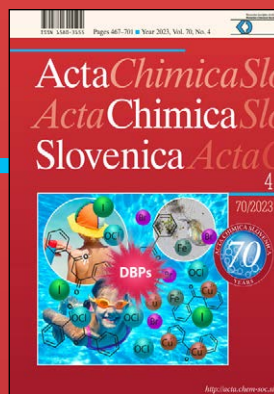


contact: [mladi@ki.si](mailto:mladi@ki.si)

# ActaChimicaSlovenica

## ActaChimicaSlovenica

Avobenzone is a widely used UV filter. Under disinfection conditions various disinfection by-products (DBPs) are formed. The presence of Br- and I- led to formation of brominated and iodinated avobenzone DBPs. Aquatic chlorination of avobenzone formulations led to the increase in toxicity. Sunscreen formulation influences on degradability of avobenzone.



Year 2023, Vol. 70, No. 4

